# *Seismic structure of the continental margin of French Guiana: implications for the rifting and early spreading of the equatorial Atlantic*

Christopher J. Greenroyd

# Seismic structure of the continental margin of French Guiana: Implications for the rifting and early spreading of the equatorial Atlantic

Christopher J. Greenroyd

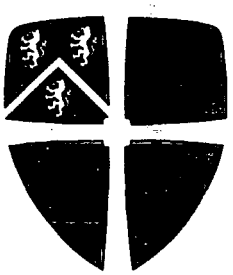

A dissertation submitted for the degree of
Doctor of Philosophy
at the University of Durham

March 2007

Software used:
This dissertation was written using LaTeX. The references and citations were produced using BibTeX. Most figures were plotted with the *Generic Mapping Tools* (GMT) written by Wessel & Smith (1991, 1998). *Gimp* was used for image conversion and manipulation. *Seismic Unix* (Cohen & Stockwell, 2000) was used for seismic data processing and plotting together with Landmark's *ProMAX*.

# Seismic structure of the continental margin of French Guiana: Implications for the rifting and early spreading of the equatorial Atlantic

**Christopher J. Greenroyd**

Recent studies of passive continental margins suggest that the rifting process produces a variety of structural styles. The along-strike continuity of these rifted margins is punctuated by significant lateral offsets, known as transform margins. Whilst many general features of both rift- and transform-style margins have been identified, the extent to which they are inter-related is not well understood.

The equatorial Atlantic exhibits a high number of large offset mid-ocean ridge transform faults and associated fracture zones, which indicate the highly segmented nature of its margins. As such, this location provides an ideal setting for a study of the deep structure of both rift- and transform-style margin structures. This investigation forms part of the Amazon Cone Experiment, a large-scale geophysical study of the French Guiana and northeast Brazil margin in the west equatorial Atlantic.

This study will provide evidence of crustal structure from recently acquired seismic, gravity and magnetic data, along two transects of the margin. The acquisition comprised 962 km of coincident multi-channel reflection and wide-angle refraction seismic data which were recorded by 20 ocean-bottom seismographs per transect, deployed at 10 km spacing. Ray-trace forward modelling of traveltime data from these instruments has resulted in two *P*-wave velocity-depth models of the subsurface structure which have been tested and further constrained by independent gravity free-air anomaly data.

Interpretation of the resulting models suggests that the pre-rift continental crust is 35-37 km thick. While at the oceanward end of each transect oceanic crust is identified which, at 3.5-5.0 km thickness, is considered to be unusually thin. The manner in which this transition is accomplished is dramatically different between the two models. In the south of the survey area the crust thins abruptly by a factor of 6.4 over a distance of ~70 km, adjacent to a ~45 km ocean-continent transition zone. To the north, however, more gradual thinning over ~320 km associated with an abrupt transition to oceanic crust is observed. Neither profile shows evidence of the tilted fault blocks characteristic of rifted margins.

There is no evidence for rift-related magmatism, commonly manifest as high *P*-wave velocity underplating or packages of seaward-dipping reflectors, along either profile. Hence, the margin is interpreted as non-volcanic, which suggests that rifting was not very rapid.

On the basis of these results, a model of transtensional rifting is proposed, in which a component of motion oblique to the margin results in the production of relatively wide, 'leaky' transform margins. This model suggests that the French Guiana margin is segmented into rift- and transform-style structures. However, the transform margins exhibit unusually wide zones of continental crustal thinning as a result of the transtensional extension.

For the Amazon Cone Experiment as a whole, anomalously thin oceanic crust is observed over a wide areal extent. This crust indicates that magma flow from the mantle is low and is interpreted to be a result of relatively cool asthenospheric mantle, slow spreading and the effect of large-scale fracture zones.

The results of this study have implications for our understanding of the effects of transtensional stresses during rifting and mode of opening of the equatorial Atlantic.

# Declaration

This dissertation describes my original work except where acknowledgement is made in the text. It does not exceed the word limit and is not substantially the same as any work that has been, or is being submitted to any other university for any degree, diploma or any other qualification.

Christopher J. Greenroyd
March 2007

# Acknowledgements

First and foremost, my sincere thanks go to Christine Peirce, my primary supervisor, without whom this project would not have been possible. Over the last three years, Chris has provided endless support, expertise and encouragement. She has found reasons for me to travel the world on several occasions and has read this thesis more times than is healthy. I am truly grateful.

Richard Hobbs has also been a fountain of knowledge and has always found time to give advice and assistance. Furthermore, whilst working on the uncertainty of geophysical data he has always been gracious enough to shred my work in a constructive manner!

Matthew Rodger and Tony Watts have shared in the pleasure and pain of this project and Matt in particular has borne the brunt of my processing and modelling frustrations with good humour and helpful advice.

Frauke Klingelhöfer and Walter Roest have provided a large amount of Guyaplac data from offshore French Guiana which have helped to develop this study. These data were acquired by Ifremer and processed by IFP.

This Ph.D. has been funded by the UK's Natural Environment Research Council through the Ocean Margins LINK programme. Thanks also to the master, officers and crew of the NERC R/V *Discovery* and to Anne Krabbenhöft and Cord Papenburg for their hard work during cruise D275.

Also, thanks to my friends in the department, Sophie, Heather, Tom, Sarah, Jim, Leanne, Matt, Gary, and of course the builders who have kindly added a very loud soundtrack to this thesis over recent months.

Finally, thanks to my parents and to Simone for their unending support.

# Contents

# List of figures

# List of tables

# Glossary of terms and abbreviations

The following terms and abbreviations are used throughout this thesis:

| | |
|---|---|
| 2D | two-dimensional |
| 3D | three-dimensional |
| ACE | Amazon Cone Experiment |
| CMP | common mid-point |
| CVS | constant velocity stacks |
| DMO | dip moveout |
| DSDP | Deep Sea Drilling Program |
| FAA | free-air anomaly |
| GMT | *Generic Mapping Tools* (Wessel & Smith, 1991, 1998) |
| GPS | Global Positioning System |
| IGRF | International Geomagnetic Reference Field |
| MAR | Mid-Atlantic Ridge |
| MCS | multi-channel seismic |
| MOR | mid-ocean ridge |
| NMO | normal moveout |
| OBH | ocean-bottom hydrophone |
| OBS | ocean-bottom seismograph |
| OCB | ocean-continent boundary |
| OCT | ocean-continent transition |
| ODP | Ocean Drilling Program |
| $P_s$ | *P*-wave sedimentary refraction |
| $P_g$ | *P*-wave crustal refraction |
| $P_n$ | *P*-wave mantle refraction |
| $P_sP$ | *P*-wave intra-sedimentary reflection |
| $P_mP$ | *P*-wave Moho reflection |
| rms | root-mean-square |
| R/V | research vessel |
| SEG-D | multi-channel seismic recording standard (Barry *et al.*, 1975) |
| SEG-Y | multi-channel seismic recording standard (Barry *et al.*, 1975) |
| SDR | seaward-dipping reflector |
| SNR | signal-to-noise ratio |
| SRME | surface related multiple elimination |
| $T_e$ | elastic thickness |
| TWTT | two-way traveltime |
| WA | wide-angle |
| $W_w$ | water wave |
| XBT | expendable bathymetric thermograph |

# Chapter 1

# Introduction and geological setting

Each of the Earth's largest oceans and seas is bordered by at least one passive continental margin. These margins are formed by intracontinental rifting and mark the dramatic juxtaposition of continental and oceanic lithosphere. Rifting results in the formation of a wide variety of crustal structures, whose study is driving forward our knowledge and understanding of global tectonics. Extensional rift-type structures are most abundant and their lateral extent along-margin-strike is truncated by transform zones, which bisect and offset them by tens to hundreds of kilometres. The structural characteristics of these transforms and their impact on the rifting process are not yet well understood. However, knowledge of this structural segmentation is vital not only to tectonics, but also to understanding the subsidence and thermal history of a margin. These factors are important for predicting the hydrocarbon potential and likely economic value of the massive sediment loads found there.

Structural segmentation is particularly abundant in the equatorial Atlantic where transforms accommodate the large offset in the trend of the Mid-Atlantic Ridge in the Central and South Atlantic Oceans. This study will focus on deep crustal structure in the equatorial Atlantic, in particular at the French Guiana passive continental margin. Here, rift and transform structures have formed in close proximity, providing an ideal setting for such a study. Thus, in this thesis, not only will our understanding of passive margins be developed but also our knowledge of the evolution of the equatorial Atlantic.

## 1.1 The structure of passive margins

In a broad sense, continental margins are either active or passive, depending on the degree of observed volcanic and/or tectonic activity. Active margins display significant activity associated with the convergence of two lithospheric plates, whilst passive margins are much less expressive and subside thermally or under the load of the great thickness of

sediment which accumulates there. Passive margins are primarily located around Australia, Antarctica, western Europe, the Arctic, Africa and along the east coast of North and South America. Of these, the Atlantic margins have been studied most extensively. Hence, the majority of examples used here will characterise the Atlantic margins which demonstrate a wide variety of structural styles and can also be compared directly with the results presented in this thesis and considered in the context of Atlantic evolution.

Figure 1.1 shows the location of the chosen example margins from the Atlantic which have also been important in the development of our current understanding of margin structure. Studies of these margins have provided evidence for both the growing understanding of the Earth processes which create them, and the dramatic improvements in the quality of marine geophysical data used to image them. Within Figure 1.1, the margins are coloured according to their broad structural type, based upon the relative orientation of rifting and subsequent oceanic spreading. Consequently, the types represent those margins which formed in an orthogonal, parallel or oblique direction.

Margins which lie orthogonal to the spreading direction are termed rifted margins and include, from North to South Atlantic: Spitsbergen (Czuba *et al.*, 2005); Vøring (Mjelde *et al.*, 2005); Møre (Breivik *et al.*, 2006); Nova Scotia (Funck *et al.*, 2004; Wu *et al.*, 2006); Rockall (Morgan *et al.*, 1989); Goban Spur (Bullock & Minshull, 2005); Galicia Bank (Whitmarsh *et al.*, 1996); Newfoundland (Funck *et al.*, 2003; Lau *et al.*, 2006; Hopper *et al.*, 2006); Iberia (Pinheiro *et al.*, 1992; Dean *et al.*, 2000); South Carolina (Holbrook *et al.*, 1994a); Virginia (Holbrook *et al.*, 1994b); Congo-Zaïre-Angola (Contrucci *et al.*, 2004); and Namibia (Bauer *et al.*, 2000). In contrast, those margins that lie parallel to the spreading direction are termed transform margins, *e.g.* Newfoundland (Todd *et al.*, 1988); Ivory Coast (Peirce *et al.*, 1996); Ghana (Edwards *et al.*, 1997); Barents Sea (Jackson *et al.*, 1990); and Exmouth Plateau (Lorenzo *et al.*, 1991). Intermediate margins which rift in an oblique direction display a degree of both strike-slip and extensional movement and are termed transtensional, *e.g.* Cameroon-Guinea-Gabon (Wilson *et al.*, 2003); Rio Muni, West Africa (Turner *et al.*, 2003).

The following sections will discuss rifted and transform margins in turn, whilst also providing an introduction to the variations in lithospheric response to rifting, including: rift-related magmatism; width over which the continental crust thins; the presence or absence of a transition zone; and the symmetry, or asymmetry, of conjugate margins. Throughout this thesis, the term rifting is used to describe not just the final plate break-up, as in some studies, but also the process of lithospheric stretching and thinning during which the structure of the final rifted margin develops.

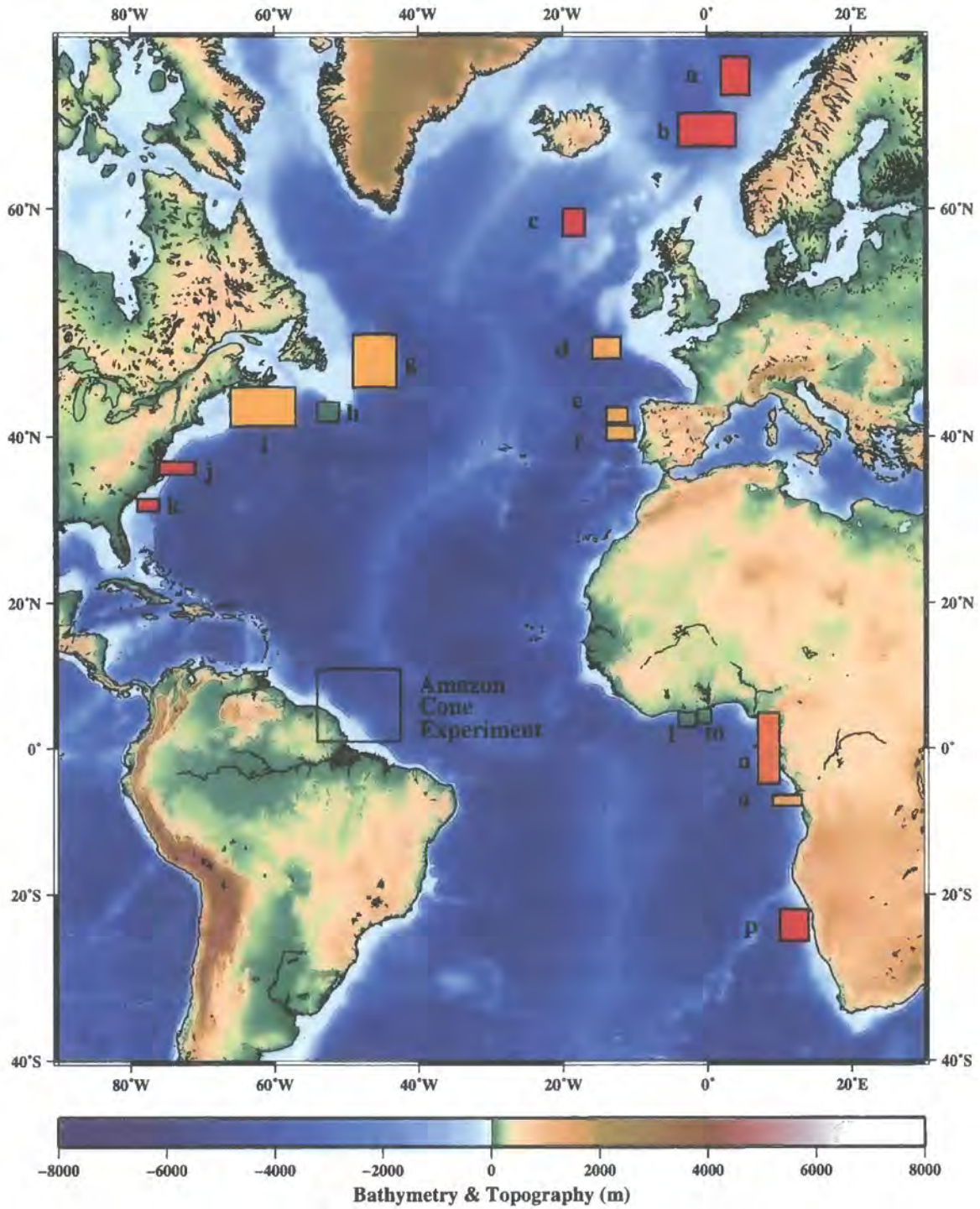


**Figure 1.1**: Locations of deep crustal studies of Atlantic margins. Each example is colour-coded for margin type (red: volcanic rift; yellow: non-volcanic rift; green: transform; orange: intermediate). The location of this study is shown for reference (black box). Examples shown are: a) Vøring (Mjelde *et al.*, 2005); b) Møre (Breivik *et al.*, 2006); c) Rockall (Morgan *et al.*, 1989); d) Goban Spur (Horsefield *et al.*, 1994; Bullock & Minshull, 2005); e) Galicia Bank (Whitmarsh *et al.*, 1996); f) Iberia (Pinheiro *et al.*, 1992; Dean *et al.*, 2000); g) Newfoundland (Funck *et al.*, 2003; Hopper *et al.*, 2006; Lau *et al.*, 2006); h) Newfoundland (Todd *et al.*, 1988); i) Nova Scotia (Funck *et al.*, 2004; Wu *et al.*, 2006); j) Virginia (Holbrook *et al.*, 1994a); k) Carolina (Holbrook *et al.*, 1994b); l) Côte d'Ivoire (Peirce *et al.*, 1996); m) Ghana (Edwards *et al.*, 1997); n) Cameroon-Equatorial Guinea-Gabon and Rio Muni, West Africa (Wilson *et al.*, 2003; Turner *et al.*, 2003); o) Congo-Zaïre-Angola (Contrucci *et al.*, 2004); and p) Namibia (Bauer *et al.*, 2000).

### 1.1.1 Rifted margins

Early studies of passive continental margins included multi-channel seismic (MCS) reflection surveys which imaged two distinctive styles of sedimentation and basement geometry (Mutter, 1993). The first showed large, rotated fault blocks infilled by small sedimentary basins (Beaumont *et al.*, 1982; Peddy *et al.*, 1989), whereas the second revealed a wedge-shaped body of seaward-dipping reflectors (SDRs) primarily within the sediment column (Hinz, 1981; Mutter *et al.*, 1982). These SDRs were thought to result from eruption of massive volumes of basaltic lava, which Eldholm *et al.* (1995) confirmed using drill samples from the Vøring Plateau. In addition, later wide-angle (WA) refraction studies observed that some margins also exhibited large extents of sub-crustal, high-velocity (7.2-7.7 $kms^{-1}$) magmatic material, termed underplating (Holbrook *et al.*, 1994b). Consequently, margins are classified as either volcanic at which SDRs and underplating are observed, or non-volcanic where these features are not present. Examples of these two types of margin are shown in Figure 1.2 – volcanic from the Vøring Plateau (Mjelde *et al.*, 2005) and non-volcanic from the Goban Spur (Bullock & Minshull, 2005).

In the case of volcanic margins, excessive amounts of magmatic material are produced by the adiabatic melting of the mantle which rises toward the Earth's surface as the lithosphere thins. This process can be exacerbated by interaction with a mantle plume which increases the mantle temperature and enhances mantle melting. However, the presence of such a plume is not a necessary prerequisite for volcanic margin formation, as evidenced by the magmatism observed at the US East Coast Margin (Holbrook & Keleman, 1993), which is a significant distance from the Iceland plume, thought to be at least partially responsible for the volcanism observed at the Hatton Bank (Morgan *et al.*, 1989) and Møre volcanic margins (Breivik *et al.*, 2006).

As progressively more crustal studies are undertaken, it has become clear that rather than being two distinct structures, volcanic and non-volcanic margins are merely end members of a continuum of structural styles (Mutter, 1993). This continuum implies that the degree of magmatism associated with rifting is dependent upon several variables, of which the most important are thought to be pre-rift asthenospheric mantle temperature, duration and degree of extension, and the initial thickness of the lithosphere (Bown & White, 1995).

When rifting occurs under relatively hot conditions, the upwelling deep mantle is more prone to melting, resulting in increased magmatism (White & McKenzie, 1989). Similarly, if extension occurs rapidly, the upwelling mantle has less time to conductively cool, again resulting in enhanced magmatism. An initially thick lithosphere will also result in a greater

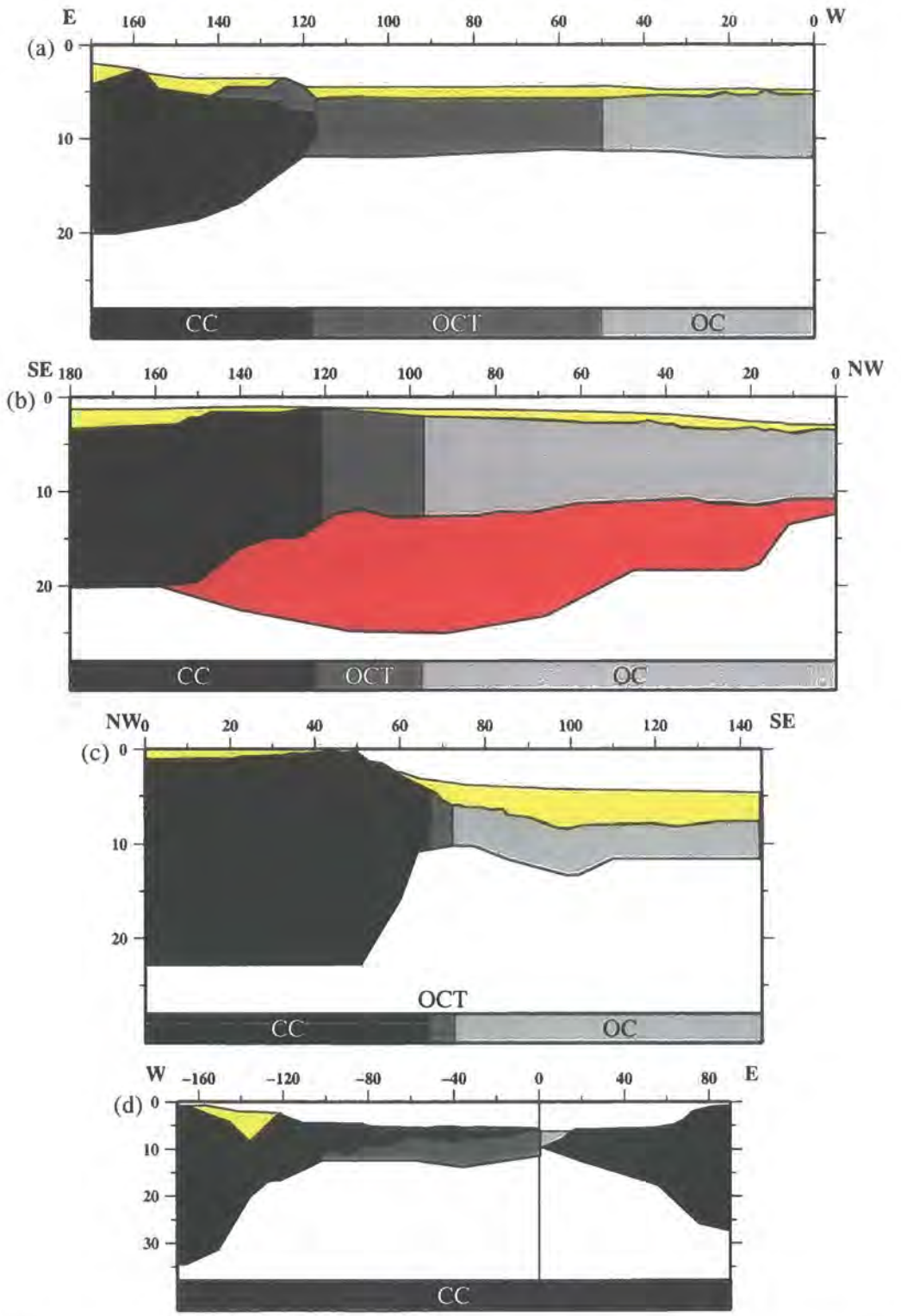


**Figure 1.2**: Comparison of volcanic and non-volcanic and rifted and transform margins. Figures a)-c) are plotted at the same scale and show (left to right): continental crust – CC (black); ocean-continent transition – OCT (dark grey); oceanic crust – OC (light grey); sediment (yellow); and magmatic underplating (red). a) Goban Spur non-volcanic rifted margin (Bullock & Minshull, 2005) exhibiting faulted blocks (~160 km offset) and a wide OCT (50-118 km offset); b) Vøring Plateau volcanic rifted margin (Mjelde *et al.*, 2005) showing large volumes of magmatic underplating; c) Ghana transform margin (Edwards *et al.*, 1997) showing a sharp thinning of continental crust and a narrow OCT; d) Reconstruction of the Newfoundland (west) – Iberia (east) conjugate margin pair (Lau *et al.*, 2006) at the time of final break-up. The Newfoundland margin shows a wider zone of continental crust, underlain by serpentinized mantle, suggesting that the margin is distinctly asymmetric.

volume of melt than an initially thin lithosphere due to the increased depth at which melting begins (*e.g.* Dean *et al.*, 2001 based on McKenzie & Bickle, 1988 and Bown & White, 1995).

Given that a range of parameters are involved, it is perhaps not surprising that the rifting process is observed to result in differing degrees of magmatism. Such simple bipolar classifications should thus be applied with caution.

In addition to the degree of magmatism, the width over which the continental lithosphere thins also varies considerably between margins. For example, whilst the Orphan Basin, Newfoundland (Chian *et al.*, 2001) exhibits a margin width as large as 400 km, the Galicia Bank (Whitmarsh *et al.*, 1996) thins over just 100 km. Watts & Fairhead (1997) classify the observed margin width, defined as the distance between the ocean-continent transition (OCT) and the full thickness crust, into two types – narrow (<75 km) and wide (>250 km). However, it is likely that these two categories are also just end members of a continuum of rift widths. Davis & Kusznir (2002), for example, study a range of margins and show that the width is related to the rate of both rifting and subsequent spreading. Highly extended margins tend to be associated with long rift durations and slow initial seafloor spreading rates, and vice versa. Transform margins display the narrowest zones of thinning of all and represent lithosphere which hasn't been extended, but instead has been sheared (Figure 1.2; Section 1.1.2).

The width of a margin is important not only in distinguishing between rifted and transform types, but also because it provides an estimate of how strain, and strain rate, affects the lithosphere as a whole. The classical view of lithospheric rifting is that of McKenzie (1978), who models stretching as a uniform process, in which a ductile lower lithosphere stretches and thins and the brittle upper lithosphere deforms via the production of tilted block and half graben basement structures, such as those observed at non-volcanic margins. The McKenzie (1978) model (Figure 1.3), however, does not explain observations of low-angle detachment faults (*e.g.* West Galicia – Boillot *et al.*, 1989), which appear to form in the final stages of crustal thinning at the boundary between shallow continental blocks and underlying transition zone material. This material most likely comprises partially serpentinized peridotite (Pérez-Gussinyé & Reston, 2001). The serpentinization reaction is catalysed by water which penetrates into the crust through cracks and faults and results in a reduction of the coefficient of friction (Escartín *et al.*, 1997). Thus, the detachment boundary becomes a relatively smooth surface, on which broken crustal blocks may slide during final break-up.

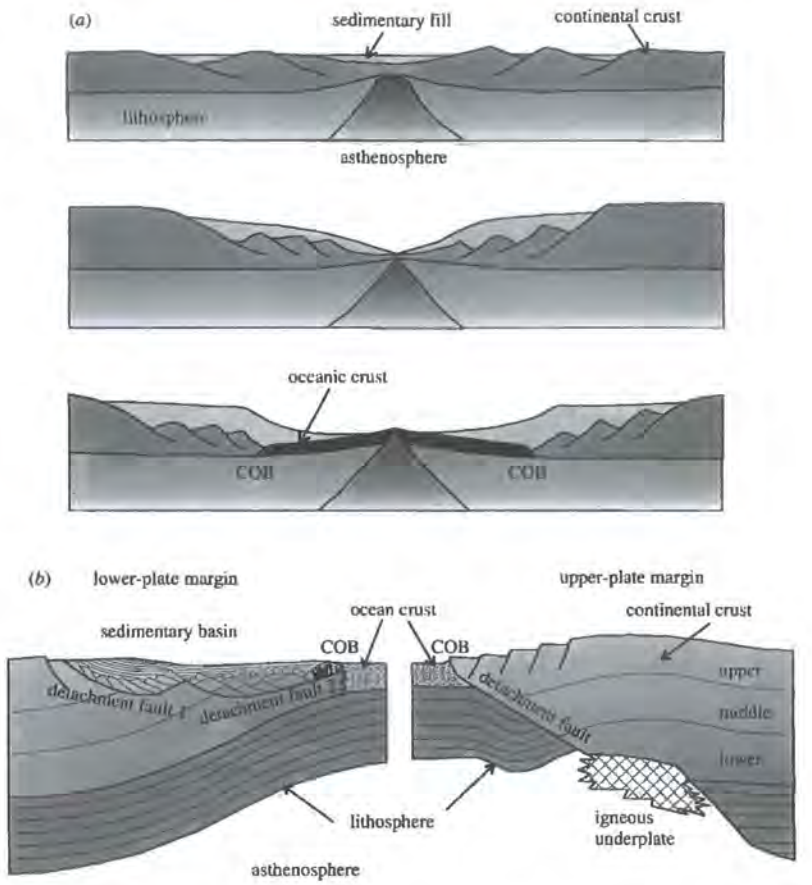


**Figure 1.3**: (a) Pure-shear and (b) simple-shear mechanisms of continental rifting, from Louden & Chian (1999), after Lister *et al.* (1986). Pure-shear (McKenzie, 1978) models indicate a symmetric rifting process in which extension is accommodated by a series of upper crustal faults and lower crustal ductile deformation. Simple-shear (Wernicke, 1985) models are asymmetric and exhibit extension along low-angle detachment faults, potential resulting in the exhumation of mantle.

The West Iberian margin is the best studied example of detachment faulting and a significant transition zone is observed between the continental and oceanic lithosphere. The term OCT is used to describe the transition between thinned continental and oceanic lithosphere, and has generally replaced the term ocean-continent boundary (OCB). The latter term is more appropriate for describing an abrupt transition between the two lithospheric types, which may be applicable to certain margins, particularly so when data resolution is insufficient to distinguish between an OCB and a narrow OCT. For the purposes of this study, the term OCB is taken to represent the very narrow end member of an OCT and, hence, unless specified directly, the term OCT will be used throughout.

The range of interpretations of the nature of the OCT is large, partly due to the observed seismic velocities being appropriate to a number of possible explanations (Bullock & Minshull, 2005). For example, OCTs have been interpreted as: thinned continental crust (Galicia Bank – Sibuet *et al.*, 1995, southwest Greenland – Chian & Louden, 1994);

oceanic crust formed during ultra-slow spreading (West Iberia – Whitmarsh *et al.*, 1996; Srivastava *et al.*, 2000, Newfoundland – Reid, 1994, southwest Greenland – Srivastava & Roest, 1999); and as serpentinized peridotite within exhumed mantle (West Iberia – Pickup *et al.*, 1996; Dean *et al.*, 2000; Whitmarsh & Wallace, 2001). The range of observed OCT widths is similarly broad and Dean *et al.* (2000) suggest a range from 10-170 km, although combined widths of both OCT and extended crust are more consistent at 100-200 km. Thus, the nature and characteristics of the OCT remain a topic of considerable debate, which will no doubt be developed (or further complicated) by studies (such as this one) from other margins, particularly those unrelated to the North Atlantic which currently dominate the literature.

The nature of the OCT and adjacent rift-related structures is not necessarily consistent between conjugate margins and asymmetry has been observed in several studies of North Atlantic margins (Figure 1.1, *e.g.* southwest Greenland – Labrador Sea, Newfoundland – West Iberia, Flemish Cap – Goban Spur; Louden & Chian, 1999). For example, the region of continental faulting observed across the Goban Spur is wider than that of the Flemish Cap (Keen *et al.*, 1989), where a low-angle detachment fault is also observed. Similarly, the Labrador margin appears wider and has subsequently undergone significantly more sediment loading and subsidence than its conjugate. Break-up is, therefore, offset toward the Greenland margin (Louden & Chian, 1999). Thus, it would appear that margin structure may also be asymmetric, which has implications for the relative evolution of conjugate margins and consequences for the McKenzie (1978) rifting model.

Asymmetric rifting is, however, captured in the simple-shear rifting model of Wernicke (1985) (Figure 1.3). This model suggests that extension occurs along low-angle detachment faults, resulting in asymmetry and significant structural differences between the resulting conjugate margins. Lau *et al.* (2006) have undertaken a reconstruction of the conjugate Newfoundland-Iberia margin (Figure 1.2) and observed significant asymmetry in the zone over which the continental crust thins. The point of final break-up is offset towards the eastern margin, resulting in a wide zone of thinned continental crust underlain by serpentinized mantle at the western margin.

Furthermore, the degree of asymmetry is not consistent along-strike. Lau *et al.* (2006) observe that: exhumed, serpentinzed mantle occupies a $\sim$10 km wide zone offshore Newfoundland and an 80-170 km wide zone offshore Iberia; continental crust thins across a wide zone offshore Newfoundland and a narrow zone offshore Iberia; a detachment surface is observed beneath the Galicia Bank but not offshore Flemish Cap (Reston, 1996); and anomalously thin oceanic crust is observed at the Flemish Cap and not at the Galicia

Bank. Exhumed mantle is associated with other asymmetric margins and is identified from seismic (Chian *et al.*, 1999; Dean *et al.*, 2000) and magnetic data (Russell & Whitmarsh, 2003). The interpretation has also been confirmed by Ocean Drilling Program (ODP) samples (Whitmarsh *et al.*, 1996; Whitmarsh & Wallace, 2001).

The symmetric McKenzie (1978) and asymmetric Wernicke (1985) models of continental rifting may represent end members of the range of possible rift processes. Other features may also be required if models are to fully capture the mechanics of rifting. For example, recent studies have also suggested that continental thinning is depth-dependent (Driscoll & Karner, 1998; Davis & Kusznir, 2002), a feature which is now incorporated into models of the rifting process.

In summary, recent studies have shown that passive rifted margins display a range of degrees of rift-related magmatism, a variety of widths of both thinned continental crust and OCTs, diverse styles of faulting, and varying degrees of asymmetry.

### 1.1.2 Transform margins

Despite the relative abundance of transform margin segments along passive margins, they remain less well studied and, hence, less well understood than rifted margins. Transform margins represent zones of sheared continental crust, which offset adjacent rifted margin segments. They are associated with fracture zones in the oceanic crust which can often be traced in gravity free-air anomaly (FAA) data from the transform margin itself to an offset in the associated mid-ocean ridge (MOR) axis. In this study, fracture zones are defined as the inactive traces of transforms at both MORs and margins. Consequently, at the MOR, the spreading centre is offset in a similar manner to along-strike continental margin structures.

In addition to their accompanying fracture zones, transform margins are most readily distinguished by their characteristically steep continental slopes, observed adjacent to, in many cases, an elevated section of the basement surface known as a marginal ridge (*e.g.* Basile *et al.*, 1993). This ridge is observed within MCS data which, in addition to drilling results, also suggests that the sharp margin edge is subjected to a higher than normal rate of erosion, resulting in the removal of significant quantities of sediment (Lorenzo *et al.*, 1991). The ridge is most likely a result of thermal expansion resulting from heat flow across the margin, between adjacent old cold continental and young hot oceanic lithosphere, as demonstrated by thermal lithospheric modelling studies (Todd & Keen, 1989; Lorenzo & Vera, 1992; Gadd & Scrutton, 1997). However, uplift has also been explained by compressional tectonics (Blarez & Mascle, 1988), sharp variations in degree of subsidence (Basile *et al.*, 1992) and magmatic underplating (Basile *et al.*, 1998).

The heat flow explanation is consistent with conceptual models of transform margins which suggest that they formed and evolved (Figure 1.4 – *e.g.* Le Pichon & Hayes, 1971; Scrutton, 1979; Mascle & Blarez, 1987; Mascle *et al.*, 1997; Peirce *et al.*, 1996) in a series of stages:

i. Initial intracontinental rifting. On a small scale, initial rifting consists of many small faults which, as rifting progresses, link together to form larger-scale rift- and transform-style structures;

ii. As rifting continues the continental crust thins orthogonal to the rift axis and several distinct rift segments form, each separated by a transform;

iii. Crustal thinning proceeds to such an extent that plate separation finally occurs and oceanic spreading centres form. Spreading results in the juxtaposition of old continental lithosphere against young oceanic lithosphere across a transform; and

iv. The continental plates continue to drift apart, with along-strike variation in the spreading orientation accommodated by strike-slip motion along fracture zones associated with the transforms. Consequently, thinned continental crust may ultimately be juxtaposed against normal thickness oceanic crust across a fracture zone.

The resultant margin structure is also dependent on the degree to which the oceanic and continental crustal blocks are mechanically coupled. Gadd & Scrutton (1997) construct a thermomechanical model of transform margin evolution and observe that at a coupled margin the two lithospheric plates will bend towards one another resulting in oceanic lithosphere which shallows towards the margin and continental lithosphere which deepens towards the margin. For example, a combined gravity and MCS study of the Falkland Plateau fracture zone, South Atlantic, suggests that the oceanic crust is 'up-warped' towards the margin (Lorenzo & Wessel, 1997). However, in order to improve estimates for the degree of coupling, thermal history and lithospheric strength, more observations of deep crustal structure are required. Furthermore, the effect of transform related serpentinization is unknown. It is possible that serpentinization may reduce the effect of friction between the two plates and, hence, facilitate the evolution of structurally segmented margins. This mechanism is similar to that for motion of crustal blocks along low-angle detachment faults at rifted margins.

The deep structure of transform margins has been modelled with both gravity and WA seismic data, which suggest that the continental crust thins sharply, over a distance of less than 30-40 km. The Barents Sea-Svalbard (Faleide *et al.*, 1991), Ghana (Figure 1.2 –

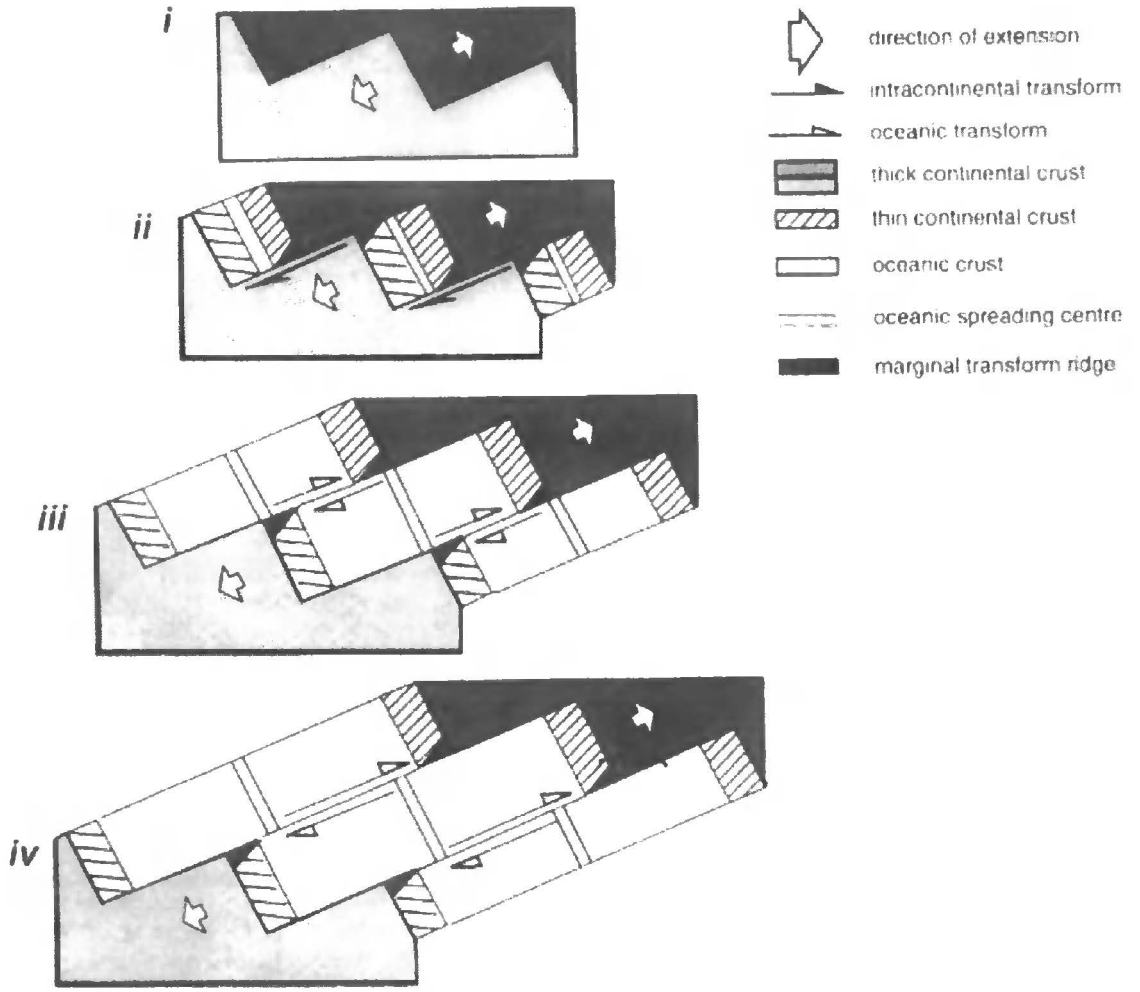


**Figure 1.4**: Schematic diagram of transform margin evolution (after Peirce *et al.*, 1996, from Mascle & Blarez, 1987 and Mascle *et al.*, 1997). The main stages of evolution are: i) initial intracontinental transform rifting; ii) continental crust thins in rift segments separated by transforms; iii) oceanic spreading results in the juxtaposition of old continental lithosphere against young oceanic lithosphere; and iv) juxtaposition of thinned continental crust against normal thickness oceanic crust across a fracture zone.

Edwards *et al.*, 1997) and Grand Banks (Keen *et al.*, 1990) margins exhibit continental crustal thinning over zones of 10-20, 15 and 40 km in width respectively.

Edwards *et al.* (1997) also note the presence of a zone of high-density (3.10 $gcm^{-3}$), high-velocity (5.8-7.3 $kms^{-1}$) and high-magnetization (1.10-1.25 $Am^{-1}$) at the OCT of the Ghana transform margin. They suggest that this zone may be a consequence of either intrusion by basic igneous rocks or serpentinization of upper mantle material. In the case of the latter, the serpentinsation occurs as a result of water ingress at the transform, a characteristic which is also observed at oceanic fracture zones (Bonatti, 1978; Fox & Gallo, 1986).

The variation in rift-related magmatism at rifted margins is also observed at transform margins. At the Southern Exmouth Plateau, Lorenzo *et al.* (1991) observe a 10 km thick layer of underplating, with *P*-wave velocity and density of 7.3 $kms^{-1}$ and 3.0 $gcm^{-3}$ respectively, which they interpret as an indication of intense magmatism during the evolution of the margin. In contrast, Edwards *et al.* (1997) find no evidence for underplating at the Ghana transform margin.

The studies upon which these observations of transform margins are made are relatively few and it is uncertain if they are sufficiently diverse to encompass all the features characteristic of transform margins, nor if the model shown in Figure 1.4 can account for them. The diversity of rift-related structures observed around the Atlantic would suggest that the lithospheric response to major structural events in highly variable. Therefore, should a similarly diverse range of transform-related structures be anticipated?

### 1.1.3 Oblique margins

Oblique continental margins result from the stretching direction not being orthogonal to the trend of the rift axis. Consequently, rifting of the lithosphere is a result of transtensional stresses. This obliquity tends to be associated with an increase in the degree of segmentation along-strike a margin, where the angular difference between the rift trend and the stress direction is accommodated by the formation of transform faults, for example in the equatorial Atlantic (Figure 1.5). However, observations of crustal structure at transform margins, both in the crust and deep lithosphere, are relatively sparse. Consequently, the mechanisms by which these transform margins are formed are poorly understood.

The abundance of fracture zones in obliquely rifted regions is observed by Wilson *et al.* (2003), who report that the transform margin offshore equatorial Guinea (West Africa) shows a 75 km transition zone between continental and oceanic crust. This zone comprises segments of proto-oceanic crust which are divided by fracture zones. Wilson *et al.* (2003) suggest that these segments are composed of serpentinized peridotite, although whether the serpentinization is associated with exhumed mantle adjacent to a magma-starved rift, or from water ingress along local fracture zones is unclear. However, the difference between these two is fundamental to understanding the degree of influence that transform faults have on the structure of a margin. Do they simply offset sections of rifted margins with structures both at and adjacent to the margin being dependent on the rifting process, or does the 'transform process' control the structures which are observed? Alternatively, and more likely, is there some degree of interplay between the two?

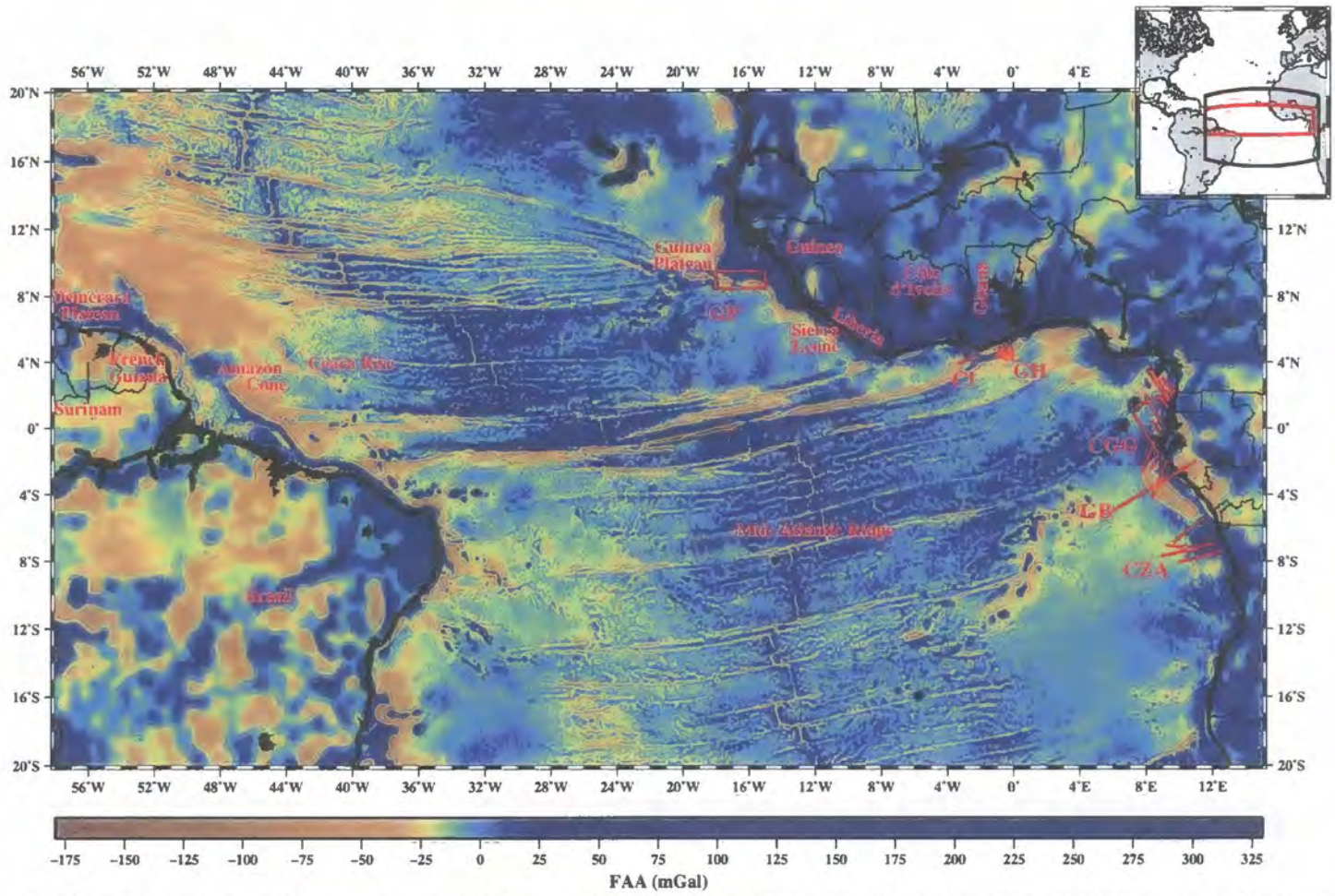


**Figure 1.5**: Satellite-derived gravity FAA of the equatorial Atlantic (Sandwell & Smith, 1997), showing the location of large-offset transform faults at the MAR and their corresponding fracture zones which can be traced, in most cases, to the adjacent continental margins. Also highlighted are the equatorial countries and prominent bathymetric features including the Demerara Plateau; Guinea Plateau; Amazon Cone deep-sea fan system; and Ceara Rise aseismic ridge. Conjugate study locations are also shown: GP – Guinea Plateau (Benkhelil *et al.*, 1995); CI – Côte d'Ivoire-Ghana (Peirce *et al.*, 1996); GH – Ghana (Edwards *et al.*, 1997); CGG – Cameroon-Guinea-Gabon (Turner *et al.*, 2003; Wilson *et al.*, 2003); GB – Gabon (Watts & Stewart, 1998); and CZA – Congo-Zaïre-Angola (Contrucci *et al.*, 2004). The inset shows the region defined as the equatorial Atlantic for this study (red) and the extent of the larger map (black).

### 1.1.4 Margin segmentation

Lithospheric segmentation is most clearly observed in bathymetric and gravity FAA data of the Earth's ocean basins, where MORs may be offset by tens to hundreds of kilometres (Figure 1.5). These offsets correspond to similar length-scale segmentation of continental margins into rift-type and transform-type structures. This segmentation is a key feature of most continental margins and is not yet fully understood. Furthermore, segmentation is of great relevance to continental margin studies which generally comprise 2D profiles rather than 3D volume-space imaging (Davies *et al.*, 2005).

Recent studies have identified examples of margin segmentation along a variety of length scales and among a number of parameters, including strength (Watts & Stewart, 1998; Wyer & Watts, 2006), structure (observed in FAA data – Sandwell & Smith, 1997 and magmatism (volcanic versus non-volcanic margins – Section 1.1.1). Furthermore, correlations have been made between patterns of segmentation at margins and MORs (Behn & Lin, 2000).

Watts & Stewart (1998) use gravity anomaly maps to analyse lithospheric strength offshore Gabon and propose that the entire African margin appears to be highly segmented in its long-term strength, exhibiting alternating sections of high and low elastic thickness, $T_e$. Wyer & Watts (2006) extend the analysis to the US East Coast and, again, segmentation is observed with weak regions abutting strong ones. Such segmentation may occur as a result of along-strike variations in the degree of thinning of the continental crust.

As described in Section 1.1.1, margin studies suggest that the degree of magmatism which occurs during rifting is highly variable. The along-strike segmentation of this magmatism has been a topic of recent investigation in order to develop our understanding of how rifting mechanisms vary both along-strike and across margins (*i.e.* their asymmetry). For example, the East Atlantic margin (Figure 1.1) is observed to switch character north to south, from volcanic (Rockall – Morgan *et al.*, 1989) to non-volcanic (Iberia – Dean *et al.*, 2000, Congo-Zaïre-Angola – Contrucci *et al.*, 2004) to volcanic (Namibia – Bauer *et al.*, 2000). The Nova Scotia margin is also an ideal setting to study such segmentation as it comprises a non-volcanic margin to the north (Grand Banks & Newfoundland – Reid, 1994; Funck *et al.*, 2003) and a volcanic one to the south (southern Baltimore Canyon Trough – Talwani & Abreu, 2000), suggesting that some form of transition between the two must exist in this region. However, modelling has thus far identified solely non-volcanic margins in the region (northern – Funck *et al.*, 2004; central – Wu *et al.*, 2006), which suggests that the transition from volcanic to non-volcanic styles of rifting may be quite abrupt.

The along-strike mechanical transition between rift- and transform-type structures is difficult to quantify given the range of current studies and is partially due to the difficulties of acquiring and modelling deep seismic data associated with rapidly varying structures, both in scale and velocity terms. In such a location, the 3D effects on WA ray paths, out-of-plane MCS reflections and off-axis influences on the gravity field are difficult to quantify.

### 1.1.5 Oceanic crustal accretion

As two plates gradually diverge from one another following rifting, hot asthenospheric mantle upwells to fill the intervening space, cools and accretes as oceanic crust at MOR plate boundaries. Although this material undergoes conductive heat loss as it rises, it reaches its solidus temperature at ~50 km depth (McKenzie & Bickle, 1988) and begins to melt. Thus, along a MOR a series of magma chambers will develop, supplying melt along dykes to the seafloor, where it erupts basaltic pillow lavas. Melt which does not reach the surface cools and solidifies at depth either as a sheeted dyke complex or as gabbroic lower crust beneath (Nicolas & Boudier, 1995). The underlying mantle rocks are comprised of melt-depleted peridotites and are divided from the oceanic crust by the Moho. Within this thesis all references to the Moho will refer to the seismic, rather than the slightly deeper petrological, Moho.

Ophiolites, boreholes, seafloor sampling and marine seismic refraction investigations (Raitt, 1963; Houtz & Ewing, 1976) have provided a detailed understanding of the structure resulting from this process. As a result, 'normal' oceanic crust is commonly subdivided into Layers 1, 2A, 2B and 3. Beneath Layer 1 sediment, the igneous Layers 2A, 2B and 3 tend to have characteristic *P*-wave velocities of 2.5-4.5, 4.5-6.5 and 6.5-7.0 $kms^{-1}$, as summarised in Figure 1.6.

White *et al.* (1992) suggest that the 'normal' thickness of oceanic crust is 7.1 ± 0.8 km thick, although there are several exceptions which provide information regarding the setting, tectonic and magmatic conditions at the time of accretion. Oceanic crust which accretes in magma-rich settings tends to be unusually thick and White *et al.* (1992) show that plume affected ridges produce crust of 10.3 ± 1.7 km thickness. In contrast, oceanic crust observed at fracture zones is often anomalously thin, typically half as thick as 'normal' oceanic crust (*e.g.* 4-5 km at the Chain Fracture Zone – Davies *et al.*, 2005). This categorisation of 'normal' crust is regularly used during crustal studies (*e.g.* Edwards *et al.*, 1997; Dean *et al.*, 2000) and will be used as the primary reference for comparison of the results of this study.

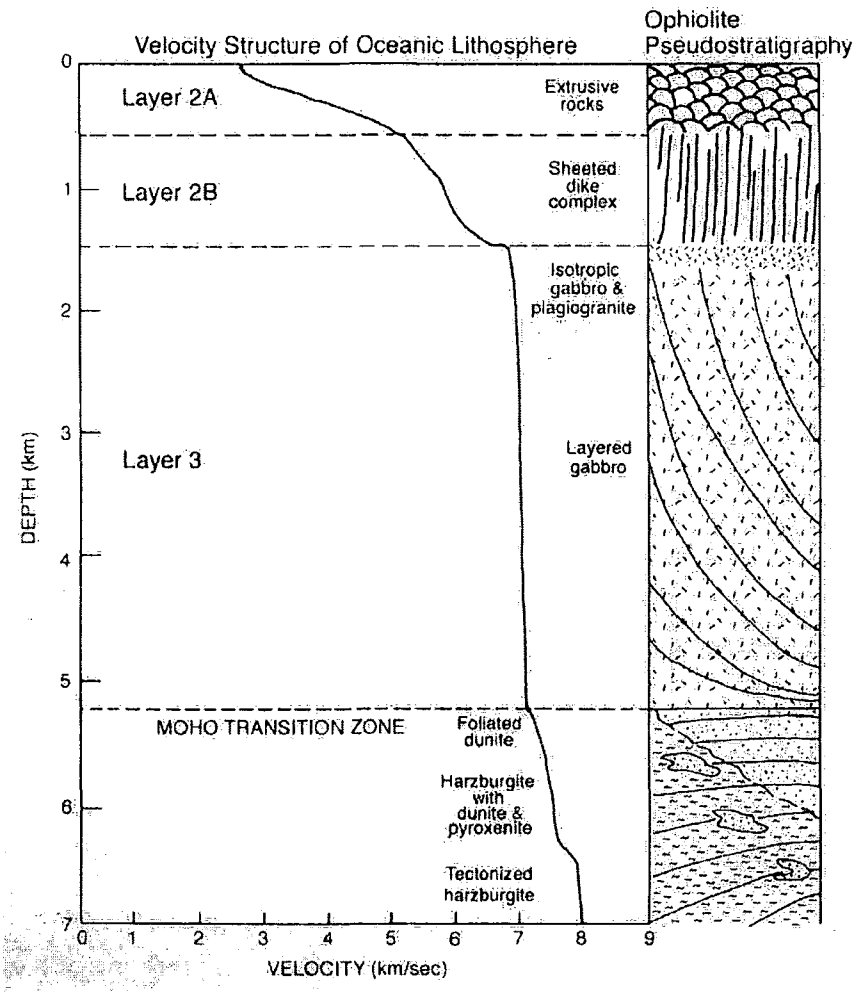


**Figure 1.6**: Characteristic velocity structure of oceanic lithosphere correlated with ophiolite pseudostratigraphy, from Gardiner (2003), after Dilek *et al.* (1998).

Crustal thickness is also observed to vary with the rate at which a plate diverges from the ridge axis, termed the half spreading rate. Half spreading rates vary significantly along present day MOR systems, and are classified accordingly into ultra-slow (half spreading rate $<10$ mmyr$^{-1}$), slow (10-28 mmyr$^{-1}$), intermediate (28-35 mmyr$^{-1}$) and fast (40-90 mmyr$^{-1}$) spreading ridges (Dick *et al.*, 2003). In general, slow to fast spreading ridges tend to accrete 'normal' thickness crust. However, thickness drops sharply at ultra-slow spreading ridges as, at these rates, conductive cooling at the ridge axis significantly reduces the available melt volume (Bown & White, 1994), and amagmatic extension predominates.

Observations of oceanic crust adjacent to transform margins are particularly varied. Edwards *et al.* (1997) suggest that structures vary from crust composed of solely Layer 2-type *P*-wave velocities off Newfoundland (Todd *et al.*, 1988), to a high velocity of 7.1 kms$^{-1}$ observed in the upper oceanic crust at the Barents Sea margin (Jackson *et al.*,

1990; Faleide *et al.*, 1991). Edwards *et al.* (1997) themselves observe unusually thin crust of just 4.4 km thickness which they attribute to a reduced magma supply due to the presence of closely spaced fracture zones and accretion within small basins bounded by cold continental lithosphere. These observations of variation in thickness and properties of oceanic crust accreted post-rift are important for our understanding of margin evolution as they inform understanding of the role played by the asthenosphere.

### 1.1.6 Post-rift sedimentation and subsidence

Present day margin structures are generally observed to be the precursors for the later development of sedimentary basins. As described in Section 1.1.1, rifting is often associated with the formation of tilted fault blocks which are progressively infilled and overlain with both terrestrial and pelagic sediment as the margin evolves. Consequently, some of the thickest sediment loads, globally, are located at continental margins and these can be home to significant hydrocarbon accumulation. The sediment loading, in addition to lithospheric cooling, results in subsidence of a margin over time.

The subsidence history is commonly inferred at margins from the sedimentary stratigraphy. For example, Watts (1988) backstripped Baltimore Canyon Trough seismic and gravity data using key sediment horizons derived from MCS reflection data to infer the gradual subsidence of the margin. In addition, evidence of faulting in both basement and sediment, and its timing (pre-, syn- or post-rift), may be used to provide information on the evolution of a margin. Of particular importance is the lithospheric strength of a margin, which controls the pattern of sediment deposition. Whilst a strong margin will tend to subside over a wide distance (a long wavelength), a weak margin will subside locally. Watts & Fairhead (1997) have shown that different margin styles will produce characteristic gravity FAA 'edge effects', which may be used to assess the along-strike segmentation of a margin (Watts & Stewart, 1998). Variable margin strength may also be a feature of transform margins, resulting in differences in the degree of thermally driven uplift and subsidence (Gadd & Scrutton, 1997). Again, such an effect may be observable in the post-rift stratigraphy which may chart the degree of crustal erosion which, in turn, may indicate the degree of uplift.

The hydrocarbon prospecting and economic potential of continental margins is highly dependent on both margin structure and degree and type of sediment loading and subsidence. These factors influence the time of formation and distribution of structures and stratigraphic traps available and also the thermal history of any hydrocarbon source rock within the continental margin succession.

## 1.2 Outstanding questions

The diversity of rift-related structures observed within the Atlantic has led to the suggestion that mantle temperature, rate and extent of rifting, rift geometry and lithospheric thickness may all potentially affect the intracontinental rifting process. These structures have resulted in margins being classified according to: orientation at rifting, from rift to transform; magmatism, from volcanic to non-volcanic; width of continental crustal thinning, from wide to narrow; and whether or not transition zones of exhumed mantle or intruded crust are observed. The conditions which result in the formation of the end members of these structural variants are broadly considered to be understood, some better than others. However, in order to fully understand the detail of the processes that form these structures, it is now perhaps necessary to focus on how the end members relate to one another. This is primarily a question of segmentation, both along-strike and between conjugate margin pairs. Particularly important aspects may include: transition from a volcanic to a non-volcanic margin along-strike; the development of wide and narrow transition zones at conjugate margins; the along-strike relation between transform and rift segments and the subsequent effect on margin evolution.

This study aims to address the along-strike segmentation of rift- and transform-style structures. In particular, how do the structures often observed at these two margin types link together? What variables control the structural division? Does magmatism play an important role? What lithospheric conditions are appropriate for such segmentation?

The role played by the lithosphere in margin segmentation may be addressed in two complimentary ways. Firstly, by surveying margin structure and inferring which features exist, which do not, and how they came to be formed. Secondly, by attempting to measure lithospheric properties either directly or indirectly by, for example, assessing the strength of the lithosphere by analysing its response to loading.

Finally, of course, until a complete global study is completed it is uncertain as to whether a complete set of structural styles has been observed. Consequently, in addressing these goals, the possibility also remains that a study in a relatively under explored region will result in the observation of features dramatically different from those described above.

To address these scientific questions, the equatorial Atlantic was chosen as the setting for a marine geophysical study of the nature of continental margins. The equatorial Atlantic has played a key role in global tectonics and represents the location of final break-up between Africa and South America. However, the deep crustal structure of the region has not yet been extensively studied. The study, known as the Amazon Cone Experiment

(ACE), was located offshore French Guiana and northeast Brazil in a setting thought to be highly segmented between rift- and transform-type margin styles. Consequently, this location is ideal for the study of structural segmentation. Additionally, the region is home to a massive accumulation of sediment offshore the Amazon River, known as the Amazon Cone, whose depositional history is well suited to a study of the temporal evolution of margin subsidence and strength.

## 1.3 Geological setting of the equatorial Atlantic

The equatorial Atlantic separates the South and Central Atlantic and, for the purposes of this study is defined as lying between 4°S and 12°N, 12°E to 58°W (Figure 1.5). French Guiana is located at the western edge of the Atlantic and shares its southern border with Brazil. Plate reconstructions suggest that, prior to break-up of the Atlantic, French Guiana and northeast Brazil were once part of Gondwanaland. So too were Guinea, Sierra Leone, Liberia, Côte d'Ivoire and Ghana, which now make up the conjugate West African margin (Blarez, 1986; Unternehr *et al.*, 1988; Nürnberg & Müller, 1991 – Figure 1.7). The reconstructions also show that rifting in the equatorial Atlantic occurred after the formation of the Central Atlantic and the South Atlantic. Consequently, the margins either side of the equatorial Atlantic were the last contact between South America and Africa. This final break-up occurred during the early Cretaceous at ~110 Ma. To the south, interpretation of commercial seismic data agrees with the plate reconstructions and geological timings (Pereira da Siva, 1989; Mello *et al.*, 2001; Cobbold *et al.*, 2004).

The gravity FAA data shown in Figure 1.5 show large offsets in the present day Mid-Atlantic Ridge (MAR), particularly between 13° and 44°W. To the east and west of these offsets, fracture zone traces are observed which stretch hundreds of kilometres from the MAR, often all the way to the continental margins where they have been imaged by 3D seismic data (Davies *et al.*, 2005). As described in Section 1.1.2, it may be anticipated that these fracture zones will intersect with transform-type margin segments, which would suggest that the French Guiana and northeast Brazil margin is heavily segmented between rift- and transform-type margin structures. Extrapolation of the fracture zone traces observed in Figure 1.5 suggests that the Amazon Cone lies upon a rift-type margin, with transform margins to the north and south. The northerly fracture zone appears to intersect with the margin at the approximate location of the Demerara Plateau.

This structural segmentation of the French Guiana margin was highlighted by a study of the seismic stratigraphy observed offshore West Africa around the Guinea Plateau. This

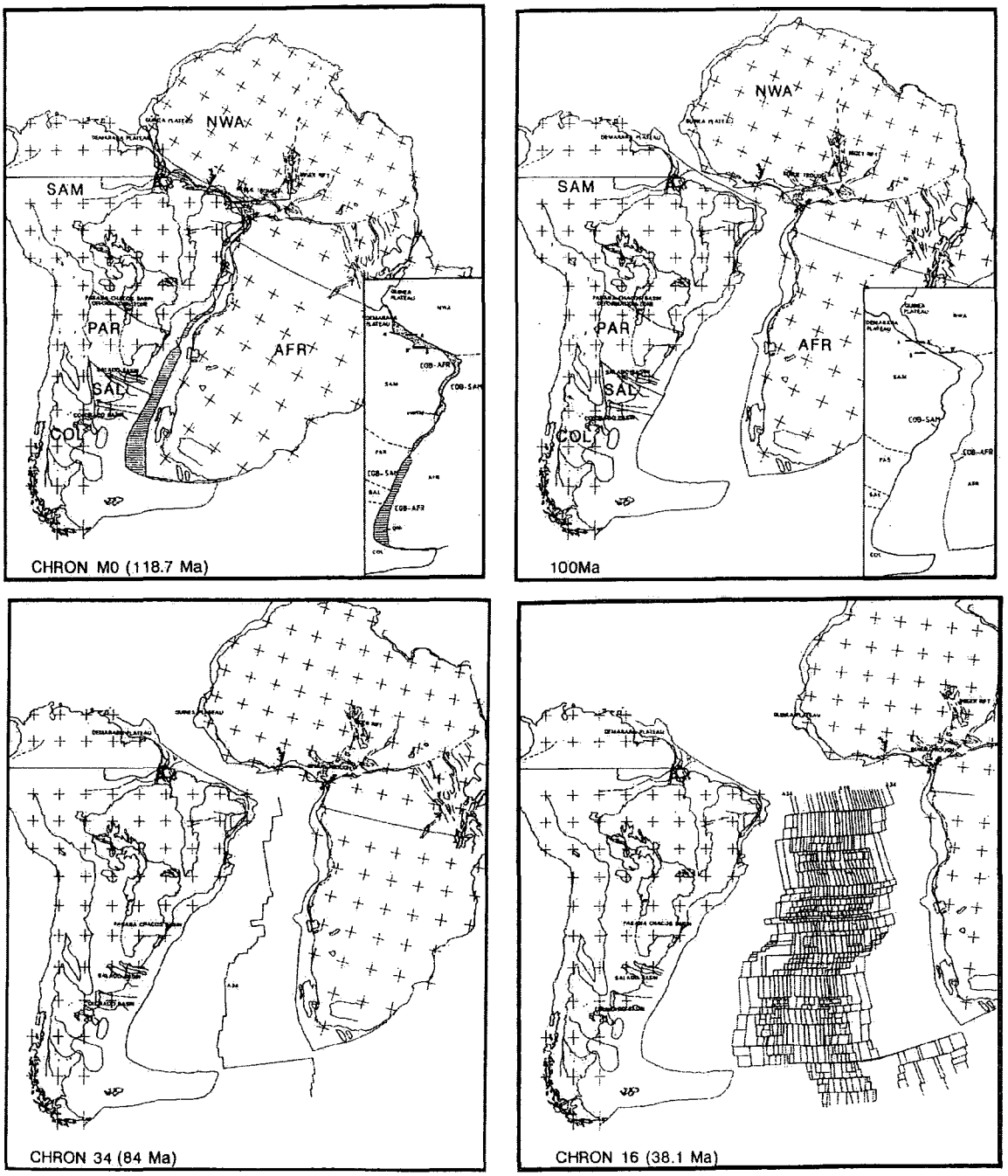


**Figure 1.7**: Plate reconstruction of the equatorial Atlantic, after Nürnberg & Müller (1991). The reconstruction shows that the North Atlantic rifted prior to 118.7 Ma and that rifting in the South Atlantic progressed northward at this time. The equatorial Atlantic was the last region of the Atlantic to open at ~110 Ma. The continents of South America and Africa are denoted by + symbols. Plates are labelled: AFR – southern Africa; NWA – northwestern Africa; SAM – South America; PAR – Parana; SAL – Salado; and COL – Colorado.

study by Benkhelil *et al.* (1995) indicates that the Guinea and Demerera Plateaux were joined prior to rifting and were shaped by polyphase tectonic activity. They also suggest a schematic for the evolution of the region (Figure 1.8) which highlights local complexities in structure. These include shallow extensional, reverse and normal faulting structures observed on top of the Guinea Plateau and Benkhelil *et al.* (1995) use this data to infer that the entire region was subject to transtensional forces during rifting.

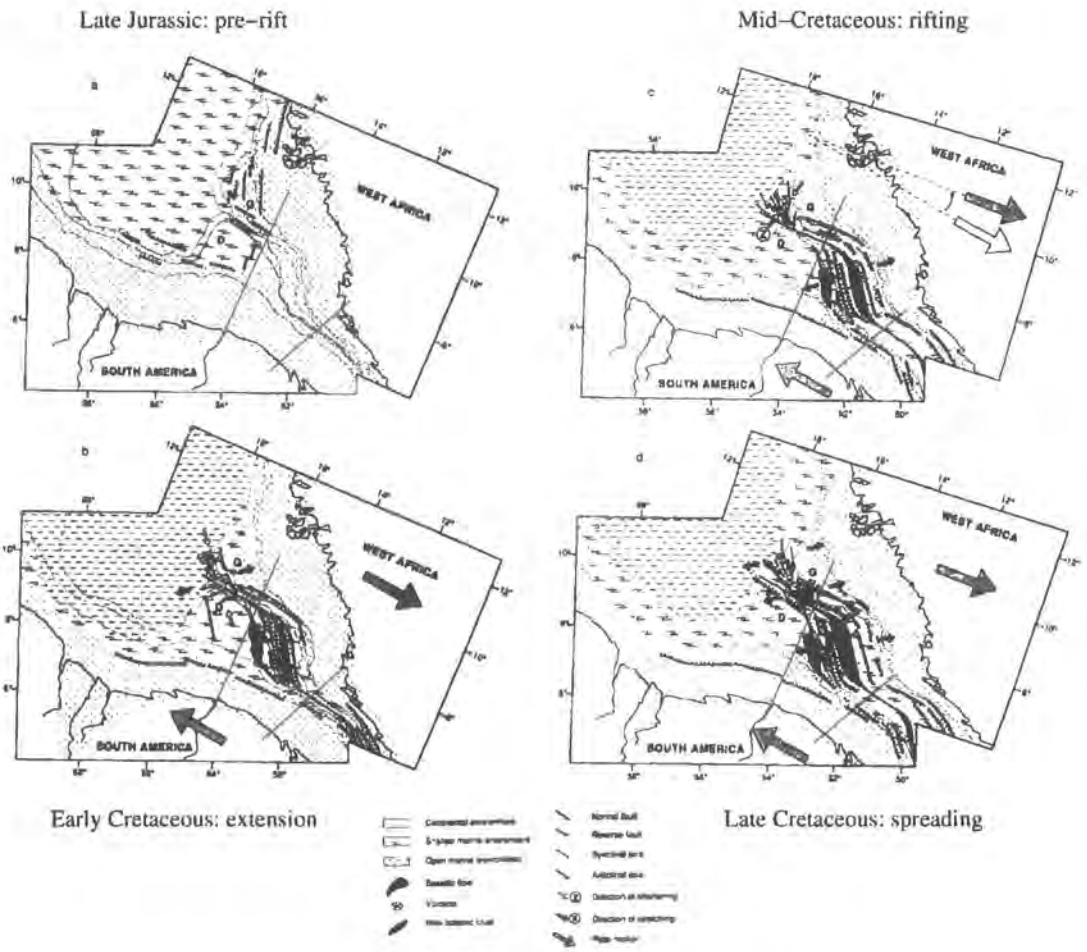


**Figure 1.8**: Initial rift geometry prior to opening of the equatorial Atlantic for the Demerara Plateau and adjacent areas offshore French Guiana, after Benkhelil *et al.* (1995). This model suggests that the initiation of continental break-up is a result of transtensional motion between the African and South American plates during the Early Cretaceous which resulted in the inception of seafloor spreading by the Late Cretaceous. Locations of the two profiles modelled in this study are shown (red lines).

Post-rift, the equatorial MAR appears to have been slow spreading, although estimates of half spreading rate vary between 9 $mmyr^{-1}$ (Le Pichon & Hayes, 1971) and 28 $mmyr^{-1}$ (Nürnberg & Müller, 1991). At ~80 Ma (Kumar & Embley, 1977), spreading was accompanied by the formation of the Ceara Rise offshore northeast Brazil and the Sierra Leone

Rise offshore West Africa, two massive crustal features which, given their conjugacy, were most likely formed at the MAR.

Adjacent to the Amazon Cone, rift-related structures are imaged within commercial seismic data on the inner shelf, where a syn-rift, mainly coarse clastic sequence of ~100-115 Ma age is overlain by a post-rift, mainly fan-delta and platform carbonate sequence of 0-100 Ma age (Brandão & Feijó, 1994). The Amazon Cone was emplaced on the northeast Brazil margin ~10 Ma before present and is attributed to an increase in sediment flux from the Amazon River (Cobbold *et al.*, 2004). This increase is associated with the uplift and erosion of the Andes mountain range along the western edge of South America (Benjamin *et al.*, 1987). This orogeny disrupted the erosional catchment basin for the Amazon River and the resulting Amazon Basin stretched almost entirely across South America, causing a massive increase in sediment flux to the Atlantic margin. This change in sedimentation rate is confirmed by piston core analysis (Damuth & Kumar, 1975) and the dating of cessation of pelagic sedimentation and influx of terrigenous material at Deep Sea Drilling Project (DSDP) site 354 (Supko & Perch-Nielson, 1977), which suggests that the increase occurred at 7.8-12.2 Ma (mid-late Miocene). The geological evolution of the northeast Brazil and French Guiana margin described above is summarised in stratigraphic terms in Figure 1.9.

### 1.3.1 Existing datasets

Several datasets have been acquired in equatorial Atlantic locations, many of which are industry owned and remain unpublished. However, the available data still enable a comprehensive evolutionary history of the margin to be determined. These data are subdivided into those which relate to the region surrounding a) the Demerara Plateau, (directly offshore French Guiana) and b) the Amazon Cone (offshore Brazil), and are described briefly below. Figure 1.10 shows the location of the datasets, which will be used in this study to: introduce an evolutionary history of the region (industry data – Gouyet *et al.*, 1994 – Section 1.3.1.1); develop an understanding of the 3D sediment distribution and basement structures (Guyaplac data – F. Klingelhöfer and W. Roest, *pers. comm.* – Section 2.5.2); and as a sedimentary stratigraphic record (ODP data – Erbacher *et al.*, 2004 – Section 2.5.1).

#### 1.3.1.1 Demerara Plateau

Hydrocarbon exploration, led by the oil and gas industry, began offshore French Guiana in 1957. Gouyet *et al.* (1994) summarise the primarily sedimentary structures observed, and divide the geological history of the Demerara Plateau into two main stages:

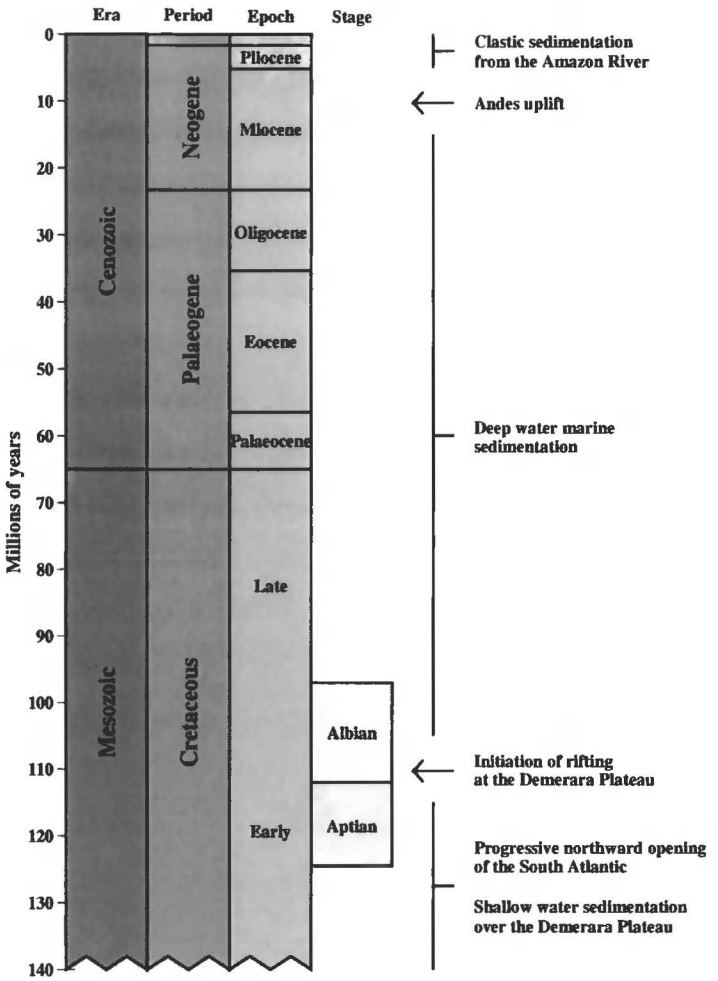


**Figure 1.9**: Summary of the temporal development of the French Guiana margin based on dating of major events: rifting – Nürnberg & Müller (1991); sedimentation – Gouyet *et al.* (1994); and Andes uplift – Benjamin *et al.* (1987). Geological timescale is based on Harland *et al.* (1990).

- Liassic to Aptian (213-113 Ma) – Prior to the equatorial rifting of South America and Africa at 118.7 Ma, the Demerara and Guinea Plateaux were adjacent parts of the southern Central Atlantic margin (Figures 1.7 and 1.8). Sedimentation at that time occurred primarily in an inner shelf environment, with significant continental influxes. The Neocomian period (145.6-131.8 Ma) also represents the start of the progressive northward opening of the South Atlantic Ocean (rifting of Argentina and South Africa); and

- Post-Aptian (113 Ma - present) – Initiated during the Albian (112-97 Ma), the break-up between the Demerara and Guinea Plateaux represents the final opening of the South Atlantic. This break-up incorporated a combination of perpendicular rifting and dextral shearing, segmenting the French Guiana and northeast Brazil margin into

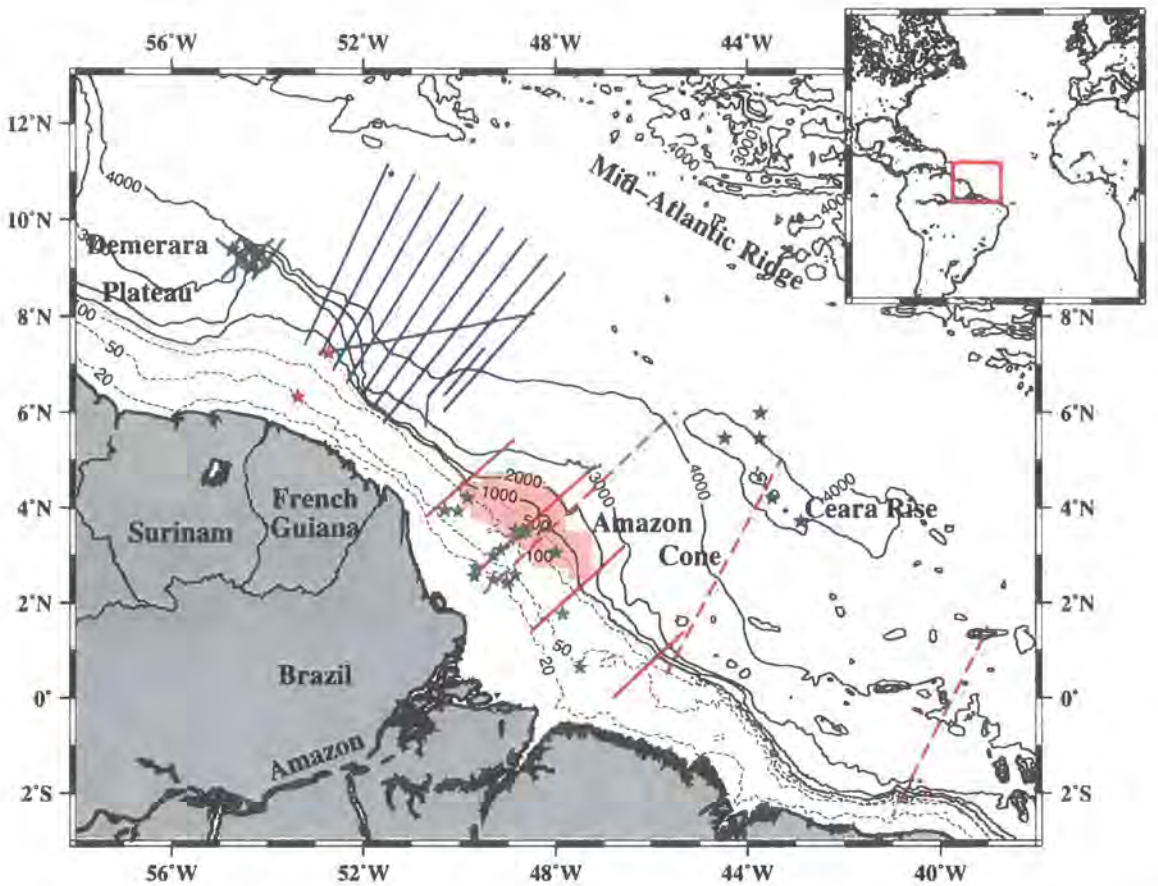


**Figure 1.10**: Datasets along the French Guiana and northeast Brazil margin prior to the ACE. Guyaplac MCS profiles – blue lines (F. Klingelhöfer and W. Roest, *pers. comm., e.g.* Loncke *et al.*, 2006); R/V *Meteor* 49-4 industry MCS profiles – green lines (Erbacher *et al.*, 2004); ODP boreholes – blue stars (Erbacher *et al.*, 2004; Curry *et al.*, 1995); Petrobrás 18 s MCS profiles and wells – solid red lines and green stars (Rodger *et al.*, 2006); two-ship sonobuoy profiles – dashed red lines (Houtz *et al.*, 1977); and industry wells – red stars (Gouyet *et al.*, 1994). Bathymetric contours are plotted at 20 m, 50 m, 100 m (dashed line), 500 m (dotted line) and then at every 1000 m (solid line) intervals.

a series of rift- and transform-type structures. Post-rift, the depositional environment shifted from shallow to open marine sediments.

The Guyaplac dataset (Section 2.5.2) was acquired in 2003 and comprises 11 MCS profiles, spanning the whole of the French Guiana margin (Figure 1.10). Ten of these profiles are oriented northeast-southwest, approximately parallel to the proposed ACE margin transects. These profiles are approximately equally spaced along-margin-strike and were located to constrain the 3D distribution of sedimentation. Although each of the profiles images the basement surface, the associated reflection event is more prominent towards the north of the survey.

ODP boreholes (Erbacher *et al.*, 2004) are located on the northwestern flank of the Demerara Plateau, offshore Surinam. Five cores were drilled to recover sections of

Cretaceous- and Palaeogene-age deep-sea sediments with the goal of investigating a) changes in the Earth's climate through geological time relative to perturbations in the global carbon cycle and associated with extinction events, and b) the progressive development of water column circulation patterns associated with the opening of the equatorial Atlantic. Erbacher *et al.* (2004) tie the borehole data to local seismic sections, which will be used in this study to extrapolate the sediment distribution across the Demerara Plateau.

#### 1.3.1.2 Amazon Cone

Prior to the ACE, the existing seismic dataset along the northeast Brazil margin comprised shallow reflection and sonobuoy refraction profiles (Edgar & Ewing, 1968; Houtz, 1977; Houtz *et al.*, 1977) which provide little information on the lower crustal and upper mantle structure. Reflection data show that the Amazon Cone is made up of a thick sediment wedge within which a major unconformity has been identified (Castro *et al.*, 1978; Braga, 1991), a result of a massive increase in clastic sedimentation rate.

The only constraint on deep crustal structure along the margin as a whole, comes in the form of a gravity transect running across the Amapa Shelf and Amazon Cone (Figure 1.10) with the only available constraint on densities at the time derived from velocities interpreted from sonobuoy data (*e.g.* Houtz, 1977) using a 1D approach to data analysis. Braga (1991) modelled the Bouguer anomaly and concluded that the continental crust beneath the shelf is about 30-35 km thick and, oceanward, the oceanic crust is about 10 km thick. This modelling could not determine the nature of the crust within the 400 km wide region defining the OCT, nor the role (if any) that magmatism played during rifting; problems which this study aims to address.

For this study, isopach maps from a comprehensive 3D seismic study have been provided by BP. However, due to the survey location, these maps only constrain the 3D subsidence of the Amazon Cone and underlying crust (Rodger *et al.*, 2006; Rodger, 2007) and will not be described further in this thesis. Further deep crustal (18 second) reflection profiles were provided by Petrobrás, in addition to several wells, the locations of which are also shown in Figure 1.10.

## 1.4 Amazon Cone Experiment

The aim of the ACE was to study the along-strike structural variation and lithospheric properties in the equatorial Atlantic. The acquisition programme was designed around the location of existing profiles on the French Guiana and northeast Brazil margin. Given

that no deep seismic margin transects were available, three new transects were planned. The locations of these transects were chosen so that data were acquired primarily over the Amazon Cone, in order to address the question of lithospheric strength in response to progressive loading, whilst also imaging deep margin structure. This transect was located coincident with a Petrobrás 18 s MCS profile (Figure 1.10) orthogonal to the current trend of the coastline and continental shelf, through the centre of the Amazon Cone. Additional transects were located to the north and south, to act as reference structures and also to address along-strike segmentation between rift- and transform-type margins. The northern profile was designed to be coincident with Guyaplac profile Guyas 44.

Failure to obtain the necessary permits to acquire data within Brazilian territorial waters resulted in several changes to the original design, although the scientific aims remained the same. The Amazon Cone transect was shortened to cover only the mid-lower Cone oceanward of the Brazilian 200 nm territorial limit. The southern transect was abandoned and an additional transect was acquired to the north, coincident with Guyaplac Profile Guyas 01. This transect crossed the Demerara Plateau and satisfied the original aim to survey structural changes along-margin-strike.

Thus, the data profiles acquired were well-distributed along the margin, to maximise the extent of the survey within the constraints of available permits and ship time. The profiles were located proximal to or coincident with existing MCS data for purposes of comparison of results and extrapolation of deep crustal models along-strike. The high quality dataset acquired during the ACE will be described in detail in the relevant chapters of this thesis.

## 1.5 Summary of this study

The previous sections have demonstrated that our understanding of lithospheric rifting and passive continental margins is not complete and several key questions have been raised regarding the structure and properties of continental margins and how these vary along-strike. The French Guiana and northeast Brazil margin has been described, as it is an ideal setting for further research. As a result, this margin was targeted for the ACE, a multi-disciplinary geophysical investigation into deep crustal structure.

As part of the ACE geophysical data were acquired during November/December 2003 and have subsequently been processed and modelled to address the original aims of the study. Consequently, seismic and gravity modelling results have been used in two complimentary studies, the first of which addresses the problem of structural segmentation along-margin-strike (this study; Greenroyd *et al.*, 2007a,b,c) and the second analyses the

subsidence history of the margin to understand how lithospheric strength has evolved (Rodger *et al.*, 2006; Rodger, 2007).

In this study interpretation of data along two profiles from the ACE will be used to construct models of the French Guiana margin, which will then be analysed in order to understand the rifting and evolution of the margin as a whole. Consequently, this thesis is subdivided into 7 chapters, of which Chapters 2, 3 and 4 are broadly focussed on model construction and Chapters 5 and 6 are used for description and development of our current understanding.

Specifically, this chapter has described the distribution and key structural features of, primarily Atlantic, passive continental margins. Recent topics of debate have been discussed, in terms of the effect of rift geometry, magmatism, post-rift spreading and oceanic crustal accretion on the structures observed at and adjacent to margins. Several questions were posed, the answers to which may potentially expand our current knowledge of margins and their role in global tectonics, of which this study will primarily address those related to deep crustal structure and segmentation of rift- and transform-style margins. Our current understanding of the evolution of the equatorial Atlantic has also been described.

In Chapter 2, the experimental configuration and MCS acquisition of the ACE will be described, prior to a detailed discussion of the processing applied to the resulting dataset. An interpretation of the MCS data will be developed in order to understand both the stratigraphic evolution of the margin and also the depth and geometry of key interfaces, which will be incorporated into the deep crustal modelling in Chapter 3.

The WA seismic dataset is introduced in Chapter 3 and a detailed description of the forward modelling procedure used to create *P*-wave velocity-depth models from the data will be provided. At this stage, the resulting models will be constrained by extensive WA ray coverage of the crust and uppermost mantle, in addition to intra-sediment and basement boundaries imaged by the MCS data. A brief interpretation of the resulting models is included to underpin subsequent approaches to model testing.

In Chapter 4, inverse modelling of the WA seismic data and forward modelling of gravity and magnetic data will be explained. This modelling is used to test the uniqueness and resolution of, and further constrain, the deep structural models. The resulting *P*-wave velocity-depth models are presented and described in Chapter 5. In order to set the models in their regional context, a detailed analysis of the regional oceanic crustal fabric will be undertaken with the aim of mapping fracture zones and margin geometries.

In Chapter 6, the modelling results will be correlated with the original aims of the study and described in terms of the role of magmatism, observations of oceanic crust, rift versus transform structures and segmentation along the margin. These features will be linked together to develop an understanding of the evolution of the equatorial Atlantic.

The main conclusions drawn from this study will be presented in Chapter 7, and suggestions for further work on the ACE dataset itself, and for additional data acquisition are proposed.

# Chapter 2

# Seismic reflection data acquisition and processing

## 2.1 Introduction

In Chapter 1 the choice of the northeast Brazil and French Guiana continental margin as the target for the ACE was discussed. In this chapter the ACE is described, comprising coincident MCS and WA seismic, bathymetric, magnetic and gravity data acquired along three margin transects (Figure 2.1). This study will focus on the profiles acquired offshore French Guiana. Each of the geophysical datasets acquired are described in detail in Section 2.2. The remainder of this chapter is devoted to the acquisition (Section 2.3), processing (Section 2.4) and interpretation (Sections 2.5 and 2.6) of the MCS data.

The final processing flow for each MCS profile includes several standard steps to improve signal-to-noise ratio (SNR), suppress multiples and migrate the data to produce sections suitable for interpretation of the sediment column to basement surface. This interpretation is used to constrain the WA data modelling (see Chapter 3). In Section 2.5, the resulting profiles are compared and contrasted with other MCS data from the same region, collected prior to the ACE. These data, and co-located well log interpretations, are used to provide geological constraint for the interpretation of both MCS profiles in this study which are presented in Section 2.6.

## 2.2 Amazon Cone Experiment

The ACE took place between October and December 2003 onboard the R/V *Discovery* (cruise D275 – Peirce & Watts, 2004). Multidisciplinary geophysical data were acquired along six profiles, as outlined below and shown in Figure 2.1. Further acquisition details, including profile locations, shooting direction and shot number are summarised in Appendix A. Each profile primarily comprises coincident, controlled-source MCS and

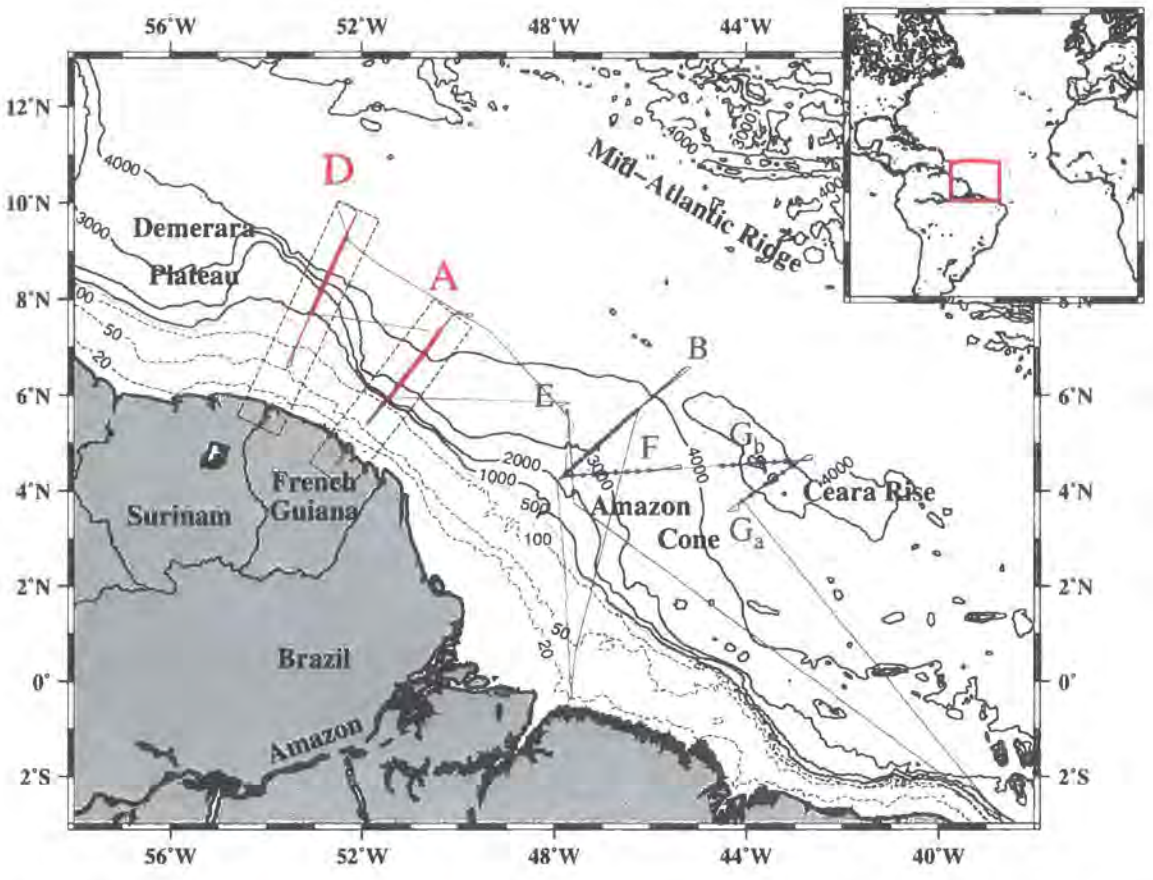


**Figure 2.1**: Geophysical data acquired during the ACE. The inset shows the location of the study area (red box) within the Atlantic Ocean. The dataset comprises six profiles, A, B, D, E, F and G. Profiles A and D (red), which cross the French Guiana continental margin, form the basis of this study. Profiles B, E and F (blue) which traverse the mid-lower Amazon Cone (offshore northeast Brazil), form the basis of a complementary flexural study (Rodger *et al.*, 2006; Rodger, 2007). Profile G crosses the Ceara Rise twice with the southwest-northeast trending section named $G_a$ and the east-west trending section named $G_b$. Seafloor bathymetry is contoured similarly to Figure 1.10. Ship tracks are plotted in light grey. Dashed boxes refer to Figure 2.2 for Profile A and Figure 2.3 for Profile D.

WA data. In addition, contemporaneous gravity, magnetic, bathymetry and expendable bathymetric thermograph (XBT) data were acquired. Profiles A and D form the basis of this study and, for each profile, locations are referenced to 0 km, defined as the site of the most southwesterly land station (described in Section 3.5) along each profile. Offsets are positive to the northeast.

### 2.2.1 Profile A

Profile A, oriented northeast-southwest, lies almost perpendicular to the French Guiana continental margin, crossing it ~400 km northwest of the Amazon Cone and ~140 km southeast of the Demerara Plateau. Coincident MCS and WA data were acquired for 266 km from the oceanward end of the profile, with a further 161 km of WA data only acquired

landward of this point, due to the shallow water depth. Profile A is therefore 427 km in total length (Figure 2.2). Of this, 45 km lies onshore and a further 137 km lies in shallow water (<150 m) above the continental shelf. Oceanward of the shelf break, located at 182 km profile offset, the seafloor deepens to in excess of 4 km. Twenty ocean-bottom seismographs (OBSs) and ocean-bottom hydrophones (OBHs) and five land stations were deployed along this profile for WA acquisition.

The primary goal of Profile A was to image crustal rift and transform structures associated with the rifting of South America from Africa. Thus the location of this profile was chosen to cross the continental margin in a region adjacent to, but less affected by, extensive Amazon Cone sedimentation, which may be expected to hinder seismic imaging of the basement surface due to its significant thickness. Consequently the profile was used to provide the crustal reference model for a study of lithospheric flexure associated with the Amazon Cone (Rodger *et al.*, 2006; Rodger, 2007) undertaken as part of the ACE.

### 2.2.2 Profile D

Oriented northeast-southwest, Profile D also crosses the Demerara Plateau and French Guiana continental margin ~140 km to the northeast of Profile A. The profile comprises 390 km of combined MCS and WA acquisition (Figure 2.3) and a 145 km WA only extension landward. Again, the profile consists of onshore-offshore data with 42 km onshore, 343 km over the Demerara Plateau (water depth <3.6 km) and 150 km further oceanward; a total line length of 535 km. WA data were acquired by 20 OBSs and four land stations. The original experimental design for the ACE did not include Profile D. This profile was incorporated during cruise D275 after failure to obtain permission from the Brazilian authorities to conduct seismic experiments within their territorial waters. However, Profile D extended the investigation of crustal structure northwest along the margin, incorporating the Demerara Plateau which, as discussed in Chapter 1, played an important role during the break-up of South America and Africa (Erbacher *et al.*, 2004).

### 2.2.3 Additional profiles

Four additional profiles were acquired during cruise D275 (Figure 2.1). These profiles do not form part of this study. Rodger (2007) presents descriptions of Profiles B and F as part of a WA study of lithospheric flexure beneath the Amazon Cone. In addition, preliminary WA modelling studies of Profiles F and G are discussed by Wilson (2006) and Hunt (2006) respectively.

In summary:

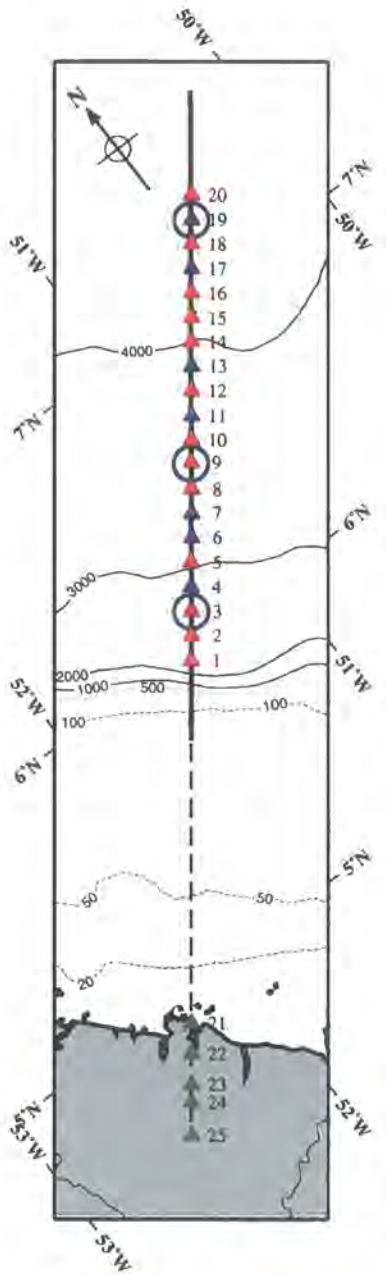


**Figure 2.2**: Acquisition geometry for Profile A. The profile (dashed and solid black line) is shown in oblique view, with the French Guiana coastline at the base of the plot. MCS shot point (solid black line), OBS (red triangles), OBH (blue triangles), land station (green triangles) and XBT (blue circles) locations are indicated. Bathymetric contours are plotted as in Figure 1.10. The dashed line shows the section of the profile for which only WA data were acquired. OBS spacing is 10 km $\pm$ 200 m and the shot interval $\sim$100 m (40 s) $\pm$ 15 m due to variations in ship speed.

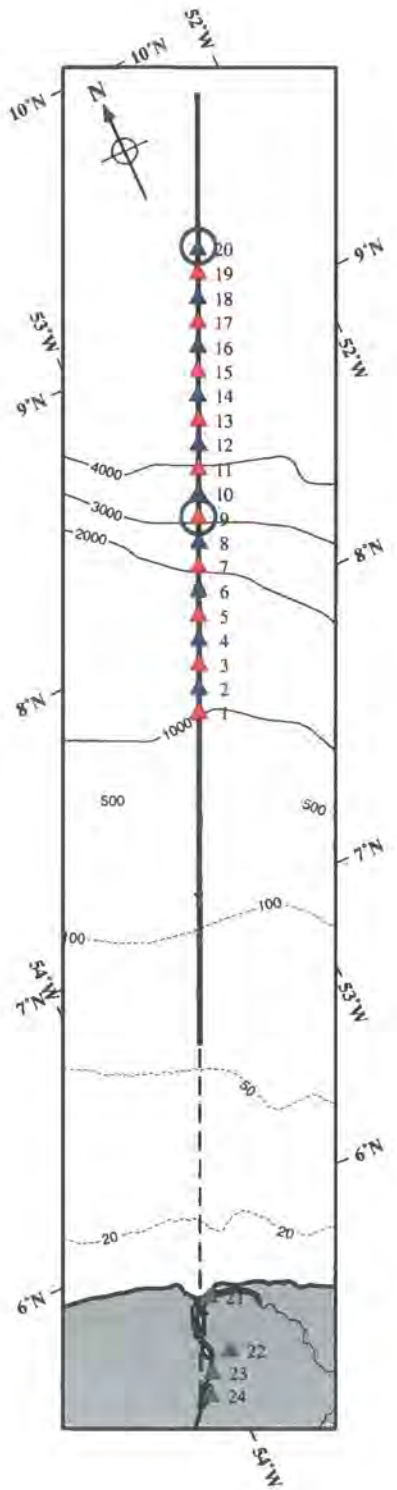


**Figure 2.3**: Acquisition geometry for Profile D. See Figure 2.2 for details. Comparison of the geometry of the bathymetric contours with those shown in Figure 2.2 shows the areal extent of the Demerara Plateau and the more subdued gradient of the continental slope in this region.

- Profile B, again oriented northeast-southwest, targets the thick sediments and flexed lithosphere of the Amazon Cone. Without permission to work in Brazilian territorial waters, this profile was limited to a region extending oceanward from 370 km (200 nm) offshore northeast Brazil, over the mid-lower Amazon Cone only;
- Profile F, oriented east-west, traverses the mid-lower Amazon Cone, intersecting Profile B at the westernmost end;
- Profile E, oriented north-south, also traverses the mid-lower Amazon Cone and, in conjunction with B and F, allows the ACE to approximate a pseudo-3D survey of the crustal structure beneath the Cone. Profile E also served as an equipment trial for the MCS acquisition and, consequently, OBSs were not deployed and WA data were not acquired along this profile; and
- Profile G, which comprises two parts. The first, $G_a$, is oriented southwest-northeast crossing the Ceara Rise, which trends southeast-northwest. Profile $G_b$ is oriented east-west. Both profiles are located such that they intersect and can be correlated with DSDP and ODP drill holes (Figure 1.10) which provide constraint on the shallow sediment lithology and geophysical parameters such as *P*-wave velocity and density.

## 2.3 Multi-channel seismic data acquisition

The source array for seismic acquisition comprised 14 Bolt 1500LL airguns, ranging in chamber volume from 160-700 $in^3$, resulting in a total array volume of 6520 $in^3$ ($\sim$107 l). Gun timing was controlled by a Seamap Gunlink system, an industry standard shot firing system. The array was designed (Figure 2.4) primarily to produce a low frequency source signature with sufficient amplitude to penetrate the whole crust and uppermost mantle for WA acquisition. Additionally, the source signature and frequency bandwidth had to be appropriate for contemporaneous MCS profiling of the stratigraphy of the sediment column and the geometry of the basement surface.

Pre-cruise source signature modelling (Figure 2.5 – Peirce & Watts, 2004) predicted a dominant frequency of $\sim$9 Hz with the array towed at 15 m. The actual tow depth achieved was $\sim$17 m, as described in the cruise report (Peirce & Watts, 2004) which also contains a full description of the acquisition and the problems encountered throughout the cruise. Such array characteristics are commonly used in the acquisition of WA data within deep-ocean and continental margin settings (*e.g.* White *et al.*, 2002). Figure 2.5 also shows that

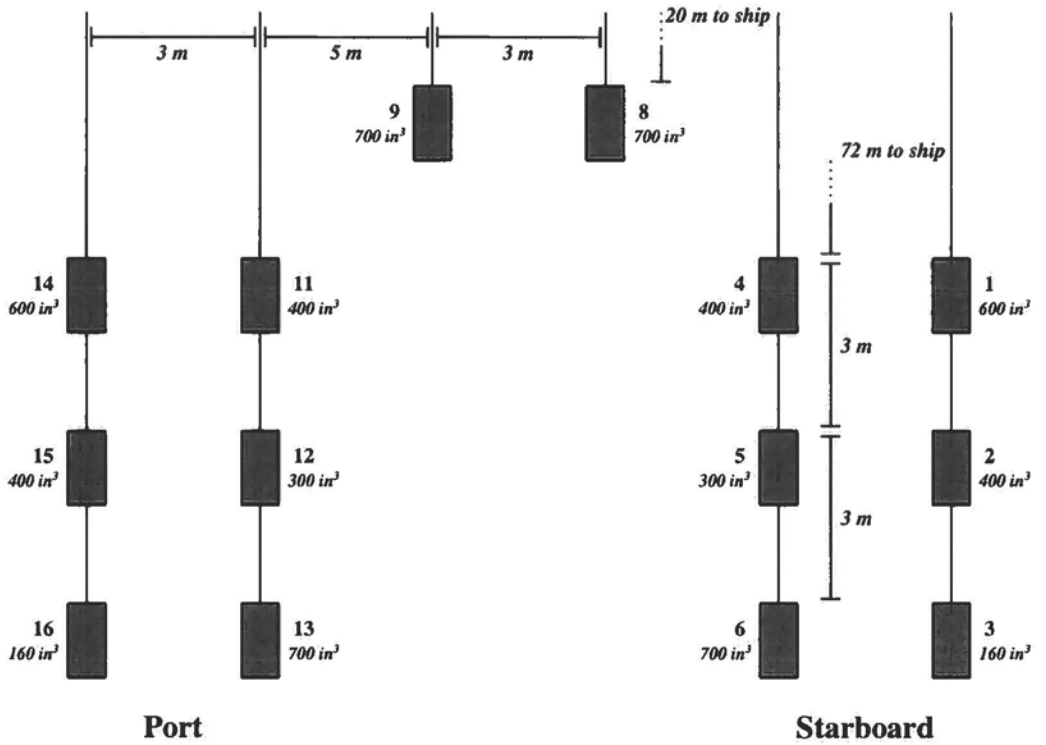


**Figure 2.4**: Schematic airgun array construction used during cruise D275. The grey boxes correspond to airguns, with numbers and chamber sizes labelled, towed from four beams. The two 700 $in^3$ guns (8 and 9) were towed from individual cables. Distances between individual guns and also to the vessel are labelled in blue.

the modelling predicts a wavelet which decays from its maximum amplitude over ~400 ms, with secondary peaks ~20-30% of the amplitude of the primaries.

The actual source signature (Figure 2.5), recorded by a shot hydrophone and Geode acquisition system, shows a wavelet of 40 ms duration, with a high amplitude primary peak, primary trough and secondary peak. This pattern is replicated 115 ms later with the primary amplitude reduced to ~30% of its inital value. When compared to these primary and secondary peaks the remainder of the source signature comprises low amplitude bubble pulses. The actual source signature shows a broader range of frequencies than predicted. However, as per the original design specifications, the target frequency of 8-10 Hz is observed in both.

Shots were fired every 40 s, with the exact trigger point randomised within a window of 128 ms about the shot instant to minimise contamination of the resulting WA sections with coherent water-borne noise. In addition, individual guns were fired at various time delays such that peak array energy output was achieved 50 ms after the shot instant – this

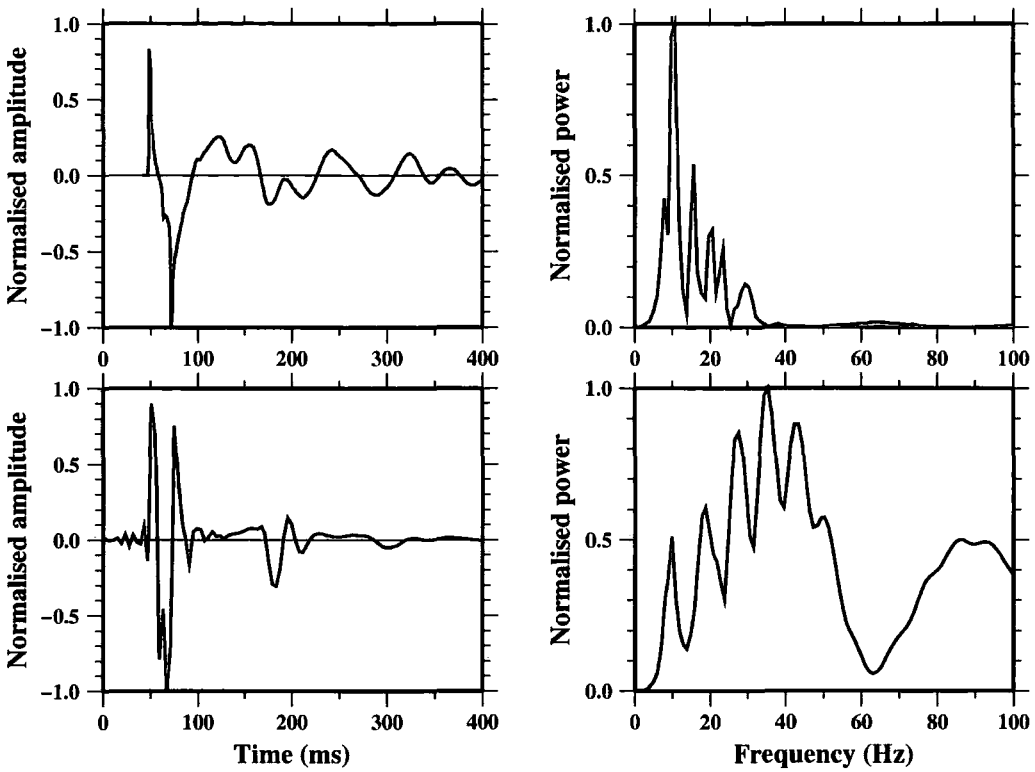


**Figure 2.5**: (Top) Pre-cruise modelling of the far-field source signature. The signature is modelled for the airgun array shown in Figure 2.4. The resulting wavelet (top left) exhibits a sharp peak followed by lower amplitude, decaying secondary peaks. The far-field frequency spectrum (top right) shows maximum power output at 9 Hz. (Bottom) Source wavelet recorded during acquisition, taken from a stack of direct water waves from channel 66 for shots 1690-2265 and 2315-3719 on Profile A. Channel 66 was chosen as it has a relatively high SNR whilst also being representative of the far-field signal, whilst also exhibiting a high SNR in comparison with the longer offset channels (*e.g.* Channel 96). Shots 2266-2314 are excluded as the source tow depth showed greater variation than normal, causing disruption to the normal source signature characteristics. Shots 3720-4171 were excluded because reflections from the shallow seafloor interfered with the direct water wave. The source wavelet (bottom left) exhibits a sharp double peak with a significant secondary arrival 110 ms later. The source frequency spectrum (bottom right) shows a clear primary peak at 9 Hz and several harmonics.

is called the aim point. A Global Positioning System (GPS) clock was used for shot timing and to locate shot points. The source signature of each airgun was recorded throughout.

A Teledyne 96-channel streamer was used to acquire the MCS data. Each active channel was 25 m long resulting in a total active length of 2.4 km. The streamer was towed at a target depth of 10 m, monitored and controlled by 13 altitude controllers (birds) with built-in depth sensors and compasses. For clarity, a cartoon of the acquisition geometry is shown in Figure 2.6 and acquisition parameters are summarised in Appendix A. For this geometry, the resulting fold of coverage was between 20 and 29. This range is due to variations in vessel speed which resulted in a shot spacing of between 86 and 116 m.

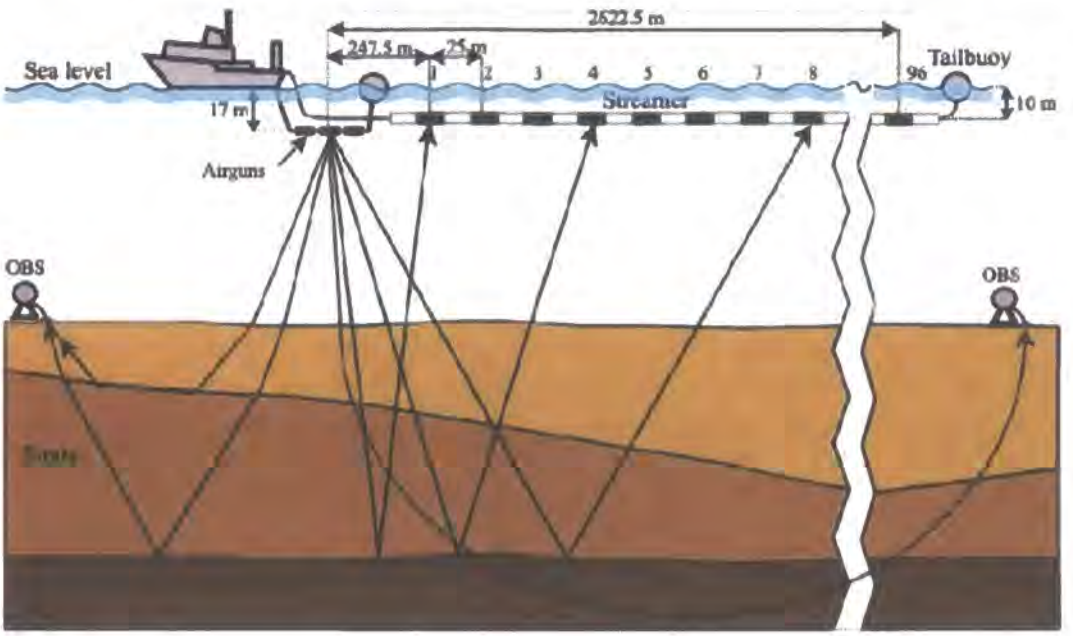


**Figure 2.6**: Seismic acquisition configuration for cruise D275. The MCS streamer, airgun array and OBSs are shown and described in the main text. Schematic ray paths from the source array to the MCS streamer and OBSs are shown in black. Instrumentation not shown here included a magnetometer towed during shooting and XBTs deployed at specific OBS locations.

MCS data were recorded, using a SmartSeis system and a sampling rate of 4 ms, for 20 s after each shot instant onto DDS3 4 mm DAT magnetic tapes in SEG-D format (Barry *et al.*, 1975).

## 2.4 Multi-channel seismic data processing

MCS data processing was divided into four main stages:

- Pre-processing (Section 2.4.1), in which the full dataset was constructed from sections stored on multiple field data tapes;
- Brute stack (Section 2.4.2), to develop an understanding of the basic geological structure upon which to base later selection of processing parameters;
- Main processing (Section 2.4.3); and
- Final production of migrated sections (Section 2.4.3.10).

Each stage of the MCS processing is described separately in the sections below and differences between the two profiles are highlighted. Tables 2.1 and 2.2 summarise the processing steps, all of which were applied using the industry standard *ProMAX* seismic

Profile A: Processing flow: Final stack

| | | |
|---|---|---|
| 1 | **Pre-processing** | Read in raw SEG-D data from DAT tapes |
| 2 | **Pre-processing** | Combine datasets and alter headers |
| 3 | **Pre-processing** | Insert 2D geometry |
| 4 | **Output brute stack** | NMO correction at 1.5 $kms^{-1}$, stack into CMP bins and output as SEG-Y (see Figure 2.7) |
| 5 | **Statics** | Source-streamer static (+18.7 ms) |
| 6 | **Statics** | Trigger delay static (-50 ms) |
| 7 | **Trace edit** | Kill spiked traces |
| 8 | **Trace edit** | Reverse polarity |
| 9 | **Filter** | 2-4-44-88 Hz minimum phase Ormsby band-pass filter (Figure 2.8) |
| 10 | **True amplitude recovery** | $(tv^2)^{-1}$ minimum phase spherical divergence correction |
| 11 | **Deconvolution** | Minimum phase predictive deconvolution ($gap$ = 32 ms, $length$ = 120 ms, $white\ noise$ = 0.1%, $gate$ = 8 s $from\ water\ bottom$) |
| 12 | **Filter** | 2-4-44-88 Hz minimum phase Ormsby band-pass filter |
| 13 | **Sort** | Sort to CMP |
| 14 | **Split data** | Split data into three distinct regions: shallow, slope and deep |
| Shallow data (CMPs 1001-2180): | | |
| 15 | **NMO** | NMO correction |
| 16 | **Trace mute** | Manually picked stretch mute |
| 17 | **Stack** | CMP stack |
| Slope data (CMPs 2181-2830): | | |
| 18 | **DMO** | Common offset DMO binning (100 m $bins$) |
| 19 | **DMO** | NMO correction |
| 20 | **DMO** | Infill dead traces |
| 21 | **DMO** | Constant velocity dip moveout correction ($velocity$ = 1.5 $kms^{-1}$, $maximum\ frequency\ analysed$ = 60 Hz) |
| 22 | **DMO** | NMO correction removed |
| 23 | **NMO** | NMO correction |
| 24 | **Stack** | CMP stack |
| Deep data (CMPs 2831-11641): | | |
| 25 | **De-multiple** | NMO correction |
| 26 | **De-multiple** | Infill dead traces |
| 27 | **De-multiple** | Parabolic Radon filter (121 $p\ values$, $over\ range$ -150 $to$ 50 ms) |
| 28 | **De-multiple** | Manually picked inner trace mute (Figure 2.12) |
| 29 | **De-multiple** | NMO correction removed |
| 30 | **NMO** | NMO correction |
| 31 | **Stack** | CMP stack |
| All data: | | |
| 32 | **Combine data** | Recombine datasets |
| 33 | **Output processed stack** | Output as SEG-Y (Figure 2.15) |
| 34 | **Migration** | Post-stack Kirchoff time migration ($maximum frequency\ analysed$ = 60 Hz, $migration\ aperture$ = 4 km) (Figure 2.18) |
| 35 | **AGC** | Automatic gain control ($operator\ length$ = 500 ms) |
| 36 | **Muting** | Top mute to remove water column |
| 36 | **Output migrated stack** | Output as SEG-Y (Figure 2.16 and Appendix B) |

**Table 2.1**: Summary of processing steps applied to MCS data for Profile A.

Profile D: Processing flow: Final stack

| | | |
|---|---|---|
| 1 | **Pre-processing** | Read in raw SEG-D data from DAT tapes |
| 2 | **Pre-processing** | Combine datasets and alter headers |
| 3 | **Pre-processing** | Insert 2D geometry |
| 4 | **Output brute stack** | NMO correction at 1.5 $kms^{-1}$, stack into CMP bins and output as SEG-Y (see Figure 2.7) |
| 5 | **Statics** | Source-streamer static (+18.7 ms) |
| 6 | **Statics** | Trigger delay static (-50 ms) |
| 7 | **Trace edit** | Kill spiked traces |
| 8 | **Trace edit** | Reverse polarity |
| 9 | **True amplitude recovery** | $(tv^2)^{-1}$ minimum phase spherical divergence correction |
| 10 | **Deconvolution** | Deconvolution filter designed to 2-4-44-88 Hz zero phase band-pass |
| 11 | **De-multiple** | NMO correction at 1.49 $kms^{-1}$ |
| 12 | **De-multiple** | Stack and pick water bottom |
| 13 | **De-multiple** | SRME *water velocity* = 1.49 $kms^{-1}$; *max. convolution dist.* = 3 km; *least square filter* : *gate spacing* = 0.5, *length* = 1 s, *gate skew* = 0.25, *filter length* = 100 ms, *max. time shift* = 50 ms, *white noise* = 0.1% (Figure 2.13) |
| 14 | **De-multiple** | NMO correction removed |
| 15 | **NMO** | NMO correction |
| 16 | **Stack** | CMP stack |
| 17 | **Output processed stack** | Output as SEG-Y (Figure 2.15) |
| 18 | **Migration** | Post-stack Kirchoff time migration (*maximum frequency analysed* = 60 Hz, *migration aperture* = 4 km) (Figure 2.18) |
| 19 | **AGC** | Automatic gain control (*operator length* = 500 ms) |
| 20 | **Muting** | Top mute to remove water column |
| 21 | **Output migrated stack** | Output as SEG-Y (Figure 2.17 and Appendix B) |

**Table 2.2**: Summary of processing steps applied to MCS data for Profile D.

processing software, with the exception of plotting which made use of *Seismic Unix* (Cohen & Stockwell, 2000) and *Generic Mapping Tools* (*GMT* – Wessel & Smith, 1998). Whilst all steps described here correspond to post-cruise processing, many were also applied onboard to quality control the data acquisition as it progressed.

### 2.4.1 Pre-processing and profile geometry

The first stage of processing was to download SEG-D data from DAT tape and undertake quality control checks. The data headers, in particular, were checked for consistent consecutive shot numbering and timing and this revealed a minor problem with shot numbering associated with data tape change-overs. For Profile A, at each tape change the last shot number on a tape was repeated at the start of the next. A few similar numbering glitches occurred elsewhere in between tape changes for both profiles. However, the data itself was unaffected and so the shot numbers in the trace headers were simply corrected by

consecutive renumbering. The data from each sequential tape were combined to produce a single dataset for each profile.

Shot point locations were calculated by back projecting ship GPS antennae locations astern of the vessel to the true source location (Figure 2.4). True receiver locations were calculated by interpolating along the streamer, from the vessel to the tailbuoy, the latter of which also had a GPS antenna housed on it. These positions were projected onto the line of the profile and source-receiver offsets calculated and loaded into the data headers. Offline shots, due to shooting commencing whilst the vessel was manoeuvring onto line, were not included (Appendix A).

Shot and receiver locations were inserted into the trace headers using the 'Inline Geom Header Load' *ProMAX* module and the geometry calculated to assign each trace to 25 m common mid-point (CMP) bins. Profile A comprises 10641 CMPs and Profile D 15607 CMPs.

### 2.4.2 Brute stack

Brute stacks (Figure 2.7) were created for each profile in order to make a preliminary assessment of the subsurface structure across the margin, such observations being used to influence future data processing. The stacks were produced using a normal moveout (NMO) correction velocity of 1.5 $kms^{-1}$, the water column velocity. With this NMO velocity the seabed is correctly stacked, which allows its two-way traveltime (TWTT) to be checked against that calculated from bathymetry measurements.

In Figure 2.7 the seafloor is clearly imaged across both profiles, and significant sedimentary reflectors are observed beneath it. The figure highlights several features which need to be addressed during processing:

- Noise – the SNR is poor throughout both sections. This feature is particularly obvious within the water column, in which no strong coherent reflections would be expected;
- Multiples – observed across the Demerara Plateau region of Profile D (between 200 km and 380 km offset) and near the continental margin in Profile A (between 190 km and 290 km offset), due to the shallow (<500 m) water depths;
- Sub-surface reflections – sedimentary and basement reflectors are the target of the MCS profiling and processing steps should aim to improve the SNR and any lateral coherence of these reflectors; and

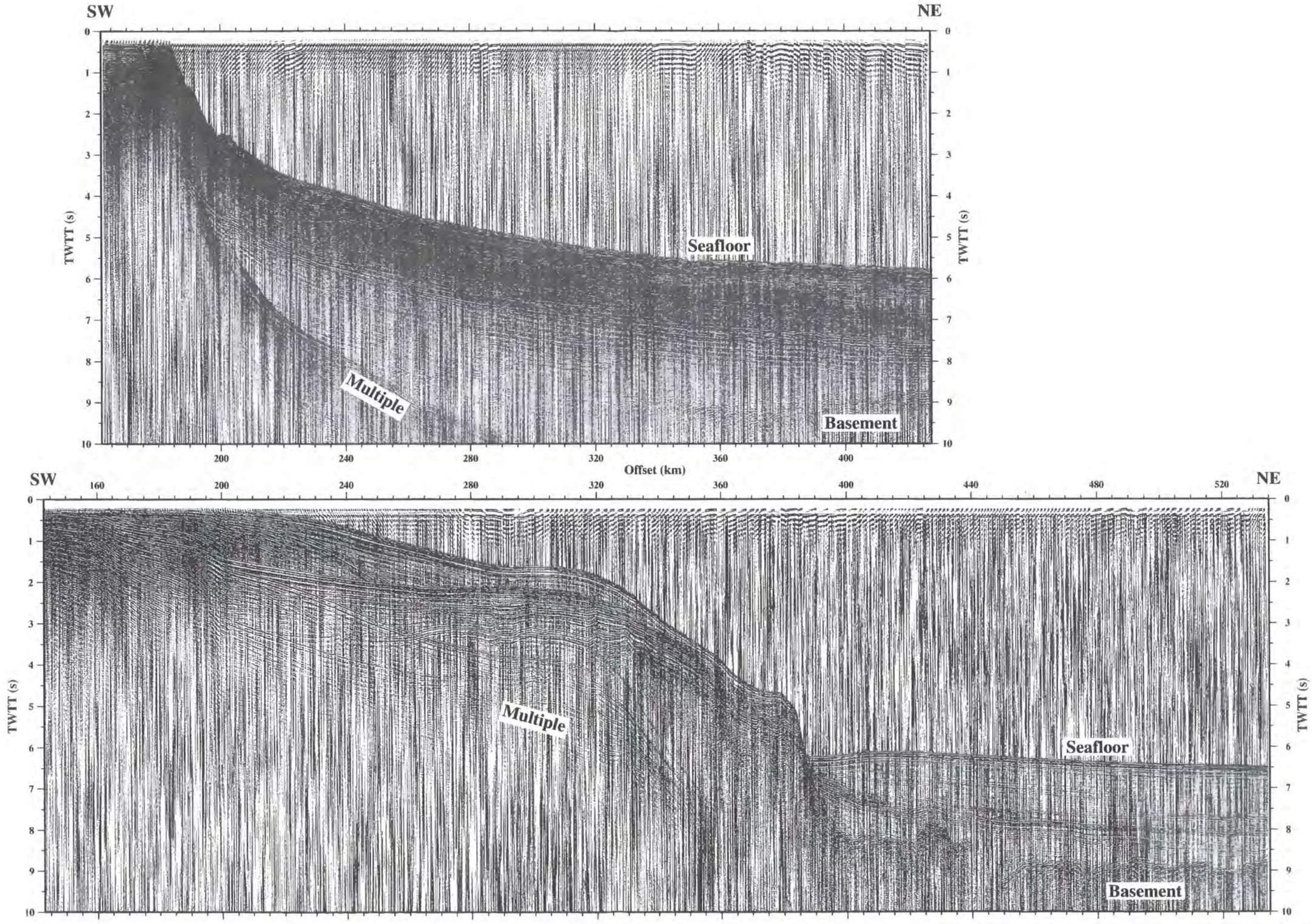


**Figure 2.7**: Brute stacks of MCS data for Profiles A (top) and D (bottom). NMO correction is applied at a constant velocity of 1.5 $kms^{-1}$. The location of each profile is shown in Figure 2.1. The stacks, whilst contaminated by low frequency noise, image a distinct seafloor reflector above several stratified layers. Additionally, both profiles display a hummocky basement surface oceanward of ~320 km along Profile A and ~400 km along Profile D and a distinct seafloor multiple which obscures primary reflections beneath the shelf and slope. The two profiles show significantly different upper crustal structures, with the Demerara Plateau (Profile D) being more structurally complex beneath the slope and exhibiting evidence of intra-sediment faulting.

- Diffraction hyperbolae – primarily associated with the rough basement surface, indicating truncated or broken reflecting horizons and/or significant basement topography.

### 2.4.3 Full processing

MCS data processing comprised several standard steps. The chosen approach (summarised in Tables 2.1 and 2.2) was designed to address the problems outlined in Section 2.4.2 and to produce as clear and accurate an image of the sediment column and basement surface as possible to inform and constrain WA seismic data modelling (Chapter 3).

#### 2.4.3.1 Static corrections and quality control

Two static corrections were applied to the data:

- A combined source-streamer correction of +18.7 ms was applied to Profile A, to project the source and streamer to the sea surface datum. The tow depths for Profile D required a correction of +16.0 ms; and
- A -50 ms correction was applied to remove the aim point delay after the shot instant.

Several traces along both profiles contained noise spikes, comprising one or two data samples of excessively high amplitude, unrelated to subsurface reflections. These spiked traces were often, although not always, limited to single channels which may have had poor electrical connections, possibly as a result of water ingress into cable connectors. Furthermore, some traces were of a significantly low SNR. All traces were checked, and spiked or very low SNR traces muted. The proportion of muted traces was too low to have a significant effect on the fold of the data. Trace polarity was also reversed for both profiles so that the seafloor reflection was of positive polarity.

#### 2.4.3.2 Frequency analysis and filtering

Figure 2.8 shows a typical shot gather acquired along Profile A. The frequency spectrum of this data contains several key features:

- A strong signal below 2 Hz;
- A significant signal between 2 Hz and 105 Hz, comprising low (<20 Hz) frequencies ideal for WA acquisition and a broad frequency range ideal for MCS acquisition;
- 'Ringing' with peaks at 9 Hz, 18 Hz, 27 Hz and so on; and

- A distinct power decrease around 54 Hz, corresponding to the source ghost notch, resulting from destructive interference between the primary pulse and the reflection from the sea surface.

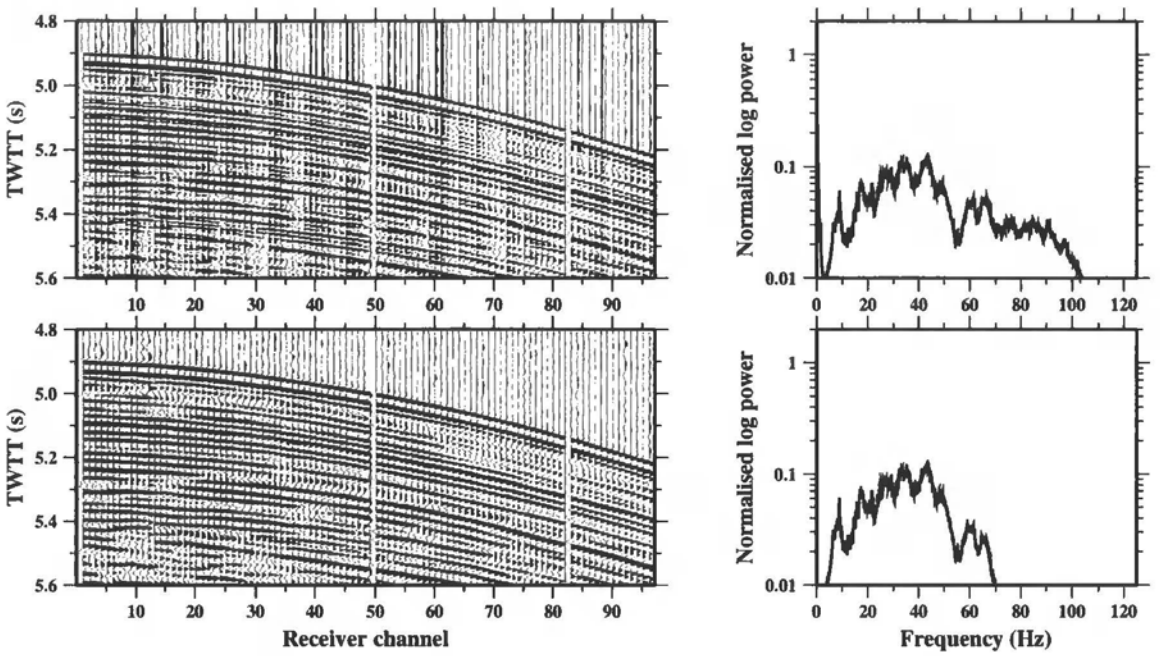


**Figure 2.8**: Application of the preferred band-pass frequency filter. (Top) Gather from shot 3000 on Profile A, typical of shot gathers from cruise D275. (Bottom) The same shot gather is displayed with a 2-4-44-88 Hz band-pass filter applied. The corresponding frequency spectra are included (right) and show that the filtering has successfully removed the very low and very high frequencies present in the data. Traces 49 and 82 have been muted (Section 2.4.3.1).

The power reduction at high frequency (>105 Hz) corresponds to anti-alias filtering above the Nyquist frequency of 125 Hz, associated with the 250 Hz sampling rate.

As a whole, the data shown in the Figure 2.8 contain several reflection events, comprising a convolution of the subsurface reflectivity and the source signature. These events are often indistinct due to varying amounts of noise and the filtering effect of the subsurface along the propagation path. Through the application of band-pass filters, the very low frequencies (<2 Hz) were found to be primarily noise and their removal significantly improved the clarity of the reflection events. Similarly, removal of very high frequencies (>88 Hz) improved the appearance and clarity of events. Following comparison of filtered and unfiltered data test panels, a 2-4-44-88 Hz filter was chosen for data processing as it significantly improved the overall SNR of the dataset. The lower panel in Figure 2.8 demonstrates that this filter significantly improves the data clarity and, post-filtering, the individual reflection events are more distinct, smoother and the DC bias has been removed.

#### 2.4.3.3 True amplitude recovery

True amplitude recovery attempts to compensate for attenuation and spherical divergence by scaling signal amplitude along each trace as a function of time, with the aim of recovering amplitudes which relate solely to changes in rock properties. Prior to velocity analysis a $t^{-2}$ function (Claerbout, 1985) was applied, where $t$ is the time since the shot. However, this is only an approximate function and after stacking velocities had been picked (Section 2.4.3.5) the true amplitude recovery step was reapplied using a $(tv^2)^{-1}$ function, where $v$ is the stacking velocity.

#### 2.4.3.4 Deconvolution

The five strong peaks within the frequency spectrum derived from shot gather data (Figure 2.8), and the relatively large secondary peak in the source wavelet (Figure 2.5), are attributed to bubble-pulse ringing of the airgun source. The source frequency spectrum has a fundamental frequency of 9 Hz (the first peak) and a series of harmonics (the higher order peaks). The higher order peaks within the source wavelet are undesirable as they may obscure true primary reflections and result in a long wavetrain. However, they are a consequence of the trade-off in design due to the requirements of contemporaneous MCS and WA acquisition and are thus to be expected. To minimise the effects of this ringing within the resulting sections, deconvolution was applied. The general aim of deconvolution is to reduce the length (in time) of the wavelet and to remove or reduce post-primary peaks, thus improving vertical resolution and event recognition.

Two different approaches to deconvolution were adopted. Minimum phase predictive deconvolution was applied to Profile A, whilst a deconvolution frequency filter was designed and applied to Profile D. Predictive deconvolution is the more widely used of the two approaches and was adopted as the starting point for the first profile to be processed – Profile A. The deconvolution filter approach was later applied to Profile D, aiming to better the result achieved with predictive deconvolution. In terms of data improvement, neither technique performed better than the other. Thus processing was completed with a different method of deconvolution applied to each profile. However, deconvolution filtering was found to be easier to design and apply and would, therefore, be the preferred future processing technique.

Within *ProMAX*, the 'spiking/predictive decon' module applies an operator using the Wiener-Levinson algorithm (Lines & Ulrych, 1977). The operator is designed by testing a range of filters on sections of data, with data and autocorrelation functions compared by eye to obtain the preferred parameters. The minimum phase predictive deconvolution

operator is dependent upon two key parameters (Figure 2.9): gap, the length of the primary pulse which we wish to retain; and filter length, the full length of the wavelet.

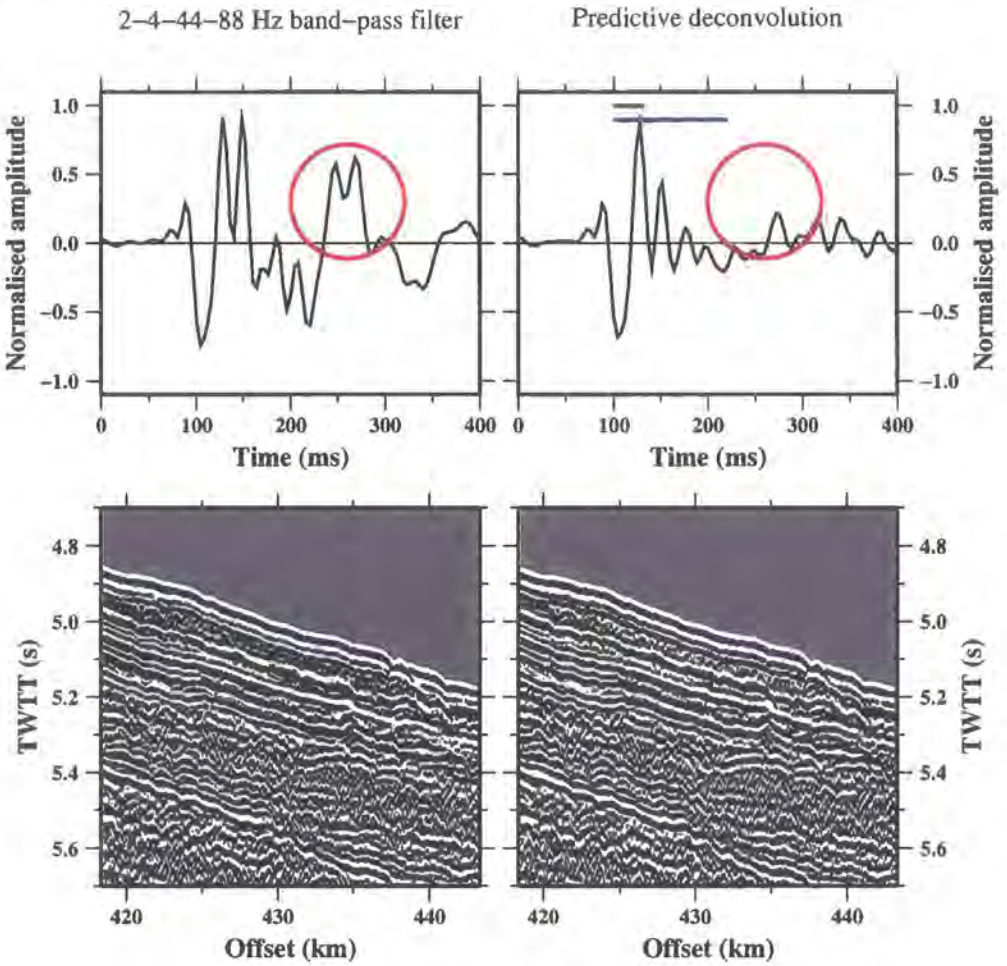


**Figure 2.9**: Results of predictive deconvolution testing on Profile A. A single wavelet is shown (top) following the application of a 2-4-44-88 Hz band-pass filter (left) and predictive deconvolution (right). For clarity, both wavelets are normalised to the maximum amplitude of the left-hand wavelet. A section of data stacked using an NMO correction at 1.5 $kms^{-1}$ is also shown (bottom). The frequency filtered wavelet contains a significant secondary peak (red circle) which is removed by the predictive deconvolution operator. Differences between the two stacked sections are hard to distinguish, but are clearest immediately beneath the seafloor. Hence, the processing step produces only minor improvement for Profile A. The gap and length of the deconvolution operator are shown in green and blue respectively.

For Profile A, these parameters were tested by first setting the gap to 30 ms and comparing autocorrelation functions for a range of operator lengths from 50 ms to 350 ms. An operator length of 120 ms was selected as the resulting autocorrelation function showed the least ringing. The operator length was then set to 120 ms and a range of gaps from 20 to 140 ms were tested. A gap of 32 ms was selected as this was the shortest gap which did not affect the primary pulse, hence maximising the length of post-primary wavelet to be removed without impinging on the primary. Additionally, the deconvolution

filter was applied with 0.1% white noise over an 8 s time window starting from the seafloor reflection. Deconvolution can boost both low and high frequency noise, hence the 2-4-44-88 Hz band-pass filter discussed earlier was also reapplied.

The effect of the deconvolution on the wavelet, and a section of stacked data, is shown in Figure 2.9. The deconvolution clearly reduces the size of the secondary peak in comparison to the effect of a band-pass filter alone, suggesting that the approach may produce significant improvement in the clarity of reflection events which arrive closely in time. Improvement is observed within the stacked data, primarily within the shallow sedimentary reflections immediately beneath the seafloor and thus the processing step was applied.

In contrast to predictive deconvolution, frequency filtering avoids the subjectivity involved in operator selection, instead relying heavily on the frequency spectrum of the data itself. The process involves convolving a pre-designed filter with the data. The design sequence aims to create a filter which will boost weak frequencies, effectively 'filling-in' the troughs between the harmonics in the frequency spectrum and, as a result, removing the ringing within the traces.

For Profile D, the filter was designed using the *ProMAX* modules 'wavelet generation', 'define average wavelet' and 'filter generation', operating on a test panel of data. The test panel consisted of every 40$^{th}$ shot across the profile, not including data from the very shallow water or data at the far northeast of the profile. The data from these two regions are not well suited for filter generation for two reasons. First, the shallow water data do not contain distinct reflections with which to observe the effect of the filter; and second the frequency spectrum of the northeast data do not contain a well defined peak and trough pattern with which to design the filter, most likely a result of rough sea conditions during acquisition of this part of the profile. Once created the filter was applied to the whole dataset, a sub-optimal approach for the rough water region. However, it was preferrable to either using bespoke filters for each trace or not applying deconvolution at all, both of which may reduce coherence across the resulting data section.

Figure 2.10 shows the operation of the deconvolution filter on the raw MCS data. Stacked data without any processing and data with a band-pass filter applied are provided for comparison. Within the frequency spectra of both the raw and band-pass filtered data, the primary and harmonic peaks are clearly visible. The frequency spectra of data convolved with the deconvolution filter shows no clear peaks, demonstrating removal of the harmonics, although possibly at the expense of some power in the target frequency band around 9 Hz. Unlike Profile A, Profile D shows a clear secondary (and arguably

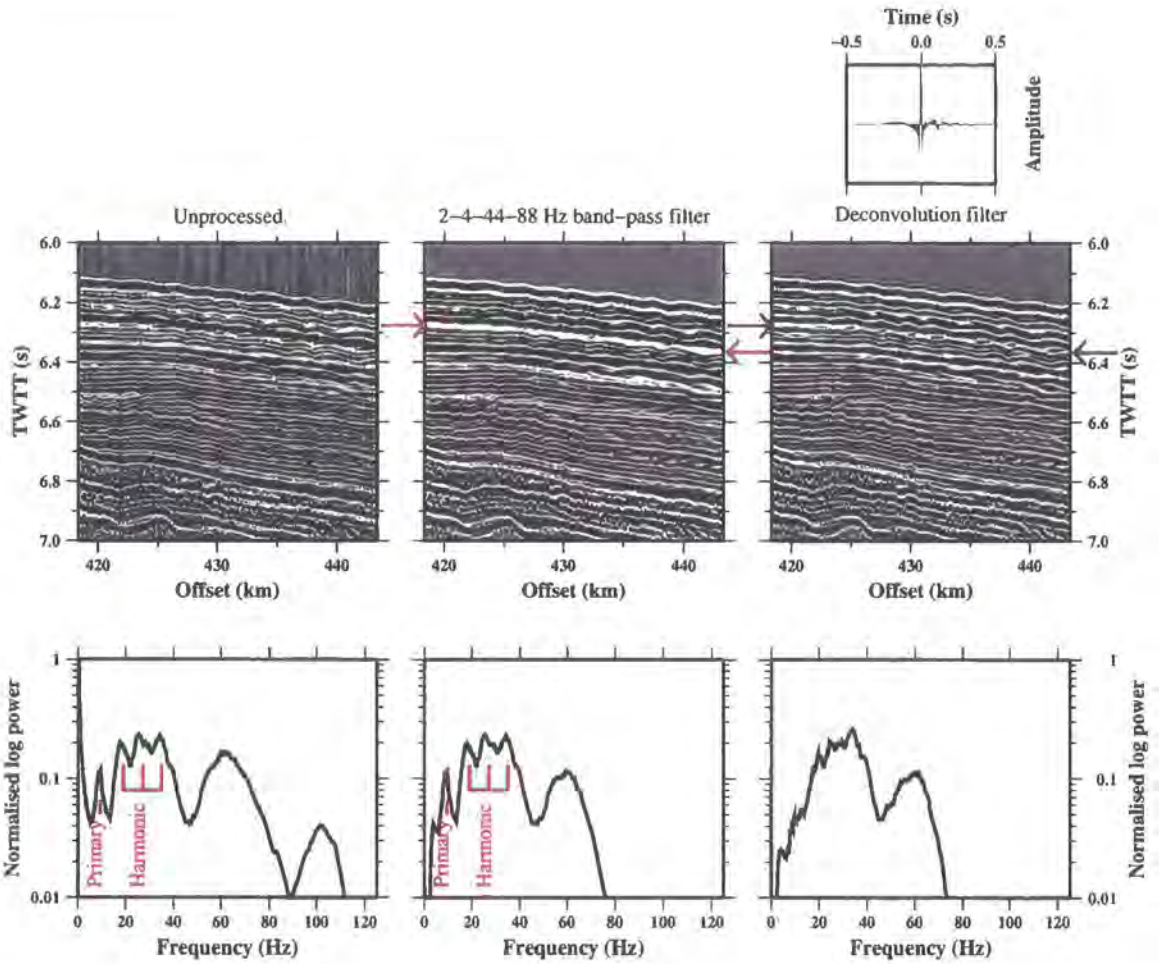


**Figure 2.10**: Results of deconvolution filter testing on Profile D. Data, stacked using an NMO correction of 1.5 $kms^{-1}$, are shown (right) following the application of a deconvolution filter (topmost right). For comparison, the same data are shown unprocessed (left) and with a 2-4-44-88 Hz band-pass filter (centre) applied. The resultant frequency spectra are also shown (bottom), normalised to the maximum power of the unprocessed data. With no processing applied the frequency spectrum contains a significant amount of low frequency noise, a primary peak at 9 Hz and several harmonics. Following application of a 2-4-44-88 Hz band-pass filter the frequency spectrum still contains the harmonics. However, the noisy high and low frequency data have been removed. Following application of the deconvolution filter the harmonics are no longer present, although the primary peak is diminished. MCS data with either band-pass filtering or deconvolution applied appear cleaner, with brighter reflections than the unprocessed data. A clear secondary arrival seen in the band-pass filtered data (red arrows) is removed by the deconvolution filter showing the underlying reflection events (blue arrows).

tertiary) peak within the stacked data, which the deconvolution filter removes (blue arrows), revealing the underlying reflection events.

### 2.4.3.5 Velocity analysis

A combined approach of semblance analysis and constant velocity stacks (CVS) was adopted for velocity analysis. The semblance approach produced a colour image of event coherence, on a velocity-time plot, from which both the best stacking velocity and an

estimate of the range of suitable stacking velocities could be estimated. In contrast, the CVS approach required the comparison of several stacks on several screens in order to estimate these two values. Thus, the semblance approach provided the clearest and quickest method for velocity picking and was primarily used in preference to CVS.

Semblance plots (Figure 2.11) were calculated from supergathers comprising five adjacent CMPs. Each plot was made at regular separations of no more than 120 CMPs (3 km) to ensure that all reflectors, even those of limited extent, were stacked as well as possible. Within regions of poor subsurface reflector continuity, such as the rapid changes in seafloor bathymetry (*e.g.* Profile D, 370-390 km offset, Figure 2.7), picks were made at shorter intervals of 40 CMPs (1 km). Interval velocity inversions were considered to be geologically unrealistic in this geological setting, due to cementation and the pressure increase with depth (Gardner *et al.*, 1974). This assumption is supported by borehole data over the Demerara Plateau (Erbacher *et al.*, 2004) which shows that the porosity decreases and the velocity increases with depth. Thus, inversions were avoided in an attempt to further constrain and minimise errors on the velocity picks. The seafloor reflection was assigned a 1.5 $kms^{-1}$ stacking velocity, similar to that of the sea water through which the reflection event has travelled, and at all locations a stacking velocity pick of 4 $kms^{-1}$ was made at 12 s TWTT, reflecting the probable increase in velocity below the basement reflector. Given the high density of velocity picks, a smoothing filter was applied to the final velocity model. Multiple passes of velocity analysis were applied in areas of significant dip, or regions of high amplitude multiples, where multiple suppression and/or dip moveout techniques were applied beforehand.

The velocity models created from the semblance picks were designed to produce a 'clean' image of the subsurface reflectors to aid interpretation. However, the velocities derived in this manner are only an approximation to the interval velocities, especially for higher velocity, deeper layers. The accuracy can be improved by use of longer seismic streamers which image reflections at greater moveout from which velocities are picked. However, for cruise D275, only a 2.4 km streamer was available but this was deemed acceptable given that the main aim of MCS data acquisition was to image the sediment column and the structure and geometry of the basement surface.

#### 2.4.3.6 Normal moveout

To enable optimal stacking of coherent reflections, corrections were required to flatten time-offset reflection hyperbola within CMP gathers. For the majority of the profiles, where reflector dips are $<15^{o}$, NMO corrections were applied using the stacking velocity

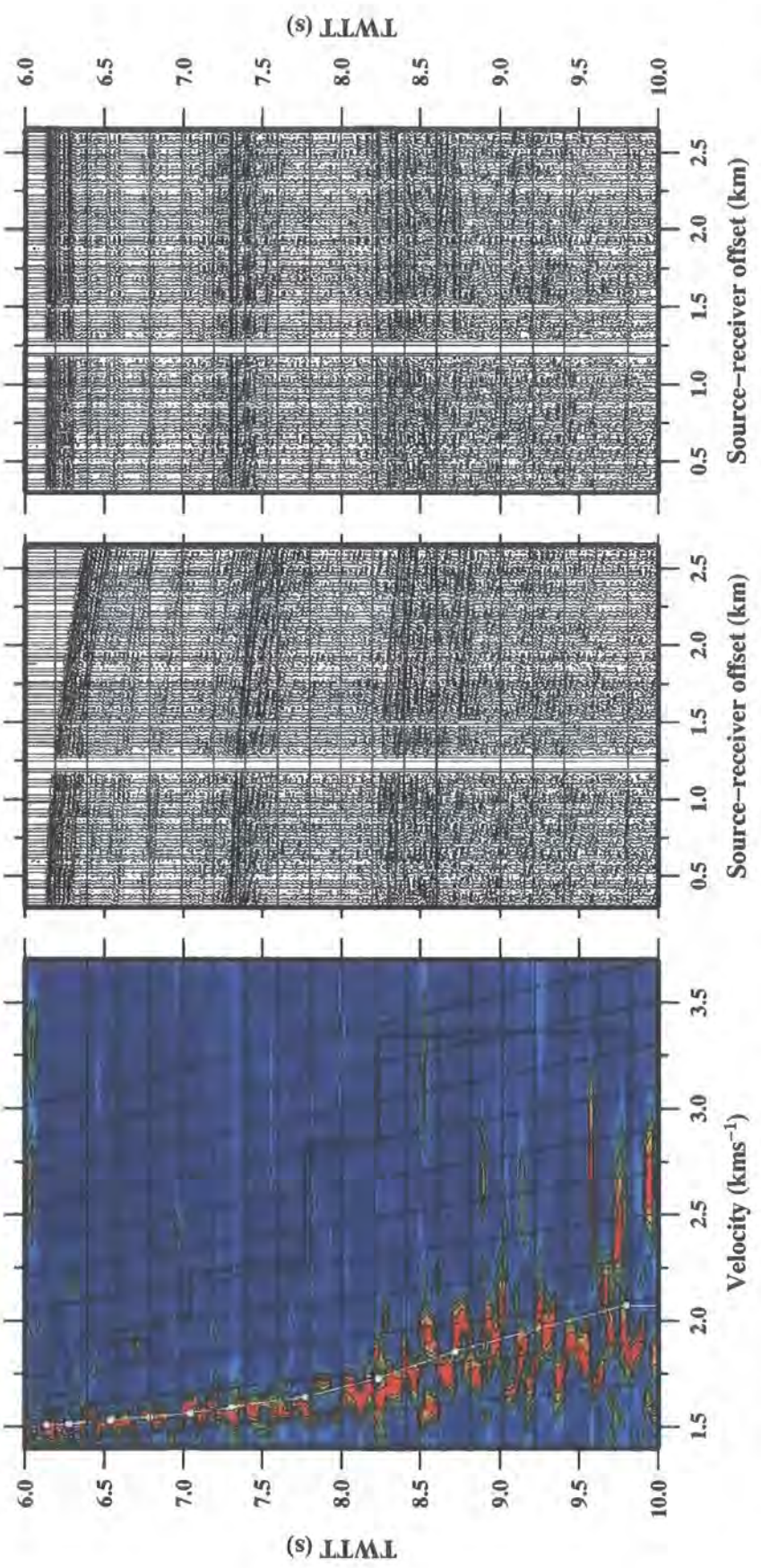


**Figure 2.11**: Velocity picking using a semblance plot. (Left) Semblance plots, created from supergathers of five adjacent CMPs, were used to pick velocities from the MCS data. Stacking velocities were chosen (white line) such that an NMO correction would flatten (right) the hyperbolic (centre) primary reflections. The traces shown are those of a supergather centred at CMP 10404, from the deep water region of Profile D. The corresponding interval velocity is also shown (black line)

fields resulting from velocity analysis. However, for the steeply-dipping region of Profile A, dip moveout (DMO) was also applied.

#### 2.4.3.7 Dip moveout

If the dip of the reflecting interface becomes greater than 15° the flat layer assumptions within NMO are no longer valid. Thus application of NMO, followed by stacking, leads to smearing of reflection events. In this case DMO (Deregowski, 1986) is used in conjunction with NMO. DMO is a partial migration process which corrects the picked velocities, allowing greater confidence in subsequent stacking and zero-offset migration.

This process was necessary at the landward end of Profile A where the seafloor and the stratified sediment interfaces all shallow, in the TWTT section, toward the continent. Thus the profile was processed in three sections: shallow water; steep sloping seafloor; and deep water. DMO was applied in addition to NMO only on the sloping section. Here, after DMO binning into 100 m bins, the data were NMO corrected, DMO corrected using a constant 1.5 $kms^{-1}$ velocity, NMO correction was removed and these data were used for $2^{nd}$ pass velocity analysis.

#### 2.4.3.8 Multiple suppression

Primary seafloor reflection events are caused by seismic energy travelling from the source to the seafloor and back to the receiver. In contrast, seafloor multiples correspond to a source-seafloor-sea surface-seafloor-receiver path. Thus, these long-path multiples pass through the water column twice (or three or four times etc.) before being recorded by the MCS streamer. Multiples tend to be of high amplitude and appear on the seismic section at twice (or integer multiples of) the TWTT of the seafloor reflection. Peg-leg, short-path multiples are of a much lower amplitude and, thus, do not have such a significant impact on the data quality and can be largely removed by deconvolution. Where multiples arrive at the same time as primary reflection events, the primary is often obscured, limiting event recognition.

In the deep water sections of each profile (seafloor reflection observed at >5 s TWTT, *e.g.* oceanward of 280 km on Profile A and 390 km on Profile D – Figure 2.7) where multiples arrive after all primary reflections, the multiples do not impact on data quality and do not necessarily need to be removed prior to interpretation. However, in shallower water the multiples are clearly visible where primary reflections are expected (this effect is most clear between 240 km and 280 km on Profile D – Figure 2.7). Thus, the clarity of

sedimentary events within the MCS data is greatly affected, particularly landward of 280 km on Profile A and 230 km on Profile D.

To address this problem three multiple suppression techniques were tested on the data prior to stacking, which in itself is an effective tool in removing multiples where moveout is large and velocities are picked accurately:

- *f-k* filtering, in which 90% NMO is applied to CMP data prior to filtering in the *f-k* domain. The NMO under-corrects the primary reflections and over-corrects the multiples, which will then appear in distinct areas of the *f-k* spectrum. The *f-k* technique was not very successful, most likely because the data does not have a significant moveout. Thus the separation between primaries and multiples in the *f-k* domain is small. The filter is therefore difficult to design without either removing too much primary energy or too little multiple energy;

- Radon transform, in which multiples are modelled and then removed from the data. Radon techniques were most effective on the deep water parts of Profile A data, where multiples obscured possible sub-basement reflectors. At the landward end of Profile A, in the shallow water and over the steeply sloping seafloor, multiples could not be distinguished from primary reflections and, thus, multiple suppression was not applied. In these regions stacking alone was the preferred method of multiple suppression, using DMO to improve the accuracy of velocity picking. In deep water areas, a parabolic Radon filter was applied using 121 p-values from -150 to 50 ms, to remove down-dip energy from the CMP gather. This technique was effective at removing the down-dip energy at large source-receiver offset (Figure 2.12), although a significant amount of energy was retained within the short offset traces. This energy was removed using a near trace mute picked to operate on the multiples and not the primaries; and

- Surface related multiple elimination (SRME), in which the arrival times of seafloor multiples are predicted from the seafloor reflection arrival time. The technique is less dependent than the other two on moveout and was most effective on the sediments of Profile D between 200 km and 330 km (Figure 2.13). In this method water bottom picks are used by the 'wave equation multiple rejection' *ProMAX* module to remove seafloor multiples using a maximum convolution distance of 3 km, a trace spacing of 25 m and a least-squares filter.

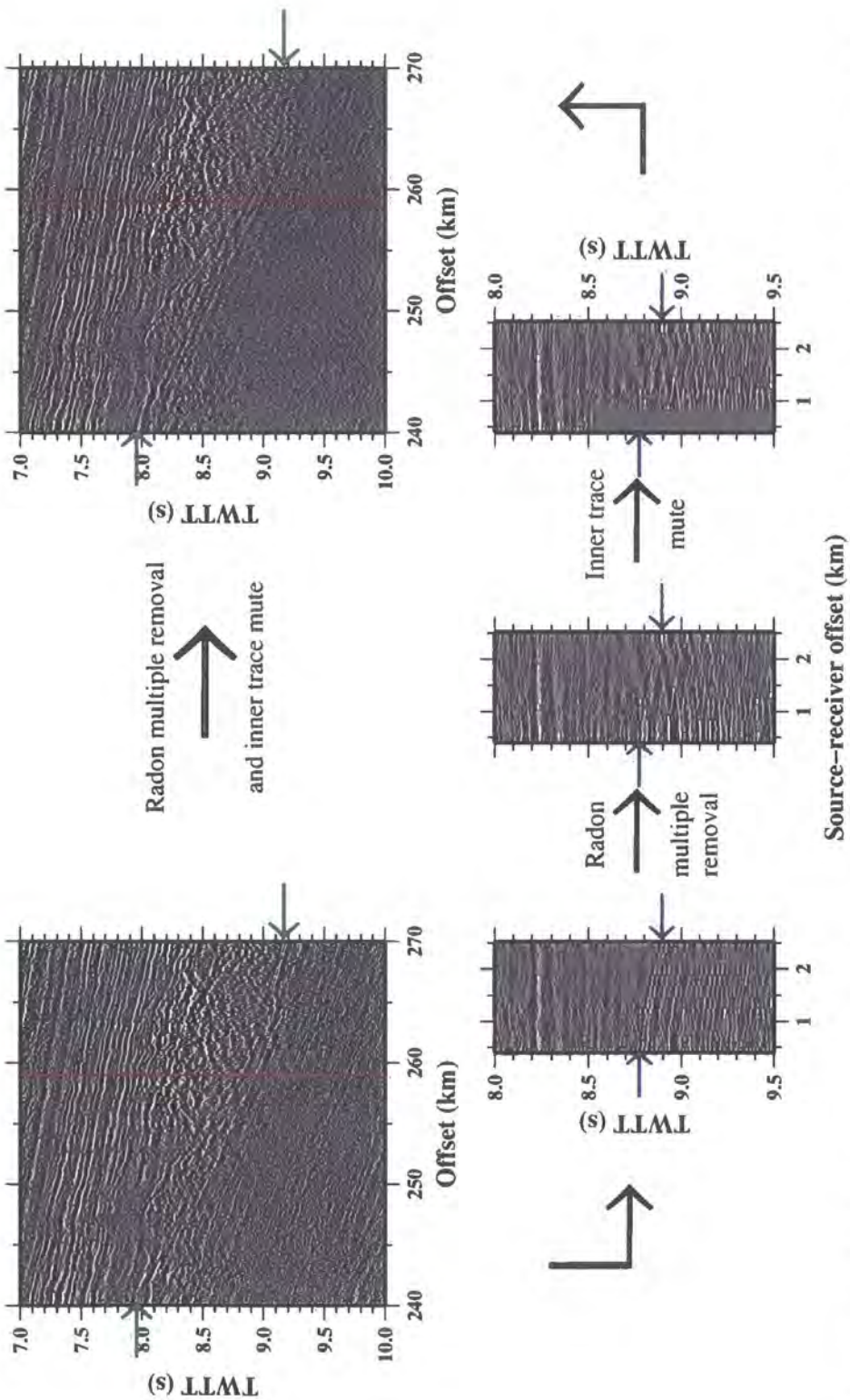


**Figure 2.12**: Multiple suppression testing for Profile A. (Top) CMPs 4140 to 5340, showing multiple energy within the stacked section before (left) and after (right) the application of a Radon transform and an inner trace mute. The seafloor multiple is highlighted (green arrows) and shows a large amplitude reduction, but falling short of complete removal. (Bottom) CMP gather 4900 (red line on top panels) showing the application of processing to a single gather. The gather has been NMO corrected using semblance picked velocities so that primaries should appear horizontal and multiples should dip downwards at larger offsets. The seafloor multiple is highlighted by the blue arrows. The panels show no de-multiple processing steps applied (left), application of the Radon transform (centre) and application of both Radon transform and inner trace mute (right).

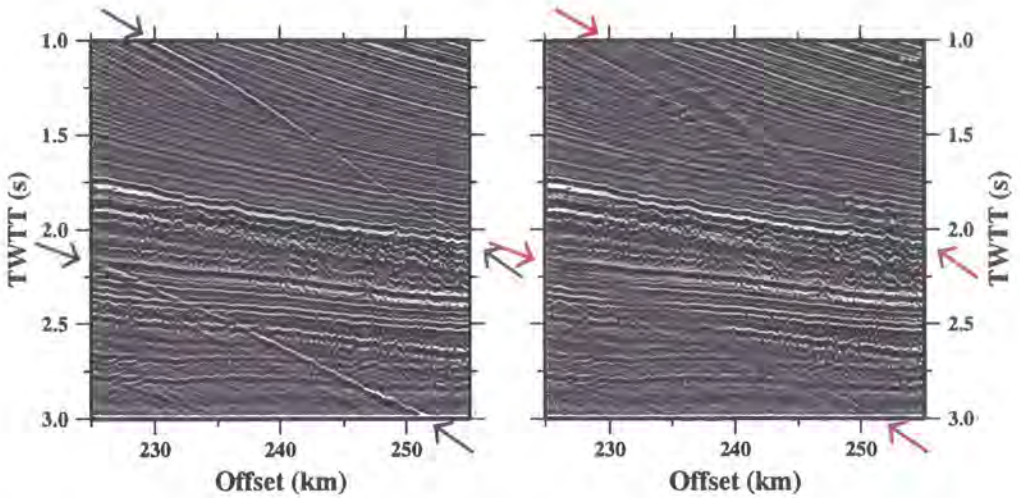


**Figure 2.13**: Multiple suppression testing for Profile D. CMPs 3266 to 4466 with (right) and without (left) SRME applied. The strong multiple events dipping from left to right (left panel – blue arrows) are suppressed by SRME. However, the technique also tends to remove some primary energy (right panel – red arrows) giving a smeared appearance.

#### 2.4.3.9 Stacking

The ~24 fold data were sorted into 25 m CMP bins and stacked following NMO correction using the final stacking velocity field, which, following conversion to interval velocity using the Dix equation (Dix, 1955), is shown in Figure 2.14. The stacked sections for Profiles A and D (Figure 2.15) when compared with the brute stacks (Figure 2.7) show a clear improvement in the clarity of reflection events primarily due to the removal of noise. Deconvolution, multiple removal and NMO correction with deliberately chosen stacking velocities have also improved the quality of the section.

#### 2.4.3.10 Migration

Kirchoff migration techniques were used to correct for scattered and diffracted arrivals, in particular from the rough basement surface in the deep basin. A Kirchoff post-stack time migration gave the best results whilst also being less time consuming than pre-stack methods. Parameter testing determined that a 4 km aperture migration was most effective for the ACE data. The final migrated sections are displayed in Figures 2.16 and 2.17 and interpreted in Section 2.6. Enlarged versions of the data sections are provided in Appendix B. The effect of migration on the Profile A basement reflection is shown in Figure 2.18.

Depth conversion and depth migration techniques were applied to selected data, but resulted in severe distortion of the stratigraphic reflections. Distortion was particularly

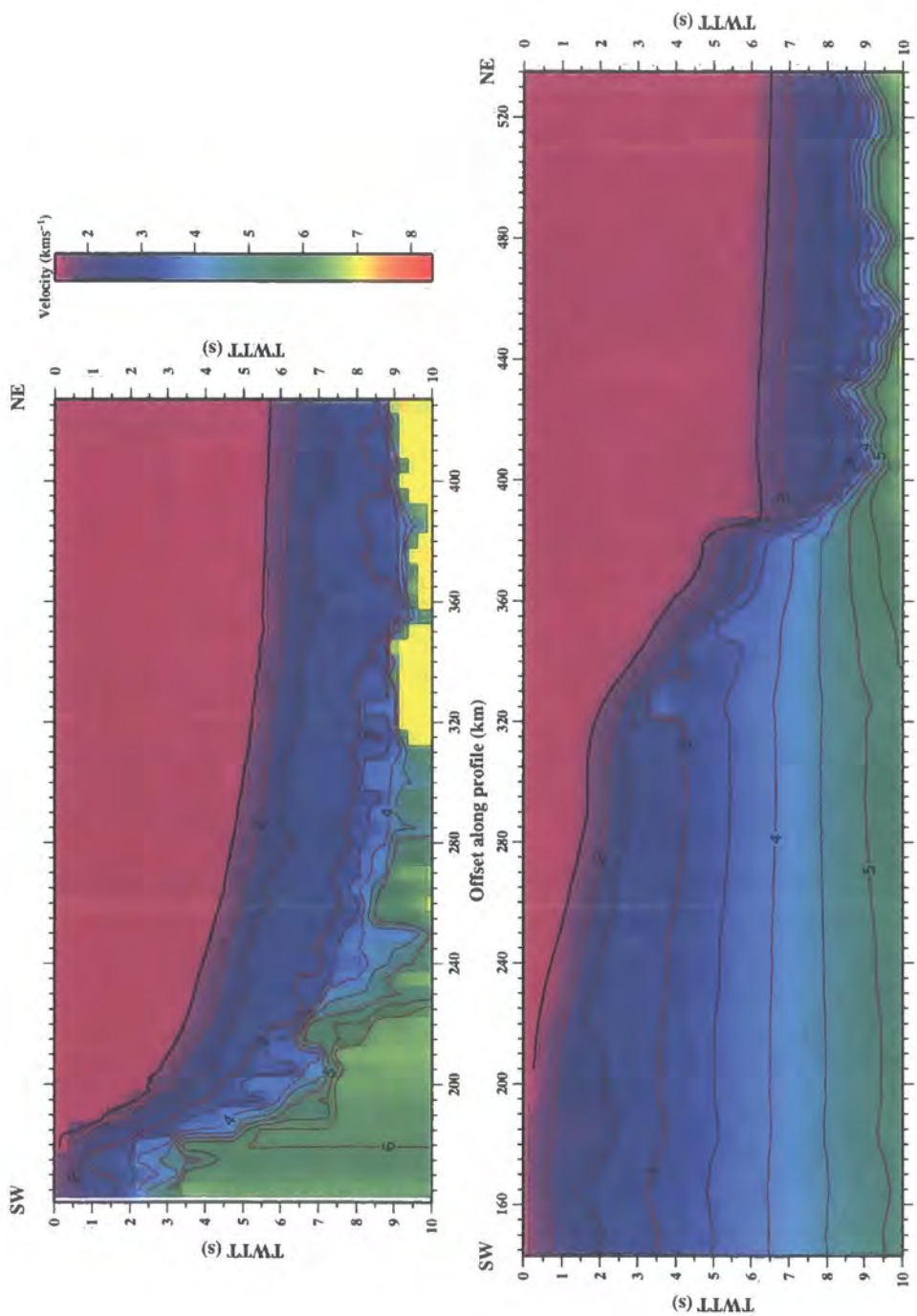


**Figure 2.14**: Interval velocity fields for Profile A (top) and D (bottom). Stacking velocity fields picked from semblance plots (Figure 2.11) were smoothed and converted to interval velocity fields using the Dix equation (Dix, 1955). Seafloor (black line) and 0.5 $kms^{-1}$ isovelocity contours (red) are plotted.

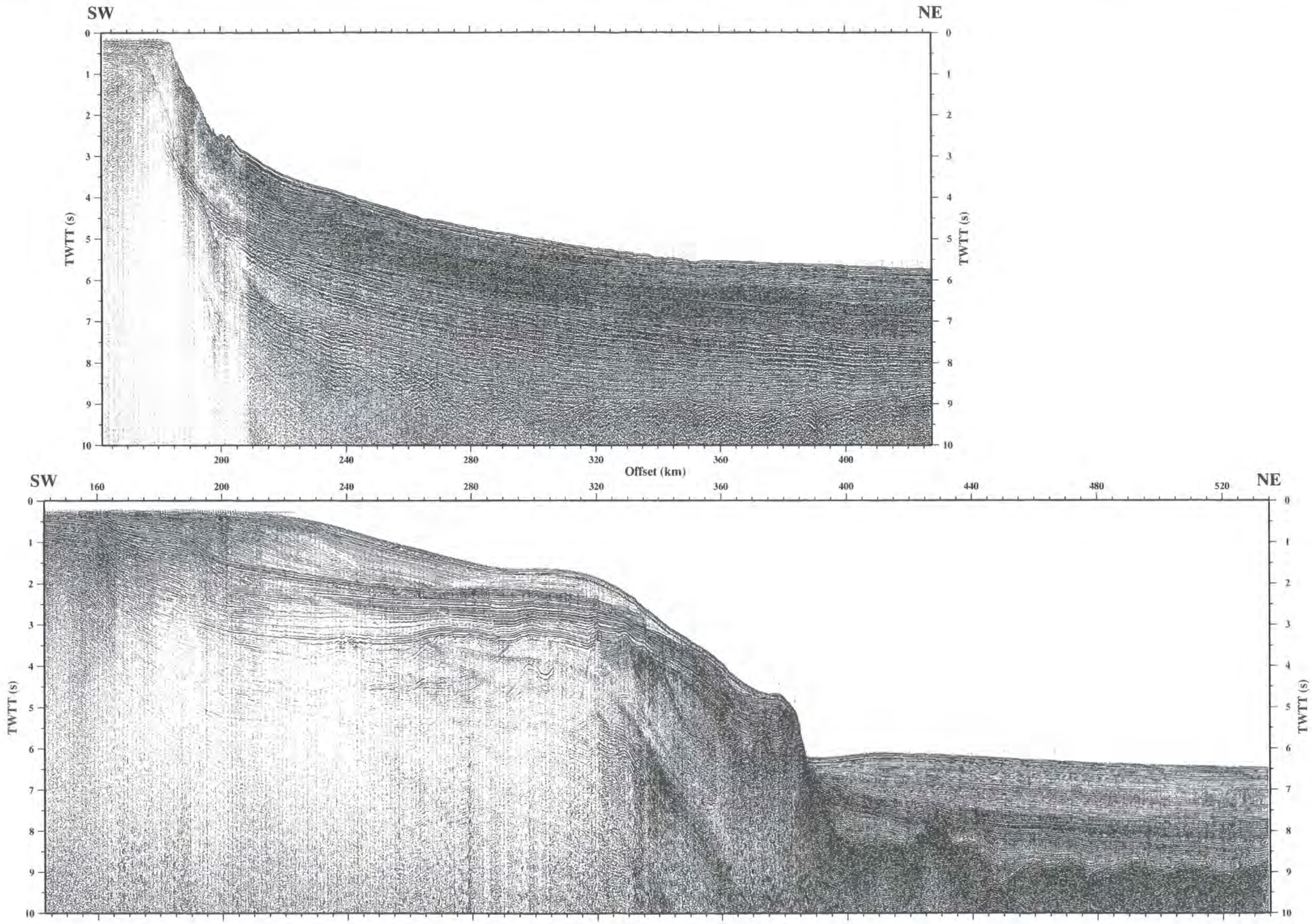


**Figure 2.15**: Final stacked sections for Profiles A (top) and D (bottom) with locations shown in Figure 2.1. Pre-stack processing has significantly improved the clarity of reflection events within the sediment column and for the basement, compared to the brute stacks (Figure 2.7).

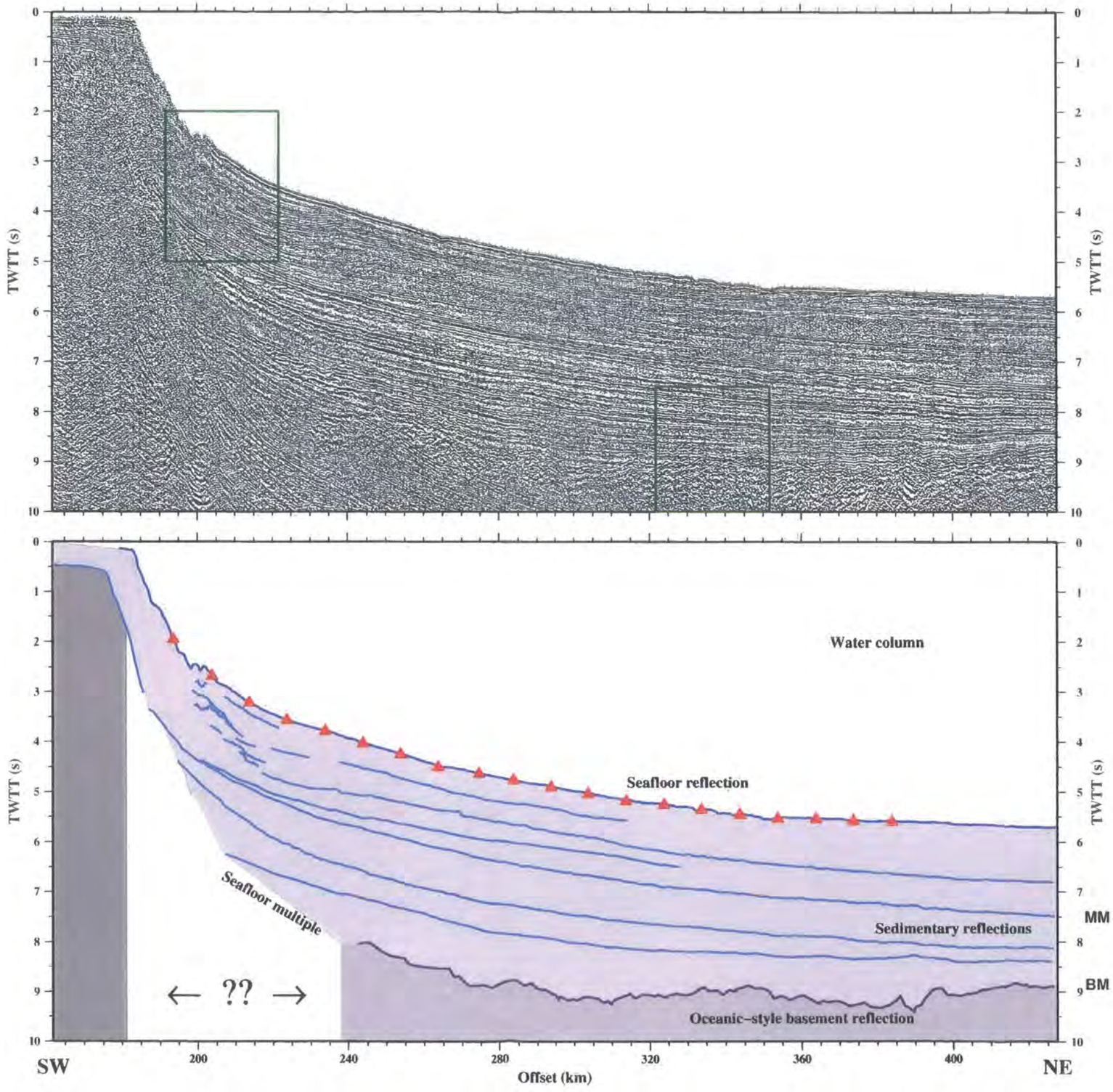


**Figure 2.16**: (Top) Time-migrated section of ACE Profile A. See Figure 2.1 for location. (Bottom) The corresponding interpretation divides the crust into three zones: (1) continental (dark grey); (2) oceanic (medium grey); and (3) sedimentary (light grey). Unassigned regions are labelled '??'. The main sedimentary reflections are also shown (light blue) beneath the seafloor reflection (dark blue) and above the basement reflection (purple). The intra-sedimentary mid-Miocene reflection is labelled MM and the basement BM. Red triangles correspond to OBS locations. Enlargements of the green outlined areas are shown in Figures 2.23 and 2.24. There is no evidence of a Moho reflection event, or the SDR sequences observed at volcanic margins. The tilted basement fault blocks and graben structures commonly associated with rifting are also absent.

C.J. Greenroyd, PhD Thesis, University of Durham, 2007

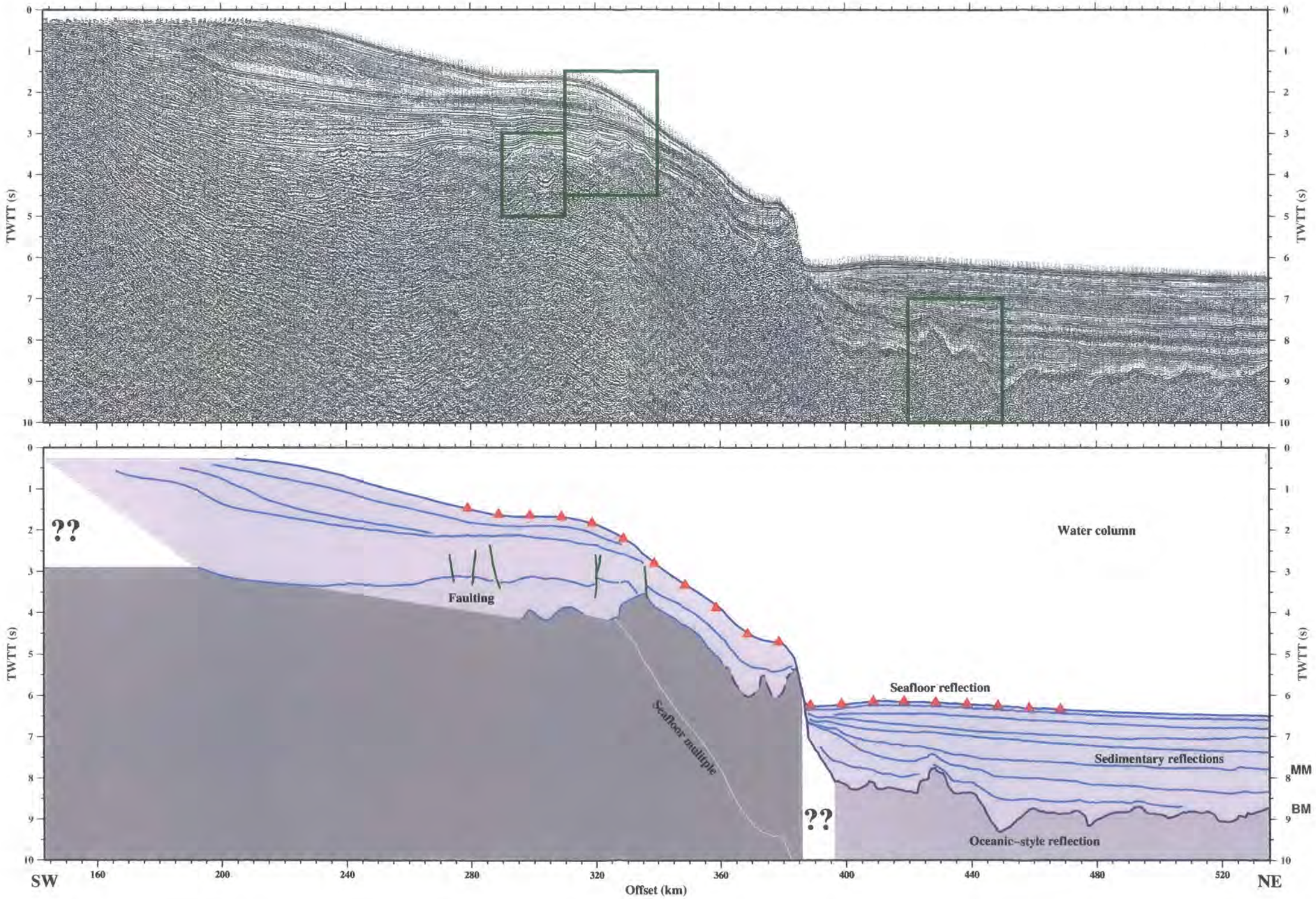


**Figure 2.17**: (Top) Time-migrated section of ACE Profile D. See Figure 2.1 for location. In the same way as Profile A, the corresponding interpretation (bottom) divides the crust into three zones: (1) continental (dark grey); (2) oceanic (medium grey); and (3) sedimentary (light grey). Reflections are coloured and annotated similarly to Figure 2.16. Enlargements of the green outlined areas are shown in Figures 2.25, 2.26 and 2.27. There is no evidence of a Moho reflection event, or the tilted basement fault blocks and graben structure commonly associated with rifting. The basement reflection between 360-385 km offset (dashed purple), interpreted as lying within the continental crustal region, is atypical of the indistinct basement observed further landward. Hence this region is tentatively interpreted as comprising a degree of intrusive volcanics.

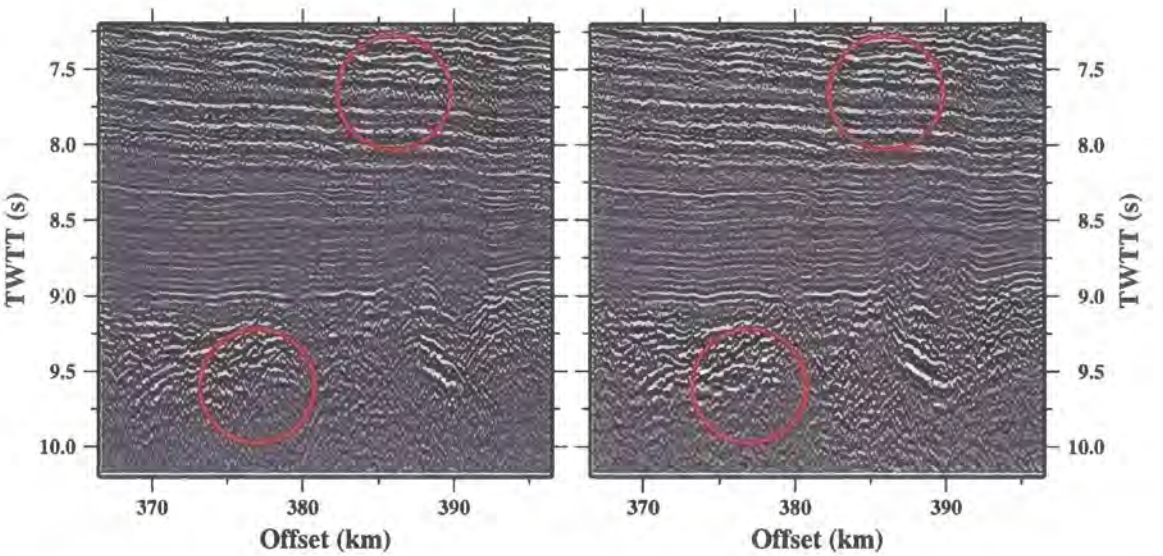


**Figure 2.18**: Results of migration. CMPs 9200 to 10400 from Profile A with (right) and without (left) post-stack Kirchoff migration applied. The migration removes the most sharply dipping diffracted events, although the improvement is limited. The result is best observed for the diffracted energy within the uppermost sedimentary layers on the panels (7.2-8.0 s TWTT) and within the basement reflections (9.0-9.7 s TWTT) (red circles).

apparent at depth, most likely due to the poor resolution of the velocity models at depth, a result of the small moveout of reflections across CMP gathers when using a relatively short MCS streamer. The small relative moveout restricts the accuracy of velocity picking to within 0.25-1.00 $kms^{-1}$. Thus final data sections are all displayed as TWTT sections.

## 2.5 Other geophysical datasets

Several other geophysical datasets have been acquired over the Demerara Plateau and French Guiana margin (Figure 2.19):

- Industry wells Sinna Mary 1 (SM1) and FG2-1 (Gouyet *et al.*, 1994);
- Industry MCS data from the R/V *Meteor* 49-4 expedition (Erbacher *et al.*, 2004);
- Borehole data from ODP sites 1257 to 1261 (Erbacher *et al.*, 2004); and
- Bathymetry, backscatter imagery, MCS, 3.5 kHz, gravity and magnetic data from the Guyaplac survey (F. Klingelhöfer, W. Roest, *pers. comm.* – *e.g.* Loncke *et al.*, 2006).

### 2.5.1 Industry data and ODP borehole sites

Several short industry MCS profiles and five ODP boreholes are located within the region 8.5° to 9.5°N, 53.5° to 55°W (Figure 2.19 – Erbacher *et al.*, 2004).

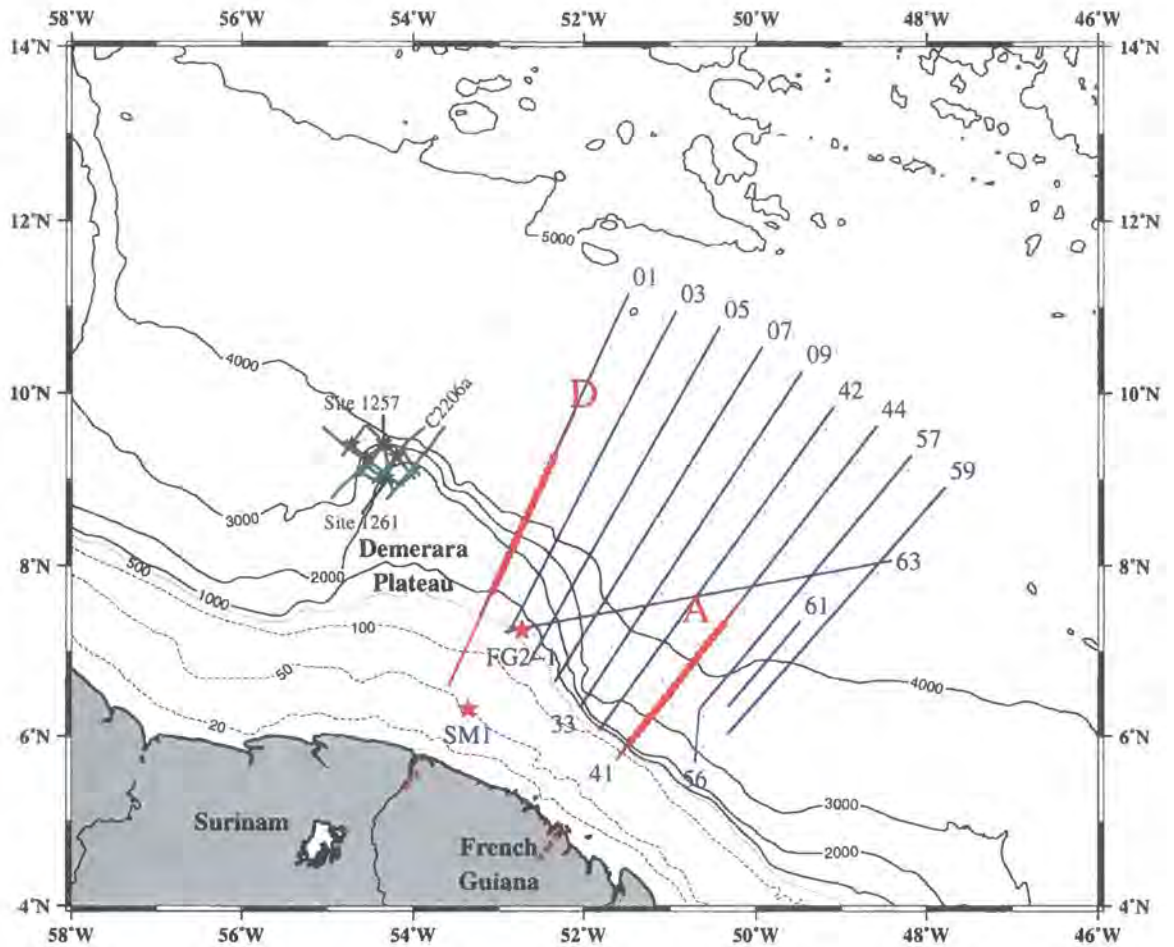


**Figure 2.19**: Location of other MCS profiles over and in the vicinity of the Demerara Plateau. Cruise D275 (red), R/V *Meteor* 49-4 industry data (green – Erbacher *et al.*, 2004), Guyaplac data (blue – F. Klingelhöfer, W. Roest, *pers. comm.*), ODP sites 1257 to 1261 (blue stars – Erbacher *et al.*, 2004) and industry wells SM1 and FG2-1 (red stars – Gouyet *et al.*, 1994) are shown. Red dots and triangles correspond to ACE OBS and land station locations respectively. Seafloor bathymetry is contoured similarly to Figure 1.10.

Erbacher *et al.* (2004) note that the Demerara Plateau is characterised by five key MCS reflections (O, A, B, B' and C) which partition the seismic stratigraphy into four major units (1-4) and one minor unit (Q). Unit Q is rarely present and is not discussed below. The five boreholes are used to interpret this seismic stratigraphy which is >1 km thick at ODP Site 1261, thinning towards the edge of the plateau. Despite the relatively wide areal distribution of the boreholes, all show a similar pattern of sedimentation (Figure 2.20), indicating that the stratigraphy may be consistent across the plateau.

Directly beneath the seafloor, Unit 1 is identified as semi-lithified sediment which thins towards the edge of the Demerara Plateau. The unit is Miocene-Pliocene nanofossil ooze and is seen in the seismic sections only at Site 1261, where it spans 415 ms. Here, Unit 1 consists of a well-defined set of coherent reflection events of varying amplitudes with a

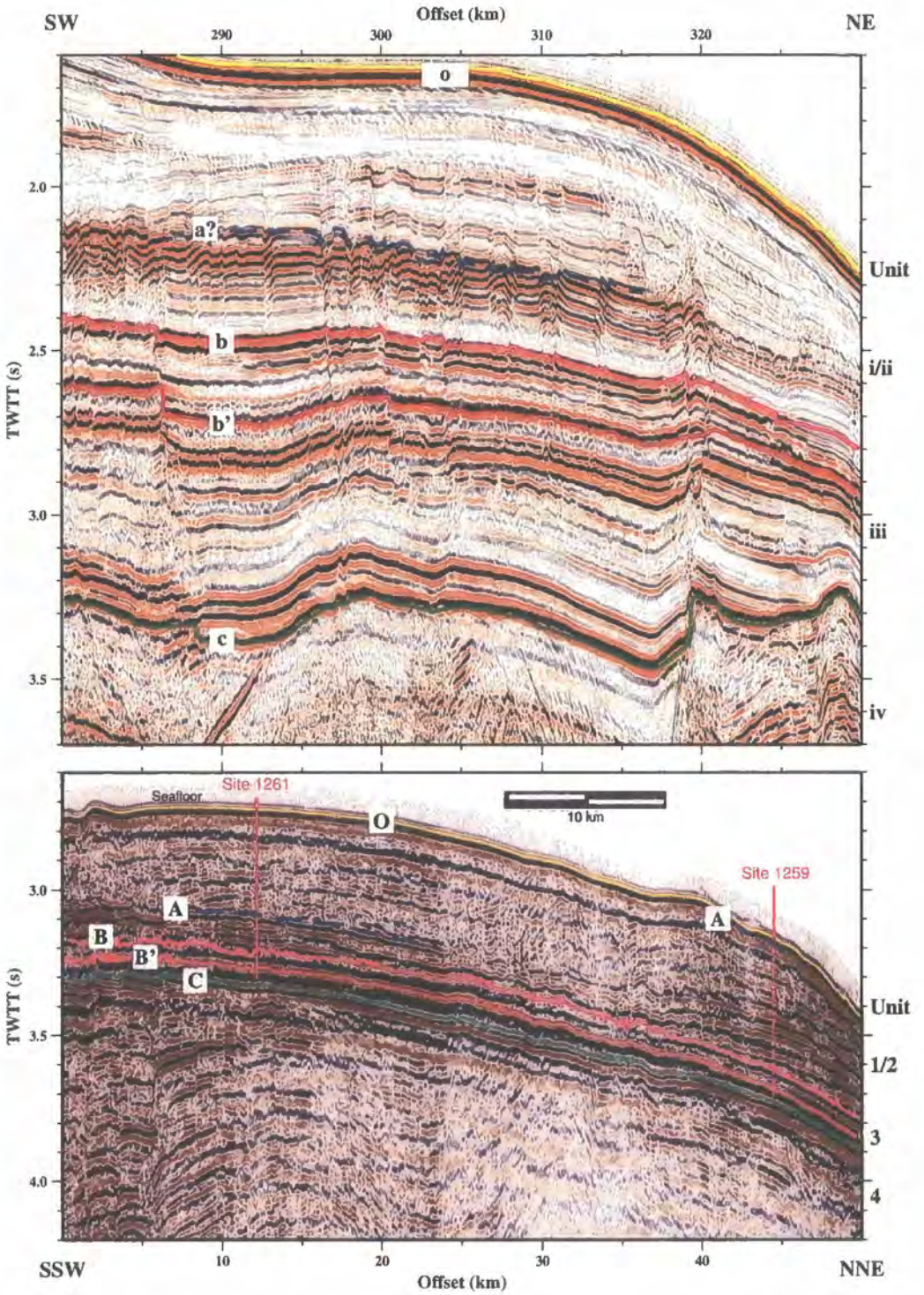


**Figure 2.20**: Seismic stratigraphic reference used as a basis of interpretation for the ACE MCS data. MCS data acquired along Profile C2206a (bottom) (Erbacher *et al.*, 2004) and cruise D275 Profile D (top). The profiles are plotted at the same scale. The locations of ODP drill sites 1259 and 1261 are shown. Coloured reflections on Profile C2206a, labelled O, A, B, B' and C, are those of Erbacher *et al.* (2004), and the corresponding reflections are interpreted, highlighted and labelled o, a, b, b' and c on Profile D. In addition the sedimentary Units 1-4 are shown on Profile C2206a and corresponding Units i-iv on Profile D. Note that the Erbacher *et al.* (2004) interpretation of sedimentary borehole log data at ODP site 1259 shows a thin layer of Unit 1 and a thick layer of Unit 2 material, whereas that of site 1261 shows the opposite. Hence the precise location of Reflection A (dashed blue) is uncertain and it does not appear to be laterally continuous.

bright reflection capping an incoherent layer in the lowest 50 ms of the unit. At the other sites the unit is too thin to be resolved in the seismic data, although a thin veneer of Unit 1 type material is observed in borehole 1259. Unit 1, therefore, is not of consistent thickness across the study area, as highlighted by Figure 2.20.

Reflection A is presumed to be a lower Miocene erosional unconformity which separates Unit 1 from Unit 2, a mainly Eocene-early Miocene nanofossil chalk sequence with Reflection B at its base. Unit 2 ranges in 'thickness' at the ODP sites, from 160 to 495 ms. The unit shows an incoherent reflection character which Erbacher *et al.* (2004) interpret as either a disturbed sediment package or the effect of side echoes from local topography. The degree of lithification within the unit may reflect variations in clay content.

Reflection B marks the top of Unit 3 and is hummocky on a local scale, probably cut by channels. The uppermost section of Unit 3, named Unit 3a, contains several high-amplitude reflections and then a thin transparent zone to the top of Reflection B'. The unit appears flat-lying and ranges in 'thickness' between the boreholes within the range 40-160 ms. Reflection B' lies within Unit 3 and represents the top of a black shale sequence. The presence of Type II kerogen within the shales indicates a marine source for the organic matter.

Reflection C is defined as the base of the black shales with Unit 4 beneath, which consists of Albian-age claystone, clayey siltstone and sandstone. Most of the acoustic energy is lost below Reflection C. At Site 1257 the reflections below Reflection C appear folded into a possible small anticline which contacts the reflection as an angular unconformity.

Dating of borehole cores suggests that sedimentation rates have varied during the last ~110 Myr. In the late Cretaceous deposition occurred at 3-9 m $Myr^{-1}$, increasing markedly across the K-T boundary to 7-15 m $Myr^{-1}$ during the Palaeocene to mid-Eocene, with deposition rates having a pronounced 20-50 kyr periodicity (Erbacher *et al.*, 2004). Recent sediments are generally too thin to obtain a good estimate of sedimentation rate. However, at Site 1261 sedimentation rates of up to 65 m $Myr^{-1}$ in the late Miocene-early Pliocene are observed.

Industry well SM1 reached the basement at a depth of 2104 m whereas well FG2-1 terminated in basaltic lava flows. These wells guide the regional interpretation by Gouyet *et al.* (1994) of the evolution of the Demerara Plateau (Section 1.3.1.1).

### 2.5.2 Guyaplac

The Guyaplac survey was conducted over the French Guiana continental margin during May-June 2003 as part of the French Extraplac (*e.g.* Loncke *et al.*, 2006) programme

whose goal was to establish the extent of the French Guiana exclusive economic zone. During this cruise, bathymetry and 3.5 kHz backscatter imagery, MCS, gravity and magnetic data were acquired along fourteen profiles (Guyas 01, 03, 05, 07, 09, 33, 41, 42, 44, 56, 57, 59, 61 and 63) which combine to produce ten margin transects, oriented northeast-southwest, and one section oriented east-west (Figure 2.19). The Guyaplac data acquisition was tuned to MCS alone and, hence, is of a higher dominant frequency then the ACE data. Thus, the Guyaplac data are better able to image the detail of the sediment column, at the expense of the deeper structure, and are therefore complimentary to the ACE data.

The northernmost (Guyas 01) and southernmost (Guyas 59) profiles run along the border between French Guiana-Surinam and French Guiana-Brazil territorial waters. Furthermore, Profiles Guyas 44 and Guyas 01 are coincident with ACE Profiles A and D respectively. Hence the Guyaplac MCS data comprise a pseudo-3D structural reference framework extending from ACE Profile D to, and ~100 km beyond, Profile A, and are used to aid interpretation of the ACE data and assess along-strike continuity of structure between the ACE profiles.

The Guyaplac data were supplied by Ifremer (F. Klingelhöfer and W. Roest, *pers. comm.*) and corresponding interpretations are by the French Petroleum Institute (IFP). Two data sections are reproduced here. The first, Profile Guyas 63 (Figure 2.21), is chosen because it is the only profile to run approximately east-west. Hence it intersects most of the other profiles. The second, Profile Guyas 03 (Figure 2.22) lies parallel to ACE Profile D and is the most westerly profile to intersect Guyas 63.

The sedimentary stratigraphy observed within the Guyaplac data is broadly divided into two main regimes:

- the abyssal plain which corresponds to all the sediments observed on Profile A and those oceanward of 385 km offset on Profile D. The uppermost 1.0-1.5 s TWTT of these sediments are interpreted as Palaeogene-Neogene in age and the underlying 1.0-1.5 s TWTT as upper Cretaceous-Palaeogene; and

- the Demerara Plateau, corresponding to the sediments landward of 385 km offset on Profile D. Here, five stratigraphic units are identified which are (from shallowest-deepest): upper Miocene-Pliocene; Oligocene-lower Miocene; Eocene; Cenomanian-Maastrictian; and Albian.

Some faulting is identified within the sections, primarily on the Demerara Plateau, although also in the abyssal sediments. More extensive faulting is observed at the basement surface, which shows several sharp offsets in TWTT. In addition, several regions

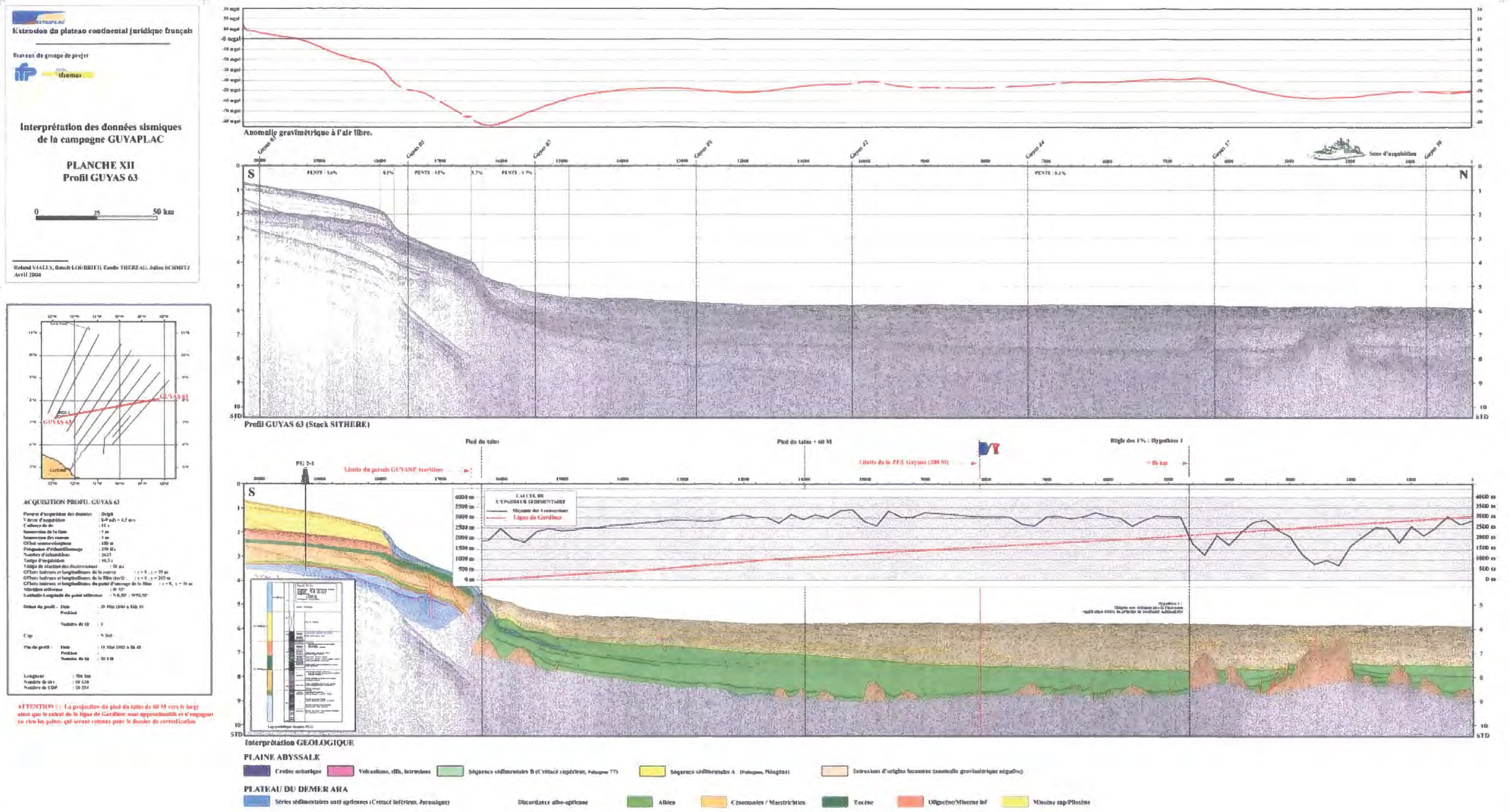


**Figure 2.21**: Guyaplac MCS Profile Guyas 63. This profile runs east-west, intersecting with several of the other Guyaplac profiles (inset and Figure 2.19). The MCS data image the sediment column across the entire profile and the basement at the oceanward end. In addition, an interpretation, performed by IFP within the Extraplac programme, is shown (bottom) and suggests that the sediment column comprises two major sequences oceanward of the toe of the Demerara Plateau compared with up to six landward. The MCS data does not image the basement across the whole section and IFP do not interpret any oceanic crust along the profile. The observed gravity anomaly is also shown (top).

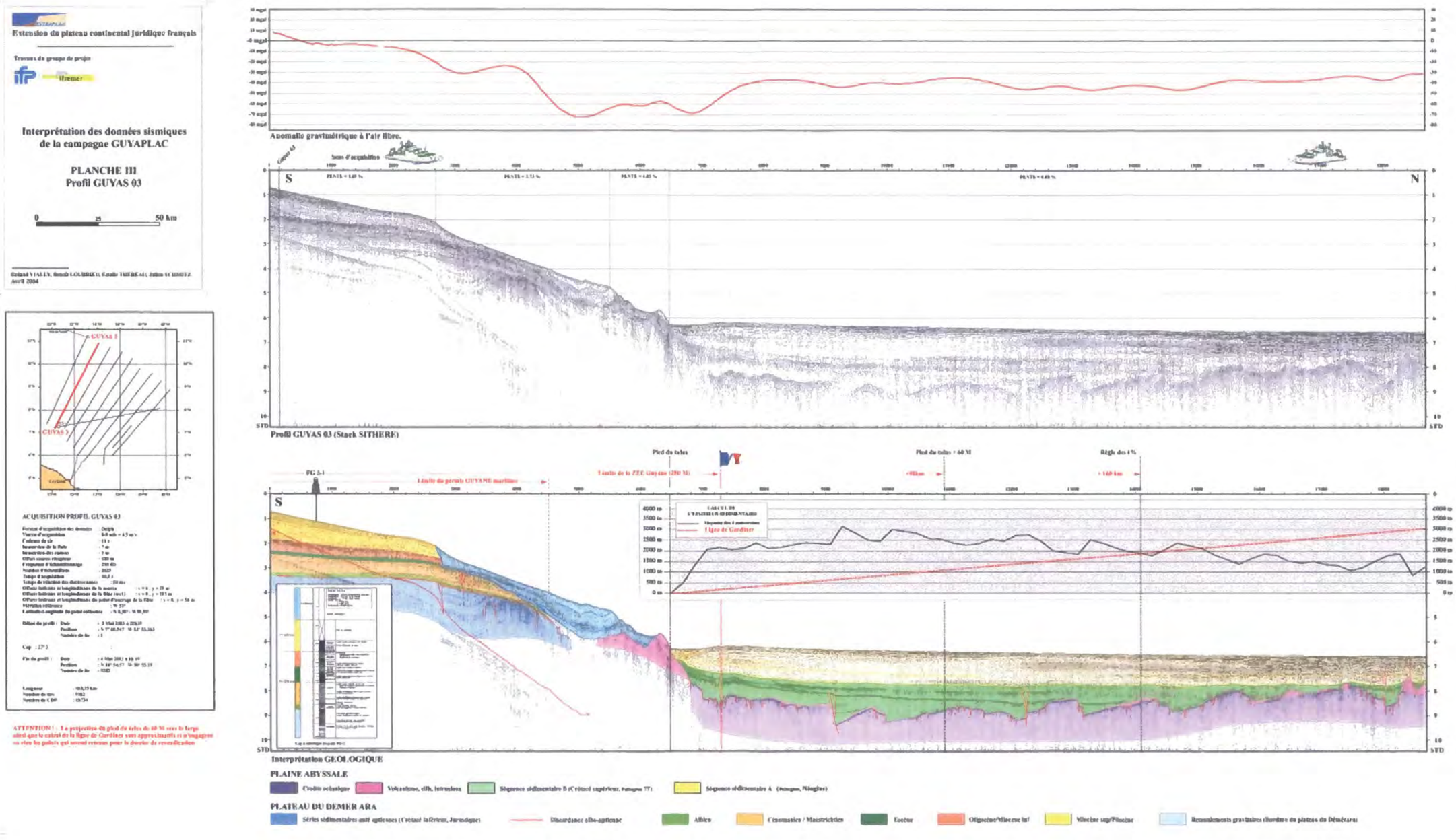


**Figure 2.22**: Guyaplac MCS Profile Guyas 03. The layout of the figure is described in Figure 2.21. This profile crosses the Demerara Plateau to the southwest of, and lies parallel to, ACE Profile D (inset and Figure 2.19). The data image basement across the entire profile and the corresponding interpretation suggests that oceanic crust is observed oceanward of the toe of the Demerara Plateau, which is interpreted as comprising sediments overlying volcanic sills and intrusives. Significant faulting of the oceanic crust is also observed, resulting in a rough basement surface.

of basement are interpreted as volcanic sills and intrusions. In particular, the two sharp rises in the basement surface observed at the toe of the Demerara Plateau on Profile D are interpreted as volcanic in nature.

Whilst surveying a wider areal extent than the ACE, the Guyaplac MCS data do not consistently image the sub-sedimentary basement. To the north, Profiles Guyas 01, 03 and 05 clearly image the basement, interpreted as oceanic crust oceanward of ~8 km from the foot of the continental slope. However, further south, the basement is less well imaged. On Profile Guyas 07 basement is first interpreted as oceanic crust ~170 km from the foot of slope and on Profile Guyas 59 no oceanic crust is observed. The basement characteristics observed across these profiles will be discussed in Chapter 5.

## 2.6 Results

In this section the interpretation of Profiles A and D is described. The lithostratigraphic interpretation is based primarily on the ODP results (Erbacher *et al.*, 2004) to the north as these data include seismic stratigraphy, geochemistry, and density and velocity measurements. In addition, the interpretations are correlated against the stratigraphy observed at nearby wells FG2-1 and SM1 which guide the IFP interpretation of the Guyaplac MCS sections.

### 2.6.1 Profile A

The final Profile A reflection section is shown in Figure 2.16, together with its interpretation which divides the profile into three major crustal zones: (1) continental; (2) oceanic; and (3) sedimentary.

The fully processed MCS data image the entire sediment column, from a relatively smooth seafloor down to the top of the basement. The water depth at the most landward end of the profile is ~100 m, and heading oceanward the seafloor deepens quickly (gradients reaching ~13°), to a maximum depth of 4.2 km by the end of the profile.

A 3.5 to 4.5 s TWTT 'thick' sedimentary zone is identified from continuous, stratified reflections and a sedimentary velocity structure with interval velocities ranging from 1.6 to ~3.5 $kms^{-1}$. The interval velocity model (Figure 2.15) indicates a large velocity gradient (~0.8 $s^{-1}$) within the top kilometre below seafloor and a lower gradient (~0.25 $s^{-1}$) in the deeper sediments. Several sedimentary packages are identified in Figure 2.16, each separated by a clear reflection event, some of which can be traced across the entire profile. A significant unconformity (labelled MM in Figure 2.16) is identified from the high ampli-

tude reflection separating sub-parallel reflectors below from those above, which onlap onto the unconformity. This unconformity shows similar characteristics to another identified within the sedimentary stratigraphy of the Amazon Cone to the south (Silva *et al.*, 1999; Rodger, 2007) which has been dated as mid-Miocene in age (Damuth & Kumar, 1975; Braga, 1991). The unconformity therefore separates shallow late-Miocene, Pliocene and Quaternary sediments above from deeper Cretaceous to early-Miocene sediments below. Braga (1991) uses this unconformity to date the onset of Amazon Cone deposition. There is little evidence of post-rift faulting within the sediments far offshore. However, as the dip of the reflections increases towards the continental shelf, there is significant distortion of the stratigraphic layering (Figure 2.23). This distortion may be a result of slumping along relatively large faults, although no clear detachment fault is observed, or alternatively may be due to contourites formed on the continental slope by strong margin parallel ocean currents.

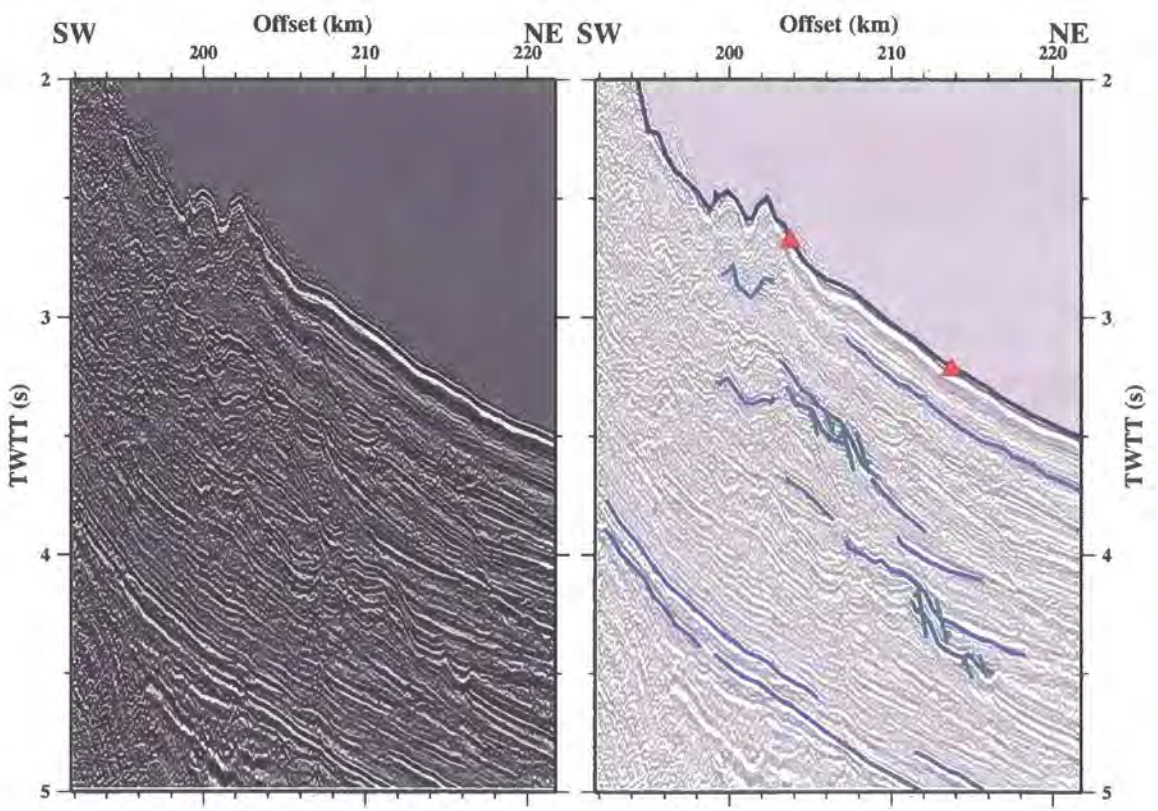


**Figure 2.23**: Sedimentary slumping under the continental slope of Profile A. Enlarged section from Figure 2.16 (left), showing slumping oceanward of the continental slope on Profile A. Significant examples of normal faulting within the sediments are highlighted in green (right), offsetting several reflections (light blue). Red triangles indicate the OBS locations on the seafloor (dark blue).

The sediments above the mid-Miocene unconformity were subdivided into three units for inclusion in the main WA model, based on the strongest, most continuous reflections.

Two further units were identified beneath the unconformity. The regional stratigraphic reference of Erbacher *et al.* (2004) identifies four units (1-4) within the sediment column of the Demerara Plateau, of which Units 2-4 are older than the mid-Miocene. Despite the inherent ambiguities of linking seismic events between unconnected profiles, the seismic character of the two sections implies that the youngest of the lower two units along Profile A most likely consists of chalk and black shale, whereas the older unit comprises claystone, clayey siltstone and sandstone.

A distinct reflection event separates the smooth, linear sedimentary reflection succession from acoustically transparent material below and is, consequently, identified as the acoustic basement. The basement reflection is characterised by a series of high amplitude, irregular, hummocky reflections (Figure 2.24), typical of oceanic basement and suggests that all sediments visible in the seismic section are post-rift. Thus, the crust beneath this reflection is identified as lying within the oceanic zone. The basement reflection extends landward to ~240 km, at which point the seafloor multiple dominates. Oceanward, the reflection increases in TWTT, most likely a consequence of a deepening of the basement surface rather than a relative lateral decrease in velocity within the sediment column. Comparison with Profile Guyas 44 does not develop the interpretation further as unfortunately no basement reflection is imaged. There is no evidence of a Moho reflection beneath the basement reflection.

The continental zone is identified southwest of the shelf break. Reverberation within the shallow water column greatly reduces the SNR in this region and, despite processing, reflections are difficult to distinguish from multiples and noise, if they are present at all. However, it seems likely that there is ~1 s TWTT and possibly up to ~2 s TWTT of sediments beneath the seafloor. The absence of a clear basement reflection is consistent with other continental crustal surveys (*e.g.* Hopper *et al.*, 2006; Edwards *et al.*, 1997). There is no evidence for tilted basement fault blocks, commonly observed at rifted continental margins (*e.g.* Goban Spur – Peddy *et al.*, 1989), nor SDR sequences often associated with volcanic margins.

### 2.6.2 Profile D

The final processed reflection section for Profile D is shown in Figure 2.17, together with its corresponding interpretation. In the same way as Profile A, the margin interpretation is divided into three major crustal zones: (1) continental; (2) oceanic; and (3) sedimentary. In contrast to Profile A, the sedimentary zone clearly extends along the entire section. Oceanward, the profile shows significant similarities with Profile A. Within the deep water

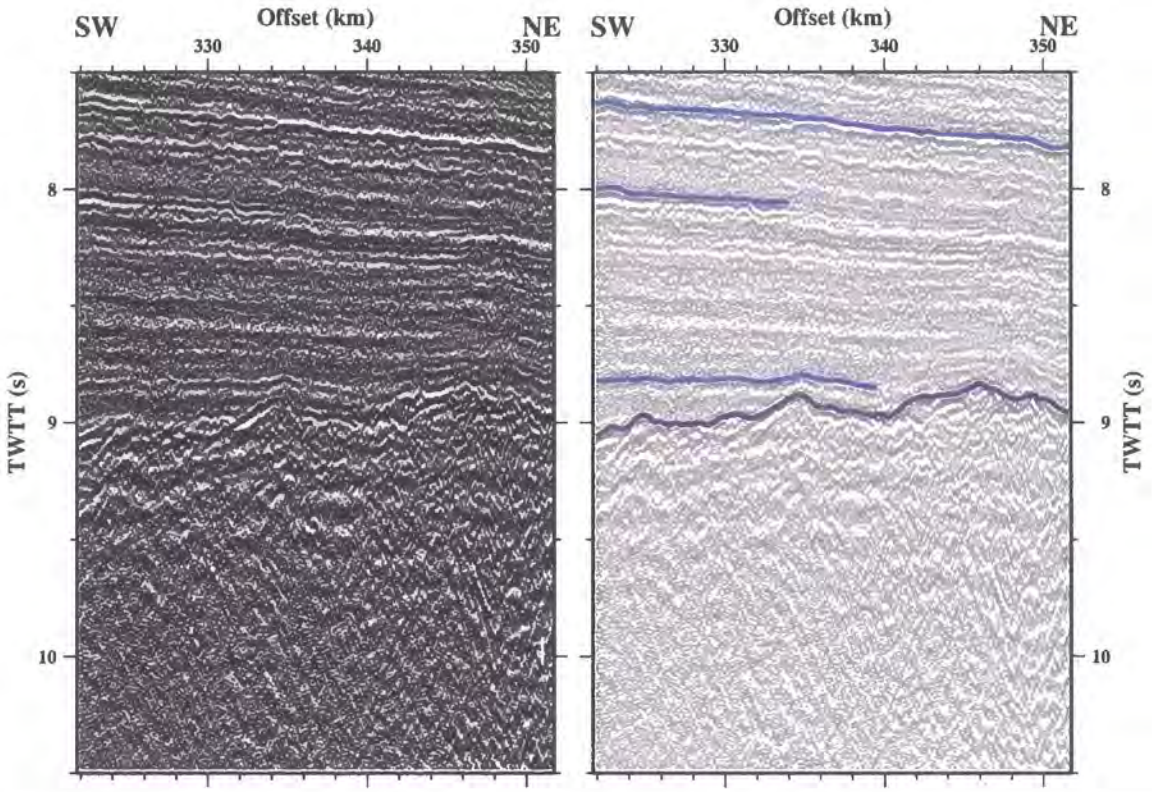


**Figure 2.24**: Oceanic basement reflection characteristics within Profile A. Enlarged section from Figure 2.16, showing the oceanic basement reflection. The reflection is of high amplitude and is hummocky in nature, separating the continuous sedimentary reflections above from the acoustically transparent oceanic crust below. The right-hand panel highlights the basement reflection (purple) and selected bright sedimentary reflections (light blue).

basin there is a ~2.5 s TWTT 'thick', well stratified sedimentary sequence overlying a distinct basement reflection. A >2.5 s TWTT 'thick' sedimentary sequence is observed on the Demerara Plateau. The two sequences are separated at 385 km by a reduction in TWTT of both the seafloor and the basement reflection underneath the toe of the plateau.

The stratigraphy within the sediments over the Demerara Plateau is also observed within the Guyaplac data and has similarities with the stratigraphy found in earlier studies ~175 km to the northwest (see Section 2.5.1; Erbacher *et al.*, 2004). Immediately beneath the seafloor, seismostratigraphic Unit i (Figure 2.20) thins oceanward towards ~290 km offset. The seismic character of the reflection at the base of the unit and the obvious thinning of the unit towards the edge of the plateau, are reminiscent of that seen on industry Profile C2206a (Erbacher *et al.*, 2004), suggesting contiguity with Unit 1, Reflection A on Profile C2206a. Similarly, the high amplitude reflections b and c beneath this unit may correspond to two of the reflections B, B' and C (Figure 2.20). However, given the significant offset between the profiles, interpretation is difficult. Beneath Reflection c the

clear sedimentary stratigraphy is absent, although Reflection d, whilst limited in extent, does suggest the presence of similar faulting to that found in Unit 4 of Profile C2206a and observed in Guyaplac Profiles Guyas 01, 03 and 05.

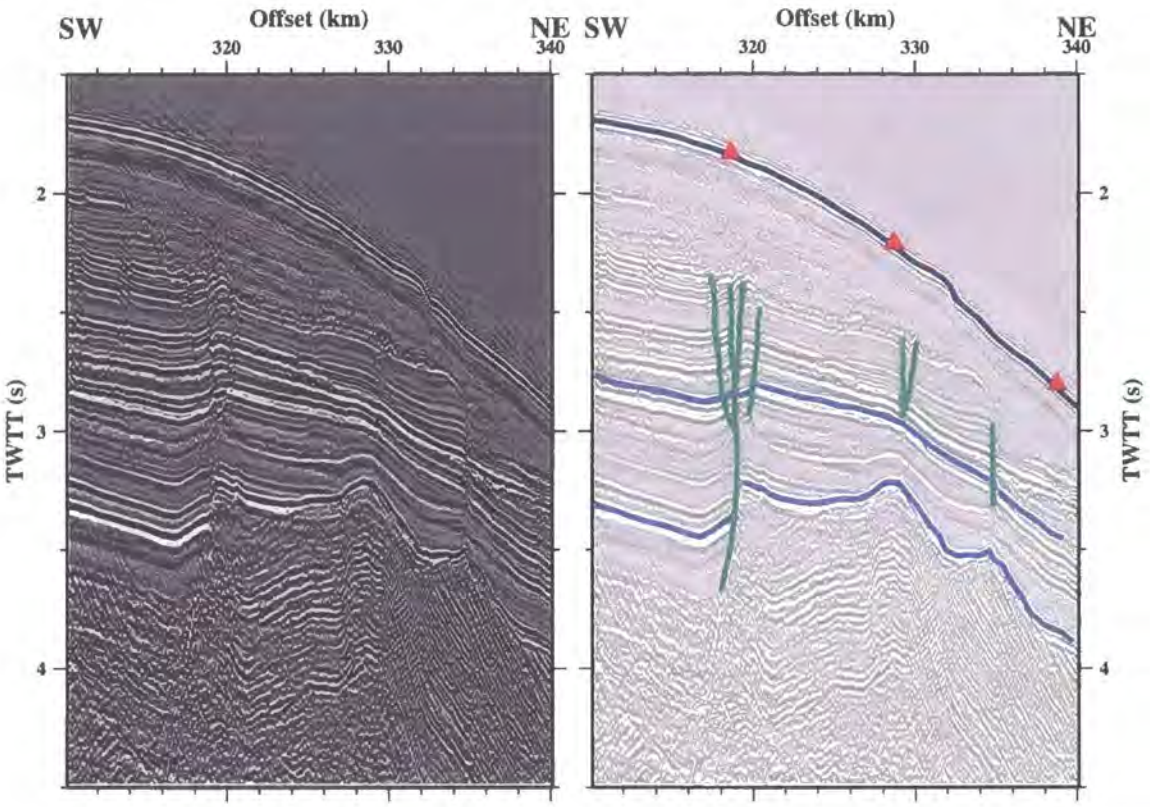


**Figure 2.25**: Faulting within the sediment column along Profile D. Enlarged plot from Figure 2.17 showing sedimentary faulting over the oceanward edge of the Demerara Plateau. Several interpreted faults are highlighted in green (right), offsetting selected bright reflections (light blue). Red triangles correspond to OBS locations on the seafloor (dark blue). Note the absence of a distinct basement reflection.

Thus, although the ACE and the industry profiles are unconnected, it seems likely that the sedimentation seen over the southeast end of the Demerara Plateau is similar to that further north. That is, faulted Albian-age claystone, clayey siltstone and sandstone with poor reflectivity, underlying younger clay and chalk sequences. Within the stratified sediments several faults are identified between ~280 km and ~360 km (Figure 2.25). The flower structures observed are commonly associated with strike-slip faulting suggesting some degree of shear motion along the margin.

The interval velocities picked from MCS semblance plots (Figure 2.11) indicate slightly different velocity gradients within the deep water sediments (~0.60 $s^{-1}$) to those seen in Profile A (0.25 $kms^{-1}$ and 0.80 $kms^{-1}$). A distinction between shallow and deep sedimentary velocity gradients is less clear.

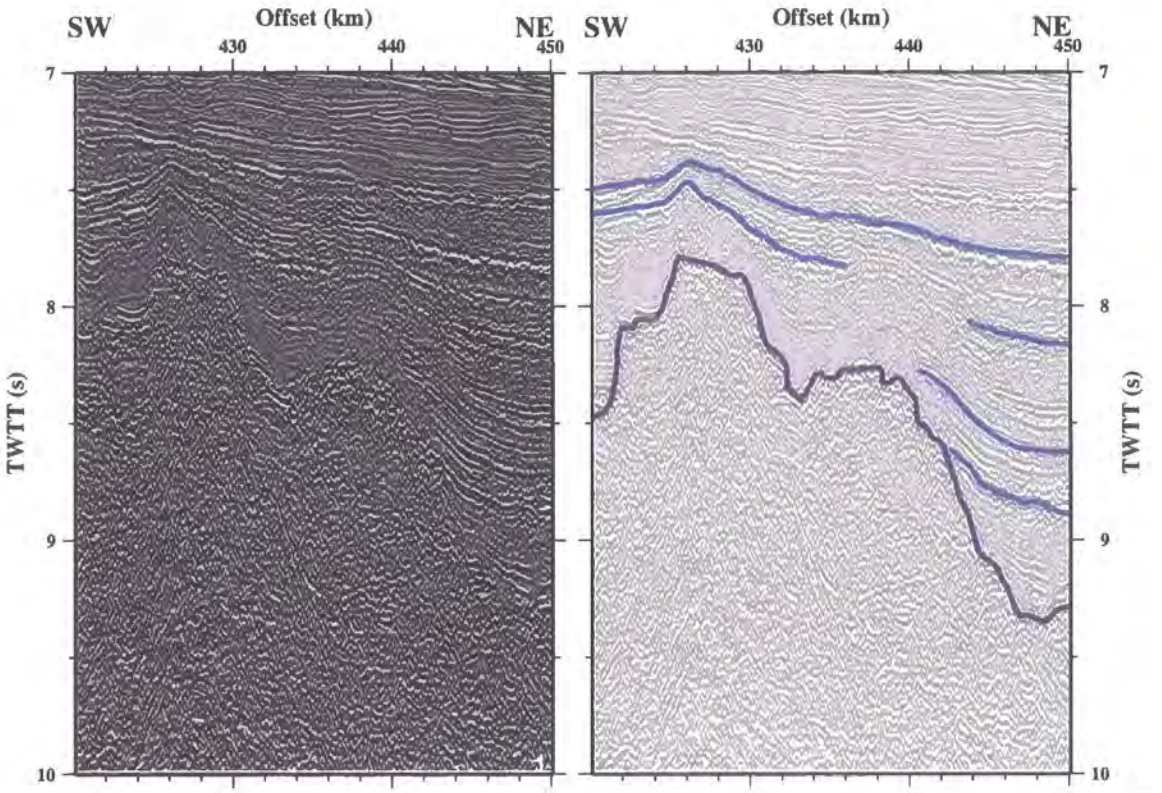


**Figure 2.26**: Oceanic basement characteristics within Profile D. Enlarged plot from Figure 2.17 showing the basement reflection in the region of the significant depth increase located at 448 km, oceanward of the Demerara Plateau. The basement reflection (purple) and selected bright sedimentary reflections (light blue) are highlighted (right).

The oceanic zone is identified similarly to Profile A, and extends landward to ~385 km. A significant basement depth increase of ~8.75 s to ~9.25 s TWTT occurs at ~450 km (Figure 2.26), a large deviation from the otherwise horizontal trend of the basement reflection. This interpretation is consistent with that of the Guyaplac data. Similarly to Profile A, there is no evidence of reflections, Moho or otherwise, beneath the basement reflection.

The continental zone is identified southwest of 360 km due to the significant shallowing of the seafloor and subsurface boundaries and the absence of a clear basement reflection which is observed oceanward of 385 km. Between 360 and 385 km a more distinct basement reflection is observed. This reflection is reminiscent of the oceanic reflection, although lower in amplitude. Additionally the reflection is ~2.0-2.5 s TWTT shallower than oceanic basement oceanward of 395 km. The region between 360 and 385 km profile offset is interpreted on the Guyaplac data as volcanic in nature, *e.g.* volcanic sills and intrusions. This interpretation is followed here to explain the anomalous nature of the

basement reflection when compared with the previously identified oceanic and continental zones.

The significant increase in acoustic basement depth at 385 km is, thus, interpreted as the transitition zone between oceanic and continental crust and, hence, the crust landward of 385 km is interpreted as continental in nature with some volcanic intrusions oceanward of 360 km.

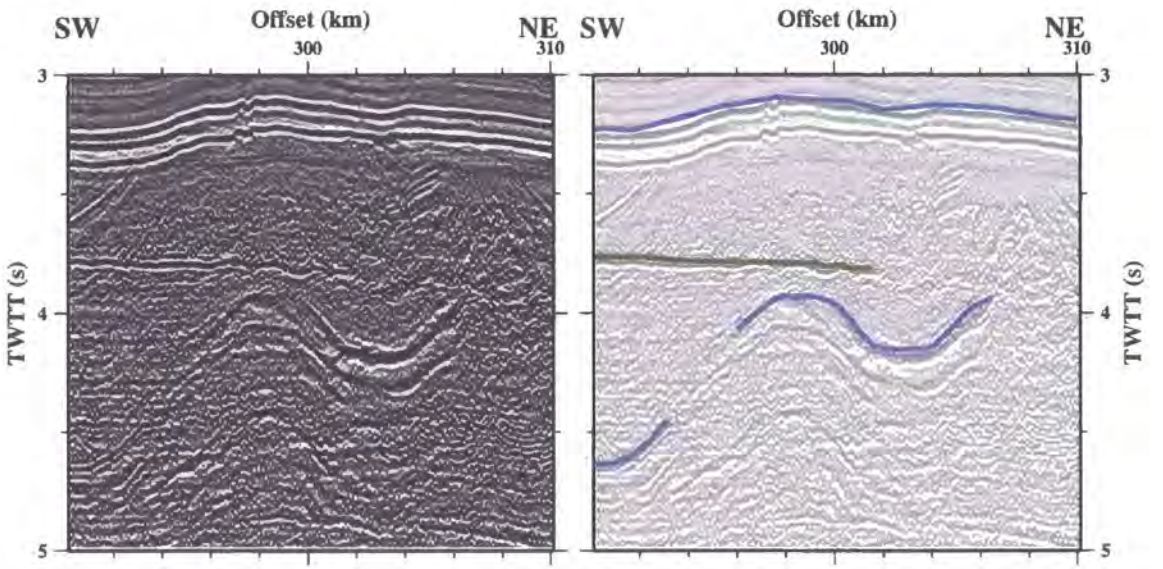


**Figure 2.27**: Deep sedimentary folding along Profile D. Enlarged plot of Figure 2.17 showing folding of sedimentary rock within the deep sediments atop the Demerara Plateau. Selected bright sedimentary reflectors are highlighted in light blue (right) and a water column multiple in green. Sedimentary folding is observed beneath relatively horizontal reflections above suggesting significant tectonic compression prior to rifting.

## 2.7 Summary

In this chapter the acquisition, processing and interpretation of MCS data from cruise D275 have been described. Migrated seismic sections have imaged the sediment column and basement reflection along two profiles offshore French Guiana. The oceanward ends of both profiles show a well stratified, up to 4.5 s TWTT 'thick', column of post-rift sediments, overlying a typical oceanic basement reflection. Profile D shows further sedimentation above the Demerara Plateau with no distinct basement reflection. In contrast, sedimentation landward of the continental slope along Profile A is less well imaged as a result of the shallow water depth.

The primary goal of cruise D275 was the acquisition of WA refraction data to image whole crustal structure. However, the MCS data described above is also required to provide

an interpretation of the sediment column to basement surface to inform WA data modelling. Additionally, estimates of interval velocity within the sediment column will guide initial WA velocity model creation.

In the next chapter, the MCS data interpretation for both profiles will be used in conjunction with the WA data analysis and modelling to develop *P*-wave velocity-depth models for the entire crust and uppermost mantle for Profiles A and D.

Chapter 3

# Wide-angle seismic data acquisition and modelling

## 3.1 Introduction

In Chapter 2 the acquisition, processing and interpretation of cruise D275 MCS data were discussed. These MCS data will be used to define the sediment column and the depth and geometry of the basement for WA data modelling, described in this chapter. Together, the WA and MCS data will be used to model seismic velocities and layer thicknesses and geometries within the sediment column, the underlying oceanic and continental crust and in the uppermost mantle.

The focus of this chapter is a description of the acquisition (Section 3.2), processing (Section 3.3), interpretation (Section 3.4) and forward modelling (Sections 3.7 and 3.8) of the WA seismic dataset. The modelling is undertaken primarily using data acquired by ocean-bottom instruments (Section 3.4), with profiles extended on land using land station data (Section 3.5). The results of this modelling are described in Section 3.9, and a preliminary interpretation provided in Section 3.10.

Tests of the uniqueness and resolution of the resulting *P*-wave velocity-depth models, undertaken by means of inverse modelling of the WA traveltime picks in addition to use of gravity and magnetic data, are described in Chapter 4.

## 3.2 Data acquisition

WA seismic data were acquired coincident with the MCS data, using a combination of OBSs and OBHs supplied by IFM-Geomar (Flüh & Bialas, 1996). Each OBS consisted of a 3-component geophone package (two orthogonal horizontal channels and one vertical channel) in addition to a single hydrophone channel. Alternatively, the OBHs had only a single hydrophone sensor (Figure 3.1). Data were recorded throughout the duration

of shooting, at sample rates of 4 or 5 ms, depending on instrument type. Instrument configurations are summarised in Appendix A.


**Figure 3.1**: Deployment of an OBS (left) and OBH (right). Both instruments consist of a large, brightly coloured buoyancy device, an anchor, a datalogger, an acoustic release transponder, an hydrophone and, in the case of the OBS, a deployment arm and 3-component geophone package.

Twenty OBSs/OBHs were deployed at 10 km intervals along both Profile A (named A1-A20) and Profile D (D1-D20) (Figures 2.2 and 2.3). This separation was designed to provide dense WA ray coverage within the entire crust, whilst maximising the lateral extent of the profile and providing redundancy in the event of instrument failure. All instruments were recovered successfully, although the hydrophones failed on instruments A1 and A8 and all geophones failed on instruments A8, A9, A14 and D11. Thus, only instrument A8 recorded no usable data at all.

Instrument locations were designed to avoid shallow water, where signal reverberation within the water column significantly swamps later arriving phases. Thus, all OBSs/OBHs were deployed in water >1100 m depth, with the deepest, D20, deployed at 4750 m depth (Appendix A). Henceforth all seabed instruments will be referred to as OBSs for simplicity.

Seismic shooting in shallow water (<100 m) posed two problems: a) the shock wave generated by the full volume array might damage the vessel's propeller stern gland; and b) the seismic streamer and/or airgun array would trail on the seafloor given the relatively deep (10-20 m) tow depth of both relative to similar water depths on the continental shelf. Consequently, seismic profile locations were designed to extend as far landward as possible without damaging equipment. Thus Profile A comprised two sections: the first, described in Chapter 2, combined shooting whilst towing the streamer; the second,

following recovery of the streamer, consisted of shooting only into the WA instruments. Recovery of the streamer when the water depth was too shallow (<83 m) allowed the effective profile length to be extended landwards by 44 km.

In contrast, Profile D was acquired in one section as shooting along Profile A demonstrated that there was more control on the tow depth of the constituent parts than originally anticipated. However, to avoid stern gland damage as the water depth decreased, the total volume of the array was reduced by turning off the large inner guns (guns 8 and 9 – Figure 2.4).

## 3.3 Data processing

OBS data processing comprised several steps to convert seismic traces from the raw instrument data files into SEG-Y format (Section 3.3.1), followed by standard processing techniques to improve the SNR of the data and the clarity of arrivals (Sections 3.3.2 and 3.3.3) for traveltime picking (Section 3.6.1). An overview of the processing applied to the raw WA data is shown in Table 3.1.

### 3.3.1 Pre-processing

Pre-processing, using IFM-Geomar in-house software packages *send2pas*, *ref2segy*, *imagerelobs* and *dat2segy*, was designed to convert the raw data into SEG-Y format (Barry *et al.*, 1975) suitable for further processing:

- *send2pas* decompresses and reads the raw data from the OBS datalogger memory cards into PASSCAL format;
- *ref2segy* converts this data to SEG-Y format, as a single seismic trace covering the entire deployment period. At this stage timing adjustments were made for clock drift during the deployment, measured by synchronising each instrument's internal clock with GPS time before and after the deployment. In all cases the clock drift was limited to a few milliseconds over the entire deployment. In addition, a 50 ms static shift was applied to correct for the difference between the shot time and the aim point of main energy release from the airgun array (Section 2.4.3.1);
- *dat2segy* uses shot times and locations (see Section 2.4.1) to split the entire deployment trace into individual shot traces (Figure 3.2). The extracted traces were 42 s long (shot interval was 40 s) to allow a 2 s buffer at the start of each trace

WA data: Processing flow

| | | |
|---|---|---|
| 1 | **Pre-processing** | |
| | *send2pas* | Decompress and read data from OBS recorder disks in PASSCAL format |
| | *ref2segy* | Write to pseudo-SEG-Y format |
| | *dat2segy* | Split data into single traces for each shot and insert offsets into headers |
| | *imagerelobs* | Recalculate instrument position (Figure 3.3) |
| | *dat2segy* | Split data into single traces for each shot and insert offsets into headers |
| 2 | **Output unprocessed data** | Output as SEG-Y (Figure 3.4) |
| 3 | **Filter** | 2-5-40-60 Hz minimum phase Ormsby band-pass filter |
| 4 | **Output processed data** | Output as SEG-Y (Figure 3.5) |
| Profile D only: | | |
| 5 | **Deconvolution** | Deconvolution filter |
| 6 | **Output processed data** | Output as SEG-Y (Figure 3.6) |

**Table 3.1**: Summary of processing steps applied to WA OBS data.

to accommodate the 'ramp-on' of filters etc.. In addition source-OBS offsets were calculated and inserted into the seismic headers;

- *imagerelobs* corrects the OBS location from its deployment location to actual location on the seabed. These positions differ because instruments drift with the ocean currents as they descend (and ascend) through the water column. The *imagerelobs* software is used to pick the near-offset water wave. If the OBS location is incorrect then the water wave will appear asymmetric. The software calculates a new instrument location from the asymmetric water wave picks, and iteratively adjusts it until water wave symmetry is achieved (Figure 3.3). This procedure will only correct the instrument location parallel to the direction of shooting, as drift perpendicular to the line of shooting does not cause water wave asymmetry, merely shifts in time; and

- *dat2segy* is repeated using the corrected instrument location to produce the WA dataset in SEG-Y format.

For viewing and traveltime picking, the seismic traces are displayed side by side with increasing offset, negative offsets to the southwest of the OBS and positive offsets to the northeast of the OBS (Figure 3.4). In addition, the time axis is plotted as reduced time, in which traces are corrected by time $\Delta t$, where $\Delta t = \frac{x}{v_{red}}$, $x$ is the source-OBS offset and $v_{red}$ is the reduction velocity chosen. In this way, data sections are plotted with relatively short time axes and arrivals which have travelled at the reduction velocity appear horizontal on the section. All OBS sections shown in this study are displayed in this manner.

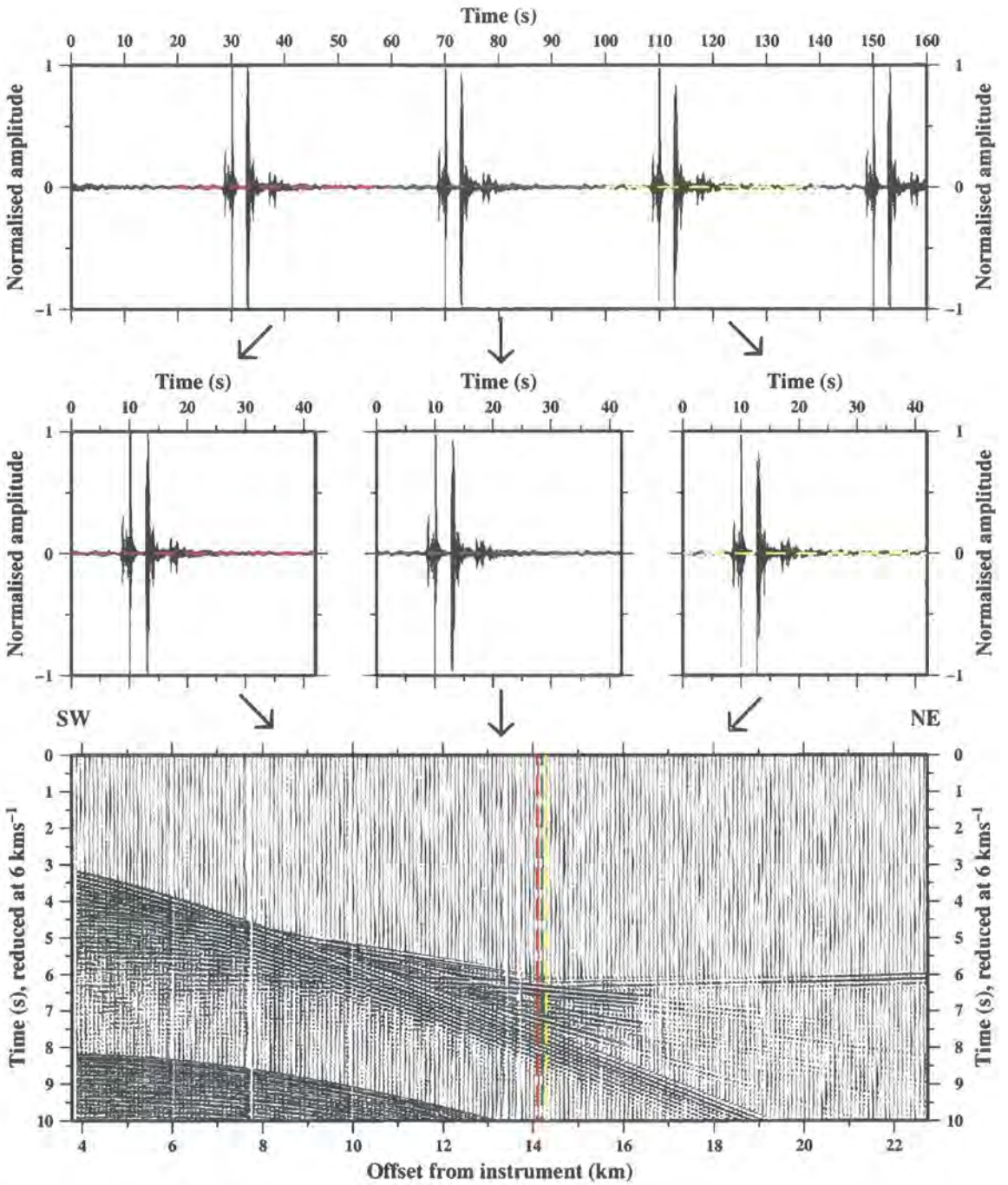


**Figure 3.2**: Receiver gather creation. A single raw data trace (top) recovered from an OBS datalogger is split into 42 s traces (middle), one for each shot. These traces are displayed side by side, often at a reduced velocity, to produce a WA seismic section for each instrument (bottom). Three 42 s traces are highlighted (red, green, yellow) to demonstrate this process. The seismic wavelets are shown normalised to the maximum trace amplitude.

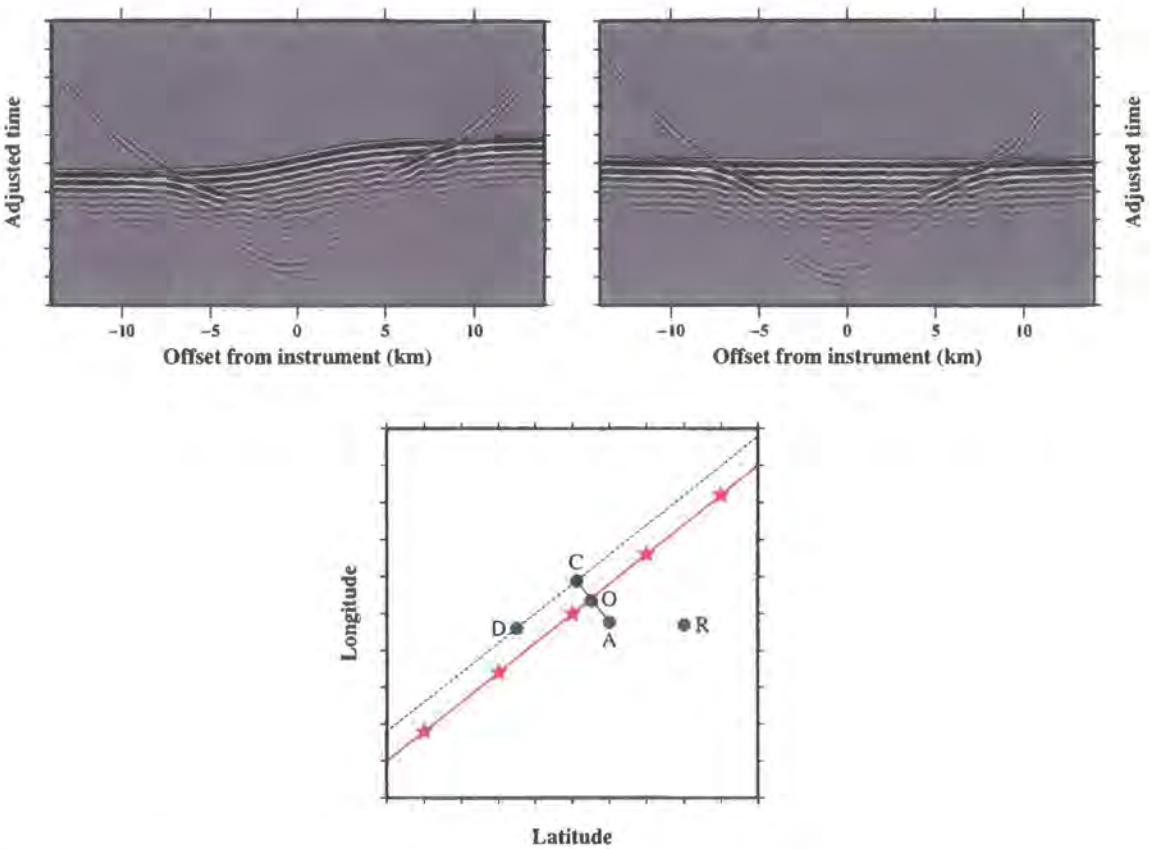


**Figure 3.3**: OBS relocation correction. OBS water wave symmetry before (left) and after (right) processing with *imagerelobs* (see main text). The data is shown reduced at 1.5 $kms^{-1}$, with an additional, trigonometrically determined time adjustment to correct the instrument to the sea surface datum, to remove the vertical component of the path length. As a consequence, if the OBS location has been correctly determined then the water wave will appear horizontal. (Bottom) Schematic diagram of the relocation correction showing: shot points (red stars); profile (red line); a line parallel to (black dashed) and perpendicular to (black solid) the profile; the OBS deployment position (Point D); the actual location of the OBS after it has drifted whilst descending through the water column (A); the OBS position as recalculated with imagerelobs (C); the on-line position (O); and the recovery position (R). The OBS location is corrected towards the actual position along a line parallel to the profile.

### 3.3.2 Frequency analysis and filtering

Unsurprisingly, the frequency spectrum of the OBS data (Figure 3.5) shows several similarities to that of the MCS data (Figure 2.8). The spectrum shows high power at low frequencies ($<\sim$4 Hz), a high amplitude primary peak at 9 Hz and a series of harmonics at 18 Hz, 27 Hz, 36 Hz and so on. These peaks are within $\pm$1 Hz of the values observed within the MCS data spectrum.

Similarly to the MCS data (Section 2.4.3.2), a minimum phase Ormsby band-pass filter was designed to remove both high- and low-frequency noise. A 2-5-40-60 Hz filter was most effective at improving the SNR across a wide-range of offsets. The application of this filter (Figure 3.5) clearly improves the data quality from which to pick individual arrivals.

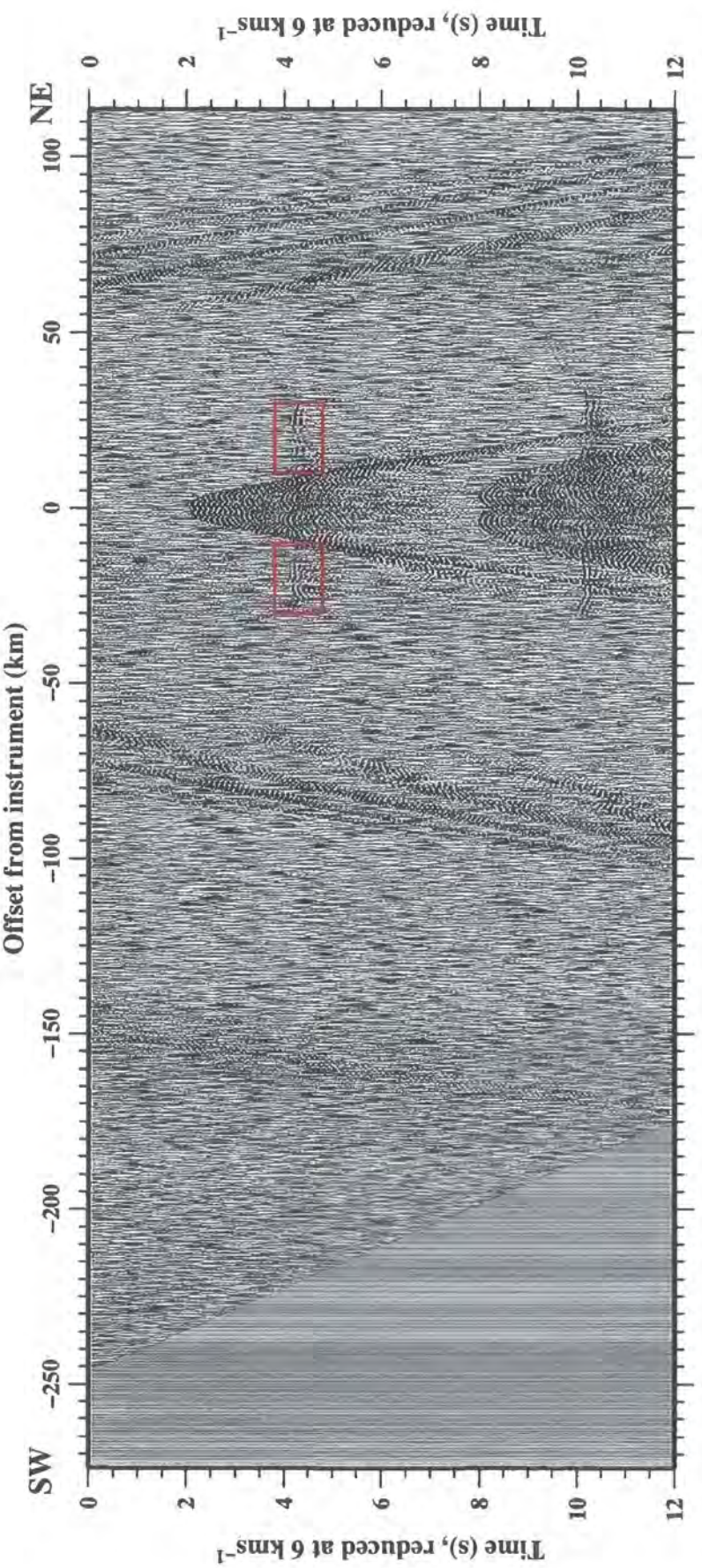


**Figure 3.4**: Raw record section for OBS D15. See Figure 2.3 for location. The data are displayed at true amplitude at a reduction velocity of 6 kms$^{-1}$, indicating that the arrivals highlighted by the red boxes have travelled at ~6 kms$^{-1}$.

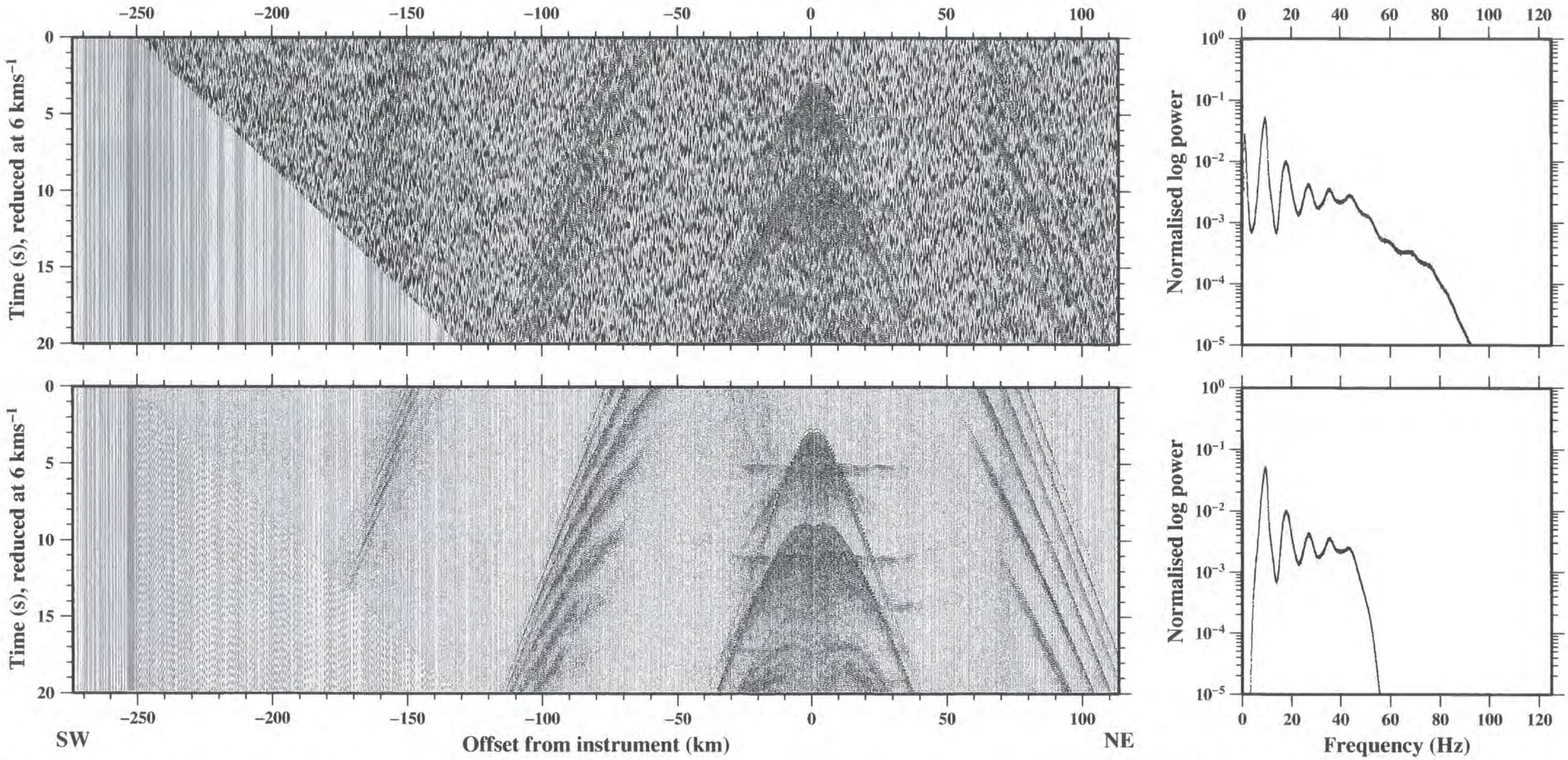


**Figure 3.5**: Application of preferred band-pass frequency filter. (Top) Unfiltered WA true amplitude data (left) and associated frequency spectrum (right) from OBS D15. (Bottom) The same data (left) and frequency spectrum (right) following the application of a 2-5-40-60 Hz band-pass filter. The filter has significantly improved the clarity of observed arrivals.

### 3.3.3 Deconvolution

The OBSs recorded a source signature containing relatively high-amplitude ringing after the primary pulse. Thus, whilst first arrivals within the data appear clean, the ringing reduces the SNR of later events, interfering with secondary phases such as reflections. To improve the clarity of secondary arrivals a deconvolution technique was applied. MCS processing (Section 2.4.3.4) demonstrated that whilst predictive and filter-based deconvolution were both effective, the deconvolution filter approach was easier to apply. Thus, the deconvolution filter approach was adopted for the OBS data. The method used to derive the filter is identical to that for the MCS data, and is described in Section 2.4.3.4.

Figure 3.6 shows data taken from OBS D15 with and without the deconvolution filter applied. The ringing of the source signature has been reduced, revealing later arriving phases which were previously either partially or wholly obscured. For this study, both primary and secondary phases will be modelled. Hence, deconvolution is an effective tool for extracting maximum information on the phases present in the data.

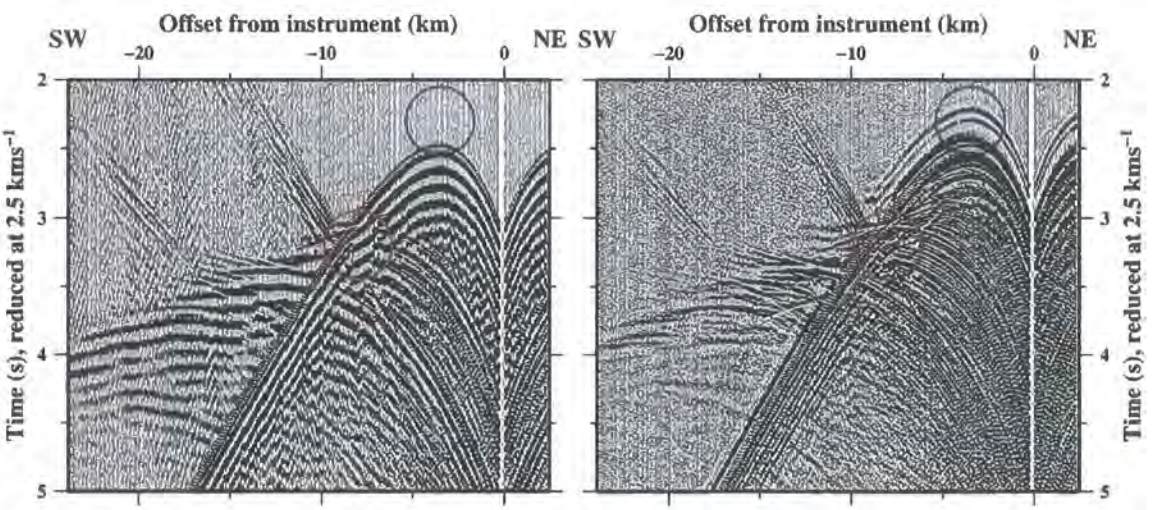


**Figure 3.6**: Deconvolution filtering of WA data. (Left) Selection of data from OBS D15 with a 2-5-40-60 Hz frequency filter applied. (Right) Same data processed using a deconvolution filter designed to remove the ringing in the source signature. Secondary, often reflected, arrivals which were previously obscured by ringing of the direct water wave are more distinct in the deconvolved data (red circles), assisting phase identification. However, the filter also produces precursory sidelobes (blue circles) above both the high amplitude direct water wave and some low velocity phases emerging from the direct water wave. As a consequence of this, the deconvolved data was not used for first break picking but instead to identify arrivals which were then picked from solely band-pass filtered data.

The technique is especially effective where arrivals overlap, for example where the water depth and sediment thickness are such that sedimentary arrivals tend to be obscured by both the water wave and deeper crustal arrivals. Thus, the deconvolution approach was

most suited to the shallow waters above the Demerara Plateau and in deep water areas where the sediments were relatively thin at the oceanward end of Profile D.

Quality control checks also revealed that, despite improving the SNR of the secondary phases, the deconvolution filter also produced a wavelet with precursory sidelobes, which give the appearance of a time shift of the seismic phases. Thus, although the peak energy remained at the same traveltime, the first break was shifted earlier along the trace. The size of this shift varied depending on the shape of the wavelet. Thus for the direct water wave, whose wavelet had an angular appearance due to clipping during recording, the time shift was large (up to ~50 ms). Secondary arrivals, whose waveshape was often formed from the stacking of multiple arrivals, were also subject to large shifts. The effect was generally much smaller for larger offset, lower amplitude arrivals as the precursory sidelobes were of lower amplitude than the background noise and hence did not impinge on the first break picking.

The variable time shift caused by the filter makes picks derived from deconvolved data unsuitable for use in modelling without large increases in the pick error. Hence the deconvolution filter was applied only to inform the decision making process when identifying phases while the picks themselves were made from solely band-pass filtered data sections.

## 3.4 Wide-angle OBS dataset

This section contains a description of the WA dataset used for modelling. Hydrophone record sections for several OBSs are shown in the accompanying figures and all OBS sections, for both profiles, are presented in Appendix C. These sections are labelled with interpreted phases, identified following the approach outlined in Section 3.4.1.

The main observations and, hence, modelling considerations for the WA data are described in Sections 3.4.2 and 3.4.3. For clarity, the profiles are described from the oceanward end of each profile (OBS A20 and D20), which exhibit the most simple pattern of phases, and these are contrasted with those from the landward end (OBS A1 and D1) where the record sections show distinctly asymmetric arrival patterns either side of an instrument. In all cases, source-receiver offsets are positive to the northeast and negative to the southwest.

### 3.4.1 Phase identification

Direct water waves ($W_w$) and crustal diving rays ($P_s$ and $P_g$) are observed as first arrivals on all WA record sections (Figure 3.7 and Appendix C). In addition, mantle diving rays ($P_n$) are also recorded by OBSs at the oceanward end of both profiles. Secondary phases are observed on many OBSs and are identified as intra-sediment and intra-crustal refracted arrivals, intra-crustal reflections ($P_gP$) and Moho reflections ($P_mP$). Coincident reflection and refraction phases often obscure one another such that the two cannot be distinguished. In this case arrivals were generally assigned to the refracted phase.

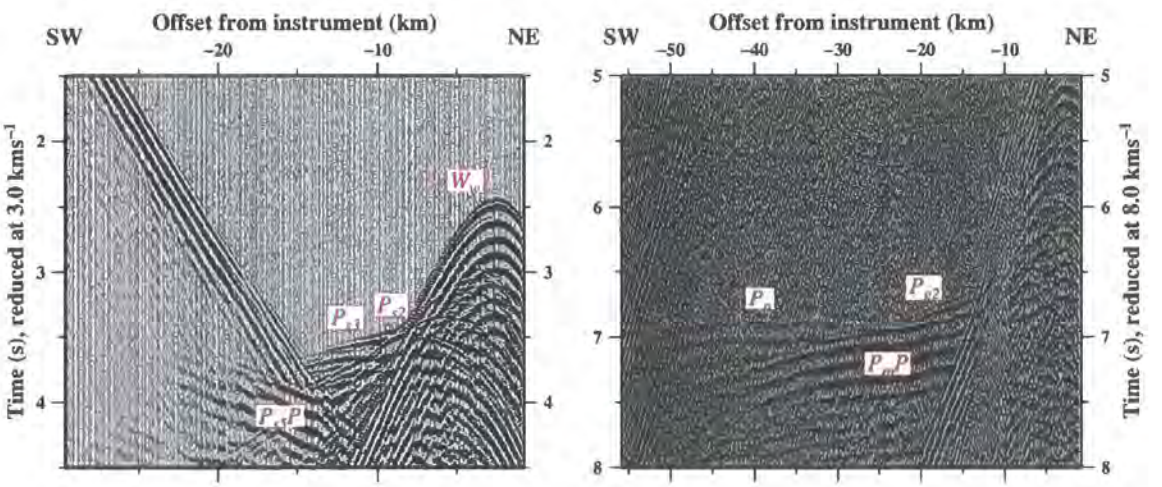


**Figure 3.7**: Phase identification. Two versions, plotted at different reduction velocities, of the OBS A20 true amplitude data are shown with associated phases labelled. (Left) Sedimentary arrivals ($P_{s2}$-$P_{s3}$) emerge from the water wave ($W_w$) at -7 km offset and can be traced to -15 km offset. (Right) Deep crustal arrivals ($P_{g2}$) and mantle arrivals ($P_n$) are accompanied by the high amplitude Moho reflection ($P_mP$). Mantle arrivals are observed beyond -50 km offset.

Crustal arrivals are subdivided into five sedimentary refractions ($P_{s1}$ to $P_{s5}$), to be consistent with MCS data, and up to two deeper crustal layers ($P_{g1}$ to $P_{g2}$) to accommodate the major changes in velocity observed on the record sections. This subdivision corresponds to refractions associated with both a two layered continental and oceanic crust, consistent with the standard models of oceanic and continental crustal structure (*e.g.* Spudich & Orcutt, 1980; Bratt & Purdy, 1984; Christensen & Mooney, 1995).

In general, phases were identified prior to traveltime picking from analysis of OBS data displayed at a range of reduction velocities. For Profile D, deconvolution aided this process. A philosophy of consistency between one instrument and the next was adopted, using the minimum number of identified phases to faithfully reflect each velocity trend within the observed arrivals. This approach was readily applied to the oceanward instruments where

the velocity structure was relatively 1D, but proved more problematic landward as the subsurface structure became progressively more complex.

In some cases phase origins were unknown and thus phase codes were not assigned until the modelling stage. At this point, phase arrival times could be predicted and compared with unknown phases. This predictive approach also led to the reidentification of some phases. In general, phases were only reassigned to the model layer above or below.

Sea surface-seabed multiples can also be identified on the WA record sections. Water wave multiples were used to aid and check the relative positioning of the instruments within the model, as described in Section 3.8.2. Other multiples were not used for the ray-trace modelling and are thus not described in detail here.

### 3.4.2 Profile A

Across the whole profile, OBS data show clear sedimentary and upper basement first arrivals emerging from the direct water wave, out to source-OBS offsets of $\sim\pm$15 km. In addition, mid-lower crustal and uppermost mantle arrivals are observed on oceanward instruments at offsets up to $\sim\pm$150 km.

OBS record section A20 (Figure 3.7), located at the oceanward end of the profile (Figure 2.2), is approximately symmetrical either side of the instrument position. Sedimentary first arrivals ($P_{s2}$-$P_{s3}$) are recorded at source-receiver offsets of $\sim\pm$7-15 km, exhibiting $P$-wave velocities less than $\sim$3 kms$^{-1}$. A clear secondary arrival ($P_{s5}P$) is also observed, which constrains the deep sedimentary layers. For the sub-sedimentary crust, first arrivals ($P_{g2}$) are observed at $\pm$15-23 km offset at velocities of 6-7 kms$^{-1}$. At larger offsets, up to $\sim\pm$60 km, upper mantle diving rays ($P_n$) are also observed at velocities $\sim$8 kms$^{-1}$. The large amplitude Moho reflection ($P_mP$), at offsets of $\sim\pm$23 km, constrains the crustal thickness. These velocities suggest normal oceanic crust overlying typical upper mantle (*e.g.* White *et al.*, 1992) at the most oceanward end of the profile.

Landward, OBSs A9 to A19 show broadly the same features as OBS A20 and, hence, their record sections are not reproduced here (see Appendix C). Some small differences are observed between these sections, for example progressively faster velocities (<0.2 kms$^{-1}$) are observed in the sedimentary phase of OBSs A9 to A14. However, there are no abrupt changes in either sedimentary, crustal or mantle structure. The largely uniform structure observed across this subset of instruments is consistent with the MCS interpretation (Section 2.6.1) of a stratified sediment column overlying oceanic crust.

OBS A8 failed to record any data and, inevitably, marks the point at which the arrivals described above begin to exhibit significant change. On OBS section A7 (Figure 3.8), fast

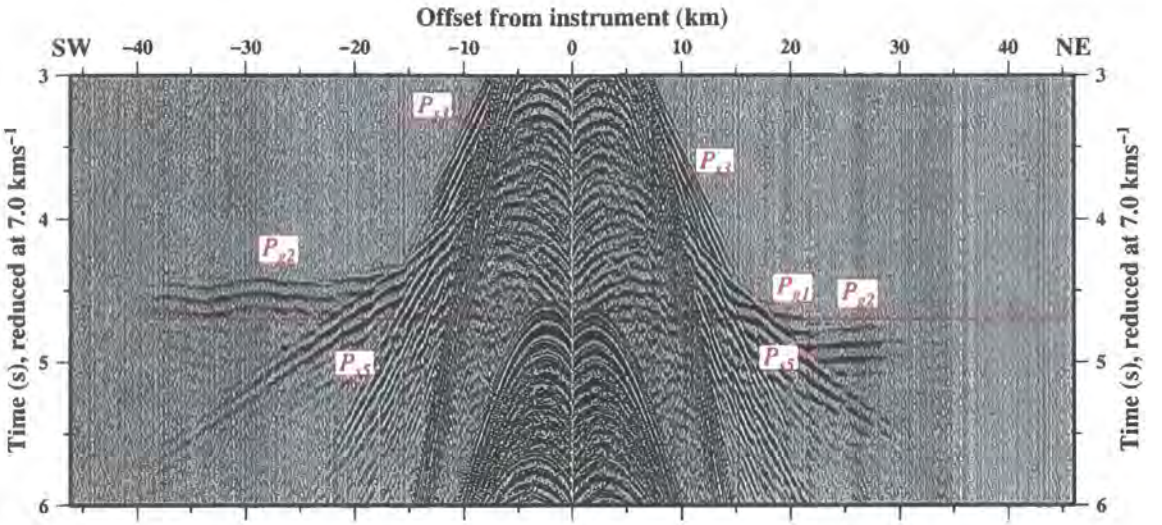


**Figure 3.8**: Asymmetry of arrivals recorded by OBS A7. The section is reduced and plotted at true amplitude and observed phases are labelled as described in Section 3.4.1. The dashed red line at 4.7 s highlights the asymmetry in arrival traveltime of the $P_{g2}$ arrivals, with those to the southwest arriving earlier than 4.7 s and those to the northeast later than 4.7 s. This asymmetry is most likely a consequence of differences in crustal structure either side of the instrument.

(6.8-7.0 kms$^{-1}$) crustal phases ($P_{g2}$) arrive before similar phases on the oceanward side of the instrument. In addition to this asymmetry, crustal phases are observed up to $\sim\pm$40 km offset, and the $P_n$ phase is no longer observed. This suggests a major structural change within the crust. Several possibilities may contribute to this change: a significant increase in thickness of the sediment column, as observed on MCS data; a rapid shallowing of the seafloor on the continental rise and slope; and an increase in crustal thickness associated with the OCT.

$P_n$ is observed to the southwest of the OBS A6 record section (Figure 3.9) at a velocity of $\sim$9 kms$^{-1}$. This velocity is much higher than the uppermost mantle velocities described above and is greater than velocities interpreted from WA data in other studies (Edwards *et al.*, 1997; Lau *et al.*, 2006), which suggests that it most likely results from refraction at a steeply dipping interface associated with a major structural change to thicker, continental-style crust.

Landward, the degree of asymmetry observed on the OBS record sections increases as the seafloor shallows rapidly. For example, when compared with OBSs further oceanward, the $P_g$ phases to the southwest of OBS A4 (Figure 3.10) are distinctly different as they rise sharply on the reduced section, which is interpreted to be a result of the progressive shallowing of the seafloor to $<$100 m depth. Interpretation of the MCS data showed that the crust underlying the shelf has continental characteristics which indicates that the WA OBS

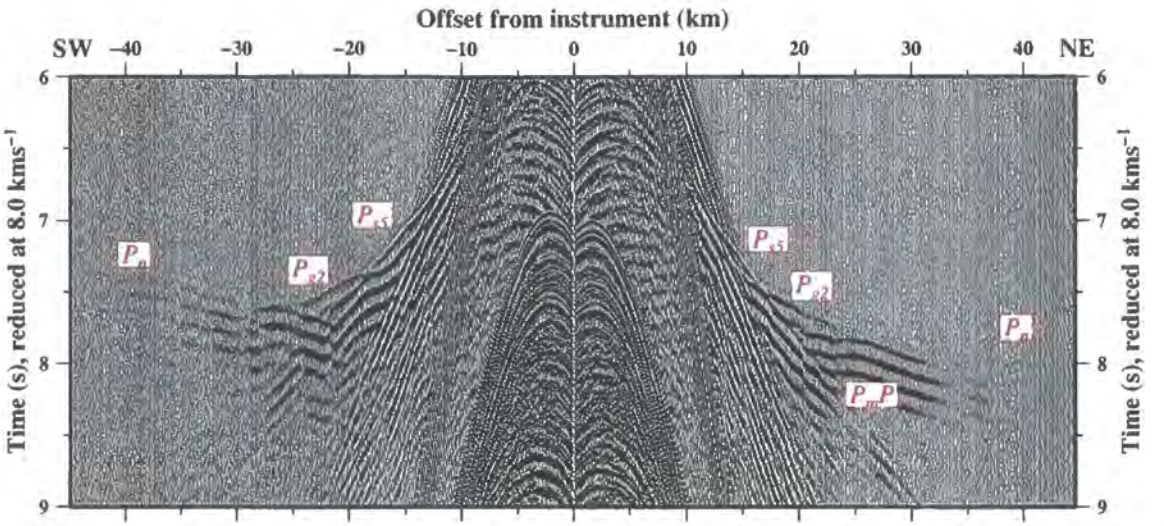


**Figure 3.9**: Indication of sharply dipping interfaces landward of OBS A6. The record section is reduced and plotted at true amplitude and observed phases are labelled as described in Section 3.4.1. The slope of arrivals to the southwest between -30 and -40 km indicates an apparent $P$-wave velocity of $\sim$9 kms$^{-1}$. Such a high apparent velocity for mantle arrivals suggests that refraction is occurring at steeply dipping interfaces.

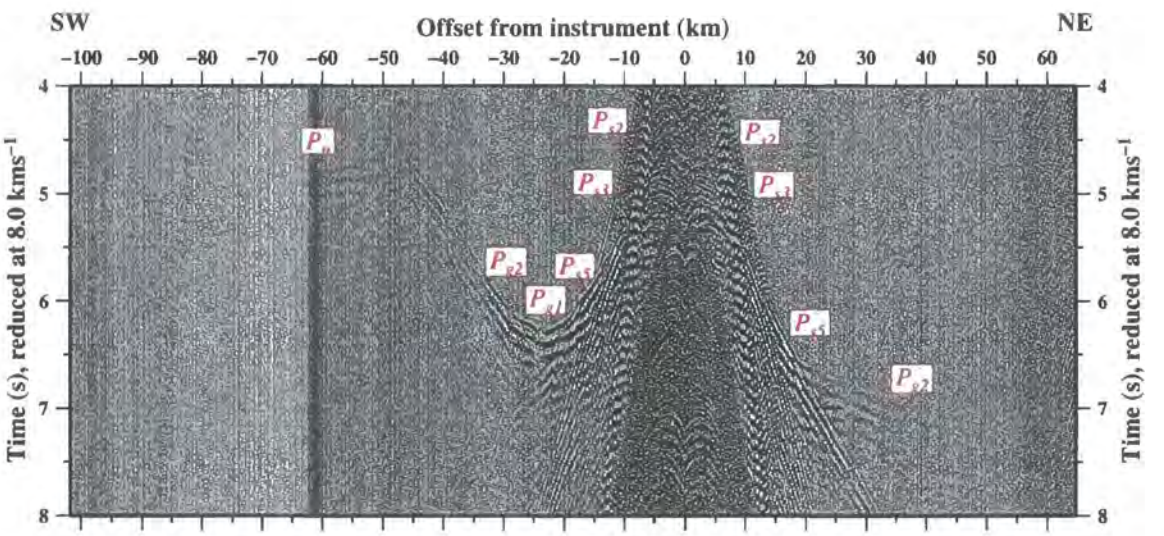


**Figure 3.10**: Major asymmetry of arrivals adjacent to the continental slope. The OBS A4 record section is reduced and plotted at true amplitude and observed phases are labelled as described in Section 3.4.1. To the southwest, arrivals rise sharply towards a plateau at $\sim$3.5 s reduced traveltime and -45 km offset. The arrivals southwest of this point are sourced from the shots fired in very shallow water ($<$100 m) above the continental shelf and, hence, have travelled through crust interpreted as continental in nature from the MCS data.

dataset comprises ray coverage of both oceanic and continental crust. Thus, the dataset crosses the OCT, a primary target of the ACE.

Furthermore, interpretation of the OBS A4 record section includes the $P_{g1}$ phase. Further oceanward, $P_{g1}$ tends to be a secondary phase often obscured by other arrivals, which may, in turn, suggest a significant thickening of the upper crust. OBSs A3-A1 have

similar characteristics to OBS A4, each showing significant asymmetry of their respective data sections.

In summary, the WA dataset from Profile A is interpreted to sample all the major structural units identified from the MCS data. Oceanward, several OBSs overlie the stratified sediment column and oceanic basement, whereas landward continental phases are observed on OBSs A1 to A4. The transition zone in between continental and oceanic crust is, hence, also imaged, which suggests that deep structural modelling is likely to reveal the margin structure for which the survey was designed.

### 3.4.3 Profile D

In contrast to Profile A, significantly more structural variation is observed along Profile D (Appendix C) For example, $P_g$ arrivals are observed on oceanward instruments at offsets up to $\sim\pm$30 km from an OBS, whereas on landward instruments $P_g$ arrivals are observed at up to $\sim\pm$60 km offset.

In broad terms, the characteristics of the OBS record sections at the oceanward end of Profile D are similar to those of Profile A. For example, the arrivals to the northeast of record section D20 (Figure 3.11) are almost identical to those to the northeast of A20 (Figure 3.7). The only significant difference is that the $P_g$ arrivals emerge from the $W_w$ arrivals earlier on section D20. This feature of the data is most likely a result of the basement along Profile D being shallower, which, given the similar water depths, implies a thinner sediment column. This observation has significant consequences for WA modelling because it results in the crustal and sedimentary phases having similar traveltimes and, hence, overlapping on the data section. As a result, uppercrustal sedimentary first arrivals ($P_{s2}$-$P_{s3}$) emerge from the water wave within a much narrower zone $\sim$3 km in width ($\pm$9-12 km offset). Additional reflected sedimentary phases ($P_{s1}P$-$P_{s3}P$) are observed. However, these are obscured to varying extents by the water wave and/or secondary refractions ($P_{s5}$).

To overcome the difficulty in identifying the arrivals, the approach to data processing was adapted to include application of the deconvolution filter described in Section 3.3.3. Oceanward of OBS D20, high velocity ($\sim$6.2 kms$^{-1}$) $P_{g2}$ arrivals are observed at offsets of $\sim$+10-20 km, adjacent to relatively high amplitude $P_mP$ arrivals at $\sim$+20 km offset. $P_mP$ and $P_n$ arrivals between $\sim$+20-40 km offset constrain the crustal thickness in this region. The maximum source-OBS offset for $P_n$ arrivals is $\sim$+60 km.

Landward of OBS D20, $P_g$ arrivals are observed between -10 and -24 km offset. Further arrivals are observed, between -24 and -30 km offset, which slope upward on the reduced time section. They are neither low amplitude, as per the majority of $P_n$ arrivals, nor of a

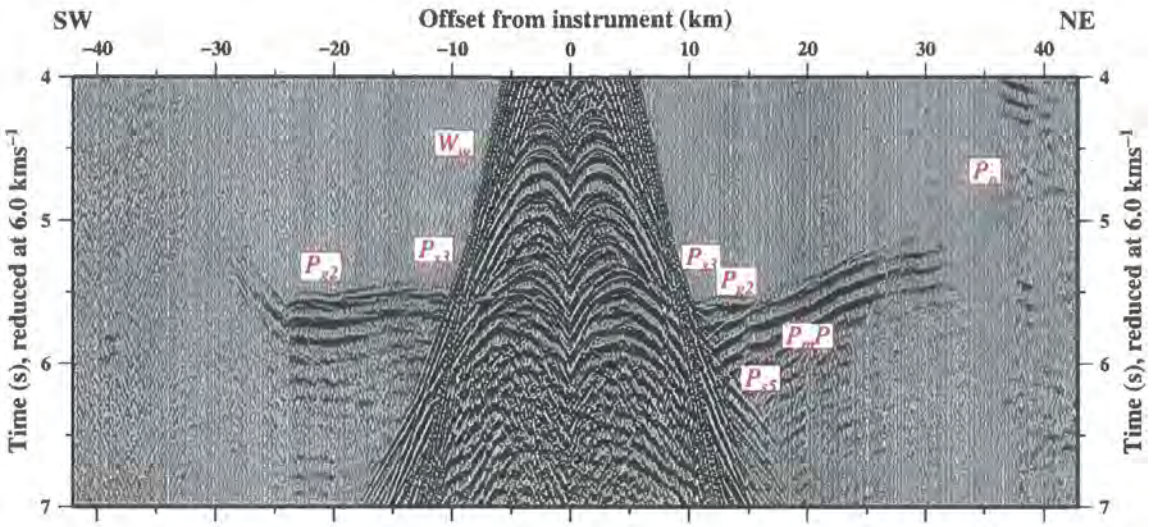


**Figure 3.11**: WA arrivals at the oceanward end of Profile D. The OBS D20 record section is reduced and plotted at true amplitude and observed phases are labelled as described in Section 3.4.1. $P_g$ arrivals are limited to a zone ~3 km in width from 8-11 km offset. Oceanward, high amplitude $P_mP$ and low amplitude $P_n$ arrivals are highlighted and are similar to those observed on the OBS A20 record section (Figure 3.7). However, the most striking feature of this section is the group of arrivals between -24 and -30 km offset. These arrivals are interpreted as crustal refractions from a steeply dipping interface.

velocity characteristic of oceanic crust. They are, hence, interpreted as crustal refractions from a steeply dipping interface.

The OBS D19 record section is similarly asymmetric, in contrast to the most oceanward instruments of Profile A in which symmetric and relatively smooth patterns of arrivals are observed. The rapid change in velocity observed on OBS D20 is also observed, at -16 km offset. The feature is not observed on OBS D18 (Figure 3.12), which shows relatively uneven, or hummocky, crustal phases, particularly to the southwest. In contrast, crustal phases were, in general, smooth along Profile A which suggests that the crust along Profile D shows more lateral structural variation, possibly at the basement surface or deeper.

Low amplitude, very far-offset $P_n$ arrivals are observed landward of OBSs D15-D17 up to ~-220 km offset. However, for OBS D14, the arrivals are more distinct and can be traced across the whole data section. Hence, approximately continuous arrivals can be traced between ~-220 and ~+120 km offset. These first arrivals show a significant step in their traveltime at ~-25 km offset (Figure 3.13), coincident with a significant shallowing of the seafloor. Although $P_n$ arrivals are identified at ~-40 km offset, the low amplitude arrivals further landward are observed at a velocity of ~6.5 kms$^{-1}$ and, consequently, they are interpreted to be a crustal phase ($P_g$). These long-offset crustal arrivals are observed on all the OBS record sections further landward.

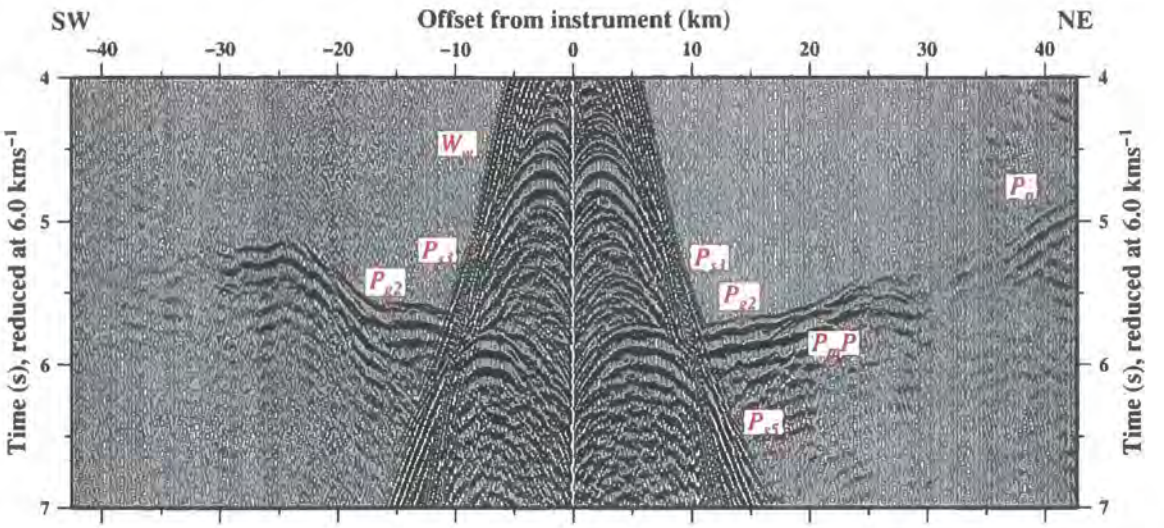


**Figure 3.12**: Hummocky arrivals observed on the OBS D18 record section. The record section is reduced and plotted at true amplitude and observed phases are labelled as described in Section 3.4.1. The crustal phase to the southwest is hummocky, suggestive of either an uneven basement surface or significant lateral structural variation within the crust

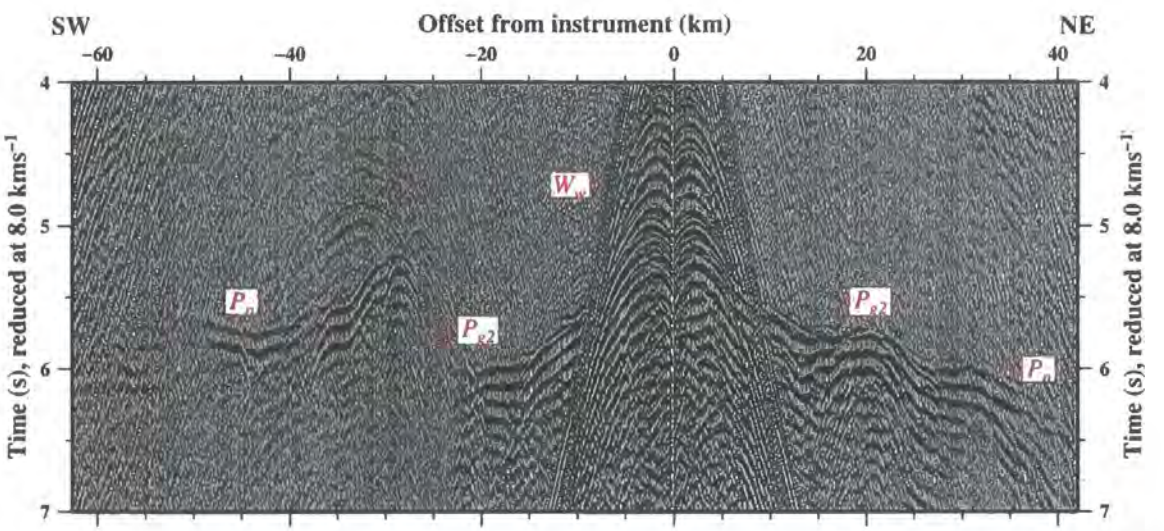


**Figure 3.13**: Observation of a step in crustal arrivals. The OBS D14 record section is reduced and plotted at true amplitude and observed phases are labelled as described in Section 3.4.1. Crustal arrivals landward of the OBS shift up the section abruptly at -25 km offset.

In addition to the lateral change in the deep crust, the shallow sediments also display significant variation toward the landward end of the profile. On the OBS data sections D17 to D20 (*e.g.* Figure 3.11), $P_s$ phases were observed within a narrow zone of first arrivals emerging from the water wave. However, landward of OBS D16 sedimentary first arrivals are no longer present. For these OBSs some secondary refracted and reflected phases were

observed on the data sections. As discussed, deconvolution aided this interpretation, which most likely indicates that the sediment column thins landward.

The reduction in distinct sedimentary arrivals landward culminates in no primary or secondary $P_s$ phases being identified on the OBS D12 record section. Here, the crustal phase to the southwest of the OBS emerges from the water wave at just -4 km offset, which is consistent with a significant shallowing of both seafloor and basement, at the toe of the Demerara Plateau, as observed in the MCS data.

OBS D11 is located on the plateau and the record section contains a distinctive feature to the northeast, in which low-velocity arrivals appear in two packages (Figure 3.14). The first package, between ~+6-12 km offset, exhibits low velocities (~2.5-3.5 kms$^{-1}$), whereas the second, between ~+12-18 km offset, shows high velocities (~4.5 kms$^{-1}$). The sharp change between the two is most likely due to refraction close to the sharp basement and seafloor boundaries.

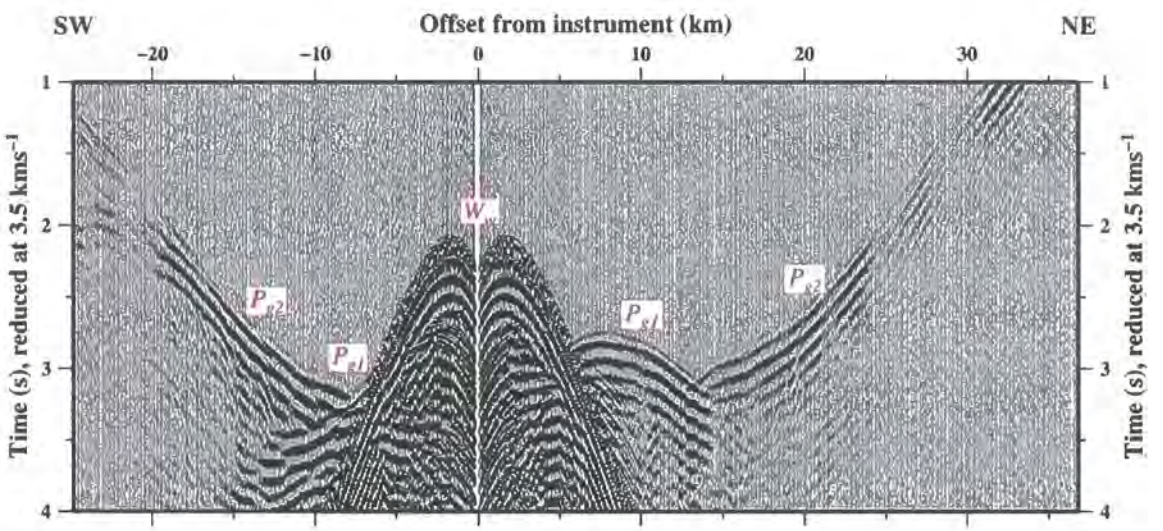


**Figure 3.14**: Traveltime arrivals at OBS D11, adjacent to the Demerara Plateau. The record section is reduced and plotted at true amplitude and observed phases are labelled as described in Section 3.4.1. Two groups of low-velocity arrivals are shown to the northeast: $P_{g1}$ exhibits velocities <3.5 kms$^{-1}$; and $P_{g2}$ exhibits velocities >3.5 kms$^{-1}$. This distinct change in phase observed at 13 km offset is not observed on the record sections further oceanward. The distinct change in velocity at this offset suggests a significant change in *P*-wave velocity structure and/or refraction at steeply dipping interfaces near OBS D11 which lies at the toe of the Demerara Plateau.

Further landward, the OBS data sections all show characteristic long-offset crustal arrivals, as shown in the OBS D6 data section (Figure 3.15). Arrivals, at velocities of up to ~6 kms$^{-1}$, are observed at relatively long offsets of up to 60 km. In contrast, the instruments at the oceanward end of the profile are only observed to ~30 km, which is indicative of significantly thicker crust landward. In addition, within the landward data sections,

long-offset arrivals are observed oceanward of the OBS to >200 km offset, completely traversing the OCT.

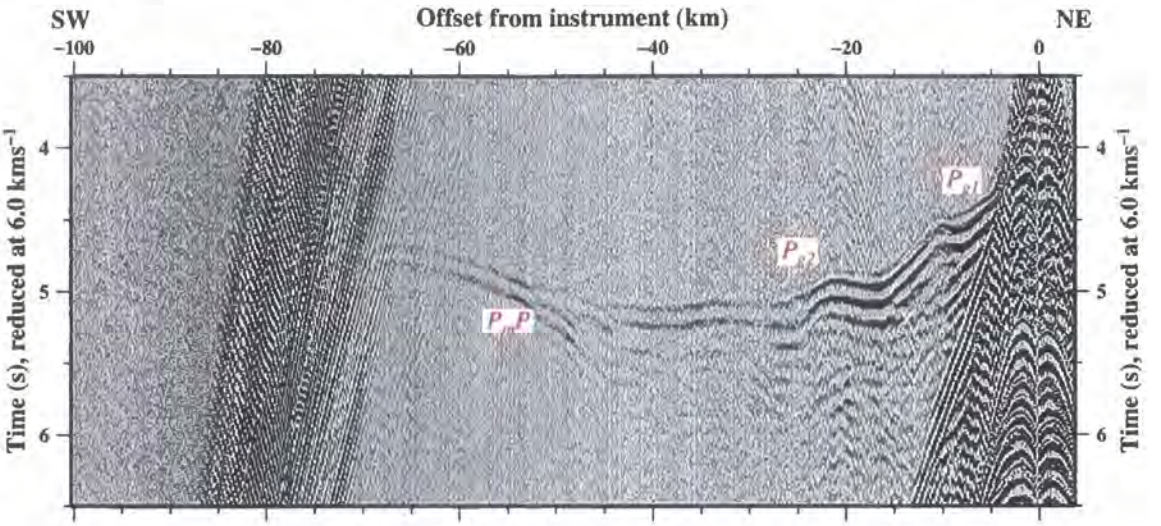


**Figure 3.15**: Crustal arrivals observed on record section OBS D6. The record section is reduced and plotted at true amplitude and observed phases are labelled as described in Section 3.4.1. Crustal arrivals of ~6 kms$^{-1}$ are observed out to 50 km offset.

In summary, $P_g$ arrivals are observed along Profile D, primarily at short offset for the oceanward instruments and also at long-offset for the landward instruments. Such a large range of offsets at which the arrivals are observed suggests that the profile traverses the transition from thick to thin crust, interpreted from the MCS data as continental and oceanic crust respectively. The profile appears to extend much further landward of the OCT than Profile A, suggesting that modelling of the Profile D data may offer greater constraint on the location of the OCT in this region.

## 3.5 Wide-angle land station dataset

In addition to the OBSs, the ACE included deployment of land-based instruments to record the marine shots at large offset. Modelling of this dataset would provide constraint on both the structure of the pre-rift crust and the rapid change in crustal thickness beneath the continental slope, adjacent to the OCT.

### 3.5.1 Data acquisition, processing and traveltime picking

SEIS-UK 6TD land-based seismographs were deployed for each profile. Five instruments were deployed at the landward end of Profile A (Figure 2.2), from Cayenne to Cacao, lying within 47 km of the coastline. For Profile D, four instruments were deployed alongside

the Maroni river, from Awala-Yalimapo to St. Jean, lying within 45 km of the coastline (Figure 2.3). Station locations and heights were measured using GPS, to ensure a consistent time and position reference between the land and marine components of the experiment. Instrument locations were chosen to avoid local noise (caused by traffic, machinery etc.) and the sensors were buried to improve coupling. All instruments recorded data throughout the offshore shooting, although instruments D21 and D23 do not contain clear seismic signals, probably due to high local noise levels and poor coupling.

Pre-processing of the data, completed in Leicester by SEIS-UK, was similar to that applied to the OBS data (Section 3.3.1), in which a continuous data trace was split into individual traces, with each trace starting at a shot instant. Source-receiver offsets were then calculated and incorporated into the trace headers. The data were converted to SEG-Y format.

The SNR of the raw, unfiltered data was too low to see clear events, and some degree of band-pass frequency filtering was necessary. A range of high- and low-cut frequencies were tested (Section 3.3.2) and a minimum phase Ormsby band-pass filter of 1-3-20-40 Hz resulted in the clearest arrivals. These filter parameters reflect the loss of high frequency signal (compared with the OBS data) due to attenuation resulting from propagation through the crust to much longer offsets.

### 3.5.2 Profile A

Land station A25 (Figure 3.16 and Appendix C) was located at the landward end of Profile A and recorded arrivals typical of all five land stations (A21-A25). The section primarily shows three phases: the first arrivals, $P_{g2}$, are observed at a velocity of $\sim$6.2 kms$^{-1}$; whereas the secondary phase, $P_mP$, appears horizontal when plotted at a reduction velocity of 8 kms$^{-1}$. The two phases converge to a triplication at an offset of $\sim$185 km, roughly coincident with the abrupt change in seafloor bathymetry associated with the continental slope. However, this offset is also dependent upon Moho depth and geometry. A relatively low amplitude $P_n$ phase is seen emerging at $\sim$195 km offset, at a velocity of $\sim$8 kms$^{-1}$, consistent with velocities typically observed within the upper mantle.

### 3.5.3 Profile D

Land stations D22 and D24 both show similar patterns of arrivals to the Profile A record sections (Figure 3.17 and Appendix C). However, whilst the Profile A arrivals show a distinct triplication associated with the sharp deepening of the seafloor and possible changes in Moho depth, the Profile D arrivals show a more gradual change, a consequence

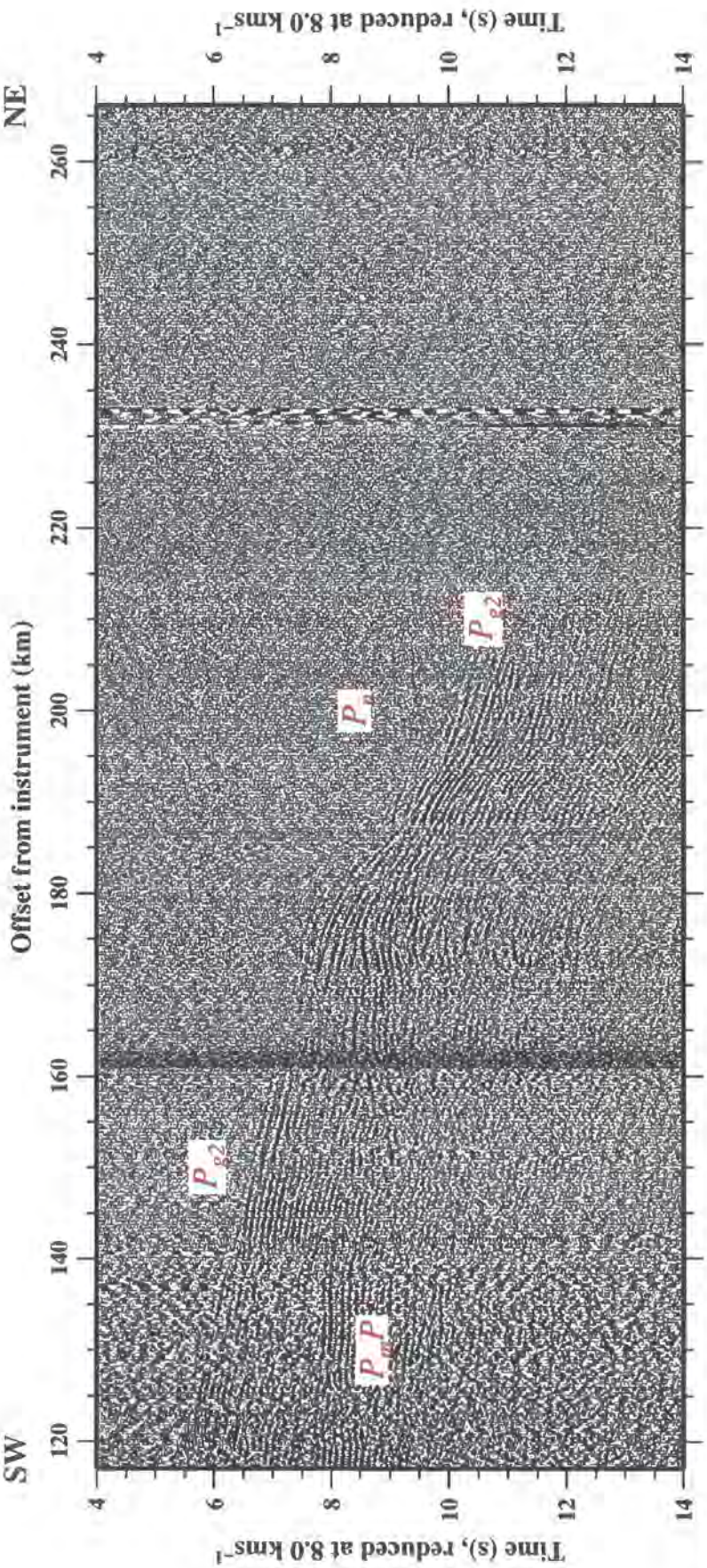


**Figure 3.16:** WA arrivals observed on the true amplitude, reduced record section from land station A25. Three distinct phases are observed. Using predictive modelling, two of these phases are identified as Moho reflections ($P_m P$) and lower crustal refractions ($P_{g2}$). The third is identified as the $P_n$ phase.

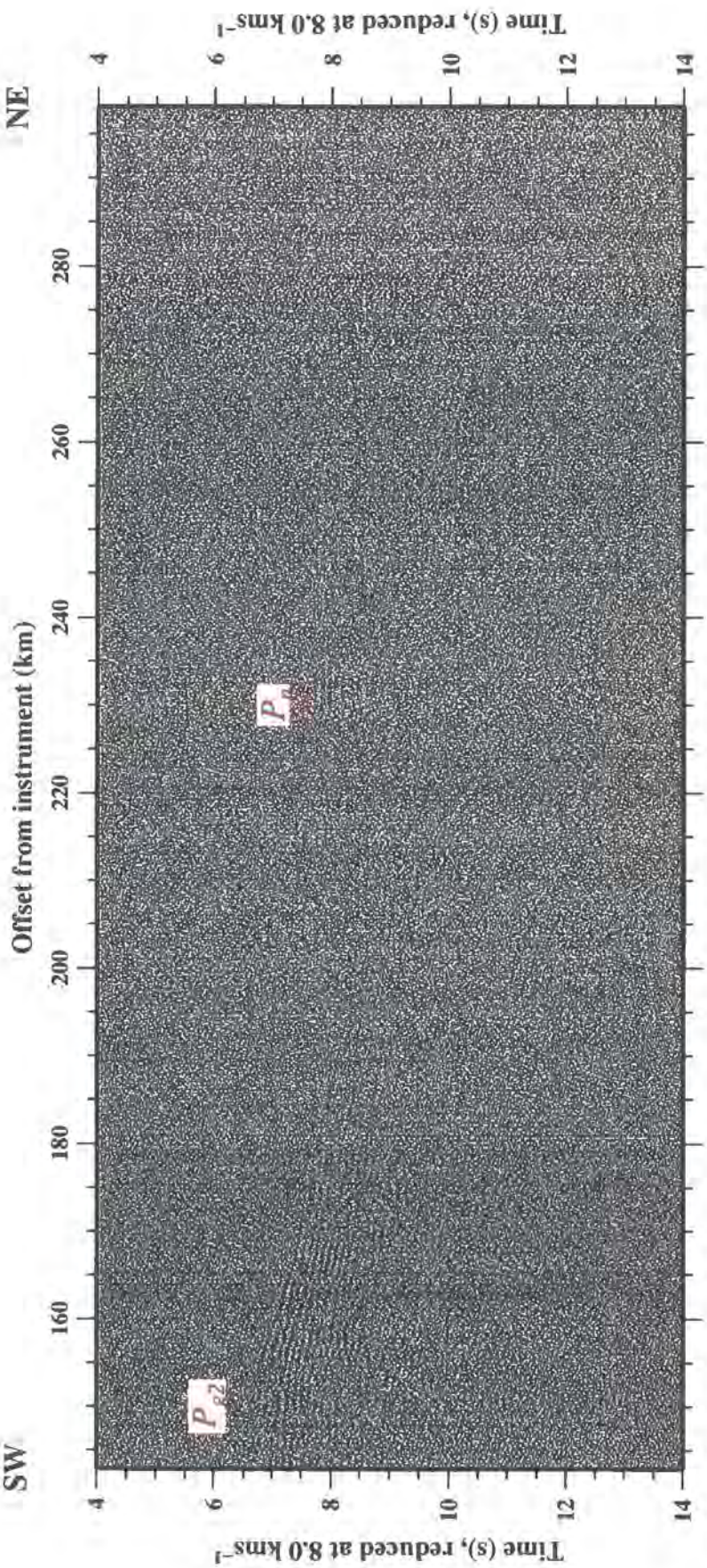


**Figure 3.17**: WA arrivals observed on the true amplitude, reduced record section from land station D24. Two phases are observed, which are identified as lower crustal ($P_{g2}$) and upper mantle refracted phases ($P_n$).

of the gently dipping seafloor over the Demerara Plateau. Within the record sections the first arrivals are of lower amplitude than their equivalents on Profile A and are, hence, less distinct. As a result, traveltimes are more difficult to pick and errors are increased accordingly.

## 3.6 Wide-angle data analysis

Prior to forward modelling of the WA data, arrival traveltimes were picked from the data sections (Section 3.6.1). Each of these picks was assigned an error (Section 3.6.2), later used to quantitatively assess the fit of the models.

### 3.6.1 Traveltime picking

The approach adopted for traveltime picking used two software packages; Landmark's *ProMAX* and *Seismic Unix* (Cohen & Stockwell, 2000). Both packages include robust pickers with a simple display to view the data at a range of scales. Short *awk* scripts were created to convert picks from *ProMAX/Seismic Unix* format to the *rayinvr* (Zelt & Smith, 1992) format required for modelling.

As described in Section 3.3.1, all WA data timings are calculated relative to the maximum energy release of the source array. Therefore, in order to pick the actual traveltime of an arrival, the first positive peak of the wavelet should be picked. However, this approach was not adopted because the arrival time of the wavelet peak varies with offset, as a consequence of attenuation of higher frequencies. Attenuation results in a narrowing of the bandwidth and, hence, a broadening effect on the wavelet, such that the first peak of the wavelet arrives later relative to the first break. Hence, picking the primary peak will result in a systematic error which increases progressively towards large offsets and should be avoided.

Instead, traveltimes were picked at the first break of the arriving wavelet and a small 5 ms pick error was incorporated to account for the time difference between it and the primary peak. Figure 3.18 shows a series of traveltime picks, illustrating the approach adopted.

Picks were made primarily on true amplitude record sections with a 'zoom-in' applied to the display so its appearance was similar to that of Figure 3.18. Also, picks were made from sections plotted with a reduction velocity similar to the velocity of the phase being picked, so that the phase ran horizontally across the display. For example, $W_w$ arrivals were picked with a reduction velocity of 1.5 kms$^{-1}$ whereas $P_n$ arrivals were picked at a

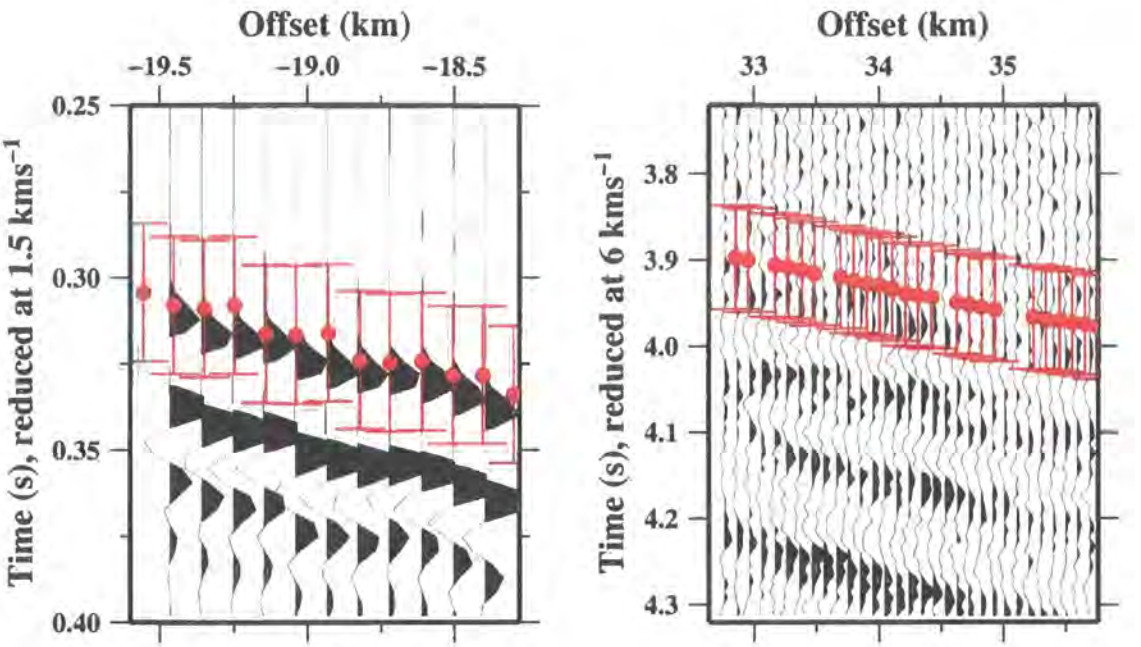


**Figure 3.18**: Traveltime picking. (Left) Eleven traces from OBS D15 showing water wave arrivals and (right) traces from OBS D5 showing lower crustal arrivals. Example traveltime picks are shown (red dots) with corresponding error bounds. Vertical exaggeration is four times greater for the left panel than the right and, hence, the true error bounds are three times greater for the lower crustal picks. The water wave picks illustrate the preferred approach to picking in which the first break of the wavelet is chosen as the pick location. The lower crustal picks show that at larger offsets, where the SNR is poor, the first break was difficult to locate precisely and so the error bounds were increased.

reduction velocity of 8 kms$^{-1}$. Short *awk* scripts were created to unreduce the traveltime picks for subsequent modelling. This approach was not always suitable and several slight modifications were made:

- As the source-receiver offset increased, arrival amplitude decreased and the first break became difficult to distinguish from background noise. Thus, at long offsets, the quality of the pick was reduced and the pick error (Section 3.6.2) was increased accordingly. Similarly, at very low SNRs, some phases cannot be seen unless a large number of traces are viewed on a single screen, *i.e.* 'zooming out'. In this case, arrival onsets are more difficult to judge and therefore pick errors are increased accordingly;

- $W_w$ arrivals were of high relative amplitude even at long offset. Thus, as the data were split into 42 s long traces (Section 3.3.1), when traces are displayed side-by-side $W_w$ arrivals appear to wrap around, obscuring subseabed travelling arrivals. Traveltime picks were not generally made within these regions; and

- The first break of secondary arrivals was often obscured by the wavetrain of primary arrivals. In this case the nearest available first break was picked and the errors increased accordingly.

The approach to traveltime picking from the land station data sections was similar to that adopted for picking of long-offset arrivals in the OBS data. There was no clear onset time on each trace, so the data were viewed 'zoomed out' so that arrival trends were clear across several traces, and picks were made at the first onset of black and white banding resulting from the trend of positive and negative polarity within the wavelet. In contrast to the OBS data, land station data has no water wave with which to check instrument location and guide picking of emergent arrivals. Hence, the error associated with land station traveltime picks is far greater than that of OBS data, generally 200 ms, sometimes increasing to 500 ms in regions where SNR is very low. Predictive modelling was used for traveltime phase identification (Section 3.8.4).

### 3.6.2 Traveltime errors

Several small errors associated with traveltime picking were combined into a total error for each traveltime pick. These errors are essential for the modelling process as they impose limits on how well the subsurface can be resolved and also allow statistical tests of the fit between synthetic and actual traveltimes. Traveltime errors include:

- Sampling error – the OBSs sample at either 4 or 5 ms depending on instrument type. Thus, first break picks can only be made to within $\pm 1$ sample;
- Pick accuracy – where the first break is clear, such as for high amplitude water waves or near-offset first arrivals, accuracy is high and error is estimated at $\pm 10$ ms. Where the first break is not distinct, errors are estimated to increase to $\pm 30$ ms. Where SNR is low errors are estimated to increase up to $\pm 20$-100 ms. Similarly, amongst secondary arrivals, where the first break is obscured by the wavetrain of first arrivals, the error is estimated to increase to $\pm 40$-100 ms;
- First break error – time zero corresponds to the point of maximum energy release from the source array. However, traveltimes are picked as the first break, *i.e.* a zero crossing rather than a peak, incorporating an estimated error of $\pm 5$ ms (Section 3.6.1);
- Instrument location – relocation of the instruments for modelling incurs an error of $<10$ ms for OBSs. In addition, uncertainty in the seafloor bathymetry of $\pm 15$ m

equates to an uncertainty in instrument depth and a corresponding uncertainty in the modelled traveltimes of ±10 ms; and

- Clock drift – on OBS recovery, clock drift is measured by synchronising to a GPS time standard, and a correction applied, assuming that the drift is linear throughout the duration of the deployment. The maximum observed drift for either profile is 23 ms, although the majority of instruments drifted by <5 ms.

Combination of these errors suggests a minimum error of ±15-20 ms. Consideration of the reduction in pick accuracy for long-offset phases suggests that this error varies between phases. Thus, the adopted approach to picking was to assign each phase an error as shown in Table 3.2. Where pick accuracy was significantly reduced the error assigned was increased from these values accordingly.

| Phase | Minimum error (ms) |
|---|---|
| $W_w$ | 15 |
| $P_{s1}$, $P_{s2}$, $P_{s3}$ | 20 |
| $P_{s4}$, $P_{s5}$ | 30 |
| $P_{g1}$, $P_{g2}$ | 40 |
| $P_n$ | 50 |

**Table 3.2**: Minimum error bounds for traveltime picks made for all identified phases. Where pick quality was poor, the error was increased accordingly.

## 3.7 Model construction

WA forward modelling was undertaken to create 2D *P*-wave velocity-depth models of the crust. Starting models were constructed in three main stages:

- The location and orientation of each model was determined by projecting the OBS and land station locations onto a best-fit straight line through the shot points (Section 3.7.1). The model extents were chosen to include all instrument and shot locations;
- Bathymetry data were used to constrain the thickness of the water column layer and the geometry of the seafloor (Section 3.7.2); and
- OBSs and land station locations were positioned slightly above the seafloor or ground in the models (Section 3.7.3).

### 3.7.1 Wide-angle profiles

The location of each of the WA profiles was determined by projecting all shot locations (Section 2.3) onto straight 'best-fit' lines. The shift required was, on average, 36 m (maximum 226 m) for Profile A and 52 m (252 m) for Profile D. To match the MCS data, all model offsets were set positive to the northeast and referenced to 0 km at the most southwesterly land station. Hence, the MCS and WA profile offsets are coincident and referenced to the same profiles and profile offsets. The location, length and orientation of each profile is shown in Table 3.3.

| Profile | Southwest end | | Northeast end | | Length | Orientation |
|---|---|---|---|---|---|---|
| | Latitude (°N) | Longitude (°W) | Latitude (°N) | Longitude (°W) | (km) | (° from N) |
| A | 4.5701<br>4° 34.21' | 52.5094<br>52° 30.56' | 7.6076<br>7° 36.46' | 50.1388<br>50° 8.33' | 427.51 | 37.695 |
| D | 5.4276<br>5° 25.65' | 54.1152<br>54° 6.91' | 9.8001<br>9° 48.00' | 52.0892<br>52° 5.35' | 535.00 | 24.541 |

**Table 3.3**: End points and extent of models, constructed from shot point and instrument locations. All components are referenced to 0 km at the most landward land station along each profile.

The models were constructed on the assumption that the Earth is flat. Zelt (1999), using the flat-Earth transformations of Aki & Richards (1980), notes that over distances less than 500 km the uncertainty caused by the assumption is negligible. Profile A is shorter than 500 km and Profile D only a short distance longer. In addition, the longest offset arrivals observed in either profile are <240 km. As a result, the error associated with this assumption is considered negligible.

### 3.7.2 Seafloor bathymetry

During cruise D275, seafloor bathymetry data were acquired using a 10 kHz SIMRAD EA500 hydrographic echo sounder. During normal operation the error on depth measurements is ±15 m. However, particularly on Profile D, the data show considerable scatter, a consequence of partial system failure which resulted in an inability to achieve seabed 'lock' unless the depth scale was fixed by the operator to the 1500 m band appropriate to actual seabed depth. As such, for Profile D, this system required constant operator attention to keep the seabed 'in band' to obtain accurate readings. Despite the scatter, the 10 kHz data are considered the most accurate measure of seafloor depth and, as such, were used to pick a multi-node seafloor for both WA models (Figure 3.19). Additionally, the depths

were checked by modelling the water waves and their multiples as described in Section 3.8.2.

### 3.7.3 Seismograph positioning

OBS locations were recorded during deployment and then corrected for drift along-strike of the profile using the *imagerelobs* software (Section 3.3.1 – Figure 3.3). To position OBSs within the 2D models, their locations were projected onto the profiles, along a line perpendicular to the strike of the profile (Figure 3.3). The maximum shift applied to any OBS was 320 m (A13) on Profile A, and 166 m (D10) on Profile D. The average OBS shifts were 158 m and 108 m for Profiles A and D respectively. These shifts correspond to a maximum difference[a] of ~13 m between the length of the actual ray path from shot to OBS and the modelled ray path, when the source is directly above the instrument. Thus, the error associated with shifting the OBSs onto the profile[b] is <9 ms.

The maximum shift applied to those land stations successful in recording data suitable for modelling was 3.4 km (A25) and 4.8 km (D23) for Profiles A and D respectively. These shifts are significantly greater than the OBS shifts, and result from difficulty in finding suitable and accessible deployment sites directly inline with the offshore part of each profile. However, the minimum source-receiver offsets corresponding to the land stations range from 71 to 126 km which, calculated trigonometrically, results in up to 90 m extra surface path length. Assuming a *P*-wave velocity of 3 $kms^{-1}$, this suggests an error of up to 30 ms, significantly less than the estimated traveltime pick errors at such long-offsets. Hence, shifting the land station locations onto the profiles does not significantly effect the accuracy of traveltimes picked directly from the data sections.

The shifts described above only apply to the relative positioning of the instruments with respect to the model. The source-receiver offsets for each individual instrument are calculated separately, as discussed in Section 3.3.1.

To position the instruments vertically within the models, each was assigned a depth corresponding to 1 m above the seafloor boundary at its relative model location, ensuring that this depth is consistent with observed seabed depth at deployment. This approach was adopted for two reasons: first, on the majority of OBSs the hydrophone was positioned about 1 m above the base of the instrument; and second, this small separation between the OBS and the model boundary minimised limitations in the modelling code when OBSs

[a]Calculated trigonometrically for OBS A13

[b]Calculated using $velocity = \frac{distance}{time}$, assuming a water velocity of 1.5 $kms^{-1}$

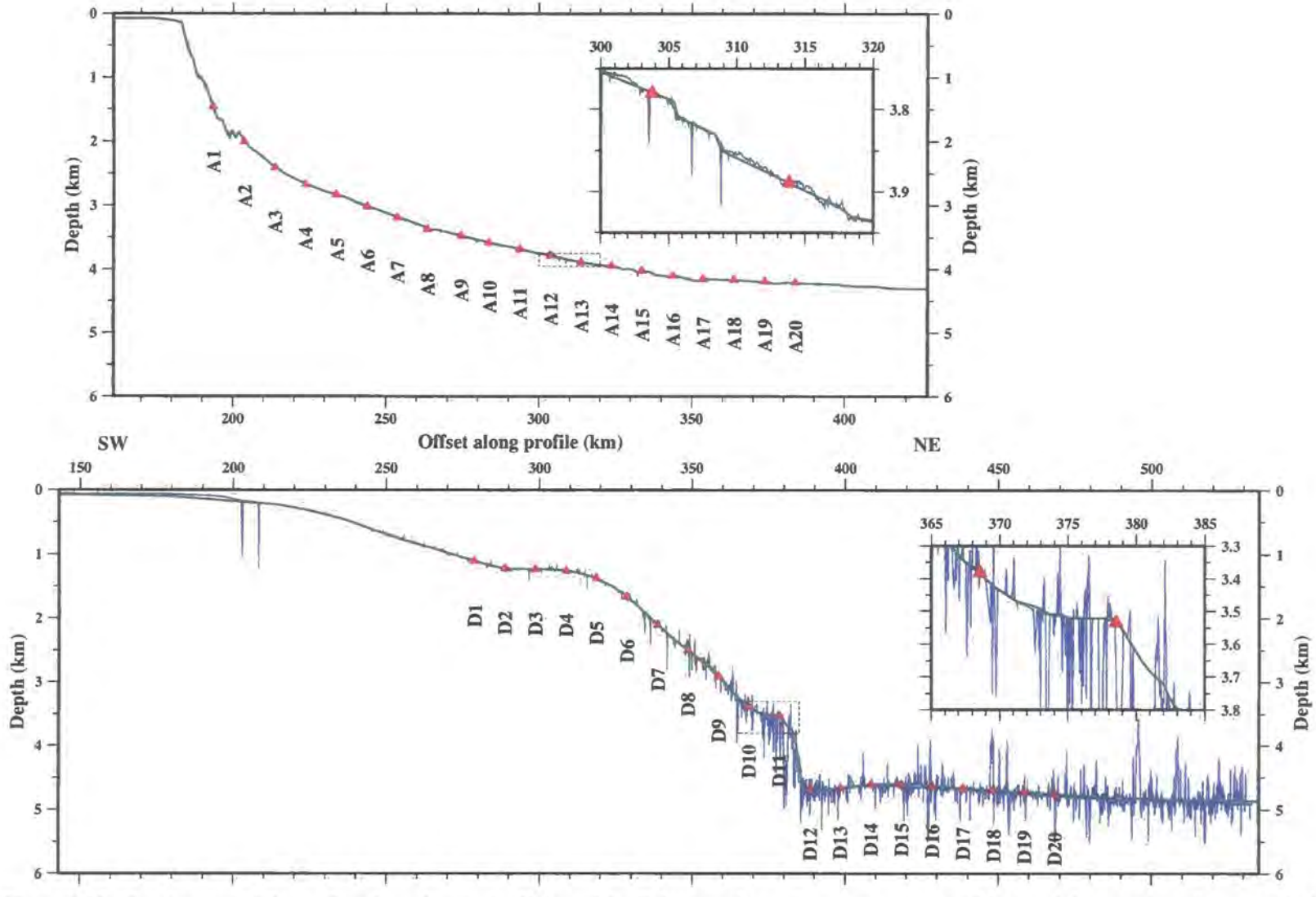


**Figure 3.19**: Construction of the seafloor boundary in the WA models. Echo sounder seafloor measurements (blue) and the corresponding smoothed seafloor picks (green) used for Profiles A (top) and D (bottom). The dashed boxes correspond to insets which demonstrate the extent of the scatter problem for Profile D. Red triangles mark OBS locations relative to each seabed model.

and nodes are too closely positioned. Figure 3.19 shows the location of OBSs with respect to the seabed in the two models.

Subseabed layers were incorporated into the models by first picking the most distinct reflections from the MCS data sections and then converting into depth using stacking velocities estimated from the semblance velocity picks (Section 2.4.3.5). Crustal layers deeper than the MCS acoustic basement were estimated based on other crustal studies and the initial observations of crustal type observed in the MCS data sections (Section 2.6).

## 3.8 Wide-angle data modelling

The initial starting models were gradually developed into final *P*-wave velocity-depth models by forward modelling of the WA traveltime data using the *rayinvr* software (Zelt & Smith, 1992). Initially, only the OBSs were modelled using an approach which comprised four main stages:

- Water wave and water wave multiple traveltimes were modelled (Section 3.8.1), coupled with XBT data analysis (Section 3.8.2), to constrain the velocity structure of the water column and check instrument depths and locations;
- All *P*-wave arrivals were modelled to develop velocity-depth models of whole crustal structure (Section 3.8.3);
- Land station data were incorporated (Section 3.8.4) to constrain the crust-mantle boundary beneath the continental slope and shelf; and
- MCS data interpretation was included as a check and further constraint on layering within the sediment column and the depth to and geometry of the basement surface.

### 3.8.1 Traveltime modelling

Traveltime modelling was undertaken using *rayinvr*, the ray-tracing and inverse modelling program by Zelt & Smith (1992). This software is considered a standard approach for WA data modelling and has been used in many other studies of continental margins (*e.g.* Funck *et al.*, 2003, 2004; Klingelhöfer *et al.*, 2005). The laterally continuous sedimentary packages, with relatively little small-scale structure (Figures 2.16 and 2.17), are particularly suited to *rayinvr* modelling as the program uses a velocity model comprising a sequence of layers separated by boundaries consisting of linked linear segments. The program also allows layers to 'pinch-out' to zero thickness against one another. Each layer is assigned

upper and lower *P*-wave velocities and the whole model is split into an irregular network of trapezoids, with associated velocities and velocity gradients, through which rays are traced and synthetic traveltimes calculated. Thus, realistic Earth models may be represented with a minimum of parameters. Rays are also traced in reverse between each OBS and all shots, for reasons of simplicity.

In addition, *rayinvr* provides a simple method for estimating the fit between observed traveltimes and those calculated for the model. Each traveltime pick is assigned an error (Section 3.6.2) based on its phase identification (*e.g.* $P_{s2}$, $P_mP$ etc. – Section 3.4.1) and an associated phase code, which ties the pick to a chosen model layer. Following ray-tracing, a statistical approach to evaluating the fit between picked and calculated traveltimes, the $\chi^2$ test, is applied. The $\chi^2$ (chi-squared) test is calculated from:

$$\chi^2 = \frac{1}{n-1} \sum_{i=1}^{n} \left( \frac{T_{0_i} - T_{c_i}}{U_i} \right)^2 \tag{3.1}$$

where $T_0$ is the observed traveltime, $T_c$ is the calculated traveltime, $U$ is the estimated pick uncertainty, and the picks are numbered from $i = 1$ to $n$ for each phase separately. A $\chi^2$ value of 1 or lower indicates an acceptable fit within the errors.

### 3.8.2 Water column

The 'top-down' approach adopted for WA crustal modelling first considers the water column which, compared to the subsurface, is relatively predictable given its effectively constant and globally consistent *P*-wave velocity of 1.49 kms$^{-1}$ $\pm\sim$2%. However, to record the *P*-wave velocity profile of the water column specifically at each profile, two additional datasets were acquired during cruise D275:

- XBT data were acquired at three locations along Profile A and two along Profile D (Figures 2.2 and 2.3). These disposable instruments record water temperature which, in turn, is converted to velocity using standard density and salinity relationships (Figure 3.20 – Shiobara *et al.*, 1997); and

- A sound velocity probe (SVP) was used to measure sound velocity, pressure and temperature against depth and, hence, may be used to calibrate the XBTs. The SVP failed to record consistently at each of the four deployment locations and as such the water column velocity structure was constrained solely from the XBT data and subsequent water wave modelling.

The XBT data show that temperature of the water column varies with depth. The variation is most easily divided into two sections, an upper and a lower layer in which the

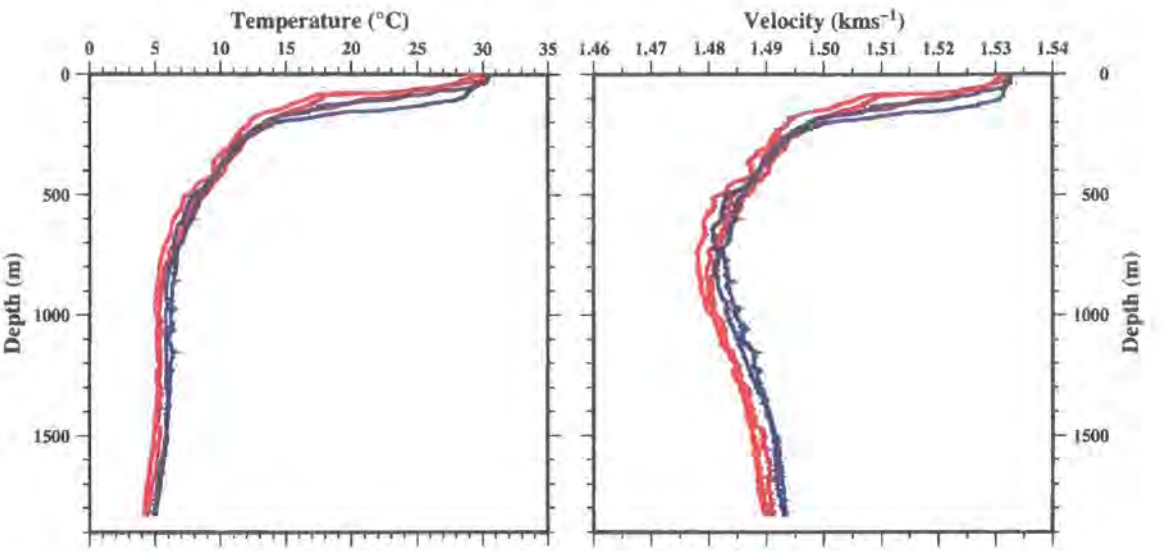


**Figure 3.20**: Velocity structure of the water column. (Left) Temperature-depth and (right) *P*-wave velocity-depth plots of XBT data, acquired at three points along Profile A (red) and two points along Profile D (blue). See Figures 2.2 and 2.3 for locations. Conversion from temperature to velocity (Shiobara *et al.*, 1997) assumed a constant salinity of 30‰. The profiles indicate that the velocity structure of the water column is relatively consistent between the sampling sites. The velocity initially decreases with depth, to a minimum velocity of 1.48 kms$^{-1}$ at ~750 m depth. Here, velocity begins to increase gradually with depth to ~1.49 kms$^{-1}$.

temperature decreases and increases, respectively, with depth. Additionally water column reflections are observed within the MCS data at ~1 s TWTT (Hobbs *et al.*, 2006) which suggest two distinct bodies of water (Figure 3.21). Thus any WA modelling of water waves needs to consider the variation in velocity with depth.

To estimate the variation, XBT temperature data were converted to *P*-wave velocities using Equation 3.2 (Shiobara *et al.*, 1997 – Figure 3.20),

$$v = 1449.2 + 4.623T - 0.0546T^2 + 0.1605P + 1.391(S - 35) \qquad (3.2)$$

where $v$ is the velocity in ms$^{-1}$, $T$ is the temperature in °C, $P$ is the pressure in bar[c], and $S$ is the salinity in ‰. Here, the pressure is assumed increase by 0.1 bar per metre depth and the salinity to be 30‰. Calculations indicate that the *P*-wave velocity at the surface is ~1.53 kms$^{-1}$, decreasing sharply with depth to a minimum of ~1.48 kms$^{-1}$ at ~750 m depth. Below this, the velocity increases gradually to ~1.49 kms$^{-1}$ at ~1800 m depth, the maximum measurement depth for the T5-type XBTs available for D275.

Water column reflections suggest abrupt changes in salinity, consistent with the theory that the uppermost body of water in this region is partially sourced from the freshwater outflow from the Amazon River, while the lowermost body is normal seawater. The upper

[c]In S.I. units 1 bar = 105 Pa = 105 kgm$^{-1}$s$^{-2}$

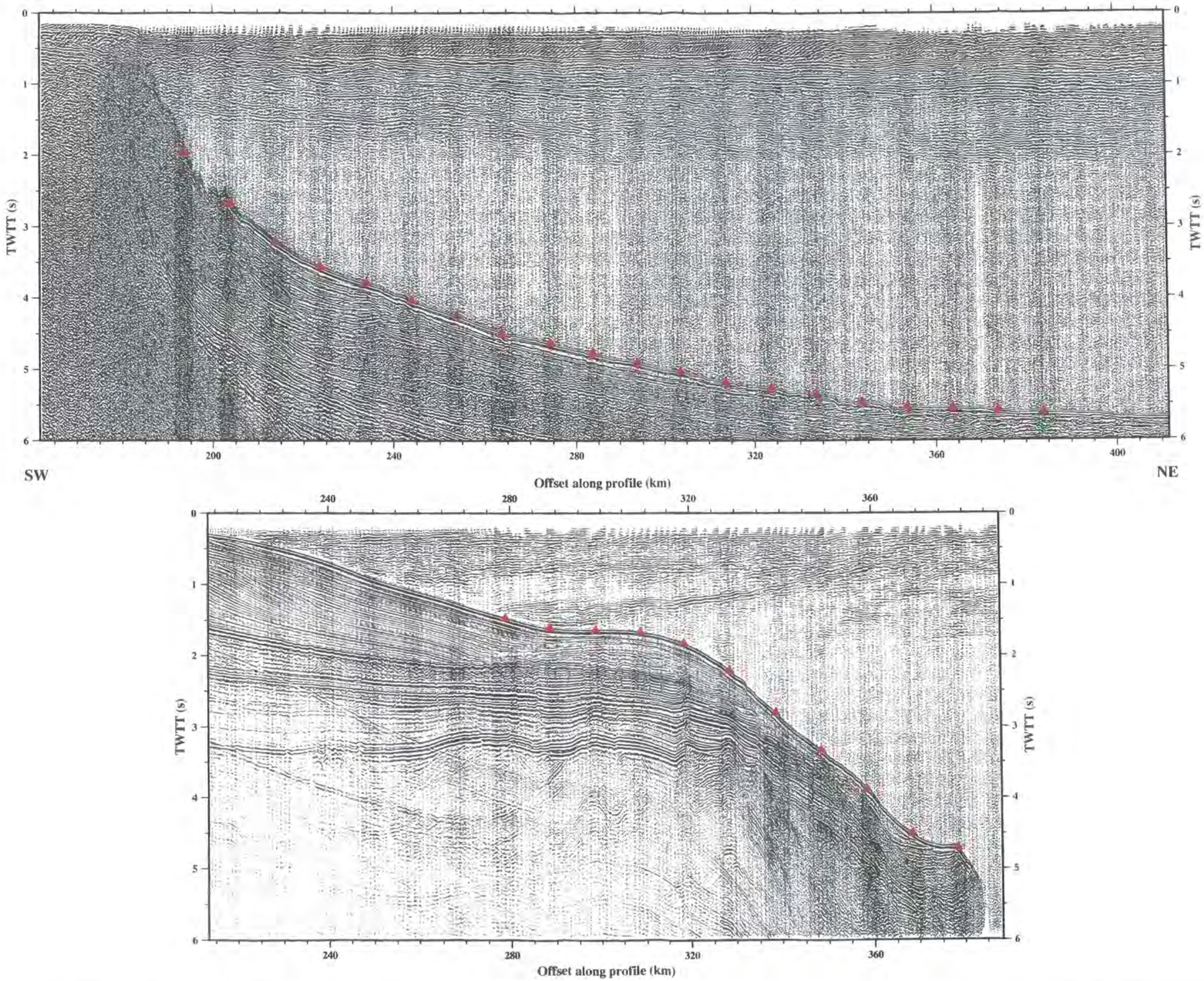


**Figure 3.21**: Reflections observed within the water column along Profile A (top) and D (bottom). Time sections, after Hobbs (2006), are processed using seismic oceanographic techniques to emphasise reflections within the water column. Distinct, relatively continuous reflections are observed along both profiles, suggesting significant variation with depth of velocity, density, temperature and/or salinity. OBS locations are highlighted by red triangles. The sections, processed to image the water column structure, can be compared with those processed to image the subseabed in Figures 2.7, 2.15 and 3.29.

body is being transported northwards by ocean currents. The likely change in salinity observed from the MCS data through the water column, suggests that the constant salinity assumption used above is inappropriate. However, a change as large as 10‰ would represent <1% change in velocity at a temperature of 20°C. Hence the assumption is considered valid within all other errors.

Using *rayinvr*, $W_w$ arrivals could not be accurately matched using a single velocity layer (Figure 3.22). Thus, the velocity structure of the water column was approximated by two layers in which the uppermost 750 m shows a decrease in velocity with depth, and the deeper water shows an increase with depth, consistent with the XBT data. Using this structure, the $W_w$ phases of 16 OBSs along Profile A and 12 along Profile D were matched.

However, water wave modelling of the remaining instruments, using this water column model, suggested that there was a likely static timing problem. A 20-80 ms timing adjustment was applied to match the water wave. These timing corrections are too large to have been caused by instrument drift and may, in part, be a result of inaccuracies in the water column model, due to the sparsity of the XBT data. Alternatively, and more likely, they may be caused by timing errors within instruments during data acquisition or data translation.

A total of 16332 $W_w$ arrivals were matched (Figure 3.23) to within errors of $\chi^2$=0.84 for Profile A and $\chi^2$=0.51 for Profile D, suggesting a high degree of confidence in the positioning of the OBSs, the velocity structure of the water column and the definition of the seabed interface within the model.

### 3.8.3 Subsurface strata

The approach adopted for modelling of the subsurface was similar to that described by Zelt (1999) and comprised several steps:

- Layers were modelled from the top down, from the shallowest sediments down to the upper mantle, starting initially with a single OBS from the oceanward end of the profile, where the subseabed was assumed to be structurally simplest;
- Initial layer velocities were estimated from the record sections for each OBS using a 1D approach separately for the landward and oceanward data for each instrument;
- For the sediment column, the lower layer boundary depth was estimated from the MCS data;

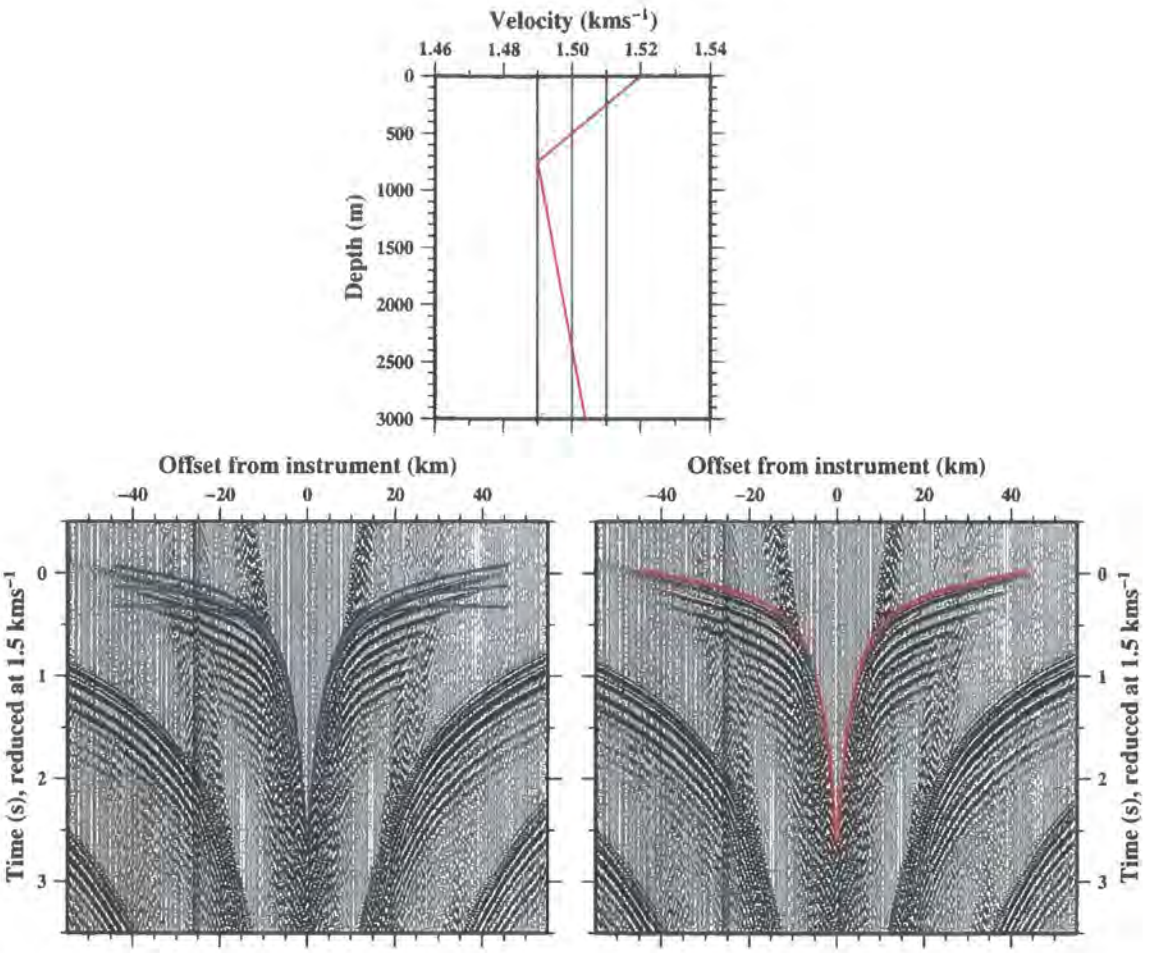


**Figure 3.22**: Direct water wave modelling. (Bottom) Modelling of water waves for OBS A16, using a constant velocity (left) of 1.49 $kms^{-1}$ (purple), 1.50 $kms^{-1}$ (green) and 1.51 $kms^{-1}$ (blue) within the water column and using the preferred two layer velocity structure (right – red). The associated velocity-depth profiles are shown (top). The two layer water column significantly improves the fit between calculated and observed traveltimes.

- Velocities and boundary depths were altered in a progressive manner to improve the fit between calculated and observed traveltimes for each phase. If necessary, phase selection was reassessed and reassigned;
- Sediment column layer boundaries were checked for consistency with the MCS data by converting the velocity model to TWTT and superimposing on the MCS sections;
- $\chi^2$ values were calculated for the layer, to check the fit with respect to error bounds;
- The process was then repeated for the next layer down;
- Often, when lower layers were incorporated into the model it was necessary to reassess upper layers;

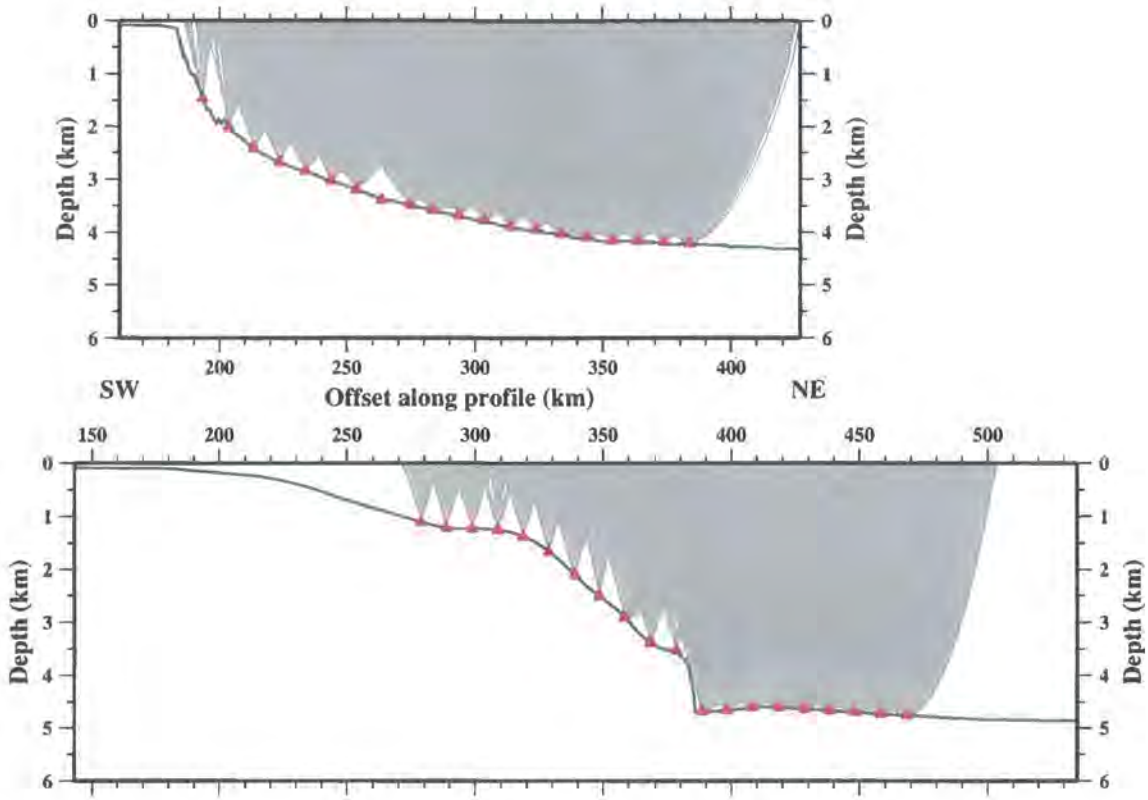


**Figure 3.23**: Ray coverage within the water column (grey) for Profile A (top) and Profile D (bottom). The relative position of OBSs (red triangles) on the seabed (green) is also indicated.

- Adjacent OBSs were then incorporated and the procedure repeated; and
- In general, the model was constructed with only small horizontal velocity gradients, avoiding abrupt lateral changes which tend to terminate ray paths or narrow ray coverage within the models.

A flexible approach was adopted and often steps were merged and multiple layers modelled together as the fit progressively improved. Similarly, multiple OBSs were incorporated at a time if the model suggested little lateral change between adjacent instruments. The relatively short (~10 km) offsets between instruments resulted in dense ray coverage across the majority of each model, with each layer constrained by multiple crossing ray paths into multiple adjacent instruments. A fit in such circumstances demonstrates reasonable model resolution and confidence.

Once the models had been created and an approximate fit achieved, final adjustments were applied, again from the top to the bottom layer, using assessment of $\chi^2$ values to pinpoint and correct any remaining discrepancies between modelled and observed data.

### 3.8.4 Land station data modelling

Once an acceptable fit to the OBS data had been achieved the land station data were incorporated into the modelling procedure. The modelling approach was very similar to that for the OBS data, and *rayinvr* (Zelt & Smith, 1992) was used to ray-trace between the land stations and the seismic shots. Traveltime phase identifications were made by first extrapolating the model landwards, using *P*-wave velocities and layer boundaries modelled with the OBS data, and setting the Moho depth to the global average continental crustal thickness of 39 km (Christensen & Mooney, 1995). Source-receiver traveltimes were then calculated and compared with those observed in the record sections. This comparison indicated that the main observed phases in the data were refractions travelling through the mid-lower continental crust ($P_{g2}$) and either diving rays from the upper mantle ($P_n$) or WA reflections from the Moho discontinuity ($P_mP$) (Figure 3.16).

As a consequence of the lack of near-offset arrivals within the land station data, the models are not constrained in the near surface adjacent to the land station locations. Thus, a much higher degree of smoothing and interpolation was required compared to the offshore modelling. Consequently, crustal velocities were estimated from velocities modelled near the continental margin and from values found in the standard velocity-depth envelopes for the continental crust (Christensen & Mooney, 1995). This approach is not ideal, but was necessary given the sparse data coverage. This model was then forward modelled to improve the fit of the data.

The greater degree of smoothing and interpolation reduces the reliability of the models in the landward regions. However, the combination of onshore and offshore instruments is very useful as it provides the only constraint on the thickness of the pre-rift crust and also the 'rapidity' of thinning.

## 3.9 Results

This section describes the results of WA modelling in terms of data fit and ray coverage. Examples of the phase identification, ray coverage and data fit are provided (Figures 3.24-3.28 and 3.30-3.34) which are typical of the range of structures observed across the margin and emphasise the relative lateral and vertical variation in structure. A complete set of record sections is provided in Appendix C. In addition, a comparison of the layer boundaries which define the WA models, converted to TWTT, with reflectors imaged in the MCS data is shown in Figure 3.29, to demonstrate the consistency between these coincident data.

Within the WA modelling, two criteria were used to assess the data fit. Firstly, travel-time picks were matched within the errors and, secondly, the $\chi^2$ measure of misfit should be $<1$. The preferred, best-fit *P*-wave velocity-depth model for each profile and the structures observed therein will be presented and described in Chapter 5, although a brief, preliminary interpretation is provided in Section 3.10.

### 3.9.1 Profile A

Examples of the ray-trace modelling are shown for OBSs A2, A7, A16, A20 and land station A25 in Figures 3.24-3.28. The statistical fit of observed and calculated phases marked on these examples is summarised in Table 3.4. At this scale, it is difficult to distinguish the calculated and observed $W_w$ phases. However, they fit to within the errors, and for the entire model the $W_w$ arrivals are matched to a $\chi^2$ fit of 0.84, which demonstrates the accurate positioning of the instruments within the model (Section 3.7.3).

Phases $P_{s2}$ and $P_{s3}$ are shown emerging from the water wave on each of the marine examples and modelling demonstrates dense ray coverage within the upper sediments. $P_{s1}$ arrivals are often obscured by the water wave. Consequently, constraint is primarily provided by comparing the WA model layer boundaries with reflectors observed in the MCS data (Figure 3.29). Within these uppermost sediment layers over 1200 traveltime picks, the vast majority with $\pm$15 ms error bounds, were modelled to a $\chi^2$ less than 1.

Whilst the record sections show that $P_{s3}$ arrivals emerge from $P_{s2}$ arrivals, this is not the case for $P_{s4}$. Thus, the boundary between the third and fourth sediment layers is modelled as a distinct change in the velocity gradient (0.65-0.30 $s^{-1}$) within the sediment column. Additionally, this boundary is coincident with a major unconformity at ~7.5 s TWTT in the MCS data. Few refracted arrivals are observed from the lower sedimentary layers, and layer velocities and depths are generally modelled from secondary or reflection phases. The basement surface, beneath the fifth sedimentary layer, is well constrained by MCS data and a combination of WA refractions ($P_{g1}$) and reflections ($P_{g1}P$).

The uppermost basement velocities at the oceanward end of the profile are poorly constrained as a consequence of few refracted arrivals being recorded that propagate within it. However, the A2, A7, A16 and A20 record sections show distinct far offset (>15 km) arrivals identified as $P_{g2}$ and $P_n$. Each of these lower crustal and uppermost mantle phases comprise a total of over 3000 picks from all OBS record sections, modelled to $\chi^2$ fits of 1.07 and 1.11 respectively. In addition to the refracted arrivals, the Moho at the oceanward end of the profile is constrained by relatively few reflection events, although they are well

| Phase | $n$ | $m_{rms}$ (ms) | $\chi^2$ |
|---|---|---|---|
| $W_w$ | 9021 | 0.014 | 0.840 |
| $P_{s1}$ | 85 | 0.011 | 0.566 |
| $P_{s2}$ | 386 | 0.016 | 1.186 |
| $P_{s3}$ | 795 | 0.014 | 0.852 |
| $P_{s4}$ | - | - | - |
| $P_{s5}$ | 650 | 0.027 | 0.995 |
| $P_{s2}P$ | 46 | 0.047 | 0.866 |
| $P_{s3}P$ | 26 | 0.020 | 0.168 |
| $P_{s4}P$ | 554 | 0.043 | 0.575 |
| $P_{s5}P$ | 917 | 0.032 | 0.313 |
| $P_{g1}$ | 435 | 0.061 | 1.678 |
| $P_{g2}$ | 3194 | 0.054 | 1.070 |
| $P_{g1}P$ | - | - | - |
| $P_n$ | 3586 | 0.073 | 1.105 |
| $P_mP$ | 398 | 0.044 | 0.787 |
| All OBS phases | 20093 | 0.042 | 0.919 |
| | | | |
| $P_{g2}$ | 962 | 0.115 | 1.067 |
| $P_mP$ | 519 | 0.144 | 1.866 |
| All land station phases | 1481 | 0.126 | 1.346 |

**Table 3.4**: Observed phases, traveltime picks and statistical analysis of WA modelling for Profile A.

distributed within a zone from 250-360 km offset. In general, the deep structure is modelled to within the error bounds and, given the dense ray coverage, high confidence.

The thinning upper crust beneath the continental slope is modelled by 1163 oceanward travelling arrivals from the first four OBSs (Figure 3.28), which fit the observed data to within a root-mean-square (rms) error of 87 ms and a $\chi^2$ of 1.77. The lower crust in the region of thinning is poorly sampled and constraint within the model is low.

The land station record sections provide an additional 1483 traveltime picks, which are matched to a $\chi^2$ of 1.35. As indicated previously, the land stations did not record any short offset arrivals as a consequence of the acquisition geometry, and hence these land stations contribute little to the shallow crustal parts of the model. However, the arrivals do provide constraint on the bulk properties of the crust at the landward end of the profile and also provide an indication of the depth to the Moho in this region and, hence, crustal thickness.

### 3.9.2 Profile D

Figures 3.30-3.34 show examples of the ray-trace modelling for OBSs D2, D7, D14 and D20 and land station D24 respectively. Table 3.5 shows the statistical fit of the observed

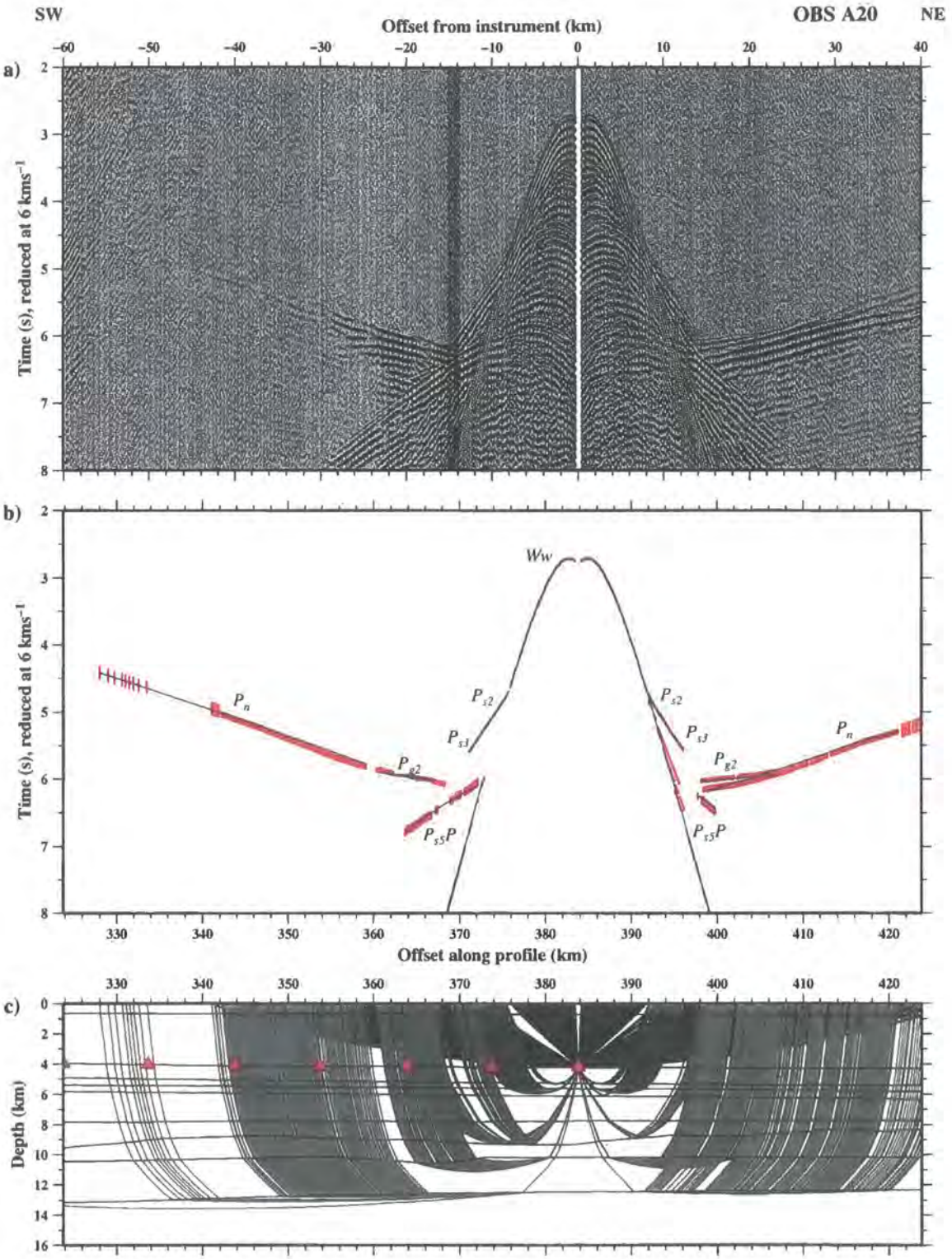


**Figure 3.24**: Ray-trace modelling of hydrophone data recorded at OBS A20 located towards the base of the continental slope (see Figure 2.2 for instrument location). (Top) Filtered record section reduced and plotted at true amplitude. The horizontal axis shows offset from the instrument position. (Middle) Record section showing observed (red vertical bars whose length represents the assigned picking error) and calculated (blue lines) traveltime picks for comparison. For this and the ray diagram (bottom), the horizontal axis shows model offset along Profile A. Phases are labelled as described in Section 3.4.1. (Bottom) Ray diagram showing modelled arrivals. Red triangles show OBS locations. Both record sections are plotted at a reduction velocity of 6 kms$^{-1}$ and at the same horizontal scale with each part aligned to the instrument position.

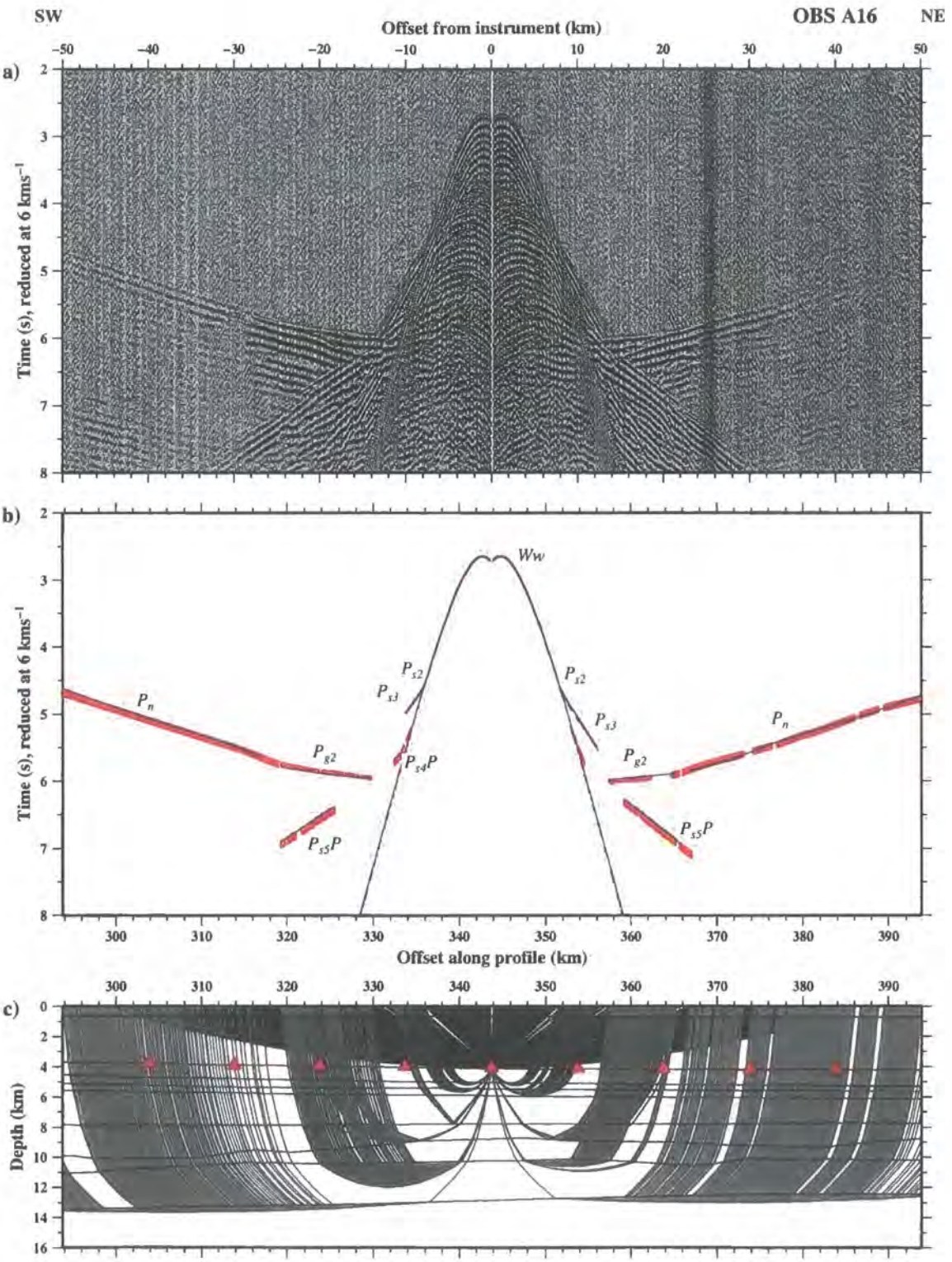


**Figure 3.25**: Ray-trace modelling of hydrophone data recorded at OBS A16 (see Figure 2.2 for instrument location). See Figure 3.24 for details.

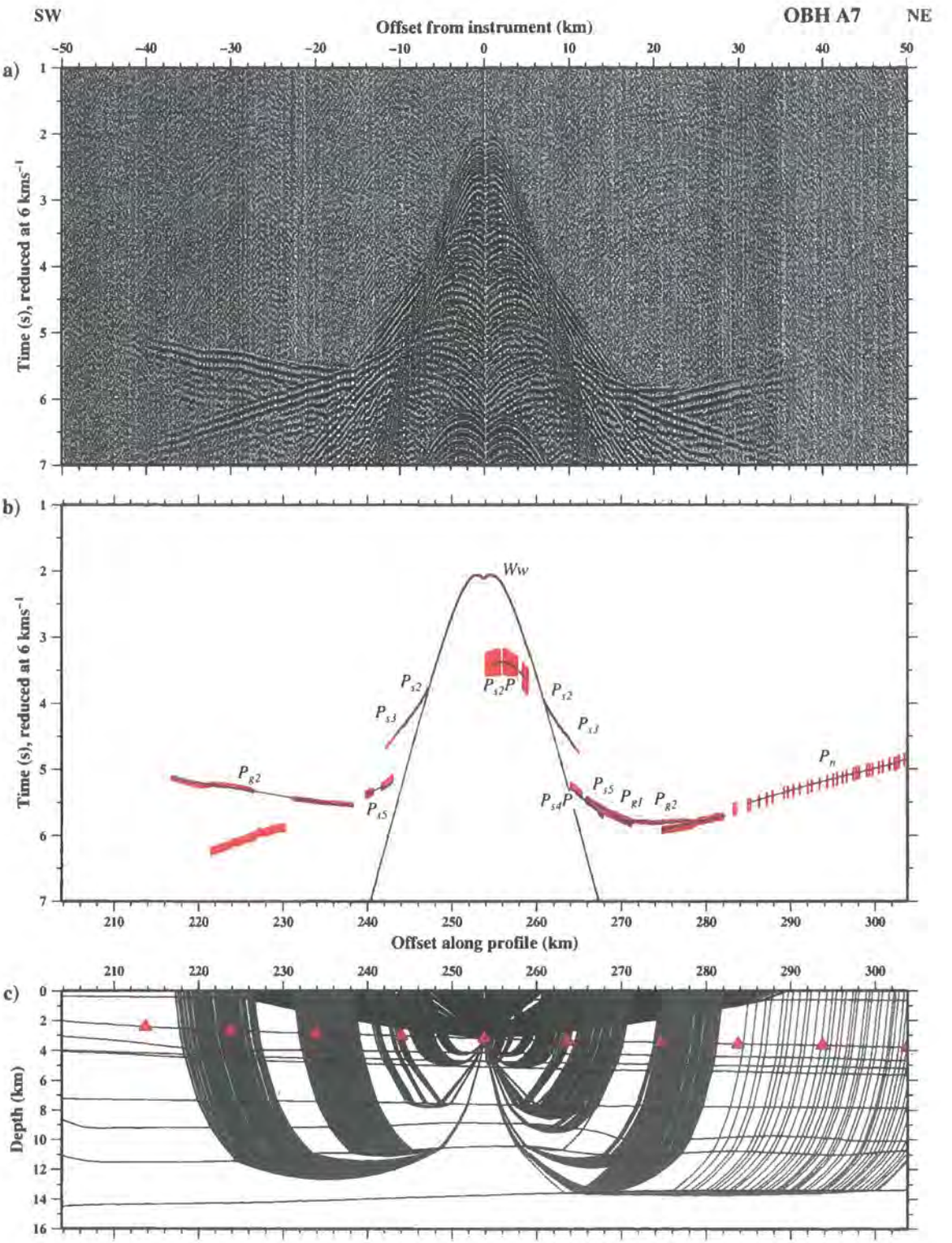


**Figure 3.26**: Ray-trace modelling of hydrophone data recorded at OBS A7 (see Figure 2.2 for instrument location). See Figure 3.24 for details.

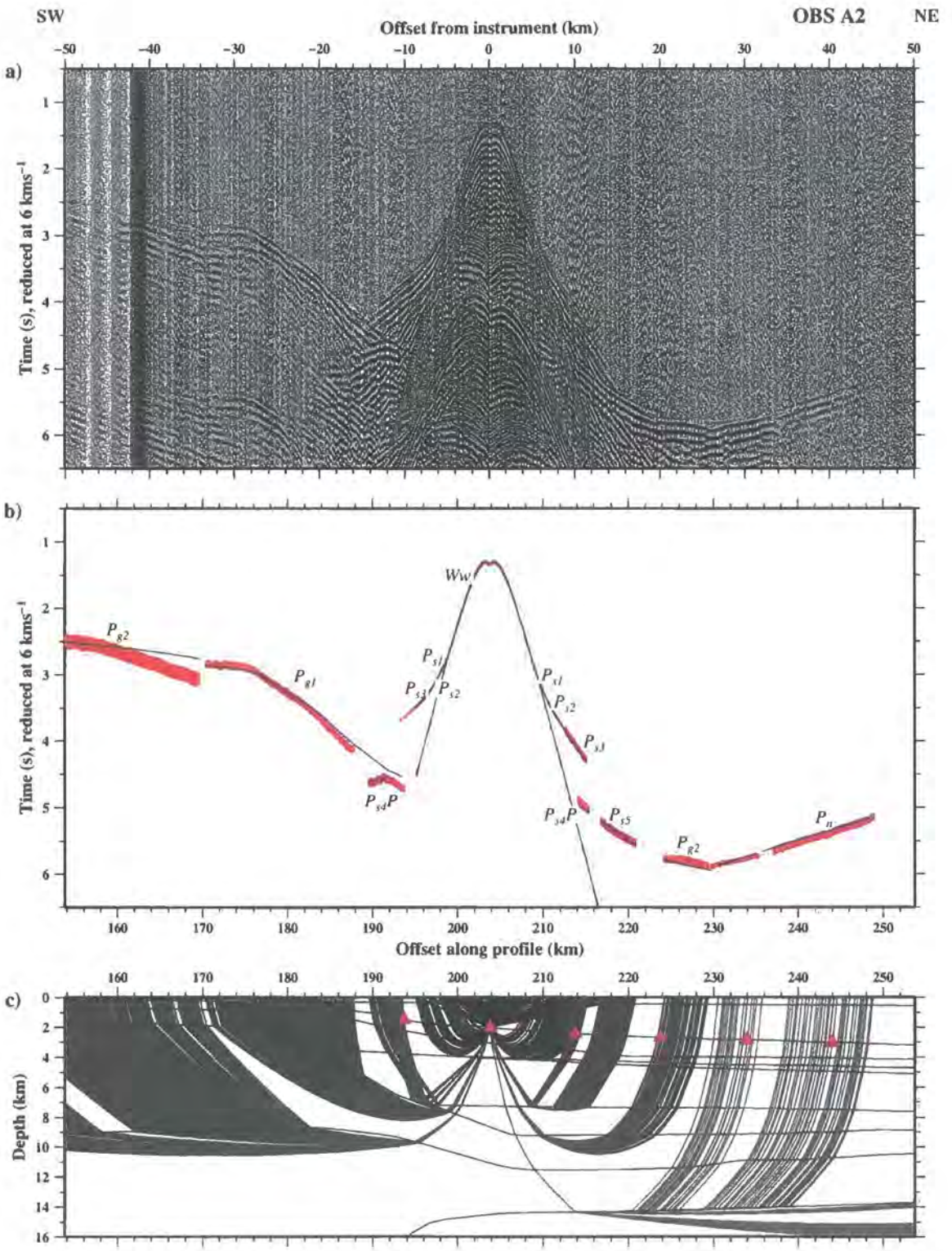


**Figure 3.27**: Ray-trace modelling of hydrophone data recorded at OBS A2 (see Figure 2.2 for instrument location). See Figure 3.24 for details.

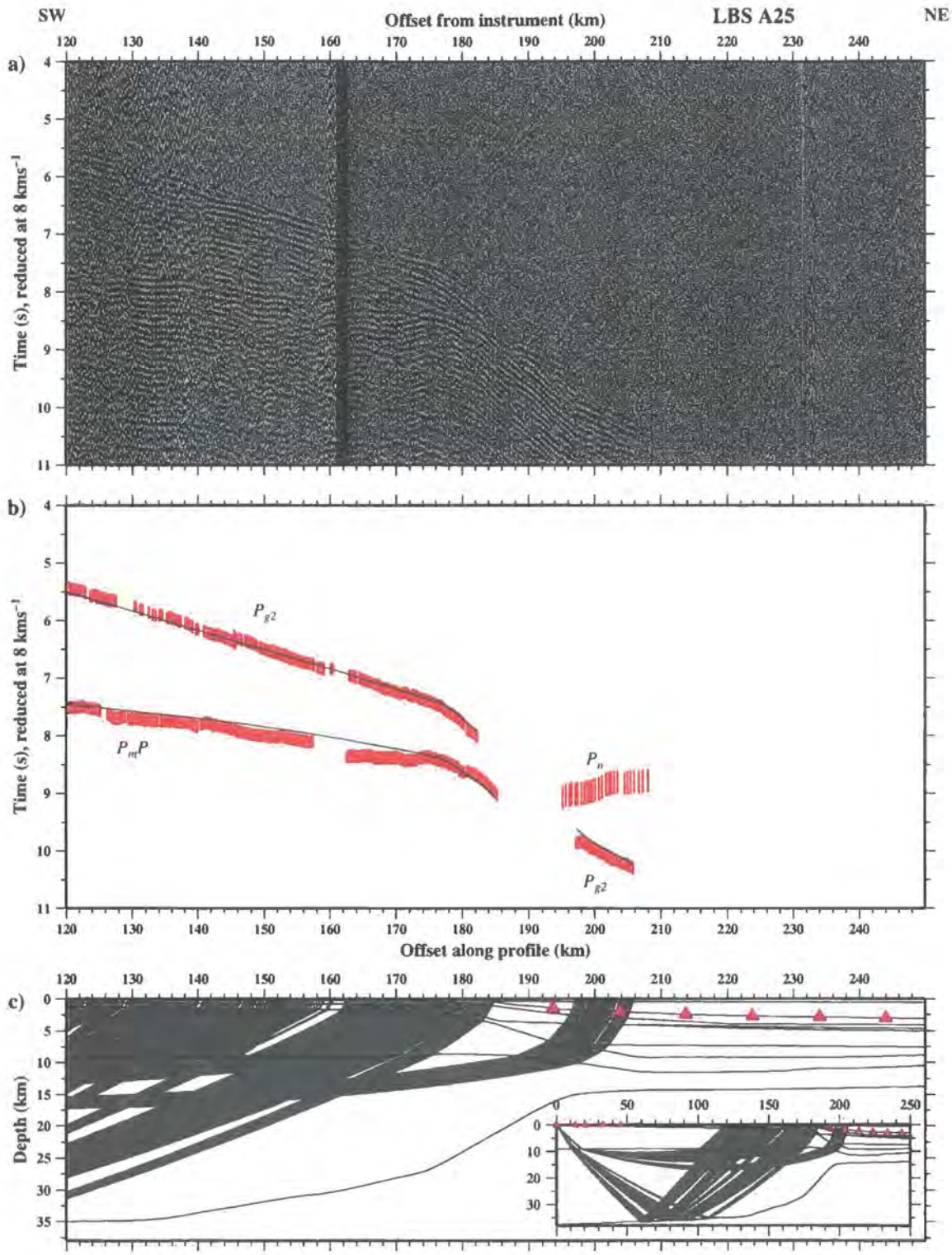


**Figure 3.28**: Ray-trace modelling of vertical geophone data recorded by land station A25 located at the southwest end of Profile A (see Figure 2.2 for instrument location). (Top) Filtered record section reduced and plotted at true amplitude. The horizontal axis shows offset from the instrument position. Arrival labels are defined in the text. (Middle) Record section showing observed (red vertical bars whose length represents the assigned picking error) and calculated (blue lines) traveltime picks for comparison. For this, and the ray diagram (bottom), the horizontal axis shows model offset along Profile A. Phases are labelled as described in Section 3.4.1. (Bottom) Ray diagram showing modelled arrivals. Red triangles show OBS locations. Inset shows the location of the five land stations (red triangles) at the southwest end of Profile A relative to the modelled arrivals. Both record sections are plotted at a reduction velocity of 8 kms$^{-1}$ and at the same horizontal scale with each part aligned to the instrument position.

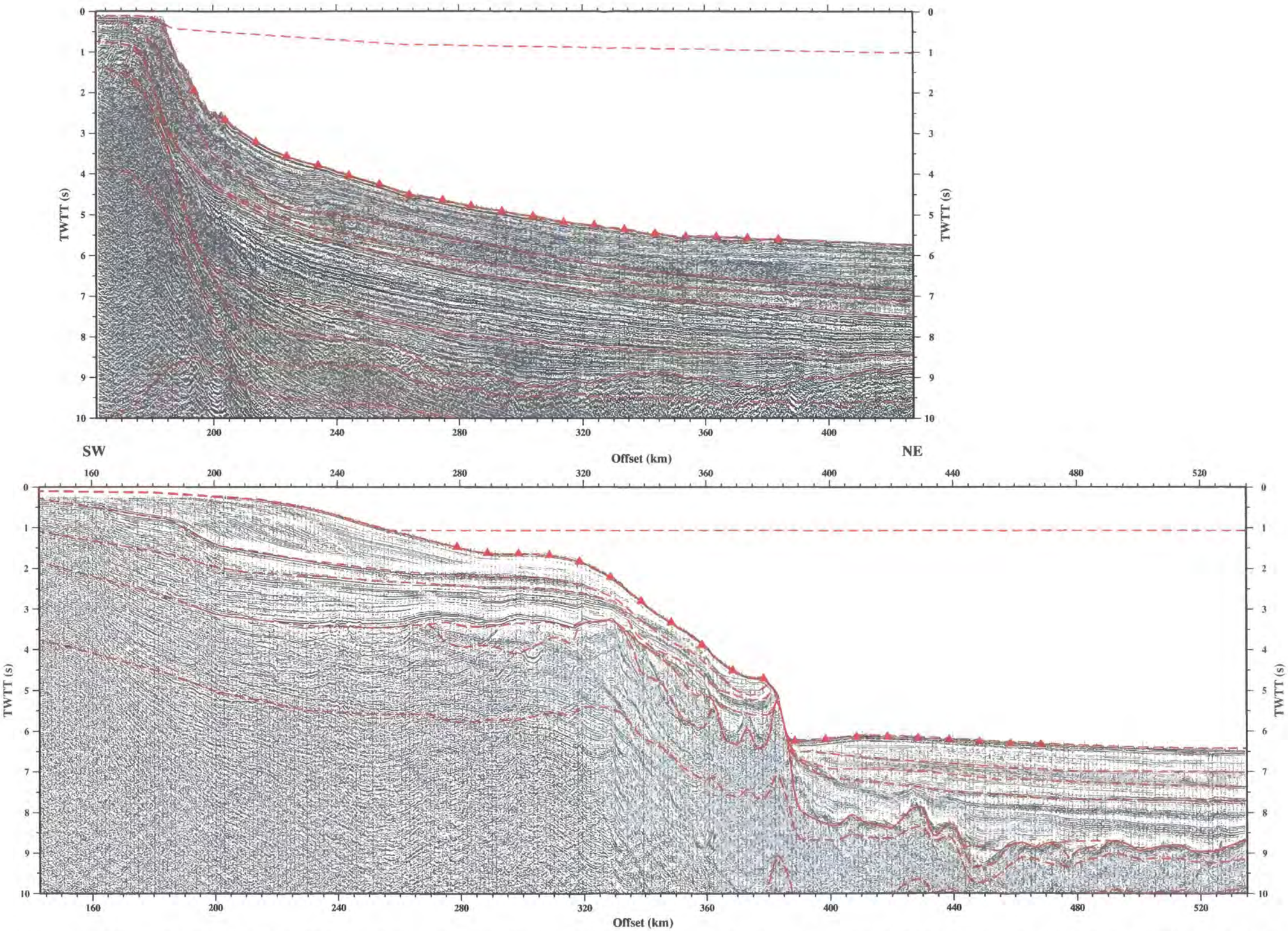


**Figure 3.29**: Comparison of WA model layer boundaries with MCS reflections for Profiles A (top) and D (bottom). Migrated time sections with layer boundaries (red) from the WA *P*-wave velocity-depth model overlain. OBS locations are indicated by red triangles.

and calculated phases marked on these examples. The $W_w$ phases fit within the errors to a $\chi^2$ of 0.51 which, similar to Profile A, illustrates the accurate positioning of the OBSs within the model.

Similar to Profile A, arrivals refracted in the uppermost sediment layer are obscured by the water wave and as a result no $P_{s1}$ phase is observed along Profile D. Furthermore, as discussed in the dataset description (Section 3.4.3), fewer sedimentary refracted arrivals (phases $P_{s2}$-$P_{s5}$) are observed along Profile D than Profile A (1341 traveltime picks compared with 1916). However, an increased number (1486 versus 626) of reflected arrivals ($P_{s2}P$-$P_{s4}P$) were modelled which improved constraint on the intra-sediment column interface geometries. Consequently, the shallow sedimentary layers are modelled to a $\chi^2$ of <1. However, the statistical fit on the deeper sediment layers is poorer, with the $P_{s5}$ matched to a $\chi^2$ of 1.88 and $P_{s4}P$ to $\chi^2$=1.77. Despite the higher $\chi^2$ values, the sedimentary layers are considered to be well constrained given the close fit between the layer boundaries and the MCS reflections (Figure 3.29).

At the oceanward end of the profile the sub-sedimentary crustal model is constrained by refractions within the lower crustal layer ($P_{g2}$) and the uppermost mantle ($P_n$). In contrast, the landward end of the profile is constrained by refractions in the upper crustal layer ($P_{g1}$) as well as $P_{g2}$. For the model as a whole, the statistical fit of $P_{g1}$ is $\chi^2$=2.84, which is relatively poor and is attributed to two main causes. Firstly, the surface which separates sedimentary and crystalline basement at the oceanward end of the profile is indistinct in the MCS data. This is a significant problem given that the surface is expected to show considerable lateral topographic variation, as indicated by the MCS section shown in Figure 2.27. The depth to the surface changes over relatively short length scales when compared with the 10 km OBS spacing and, thus, is difficult to resolve from the WA data. Secondly, in the vicinity of ~385 km offset, the depths to the seafloor and basement change sharply, resulting in steep interfaces and several layers 'pinching' together. In this region ray-tracing through the upper crustal layer, in particular, is highly dependent upon these steep boundaries and associated steep velocity gradients. Thus, for nearby instruments (OBSs D11 and D12) the fit obtained is poorer than elsewhere within the model.

Calculated and observed $P_g$ and $P_n$ phases match to $\chi^2$=1.95 and $\chi^2$=1.22 respectively. The problems associated with the upper crustal layer described above, result in a slightly poorer fit than anticipated for these two phases. However, they are modelled to within reasonable errors. Steep changes in depth to Moho are more densely sampled along Profile D than Profile A, indicating that the WA modelling has constrained the Moho more tightly around the probable OCT region.

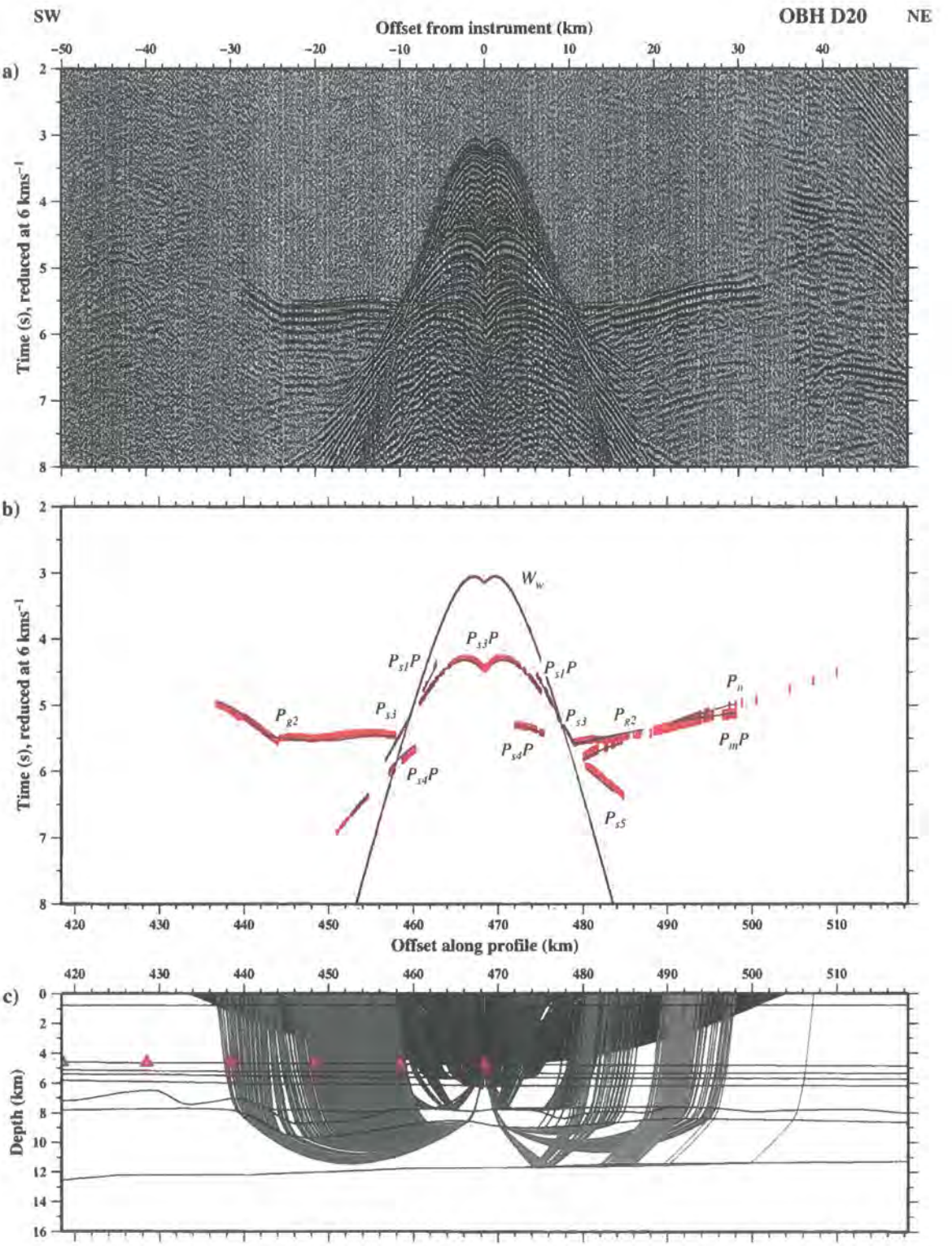


**Figure 3.30**: Ray-trace modelling of hydrophone data recorded at OBS D20 (see Figure 2.3 for instrument location). See Figure 3.24 for details.

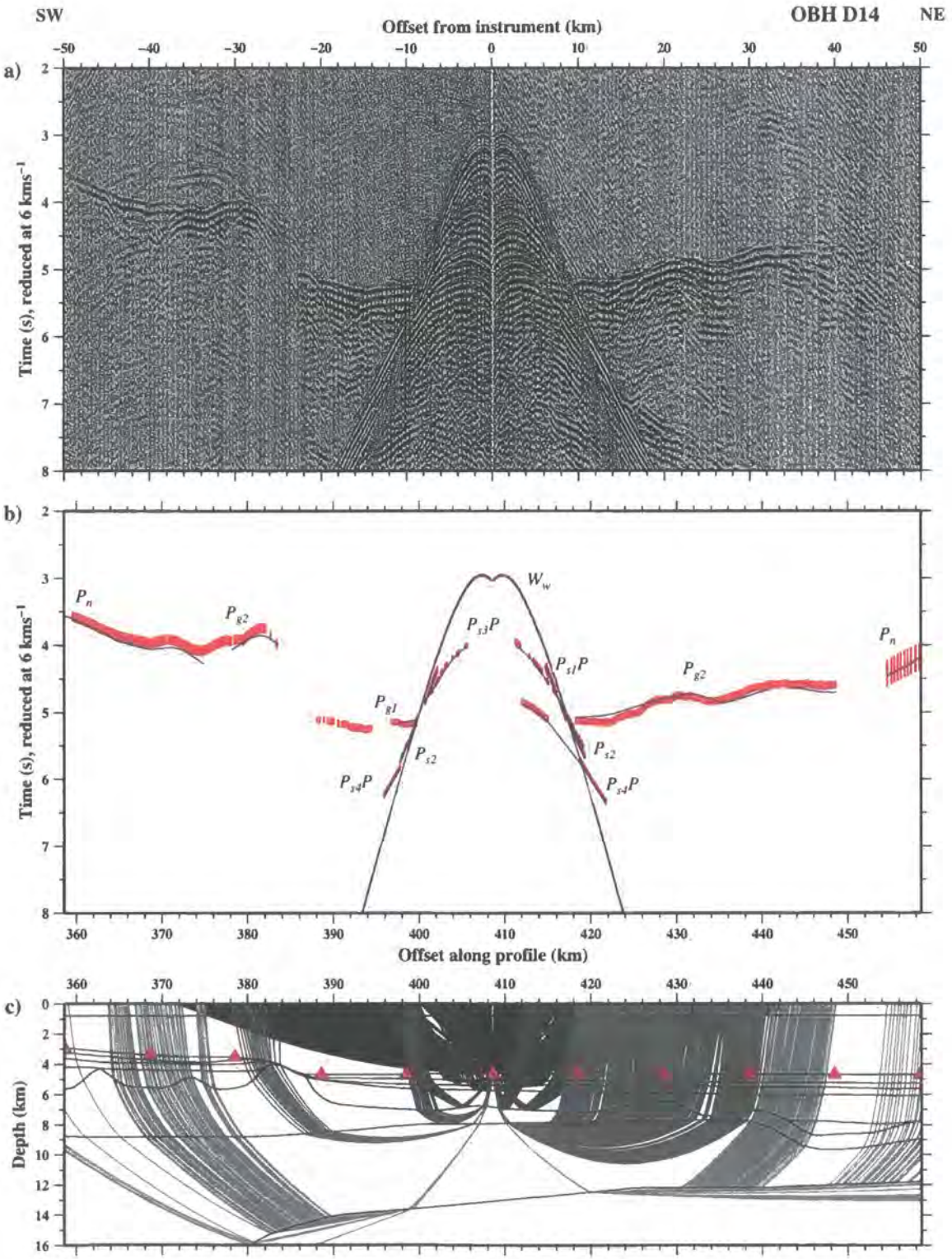


**Figure 3.31**: Ray-trace modelling of hydrophone data recorded at OBS D14 (see Figure 2.3 for instrument location). See Figure 3.24 for details.

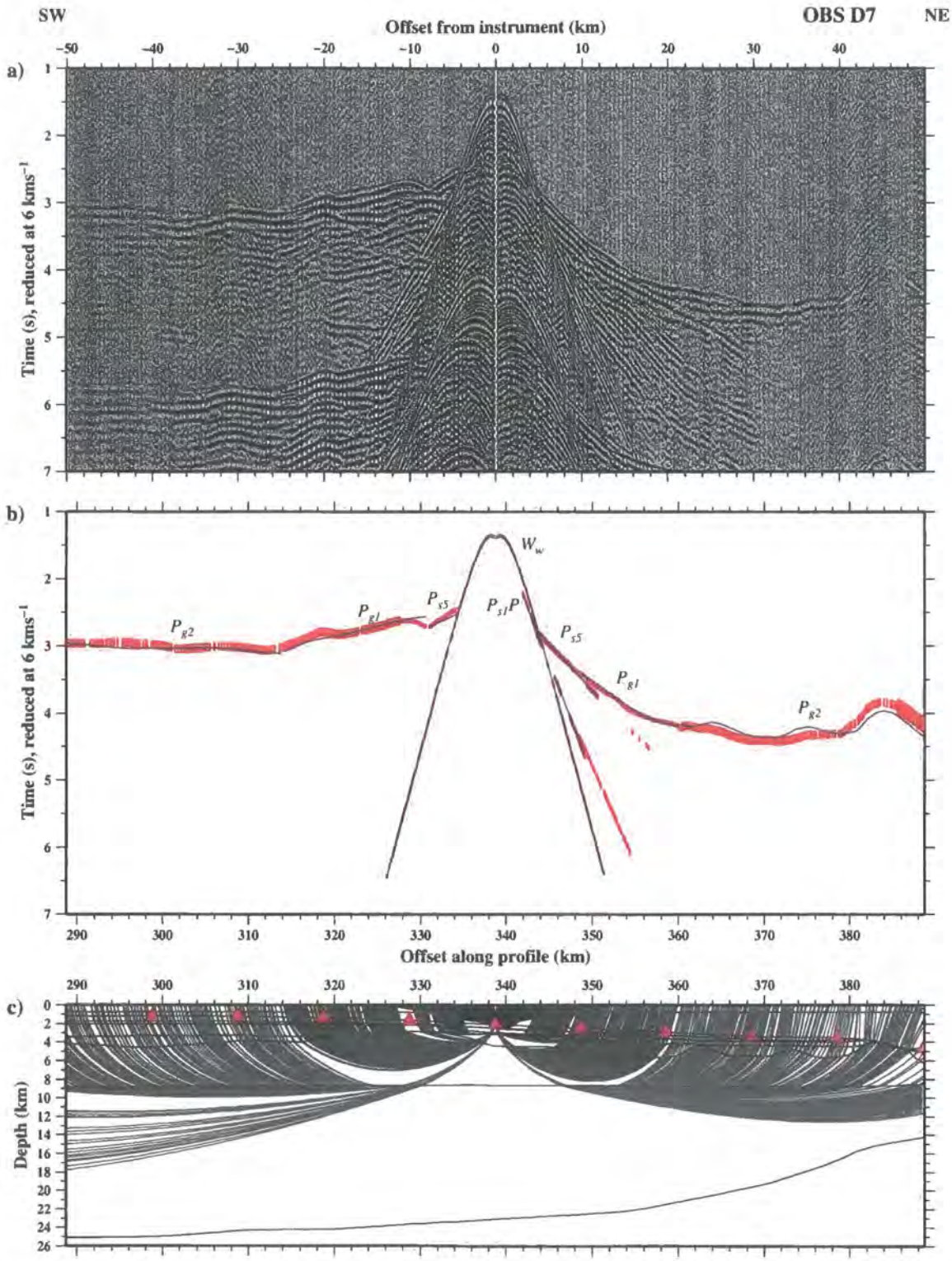


**Figure 3.32**: Ray-trace modelling of hydrophone data recorded at OBS D7 (see Figure 2.3 for instrument location). See Figure 3.24 for details.

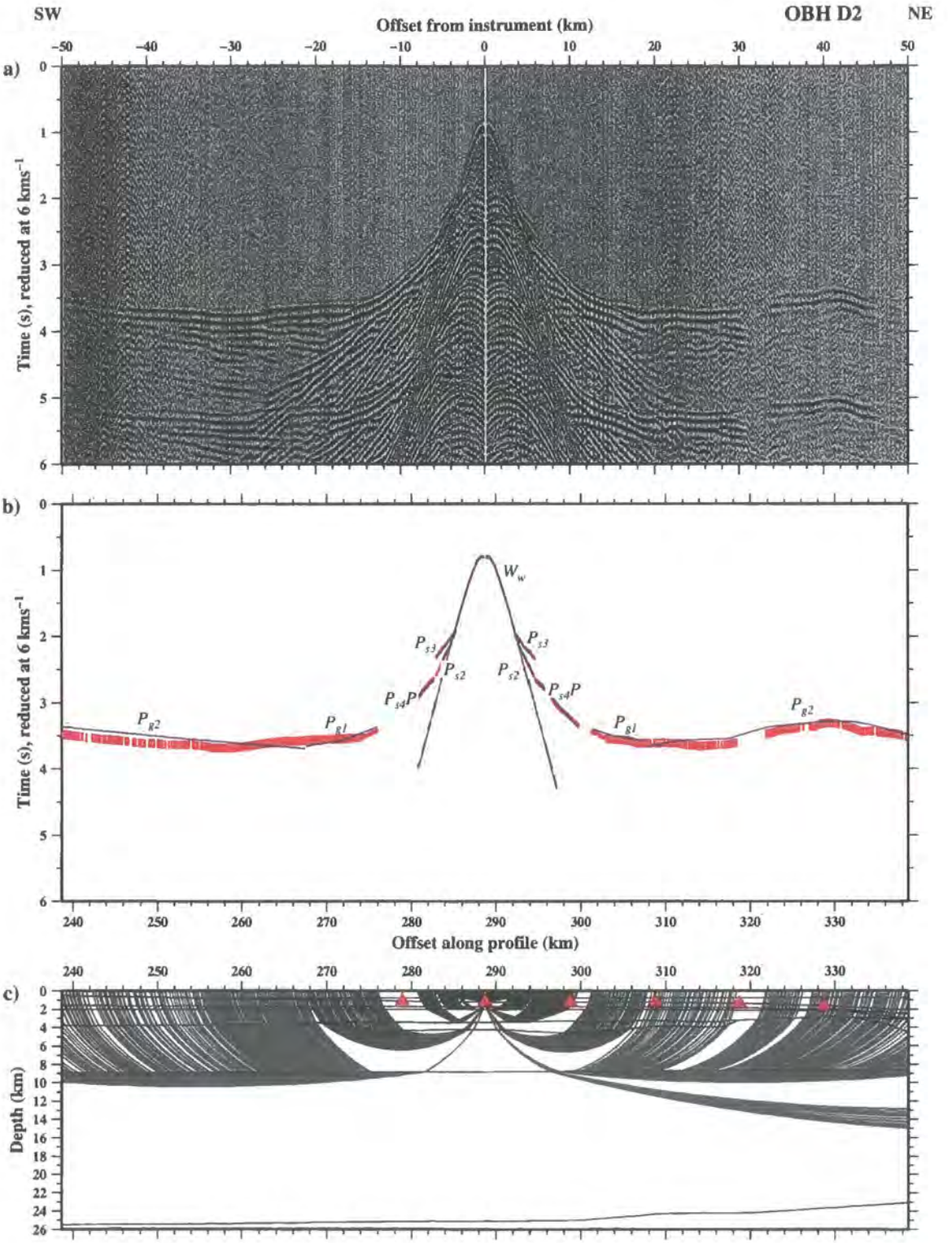


**Figure 3.33**: Ray-trace modelling of hydrophone data recorded at OBS D2 (see Figure 2.3 for instrument location). See Figure 3.24 for details.

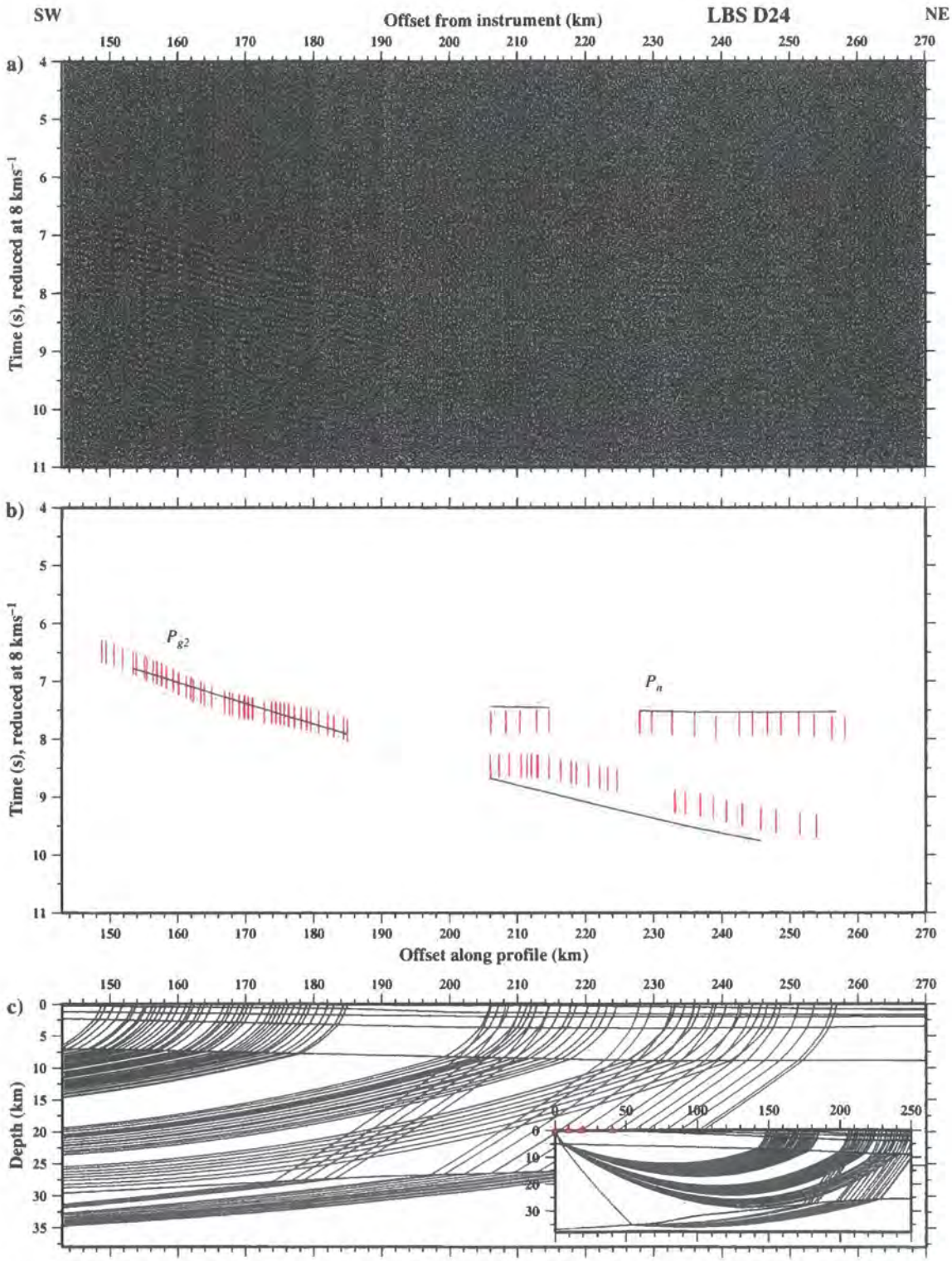


**Figure 3.34**: Ray-trace modelling of vertical component geophone data recorded at land station D24 (see Figure 2.3 for instrument location). See Figure 3.28 for details.

| Phase | $n$ | $m_{rms}$ (ms) | $\chi^2$ |
|---|---|---|---|
| $W_w$ | 7311 | 0.014 | 0.512 |
| $P_{s1}$ | - | - | - |
| $P_{s2}$ | 496 | 0.016 | 0.380 |
| $P_{s3}$ | 455 | 0.023 | 0.998 |
| $P_{s4}$ | 27 | 0.021 | 0.186 |
| $P_{s5}$ | 363 | 0.049 | 1.883 |
| $P_{s2}P$ | 73 | 0.030 | 0.531 |
| $P_{s3}P$ | 946 | 0.026 | 0.503 |
| $P_{s4}P$ | 467 | 0.063 | 1.771 |
| $P_{s5}P$ | 202 | 0.051 | 0.854 |
| $P_{g1}$ | 2013 | 0.082 | 2.839 |
| $P_{g2}$ | 7434 | 0.093 | 1.954 |
| $P_{g1}P$ | - | - | - |
| $P_n$ | 980 | 0.120 | 1.216 |
| $P_mP$ | 386 | 0.072 | 0.893 |
| All OBS phases | 21639 | 0.068 | 1.316 |
| | | | |
| $P_{g2}$ | 101 | 0.232 | 1.363 |
| $P_n$ | 90 | 0.148 | 0.553 |
| All land station phases | 191 | 0.197 | 0.976 |

**Table 3.5**: Observed phases, traveltime picks and statistical analysis of WA modelling for Profile D.

The land station record sections provide limited ray coverage at the landward end of the profile. Unfortunately, only two of the four deployments acquired usable data and observed phases were less well defined than the data from the Profile A land stations, resulting in a reduced pick accuracy. However, 191 traveltime arrivals were picked and these were modelled to a $\chi^2$ of $<1$. These included 90 $P_n$ arrivals which constrain the crustal thickness at the southwestern extreme of the Profile.

## 3.10 Preliminary interpretation

Forward modelling of the WA data has resulted in $P$-wave velocity-depth models of the deep crustal structure along Profiles A and D (Figure 3.35). An interpretation is required at this stage in order to guide further testing of resolution and uniqueness, primarily in order to define the density field for gravity modelling. This interpretation is considered to be preliminary and a final interpretation will be described, and the models shown in detail, in Chapter 5.

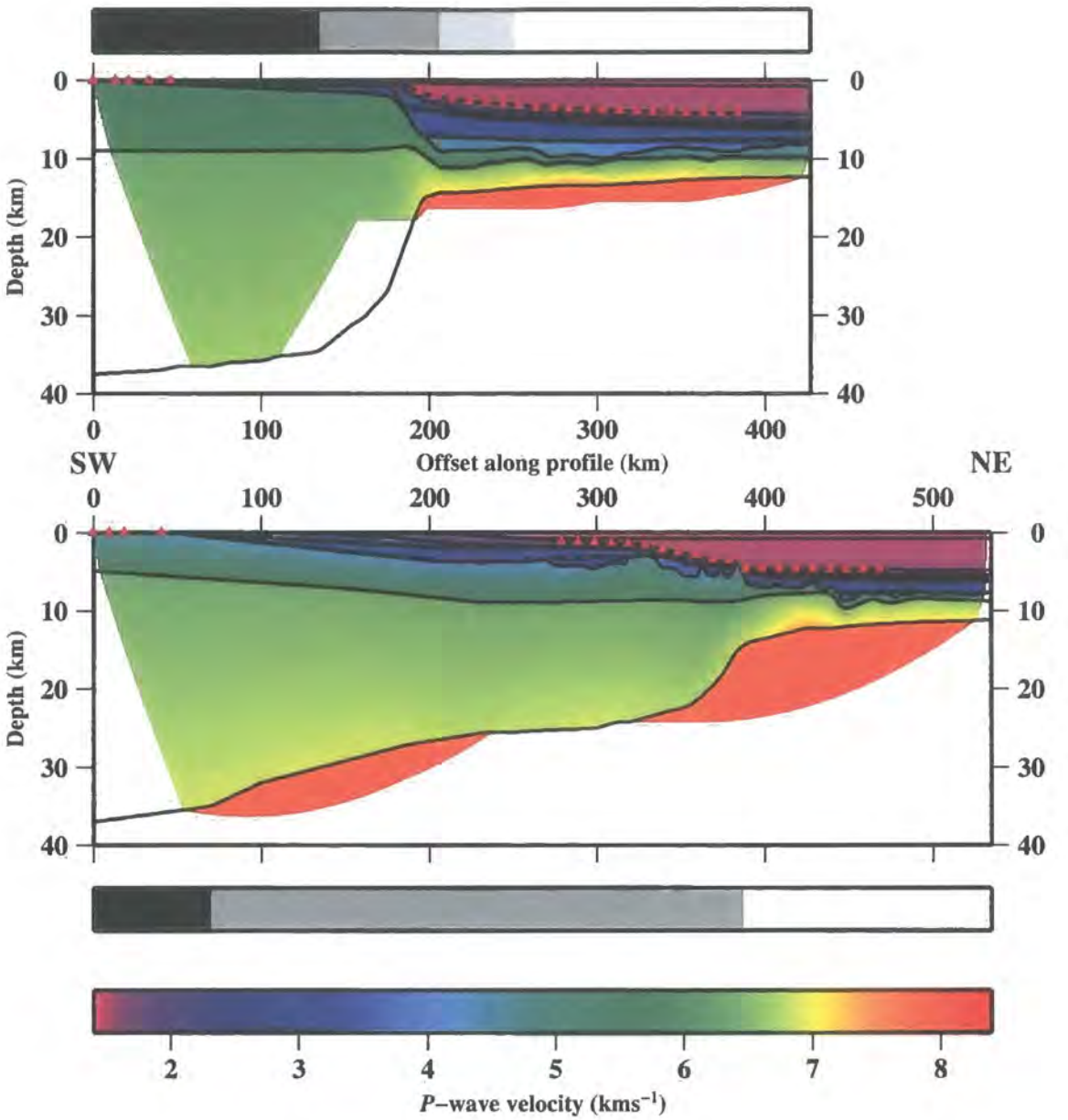


**Figure 3.35**: Preliminary results of WA modelling. *P*-wave velocity-depth models of Profiles A (top) and D (bottom) with preliminary interpretation (bar above Profile A and below Profile D). OBS and land station locations are shown (red triangles). Vertically, both models are subdivided into water column (purple colour), five layer (S1-S5) sediment column (dark blue-light blue), two layer crust (green-yellow) and mantle (red). Preliminary interpretation of the lateral changes in structure indicate that the models comprise continental crust (black), thinned continental crust (dark grey), transition zone (light grey) and oceanic crust (white).

Profile A is interpreted to consist of five broad structural subdivisions – sediment column, pre-rift and thinned continental crust, oceanic crust and a transition zone. Similarly, Profile D is subdivided into the sediment column, pre-rift and thinned continental crust and oceanic crust. No transition zone is interpreted along Profile D which, instead, is modelled with a relatively sharp OCT. Beneath the seafloor, the sediment column within each *P*-wave velocity-depth model comprises five layers. In addition, given the partitioning of both continental and oceanic crust into two layers, the terms Upper and Lower and Layer 2 and Layer 3 will be used for the respective layers and crustal types. These classifications are consistent with standard models of continental and oceanic crust (Spudich & Orcutt, 1980; Bratt & Purdy, 1984; Christensen & Mooney, 1995) and continental margins (*e.g.* Funck *et al.*, 2004).

### 3.10.1 Resolution

In order to further test the uniqueness of the two models (Figure 3.35), an understanding of the current resolution of the models must be developed. Further methods to determine resolution will be described in Chapter 4.

Quantitative analysis of the ray-trace traveltimes and the data picks demonstrates that both models fit the data within the error bounds (Table 3.4 and Table 3.5). For the land instruments, arrivals were modelled to an error of 126 ms and $\chi^2$ of 1.3 for Profile A and 197 ms and a $\chi^2$ of 1.0 for Profile D. However, for both models, the distribution of OBSs provides dense ray coverage laterally in the region beneath the OBSs, *i.e.* 193-383 km along Profile A, 278-468 km along Profile D. This is reflected by a great improvement in resolution oceanward of OBS A1 and D1, with over 20000 observed traveltime picks per profile producing total misfits and $\chi^2$ values of just 42 ms and 0.9 for Profile A and 68 ms and 1.3 for Profile D. These $\chi^2$ values may be considered an 'over fit', due in part to the relatively large errors assigned to secondary arrivals resulting from their onsets being obscured by the wavelet of the preceding first arrivals (Section 3.4.1).

However, a fit to within these criteria does not guarantee the uniqueness of the model as traveltimes are dependant upon both seismic velocity and propagation path length. Thus, an adequate data fit can often be obtained by increasing one and decreasing the other of these parameters and vice versa. The resulting model uncertainties associated with this trade-off have been estimated by systematically varying the model parameters and, hence, sensitivity testing modelled horizons and layer velocities. When testing the model uncertainties, the model was considered to fit while rms errors remained within twice the standard error (Table 3.2) for the picks of the layer being tested – *i.e.* 40 ms for S1-S3 picks; 60 ms for

S4-S5; 80 ms for sub-basement crustal layers oceanward of the shelf break G1-G2; and 100 ms for the mantle.

The maximum variation which may be applied to the layer velocities is shown in Table 3.6, where a high value indicates that several models with slightly varying velocities can produce a fit to the data. A small value indicates that the model is more unique and that only a small range of velocities will produce a satisfactory fit.

| Layer | Profile A ($\pm$kms$^{-1}$) | Profile D ($\pm$kms$^{-1}$) |
|---|---|---|
| S1 | 0.1 | 0.1 |
| S2 | 0.1 | 0.2 |
| S3 | 0.2 | 0.2 |
| S4 | 0.1 | 0.1 |
| S5 | 0.2 | 0.2 |
| Continental G2 | 0.2 | 0.1 |
| Oceanic G1 | 0.3 | 0.3 |
| Oceanic G2 | 0.4 | 0.1 |

**Table 3.6**: Summary of the velocity resolution testing of the WA models. Errors shown indicate that the ray-trace modelling does not adequately match the traveltime data when the model velocity is altered to original value $\pm$ error, in kms$^{-1}$.

Applying this method to both models shows that the upper sedimentary layer velocities are well constrained to within 0.1-0.2 kms$^{-1}$ errors. Along Profile A, these error values increase with depth, indicating that deeper crustal layers are associated with greater uncertainty. In contrast, the deeper layers along Profile D show smaller uncertainties among lower crustal layers.

This apparent decrease in uncertainty with depth highlights an inherent problem with this approach to assessing model errors. If WA data has been modelled poorly, with too many or too few lateral variations in structure, then it will only just fit to within the error bounds. Consequently, varying the velocities only slightly will result in the model no longer adequately matching the data. Hence, this approach to analysing model uncertainty will result in the suggestion that the layer has a small uncertainty, when this is not the case. To overcome this problem, the approach to uncertainty analysis requires that the positions and velocities of individual model nodes are varied, rather than entire layers. Thus, lateral variations in structure will be incorporated into the uncertainty analysis and improved estimates will be obtained. This development and its results will be undertaken and described in Section 4.3.

Varying the depth of an entire layer of the model suggests that the intracrustal boundary has an uncertainty of $\pm$400 m along both profiles. The oceanic Moho uncertainty is

estimated to be ±600 m along Profile A and ±400 m along Profile D, whereas continental Moho uncertainty is estimated to be ±2.5 km.

## 3.11 Summary

In this chapter the acquisition, processing and modelling of two profiles of ACE WA data have been described. The chapter has addressed the primary goal of this study, to construct deep crustal models of the continental margin of French Guiana, the first models to explore the sub-sedimentary crustal structure in this region. Modelling confidence has been assessed statistically and the $\chi^2$ test demonstrates that the models produce an acceptable fit to the observed data, within the errors. The models have been compared with the MCS data to provide additional constraint and to check consistency. A preliminary interpretation of the resulting models was presented and the resolution of these models was tested by systematically varying the depths and velocities of each layer and recalculating the statistical fit of the observed and calculated traveltimes.

In Chapter 4 several methods used to test the uniqueness of the *P*-wave velocity-depth models will be described. These include inverse modelling of the WA data, in addition to the use of gravity and magnetic data.

# Chapter 4

# Model resolution and testing

## 4.1 Introduction

In Chapters 2 and 3, the MCS and WA seismic data acquisition and processing were described. In addition, the approach to modelling these data to create two *P*-wave velocity-depth models of the sediment column, crust and upper mantle across the continental margin of French Guiana was explained.

Ideally, the models created are unique, containing no ambiguity. However, realistically this is not the case due to the nature of the dataset and chosen modelling approaches, which result in some degree of non-uniqueness. In this chapter, approaches to assessing and minimising such non-uniqueness will be described.

The forward modelling approach, for example, is inherently dependent upon the modeller, who assesses the quality of fit and decides on model adjustment given geological background knowledge. This close relationship to the modelling process also inevitably results in a degree of bias towards their expectation of likely structures and velocities given the geological setting of the study. Inverse modelling techniques, however, are independent of such bias and will be used here as a check on the uniqueness of the forward models. The techniques used will be described in Sections 4.2 and 4.3, and their results compared with the forward models in Sections 4.2.3 and 4.3.2. An additional source of non-uniqueness within the models is the current dependence solely on seismic data. Thus, further tests of the models will be described using independent, *i.e.* non-seismic datasets such as gravity and magnetics.

In Section 4.4.1, the acquisition of shipboard gravity data during the ACE will be described. These data are checked against satellite-derived data for consistency. Section 4.4.2 contains a description of the 2D modelling of the gravity anomaly, using density models created from the *P*-wave velocity-depth models. The results of this modelling are discussed in Section 4.4.5. This modelling also provides additional constraint on the

variation in crustal thickness and Moho geometry beneath the continental slope and shelf where the ray coverage is limited and, consequently, the *P*-wave velocity-depth models are poorly constrained. Section 4.5 will then be used to describe the modelling of magnetic anomaly data, which will primarily be used to identify true oceanic crust and consequently the location of the OCT.

Discussion of gravity and magnetic data in this chapter is restricted to variation along the ACE profiles. However, following a description of the velocity models in Chapter 5, the regional gravity and magnetic data will be used to assess crustal structure adjacent to the profiles in order to develop an understanding of the 3D margin structure.

## 4.2 Inverse modelling of wide-angle data

The forward modelling approach (Section 3.8) is an informative and useful method of modelling WA refraction seismic data. However, a range of models may fit the traveltime data within the error bounds which are the primary constraint used to determine model uniqueness. Thus, the uniqueness of a model is dependent upon the following:

- *dataset* – *e.g.* ray coverage and resolution provided by the acquisition geometry and the nature of the seismic source characteristics;
- *modelling approach* – *e.g.* can the modelling software reproduce the range of ray paths and arrivals observed at each OBS?; and
- *modeller* – *e.g.* skill, expectations and experience.

As previously discussed, the models created from this dataset have been assessed in terms of ray coverage and resolution to determine the regions of the model which are most well constrained and those which are less so. In this section an alternative approach to modelling the WA data, free from modeller intervention will be described. Thus, the inverse modelling approach will test the uniqueness of the models with respect to the modeller.

### 4.2.1 Methodology

For tomographic inverse modelling of the WA data, *tomo2d* was used (Korenaga *et al.*, 2000), which has been applied in similar WA studies (*e.g.* Holmes *et al.*, 2005) and, following testing, was found to be more suitable than *TTT* (Trinks, 2003) and *FAST* (**F**irst **A**rrival **S**eismic **T**omography – Zelt & Barton, 1998). *TTT* was designed for use with

land, rather than marine refraction data and was unstable when OBSs were located on or close to the seafloor boundary. Both *FAST* and *tomo2d* were considered suitable for use with the ACE data. However, *tomo2d* was selected in order to avoid a dependence on the work of Zelt (*rayinvr* – Zelt & Smith, 1992; *FAST* – Zelt & Barton, 1998) which, given the approach adopted to coding might produce a systematic error or system dependent characteristic which would otherwise go unnoticed, even though the likelihood of this is considered small given the wide range of studies to which *rayinvr* and *FAST* have been applied.

To test the suitability of the chosen approach, two synthetic datasets were created by ray-tracing through the forward model for Profile A (Figure 3.35). The first was considered 'ideal' as it comprised traveltime arrivals from each and every shot point. The second was representative of the observed data, comprising arrivals from near-offset and a selection of far-offset shot points. Both datasets were inverted and the results compared with the model used to ray-trace, *i.e.* create, the synthetic data. Thus, if the technique recovers the original model, inverting the observed data should recover a model representative of the actual subsurface structure.

The first stage of testing the suitability of the inverse modelling approach was the creation of a synthetic dataset by ray-tracing through the final *P*-wave velocity-depth model for Profile A. Where possible, the ACE acquisition parameters were chosen for the synthetic dataset, for example traveltimes were calculated for 20 OBSs, using a 100 m shot spacing, between 116 and 427 km offset. *tomo2d* inverts first arrival refractions and Moho reflections and, hence, traveltimes were calculated for these phases only. This synthetic dataset is considered 'ideal' as it comprises first arrival traveltimes corresponding to each and every shot. The observed OBS record sections have low SNRs across a wide range of offsets and hence traveltimes cannot always be picked. Consequently, the 'ideal' synthetic dataset comprises many more traveltime picks than the observed dataset. As such, inverse modelling of these data cannot, on its own, demonstrate that the technique is suitable for the ACE data. However, a failure of the technique to recover a model within reasonable error bounds would suggest that the technique is not suited to the ACE data.

Following the creation of the 'ideal' dataset, parameter testing was performed to assess the effect of a variety of parameters and starting models. A grid parametrization of 1 km horizontally and 0.25 km vertically was chosen. This resolution avoids the creation of too fine a grid, which significantly increases computational run-time. However, the grid is small enough to allow parameterization of the thinnest sedimentary layers observed in the WA modelling.

The chosen starting model was constructed with velocities which are significantly lower than the actual model. This approach ensures propagation of rays to great depths. This is sometimes a problem with inverse modelling methods, in which shallow, high velocity gradients tend to refract rays toward the surface. The consequence is little-to-no ray coverage at depth and, hence, failure of the approach to model the deep structure. The starting model chosen is shown in Figure 4.1, with a velocity of 1.6 $kms^{-1}$ immediately below the seafloor, increasing linearly to a velocity of 7.0 $kms^{-1}$ at 20 km depth. Beneath this, velocities increase from 7.0 to 8.0 $kms^{-1}$ between 20-40 km depth and 8.0 to 8.2 $kms^{-1}$ from 40-50 km. Thus, with the exception of the seafloor, the starting model shows no lateral variation, and incorporates a complete range of velocities which are commonly observed at continental margins.

During testing, the joint modelling of refractions and reflections proved unstable and the resulting models often contained abrupt, geologically unrealistic changes in Moho depth. To avoid this, the initial approach was modified to include only refracted first arrivals.

In contrast to the forward modelling technique, the inverse approach adopted cannot give accurate estimates of sharp velocity changes associated with layer boundaries. Thus, the output models will appear highly smoothed in comparison to the forward models.

The inverse modelling methodology was designed, using 'ideal' synthetic data as a test case, to create a smooth output model. In the same way as the forward modelling technique, a $\chi^2$ test was applied to calculate the statistical fit of the traveltimes. As the inverse modelling was computationally intensive, the final approach to modelling was segmented. This allowed progress to be monitored during modelling, which comprised several steps:

- Use traveltimes from shots within $\pm$25 km offset of the instrument and invert over 5 iterations;
- Smooth the data heavily to bias the outcome to the creation of a smooth model;
- Invert these data again, over 5 iterations, and smooth;
- Include traveltimes from shots within $\pm$50 km offset, invert over 5 iterations and smooth;
- Invert these data again, over 5 iterations, and smooth;
- Include all available data, invert over 5 iterations and smooth;

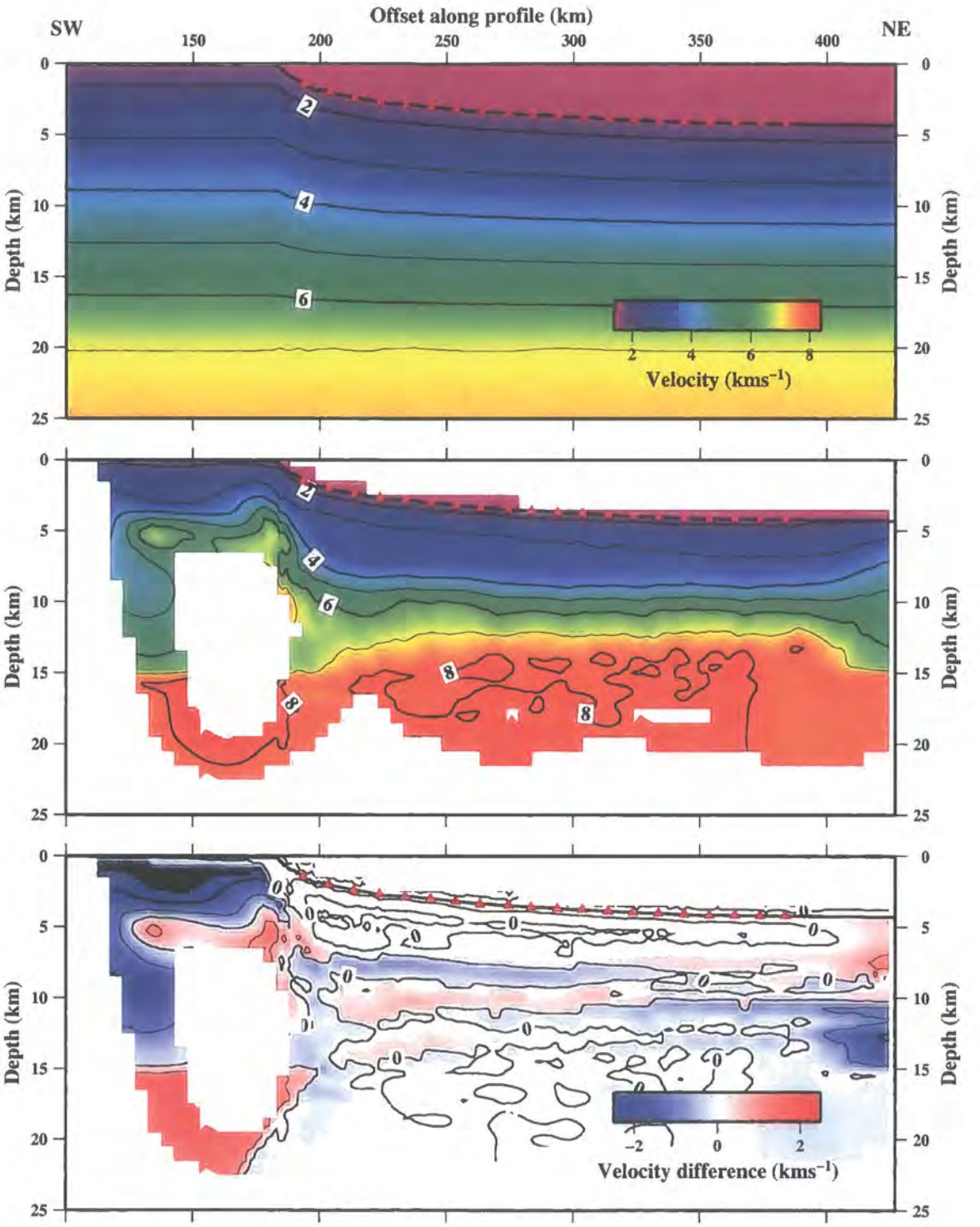


**Figure 4.1**: Results of inverse modelling of the 'ideal' synthetic dataset (see text) for Profile A. A starting *P*-wave velocity-depth model (top) was inverted to produce a model (centre). Blanked out regions did not have any ray coverage. The original model (Figure 3.35) was subtracted from the inverse modelling result to produce a comparison of these models (bottom). OBSs are highlighted by red triangles and isovelocity contours are shown every 1 kms$^{-1}$.

- Invert until the $\chi^2$ value approaches 1, or converges to a stable value.

This methodology incorporates several inversion independent smoothing steps to ensure the creation of a smooth model. Alternatively, large smoothing parameters could have been applied within the code. However, the former approach was preferred as the output at each stage provided an understanding of the progress of the inverse modelling.

### 4.2.2 Synthetic inverse modelling results

Comparison of the inverse modelling results (Figure 4.1) with the original model from which the synthetic data were created, shows that the inverse modelling has recovered the velocity structure beneath the OBSs (190-390 km offset) very well.

However, landward of ~190 km the structure is poorly recovered, most likely due to the sparse OBS and, hence, short-offset ray coverage in this region. These short-offset shots constrain the near surface velocities and so, with no control, the inverse modelling tends to retain the low velocities from the starting model. As a result, deeper velocities tend to be unrealistically high in order to reproduce the necessary traveltimes. For example, velocities of >9 $kms^{-1}$ are observed at 20 km depth. Similarly, oceanward of OBS A20, the original model is poorly recovered and velocities tend to resemble those of the starting model.

Following the successful test of model recovery by the inverse modelling approach, the traveltimes were sub-sampled to produce a synthetic dataset representative of the ACE data. Thus, where arrivals were not observed in the ACE data, these arrivals were removed from the synthetic data. Sub-sampling was done on an OBS-by-OBS basis and was equivalent to reducing the number of traveltimes in the dataset by a factor of ~6 (from 100 to ~16%). The same approach as described above was used to invert this dataset and the results are shown in Figure 4.2.

Despite the large reduction in the quantity of arrivals comprising the dataset, the resulting model also recovers the original model (Figure 4.2). Beneath the OBSs the 'ideal' data and the subset of this data produce almost identical models. Landward of OBS A1 and oceanward of OBS A20, the model is still poorly recovered, as would be expected given the acquisition geometry.

### 4.2.3 Real inverse modelling results

Inverse modelling the synthetic data created using the ACE acquisition parameters suggests that the inverse modelling approach is suited to the ACE WA data from Profiles A and D. *tomo2d* was therefore used to invert the real data and the results are described below.

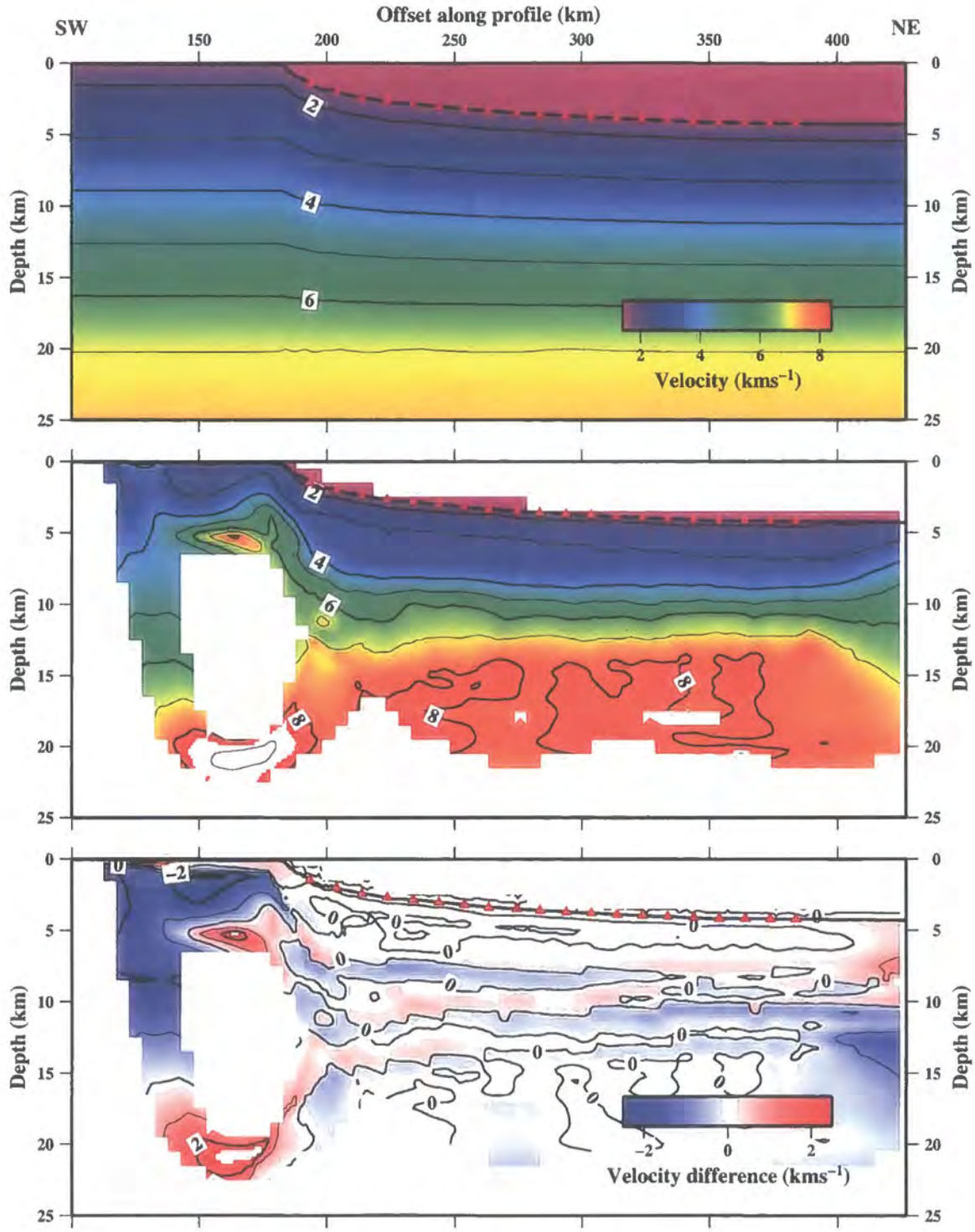


**Figure 4.2**: Results of inverse modelling of a synthetic dataset representative of the real Profile A data. See Figure 4.1 for details.

#### 4.2.3.1 Profile A

The inverted *P*-wave velocity-depth model for Profile A (Figure 4.3) matched the real data to a $\chi^2$ of 1.26 and clearly shows a velocity-depth profile in which velocity increases with depth. Between 200-370 km offset, the upper 3 km comprises velocities ranging from 1.6-3.0 kms$^{-1}$ corresponding to a velocity gradient of 0.5 s$^{-1}$. Beneath the 3 kms$^{-1}$ contour, the velocity gradient increases to ~0.7 s$^{-1}$ (landward end) and ~0.9 s$^{-1}$ (oceanward end). In contrast, the forward model shows a decrease in velocity gradient with depth in the sediments. This is most likely a consequence of the inverse modelling approach not having included secondary phases such as reflections and instead being based on first arrivals, none of which were identified as deep sedimentary refractions ($P_{s4}$-$P_{s5}$ – Section 3.4.1).

The 4 kms$^{-1}$ contour runs parallel to the seafloor, becoming progressively deeper oceanward, whereas the 7 kms$^{-1}$ contour shallows oceanward. Thus, the range of depths over which the intermediate velocities are observed narrows slightly oceanward, consistent with a thinning of the oceanic crust. As anticipated with this approach, there is no clear boundary defining the Moho, although it is likely to lie between the 7 kms$^{-1}$ and 8 kms$^{-1}$ contours, at ~12-15 km depth, suggesting a total crustal thickness of ~9 km at the oceanward end of the profile and ~12 km landward. This thickness is similar to the total thickness of 8-11.6 km observed within the forward model, which will be described in Chapter 5.

Within the region of dense ray coverage beneath the OBSs, the correlation between the inverse and forward modelled velocity profiles is good (Figure 4.3). The inverse model appears to be a smoothed version of the forward model with no obvious discrepancies. However, around 200-220 km offset the velocities at ~15-20 km depth decrease, indicating a thickening of the crust in this region. At these offsets ray coverage is still relatively dense and includes rays traced both to the northeast and the southwest. Thus, this crustal thickening is likely to be a real feature of the data rather than an artefact of modelling. Landward of 190 km offset, ray coverage decreases and, as demonstrated by the synthetic modelling (Section 4.2.2), modelled velocities may become unrepresentative of the true velocities. Similarly, oceanward of ~370 km offset the velocities are calculated from sparse, unidirectional rays and, hence, the model retains the low velocities from the starting model.

Thus, for Profile A, the inverse modelling is complimentary to the forward modelling, suggesting that between 190-390 km offset the forward model is relatively independent of modeller bias. However, this does not yet indicate that the model is unique as both the

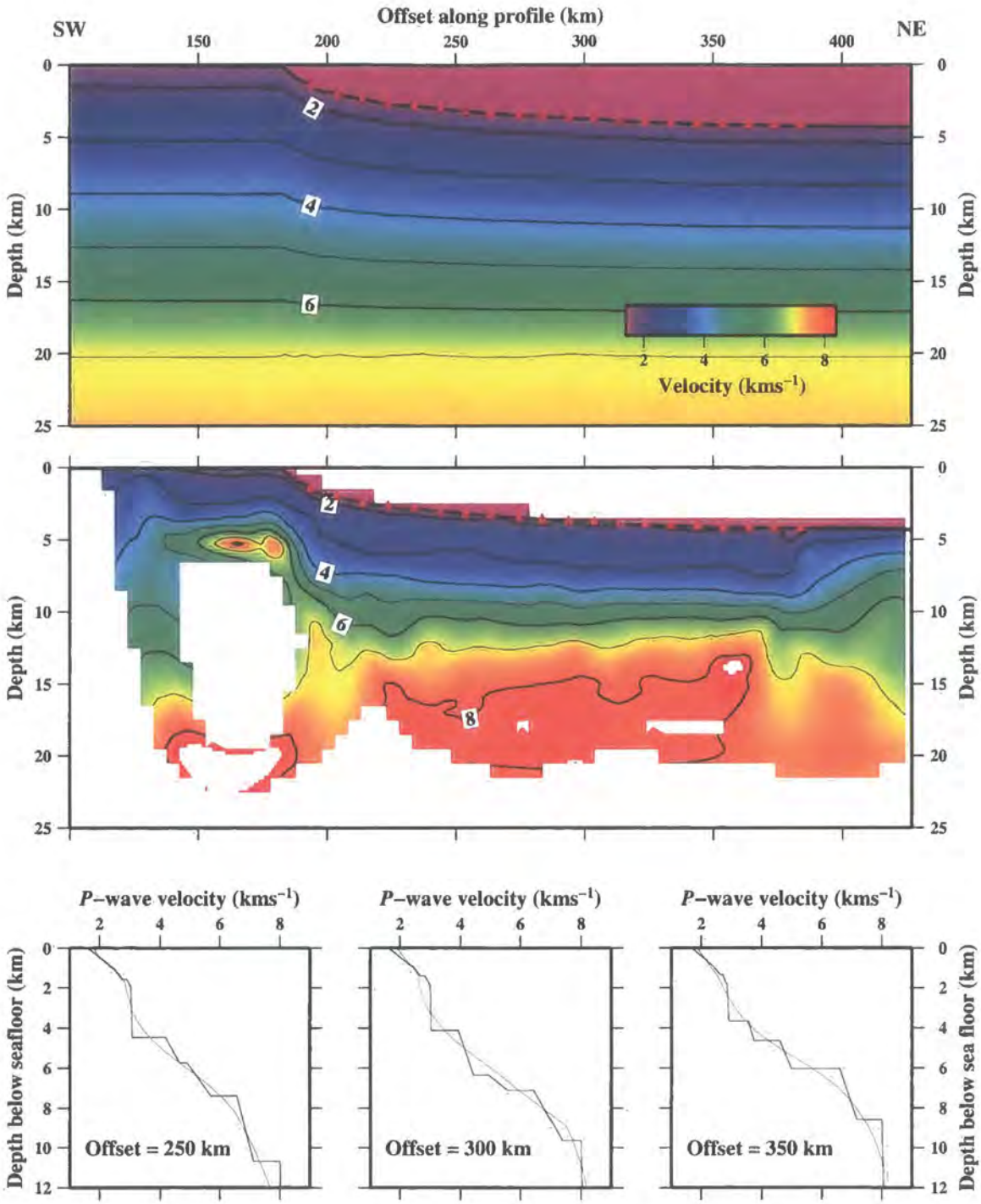


**Figure 4.3**: Results of inverse modelling of the observed traveltimes (see text) for Profile A. A starting *P*-wave velocity-depth model (top) was inverted using OBS first arrival traveltimes to produce a velocity model (centre). 1D velocity-depth profiles (bottom) through the inverted model (blue) and the forward model (black) are compared. The velocity-depth profiles are calculated at 250, 300 and 350 km offset, a region identified from the MCS data as most likely oceanic in nature. The profiles show distinct similarities between the velocity models produced by the forward and inverse modelling techniques. OBS locations are highlighted by red triangles.

approaches described thus far have been dependent upon WA seismic data and are not yet supported by independent datasets.

#### 4.2.3.2 Profile D

The inverted velocity-depth structure ($\chi^2$=2.48) for Profile D is shown in Figure 4.4. The contours oceanward of 400 km are relatively uniform, except for a dip at 450 km offset. At 385 km offset, beneath a large change in seafloor bathymetry, a significant reduction in the thickness of low velocities is observed. At this point the 7 $kms^{-1}$ contour dips sharply, indicating a thickening of the lower crust.

In addition, velocities of ~3 $kms^{-1}$ are observed just below the seafloor at 380 km offset, a point at which the basement reflector shallows in the MCS data sections (Section 2.4.3.10). Landward of OBS D1, velocities of ~8 $kms^{-1}$ are observed at a depth of ~20 km, although this may be a result of sparse, unidirectional ray coverage in this region as described for Profile A. Landward of 220 km offset, the model closely resembles the starting model and is unlikely to represent the true velocity structure. Similarly, oceanward of OBS D20 the velocity structure tends towards that of the starting model.

In contrast to Profile A, the velocity-depth profiles shown for Profile D show a relatively poor fit to the forward model. This is particularly apparent in the uppermost, low velocity crust (<5 $kms^{-1}$) and is most likely a consequence of a lack of sedimentary first arrivals (Section 3.4.3) observed along Profile D. Instead, due to the thinner sediment cover, arrivals from the igneous crust appear earlier on the OBS data sections, and, consequently, sedimentary arrivals are observed as secondary arrivals, which are not included in the inverse modelling process. The absence of secondary arrivals is a modelling limitation which inevitably causes a reduction in the accuracy of the inverse model.

### 4.2.4 Inverse modelling conclusions

The inverse modelling-based models discussed above have been constructed independently of modeller bias. In the same way as the forward models, they are reliant upon traveltime picks (Section 3.6.1) and their associated errors (Section 3.6.2). However, while first arrivals are assumed to be refractions, the inversion process does not depend upon correct phase identification (Section 3.4.1). Thus, any error in the forward model caused by a modeller incorrectly identifying phases is avoided. Furthermore, the use of a 1D starting model, which contains no preconceived ideas of what crustal velocities should be (with the exception of being greater than water velocity and increasing with depth), also avoids the inclusion of any predetermined structure. It has been demonstrated here that the inverse

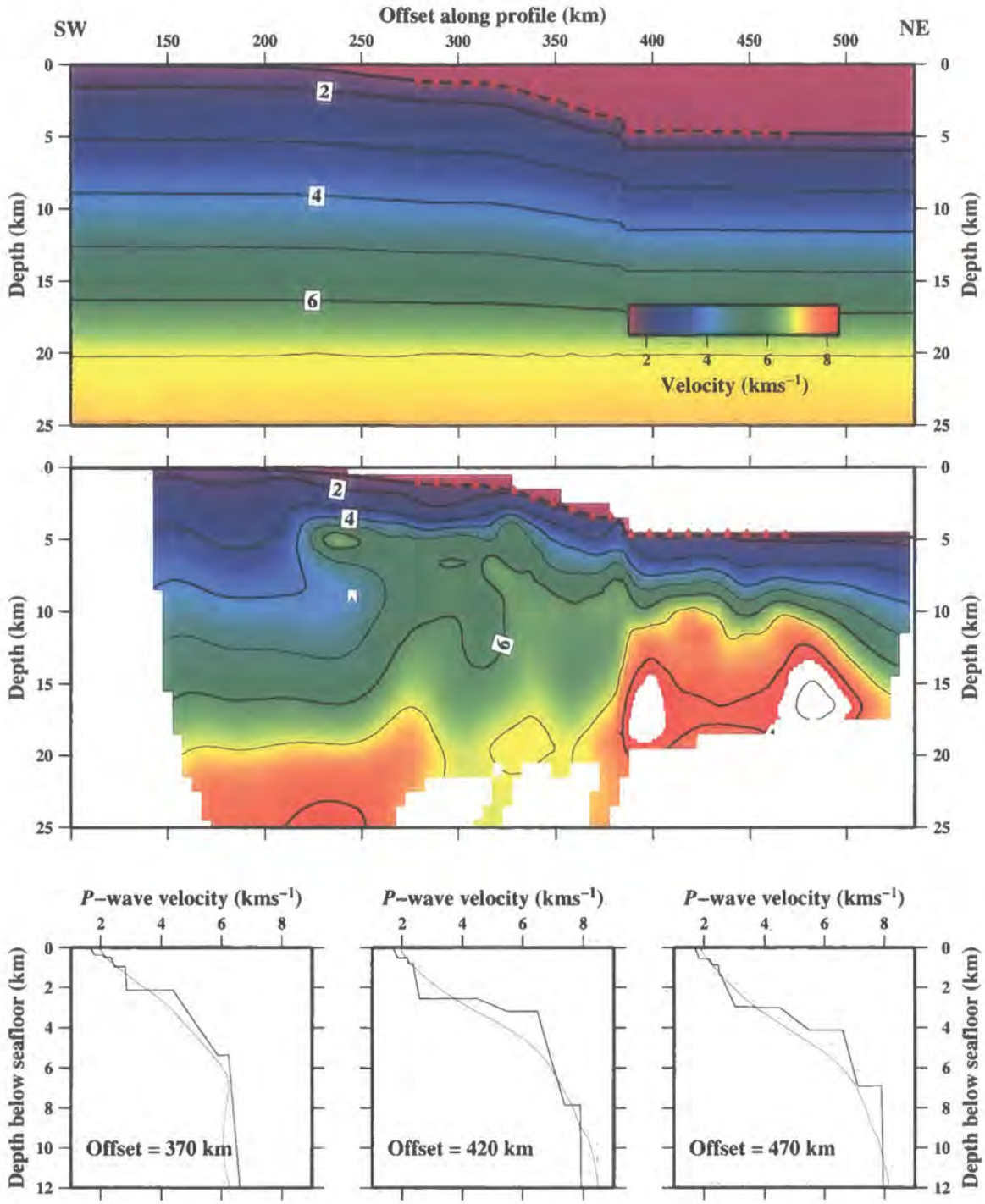


**Figure 4.4**: Results of inverse modelling of the observed traveltimes (see text) for Profile D. A starting *P*-wave velocity-depth model (top) was inverted using OBS first arrival traveltimes to produce a velocity model (centre). 1D velocity-depth profiles (bottom) through the inverted model (blue) and the forward model (black) are compared. The velocity-depth profiles are calculated at 370, 420 and 470 km offset along Profile D, a region identified from the MCS data as most likely oceanic in nature. The profiles show some similarities between the velocity models produced by the forward and inverse modelling techniques. However, the uppermost velocities in the models at 420 and 470 km do not match, a consequence of the small number of sedimentary first arrivals observed within the record sections. OBS locations are highlighted by red triangles.

modelling methodology is suitable for use with the ACE acquisition geometry and two models have been produced which share many similarities with the forward models.

Despite the success of the inverse technique, the forward modelling still offers a much greater degree of control on the models and, hence, more insight into the crustal structure. In the case of Profiles A and D, this control is a consequence of the inclusion of secondary arrivals within the data. For Profile D, in particular, many of the sedimentary phases are secondary arrivals and provide significantly increased constraint. Furthermore, when constrained by the reflection events in the MCS data, several sedimentary layers can be distinguished from one another. This degree of modelling is not possible with the methodology outlined above. Thus, the forward models are preferred over the inverted ones. However, the inverse modelling has provided a greater degree of confidence in the forward models and suggests that the major features observed are unique. For example the data may only be satisfied by ray-tracing through a model with significant crustal thickening at the continental margin and also by crust which, at the oceanward ends of the profiles, is limited to $<12$ km in total thickness.

## 4.3 *Metropolis*

To further assess the resolution of the *P*-wave velocity-depth models, the models and their associated traveltime data were used as a test dataset for the *Metropolis-Hastings* algorithm (Pearse, 2002; Tarantola, 2005; Hobbs, 2006). The algorithm is not an inverse technique, although it is computationally intensive and modeller independent similar to the *tomo2d* inverse modelling. The *Metropolis* approach is, in effect, a more detailed version of the resolution testing described in Section 3.10.1, which is able to test lateral and vertical velocity and depth variations simultaneously. This algorithm was originally designed to operate on 1D models (Pearse, 2002) and has recently been developed by R. Hobbs to work with 2D models. The following sections describe the results of Hobbs' work in the context of the ACE data.

### 4.3.1 The *Metropolis-Hastings* algorithm

The *Metropolis-Hastings* algorithm is designed to quantify uncertainty within a model by extensively testing models close to the final forward model. This is a Markov Chain Monte Carlo-based algorithm which uses an approximation to the final forward model as a start point. The algorithm then applies small, random perturbations to the model and assesses each resulting model in terms of the statistical fit, calculated using the *rayinvr* software

(Section 3.8.1). If the fit has improved then the new model is retained and used as the starting model for the next perturbation. However, if the fit has worsened the decision on whether or not to retain the model is dependent on a randomly generated number, $u$, between zero and one. If $u$ is less than the likelihood of the new model divided by the likelihood of the previous model then the model is retained. In this way, models which exhibit a poorer fit may be retained although those that display very much poorer fits are less likely to be retained. The algorithm thus creates a chain of models which effectively 'search' the model space around the final forward model. As a consequence, this approach extracts quite different information from the data when compared with the inverse modelling approach. While the inverse modelling has shown that the large-scale structural features of the models are not manifestations of modeller bias, this approach will test the resolution of these features. If, for example, a particular layer is poorly resolved due to a lack of traveltime picks then a variety of models, each with a slightly different velocity or depth structure, may fit the data.

To use this algorithm, in its current stage of development, the final forward models are assumed to be a close representation of the true structure. If this were not the case then there is no guarantee that the algorithm would be able to explore a wide enough region of model space to recover the true model. In addition, because the *rayinvr* software is used, the traveltime picks retain their predetermined phase allocations. Thus, modeller bias is inherent in the technique, although it proceeds automatically.

Hobbs (2006) has conducted tests of the software on synthetic 1D models and reports that "the algorithm is very effective in mapping uncertainty from the data into the model. It identifies parts of the model that are under- or over-parametrised and in extreme cases can be used to identify model inadequacies." The use of the algorithm on the ACE data from Profile A provided an opportunity to test the algorithm on 2D models and crustal structures.

The starting models for the algorithm were created by resampling the final forward models at points coincident with the OBS locations (Appendices A.3 and A.4), *i.e.* every 10 km along each profile. While the whole of Profile D was included in the modelling, Profile A only spanned from 185 to 427 km. This landward termination of the latter model was necessary due to the complexity involved in perturbing layers which pinch together and dip sharply. Such overlap of layers resulted in failure of the *rayinvr* code and, hence, the *Metropolis* algorithm.

### 4.3.2 Results

Approximately 20000 models were created along Profiles A and D and from these the statistical means were calculated. In addition to the mean model, the standard deviation, $\sigma$, of the models was also calculated. Standard deviation is a measure of how tightly the various models are clustered around the mean, where 66% of models lie within $1\sigma$ of the mean and 86% within $2\sigma$. Figures 4.5 and 4.6 show the results of this Monte Carlo based modelling, divided into the error estimates for the model boundaries and also the *P*-wave velocities.

The approach was quite successful for Profile A, and the best-fit forward model lay approximately in the centre of the suite of models created by *Metropolis*. Given the pick assignments used, the uppermost layers are well constrained across the model. Errors increase with depth, but are not excessively large and at the Moho the error within which $1\sigma$ of the models lie is $\pm$0.2-0.5 km. These errors increase landwards, partly as a result of the lack of MCS control on the basement surface and partly due to the lack of ray coverage approaching OBS A1. Similarly, the velocities are well constrained and $1\sigma$ errors are estimated at 0-0.2 $kms^{-1}$ in the sediment layers and 0.2-0.4 $kms^{-1}$ in the underlying crust. Errors in the mantle appear slightly banded, primarily as a result of the reduction in ray coverage at depth.

The banding also highlights an issue regarding how model parameterisation can affect the results. A typical upper mantle ray path is 20-60 km in length, whereas the model is laterally sampled every 10 km. The banding therefore shows that the Moho boundary and upper mantle velocity may be oversampled, resulting in instabilities on a wavelength of $\sim$20 km. Hence, the ray-trace approach to modelling cannot resolve anomalies in the mantle of $<\sim$20 km.

Model results for Profile D were similar to those of Profile A. The model boundaries are again well constrained at the oceanward end of the profile. Beneath the continental shelf the Moho is less well constrained with errors of the order of 1-3 km. The errors on the Moho appear to vary significantly in a lateral direction, which may indicate that individual nodes of the model are well constrained as several rays are traced through them, whilst others are not. However, this may also indicate that the algorithm has not adequately sampled the model space and that significantly more iterations and, hence, models are required.

Profile D velocity errors are again relatively small and are also banded, particularly beneath the Moho. The largest velocity errors above the Moho are observed at 440 km offset in the deep sediments. In this region the uncertainty may be large due to the effect of a sharp dip in the basement surface, although the MCS processing has shown that the

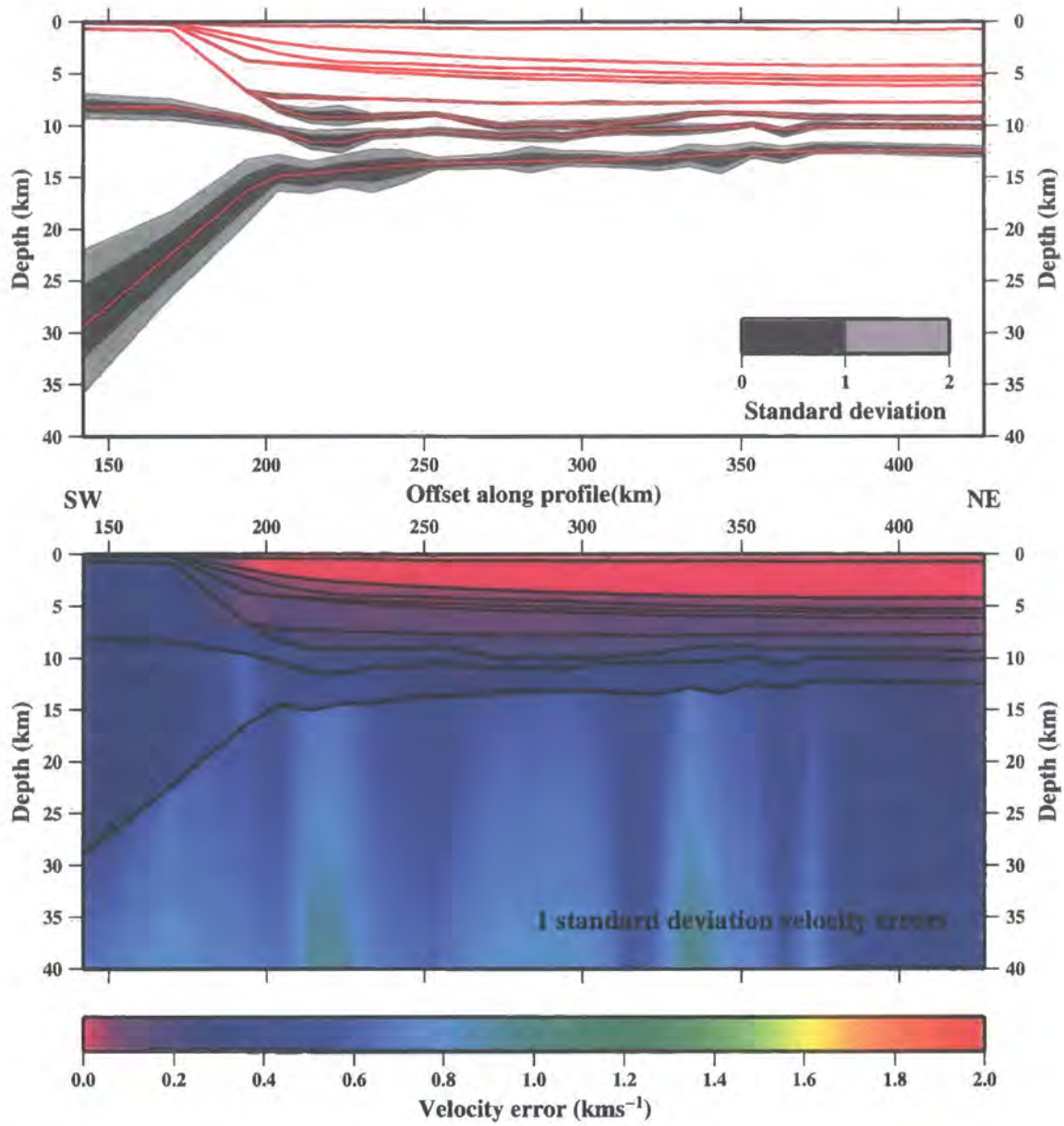


**Figure 4.5**: Results of *Metropolis* uncertainty analysis on Profile A. (Top) The distribution of model boundaries produced by the *Metropolis* algorithm, where 66% of the boundaries lie within one standard deviation (dark grey) and 86% within two. The input model (red lines) is the best-fit forward model, subsampled every 10 km. (Bottom) One standard deviation velocity errors - where 66% of models created by the *Metropolis* algorithm lie within the mean $\pm$ the velocities shown.

geometry of the sediment layers is relatively consistent laterally. Hence, it is unlikely that a significant velocity change occurs in this region.

### 4.3.3 Summary

Use of the *Metropolis* approach has improved our understanding of which regions of the model are reliable and those which are not. The modelling and subsequent statistical analysis of both profiles suggests error estimates similar to those in Section 3.10.1,

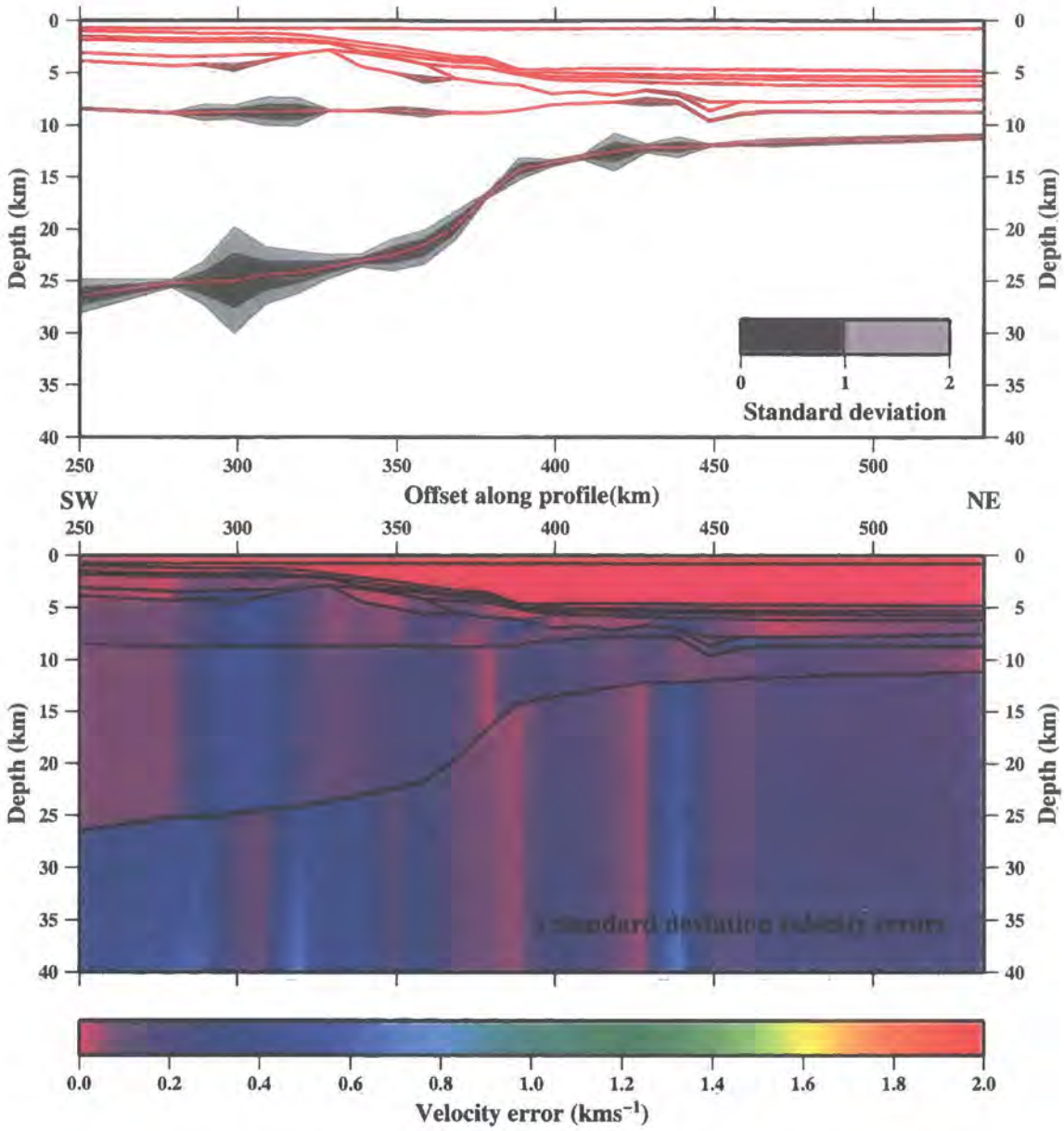


**Figure 4.6**: Results of *Metropolis* uncertainty analysis on Profile D. See Figure 4.5 for details.

which increase with depth but are still considered to be good, especially in areas where oceanic crust has been identified and the crust is significantly thinner. Landward, the uncertainties on depth to the Moho increase, although they are not excessive. The banding effect in the mantle velocities suggests that along both profiles structural variations over a distance $<\sim$20 km cannot be resolved. A potential improvement to the algorithm may be to introduce a depth-dependent smoothing factor to prevent small features which are laterally unresolvable from becoming dominant, *i.e.* remove the unrealistic banding effect to produce a better estimate of deep lithospheric uncertainty.

Following the inverse modelling and uncertainty analysis, significant confidence has been developed in the seismically constrained *P*-wave velocity-depth models. However, to improve this confidence further, an independent, non-seismic dataset is required.

## 4.4 Gravity data

Gravity modelling was undertaken primarily as a test of validity and uniqueness of the WA models, and secondly to provide additional constraint on the variation in crustal thickness and Moho geometry. Additional constraint is required, in particular, beneath the continental shelf where the ray coverage was limited. In addition, the gravity data is independent of the seismic data on which the modelling and model testing described previously, have been based.

### 4.4.1 Acquisition

The ACE acquired gravity data continuously along all six seismic profiles and also during transit between profiles. The R/V *Discovery* was fitted with a LaCoste-Romberg gravimeter, housed in the 'stable lab', 2 m below the water level. The shipboard data extend landward only as close to the shore as the ship travelled, *i.e.* to 116 km and 141 km offset along Profiles A and D respectively.

The gravity data were correlated with pre- and post-cruise gravity reference stations in Fortaleza to produce absolute measurements. The reference measurements indicated that the gravimeter drifted by 3.37 mGals over the 38 day cruise, *i.e.* <0.1 mGals per day. It was assumed that this drift occurred at a constant rate during the cruise and the data were corrected accordingly.

The gravity FAA was then calculated from the absolute value ($g_{obs}$) using Equation 4.1,

$$FAA = g_{obs} - g_{\phi} + FAC + EC \tag{4.1}$$

where $g_{\phi}$ is the absolute gravity on a reference spheroid calculated from the International Gravity Formula 1967 (IAG, 1971; Woollard, 1979) using Equation 4.2, $FAC$ is the free-air correction (Equation 4.3) and $EC$ is the Eötvös correction (Equation 4.4).

$$g_{\phi} = 978031.85 \times (1 + 0.005278895 \sin^2\theta + 0.000023462 \sin^4\theta) \tag{4.2}$$

$$FAC = 0.3080h \tag{4.3}$$

$$EC = (7.503V \times \sin\xi \times \cos\theta) + 0.004154V^2 \quad (4.4)$$

Here, $\theta$ is the latitude, $h$ is the height of the measurement above sea level, $V$ is the ship speed in knots and $\xi$ is the ship heading. The 2D FAA data along Profiles A and D (Figure 4.7) are correlated with 3D satellite gravity, taken from the compilation of Sandwell & Smith (1997). Although these two datasets were acquired independently, they show a strong correlation.

A significant change in FAA is observed across both profiles. However, the FAA of Profile A is striking in that it is, given the significant changes in crustal structure suggested by the MCS imaging and WA modelling, remarkably simple. The most prominent feature is a 125 mGal increase in the anomaly at 180 km profile offset, interpreted as the margin edge effect (Watts & Marr, 1995). However, edge effects are commonly observed to comprise a large peak accompanied by an oceanward flanking trough. This trough is absent from the Profile A anomaly, suggesting that the margin does not conform to the normal rifted structure at which edge effects have previously been observed.

Profile D shows a smaller anomaly range than Profile A, with the shipboard observations showing peaks at 325 and 380 km offset in addition to adjacent troughs at 290, 365 and 395 km offset. The third of these troughs is approximately coincident with the sharp increase in seafloor depth at the toe of the Demerara Plateau. However, the largest anomaly change, at 340 km, is not centred over a significant bathymetric feature, suggesting the anomaly is a consequence of a deeper structural change. The two peaks observed in the FAA are similar in appearance to an 'offshore dipping double', as observed by Watts & Marr (1995) offshore Africa, who interpret this as resulting from weak continental crust abutting weak oceanic crust.

In addition to sharp changes in FAA, a longer wavelength variation is also observed along both profiles. The continental region has a higher FAA than the oceanic region, corresponding to an increase of 50-60 mGal across the profile. Both profiles show a FAA of $\sim$-40 mGal at their oceanward ends.

These features of the 2D FAA extend along-strike the margin, as shown in Figure 4.7. For example, the edge effect observed along Profile A is also observed to extend for $\sim$50 km both north and south of the profile. To the south, over a region of 150-200 km, the edge effect appears to diminish slightly in amplitude and display a more prominent trough, oceanward of the continental slope. The Amazon Cone lies to the south of this region and its effect is observed in the FAA. Here, the edge effect is smaller in amplitude and much less abrupt, most likely a consequence of the thicker (up to 12 km) sediment cover (Rodger

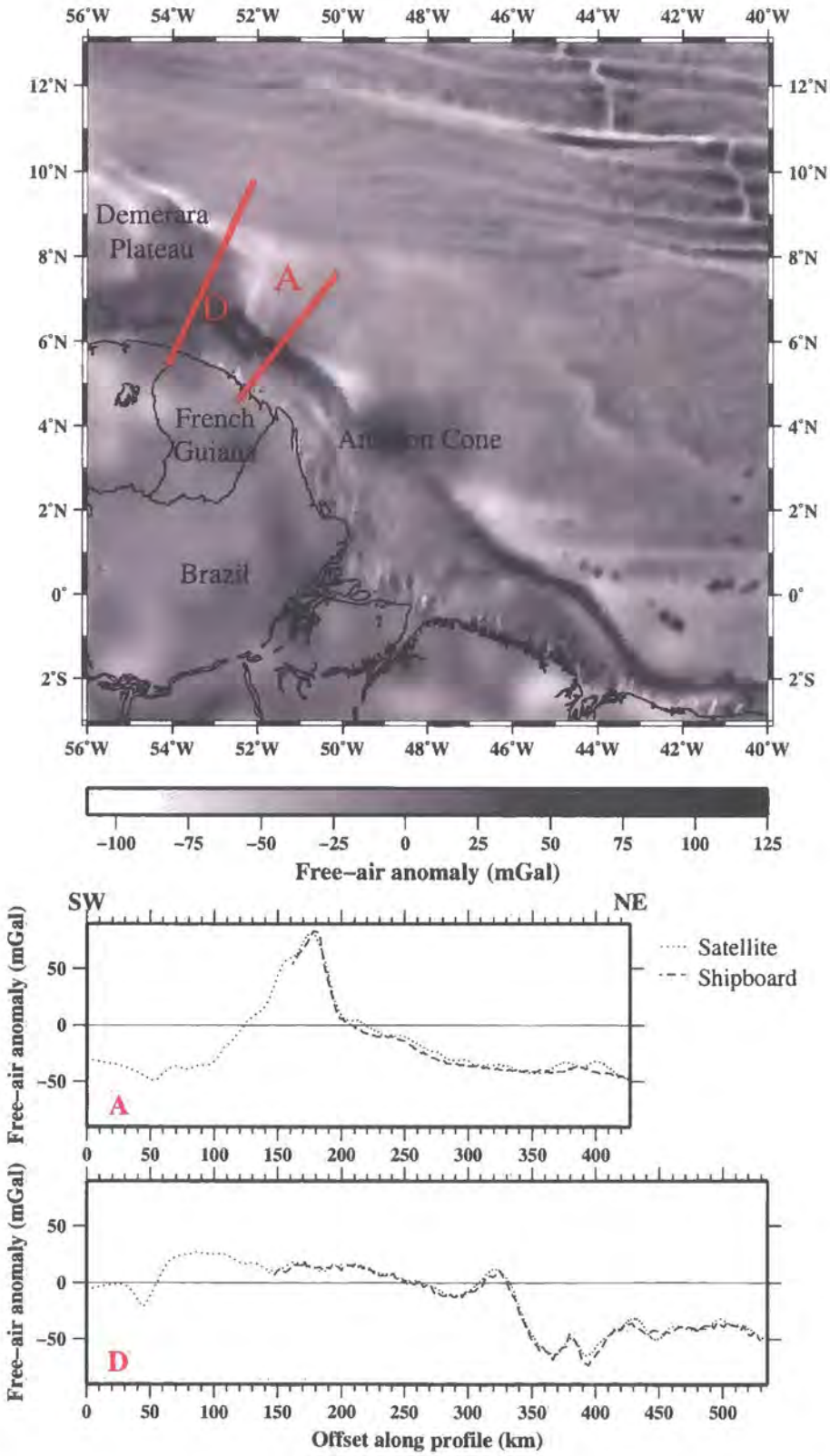


**Figure 4.7**: Gravity FAAs within the equatorial Atlantic (Sandwell & Smith, 1997) (top). Profiles A and D are shown in red. FAA along Profiles A (middle) and D (bottom) indicate that the shipboard (dashed line) and satellite anomalies (dotted line) show a strong correlation.

*et al.*, 2006). To the north of Profile A the edge effect appears to divide from a single into a double peaked anomaly (Watts & Marr, 1995).

Watts & Marr (1995) associate this double peak with relatively weak (low $T_e$) margins in which significant crustal flexure is localised underneath the associated causative sediment load. In contrast, a strong (high $T_e$) margin exhibits flexure and subsidence over a wider region, resulting in a single edge effect. However, the 'double' may also indicate the presence of a small sedimentary basin ~50 km landward of the shelf break, as suggested by the presence of two gentle east-west trending basement flexures within the submarine region landward of the Demerara Plateau (Gouyet *et al.*, 1994). Unfortunately, neither the ACE, nor the Guyaplac MCS data (Section 2.5.2) extend far enough landward to image this basin. Both Profile D and the Demerara Plateau lie to the north of this double peaked anomaly. Thus, there are significant differences in the nature of the FAA (as would be expected given the structural variation observed in the MCS and WA data) between Profiles A and D.

## 4.4.2 Two-dimensional modelling

This section contains a description of the approach adopted for 2D modelling of the FAA data, which utilises the program *grav2d*, described in Section 4.4.2.1. In Section 4.4.2.3 an explanation of the 'large block' approach is given, in which a *P*-wave velocity-depth model is split into individual blocks, each of which is assigned a density corresponding to the average *P*-wave velocity observed within it (Section 4.4.2.2). The results of this modelling are described in Section 4.4.3.

In Section 4.4.4 an alternative to this approach is described, in which the conversion from *P*-wave velocity-depth model to density model is automated using the *GMT* tool *grdcontour*. This method offers a fast and simple way to create smoothly varying density models with layers matching the geometry of velocity contours, whilst also including finer detail density structure. The results of this alternative approach are presented in Section 4.4.5.

### 4.4.2.1 *grav2d*

The program *grav2d*, written by J.H. Leutgart and based on the algorithm of Talwani *et al.* (1959), was used to calculate the FAA. *grav2d* has been used for other surveys of crustal structure, *e.g.* Lau Basin – Turner *et al.* (1999); Peirce *et al.* (2001) and Reykjanes Ridge – Gardiner (2003).

This method is based upon the assumption that the structure is uniform for an infinite distance perpendicular to the 2D model. The sensitivity of the models to this assumption can be estimated by considering the effect of a major along-strike structural change on the FAA.

The potential locations of such a change can be isolated by considering the local bathymetry and FAA. The bathymetry (Figure 2.1), neither deepens nor shallows significantly for ~100 km along-margin-strike. Similarly, the FAA also shows little variation either side of the profiles (Figure 4.7). These observations imply that the deep crustal structure is relatively uniform for ~100 km perpendicular to both profiles.

The effect of a structural change 100 km from a 2D profile is calculated by comparing the FAA of two models (Figure 4.8). The first model comprises three layers with densities commonly associated with water, crust and mantle. The second model is identical to the first, except that it contains a 10 km step in the Moho at 0 km profile offset. Such a structural change is larger and more abrupt than would be expected across-strike the margin. Consequently, the change in FAA caused by this structural change will be the largest possible discrepancy caused by the across-strike uniformity assumption.

Figure 4.8 shows that a 10 km step in the Moho at 0 km profile offset causes the FAA to decrease by ~9 mGal at 100 km profile offset. Thus, errors associated with the 2D assumption in this region are estimated to be up to 9 mGal, but are most likely smaller than this.

All density models discussed below have been extended 1000 km beyond the ends of the model displayed. The extension consists of the 1D structure at the end of the model and no attempts have been made to extrapolate structural trends. For example, if the Moho shallows towards the edge of the model then this trend will not be continued into the extension. The extensions prevent edge effects associated with modelling distorting the results. However, the obvious problem with this approach is that the structure in the edge extensions may not be representative of true structure beyond the observed data profile.

#### 4.4.2.2 Velocity-density conversions

The *grav2d* software described above operates on an input density model, obtained by conversion of the *P*-wave velocity-depth model to density. Separate conversions were used for the three major crustal components identified in Section 3.10: sediments, oceanic crust and continental crust, using studies specific to each. This approach was designed to avoid any skew along the profile caused by using conversions not appropriate for a particular crustal type. The individual conversions are summarised in Figure 4.9.

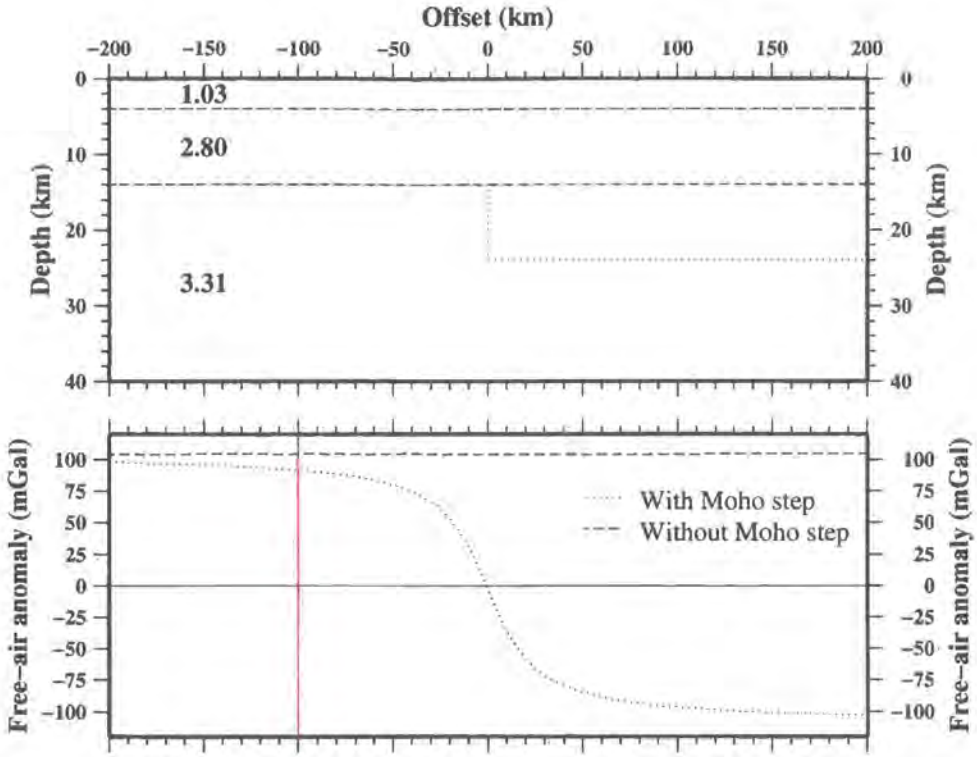


**Figure 4.8**: Testing the 2D gravity modelling approximation. (Top) A 2D, three layer density model with (dotted line) and without (dashed line) a large step in the deeper interface at 0 km offset. (Bottom) The FAA produced by these density models, calculated using *grav2d*. The model densities are chosen to represent typical layer densities (water: 1.03 $gcm^{-3}$; crust: 2.80 $gcm^{-3}$; mantle: 3.31 $gcm^{-3}$). The interface step is chosen to over-exaggerate possible steps in the Moho. The figure estimates a maximum reduction in FAA of ~9 mGal at an offset of 100 km (red line) – the minimum distance between Profile A or D and a major structural change, as suggested by the regional gravity.

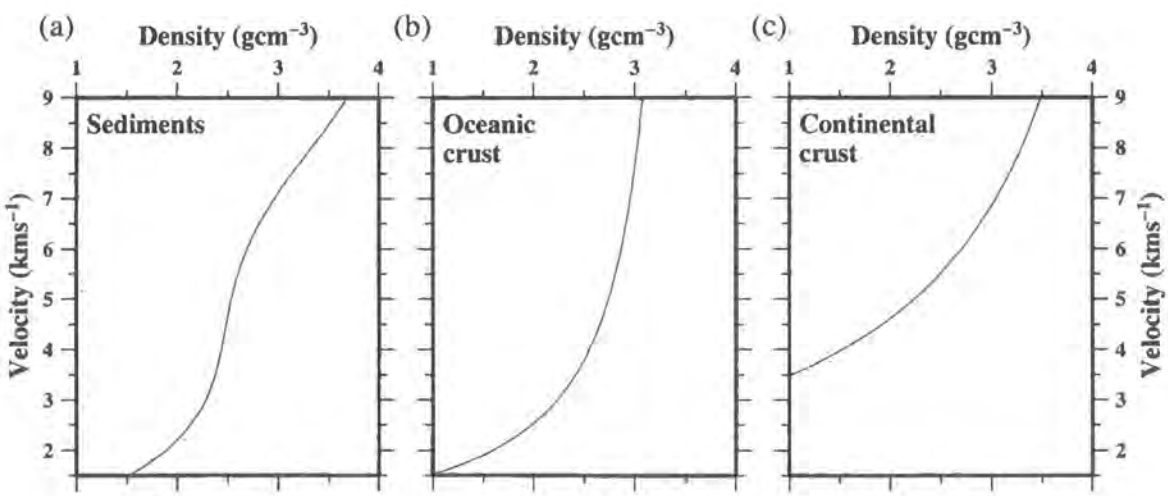


**Figure 4.9**: Summary of velocity-density conversion relationships. (a) Ludwig *et al.* (1970), after Nafe & Drake (1957), for sediments; (b) Carlson & Raskin (1984) for oceanic crust; and (c) Christensen & Mooney (1995) for continental crust.

For the sediments, the empirical relationship (Equation 4.5) of Ludwig *et al.* (1970), after Nafe & Drake (1957), based on measurements of velocity and density in sediments, was used for the velocity-density conversion,

$$\rho = -0.00283v^4 + 0.0704v^3 - 0.598v^2 + 2.23v - 0.7 \tag{4.5}$$

where $\rho$ is the density in gcm$^{-3}$ and $v$ the *P*-wave velocity in kms$^{-1}$. Within the regions identified as oceanic crust, the relationship of Carlson & Raskin (1984) (Equation 4.6) was used. For both the thinned and pre-rift continental crust, with velocity greater than 6.0 kms$^{-1}$, the relationship of Christensen & Mooney (1995) (Equation 4.7) was applied. The relationship for continental crust is not applicable to velocities less than 6.0 kms$^{-1}$, thus the sedimentary relationship of Ludwig *et al.* (1970) (Equation 4.5) was used for such velocities. A density of 1.03 gcm$^{-3}$ was assigned to the water column and the uppermost mantle was assigned a density of 3.31 gcm$^{-3}$ (Kuo & Forsyth, 1988). Note that, primarily for brevity in figure annotations, model densities are quoted in gcm$^{-3}$, where 1 gcm$^{-3}$ is equivalent to 1000 kgm$^{-3}$ in S.I. units.

$$\rho = 3.81 - \frac{5.99}{v} \tag{4.6}$$

$$\rho = 5.055 - \frac{14.094}{v} \tag{4.7}$$

#### 4.4.2.3 Large block modelling

The final *P*-wave velocity-depth models were divided into several large blocks for modelling. Each block comprised a region exhibiting broadly similar velocities. Profiles A and D were both split into five blocks – the water column, sediments, oceanic crust, continental crust and mantle. Each block was then assigned a velocity representative of the material within it by calculating the average of the velocities observed and converting these to density (Table 4.1), an approach which follows that of several other studies (*e.g.* Holbrook *et al.*, 1994a; Bullock & Minshull, 2005).

### 4.4.3 Large block modelling results and discussion

Figures 4.10 and 4.11 show the models and calculated FAA for Profiles A and D respectively. Profile A shows a significant misfit between observed and calculated FAA, whereas Profile D fits quite closely. The mismatch for Profile A suggests a problem with either the model or the assumptions that underpin the modelling, such as:

| Block | Material | Velocity ($kms^{-1}$) | Conversion relationship | Density ($gcm^{-3}$) |
|---|---|---|---|---|
| A1 | Sea water | 1.49 | Fixed value | 1.03 |
| A2 | Sediments | 3.01 | Nafe & Drake | 2.28 |
| A3 | Oceanic crust | 6.24 | Carlson & Raskin | 2.85 |
| A4 | Continental crust | 6.37 | Christenson & Mooney | 2.84 |
| A5 | Mantle | 8.00 | Fixed value | 3.31 |
| D1 | Sea water | 1.49 | Fixed value | 1.03 |
| D2 | Sediments | 2.59 | Nafe & Drake | 2.16 |
| D3 | Oceanic crust | 6.50 | Carlson & Raskin | 2.89 |
| D4 | Continental crust | 6.35 | Christenson & Mooney | 2.84 |
| D5 | Mantle | 8.00 | Fixed value | 3.31 |

**Table 4.1**: Summary of densities used in large block gravity modelling. The densities are calculated from average layer velocities using the conversion relationships described in the text.

- The *P*-wave velocity-depth models are incorrect – this is, in effect, what the gravity modelling is designed to test;
- The velocity conversions used do not produce appropriate density values. Whilst the relationships used are based upon empirical evidence (Nafe & Drake, 1957; Ludwig *et al.*, 1970; Christensen & Mooney, 1995; Carlson & Raskin, 1984), this has often been acquired in standard conditions, *i.e.* atmospheric pressure and temperature in a laboratory. Hence, the relationships may not be entirely suitable for use at depth. However, they have been used successfully in a wide range of other crustal structural studies;
- There is considerable out-of-plane variation in crustal structure although, as discussed in Section 4.4.2.1, there is no evidence for this in local FAA or bathymetry data; and/or
- The blocking methodology is not suitable. This is the favoured explanation for the misfit and is a likely explanation given that the large block density models do not accurately account for the crustal complexity and lateral and vertical density variations within a block. This may also explain why Profile A, which shows lateral velocity variation within the crust oceanward of the continental slope, fits poorly, whereas Profile D, which is constructed from layers whose depth may vary but whose velocities are relatively consistent laterally fits well. To address this problem, Section 4.4.4 describes an approach in which layers are created which mirror velocity contours and are assigned density values which have been averaged over significantly smaller regions in much thinner layers than the large block approach.

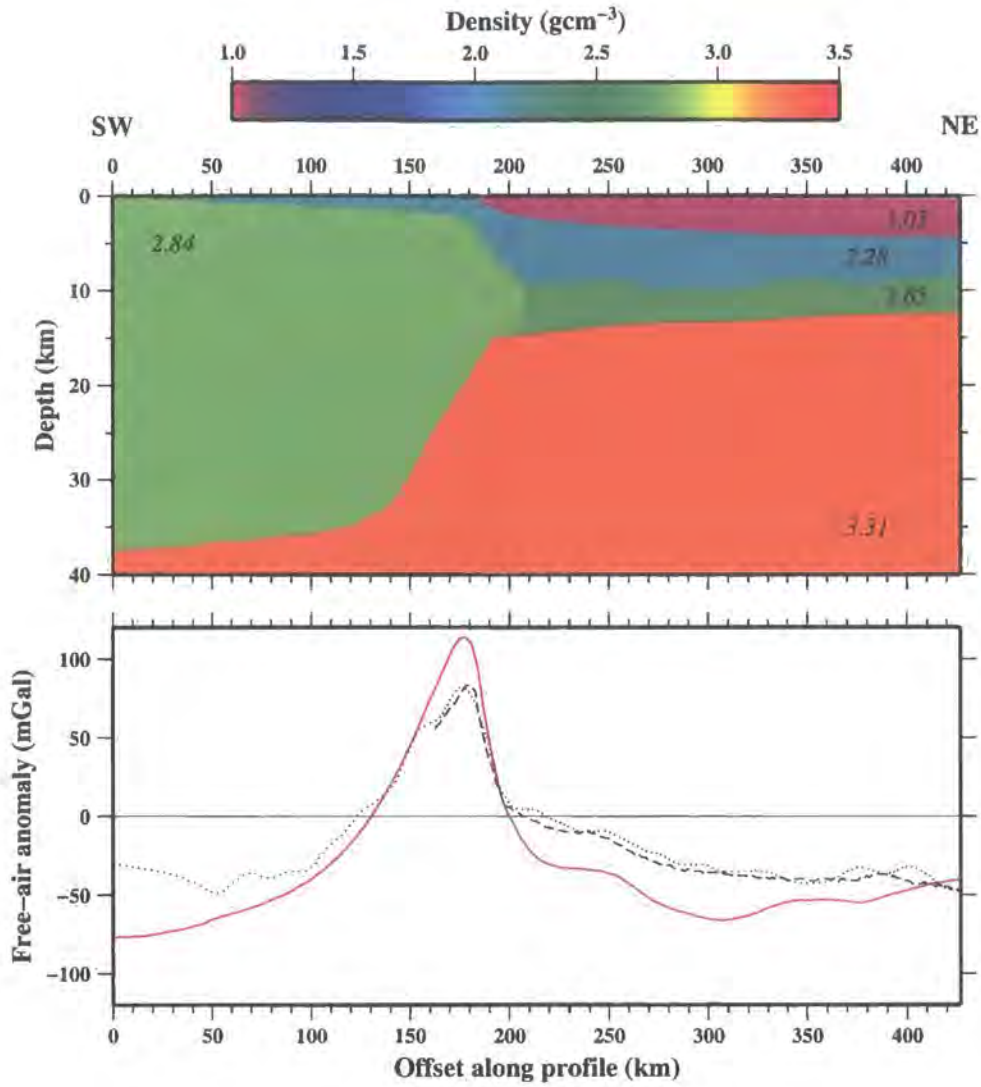


**Figure 4.10**: Results of large block 2D gravity modelling for Profile A. (Top) Density model comprising five blocks (A1-A5) with densities shown in gcm$^{-3}$. (Bottom) Calculated FAA (red line) compared with shipboard (dashed line) and satellite (dotted line – Sandwell & Smith, 1997) observations. The figure illustrates a distinct misfit, at all offsets, between the observed and calculated anomalies.

### 4.4.4 Reducing the block size

To represent the observed lateral and vertical velocity changes within the crustal models more accurately, a method was developed to convert the *P*-wave velocity-depth models to density. The method uses the *GMT* contouring program *gmtcontour* (Wessel & Smith, 1998) to contour the velocity models every 0.1 kms$^{-1}$ between 1.6 kms$^{-1}$ (just below the seabed) and 7.5 kms$^{-1}$ (Moho). As a result, density gradients closely follow velocity gradients. The contours were used to create layers in the format required for input to *grav2d* and each layer was assigned a density obtained from the velocity-density conversions discussed in Section 4.4.2.2. This contouring methodology is equivalent to a layer for

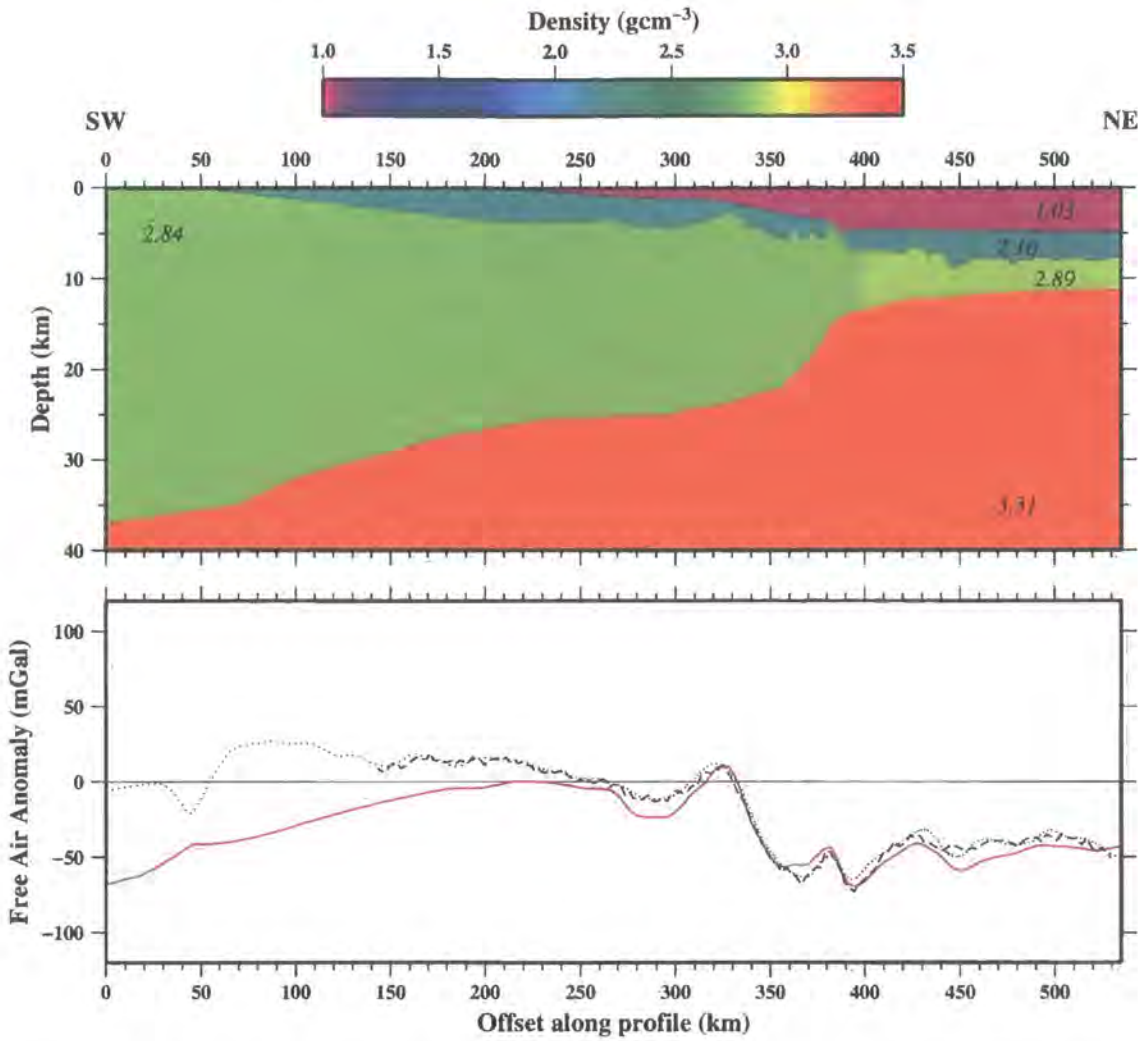


**Figure 4.11**: Results of large block 2D gravity modelling for Profile D. (Top) Density model comprising five blocks (D1-D5) with densities shown in gcm$^{-3}$. (Bottom) Calculated FAA (red line) compared with shipboard (dashed line) and satellite (dotted line – Sandwell & Smith, 1997) observations. The figure illustrates a close fit between the observed and calculated anomalies.

every ~0.02 gcm$^{-3}$ increase in density. The water column and seafloor were fixed within the models. The shell script written to create the models, *gravcontour*, largely automates the model production for a given *rayinvr* velocity model.

To obtain the final Profile A margin model, the depth of the Moho beneath the continental slope was adjusted to minimise the misfit of the FAA associated with the edge effect. Here, the Moho is poorly constrained by the WA data. The Moho either side of this region was constrained by $P_n$ and $P_mP$ arrivals and, hence, was not modified. The FAA above the continental slope is very sensitive to changes in Moho depth and, hence, provides greater constraint than elsewhere along the profile. The changes in Moho geometry were incorporated into the *P*-wave velocity-depth models and the WA ray-tracing rechecked to

ensure that the WA models still fit the observed data within the errors and fit criteria. The approach was identical for Profile D, although no significant change in the Moho position was required to enhance the fit.

### 4.4.5 Results

The results of gravity modelling are shown in Figures 4.12 and 4.13 and described below. No single model that perfectly matches both the FAA and seismic data (within all error bounds) in these regions could be found, and the models shown represent the best compromise that could be achieved between the two. The models are, inevitably, biased toward the WA/MCS data since they better image the vertical and lateral structural variation along the profile.

#### 4.4.5.1 Profile A

In the same manner as the seismic model, the sediment column of the gravity model is divided into five main layers, with densities in each layer: S1 – 1.62-2.18 $gcm^{-3}$; S2 – 2.08-2.27 $gcm^{-3}$; S3 – 2.21-2.29 $gcm^{-3}$; S4 – 2.24-2.32 $gcm^{-3}$; and S5 – 2.32-2.50 $gcm^{-3}$ respectively and with boundaries matching those of the seismic model. For continental regions the crust is divided into two layers with densities of 2.54-2.67 $gcm^{-3}$ for the upper and 2.85-2.95 $gcm^{-3}$ for the lower layer. The oceanic crust was subdivided into Layer 2 – 2.49-2.81 $gcm^{-3}$ and Layer 3 – 2.87-3.01 $gcm^{-3}$.

The most significant misfit to the shipboard FAA is centred on 180 km offset, the peak of the margin edge effect. As previously stated, this is the region of the model most sensitive to changes in geometry of the Moho associated with the thinning continental crust. This misfit is most likely a consequence of inaccuracies in the depth and geometry of the Moho, although may also reflect the lack of constraint on sediment thickness on the continental shelf. This poor constraint is caused by an absence of clear MCS reflections and a lack of shallow WA constraint on the model due to the OBSs being distributed oceanward of 193 km only.

A further misfit is centred on ~240-280 km model offset, the region in which the characteristic flanking low associated with the margin edge effect high would be expected (*e.g.* Watts & Marr, 1995). This anomaly misfit correlates with the region interpreted as the oceanward limit of the transition zone between thinned continental and oceanic-type crust. The nature of the misfit implies either that the crust and/or sediment layers are too thin or that the density is too high, or some degree of both of these.

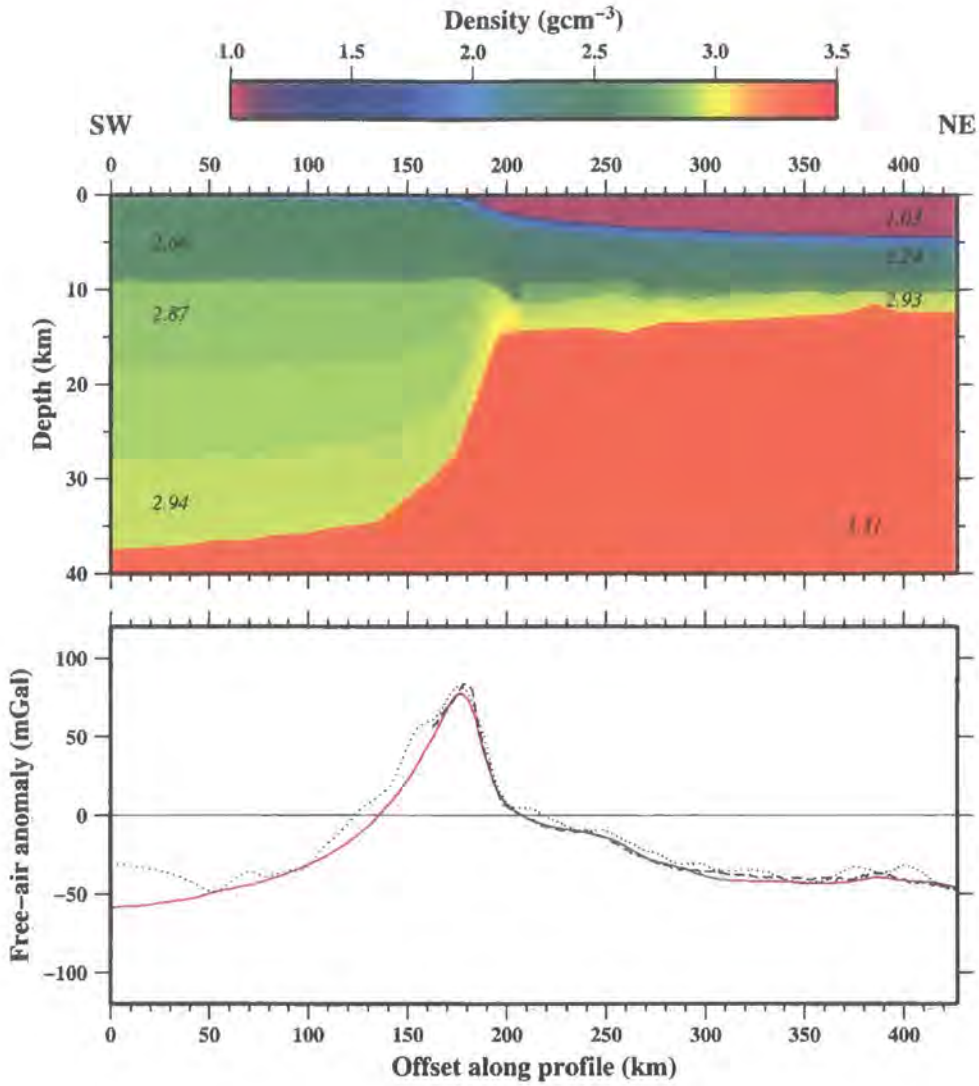


**Figure 4.12**: Results of contoured 2D gravity modelling for Profile A. (Top) Density model, with densities shown in gcm$^{-3}$. (Bottom) Calculated FAA (red line), compared with observed shipboard (dashed line) and satellite (dotted line – Sandwell & Smith, 1997) data.

Another region of misfit is located between ~370-400 km model offset. Towards these longer profile distances the seismic resolution of the sub-sediment crustal layers is reduced due to the limited offset between shots and the OBSs at the oceanward end of the profile. The gravity misfit implies thinner crust and/or sediment layers or that the model density within this region is too low or some combination of these.

The density-depth model was used to test the origin of these misfits, fixing the Moho depth outside of the misfit region (where the gravity fit was acceptable) and varying the model within the two misfit locations (240-280 km and 370-400 km model offset). Modelling suggests that an improved fit can be achieved by an increase in crustal thickness at 260 km offset of around 750 m, and by thinning of the crust at 385 km offset by around

600 m. Despite the dense ray coverage in both these localities, the seismic resolution is not capable of accurately distinguishing between the original model and the adjusted model. However, the results of gravity modelling would suggest that either a slight increase in Moho depth or a slight decrease in crustal density, perhaps as a result of serpentinization, is the cause of the misfit around 240-280 km offset, and that crustal thinning is the most likely origin of the misfit around 385 km offset.

#### 4.4.5.2 Profile D

The Profile D density model comprises: five sedimentary layers, S1 – 1.65-1.82 $gcm^{-3}$, S2 – 1.91-2.04 $gcm^{-3}$, S3 – 2.02-2.13 $gcm^{-3}$, S4 – 2.09-2.30 $gcm^{-3}$ and S5 – 2.36-2.41 $gcm^{-3}$; continental crust, G1 – 2.45-2.78 $gcm^{-3}$ and G2 – 2.85-3.01 $gcm^{-3}$; and oceanic crust, G1 – 2.46-2.78 $gcm^{-3}$ and G2 2.87-3.00 $gcm^{-3}$. In general, the calculated and observed gravity FAA fit well. However, oceanward of ~440 km the misfit increases to ~10 mGal and between ~190 and ~275 km the calculated FAA is again too low. This misfit is small but may suggest that the density of the oceanic crust is too low, or that the crust is too thick. Similarly, the second region of misfit may indicate that the densities are too high or the thicknesses too large for a section of the thinned continental crust.

These regions of misfit were analysed by varying the density-depth model in a similar manner to that of Profile A. Between 440-475 km offset, an improved misfit was obtained by shallowing the Moho by ~600 m, approximately the same depth variation as is permitted by the errors involved in WA modelling. The landward misfit between 190-235 km offset was improved by shallowing the Moho by 2 km. However, given that the MCS data were suggestive of significant lateral variation in structure deep within the sediment column, which could not be resolved in the WA modelling, this misfit may be a result of inaccuracies in the shallow part of the model.

An alternative interpretation of the misfit at the far landward and oceanward ends of the profile is that the background density is slightly inaccurate and that it is the central portion of the model that is misfit rather than the ends. An improved fit may be obtained by deepening the Moho by 500 m between 270 and 430 km offset. However, this is the region of the model that is best constrained by the WA data and, hence, the preferred interpretation is that it is the ends of the model which are misfit.

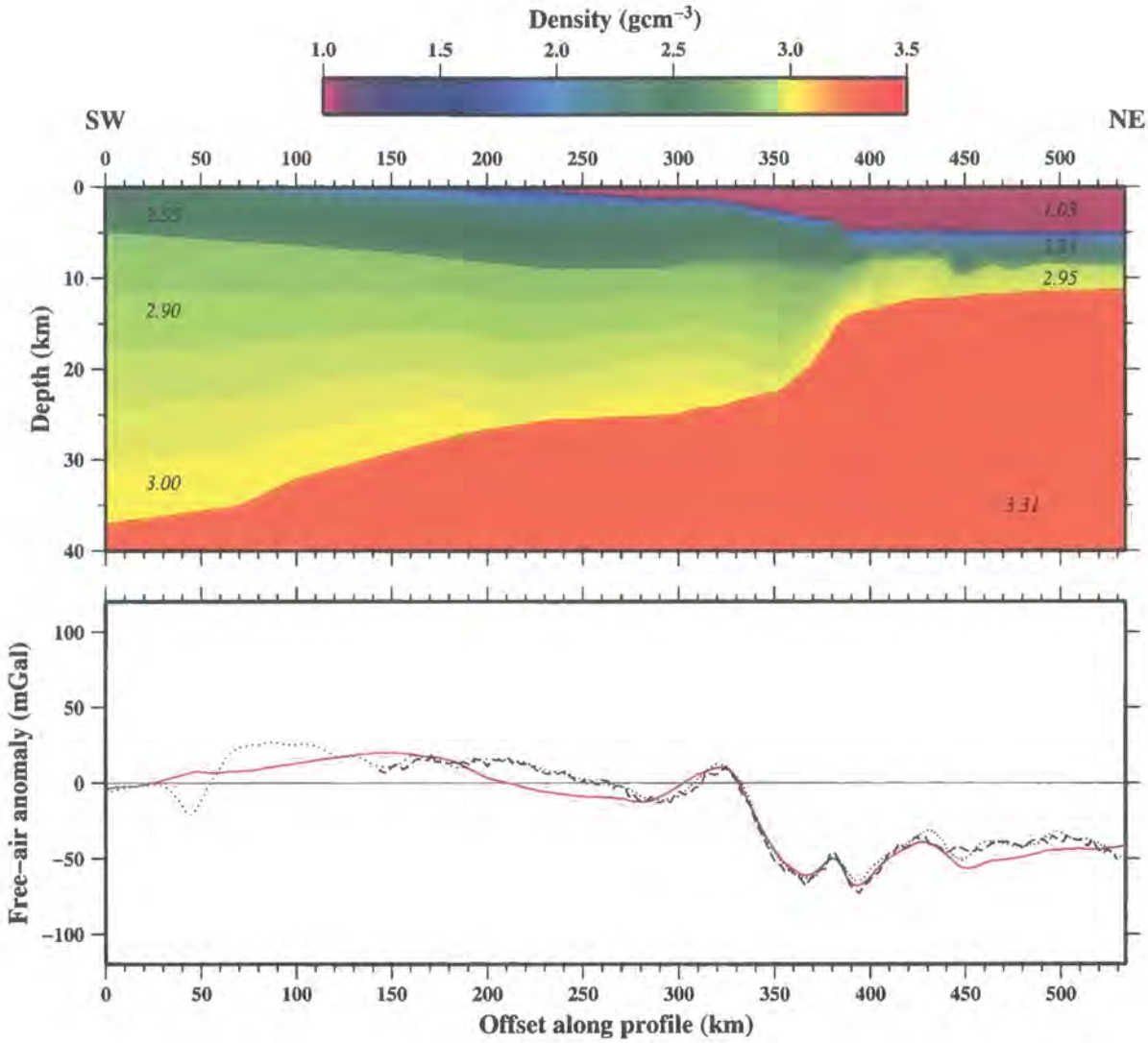


**Figure 4.13**: Results of contoured 2D gravity modelling for Profile D. (Top) Density model, with densities shown in gcm$^{-3}$. (Bottom) Calculated FAA (red line), compared with observed shipboard (dashed line) and satellite (dotted line – Sandwell & Smith, 1997) data.

## 4.5 Magnetic data

Magnetic data offers another non-seismic approach by which to constrain crustal properties at a continental margin. In previous studies, cross-strike variations in crustal magnetization have been observed at several margins (*e.g.* Ghana – Edwards *et al.*, 1997; Nova Scotia – Wu *et al.*, 2006). They are generally used to locate magnetized oceanic crust and also to assess spreading rate with respect to magnetic field reversals. However, changes in magnetization may also be associated with serpentinization and the presence of fracture zones (Lin *et al.*, 2005). As such, magnetic modelling of the French Guiana profiles was conducted with three aims: to analyse structural variations which may resolve the cause

of minor discrepancies between the observed and modelled gravity FAA; to distinguish between oceanic and non-oceanic crust, *i.e.* the location of the OCT; and to correlate magnetic spreading anomalies along-strike the margin for the purpose of accurate spreading rate calculations.

### 4.5.1 Oceanic crustal magnetization

Magnetization of crustal rocks takes two forms: *induced*, a temporary magnetization due to the presence of the Earth's magnetic field, and *remanent*, a permanent magnetization which forms as the rock cools through the Curie temperature and persists in the absence of an external magnetic field. The remnant magnetization is, hence, orientated relative to the Earth's magnetic field at the time of crustal accretion. The field from each of these combines to produce the total magnetic anomaly, which, when summed with the dipole component of magnetic field from the Earth's core, make up the total magnetic field.

Magnetization intensities vary with depth within oceanic crust (Figure 4.14). The majority of natural remnant magnetization results from the magnetic minerals contained within the pillow basalts of Layer 2A, although Layers 2B and 3 also contribute (Smith & Banerjee, 1986; Gee & Kent, 1994). The vertical magnetization model of Dunlop & Prevot (1982) suggests that Layer 2A will have a magnetization of 3.0 $Am^{-1}$, in comparison to 0.5, 1.0 and 0.2 $Am^{-1}$ for Layers 2B, 3A and 3B respectively. Serpentinized crust tends to have a significantly higher magnetization, which Matveenkov *et al.* (1996) estimate to be 5-20 $Am^{-1}$ from a drilling and marine study of the Gorringe ridge at the Azores-Gibraltar fracture zone.

Lateral variations in crustal thickness and magnetization may generally be observed in magnetic anomalies. However, at the French Guiana margin, this is complicated in two ways. Firstly, according to plate reconstructions (Figure 1.7 – Nürnberg & Müller, 1991), the onset of crustal accretion in the equatorial Atlantic coincided with the Cretaceous magnetic quiet zone of constant normal polarity (Chron 34, 118-84 Ma – Harland *et al.*, 1990). Thus, seafloor spreading anomalies are not expected offshore French Guiana. This problem is exacerbated by the area having lain in equatorial latitudes since the Cretaceous (McElhinny, 1973). Therefore, the inclination of the remnant magnetic vector is very low and thus only a small component of the total magnetic field is measured with towed marine magnetometers.

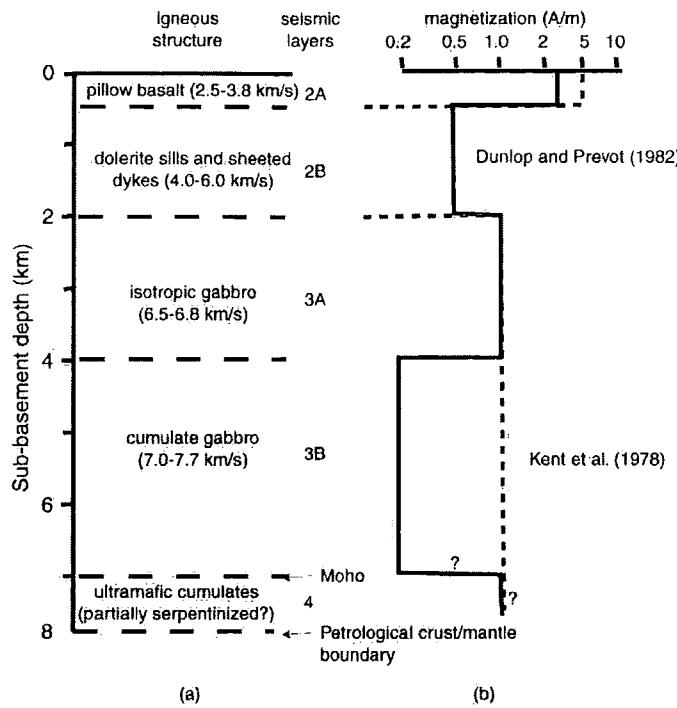


**Figure 4.14**: Variation in magnetization intensity with depth in igneous crust, after Russell (1999). (a) Seismic and igneous structure of typical layered oceanic crust, as described in Section 1.1.5. (b) Magnetization of these crustal layers, according to the the models of Kent *et al.* (1978) (dashed line) and Dunlop & Prevot (1982) (solid line). Layer 2A is indicated to be the most strongly magnetized crustal layer.

### 4.5.2 Data acquisition

Available magnetic data in the region comprise the magnetic profiles acquired as part of cruise D275 and Guyaplac data (Section 2.5.2). During cruise D275, total magnetic field was measured using a Varian V-75 proton precession magnetometer, which was towed ~125 m behind the stern of R/V *Discovery* during seismic profiling. Magnetic data were processed onboard to remove the component of the field from the Earth's core, modelled by the International Geophysical Reference Field (IGRF 2000 – Mandea & Macmillan, 2000), to leave the magnetic anomaly. The Guyaplac data were primarily acquired along ten cross-strike margin transects. These 2D data were combined into a 3D dataset, shown in Figure 4.15, and are also referenced to IGRF 2000 (F. Klingelhöfer – *pers. comm.*).

In addition to the regional magnetic anomaly, Figure 4.15 also shows the anomaly along the Profile A and D transects, as observed within the ACE and Guyaplac data. The datasets were acquired separately but show similar patterns of anomalies, corroborating one another. Magnetic anomalies are observed along both profiles and are generally small. The largest anomaly is -290 nT at 490 km offset along Profile A, although this is oceanward of the northeast limit of the *P*-wave velocity-depth model. Between 0 and 427 km offset,

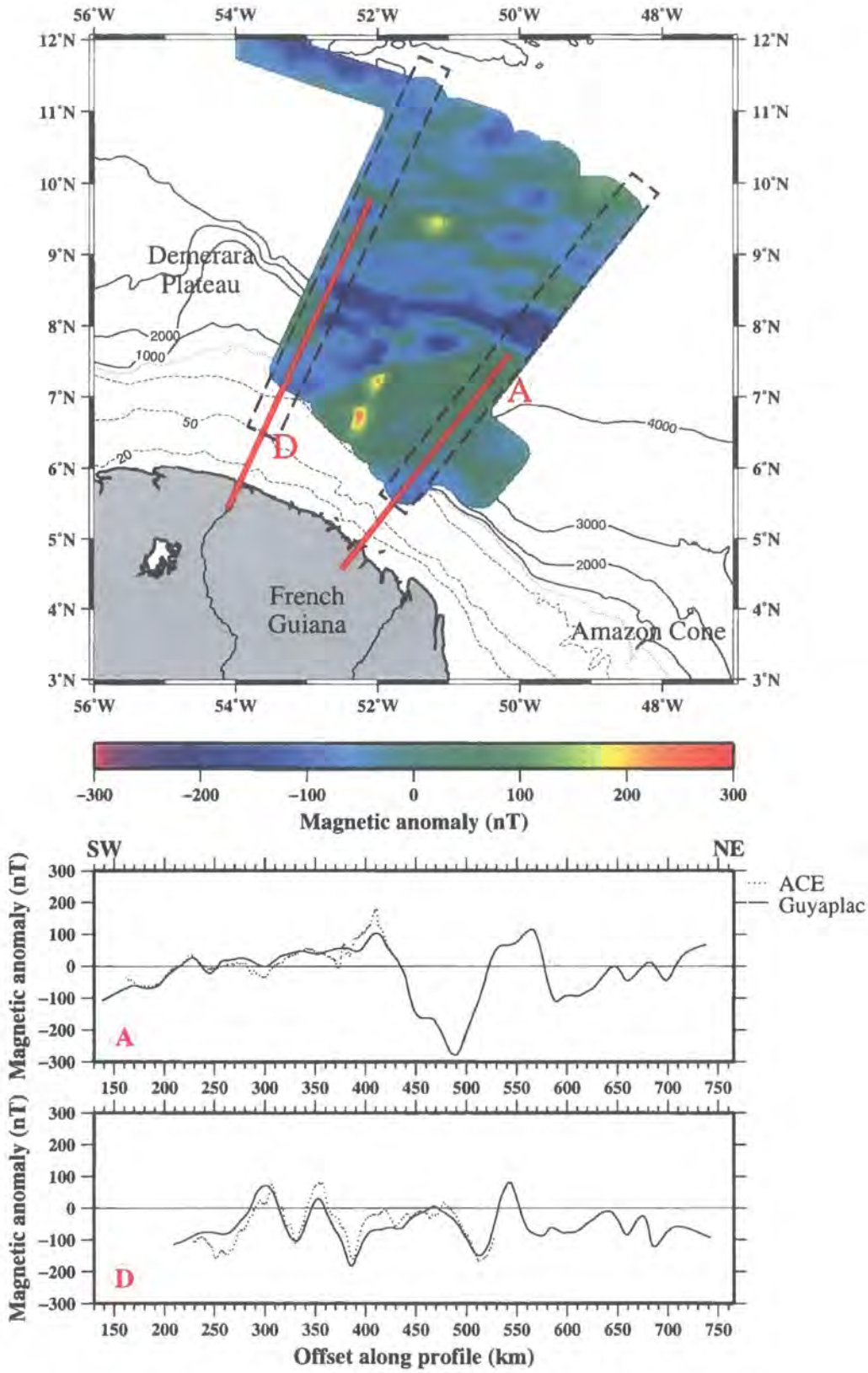


**Figure 4.15**: Magnetic anomalies within the equatorial Atlantic (top). Profiles A and D are shown in red. The lateral extent of the lower panels is shown by the by the black dashed boxes. Anomaly along Profiles A (middle) and D (bottom) indicate that the ACE shipboard (dotted line) and Guyaplac anomalies (dashed line) show a strong correlation.

the region modelled with WA data, no significant anomalies are observed, although the anomaly increases gradually oceanward. Along Profile D, three main troughs are observed, each of ~150 nT. The first of these troughs is located at 330 km offset, above the Demerera Plateau; the second at 385 km, near the OCT identified from the WA modelling; and the third at 510 km offset above oceanic crust. The different settings of these anomalies suggests that they may have different causal factors, which may include the presence of highly magnetized material such as serpentinite, changes in basement topography or the juxtaposition of continental and oceanic crust.

### 4.5.3 Magnetic modelling

The aim of magnetic modelling was to check for structural variation not recovered by the seismic or gravity datasets analysed thus far. In particular, the location of the OCT and the presence of oceanic fracture zones, which may be accompanied by changes in magnetization due to the ingress of water into the crust resulting in serpentinization. Thus, the approach adopted did not attempt to recover absolute values of magnetization but instead modelled variation along the Profiles in a relative sense. Furthermore, the modelling assumed that the magnetized layer consisted of the whole crust, whose topography and thickness were taken from the WA velocity models.

The whole crustal approach is appropriate, despite the magnetized material generally being concentrated in the uppermost oceanic crust, because the magnetic modelling is being used to assess crustal-scale features. Furthermore, this approach was adopted by Edwards *et al.* (1997) whilst modelling the Ghana margin, also in the equatorial Atlantic, which will be the primary source for comparison of the results. Edwards *et al.* (1997) model the magnetization of the oceanic crust as a remnant magnetization, *i.e.* with a magnetic susceptibility equal to zero. Here, the vector for the magnetization direction is calculated from the palaeomagnetic pole at the time of crustal accretion and the present day location of the survey, taken as 6.5°N, 309°E. Gordon & Van der Voo (1995) calculate the palaeomagnetic polar wander paths for the major continents and estimate that, for South America at 98-144 Ma, the palaeomagnetic pole was at 84°N, 224°E. This information may be used with several standard equations to calculate the declination and inclination of the remnant magnetization of the oceanic crust at the margin. The equations are included below as Equations 4.8, 4.9 and 4.10,

$$\sin\left(\phi_p - \phi_x\right) = \frac{\cos\lambda \sin D}{\cos\lambda_p} \tag{4.8}$$

where $D$ is the declination of magnetization, $\lambda$ is the magnetic latitude, and the palaeomagnetic pole is at longitude $\phi_p = 224°$E and latitude $\lambda_p = 84°$N.

$$\sin \lambda_p = \sin \lambda_x \sin \lambda + \cos \lambda_x \cos \lambda \cos D \tag{4.9}$$

where the survey longitude, $\phi_x = 309°$E, and latitude, $\lambda_x = 6.5°$N. In addition,

$$\tan I = 2 \tan \lambda \tag{4.10}$$

where $I$ is the inclination of magnetization. By solving these equations, the inclination and declination of the remnant magnetization are calculated to be 13° and 6° respectively.

These modelling parameters were used with *gravmag*, a magnetic modelling program written by the British Geological Survey and based on the theory of Shuey & Pasquale (1973). The WA crustal models were divided into their major components – water, sediment, continental and oceanic crust and mantle. The continental and oceanic crustal blocks were assumed to be the only sources of magnetization. The crust was then laterally subdivided into blocks, such that boundaries were positioned close to peaks and troughs observed in the anomaly data. The magnetizations of these blocks were then adjusted in order to produce a model which recovered the major anomalies observed in the data.

### 4.5.4 Results

Both ACE profiles were modelled and the major magnetic anomalies were reproduced. However, the range of model magnetizations which could reproduce the anomalies was relatively large and the magnetizations are considered to be poorly constrained. Despite this lack of uniqueness, a preferred model was created for each profile which are both consistent with the data and highlight potential crustal features.

#### 4.5.4.1 Profile A

Figure 4.16 shows the model used for magnetic modelling and the resulting magnetizations and anomaly fit. The region of the magnetic model for which the crustal thickness is constrained by WA modelling extends to 427 km. The most significant magnetic anomaly observed along either profile is located slightly oceanward of this WA model limit. Hence, the crustal structure observed along Profile A was extrapolated oceanward in order to model this feature. The Guyaplac (Section 2.5.2) MCS data were used to constrain the basement surface for this extension, and do not suggest the presence of any significant structural variations in the region. Thus, the approach is considered valid.

The preferred model shows that a satisfactory fit can be attained for Profile A using relatively weak crustal magnetizations of $<1$ $Am^{-1}$ landward of 420 km. There appears to be some variation in magnetization along this section of the profile (Figure 4.16) ranging from 0.0-0.9 $Am^{-1}$. These values are comparable in size to those observed at the conjugate margin (Edwards *et al.*, 1997). However, several similar models were able to reproduce these results and the actual values and block locations are not considered to be well constrained. Consequently, this region is simply identified as weakly magnetized oceanic crust.

Slightly oceanward of this region, however, the magnetization increases by an order of magnitude, although the dimensions of this increase are not well defined. The amplitude of the magnetic anomaly at this point could not be modelled by weakly magnetized oceanic crust. Hence, another explanation is proposed, that the large anomaly is a result of fracturing of the crust, accompanied by serpentinization, which has increased the crustal magnetization. This may suggest that the extension of this anomaly to the west in the regional anomaly (Figure 4.15) may be representative of a local fracture zone.

#### 4.5.4.2 Profile D

Figure 4.17 shows the results of magnetic modelling for Profile D. The crust at the oceanward end of the profile is of a slightly higher magnetization than observed along Profile A. At 520 km offset, near the oceanward extent of the WA crustal modelling a relatively large lateral variation is observed, perhaps suggestive that the crust further landward is of a higher magnetization than would otherwise be anticipated. However the change is only half that observed on Profile A and, hence, this finding is only suggested tentatively.

The continental crust is, similarly to Profile A, modelled with relatively low magnetizations. However, the zone from 360-400 km offset is modelled with a magnetization of 1.4 $Am^{-1}$. This result indicates that the thinned continental crust is likely to be of a slightly higher than normal magnetization, possibly as a result of some serpentinization at the OCT. Further landward the amplitude of the anomaly at 330 km offset is not fully recovered and may suggest that the basement has more lateral structural variation than the WA models. If more structural variation were present then the extra lateral change in magnetization may improve the fit of the models. Given the resolution of the magnetic modelling it is not feasible to assess the specifics of such structures from the magnetic data.

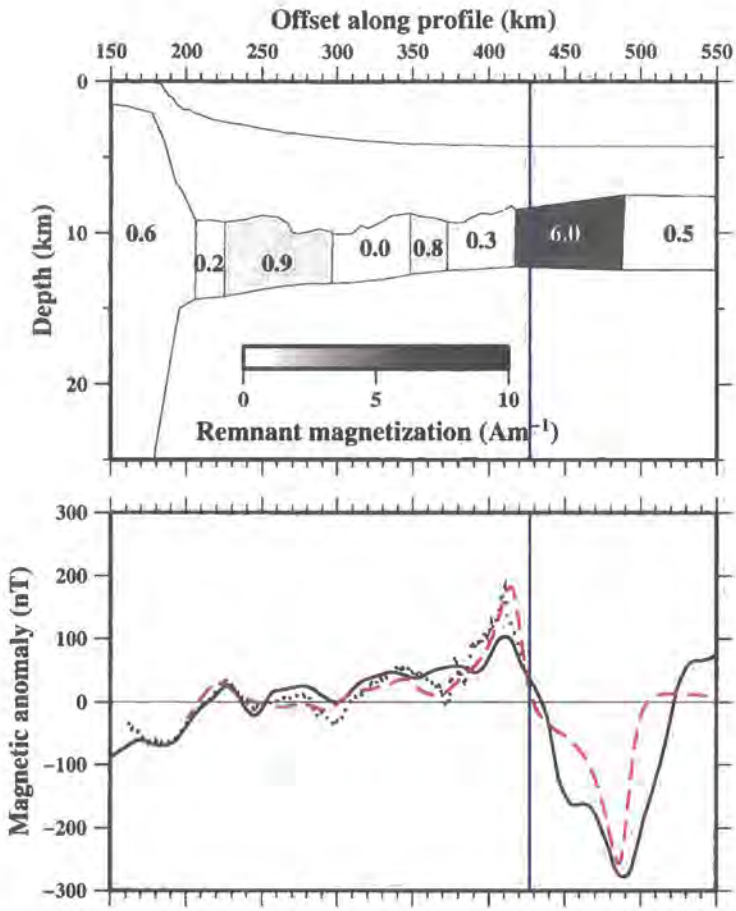


**Figure 4.16**: Results of magnetic modelling along Profile A. The magnetic model is shown (top) divided laterally into several blocks. Assigned magnetizations are labelled in $Am^{-1}$. The calculated magnetic anomaly (red dashed) is shown for comparison with the shipboard (black dotted line) and Guyaplac (Black solid line) data. A significant increase in magnetization is observed between 420-490 km offset, slightly oceanward of the extent of the WA modelling (blue solid line).

## 4.6 Summary

In this chapter the uniqueness of the best-fit WA *P*-wave velocity-depth models was tested by remodelling the WA data, independent of modeller intervention. Both an inverse and a Monte Carlo-based forward modelling approach were used, and the velocity-depth models were converted into density models in order to calculate the FAA for comparison with observations.

All of these independent tests have demonstrated and confirmed the goodness of fit and the apparent uniqueness of the seismic models and, in turn, also provided additional constraint in areas unconstrained by seismic forward modelling. The FAA calculated from density models was in excellent agreement with observations and improved estimates of Moho depth and geometry in regions of low WA ray coverage.

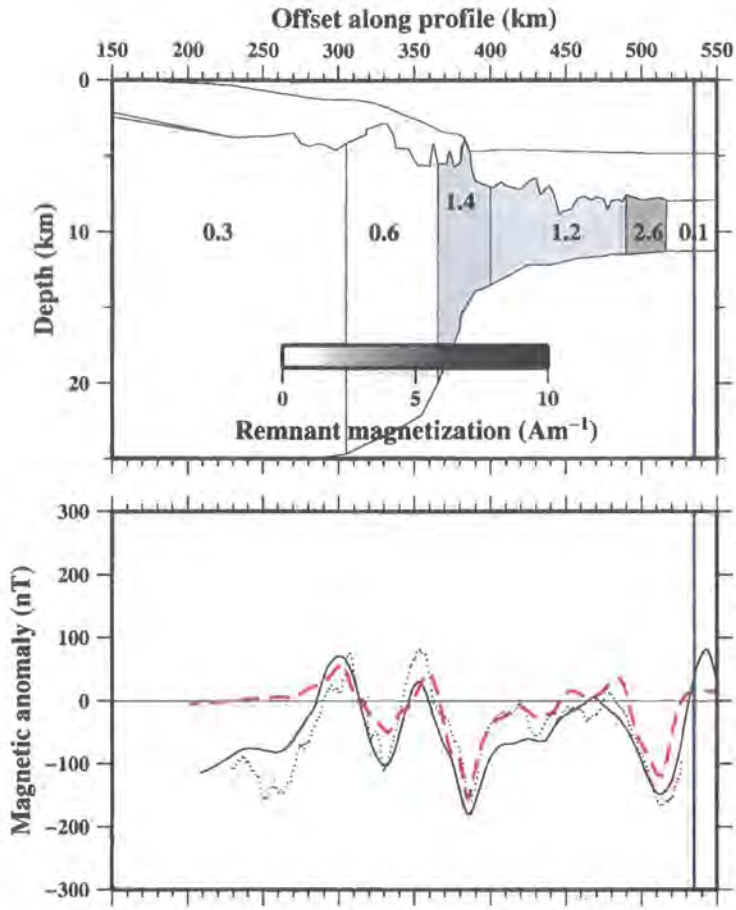


**Figure 4.17**: Results of magnetic modelling along Profile D. See Figure 4.16 for a description of the panels shown. The magnetization of the continental crust is increased between 360-400 km offset, the approximate location of the OCT.

Finally, this chapter has included a description of the magnetic anomaly along the profiles, developing estimates of relative crustal magnetization with the aim of highlighting variation in crustal structure and defining and characterizing the oceanic crust. Unfortunately this modelling has not clearly identified the edge of the oceanic crust, *i.e.* the most oceanward boundary of the OCT. However, the magnetic modelling has suggested the presence of a significant fracture zone slightly oceanward of Profile A and also that the OCT of Profile D is of a relatively high magnetization.

In Chapter 5 the *P*-wave velocity-depth models developed thus far will be described.

Chapter 5

# Deep crustal models: Results and model description

## 5.1 Introduction

Chapters 2, 3 and 4 contained a description of the development of two deep crustal models along transects of the French Guiana continental margin. MCS data, described in Chapter 2, were used to image the sedimentary structure within the deep basin and also over the Demerara Plateau in order to constrain the depth to, and geometry of, the intra-sedimentary and basement boundaries. In Chapter 3 a description of the WA data modelling was given, which produced *P*-wave velocity-depth models of the sediment column, underlying crust and uppermost mantle. Model testing (Chapter 4) incorporated inverse and Monte Carlo-based forward modelling of the WA data, in addition to 2D gravity and magnetic modelling as a check of model resolution and uniqueness of fit to all available datasets. The resultant models are consistent with the majority of the available data and are constrained within the error bounds.

This chapter will present and discuss the final *P*-wave velocity-depth models, including their strengths, weaknesses, constraints and inconsistencies. It will also highlight key features within the models, which will be used to develop an understanding of the evolution of the equatorial Atlantic in Chapter 6.

## 5.2 Results

As discussed in Section 3.10, the *P*-wave velocity-depth models were initially subdivided into crustal types to assist model testing as described in Chapter 4. For example, gravity modelling involved converting the *P*-wave velocities into densities using empirical relationships. Following assessment of model resolution, fit within the errors of the seismic data and further modelling using all available data, a full description of the final model

along each transect is provided below. Each profile is described separately prior to a discussion of similarities and differences in Section 5.2.3.

## 5.2.1 Profile A

The preferred, best-fit *P*-wave velocity-depth model of Profile A is shown in Figure 5.1, and is defined by the water column, five sediment layers (S1-S5), the basement crust and the underlying upper mantle. The basement crust is further subdivided into two layers: Layer 2 and Layer 3 to reflect the oceanic crust at the oceanward end of the profile; and Upper and Lower Crust, at the landward, continental-style, end of the profile.

The model was divided into the following regions and the characteristics of each are discussed in separate sections below:

- Continental crust (0-135 km offset);
- Thinned continental crust (135-206 km);
- Sediment column (180-430 km);
- The transition zone (206-250 km); and
- Oceanic crust (250-427 km).

### 5.2.1.1 Continental crust

The crust landward of 135 km offset is identified as continental and its structure and velocity are constrained by over 950 refracted arrival traveltime picks ($\chi^2$ of $\sim$1.1) within the crust and over 500 ($\chi^2$ of $\sim$1.8) Moho reflection picks from the land station data. However, the ray coverage provided by the ray-tracing of these picks is quite limited, particularly in the uppermost $\sim$8 km, a consequence of the large $\sim$150 km separation between OBS A1 and land station A21. This acquisition geometry was necessary to avoid placing seafloor instruments in shallow ($<$100 m) water, and was further compounded by not firing seismic shots in the very shallow water for safety reasons. Despite these limitations, the pre-rift continental crust is modelled as two layers. The Upper Crust is 8 km thick with velocities ranging from 5.6-6.0 kms$^{-1}$. The Lower Crust has a lower velocity gradient, with velocities between 6.4-6.7 kms$^{-1}$ below $\sim$9 km depth. The base of the crust is constrained at a maximum depth of $\sim$37.5 km by $P_mP$ arrivals, and the Moho shallows slightly oceanward to a depth of $\sim$34.5 km at 135 km offset.

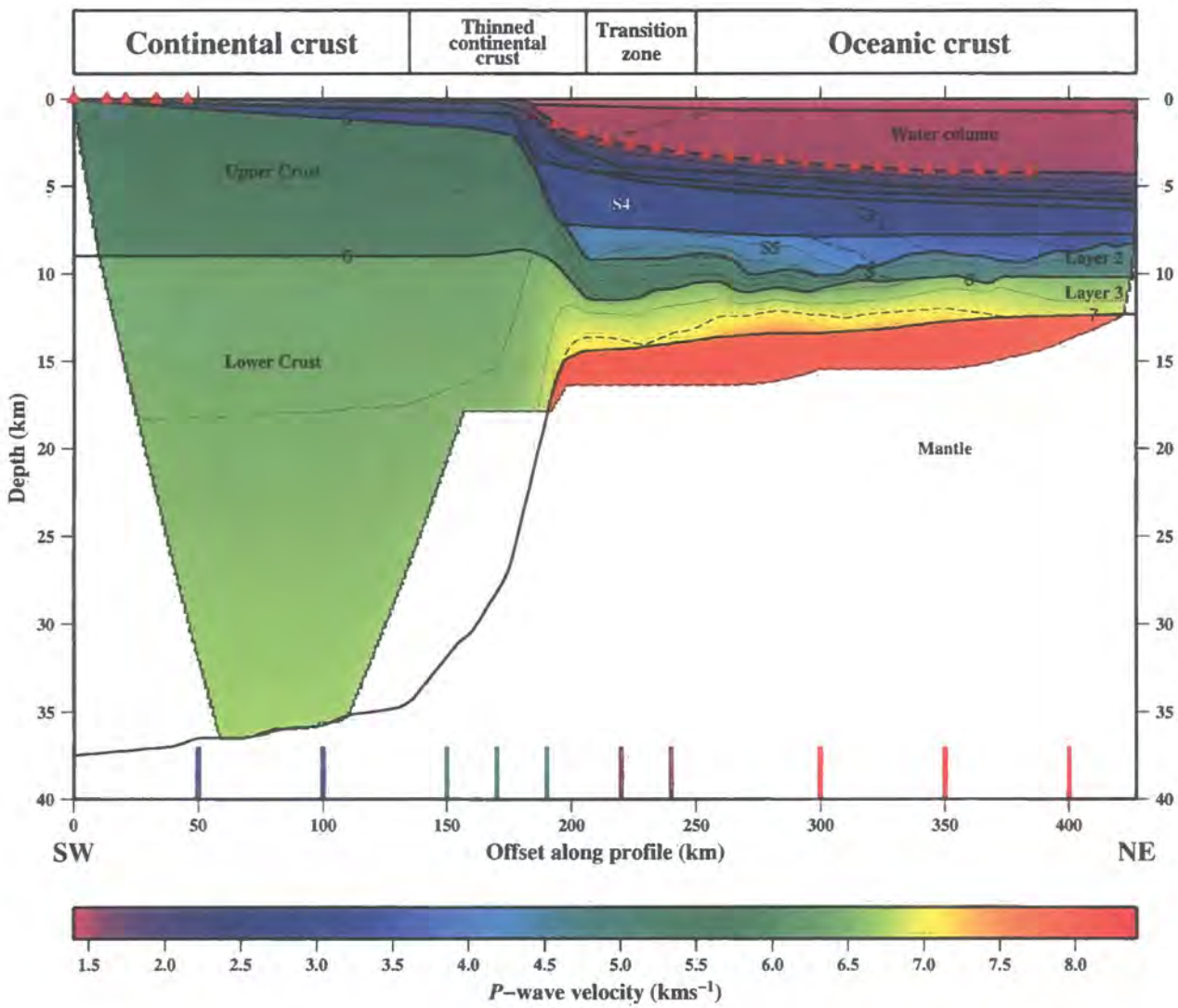


**Figure 5.1**: *P*-wave velocity-depth model of the French Guiana margin along Profile A. A simplified illustration of the interpreted crustal units is also shown (top). The region sampled by WA ray paths is colour-coded according to velocity and contours annotated every 1 $kms^{-1}$. Red triangles mark OBS and land station locations. Labels S4 and S5 refer to the two deepest sedimentary layers and layers S1-S3 are unmarked above S4. Layer 2 and Layer 3 refer to interpreted oceanic crust, while the continental crust is divided into Upper Crust and Lower Crust layers. In both cases the 6 $kms^{-1}$ velocity contour marks the transition between the two crustal layers. The coloured markers at the base of the plot indicate the locations of the 1D velocity-depth profiles shown in Figure 5.2 (red – oceanic; purple – transition zone; green – thinned continental crust; blue – continental crust).

#### 5.2.1.2 Thinned continental crust

The crust from 135-206 km offset is identified as thinned continental in type from its crustal velocity-depth profile which is consistent with global averages from thinned crust imaged in continental margin settings (Figure 5.2 – Peirce *et al.*, 1996). However, the top of the Upper Crust layer shows no evidence, either in the WA model or in the MCS data (Figure 2.16), of the large-scale rotated fault blocks and half graben observed at many rifted continental margins (*e.g.* Goban Spur – Peddy *et al.*, 1989).

By ~206 km offset the crust has thinned from ~37.5 km to ~5.2 km thick. This thinning is largely accommodated within the Upper Crust (from 6.5 km to 2.2 km) between 175-206 km offset and in Lower Crust (25.5 km to 3.0 km) from 135-205 km offset. This is equivalent to a shallowing of the Moho from 34.5 to 14.4 km between the continental shelf and the base of the continental rise, and corresponds to thinning by a factor of ~6.4 over a distance of 70 km.

#### 5.2.1.3 Sediment column

Beneath the seabed, the *P*-wave velocity-depth model comprises five sedimentary layers within the Sediment unit – termed S1-S5. Within this unit the *P*-wave velocity increases from 1.62 $kms^{-1}$, immediately beneath the seafloor, to 4.7 $kms^{-1}$ at the base of the sediment column. The initial subdivision of the Sediment unit into five layers stems largely from the interpretation of the most prominent horizons/reflection events within the MCS data.

| Layer | Range of thicknesses (km) | Range of *P*-wave velocities ($kms^{-1}$) |
|---|---|---|
| S1 | 0.95 | 1.62-2.46 |
| S2 | 0.50 | 2.38-2.75 |
| S3 | 0.45 | 2.70-3.06 |
| S4 | 1.55-2.55 | 2.85-3.12 |
| S5 | 1.00-2.20 | 3.20-4.70 |

**Table 5.1**: Observed sediment layer thicknesses and *P*-wave velocities for Profile A.

The thicknesses of, and velocities within, layers S1-S3 (Table 5.1) are constrained by extensive ray coverage. Within the uppermost layer (S1) the large velocity gradient (~0.8 $s^{-1}$) is consistent with shallow compacted sediments. As identified in Section 2.6.1, a major unconformity at ~7.5 s TWTT separates these upper sediments from those below (S4-S5) and is associated with a large change in velocity gradient (0.65 $s^{-1}$ in S1-S3 to 0.30 $s^{-1}$ in S4-S5) and ray coverage in the model (Section 3.9.1). The lower sedimentary layers are modelled with a wider range of velocities and thicknesses (Table 5.1) than the upper

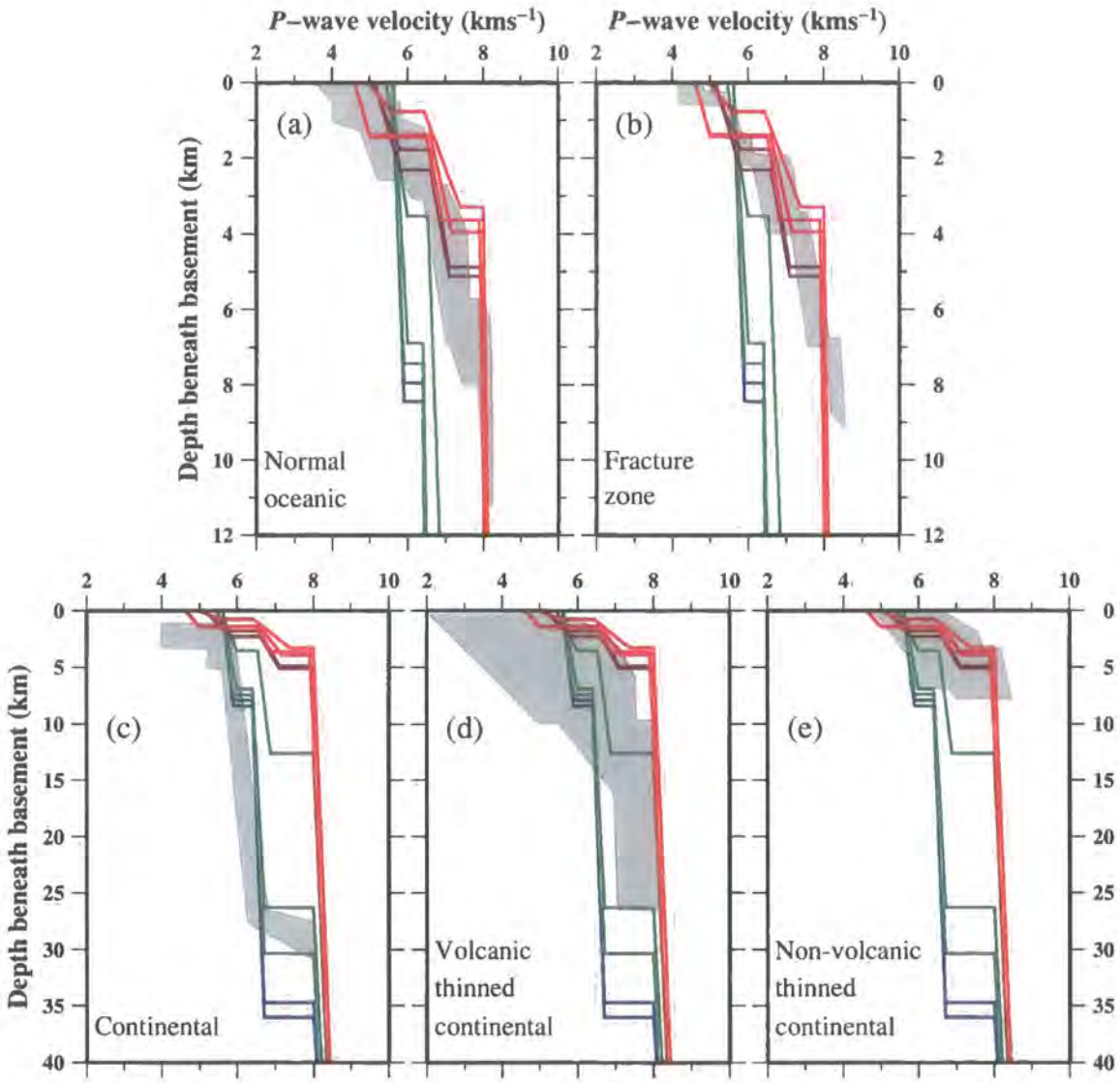


**Figure 5.2**: Comparison of velocity-depth profiles from the Profile A *P*-wave model with compilations (shaded grey) for a) normal oceanic crust, b) oceanic crust adjacent to fracture zones, c) continental crust, d) volcanic thinned continental crust and e) non-volcanic thinned continental crust. a) and b) are plotted to 12 km depth, c), d) and e) to 40 km depth. Compilations, after Peirce *et al.* (1996), taken from Hinz *et al.* (1982), Morgan *et al.* (1989), Morgan (1988), Mutter & Zehnder (1988) and White (1979, 1984). The ACE velocity-depth profiles are colour-coded for oceanic crust (red), pre-rift continental crust (blue), thinned continental crust (green) and transitional crust (purple). The oceanic crust is significantly thinner than normal.

layers and display a significant thinning and velocity decrease oceanward. The velocity gradient in these layers (0.30 $s^{-1}$) is consistent with the very low interval velocity gradient immediately below the unconformity observed in the MCS data (Figure 2.14).

The sediments are also interpreted to extend onto the continental shelf, landward of 180 km offset. However, within this region the MCS reflections are difficult to distinguish from seafloor multiples and, hence, the sediment layer thicknesses are not well constrained. Furthermore, the lack of OBSs on the shelf prevents near-offset modelling of the WA data in this region.

The basement surface is modelled by a series of segments which show it to be relatively smooth, within the resolution of the WA data at that depth. Despite this smoothing, up to ~2 km of topography is observed along the entire profile. However, the MCS data (Figure 2.16) reveals that the basement surface is in fact quite hummocky, particularly oceanward of the continental rise, and underlies a maximum sediment cover of 6.4 km, thinning oceanward to 4.0 km.

#### 5.2.1.4 The transition zone

The region between 206 and 250 km offset is identified as a transition zone between continental- and oceanic-style crust. This zone is most similar to the oceanic crust, as it contains oceanic Layer 2 and Layer 3 velocities (4.9-5.8 $kms^{-1}$ and 6.6-7.1 $kms^{-1}$ respectively) and is only slightly thicker (5.0 versus 3.5 km). However, the MCS data do not clearly image the basement surface, partly due to the seafloor multiple and basement reflection arriving contemporaneously, and partly due to a thicker sediment column close to the continental slope.

The transition zone lies landward of a region of high velocities identified within the base of the oceanic crust whose location also corresponds to a 1.00-1.25 km depression in the basement surface and a thinning of Layer 2. The high velocities are approximately coincident with a region of the density model (Section 4.4.5.1) for which lower densities were required to improve the final misfit, and is suggested to be a result of some degree of serpentinization. Thus, it may be possible that the oceanward end of the transition zone is coincident with partially serpentinized crust, suggesting that some some form of transition zone is present. Consequently, the precise nature of this region is unclear and it is classified as transitional because it does not conform to the style of the crust either landward or oceanward of it.

#### 5.2.1.5 Oceanic crust

The crust oceanward of 250 km offset is identified as oceanic from its hummocky basement surface (MCS data) and the distinctive three-layered velocity structure in the WA model (White *et al.*, 1992). Immediately beneath the basement surface, oceanic Layer 2 velocities are poorly constrained between 4.6-5.7 $kms^{-1}$. However, Layer 3 is well constrained, with modelled velocities ranging from 6.4-7.5 $kms^{-1}$, with the highest velocities (7.2-7.5 $kms^{-1}$) found in the lowermost crust between 255 and 340 km offset. The position and geometry of the Moho is constrained to a depth of ~17 km below sea surface beneath the edge of the continental shelf, to 12.5 km beneath the abyssal plain. Layers 2 and 3 together range in thickness from 3.5-5.0 km (Figures 5.1 and 5.2), of which 2-3 km is Layer 3.

The high velocities (7.2-7.5 $kms^{-1}$) observed at the base of the oceanic crust occupy a region less than 0.7 km thick. These velocities are consistent with those observed within regions interpreted as underplating (Morgan & Barton, 1990; Holbrook *et al.*, 1994a). However, there is no evidence of SDR sequences within the MCS data to support this as an interpretation for the high velocities within the model for Profile A. Alternatively, they may represent some degree of serpentinization, possibly as a result of water ingress along large-offset faults or fracture zones within the crust (*e.g.* Bonatti, 1978; Fox & Gallo, 1986). The WA uncertainty analysis (Section 4.3.2) and the testing of the density model (Section 4.4.5.1) both indicate that these velocities and thicknesses are at the limit of the resolution of the modelling and, hence, this interpretation is made tentatively.

### 5.2.2 Profile D

The preferred, best-fit *P*-wave velocity-depth model of Profile D is shown in Figure 5.3 and, like Profile A, is defined by the water column, five sediment layers (S1-S5), the basement crust and the underlying upper mantle. Again, the oceanic crust is further subdivided into Layer 2 and Layer 3 and the continental crust into Upper and Lower Crust.

The lateral interpretation of Profile D is different from that of Profile A in that it comprises four, rather than five regions. No transition zone is identified between the thinned continental and oceanic crust. However, the possible existence of a transition zone will be discussed below, together with the other subdivisions of the crust, which are:

- Continental crust (0-70 km offset);
- Sediment column (50-535 km);
- Thinned continental crust (70-387 km); and

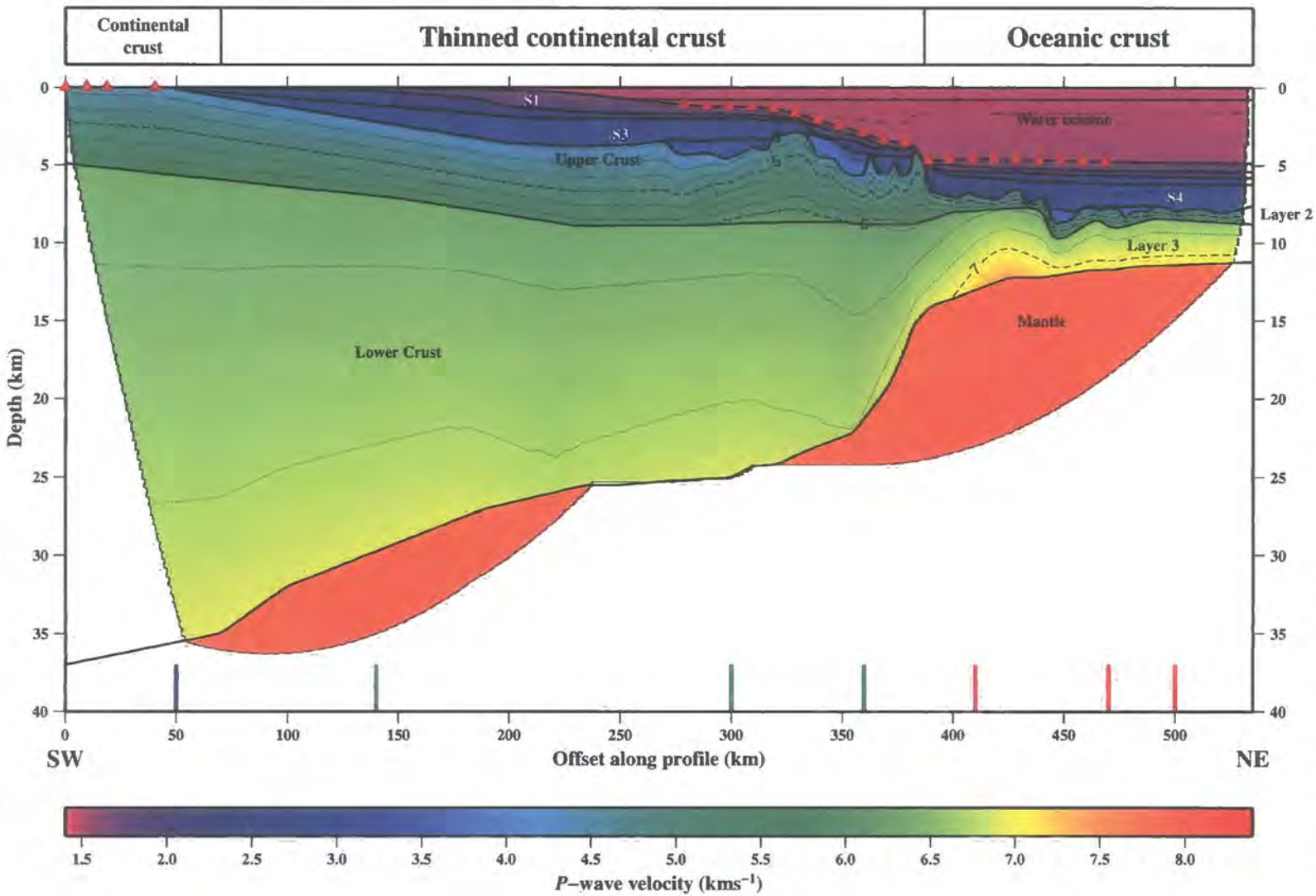


**Figure 5.3**: *P*-wave velocity-depth model of the French Guiana margin along Profile D. A simplified illustration of the interpreted crustal units is also shown (top). The region sampled by WA ray paths is colour-coded according to velocity and contours annotated every 1 $kms^{-1}$. Red triangles mark OBS and land station locations. Labels S1, S3 and S4 show sedimentary layers. Layers S2 and S5 are not labelled. Layer 2 and Layer 3 refer to interpreted oceanic crust, while the continental crust is divided into Upper Crust and Lower Crust layers. In both cases the 6 $kms^{-1}$ velocity contour marks the transition between the two crustal layers. The coloured markers at the base of the plot indicate the locations of the 1D velocity-depth profiles shown in Figure 5.4 (red – oceanic; green – thinned continental crust; blue – continental crust).

- Oceanic crust (387-535 km).

#### 5.2.2.1 Continental crust

Full thickness, pre-rift, continental crust is tentatively identified landward of 70 km offset. At this offset the model is constrained only by long-offset lower crustal and upper mantle refractions. Consequently, the lateral resolution is poor and it is unclear whether the crust is full thickness or is partially thinned. Similarly, it is uncertain what the full crustal thickness is in this region, and the only references on which to judge this value come from the analysis of the ACE data along Profile A and the non-unique gravity modelling, which is broadly consistent with the final model. However, the calculated FAA does not match the satellite data exactly, as it does not show a trough at ~50 km offset (Figure 4.13), which is most likely a result of switching from offshore to onshore data at the coastline. On this profile, pre-rift continental crust was determined to be ~37 km thick and, within the 2.5 km error bound, this depth is observed on Profile D landward of 70 km offset.

The velocities observed within the crust at these offsets are modelled using a combination of seismic data recorded at the land stations and an extrapolation of velocities observed beneath the OBSs further oceanward. The land station data comprise over 1400 traveltime picks which are modelled to an error of 126 ms ($\chi^2$ of 1.35). Despite the sparse data coverage, the structure observed is similar to Profile A in that it comprises two layers. The uppermost layer is ~5 km thick with velocities ranging from 4.3-5.7 $kms^{-1}$, whereas the deeper layer is ~31 km thick with velocities from 6.4-6.9 $kms^{-1}$.

#### 5.2.2.2 Sediment column

The sediment column observed along Profile D is different from that of Profile A in that it extends over 300 km onto the thinned continental crust, contributing to the extent of shallow seafloor on the shelf which marks the Demerara Plateau. Upon, and oceanward of, the Demerara Plateau the sediment column is primarily subdivided into five layers – labelled S1-S5. The deepest layer (S5) is incorporated into the model to reflect the deepest sediments at offsets of 443-448 km and 475-490 km. However, the sediments from 338 to 362 km offset are also identified as S5, despite the absence of S4, because they are of a higher velocity than those around them. This layer of sediment shows similar characteristics to those observed in the landward S5 layer than the S4 layer.

Within the entire sediment column the velocities range from 1.65-3.80 $kms^{-1}$. Thus, the maximum velocity observed within the sediments is significantly lower than the maximum of 4.7 $kms^{-1}$ observed along Profile A. This is most likely a consequence of the smaller

| Layer | Range of thicknesses (km) | Range of *P*-wave velocities ($kms^{-1}$) |
|---|---|---|
| Demerara Plateau | | |
| S1 | 0.49-1.25 | 1.65-2.00 |
| S2 | 0.15-1.25 | 2.05-2.45 |
| S3 | 0.10-1.80 | 2.28-2.96 |
| S4 | 0.00-0.86 | 3.20-3.45 |
| S5 | 0.00-1.30 | 3.40-3.80 |
| Abyssal plain | | |
| S1 | 0.33-0.54 | 1.68-1.85 |
| S2 | 0.26-0.39 | 1.95-2.23 |
| S3 | 0.28-0.55 | 2.33-2.50 |
| S4 | 0.53-1.93 | 2.37-3.08 |
| S5 | 0.00-1.06 | 3.50-3.65 |

**Table 5.2**: Observed sediment layer thicknesses and *P*-wave velocities for Profile D.

degree of compaction resulting from the reduced sediment load along Profile D, which comprises, at most, a 3.9 km thick sediment unit (at 450 km offset) compared with 6.5 km along Profile A.

The identification of the sedimentary layers S1-S5 is primarily from the MCS data and correlation between the velocity-depth model boundaries and prominent MCS reflectors is good (Figure 3.29). On the Demerara Plateau (landward of 387 km offset) the thicknesses of, and velocities within, layers S1-S5 (Table 5.2) are constrained by extensive ray coverage. Given the lack of a distinct basement reflector in the MCS data, the precise depth to, and geometry of the boundary separating the sediments from the continental crust is poorly constrained.

The sediment layers which overlie the region identified as oceanic crust have similar thicknesses and velocities to those in Profile A , although they display a lesser degree of lateral variation. Similar to Profile A, these sediments contain an unconformity at ~6.5 km depth which marks a change in the velocity gradient from 0.6 $s^{-1}$ to 0.3 $s^{-1}$.

The oceanic basement surface in the model has 2.4 km of topography, which is primarily accommodated by a step in the basement between 435 and 448 km offset, potentially indicating the presence of a large fault within the basement.

#### 5.2.2.3 Thinned continental crust

The thick continental crust at the landward end of Profile D appears to thin gradually from 70 to 387 km offset. This thinning occurs primarily in two regions: 70-235 km where the crust thins gently from 34.4 to 21.7 km thickness; and 320-387 km where the crust thins

sharply from 21.0 to 10.6 km. Thus, the oceanward zone of thinning occurs over a region of approximately half the width of the landward zone.

*P*-wave velocities within the thinned continental crust are well constrained oceanward of ~280 km offset, beneath the OBSs. In general, they range from 4.2 to 6.2 $kms^{-1}$ in the upper layer and from 6.2 to 6.9 $kms^{-1}$ in the lower layer. However, landward of 363 km offset the upper velocities drop to 3.7 $kms^{-1}$, although this may be partially a result of slight misplacement of the steep boundary which separates the sediments from the continental crust.

The surface of the continental Upper Crust, beneath the sediments, is rough with ~2.8 km of relief. Indeed, the surface may even be rougher than the WA models suggest as the resolution the modelling provided on this surface was insufficient to model the relatively small scale undulations in the basement, as observed in the MCS data (Figure 2.27). Thus, given the irregularity of the basement, the surface is not interpreted as comprising rifted fault blocks or half graben and, instead, is a result of transtensional motion along the margin.

#### 5.2.2.4 The transition zone

Along Profile A the presence of a transition zone was inferred from the absence of features which clearly define the crust as either oceanic or thinned continental. In addition, clear MCS reflections were absent or indistinct due to steep gradients and the overlap of seafloor multiple within this region. Data from the Profile D transect do not exhibit these features, primarily because the seafloor multiple does not obscure the basement reflection in this region. As a result, an oceanic-style basement reflection is identified landward to ~390 km. Within the WA model a two-layer crust with velocities characteristic of oceanic crust is observed to ~400 km. Although a slight thickening of this crust is observed, compared with the crust oceanward of 450 km, it is insufficient to suggest that the crust does not conform to standard models of oceanic crust.

The rapid thickening of the continental crust landward of 387 km suggests that this region is continental in nature and, hence, implies a relatively thin OCT. Although, given the limits of the lateral resolution at this depth, the OCT could alternatively be described as an OCB, with an abrupt contact between continental and oceanic crust.

#### 5.2.2.5 Oceanic crust

The crust oceanward of 387 km offset is identified as oceanic in nature from the hummocky basement reflection observed in the MCS data (Figure 2.26) and the characteristic three-

layer velocity structure in the WA model. Beneath the Layer 1 sediments, the crust comprises Layers 2 and 3 with thicknesses and velocities of 0.6-1.2 km / 4.3-6.2 $kms^{-1}$ and 2.3-4.5 km / 6.4-7.4 $kms^{-1}$ respectively; a total thickness of 3.3-5.7 km (Figure 5.4).

Comparison with Profile A shows that Layer 2 is thinner (and Layer 3 thicker) along Profile D. However, both profiles show a similar range of velocities, including high velocities of up to 7.4 $kms^{-1}$ at the base of the crust at around 425 km offset. The preferred explanation is some degree of serpentinization as described in Section 5.2.1.5.

The rapid increase in the depth of the basement surface between 435 and 448 km offset is accompanied by a similar increase in the depth of the intra-crustal boundary, suggesting the possibility of a fault cross-cutting the entire crust. However, within the limits of resolution, no significant change is observed in the depth to Moho. The high velocity zone discussed above is located close to, although slightly landward of this region.

### 5.2.3 Similarities and differences

Profiles A and D are, at first glance, strikingly different. These differences include:

- Distribution of sediments – whilst Profile A displays a thick sediment column oceanward of the continental slope and relatively thin sediments on the continental shelf, Profile D shows a sediment column of approximately constant thickness from close to the shoreline to the deep basin, which is most likely due to subsidence associated with thinning of the continental crust;

- Zone of thinning – the difference is significant given that the margins are located relatively close together along-strike of the margin. Profile D thins over a zone which is ~4.5 times the width of this zone on Profile A, despite both sections of the margin (~125° from north) and both profiles (~30° from north) trending in roughly the same directions; and

- Crustal velocities – the uppermost continental crust shows a higher velocity gradient along Profile D than along Profile A, possibly a consequence of some degree of fracturing associated with the stretching phase of rifting. An alternative explanation is that the uppermost crystalline crust has been progressively compacted as it has subsided following deposition of greater thicknesses of sediment. However, more likely the difference in velocity gradient is an artefact of modelling which reflects the lack of ray coverage in this region of Profile A as the OBSs were located oceanward of the continental shelf. The velocity structure observed along Profile D was better constrained.

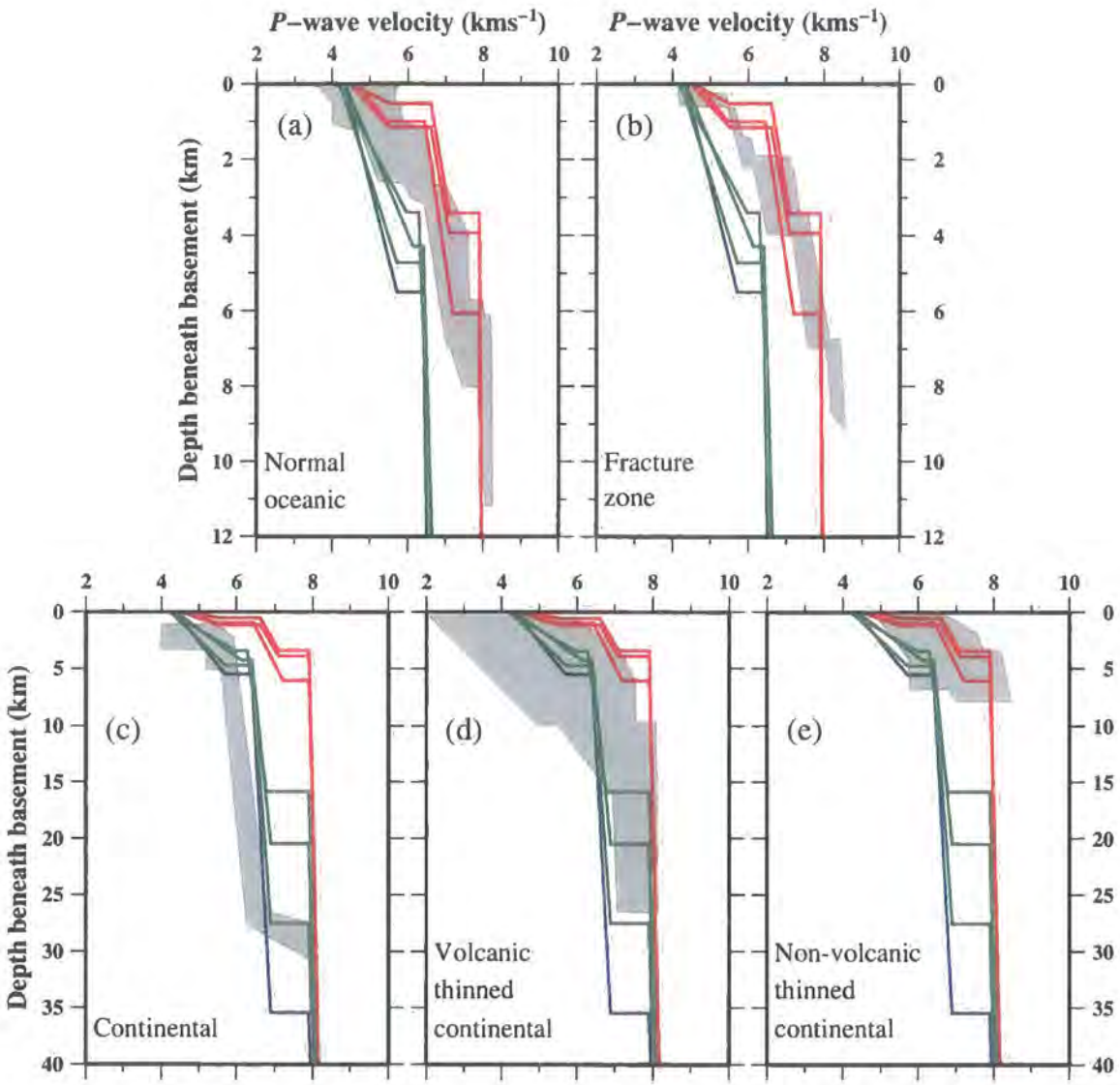


**Figure 5.4**: Comparison of velocity-depth profiles from the Profile D *P*-wave model with compilations (shaded grey) for a) normal oceanic crust, b) oceanic crust adjacent to fracture zones, c) continental crust, d) volcanic thinned continental crust and e) non-volcanic thinned continental crust. a) and b) are plotted to 12 km depth, c), d) and e) to 40 km depth. Compilations, after Peirce *et al.* (1996), taken from Hinz *et al.* (1982), Morgan *et al.* (1989), Morgan (1988), Mutter & Zehnder (1988) and White (1979, 1984). The ACE velocity-depth profiles are colour-coded for oceanic crust (red), pre-rift continental crust (blue) and thinned continental crust (green). The oceanic crust is significantly thinner than normal.

In addition, the profiles share several similarities:

- Continental crust – the full thickness, pre-rift continent crust at the landward end of both profiles is approximately the same thickness (~35.0-37.5 km);
- Oceanic crust – is very similar in terms of velocities and overall thickness observed. However, the relatively poorly constrained Layer 2 is slightly thicker along Profile A than Profile D. Across much of both profiles this difference is considered to be within the limits of resolution and, hence, the profiles show effectively the same layer thickness. However, there also exist regions for which this is not the case and, hence, the feature is considered to be real; and
- Mantle – velocities are approximately 7.9-8.0 $kms^{-1}$, consistent with other WA refraction studies.

## 5.3 Model features

In this section several features observed within the models will be discussed. These merit further analysis because they may have implications for the rifting and early evolution of this margin, and include:

- the degree of continental crustal thinning (Section 5.3.1), which shows considerable variation globally (Section 1.1.1);
- the roughness of the oceanic basement (Section 5.3.3), which has been observed to be inversely related to spreading rate at rifted margins (Malinverno, 1991; Minshull, 1999), *i.e.* a relatively smooth crustal surface results from accretion at fast-spreading rates and vice versa; and
- the nature of crustal faulting and other lineations, suggested as an explanation for high velocities within the oceanic crust, which may be observed on a regional scale as well as within the two ACE profiles.

### 5.3.1 Continental crustal thinning

As discussed within Sections 5.2.1.2 and 5.2.2.3, significant crustal thinning is observed along both ACE Profiles. Along Profile A this is evidenced by WA data which constrain the thick continental crust landward of, and the thin oceanic crust oceanward of, the zone of thinning. The geometry of the Moho in between is primarily constrained by gravity

modelling. Along Profile D the Moho is better constrained by the WA data, and modelling of this is, largely, in agreement with the geometry of the Moho suggested by gravity modelling (Section 4.4.4).

The distance over which this thinning is accommodated varies dramatically between the two profiles. Whilst the crust thins by a factor, $\beta$ (= full crustal thickness / crustal thickness at a given offset), of $\sim$6.4 over a distance of 70 km along Profile A, the crust thins by a factor of $\sim$3.8 over 320 km along Profile D. Additionally, the thinning along Profile D may be subdivided into two phases – a $\beta$ of $\sim$1.6 over 165 km and a $\beta$ of $\sim$2.0 over 67 km – which are separated by a zone of $\sim$88 km in which no significant thinning is observed.

Figure 5.5 illustrates this point and compares the two profiles with several others from a study by Watts & Fairhead (1997), who divide margins into wide (>250 km) and narrow (<75 km) types based on the width over which the continental crust thins. As more recent studies have shown this terminology is an oversimplification of the rifting process, and a wide range of widths have been observed (*e.g.* Davis & Kusznir, 2002). However, to compare the ACE profiles with a wide range of rifts, without overcomplicating the plot, this terminology is used here. Figure 5.5 shows that Profile A lies at the narrowest end of the narrow rifts and that, in contrast, Profile D is a relatively wide rift. This significant difference in the width of continental thinning between the two transects clearly demonstrates a large degree of along-strike margin segmentation. Several factors influence the width over which continental thinning occurs, including rate and orientation of rifting and crustal strength, which will be considered in due course.

### 5.3.2 Spreading rate in the equatorial Atlantic

In the next two sections, the basement roughness and overall thickness of oceanic crust will be discussed. Both of these variables have been observed to be related to spreading rate during crustal accretion. Therefore, in this section, spreading rate will be introduced and estimated for the equatorial Atlantic.

Post-rift full spreading rate is the speed at which two adjacent lithospheric plates are separating from a central spreading axis. Hence, half spreading rate is the speed at which one plate is moving away from the axis which, in the case of symmetric spreading, is exactly half of the full spreading rate. As the primary consideration of this study is the western margin of the equatorial Atlantic, the half spreading rate will be used and, where comparisons are made with other studies, values of full spreading rate will be halved. To avoid confusion between these two definitions, the term 'spreading rate' will be avoided

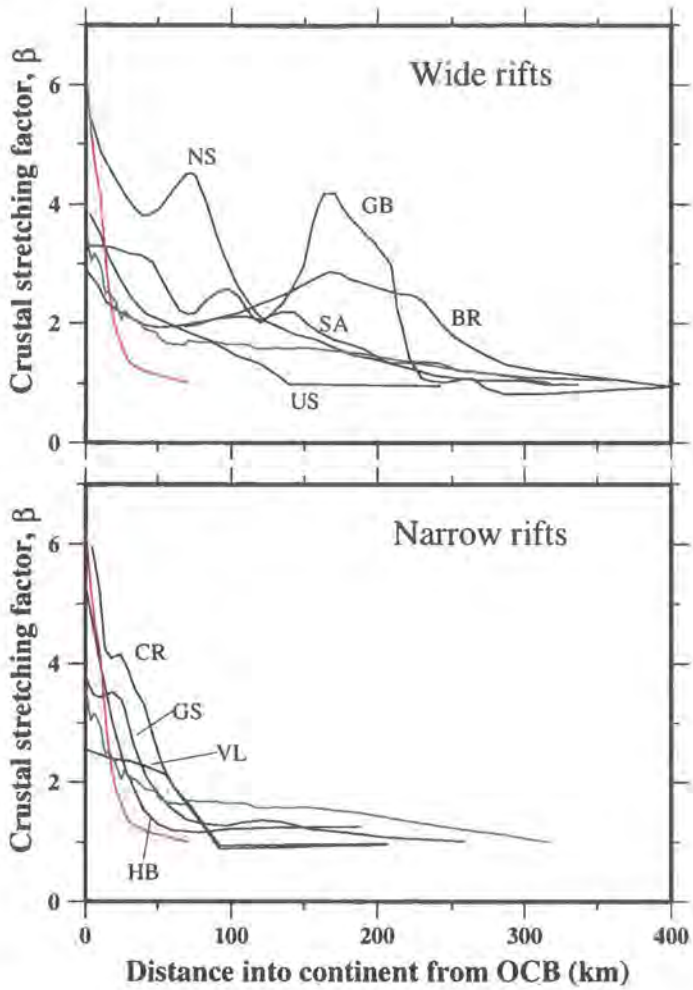


**Figure 5.5**: Width over which continental thinning occurs for Profiles A (red) and D (green). The degree of thinning is shown in terms of crustal stretching factor, $\beta$, for which a value of 1 is equivalent to no thinning, *i.e.* full crustal thickness. The two profiles are compared with several 'wide' rifts (top) and several 'narrow' rifts (bottom), after Watts & Fairhead (1997). The comparison indicates that, in terms of the Watts & Fairhead (1997) width terminology, Profile A, which thins over ~70 km is at the narrow end of the narrow rifts. Profile D, which thins over 320 km, is more readily compared with wide rifts. The rifted margins shown are NS – Nova Scotia (Mohriak *et al.*, 1990); GB – Gabon (Watts & Fairhead, 1997); BR – Brazil (Hutchinson *et al.*, 1983); SA – South Africa (Young, 1992); US – US East Coast (Watts & Torné, 1992); CR – Carolina (Beaumont *et al.*, 1982); GS – Goban Spur (Horsefield, 1991); VL – Valencia (Watts, 1988); and HB – Hatton Bank (Watts & Fairhead, 1997).

and 'half spreading rate' used instead. This approach assumes that spreading was, and has remained to the present day, symmetrical about the ridge axis. The likelihood of this assumption being valid will be addressed shortly.

The half spreading rate in the equatorial Atlantic is estimated from the global, 6′ seafloor age grid of Müller *et al.* (1997) (Figure 5.6). In their study, best-fit isochrons are calculated by using magnetic anomaly and fracture zone picks, in addition to consideration of the rotation poles about which spreading occurs. Isochrons are then extrapolated from

the oldest observed magnetic anomaly to the continental margins, the location of which is identified using the satellite gravity data of Sandwell *et al.* (1994).

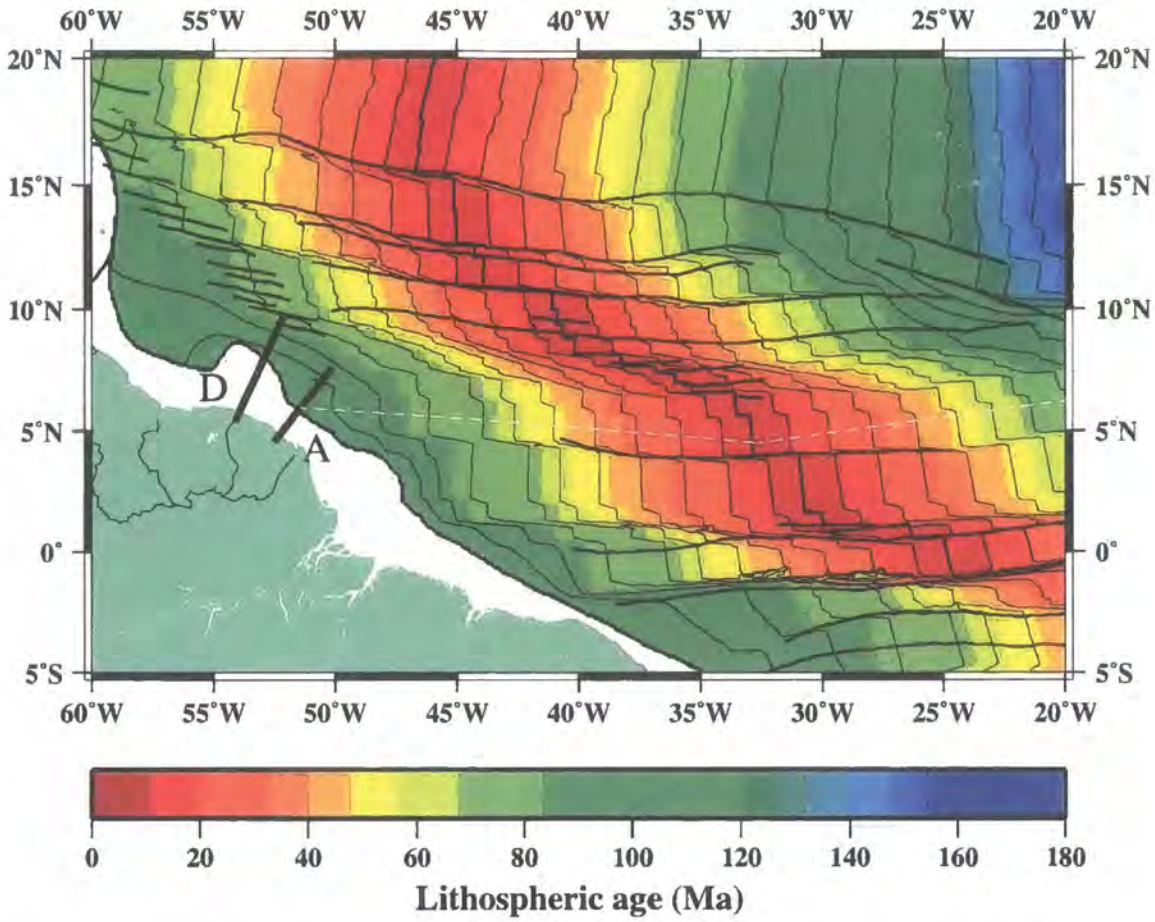


**Figure 5.6**: Oceanic lithospheric ages in the equatorial Atlantic. Ages are taken from the grid of Müller *et al.* (1997) and illustrate young lithosphere at the MAR and 100-110 Ma old lithosphere at the French Guiana margin. Profiles A and D (black) and the pseudo-flowline (dashed white) used to calculate spreading rates (Figure 5.8) are shown.

Total errors associated with each cell of the grid are determined by considering errors due to uncertainty in the identification of magnetic anomalies, distance from these anomalies and the gradient of the age grid, which is large at fracture zones. Consequently, relatively large errors are estimated for certain regions including the Bay of Bengal, Polynesia and the equatorial Atlantic (Müller *et al.*, 1997). These regions are either equatorial, reflecting the lack of distinct magnetic anomalies, or adjacent to margins formed during the Cretaceous quiet zone, in which extrapolation between magnetic anomalies and the margin occurs over large distances. As a result, the ages adjacent to the French Guiana margin are, unfortunately, poorly constrained. However, the age grid is still the best available dataset for this approach.

Figures 5.6 and 5.7 show the age grid and the associated errors for the equatorial Atlantic. From the grid, the lithosphere immediately adjacent to the margin is between 100 and 110 Ma old. Additionally, the errors on the lithospheric age are estimated to be ~7-8 Ma in the region of the two profiles, although they are as high as 13 Ma adjacent to fracture zones further south.

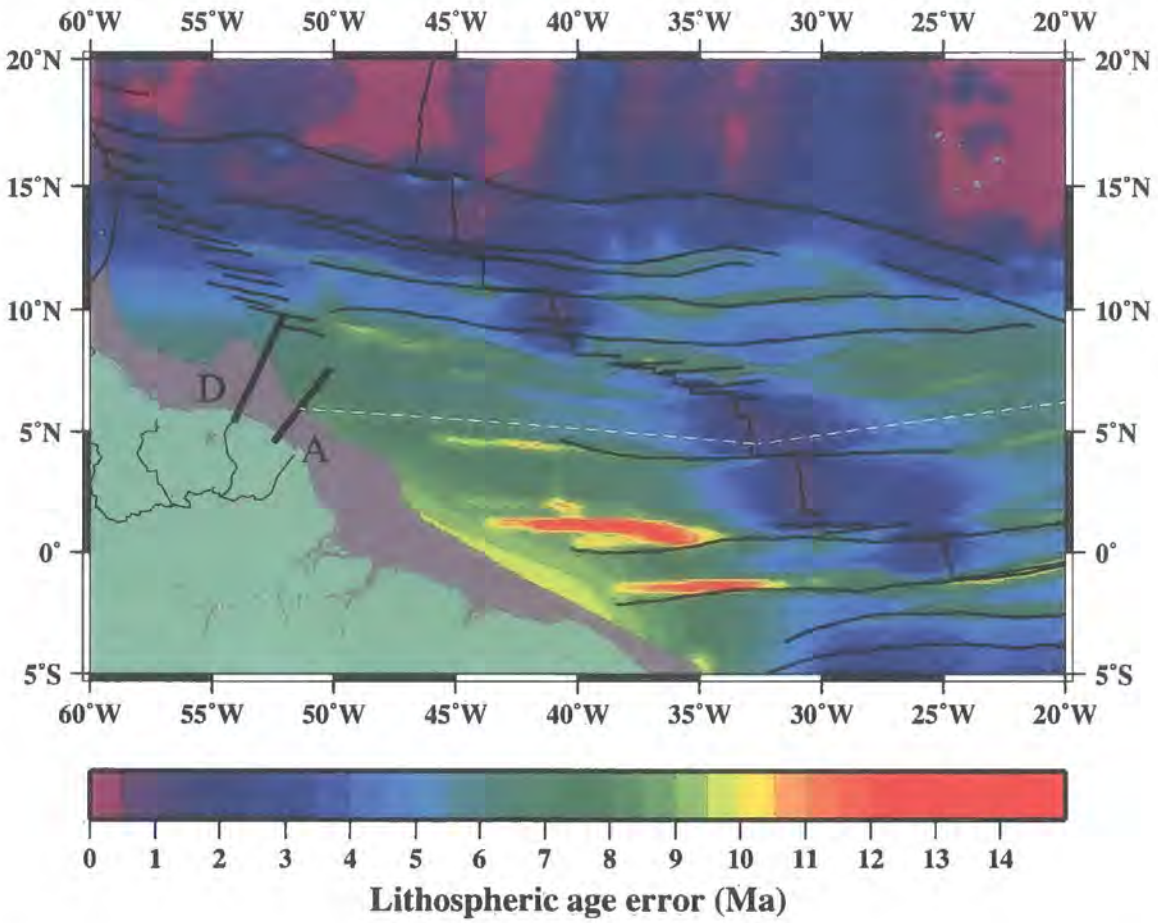


**Figure 5.7**: Errors on the oceanic lithospheric ages shown in Figure 5.6. Errors are relatively large within the equatorial Atlantic due to the sparsity of magnetic anomalies. Very large errors are observed at fracture zones due to the increased age gradient resulting from uncertainty in the precise location of the fractures in these regions. Profiles A and D (black) and the flowline (dashed white) used to calculate spreading rates (Figure 5.8) are shown.

Figure 5.8 shows the half spreading rate calculated along a pseudo-flowline, following the general trend of nearby fracture zones, from OBS A1 to the MAR. This figure illustrates that the half spreading rate has been relatively stable at ~20 $mmyr^{-1}$ since the inception of seafloor spreading. The only major exception to this occurred between 68 and 55 Ma, when the half spreading rate decreased to ~11 $mmyr^{-1}$. This reduction, and the general trend, is consistent with the calculations by Cogné & Humler (2004, 2006) from the South, Central and North Atlantic. The period of reduced half spreading rate is roughly contemporaneous

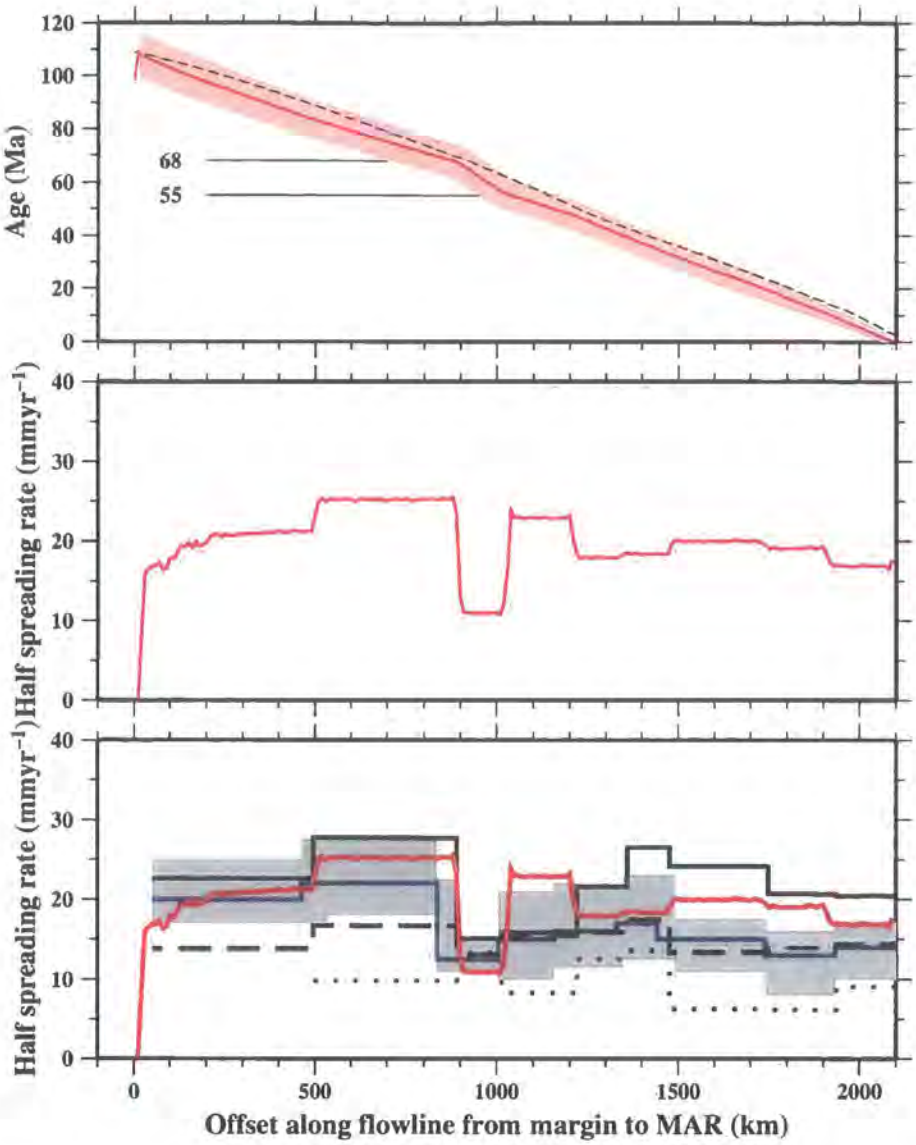


**Figure 5.8**: Seafloor half spreading rate at the French Guiana margin. (Top) Age (red line) of oceanic lithosphere versus distance, along a pseudo-flowline from OBS A1 to the MAR, taken from the age grid shown in Figure 5.6 (Müller *et al.*, 1997). The shaded background shows the age ± the error (Figure 5.7). Lithospheric age (black dashed line) along a second pseudo-flowline across the eastern equatorial Atlantic shows that spreading is relatively symmetric. Locations of the pseudo-flowlines are shown in Figures 5.6 and 5.7. (Middle) Half spreading rate calculated by taking the gradient of the age-distance relationship (top). (Bottom) Half spreading rate compared with the rates calculated by Cogné & Humler (2004, 2006) for the South (solid black line), Central (dotted black line) and North (dashed black line) Atlantic. In addition, the Atlantic average (solid blue line) and variation (shaded grey) are also shown.

with the onset of northward movement of the Indian subcontinent (65-47 Ma – Patriat & Achache, 1984).

In addition, Figure 5.8 also shows the half spreading rate for the east equatorial Atlantic, calculated along a second pseudo-flowline from the intersection between the first pseudo-flowline and the MAR, to the West African margin. Within the error bounds, the

half spreading rates to the east and west of the MAR are equal. This suggests that spreading was symmetrical about the ridge axis, validating the earlier assumption in this regard.

When the age grid errors are considered, the initial half spreading rate at the margin is estimated to be between 15 and 31 $mmyr^{-1}$. These values are consistent with other studies which suggest a range of half spreading rates from 9 $mmyr^{-1}$ (Le Pichon & Hayes, 1971) to 28 $mmyr^{-1}$ (Nürnberg & Müller, 1991) and suggest that accretion occurred at slow spreading rates immediately after rifting. Hence, spreading was approximately twice as fast as that observed at margins adjacent to ultra-slow (half spreading rate $<10$ $mmyr^{-1}$ – Bown & White, 1994) speading centres.

### 5.3.3 Oceanic basement roughness

The combination of ACE and Guyaplac data provides a wealth of information about the roughness of oceanic basement offshore French Guiana. The topography observed along the boundary between oceanic Layers 1 and 2, parallel to the spreading direction, has been demonstrated to be a proxy for post-rift spreading rate. Several studies detail this effect close to the ridge axis where sediment cover is minimal (Malinverno, 1991; Goff, 1991, 1992; Small, 1994). However, older basement located within ocean basins and adjacent to continental margins, where relief can only be detected by MCS profiling, is more problematic to study due to the difficulties of imaging and accurately resolving the sub-sediment basement surface. Minshull (1999), in a study of Mesozoic age oceanic crust in the North Atlantic, notes that "there is no obvious way for roughness created at the spreading centre to be lost as the crust evolves" and suggests that present day observations of basement roughness are a measure of spreading rate. Hence, discounting the possibility of some form of glacial scouring, as is observed at high latitudes, anomalous roughness may be due to anomalous accretion or some tectonic process which occurs as the crust moves away from the ridge axis. As such, it follows that basement roughness offshore French Guiana may act as an indicator of spreading rate and/or the 'normality' of crustal accretion.

The basement surface along Profiles A and D can be determined in two ways (Figure 5.9):

- The layer boundary can be extracted directly from the *P*-wave velocity-depth models. However these boundaries are constructed from a series of nodes, which given the resolution of the WA data, are effectively smoothed versions of the true surface. Hence, most fine detail will be lost in this definition of the basement; and

- The topography may be taken directly from the MCS data sections. However the measurements will be in TWTT and an estimate of velocity is required to convert to distance.

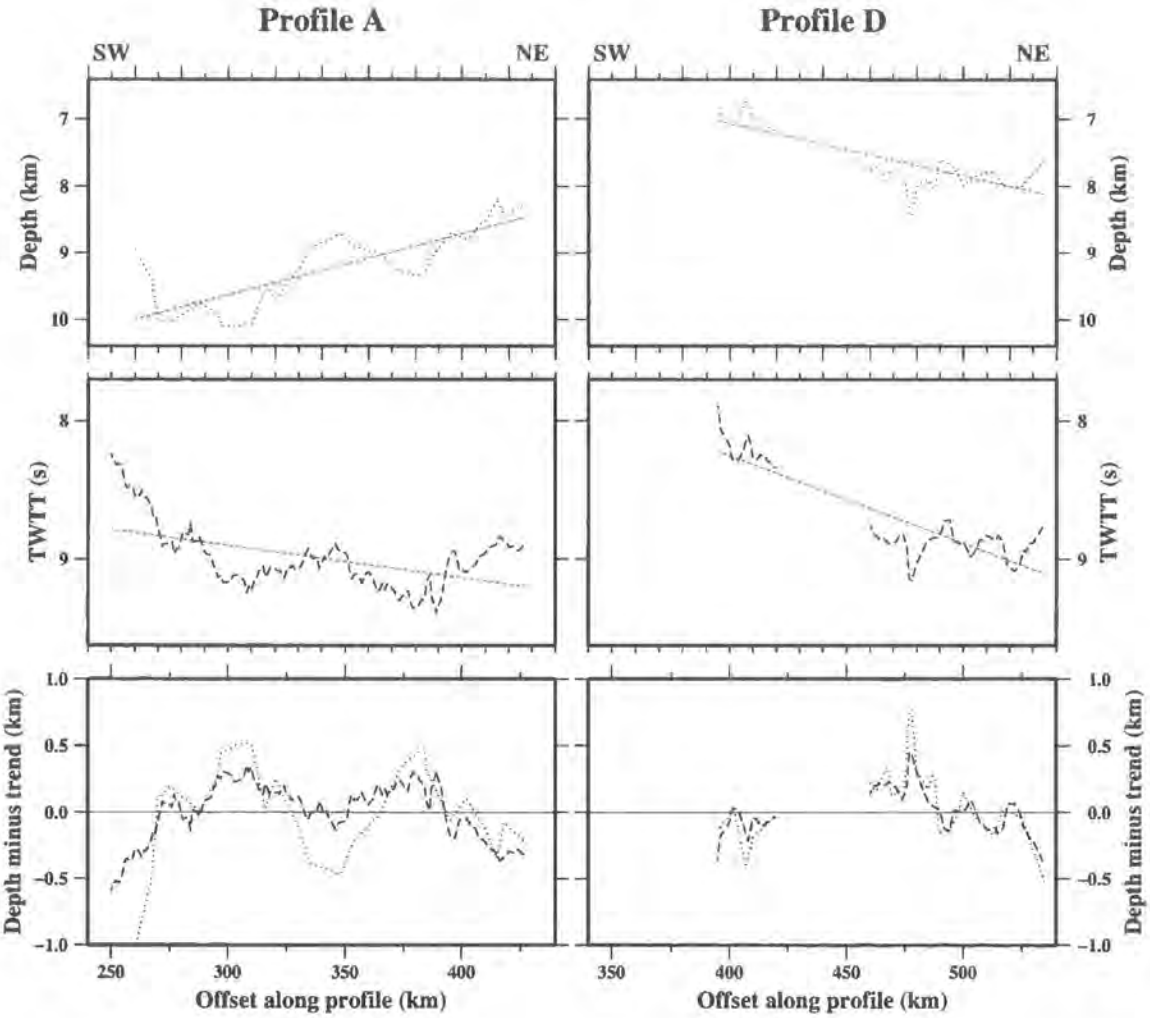


**Figure 5.9**: Analysis of basement roughness along Profiles A (left column) and D (right column). (Top) Basement surface taken from the *P*-wave velocity-depth models (black dotted line) and a best-fit basement trend (red dashed line). (Middle) The same surface picked from the MCS sections. (Bottom) Difference between the surfaces and their trends, where values in TWTT have been halved and multiplied by a stacking velocity of 2.2 $kms^{-1}$ to convert to depth. The rms difference is known as the basement roughness (Table 5.3).

The roughness of the surface is defined as its rms deviation from a best-fit line through the entire profile (Malinverno, 1991). Using this approach, systematic variation resulting from normal faulting has been observed when profile lengths are short, typically less than 100 km in length. However, each of the ACE profiles was of sufficient length to avoid this potential error. The accuracy of roughness measurements is also subject to the influence of fracture zone traces, which may be associated with large changes in basement

topography. Such lineations are often difficult to identify especially within regions where the bathymetry or FAA is masked by an overlying sediment column. The only potential fracture zone trace observed thus far, within these data, is that bisecting Profile D at ~440 km (Section 5.2.2.5). The topographic change as a result of this zone is removed from the following analysis. However, the effects of further, less distinct, fracture zones associated with smaller topographical variation may remain.

The results of both types of roughness analysis are shown in Figure 5.10 and summarised in Table 5.3. In addition to the ACE data, the basement is also imaged along many of the Guyaplac MCS profiles (Section 2.5.2). Hence, the same analysis was used to calculate the roughness along these profiles. No velocity information is available for the Guyaplac profiles and, to ensure a consistent approach, a *P*-wave stacking velocity of 2.2 $kms^{-1}$ was chosen to convert between roughness in TWTT to roughness in km for both ACE and Guyaplac profiles.

| Profile | Basement roughness (m) | |
|---|---|---|
| | from WA model | from MCS data |
| A | 316 | 215 |
| D | 225 | 160 |
| 01 | | 234 |
| 03 | | 299 |
| 05 | | 315 |
| 07 | | 434 |
| 09 | | 372 |
| 42 | | 348 |
| 44 | | 311 |
| 57 | | 383 |
| 59 | | 385 |
| 63 | | 434 |

**Table 5.3**: Summary of basement roughness for seismic profiles offshore French Guiana. For Profiles A and D two measures were used; roughness of the basement boundary within the *P*-wave velocity-depth model and roughness of the basement in the MCS data, converted to depth using a velocity of 2.2 $kms^{-1}$. No WA data are available for the Guyaplac profiles and, hence, roughness is calculated from the MCS data only.

The Guyaplac and ACE MCS data image basement which has a broad range of rms roughness, from 160 to 434 m. However, given the likelihood that some fracture zones may be present whose effect have not been removed from the data, the rms roughness values calculated here are likely to be overestimates.

Using a half spreading rate of 20 $mmyr^{-1}$ (Section 5.3.2), Figure 5.10 shows a comparison of the roughness observed offshore French Guiana with the results from Malinverno (1991) and Goff (1991, 1992). The profiles which express the least topographic variation

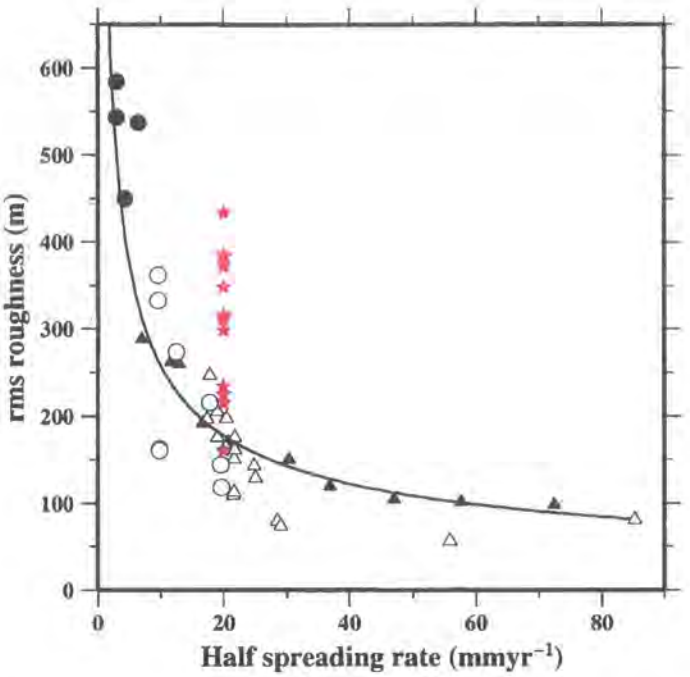


**Figure 5.10**: Relationship between basement roughness and half spreading rate, after Minshull (1999). Black and white triangles represent values from Malinverno (1991) and Goff (1991, 1992) respectively. Similarly, black and white circles are taken from Weigelt & Jokat (2001) and Minshull (1999) respectively. The power-law relationship of Malinverno (1991) is also shown (black line). Basement roughness measurements, offshore French Guiana, are shown as red stars, assuming a half spreading rate of 20 mmyr$^{-1}$. The range of these measurements suggests that a half spreading rate as low as 5 mmyr$^{-1}$ may be more appropriate to such basement characteristics or that the roughness isn't a result of processes associated with accretion alone.

and, hence, roughness, are located on the graph in the approximate position expected, given the roughness-half spreading rate relationship of Malinverno (1991). However, several of the profiles are significantly rougher than would be expected, which suggests that either the abundance of fracture zones in the region has contaminated the measurements and resulted in overestimates of the roughness, or that the half spreading rate is significantly lower than the age grid calculations (Section 5.3.2) have suggested. A projection of the roughness calculations onto the power-law relationship of Malinverno (1991) indicates that half spreading rate may be as slow as 5 mmyr$^{-1}$, *i.e.* ultra-slow spreading. Consideration of the errors on the age grid suggests that such a low spreading rate is unlikely and, hence, a more thorough assessment of regional fracture zones is required to fully understand the evolution of the oceanic crust offshore French Guiana.

### 5.3.4 Regional lineations

Given that fracture zones have been suggested by the 2D MCS and WA data modelling, it is likely that these extend laterally away from the profiles, into 3D. Here, the 3D basement

surface is analysed to ascertain its origin which, for example, may be caused by along-axis ridge segmentation preserved within the crustal fabric. Lineations are assessed in 3D using three different methods:

- Gravity – regional variation in the FAA;
- MCS – in particular the variation in TWTT to the basement surface; and
- Magnetic – variation in the magnetic anomaly.

#### 5.3.4.1 Gravity field

In general, within the Atlantic Ocean, lineations within the FAA gravity field can be traced easily away from the MAR. However, closer to the continental margins lineations are less distinct, especially between 1° and 7°N in the equatorial Atlantic, precisely where ACE Profiles A, B, F and G are located. This observation partially reflects the reduction in the frequency of fracture zones in this region in comparison to those slightly to the north and the south which can be seen clearly in the trend of the MAR. However, it is also a likely consequence of the thick sediment column in this region which masks the gravity signature of the underlying basement.

Figure 5.11 shows several of the more distinct fracture zones picked from satellite FAA data (Sandwell & Smith, 1997). To improve fracture zone identification, some of these picks were made from the first derivative of the FAA (Figure 5.12), calculated using the *GMT* module *grdgradient*, by taking the derivative with respect to distance in two primary directions, 10° and 100° from north; the approximate orientations of the MAR and the fracture zones respectively. Of these two derivatives, the larger was retained and the smaller discarded to produce the final image. This technique strongly highlights 'edges' in the data which run parallel to the two chosen directions, *i.e.* the fracture zones and the MAR.

#### 5.3.4.2 Basement characteristics

Whilst a 3D description of the basement is not possible with the MCS data available, a pseudo-3D description can be approximated from the 2D profiles. This analysis will be limited by the ~50 km separation of the Guyaplac profiles along-margin-strike. Thus, only large scale features with a reasonable degree of east-west orientation may be observed. However, given the general trend of lineations in this region (Figure 5.12), significant fracture zones are likely to be among these.

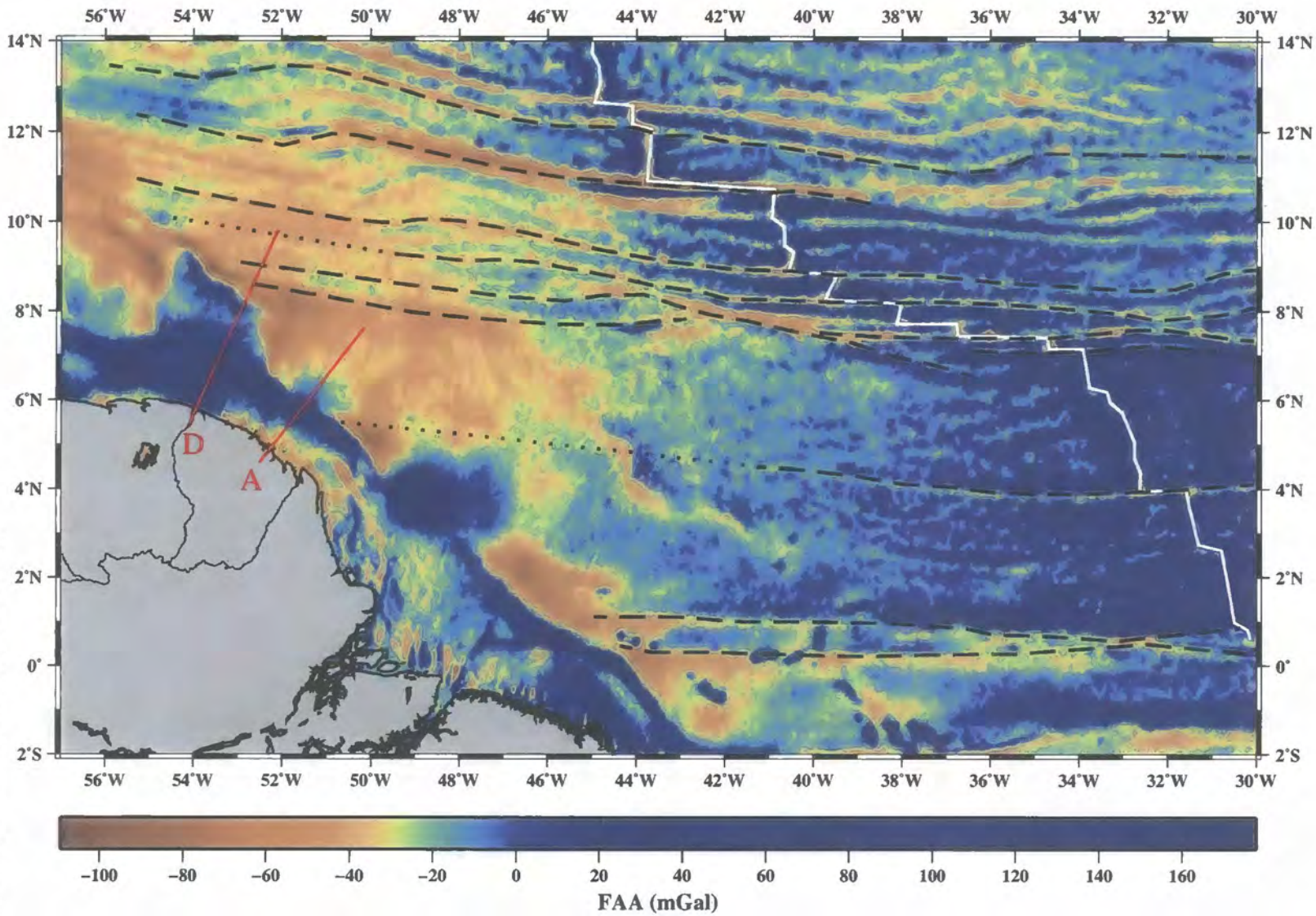


**Figure 5.11**: Lineations observed in the FAA of the equatorial Atlantic. Distinct lineations (black dashed), the MAR (white) and ACE Profiles A and D (red) are shown on satellite-derived FAA data (Sandwell & Smith, 1997). Two lineations which do not extend to the margin are extrapolated and shown (black dotted).

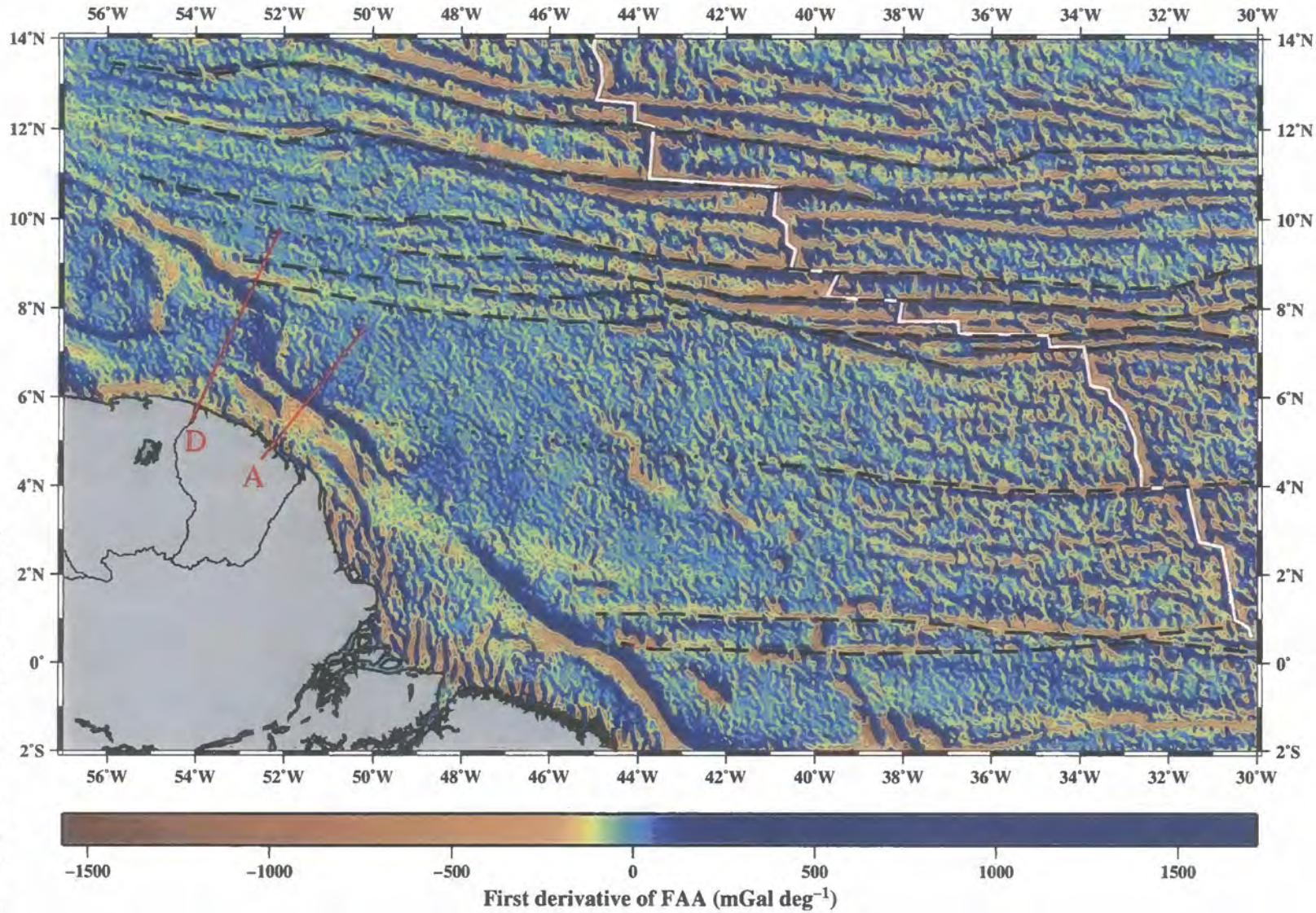


**Figure 5.12**: Lineations observed in the first derivative of the FAA. Calculation of the first derivative is an approach which highlights the MAR and lineations which run perpendicular to it. Distinct lineations (black dashed), the MAR (white) and ACE Profiles A and D (red) are shown. Two lineations which do not extend to the margin are extrapolated and shown (black dotted). Comparison with Figure 5.11 shows that this approach improves the clarity of lineations and trends within the data, from which to pick fracture zones across the entire Atlantic.

The chosen approach comprised picking the basement from the ACE and Guyaplac MCS data, colour-coding the picks according to TWTT and displaying them at their true geographic location (Figure 5.13). The figure also shows a tentative identification of the most distinct linear features across these profiles.

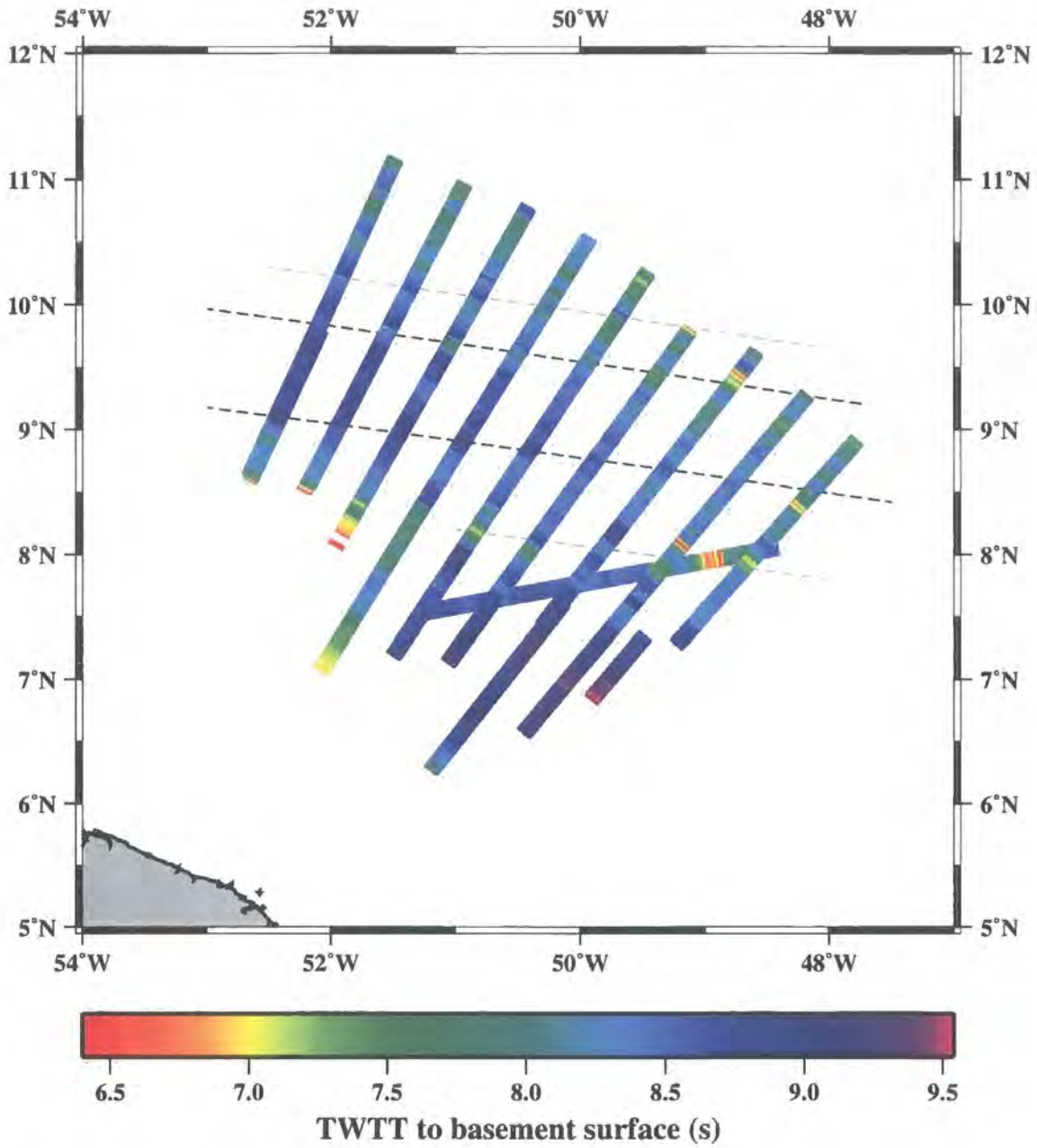


**Figure 5.13**: Along-margin variation in basement surface plotted as TWTT picks from both ACE and Guyaplac sections. Two distinct features are highlighted by the black dashed lines and two additional, less distinct, features are shown in grey. The trend of these features is approximately east-west.

#### 5.3.4.3 Magnetic field

In Section 4.5, the 2D magnetic modelling of both profiles was described. This modelling proved to be highly non-unique, although oceanward of the Profile A WA model a region of increased magnetization was observed. This region was suggested to result from a fracture zone in the oceanic crust. Consequently, the areal extent of certain fracture zones may be observed in the regional magnetic data.

Figure 5.14 shows the Guyaplac regional magnetic anomaly data and an interpretation of possible lineations within the data. A distinct low runs approximately east-west at ~8°N and correlates with the east-west trending features identified in basement and gravity data. Using this trend, three areas of positive anomaly can be identified between 8° and 10°N. These areas are displaced from one another by ~90-130 km in an east-west direction and, in conjunction with the 2D magnetic modelling, imply the presence of fracture zones.

#### 5.3.4.4 Summary of regional lineations

In this section, analysis of three independent datasets has been undertaken to map lineations within the western equatorial Atlantic. These lineations, identified from the basement surface, gravity FAA and magnetic anomaly, are summarised in Figure 5.15. This compilation shows that the lineations identified from the basement surface and the FAA are approximately coincident. Given that these are not associated with any rapid changes in the seafloor bathymetry, they most likely represent first-order fracture zones at which there is some vertical displacement in the basement surface.

The two lineations at ~8°N, identified from the regional magnetic anomaly, are coincident with the basement and FAA lineations, suggesting changes either in crustal magnetization or the depth to the magnetic anomaly source. Further north, the lineations do not coincide as well and are more closely spaced, which may indicate the presence of an additional fracture zone, not identified from the FAA or basement data. This interpretation may be possible if the fracture zone is not associated with any change in the topography of the basement and, hence, no lateral density variation.

Two interesting features highlighted by this analysis are the fracture zones which intercept Profile D at ~385 and ~440 km offset. The first of these corresponds to the location of the OCT in the WA model (Section 5.2.2), which indicates that the thinned continental crust along Profile D terminates at a fracture zone and, despite the wide zone of thinned crust, the margin here should be termed a transform margin. The second of these zones intersects the profile at the site of the large topographical change in the basement

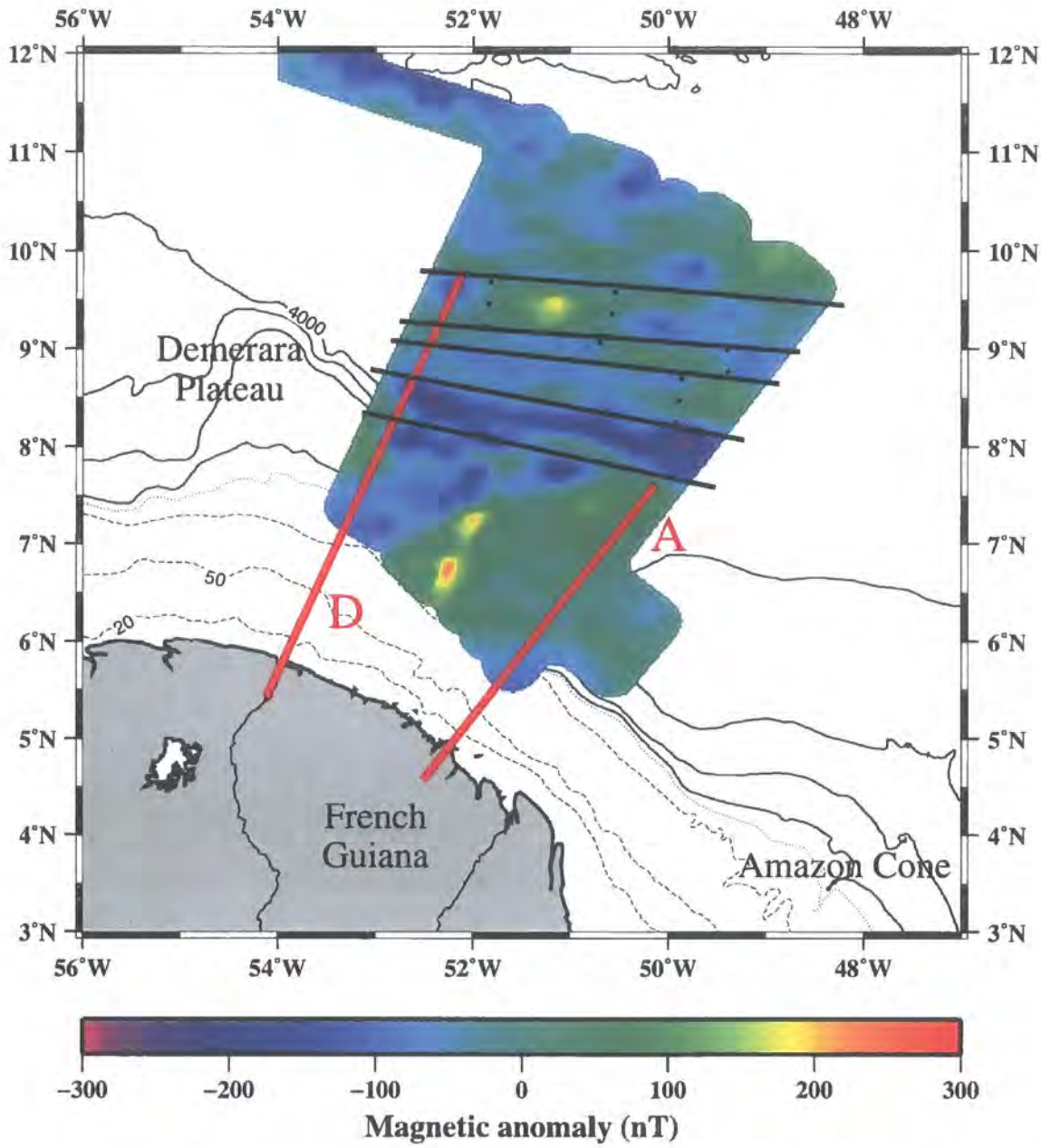


**Figure 5.14**: Interpretation of magnetic lineations within the regional magnetic anomaly. The Guyaplac magnetic anomaly (F. Klingelhöfer and W. Roest – *pers. comm.*, processed by IFP) shows a clear east-west trending low at ~8°N and a series of positive anomaly blocks between ~8° and 10°N. Lineations (solid black), block divisions (dotted black) and Profile A and D (red) are shown.

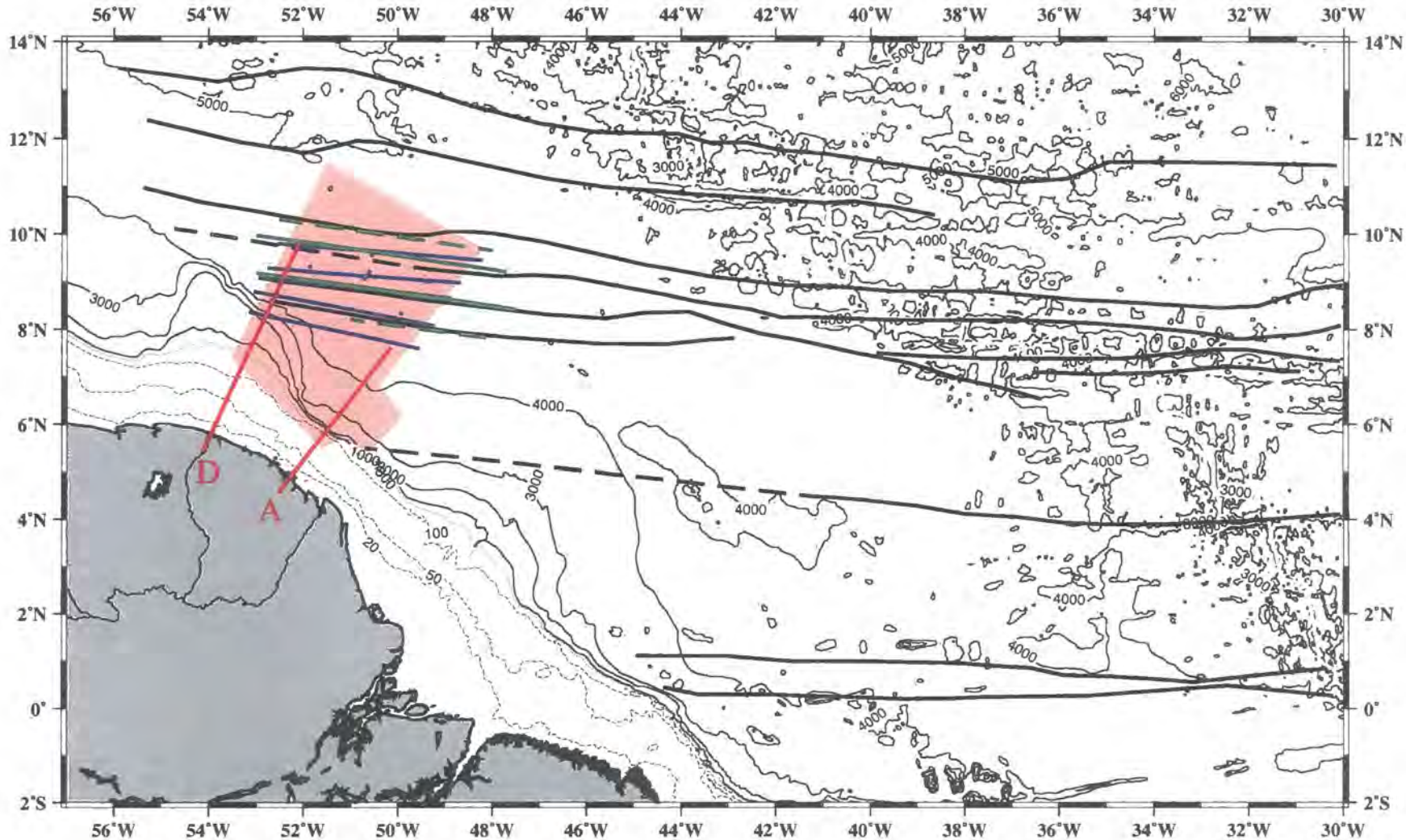


**Figure 5.15**: Compilation of interpreted lineations within the western equatorial Atlantic. Lineations identified from MCS basement picks (green – Figure 5.13), FAA (black – Figure 5.11) and magnetic anomaly (blue – Figure 5.14) are shown together with Profiles A and D (red). Bathymetric contours are shown, as in Figure 1.10, to illustrate the current seafloor topography.

surface identified in both the WA and MCS data. Two further fracture zones are interpreted to lie at ~530 and ~470 km offset.

No fracture zones are interpreted to cross Profile A, although one is extrapolated, from a gravity signature further oceanward, to intersect the margin at ~5.5°N, close to the continental slope on Profile A. The location of fracture zones in relation to the structural variation observed, along Profile D in particular, highlights their importance in the evolution of the French Guiana margin.

## 5.4 Summary

In this chapter, two *P*-wave velocity models of transects of the French Guiana continental margin have been presented. Constructed primarily from WA seismic data, these models are also consistent with MCS and gravity FAA data. Each model has been described in terms of its major structural components – pre-rift and thinned continental crust, oceanic crust, sediment column and, in the case of Profile A, a transition zone. The main similarities and differences between the two models have been highlighted and several observations of key features discussed. The rate and extent of continental thinning has been analysed to illustrate that the margin imaged by Profile A is comparable to very narrow rifted margins and by Profile D to those classified as 'wide'. In addition, the half spreading rate of the equatorial Atlantic has been calculated and used to explain observations of oceanic basement roughness. The results of the analysis suggest either that the half spreading rate is overestimated, or alternatively that the basement roughness is uncharacteristically high. Consequently, the pattern of local fracture zones were considered to explain the observations and were found to correlate particularly well with features modelled in the basement surface along Profile D. These observations will be further discussed in the context of overall structure and evolution of the margin in Chapter 6.

# Chapter 6

# Discussion and implications

## 6.1 Introduction

This thesis contains a discussion of the processing, modelling and interpretation of MCS reflection and WA seismic refraction, gravity and magnetic data acquired offshore Brazil and French Guiana as part of the ACE. In the previous chapter's the creation, testing and interpretation of two deep crustal models has been described. In this chapter their contribution to our understanding not only of the mode of margin evolution but also the opening of the equatorial Atlantic will be discussed.

One of the key aims of this study has been to improve our understanding of structural variation along-strike continental margins. In order to develop such an understanding, this chapter will contain a discussion of the modelling results from the French Guiana and northeast Brazil margins, primarily within a regional context. The results will also be used to construct a model of the geometry and mode of opening of the region, which will be accompanied by a discussion of: the role of magmatism (Section 6.2); the thickness of oceanic crust (Section 6.3); rifting versus transform margins and their segmentation along-strike (Sections 6.4 and 6.5); the role of sedimentation (Section 6.6) and, finally, the evolution of the equatorial Atlantic (Section 6.7).

## 6.2 The role of magmatism

Deep crustal seismic studies have identified several structural styles at geographically distinct passive margins formed as a result of continental rifting. For example, significant structural differences are observed as a result of variations in the role of magmatism at a margin. Whilst rifting can often be thought of in terms of simple amagmatic stretching followed by thermal subsidence (McKenzie, 1978; Sleep, 1971), it often occurs in conjunction with the accretion of massive thicknesses of igneous material into the crust (Mutter

*et al.*, 1984; White *et al.*, 1987; Holbrook *et al.*, 1994a; Eldholm *et al.*, 1995). As a result, passive margins have traditionally been divided into two contrasting types – volcanic and non-volcanic.

Volcanic margins are characterised by the presence of thick (up to 25 km) lower crustal bodies (White & McKenzie, 1989; White *et al.*, 1987), which are often observed to have high *P*-wave velocities of 7.2-7.7 $kms^{-1}$ and are termed underplating. These bodies of underplating have been observed, for example, in seismic refraction data at several of the plume-influenced margins surrounding the North Atlantic (Fowler & McKenzie, 1989; White, 1992; Breivik *et al.*, 2006) and are thought to reflect mafic to ultra-mafic magma, generated deep in the mantle, which has become trapped near the Moho. In addition, an associated series of SDR sequences, identified as extrusive basalts, are commonly observed in MCS data (Hinz, 1981; Mutter *et al.*, 1984).

In contrast, the extensional fabric of non-volcanic margins has not been affected by significant volcanism and, hence, lacks these features. Instead, fault-bounded basement blocks (*e.g.* Goban Spur – Peddy *et al.*, 1989) and/or low-angle detachment faults (*e.g.* West Iberia – Hoffman & Reston, 1992; Krawczyk & Reston, 1995; Galicia Bank – Krawczyk *et al.*, 1996) are often observed. Furthermore, a transition zone often separates thinned continental and oceanic crust (Dean *et al.*, 2000) at these margins.

However, volcanic and non-volcanic margins are merely the end-members of a continuum of marginal styles, resulting from varying degrees of magmatism. Consequently, margins are likely to express a range of volcanic characteristics (Geoffroy, 2005; Eldholm *et al.*, 1995). This variation is primarily due to differences in mantle temperature, rate and duration of extension and the initial lithospheric thickness (Bown & White, 1995).

Interpretation of the ACE MCS data shows no evidence for SDRs. However, this is not always a clear indicator of volcanism as extrusive sequences are not always expressed by seismic reflections (Geoffroy, 2005; Eldholm *et al.*, 1995; Planke & Eldholm, 1994; Planke *et al.*, 2000). Furthermore, neither WA model shows any significant deep crustal high velocity zone. A relatively narrow zone of thinned continental crust is observed along Profile A, with a maximum velocity of 6.9 $kms^{-1}$. Also, despite a much broader region of thinning, Profile D shows no evidence for such high velocities. In addition, studies to the south (Rodger *et al.*, 2006; Rodger, 2007) have not shown any evidence for magmatism, although the majority of the data used for this study were located oceanward of the margin.

As a consequence, the continental margin in the vicinity of ACE Profiles A and D, offshore French Guiana is interpreted as non-volcanic. Furthermore, given the absence of evidence to the contrary, a wider region of the margin is tentatively interpreted to be non-

volcanic, from the northern limit of French Guiana territorial waters to the Amazon Cone in the south, from ~3° to 8°N.

This interpretation is consistent with studies of the conjugate West African margin, for example: offshore Congo, Zaïre and Angola – Contrucci *et al.* (2004); Côte d'Ivoire – Edwards *et al.* (1997); Cameroon-Guinea-Gabon – Wilson *et al.* (2003). A number of these non-volcanic margins have also been identified in the North Atlantic, including: the Northern Bay of Biscay – Thinon *et al.* (2001); the Iberia Abyssal Plain – Dean *et al.* (2000); the Galicia Bank and Goban Spur – Whitmarsh *et al.* (1996); Horsefield *et al.* (1994); Bullock & Minshull (2005); the Orphan Basin – Chian *et al.* (2001); the Greenland and Labrador margins – Chian & Louden (1994); Chian *et al.* (1995); and the Newfoundland margin – Reid (1994). However, the margin offshore French Guiana is somewhat unique in comparison to these examples, given the complex rifting and post-rift geometry which have resulted in a dense cluster of fracture zones, as discussed in Section 5.3.4.4.

The classification of this margin as non-volcanic has great significance for our understanding of the nature of the lithosphere and properties of rifting in this region. The observation that little or no volcanism accompanied the rift process suggests that there was no significant melting of the deep mantle. This has several implications: the rifting event was not plume-related, *i.e.* there was no deep asthenospheric heat source causing excessive amounts of melting, as is observed at some North Atlantic margins (*e.g.* Møre – Breivik *et al.*, 2006); that rifting occurred over a relatively long time period, resulting in the gradual dissipation of heat from the system and the creation of only small volumes of melt; or, alternatively, the lithosphere was unusually cold both before and during rifting which minimised melt production. The latter two implications may be developed by analysing the models further.

Crustal thinning factor, $\beta$, has been modelled to relate directly to the rift duration, for example Bown & White (1995) use a rifting model to estimate the melt production at a rifted margin for a range of rift durations and $\beta$ factors. The resulting relationship is shown in Figure 6.1 and indicates that a combination of high $\beta$ factor and short rift duration causes the production of excess melt and, hence, results in volcanism at a margin. Conversely, long rift durations in conjunction with small $\beta$ factors result in non-volcanic margins. Given that the French Guiana margin has been identified as non-volcanic the melt thickness may be assumed to be ~0 km. Thus, a $\beta$ factor of 6.4 for Profile A suggests a rift duration of at least 18 Ma. This is consistent with estimates of rift duration of 15-30 Ma at the approximately conjugate non-volcanic margin offshore Angola (Moulin, 2003).

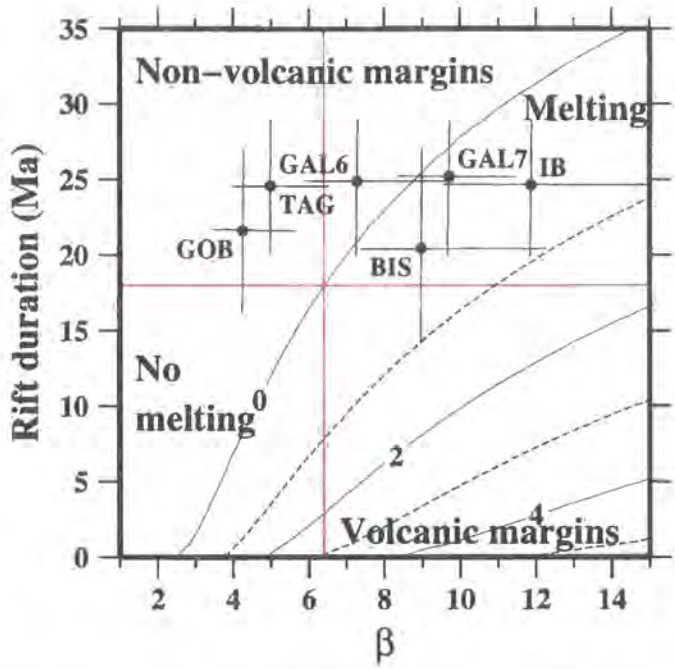


**Figure 6.1**: Variation in melt thickness relative to crustal thinning factor, $\beta$, after Bown & White (1995). ACE Profile A is marked in red and, assuming a total melt thickness of ~0 km and a $\beta$ of ~6.4, suggests a rift duration of ~18 Ma. Other non-volcanic margins are shown for comparison: GOB = Goban Spur line 3 (Horsefield *et al.*, 1994); TAG = Tagus line AR (Pinheiro *et al.*, 1992); GAL6, GAL7 = Galicia lines 6 and 7 (Whitmarsh & Miles, 1995); BIS = Biscay line 2 (Montadert *et al.*, 1979); and IB = average of Iberia lines 1 and 2 (Whitmarsh *et al.*, 1990). See Bown & White (1995) for further details.

However, the interpretation of only a narrow zone of thinned continental crust suggests that Profile A is not a typical rifted margin, and as such this estimate for rift duration is only made tentatively.

Pre-rift lithospheric temperature at the French Guiana margin is difficult to estimate and this study has acquired no direct measurements of this. However, the French Guiana margin borders the Guiana Shield, which represents the northern segment of the Amazonian Craton (Voicu *et al.*, 2001). Prior to rifting this craton was joined to the West African Craton, both of which are Archean age (Figure 6.2 – Artemieva & Mooney, 2001). The thermal thickness of these and other Precambrian cratons was modelled in a study by Artemieva & Mooney (2001) to calculate temperature distribution. Their modelling is based on heat flow data (*e.g.* Pollack *et al.*, 1993) from around the world, which unfortunately tend to be concentrated around Europe and North America. No data are used from around the French Guiana margin. However, around 16 measurements are incorporated from West Africa, at the conjugate margin. Despite this sparsity of data, Artemieva & Mooney (2001) have calculated the temperature distribution shown in Figure 6.2.

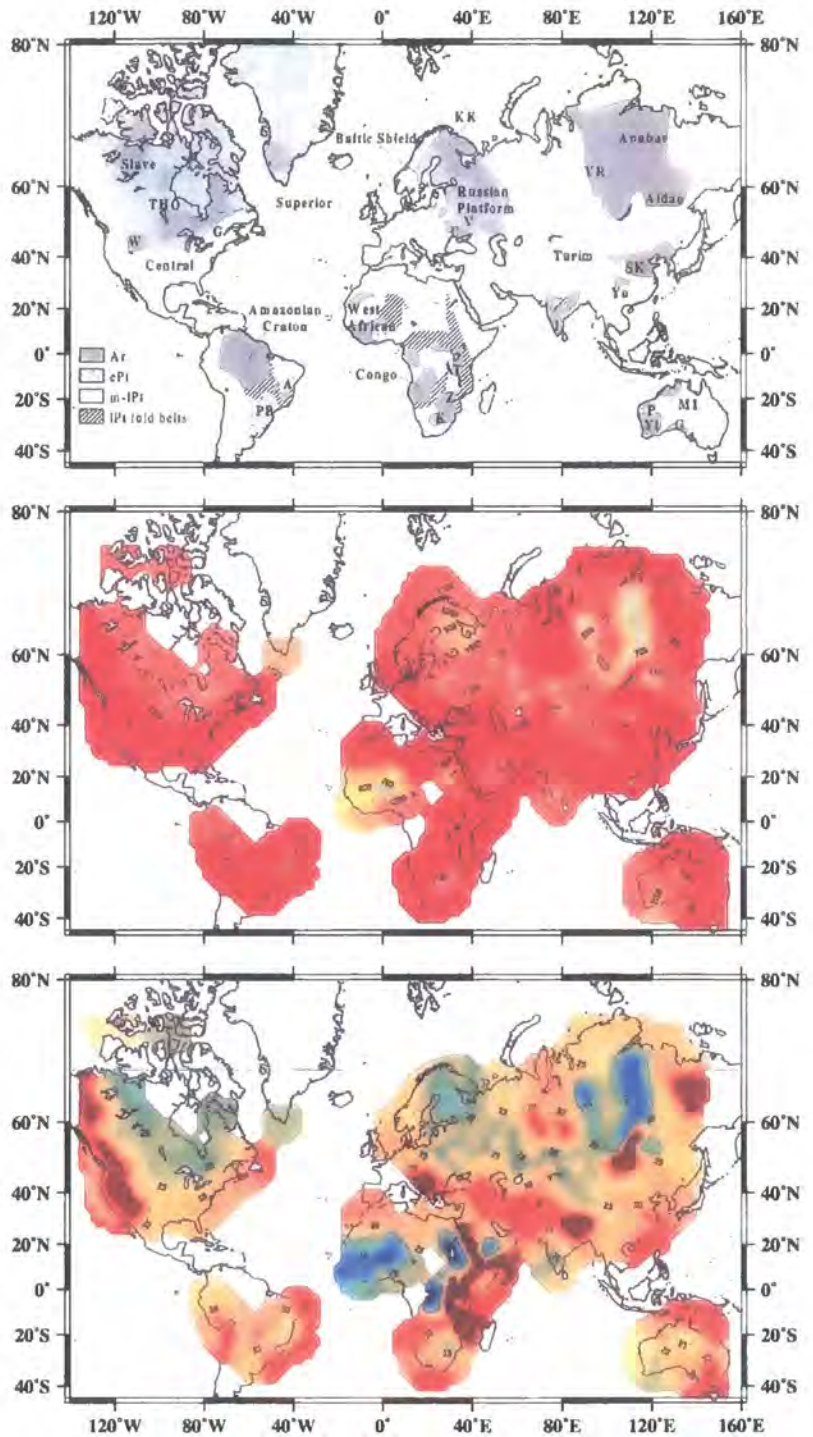


**Figure 6.2**: Global craton, lithospheric temperature and sub-lithospheric mantle heat flow distribution, after Figure 2 and Plates 1 and 4 of Artemieva & Mooney (2001). (Top) French Guiana is underlain by the Archean age Amazonian Craton, which, prior to equatorial Atlantic rifting, was joined to the West African Craton. (Middle) Estimated lithospheric temperatures at 50 km depth are shown (red – relatively hot; yellow – relatively cold). No data is available for French Guiana, although relatively cold (~400°C) lithosphere is observed around the conjugate margin of West Africa, a potential explanation for the observation of non-volcanic rifting. (Bottom) Modelled sub-lithospheric mantle heat flow beneath the West African Craton is relatively low (relatively high – red; relatively low – blue). Given that the West African and Amazonian Cratons were joined prior to the rifting of the Atlantic, it is likely that, in addition to the lithosphere, the asthenosphere at the French Guiana margin is relatively cold (see text). This low asthenospheric temperature is a potential explanation for the observation of unusually thin oceanic crust in the region.

This figure indicates that global lithospheric temperature lows are observed around the White Sea in northeast Russia, the Central Siberian Plateau in central Russia and in West Africa in the region conjugate to French Guiana. The temperature low in this region persists into the mantle to depths in excess of 150 km (Artemieva & Mooney, 2001) and is largely centred around the West African Craton, which implies that at the time of rifting and subsequently, the lithosphere at the French Guiana margin has been relatively cold, consistent with the observations that this is a non-volcanic margin.

Thus, the margins non-volcanic origins would appear to result from rifting of cold lithosphere over a time period which was neither remarkably fast nor slow. Both of these factors tend to result in non-volcanic margins.

In developing an understanding of the nature of the lithosphere at the French Guiana margin, the underlying asthenosphere has been suggested to be unrelated to any plume event, but has otherwise been neglected. However, the oceanic crust adjacent to the margin may offer insight into this deeper structure associated with the post-rift accretion of oceanic lithosphere.

## 6.3 Oceanic crustal thickness

Beneath the Earth's oceans, the structure of oceanic crust is remarkably uniform in terms of its bulk composition, rare earth element concentrations and thickness, which is, on average, 7.1 $\pm$ 0.8 km thick (White *et al.*, 1992). However, as shown in Figure 6.3, the oceanic crust identified offshore French Guiana and northeast Brazil is anomalously thin when compared with this average. Whilst Profiles A and D show slightly thicker crust adjacent to the margin, $\sim$60 km oceanward the crust is consistently thin at between 3 and 4 km. Furthermore, this feature appears to be quite widespread in the region, as the oceanic crust is also thin (4-5 km) to the south across the whole of Profile F and the landward portion of Profile B (Rodger *et al.*, 2006; Rodger, 2007). At the oceanward end of Profile B the crust increases to $\sim$10 km thick, which Rodger *et al.* (2006) interpret to be related to the nearby Ceara Rise. The thickness of the crust oceanward of the Ceara Rise is unknown and, hence, this feature may or may not represent the onset of 'normal' thickness crustal accretion.

To understand the significance of this regional feature it is important to assess how unusual it is in the wider context of global crustal structure. For example, there exist several exceptions for which thickness is notably different from the average. These include unusually thick crust accreted near hotspots and anomalously thin crust near fracture zones

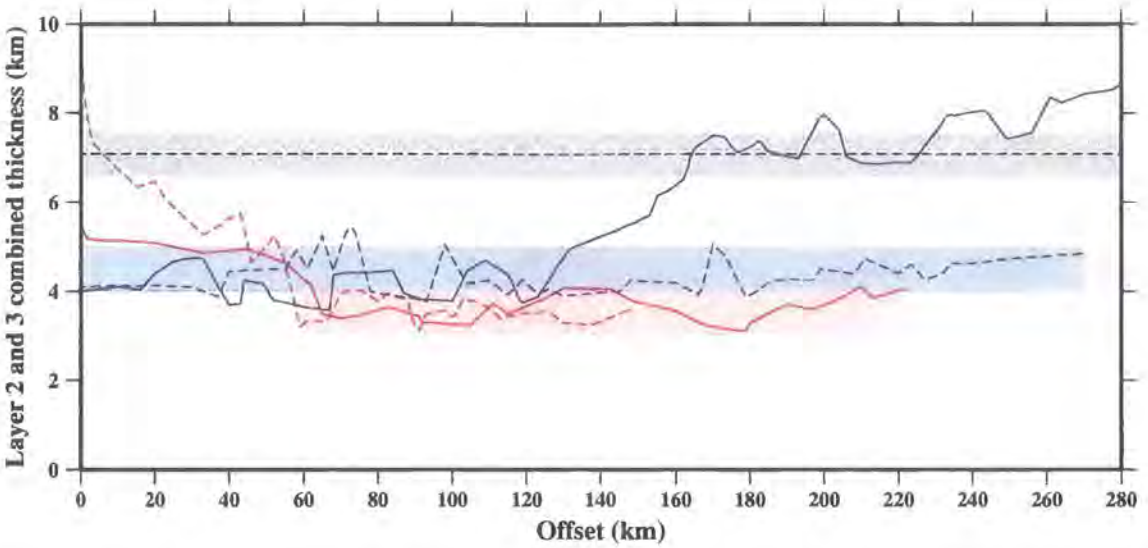


**Figure 6.3**: Oceanic crustal thickness offshore French Guiana and northeast Brazil. The combined thickness of oceanic Layers 2 and 3 is shown for Profiles A (solid red line), D (dashed red), B (solid blue) and F (dashed blue). Profiles A and D are plotted from the oceanward limit of the thinned continental crust shown in Figures 5.1 and 5.3. The full extent of Profiles B and F, shown in Figure 2.1, is plotted. In general, the oceanic crust along Profiles A and D is 3-4 km thick (shaded red) and along Profiles B and F (Rodger *et al.*, 2006; Rodger, *in prep.*) is 4-5 km thick (shaded blue), with the exception of the landward ~60 km of Profiles A and D and the oceanward end of Profile B which are all thicker than this. Compared with the Atlantic average of 7.1±0.8 km (black dashed line and grey shading – White *et al.*, 1992), each of the ACE profiles exhibits unusually thin crust.

(Bown & White, 1994; White, 1984; White *et al.*, 1984; Minshull *et al.*, 1991; White, 1992; White *et al.*, 1992). In addition, the crust adjacent to some non-volcanic rifted margins has also been observed to be uncharacteristically thin. For example, Hopper *et al.* (2004) interpret thin oceanic crust offshore Newfoundland as having accreted in a magma-limited setting in which mantle was eventually exhumed. Whilst the North Atlantic is presently slow-spreading, they conclude that the thin crust formed as a result of ultra-slow spreading. The same explanation has previously been invoked to explain the thin crust observed at ACE Profile B (Rodger *et al.*, 2006).

Compilations of observations of oceanic crustal thickness (*e.g.* Bown & White, 1994) indicate that there exists a relationship between crustal thickness and spreading rate, in which ultra-slow spreading gives rise to thin crust, while faster spreading rates produce thicker, more 'normal' crust. The primary reason for this is that during normal spreading, melt is generated from the ascent and associated decompression melting of deep asthenospheric mantle material which is subsequently accreted as oceanic crust. However, during ultra-slow spreading the material rises less quickly and, consequently, there is a greater

amount of time available for conductive cooling and, hence, less melt is generated. Thus, the resulting oceanic crust is significantly thinner.

Figure 6.4 summarises empirical models of the relationship between spreading rate and crustal thickness (after Reid & Jackson, 1981; Bown & White, 1994; Su *et al.*, 1994). In Section 5.3.2, an estimate of 20 mmyr$^{-1}$ was made for the half spreading rate at the French Guiana margin, using the seafloor age grid of Müller *et al.* (1997). At this rate the relationships of Reid & Jackson (1981), Bown & White (1994) and Su *et al.* (1994) all predict a crust of ~6-7 km thickness, slightly thinner than the Atlantic average. However, the oceanic crust offshore French Guiana is observed to be significantly thinner than this estimate. If the crustal thickness at the French Guiana margin were compatible with these relationships then they would predict a half spreading rate of 0-10 mmyr$^{-1}$.

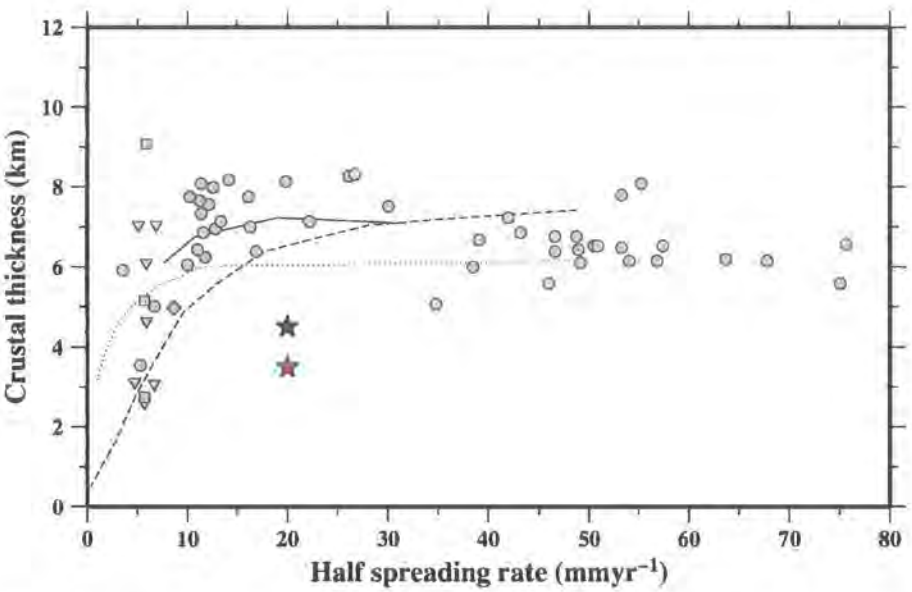


**Figure 6.4**: Various empirical models of the relationship between crustal thickness and half spreading rate (after Weigelt & Jokat, 2001). Three relationships are shown: Bown & White (1994) – dotted; Reid & Jackson (1981) – dashed; and Su *et al.* (1994) – solid. Grey circles indicate data from these studies. Grey triangles are values for the Gakkel Ridge from studies by Jackson *et al.* (1982), Kristoffersen *et al.* (1982), Duckworth & Baggeroer (1985), and Duckworth *et al.* (1982). Grey squares are from the study of the Eurasian Basin, Arctic Ocean by Weigelt & Jokat (2001) and the grey diamond from a study of the Southwest Indian Ridge (Muller *et al.*, 1995). ACE Profiles A and D (red star) and B and F (blue star) are shown for comparison and suggest unusually thin crust.

As discussed in Section 5.3.2, within the Cretaceous magnetic quiet zone of the equatorial Atlantic adjacent to the French Guiana margin, data used to create the seafloor age grid are sparse. This limitation is reflected in the large age errors (Figure 5.7) in this region. Hence, it seems feasible that the half spreading rate of 20 mmyr$^{-1}$ estimated from this grid may not be accurate. Indeed, Rodger *et al.* (2006) attribute the thin oceanic crust

observed along ACE Profile B to ultra-slow spreading (half spreading rate <10 $mmyr^{-1}$ – Bown & White, 1994). Such an interpretation is consistent with the calculations of basement roughness (Section 5.3.3) which, given the relationship suggested by Malinverno (1991), imply a spreading rate as low as 5 $mmyr^{-1}$. However, as noted in Section 5.3.3 and evidenced in Section 5.3.4, there are a significant number of fracture zones in the region, which may increase the observed roughness and limit the accuracy of this approach. Hence, 5 $mmyr^{-1}$ may be an underestimate of the true half spreading rate. Furthermore, studies by Cogné & Humler (2004, 2006) do not observe ultra-slow spreading rates during this time period in either the North or South Atlantic. These studies are based on the same seafloor age grid as this study, although in general the Atlantic margins which dominate the analysis are not limited by having rifted during the Cretaceous quiet zone. Hence, it seems unlikely that ultra-slow spreading is the major cause of the thin oceanic crust.

Crust of 4.4 km thickness has also been observed at the approximately conjugate margin offshore Côte d'Ivoire-Ghana (Edwards *et al.*, 1997). In addition to ultra-slow spreading MORs, discussed above, Edwards *et al.* (1997) note that thin oceanic crust is found in two further settings:

- Adjacent to non-volcanic rifted margins; and
- At oceanic transform/fault zones.

Examples of the first of these possibilities exist around the Atlantic, including Iberia – Whitmarsh *et al.* (1990, 1993), Pinheiro *et al.* (1992), and Goban Spur – Horsefield *et al.* (1994). Here, long-lasting stretching of the continental lithosphere prior to break-up results in conductive heat loss in the mantle and, hence, a lower volume of melt generated (Whitmarsh *et al.*, 1993; Bown & White, 1995). Bown & White (1995) use the $\beta$ versus rift duration relationship to attribute the 15 km of thin oceanic crust adjacent to the OCT at the Galicia Bank margin to conductive cooling of the upwelling mantle during continental stretching. Further oceanward of the Galicia Bank margin normal thickness crust is observed, suggesting that this effect is localised to a relatively narrow zone adjacent to the OCT, *i.e.* the 'zone of influence' of the margin itself. If this is the case then the observation of thin crust for more than 100 km from the French Guiana margin indicates that this explanation is unlikely regardless of the rift duration.

However, Minshull *et al.* (2001) conclude, from a study of the West Iberia margin, that the model of Bown & White (1995) over-estimates the melt volume for non-volcanic margins. Instead, they propose that melt generation remains limited after break-up and during the formation of the transition zone, and increases when the thermal lithospheric

flow becomes focused as a steady-state spreading ridge system evolves. As a result, thin oceanic crust may be produced at much greater distances from the margin. However, it is still unlikely that the areal extent of the thin crust far from the French Guiana margin may be explained by this mechanism. Furthermore, the WA models suggest the converse is true, *i.e.* the crust immediately adjacent to the OCT is slightly thicker than that further oceanward (Figure 6.3). Consequently, the rift duration at the French Guiana margin is not considered to be the cause of the unusually thin crust and is likely to have occurred over at least 18 Ma.

The second suggestion is that the thin oceanic crust is a consequence of oceanic transform faults/fracture zones, which White *et al.* (1984, 1992) and Minshull *et al.* (1991) attribute to a reduced magma budget at the ends of ridge segments adjacent to the fracture zone. However, Stroup & Fox (1981) and Fox & Gallo (1984) attribute the crustal thickness to a thermal edge effect resulting from the juxtaposition of the MOR against relatively cold oceanic lithosphere, particularly where offsets are large. The large number of fracture zones identified to the north of the ACE study area (Section 5.3.4.4) indicates that such an interpretation is feasible, even likely. Consequently, Greenroyd *et al.* (*in press*) suggest this hypothesis as an explanation for the thin crust observed along ACE Profile A.

In the south, in the area surrounding Profiles A, B and F, fewer fracture zones are observed than around Profile D. Therefore, it would be logical for thicker crust to be observed here. This is indeed the case (Figure 6.3) and Profiles B and F (Rodger *et al.*, 2006; Rodger, 2007) exhibit oceanic crust which is ~1 km thicker than in the north, slightly greater than the ~600 m resolution of the seismic data modelling. However, the crust is still only 4-5 km thick and, hence, the effect of the fracture zones appears to be a contributing factor, but not the sole cause of the thin crust.

At this stage, three commonly used explanations for observations of thin oceanic crust have all been, at least partially, discounted. Ultra-slow spreading is unlikely given estimates of seafloor age; slow rifting is unlikely given the extent of the thin crust away from the margin; and fracture zones contribute but don't sufficiently account for the large areal extent of the thin crust. The mechanism resulting in the creation of thin oceanic crust by each of these hypotheses is very similar and can be summarised as a reduction in melt generation due to excessive heat loss, the first two due to slow upwelling of the mantle and the third due to juxtaposition of hot and cold lithosphere. Therefore, a fourth explanation may be more appropriate. Rather than invoking excess heat loss to explain the reduced melt generation, maybe the heat was never available to be lost, *i.e.* the asthenosphere in the equatorial Atlantic is simply colder than elsewhere.

Artemieva & Mooney (2001), in addition to estimating the temperature of Precambrian lithosphere described in Section 6.2, model the heat flow within the crust, lithosphere and sub-lithospheric mantle. They estimate that the heat flow (Figure 6.2) around the West African Craton is just 15 $mWm^{-2}$, which is one of the three lowest heat flows observed world-wide. In conjunction with the relatively cold lithosphere above, the low heat flow between asthenosphere and lithosphere most likely implies that there is a relatively small temperature gradient at this boundary and, hence, the asthenosphere is also unusually cold. A potential consequence of cold asthenosphere is low melt generation at the MAR and, hence, the accretion of thin oceanic crust as observed along the ACE profiles.

The existence of a relatively cold asthenosphere in the equatorial Atlantic is also suggested by Bonatti (1996). Within the equatorial Atlantic, Bonatti (1996) observes a maximum in mantle shear wave seismic velocity, a minimum in zero-age topography and a minimum in degree of melting, as evidenced by geochemical analysis of MAR basalts and peridotites. These observations are explained by the existence of a thermal minimum which has probably been present since prior to break-up. As a result of this thermal minimum, Bonatti (1996) suggest that the pre-rift continental lithosphere will be cold and thick and that little mantle melting will occur during rifting and subsequent oceanic crustal accretion. Each of these effects is consistent with the findings of this study of the French Guiana margin.

## 6.4 Rifting versus transform motion

The pre-rift crust imaged along Profiles A and D is 35-37.5 km thick and is comparable with several other locations around the Atlantic. For example, rifted margins offshore Nova Scotia (Funck *et al.*, 2004) – ~36 km; Orphan Basin (Chian *et al.*, 2001) – ~36 km; US East Coast (Holbrook & Keleman, 1993; LASE Study Group, 1986; Sheridan *et al.*, 1993; Tréhu *et al.*, 1989; Holbrook *et al.*, 1994a,b) – 36-41 km; and the transform margin offshore Ghana (Edwards *et al.*, 1997) – 35 km. However, there also exist several examples of significantly thinner crust, *e.g.* Goban Spur (Horsefield *et al.*, 1994) – ~27 km; and Iberia (Dean *et al.*, 2000) – ~27 km. Thus, the continental crust at the French Guiana margin is of a thickness typical of other Atlantic margins, although these may show considerable variation.

Although the pre-rift continental crustal thickness is observed to be relatively consistent along the French Guiana margin, the degree of thinning is not. Profile A shows a relatively narrow, high $\beta$ factor zone of thinning whereas Profile D shows a wide zone of

thinning, including an abrupt thinning at the oceanward termination of the zone of thinned continental crust. These two structural styles are very distinct from one another and will be discussed separately and then together.

The WA model for Profile A shows continental crust which thins by a factor of ~6.4 over ~70 km distance. Section 5.3.1 (Figure 5.5) contained a discussion of these values and concluded that this is a very narrow zone of thinning when compared with other rifted margins. Although the comparison used in Section 5.3.1 was limited to the wide and narrow rifts of Watts & Fairhead (1997), this conclusion applies when comparison is made with other studies. For example, Dean *et al.* (2000) find that the typical width over which continental thinning occurs is between 80 and 150 km. Dean *et al.* (2000) also incorporate measurements of the transition zone, which is found to be 10 to 120 km wide, to yield a total margin width of 100-200 km. The transition zone along Profile A is at most 45 km wide. Thus, even if the largest possible transition zone is assumed, the width of the margin along Profile A is 115 km and at the narrow end of this range.

Furthermore, rifted margins are often characterised by large fault blocks or low-angle normal faults through the brittle upper crust. There is no evidence for such blocks or faulting along Profile A. The MCS data suggest flat lying sediments landward of the continental slope, although their thickness is difficult to gauge, as the reflections are generally contaminated by seafloor multiples in this shallow water region. The absence of fault blocks and the observation of a narrow zone of thinning suggests that the margin may not be a rifted margin at all. Instead, interpretation as a transform margin may be more appropriate.

Transform margins (*e.g.* Scrutton, 1979; Newfoundland – Todd *et al.*, 1988; Barents Sea – Jackson *et al.*, 1990; Exmouth Plateau – Lorenzo *et al.*, 1991) are generally characterised by thinning over a distance of 5-30 km, much shorter than rifted margins. For example Edwards *et al.* (1997), in a study of the Ghana margin, observe continental thinning over a distance of ~15 km. In addition, transform margins tend not to be accompanied by either high lower crustal velocities, normally indicative of magmatism, or basement rotated fault blocks, indicative of rifting. Whilst the Profile A model is consistent with these latter two characteristics, it thins over a wider zone than would be expected for a normal transform margin.

Given that Profile A exhibits aspects of both rifted and transform margins, the evidence is inconclusive for either rifted or transform motion alone. Consequently, other possibilities are suggested. Firstly, is it possible that the margin is a transform margin which displays a narrow zone of thinned continental crust and that Profile A has crossed the margin oblique

to the direction of the transform motion? As a result, a relatively wide zone of thinned crust would be observed along Profile A. The angle between the profile and local fracture zones, located from basement, gravity and magnetic data in Section 5.3.4, is ~30°. Thus, trigonometrically, the perpendicular width of the zone of thinning is $70 \times \cos 30 = 61$ km. So, whether or not an obliquity correction is required, the margin is not typically transform in style.

Secondly, an alternative structural explanation may be required, for example the South American and West African plates may have separated in a direction which is not quite perpendicular to the MAR. As a result, along the equatorial Atlantic margin, rifted margins may have formed with an element of shear motion, and transform margins with a degree of rift motion perpendicular to the strike of the transform, termed oblique rifts and 'leaky' transforms respectively. Profile A is interpreted as a 'leaky' transform, which explains the relatively narrow zone of thinned continental crust and the absence of fault blocks. This interpretation suggests that, whilst the majority of passive margins may be classified as either rift or transform margins, structures in between these two end members may also exist. Thus, the structure of the French Guiana margin adjacent to the Profile A transect may represent an intermediate structural style which lies in between the rift and transform end members. Alone, however, the results from Profile A do not suggest that passive margins may develop along a continuum of styles ranging from rift to transform, merely that the potential range of structures may be slightly broader than previously thought.

The WA model for Profile D shows a much wider zone of thinning than Profile D. This zone is comparable to many rifted margins (Figure 5.5) and at first glance the profile lies across a non-volcanic rifted margin. However, topographic variation of the oceanic basement surface oceanward of the OCT prompted a further investigation of local fracture zones (Section 5.3.4). This analysis has highlighted several fracture zones which cross the equatorial Atlantic, including one which intersects the margin at approximately the same location as the interpreted OCT location. The location of this intersection suggests that, whilst a significant proportion of the crust observed along Profile D is thinned continental in nature, the actual OCT is a transform fault. Given the general east-west trend of the fracture zones, the thinned continental crust is interpreted as having extended in an east-west direction. Hence, Profile D actually cuts across the thinned continental crust in a direction roughly perpendicular to the rift direction. This interpretation also explains the apparent absence of faulted blocks, which are typically observed at rifted margins when surveyed along the rift direction. Such rift blocks are observed along the eastern flank of the Demerara Plateau (Gouyet *et al.*, 1994), again supporting the interpretation.

Above the toe of the Demerara Plateau, at the oceanward end of the thinned continental crust along Profile D (Figure 5.3), the MCS data show two small sedimentary basins (360-380 km offset) separated by an upward protrusion of the basement surface (~370 km). In addition, immediately adjacent to the OCT is a second, larger rise in the basement (~380 km). These features are not interpreted as faulted blocks given their large topography and relative sharpness. Furthermore, their MCS basement surface reflection is unlike the continental basement further landward and is similar in style to the oceanic-style basement, although the sharp increase in depth to basement further oceanward indicates that this is not oceanic crust. Two hypotheses are suggested for these features.

Firstly, they are volcanic extrusions possibly formed as a result of magmatic material rising to the surface along the previously identified fracture zone. The volcanism may also be associated with perpendicular motion of the plates either side of the transform fault, *i.e.* 'leakiness' along the fault.

Secondly, the features are marginal highs associated with the formation of the transform zone. The highs may result from either thermal effects and/or density changes associated with serpentinization. The juxtaposition of relatively hot oceanic crust and cold continental crust at a margin results in heat flow across the margin. As a result of the thermal contrast, thermal expansion occurs on the continental side and thermal contraction on the oceanic side of the margin. Consequently, the continental side undergoes uplift, creating a marginal high, or ridge (Gadd & Scrutton, 1997). Alternatively, serpentinization of crustal material at the OCT could reduce the density of the crust, also resulting in uplift. Given the close fit of the calculated and observed gravity FAA, modelled without such a density reduction, it seems unlikely that such a large ridge may result solely from serpentinization and thus the thermal effects may play the dominant role in formation of the marginal high.

Marginal highs have been observed at the Newfoundland (Todd *et al.*, 1988) and the Côte d'Ivoire-Ghana margin (Basile *et al.*, 1993, 1998). The latter of these locations is approximately conjugate to the French Guiana margin and Figure 6.5 contains a comparison with the French Guiana ridge. The ridges are similar in both appearance and extent and, consequently, the preferred interpretation of the feature is as a marginal ridge which, given the relatively large topography of the ridge, suggests that the MAR may have passed adjacent to the edge of the Demerara Plateau during early seafloor spreading, maximising the thermal gradient.

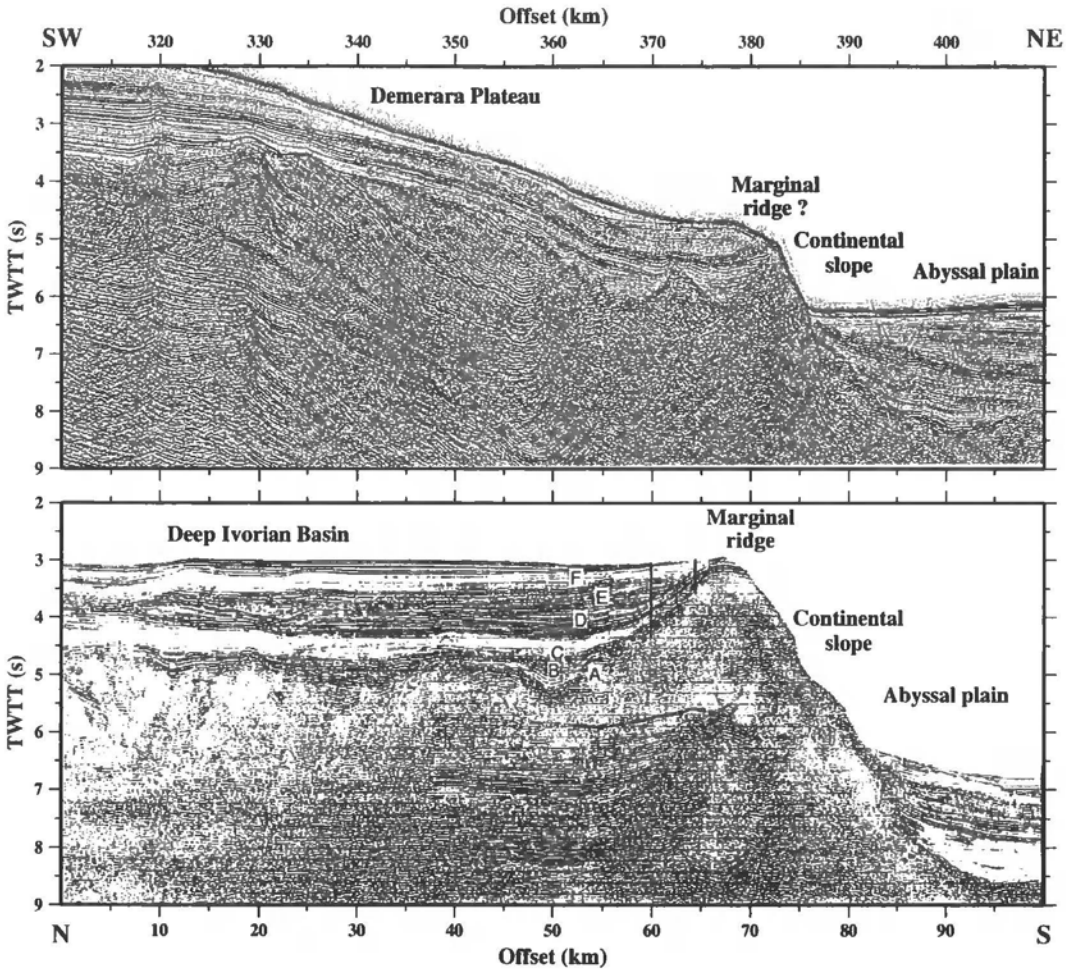


**Figure 6.5**: Comparison of marginal ridges either side of the equatorial Atlantic. (Bottom) A MCS section of the marginal ridge observed at approximately 3.5°N 2.5°W along the Côte d'Ivoire-Ghana ridge (Basile *et al.*, 1998). (Top) A similar section of a marginal ridge observed landward of the OCT along Profile D. Both sections are plotted at the same scale. The ridges are broadly similar in both lateral and vertical extent and may have been formed by the same thermal mechanism (see text).

## 6.5 Segmentation of the margin

Chapter 5 has contained a description of the deep structure of the two ACE profiles and in Section 6.4 the margin was classified as a 'leaky' transform at Profile A and as a transform at Profile D. However, Profile D also crosses a wide zone of thinned continental crust resulting from an adjacent rifted segment of the margin. Using these interpretations structure and segmentation along the margin may be inferred.

Structural segmentation is observed at continental margins, active spreading centres and in the oceanic crustal fabric in between (Behn & Lin, 2000). At spreading ridges, first-

order discontinuities are manifest as transform faults offsetting ridge segments by 50 km or more. Second-order discontinuities are observed as smaller offset (2-50 km) features which may migrate along the ridge axis over time and third- and fourth-order discontinuities are either smaller still (MacDonald *et al.*, 1991; Gardiner, 2003) or geochemically based. The first-order transform faults are clearly observed as fracture zones across the ocean basins in gravity FAA (*e.g.* Figure 5.11) and magnetic data. In addition, traces of non-transform offsets are also observed (Grindlay *et al.*, 1991; Sempéré *et al.*, 1993; Tucholke & Lin, 1994).

Further segmentation has been observed along continental margins. For example Behn & Lin (2000), in a study of the US East Coast margin, observed segmentation of the magnetic and gravity anomalies and conclude that short wavelength (100-150 km along-strike) segmentation may be a result of non-transform, second-order discontinuities at the MAR, whilst long wavelength (300-500 km) segmentation is a consequence of variations in tectonism. Their work demonstrates that there is a direct link between segmentation at the MAR and the margin which indicates that segmentation is highly important for margin evolution. Furthermore, Watts & Stewart (1998) studied lithospheric strength of the Gabon margin, which is south of, but approximately conjugate to, the French Guiana margin. Watts & Stewart (1998) observe segmentation of the gravity FAA along the margin which they suggest is a consequence of variations in long-term strength.

Distinct structural segmentation is observed along the French Guiana margin. The key structural features (continental, thinned continental, and oceanic crust and transition zone) from Profiles A and D (this study) and B and F (Rodger *et al.*, 2006; Rodger, 2007) have been used to map out this segmentation. In addition, the OCT is traced along the margin in two ways. Firstly, to the south, the location of the 8 km depth below surface contour, *i.e.* the base of the sharp increase in depth to basement, is taken from the 3D basement grid of Rodger *et al.* (2006). Secondly, to the north of this basement grid, the zero crossing of the gravity FAA was traced along the margin. Both of these have been observed to be good indicators of the OCT location at the points at which they intersect the ACE profiles. In addition, the fracture zones picked from the gravity data (Section 5.3.4.1) were added and used to guide interpretation of rift and transform segments of the margin.

Within Figure 6.6, two rifted segments of the margin lie roughly north-south. To the far south of these rifted segments is a transform margin which, given that this segment of the margin lies approximately parallel to local transform faults, is likely to be a 'standard' transform margin. The segment of margin modelled by Profile A lies in between the two rifts, and is interpreted as a 'leaky' transform margin. The strike of the northern

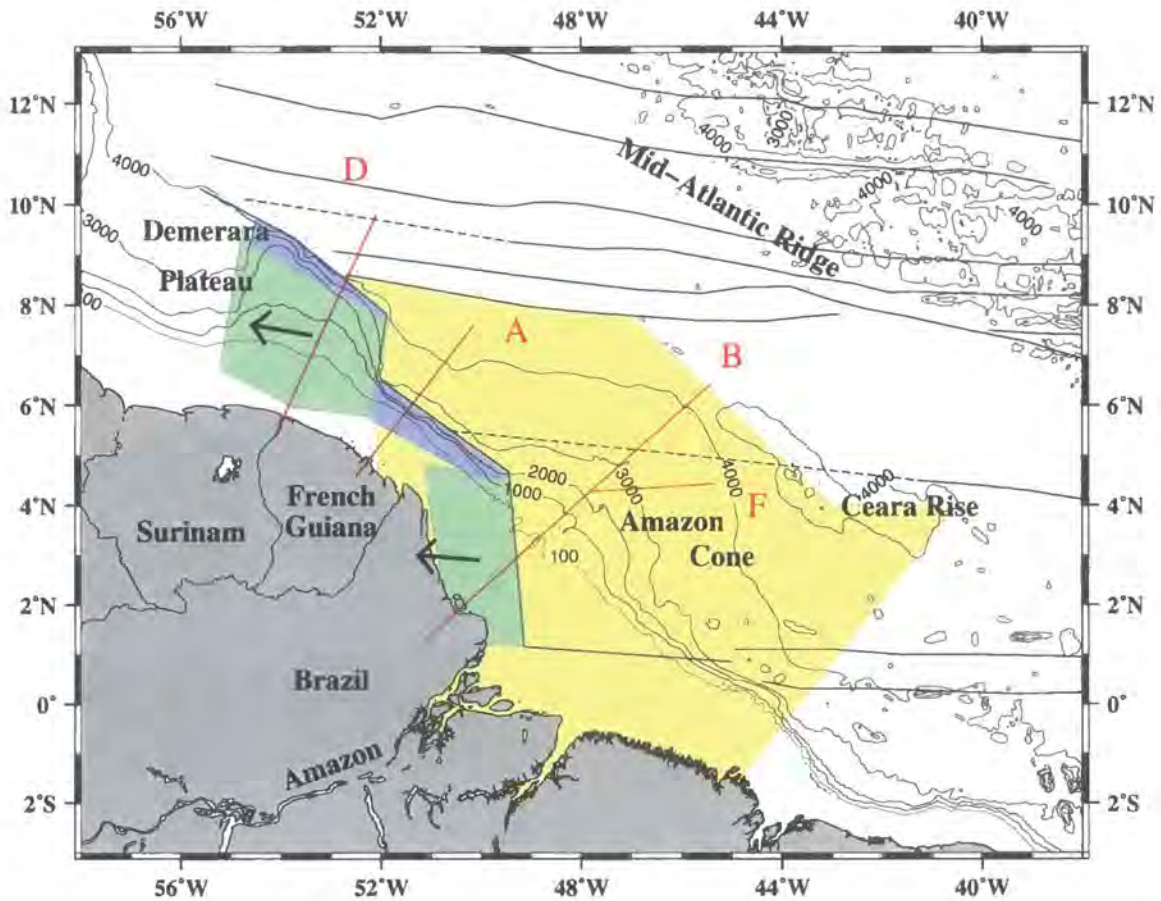


**Figure 6.6**: Interpretation of structural segmentation along the margin of French Guiana and northeast Brazil. Following interpretation of Profiles A and D, the margin is subdivided into its likely structures. Two sections of rift (green lines) are identified striking roughly north-south at ~49° and ~52°W. The thinned continental crust resulting from this rifting is shaded green. Transform margins (blue lines) are also shown with zones (shaded blue) of thinned continental crust of varying widths. The area of particularly thick sedimentation, discussed in Section 6.6, is shown (yellow). The locations of the ACE profiles used for this study and for the study of Rodger (2007) are shown (red).

and southern rifts differs by ~15°, a change which is most likely accommodated by the transtensional motion observed along Profile A, *i.e.* the plate rotation required to shift from the southern rift direction to the northern rift direction is the cause of a degree of oblique motion along the transform fault separating the two. This rotation may be part of a very long lasting shift in the plate orientations or may represent a 'shimmy' which occurred over a shorter time scale, possibly related to the release of tension when the South American and African plates finally parted, at or close to the Demerara Plateau which Gouyet *et al.* (1994) identify as the last point of contact between the two plates.

The northernmost transform segment on the figure is oriented similarly to the segment which is crossed by Profile A. However, the structure appears to be more similar to a 'standard' transform margin than the Profile A segment. For example, a marginal ridge

is observed whilst no ridge is seen further south, possibly a consequence of the greater incidence of first-order fracture zones intersecting this segment of the margin.

The obliquely rifted section of the margin described above is not easily explained by current models of margin evolution and, hence, a revised model is proposed. This is based largely on current models (after Peirce *et al.*, 1996; and developed from Mascle & Blarez, 1987 and Mascle *et al.*, 1997), shown in Figure 1.4. The revised model created to explain the oblique rifting observed in the equatorial Atlantic is shown in Figure 6.7 and comprises five main stages:

i. Initial intracontinental rifting begins between South America and Africa;

ii. Rifting continues and the lithosphere extends, thinning the continental crust. However, stresses are transtensional, *i.e.* rifting is oblique to the rift axis, and rather than forming strike-slip transform faults, crustal thinning occurs parallel with the rift axis; Consequently, segments of highly thinned continental crust are offset by regions of sharply thinned crust rather than abrupt transform faults;

iii. Crustal thinning proceeds to such an extent that break-up occurs and oceanic spreading centres form.

iv. As the two lithospheric plates drift apart, strike-slip motion occurs within the sharply thinned segments of crust. This results in the juxtaposition of old continental lithosphere against young oceanic lithosphere at a 'leaky' transform margin;

v. The continental plates continue to drift apart, with the spreading accommodated by strike-slip motion along fracture zones stemming from the 'leaky' transforms. The structure associated with rifting has now developed, showing typical rifted segments and atypical 'leaky' transform segments. The margin then continues to evolve as sedimentation causes progressively larger amounts of subsidence.

Post-rift, the continents of South America and Africa spread apart, with associated accretion of oceanic crust. This spreading may be described by movement of the continents relative to a pole of rotation which describes a series of arcs connecting the two plates. Recent poles of rotation for the Atlantic have been described by several authors (*e.g.* Rabinowitz & LaBrecque, 1979) and are generally located within the North Atlantic between 15-45°W 40-70°N. Prior to ~107 Ma the poles of rotation are often placed further south, in West Africa (Rabinowitz & LaBrecque, 1979). Using the margin orientations shown in Figure 6.6 the French Guiana and northeast Brazil margin may be projected eastwards

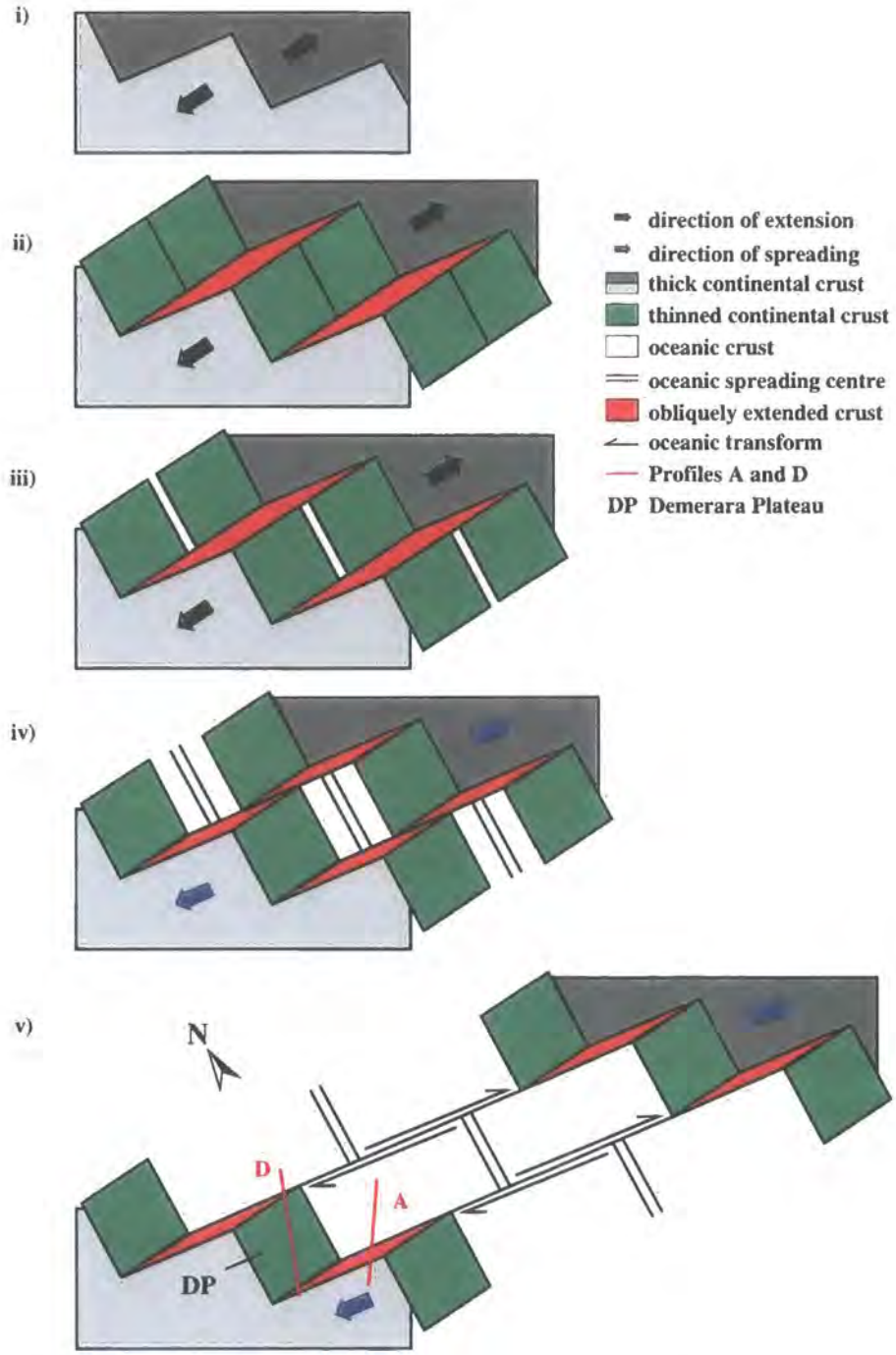


**Figure 6.7**: New model of 'leaky' transform margin evolution, developed from Peirce *et al.* (1996), Mascle & Blarez (1987), Mascle *et al.* (1997) (Figure 1.4) to explain the deep structure observed at the French Guiana margin. i) Initial intracontinental rifting; ii) Transtensional rifting creates segments of broad crustal thinning offset by regions of narrow crustal thinning; iii) Final rifting and development of oceanic spreading centres; iv) Strike-slip motion within segments of sharply thinned crust juxtaposes old continental crust against young oceanic crust and completes the formation of the 'leaky' transform; v) Further spreading is accommodated along fracture zones. The present day setting of both profiles at the margin is shown in v), where Profile A crosses a 'leaky' transform, and Profile D crosses thinned continental crust and a transform.

toward the conjugate West African margin using such poles of rotation. Figure 6.8 shows a reconstruction of the conjugate margin using a single pole of rotation positioned at 35°W 60°N and suggests that the conjugate margins can be located accurately using projection about a single pole. Hence, the margin orientations observed in this study do not suggest a significant shift in the location of the pole. This absence of a shift may be a result of final break-up occurring around the time of the shift of the pole and hence the interpretation is inconclusive. The reconstruction shown in Figure 6.8 also suggests that the southern margin has spread ~370 km futher than the northern margin within the ACE study area which, at a full-spreading rate of 40 mm $yr^{-1}$, corresponds with a 9 Ma difference in the time of final break-up between the two sections of the margin. This gradual break-up may suggest that the transtension observed at this margin may be a result of the gradual northward motion of both the rift and the stress field which, given the progressive development of the margin, is always oriented obliquely to the rift direction.

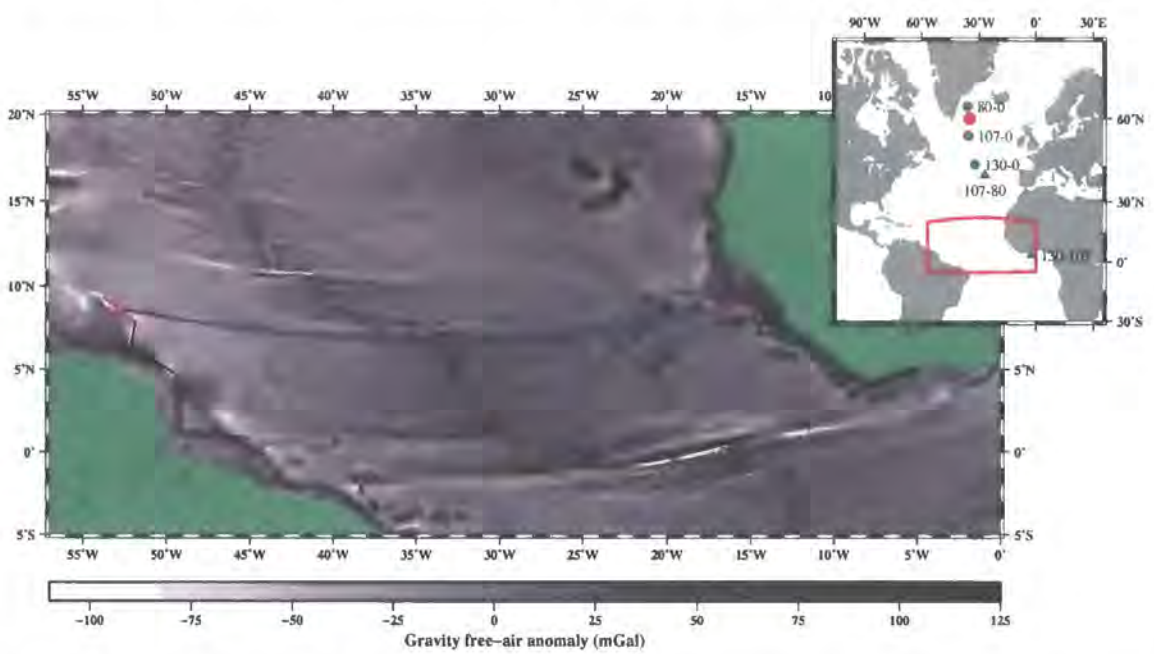


**Figure 6.8**: Reconstruction of the equatorial Atlantic conjugate margins. The margin orientations (Figure 6.6), shown as black lines, are rotated toward the West African margin about a pole located at 35°W 60°N. The inset shows this pole of rotation (red) compared with poles derived by Rabinowitz & LaBrecque (1979) (total rotation poles – green circles, early poles of opening – green triangles). Pole labels are in Ma. The West African margin orientation can be recovered using a single pole of rotation. The distance that the margins have spread varies along-strike with the total distance separating the conjugate margins labelled on the main figure in kilometres. The southern margin has spread 370 km further than the northern margin (red; spreading path shown in blue), which at a full spreading rate of 40 mm $yr^{-1}$ suggests that the southern margin rifted 9 Ma prior to the northern margin.

## 6.6 Controls on sedimentation

The assessment of fracture zones within the equatorial Atlantic (Section 5.3.4) has shown that the oceanic crust along Profile D is transected by at least two, possibly three transform faults. The most distinct of these, located at 440 km offset, is associated with a 1.9 km change in basement topography along Profile D. Furthermore, the fault can be traced across several of the Guyaplac MCS data sections in which associated basement topography gradually decreases eastward, *i.e.* oceanward. In addition to the basement topography the fault is also clearly observed in the gravity FAA.

This first-order transform fault is associated with a >100 km offset in the MAR and, hence, appears to be very significant in the post-rift evolution of the region. To the north of the fault, several further fracture zones are clearly identified (Figure 5.11), some of which can be traced over 1800 km from the MAR toward the Caribbean at ~54°W. To the south no fracture zones are observed in the FAA to the west of 46°W, although several hundred kilometres south of the Amazon Cone, they can once more be traced to the margin. Such an observation would be readily explained if the margin in this region was formed by purely rift type processes. However, as established in the last section, this is not the case and rifted and transform structures are observed.

A possible explanation for the lack of fracture zones observed within the regional gravity data (Figure 5.11) is the thick sediment cover which, despite their close proximity, differs significantly between Profiles A (6.5 km) and D (3.9 km). The extra ~3 km of sediment observed along Profile A may result in higher densities within the lower sediment column, which would reduce the density contrasts and, hence, reduce the FAA changes associated with fracture zones. Additionally, following subsidence, the density contrast is located further from the observation point. The reason for this change in sediment thickness along-margin-strike is partly related to the Amazon River, the major local source of suspended sediment (Cobbold *et al.*, 2004). However, the fracture zones observed in this study may also play a role in controlling the distribution of sediment.

It is likely that the large rise in basement topography, observed at a fracture zone along Profile D, has dammed the sediment which has been carried northward up the coast, from the mouth of the Amazon River, by prevailing currents (Johns *et al.*, 1998). The Ceara Rise has had a similar effect, damming the eastern edge of the thick Amazon Cone. This has resulted in an unusually thick sediment column not just within the Amazon Cone fan, but also within the region south of 8°N and west of ~46°W, as shown in Figure 6.6.

## 6.7 Evolution of the equatorial Atlantic

The margins of the equatorial Atlantic are of great importance, both in terms of their economic value and the control they have placed over the tectonic evolution of the Atlantic Ocean. This study has produced two deep models of the structure of the French Guiana margin which help develop our understanding of this region. Within the preceding sections various elements of these models have been described and here this work is briefly summarised into a possible model of the evolution of the equatorial Atlantic around French Guiana.

In chronological order:

- Europe and North America (180 Ma) and South Africa and South America (140 Ma) began to rift apart, forming the North and South Atlantic Oceans respectively. In both cases, rifting progressed gradually towards equatorial regions, eventually resulting in a roughly east-west tensional stress between South America and Africa across the area which is now known as French Guiana, northeast Brazil, Liberia, Sierra Leone and Guinea.

- This tension stretched the relatively cold, thick lithosphere of the region. Thinning of the crust itself proceeded over ~18 Ma and was not accompanied by significant melting of the mantle. Hence, the resulting margin is non-volcanic.

- The initial lateral offset between the MAR of the North Atlantic and South Atlantic resulted in a relatively large degree of transform motion during the rifting of the equatorial Atlantic.

- Thus, when Africa and South America finally rifted apart, around 110 Ma, the margins were highly segmented, displaying a series of rift and transform structures. This rifting proceeded northwards resulting in a gradual shift in the rift direction. Consequently, some transform margins developed with a degree of motion perpendicular to the transform, producing 'leaky' transforms.

- Oceanic crustal accretion begins. As a result of the relatively cool asthenosphere, heat loss due to a relatively slow spreading rate and a large number of fracture zones, the crust that forms is unusually thin.

- Sedimentation occurs across the whole margin at a relatively slow rate, with the Ceara Rise and the transform fault at ~8°N acting to dam the sediments offshore northeast Brazil and southern French Guiana.

- At ~12 Ma the uplift of the Andes mountain range in the west of South America results in a rapid increase of sediment flux from the Amazon River. A thick sediment column develops offshore Brazil and French Guiana causing associated subsidence.

## 6.8 Summary

This chapter has contained a final discussion of the results of this thesis. The deep structural models resulting from earlier data modelling and testing have been used to conclude that the margin is non-volcanic. This interpretation has been discussed relative to other studies and, consequently, the lithosphere is suggested to be relatively cold and rifting not plume-related. The unusually thin oceanic crust observed during the ACE is interpreted to result from relatively cold asthenosphere, slow spreading and the existence of several fracture zones, all of which result in a relatively small amount of melt available for accretion.

The primary aim of this study has been addressed through a discussion of rifting versus transform motion, which has resulted in the interpretation of two distinct crustal structures. The first, along Profile A, is a 'leaky' transform and the second, along Profile D, is a transform margin adjacent to thinned continental crust. These structural interpretations have been used to develop a model of the structural segmentation of the margin. In turn, this model has been used to adapt existing models of transform margin formation to explain the formation of the 'leaky' transform.

The next chapter will condense the final conclusions of this study and discuss the potential for further research.

# Chapter 7

# Conclusions and further work

## 7.1 Conclusions

This thesis has described an investigation of the deep crustal structure of the continental margin of French Guiana in the west equatorial Atlantic. This work was completed with several aims, including the development of an understanding of the role of magmatism, mode of rifting and influence of segmentation along this margin. These aims have been addressed through the acquisition and modelling of a multidisciplinary geophysical dataset and the key results and conclusions are:

- Deep crustal *P*-wave velocity-depth modelling of two margin transects has demonstrated significant structural variation along the French Guiana passive continental margin. To the north, Profile D exhibits a 320 km wide zone of thinned continental crust adjacent to a sharp OCT. The margin is interpreted as a transform margin and the wide zone of thinning a consequence of rifting perpendicular to the transect modelled. Further south, a 70 km wide zone of thinned continental crust is observed along Profile A, which shows characteristics of both transform and rifted margins and is, hence, interpreted as a 'leaky' transform.

- Observation of a 'leaky' transform margin offshore French Guiana has implications for our understanding of both passive margin structure and equatorial Atlantic evolution. Existing models have been developed to describe the formation of this structure in terms of plate motion oblique to the strike of the rift axis.

- Extrapolation of the structures observed across the two transects along-margin-strike, coupled with an analysis of local fracture zones observed within basement, gravity and magnetic data, indicates a segmented pattern of adjacent rift and transform margin segments. However, interpretation of the 'leaky' transform along Profile

A suggests that at least one of the transform segments was influenced by oblique motion, *i.e.* transtension.

- The two models, in conjunction with coincident MCS reflection data confirm that the margin is non-volcanic. Neither SDR sequences, nor high sub-continental velocities are observed. Thus, margin formation was not plume-related and the cratonic lithosphere was likely to be relatively cold.

- The structural models presented as part of this study, combined with other profiles from the ACE (Rodger *et al.*, 2006; Rodger, 2007) suggest that the oceanic crust in the west equatorial Atlantic from 4° to 10°N and 46° to 53°W is anomalously thin when compared to 'normal' Atlantic crust (White *et al.*, 1992). The thin crust implies low melt generation which is interpreted be a consequence of relatively cold asthenosphere, combined with heat loss during rifting and multiple fracture zones, particularly in the north.

- Sedimentary control in the region is inferred from an analysis of the basement topography which suggests that a transform fault which intersects the MAR at ~7° and the margin at ~8°N is associated with a large topographic displacement of the basement surface. This, in conjunction with the Ceara Rise feature to the east, dam the Amazonian sediments.

## 7.2 Further work

Two *P*-wave velocity-depth models of the French Guiana margin have been developed as part of this study. However, neither the 3D characteristics of the margin nor the full extent of the unusually thin oceanic crust are fully constrained. Furthermore, the along-strike margin structure outside of the ACE study area is unknown and, hence, it is unclear how representative of the equatorial Atlantic structure these two profiles are. It may be possible to extend this study to improve our understanding using existing data and also by acquiring further data.

### 7.2.1 Existing data

In this study, two margin transects have been modelled and used to infer structural variation along-margin-strike. However, in order to better understand this variation, a model of 3D margin structure should be developed. This may be attempted by combining the existing seismic and satellite-derived FAA data. The seismic data provide good constraint on

structural variation along 2D profiles. The FAA data cover a wide areal extent but do not reveal the depth at which the subsurface structural variation is located.

The velocity structure observed in the WA data may be extrapolated along-margin-strike and used, in addition to the Guyaplac MCS dataset, to create depth estimates for the intra-sediment boundaries and basement surface. Thus, a 3D *P*-wave velocity-depth model of margin structure may be developed which comprises: a seafloor boundary which has excellent constraint from bathymetry data; a sediment column and basement boundary which have moderate constraint, primarily from MCS data; and a deeper crustal structure which is constrained at just two points along the margin by the ACE profiles. This model may be converted to density using similar methods to those described in this thesis and then used to calculate the FAA in 3D with which to compare with the satellite-derived FAA. Given the constraint on the shallow structure provided by existing data, the main uncertainty that remains is the depth to the Moho. Consequently, a good fit between the calculated and satellite-derived FAAs would indicate a correctly positioned Moho and, hence, constraint on the 3D deep crustal structure.

Existing data may also be used to better understand the unusually thin oceanic crust observed in this study. In order to fully understand the reasons for the accretion of this crust, it would be useful to map out its areal extent. At present, studies of the ACE data have shown the thin crust to be a feature of each of the profiles modelled. However, it is uncertain how far oceanward the thin crust extends and it may extend only as far as the oceanward limit of the ACE profiles or, alternatively, across the entire Atlantic indicating that some type of anomalous accretion is still occurring today. One hypothesis may be that the Ceara Rise marks the onset of 'normal' accretion, as evidenced by a significant thickening of the oceanic crust along Profile B (Rodger *et al.*, 2006). However, crustal thickness is unknown oceanward of the Ceara Rise and should be investigated in order to test this hypothesis. Modelling of the existing ACE WA data from Profile G (Figure 7.1), which crosses the Ceara Rise, should be the first stage in such an investigation.

### 7.2.2 Further data acquisition

An alternative approach would be to acquire further WA data. Thus, rather than focussing on the 3D structure of a relatively small section of the margin, studies would address the wider context of structural variation in the equatorial Atlantic. There are two primary locations for acquisition which may lead to a better understanding. Firstly, additional profiles could be acquired at, and adjacent to, the French Guiana margin (Profiles H, J,

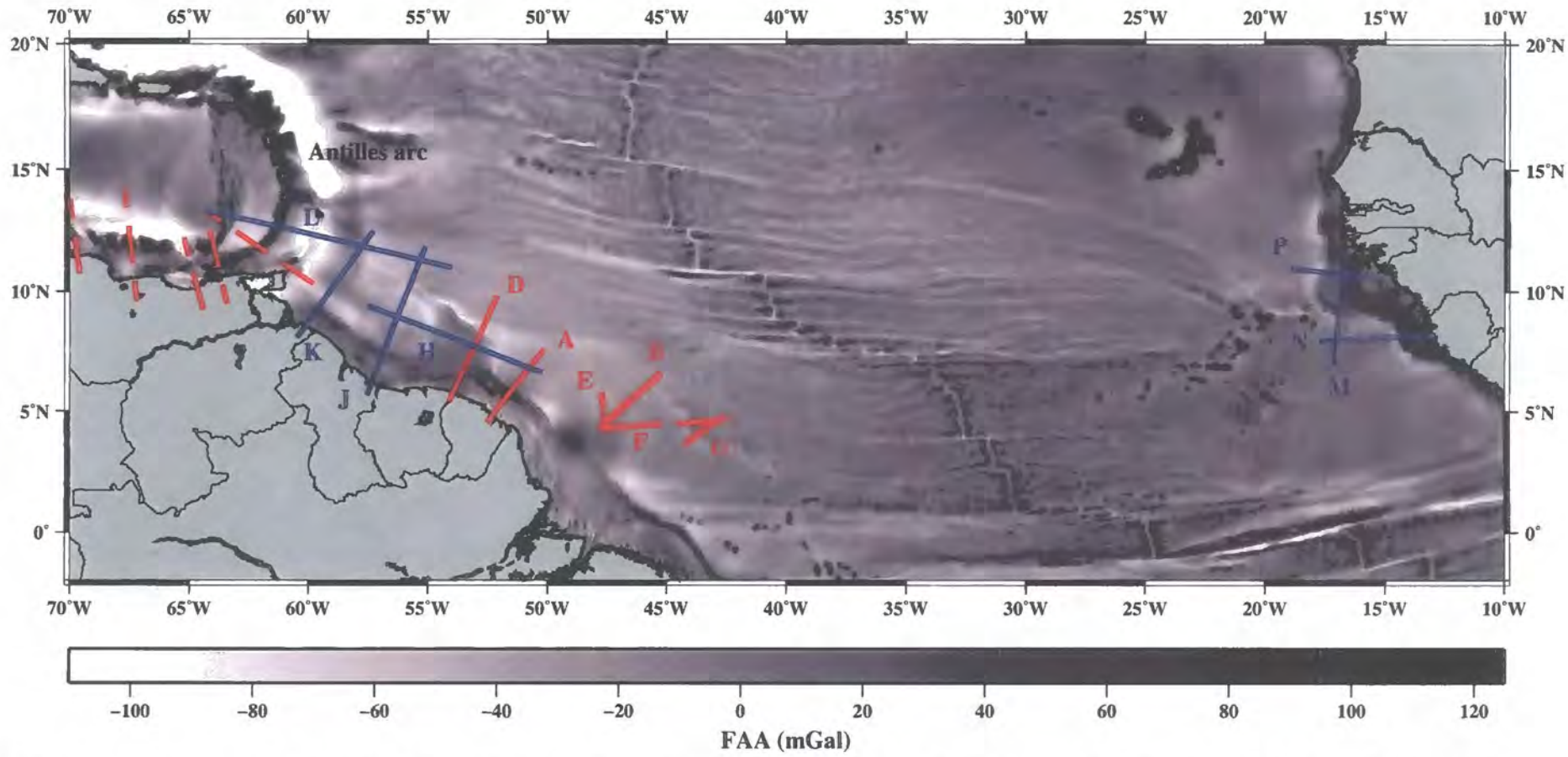


**Figure 7.1**: Acquisition of further data in the equatorial Atlantic. Seven coincident WA and MCS profiles are proposed (blue lines). Profile H transects the margin inbetween ACE Profiles A and D (red solid lines), which the model developed during this study suggests is a rift-style segment of the margin. The profile also intersects Profiles A, D and J to allow cross checking of the resultant models. Profiles J, K, and L extend the margin study northwards from the region surveyed by the ACE towards the Caribbean, home to the BOLIVAR margin study (red dashed lines – *e.g.* Guedez *et al.*, 2005). Profiles N, P and Q are located at the conjugate margin in order to investigate the symmetry, or asymmetry, or rifting.

K and L – Figure 7.1). Secondly, additional studies of the conjugate West African margin could be made (Profiles M, N and P).

The model of margin segmentation proposed in this study suggests that between profiles A and D the French Guiana margin is rift in type. This segment of the margin would make an ideal target for a WA profile for three reasons. Firstly the structures observed would provide constraint on how transtensional motion affects rifting, complimenting the observations described within this study which suggest that transform margins which have evolved under the influence of transtension are wider than would normally be expected, *i.e.* 'leaky'. Secondly, the profile may be oriented to intersect both of the profiles modelled during this study, in order to compare and contrast the resulting models. Thirdly, the profile could lie parallel to the general trend of fracture zones in the region and hence provide an estimate of basement roughness in the absence of fracture zone related topographic offsets. This profile is named Profile H and is shown in Figure 7.1. The profile is proposed to extend far enough to the west to completely cross the Demerara Plateau, in order to better constrain the 3D deep crustal structure of this feature.

Additionally, targets for WA acquisition may be selected along-strike the margin, to the north of the ACE target area. In this region, offshore Surinam, Guyana and Venezuela the crustal structural variation is complicated by the presence of the Caribbean-South America plate boundary and subduction of the Atlantic plate. However, by extending this research northwards the study may link up with a recent study onshore-offshore Venezuela, allowing a thorough understanding of margin development 2500 km along-margin-strike. Three potential profile locations, named J, K, and L, are proposed shown in Figure 7.1.

Profiles J and K both transect the continental margin and may include onshore-offshore data acquisition in the same manner as ACE Profiles A and D. The third profile lies approximately east-west, intersecting Profiles K and J and also the junction between two BOLIVAR profiles (*e.g.* Guedez *et al.*, 2005). BOLIVAR is a large-scale project to investigate the collision between the Antilles arc and the continent of South America at the Caribbean-South America plate boundary. The project comprised five coincident MCS and WA seismic profiles which constrain the deep crustal structure both along the Venezuela margin and to the northeast, through the Antilles arc. Thus, by combining the data from ACE, BOLIVAR and the proposed profiles, along-strike structural variation may be studied at a margin which exhibits rift-, transform, and subduction-style structures.

Alternatively, the conjugate margin may be targeted, in order to understand the symmetry of the margin. Significant asymmetry has been observed among the non-volcanic margins of the North Atlantic. For example, conjugate margins have been observed to

exhibit significant low-angle detachment faults, zones of exhumed mantle of various widths and continental crust which thin sharply or gradually. Low-angle detachment faults are thought to result from serpentinization within the crust which, given the abundance of fracture zones, may potentially be formed in greater quantities in the equatorial Atlantic. The possible effect that this may have is unknown. Thus, a WA study of the rift- and transform-style structures around the Guinea Plateau may allow direct observation of equatorial Atlantic asymmetry and, in particular, the asymmetry of transform margins which has not yet been studied.

Profile M is approximately conjugate to ACE Profile D allowing the direct comparison of conjugate transform margins. Similarly, Profile N to the south transects the margin in a region which most likely exhibits rift-style structures. This profile is, hence, conjugate to proposed Profile H. Profile P to the north also transects what is likely to be a rifted margin, in order to understand the segmentation between rift- and transform-style structures at the West African margin. These three profiles are oriented so that they intersect one another in order to tie together the structures observed along each profile.

# References


**Aki**, K. & Richards, P.G. (1980). *Quantitative Seismology, Volume 2*. W.H. Freeman, New York.

**Artemieva**, I.M. & Mooney, W.D. (2001). Thermal thickness and evolution of precambrian lithosphere: A global study. *J. Geophys. Res.*, 106(B8), 16387–16414.

**Barry**, K.M., Cavers, D.A. & Kneale, C.W. (1975). Report on recommended standards for digital tape formats. *Geophysics*, 2, 344–352.

**Basile**, C., Brun, J.P. & Mascle, J. (1992). Structure et formation de la marge transformante de Côte d'Ivoire-Ghana: apports de la sismique réflexion et de la modélisation analogique. *Bull. Soc. Geol. Fr.*, 163, 207–216.

**Basile**, C., Mascle, J., Benkhelil, J. & Bouillin, J.-P. (1998). Geodynamic evolution of the Côte d'Ivoire-Ghana transform margin: An overview of Leg 159 results. In: *Mascle, J., Lohmann, G.P. and Moullade, M.* (eds.), *Proc. ODP, Sci. Results*, 159, 101–110.

**Basile**, C., Mascle, J., Popoff, M., Bouillin, J.P. & Mascle, G. (1993). The Ivory Coast-Ghana transform margin: a marginal ridge structure deduced from seismic data. *Tectonophysics*, 222, 1–19.

**Bauer**, K., Neben, S., Schreckenberger, B., Emmerman, R., Hinz, K., Fechner, N., Gohl, K., Schulze, A., Trumbull, R.B. & Weber, K. (2000). Deep structure of the Namibia continental margin as derived from integrated geophysical studies. *J. Geophys. Res.*, 105(B11), 25829–25853.

**Beaumont**, C., Keen, C.E. & Boutilier, R. (1982). On the evolution of rifted continental margins: Comparison of models and observations for the Nova Scotian margin. *Geophys. J. R. Astr. Soc.*, 70, 667–715.

**Behn**, M.D. & Lin, J. (2000). Segmentation in gravity and magnetic anomalies along the U.S. East Coast passive margin: Implications for incipient structure of the oceanic lithosphere. *J. Geophys. Res.*, 105(B11), 25769–25790.

**Benjamin**, M.T., Johnson, N.M. & Naeser, C.W. (1987). Rapid uplift in the Bolivian Andes. *Geology*, 15, 680–683.

**Benkhelil**, J., Mascle, J. & Tricart, P. (1995). The Guinea continental margin: an example of a structurally complex transform margin. *Tectonophysics*, 248, 117–137.

**Blarez**, E. (1986). La marge continentale de Côte d'Ivoire-Ghana: Structure et evolution d'une marge continentale transformante. *Ph.D. thesis*, Université Pierre et Marie Curie, Paris, France.

**Blarez**, E. & Mascle, J. (1988). Shallow structure and evolution of the Ivory Coast and Ghana transform margin. *Mar. Petr. Geol.*, 5, 54–64.

**Boillot**, G., Féraud, G., Recq, M. & Girardeau, J. (1989). 'Undercrusting' by serpentinite beneath rifted margins: the examples of the West Galicia Margin (Spain). *Nature*, 341, 523–525.

**Bonatti**, E. (1978). Vertical tectonism in oceanic fracture zones. *Earth Planet. Sci. Lett.*, 37, 369–379.

**Bonatti**, E. (1996). Anomalous opening of the Equatorial Atlantic due to an equatorial mantle thermal minimum. *Earth Planet. Sci. Lett.*, 143, 147–160.

**Bown**, J.W. & White, R.S. (1994). Variation with spreading rate of oceanic crustal thickness and geochemisty. *Earth Planet. Sci. Lett.*, 121, 435–449.

**Bown**, J.W. & White, R.S. (1995). Effect of finite extension rate on melt generation at rifted continental margins. *J. Geophys. Res.*, 100(B9), 18011–18029.

**Braga**, L.F.S. (1991). Isostatic evolution and crustal structure of the Amazon continental margin determined by admittance analysis and inversion of gravity data. *Ph.D. thesis*, Oregon State University, US.

**Brandão**, J.A.S.L. & Feijó, F.J. (1994). Bacia do Foz do Amazonas. *Boletim de Geociências da Petrobrás (Rio de Janeiro)*, 8(1), 91–100.

**Bratt**, S.R. & Purdy, G.M. (1984). Structure and Variability of Oceanic Lithosphere on the Flanks of the East Pacific Rise Between 11° and 13°N. *J. Geophys. Res.*, 89, 6111–6125.

**Breivik**, A.J., Mjelde, R., Faleide, J.I. & Murai, Y. (2006). Rates of continental breakup magmatism and seafloor spreading in the Norway Basin-Iceland plume interaction. *J. Geophys. Res.*, 111, B07102, doi:10.1029/2005JB004004.

**Bullock**, A.D. & Minshull, T.A. (2005). From continental extension to seafloor spreading: crustal structure of the Goban Spur rifted margin, southwest of the UK. *Geophys. J. Int.*, 163, 527–546.

**Carlson**, R.L. & Raskin, G.S. (1984). Density of the ocean crust. *Nature*, 311, 555–558.

**Castro**, J.C., Miura, K. & Braga, J.A.E. (1978). Stratigraphic and structural framework for the Foz do Amazonas basin. *Society of Petroleum Engineers 10th Annual Offshore Technology Conf. Proc.*, 3, 1843–1847.

**Chian**, D. & Louden, K.E. (1994). The continent-ocean transition across the southwest Greenland margin. *J. Geophys. Res.*, 99(B5), 9117–9135.

**Chian**, D., Louden, K.E., Minshull, T.A. & Whitmarsh, R.B. (1999). Deep structure of the ocean-continent transition in the southern Iberia Abyssal Plain from seismic refraction profiles: Ocean Drilling Program (Legs 149 and 173) transect. *J. Geophys. Res.*, 104(B4), 7443–7462.

**Chian**, D., Louden, K.E. & Reid, I.D. (1995). Crustal structure of the Labrador Sea conjugate margin and implications for the formation of nonvolcanic continental margins. *J. Geophys. Res.*, 100(B12), 24239–24254, doi:10.1029/95JB02162.

**Chian**, D., Reid, I.D. & Jackson, H.R. (2001). Crustal structure beneath Orphan Basin and implications for nonvolcanic continental rifting. *J. Geophys. Res.*, 106, 10923–10940.

**Christensen**, N.I. & Mooney, W.D. (1995). Seismic velocity structure and composition of the continental crust: a global view. *J. Geophys. Res.*, 100(B6), 9761–9788.

**Claerbout**, J.F. (1985). *Imaging the Earth's interior.* Blackwell Scientific Publications Inc.

**Cobbold**, P.R., Mourges, R. & Boyd, K. (2004). Mechanism of thin-skinned detachment in the Amazon Fan: assessing the importance of fluid overpressure and hydrocarbon generation. *Mar. Petr. Geol.*, 21, 1013–1025.

**Cogné**, J.-P. & Humler, E. (2004). Temporal variation of oceanic spreading and crustal production rates during the last 180 My. *Earth Planet. Sci. Lett.*, 227, 427–439.

**Cogné**, J.-P. & Humler, E. (2006). Trends and rhythms in global seafloor generation rate. *Geochem. Geophys. Geosyst.*, 7, Q03011, doi:10.1029/2005GC001148.

**Cohen**, J.K. & Stockwell, Jr. J.K. (2000). CWP/SU: Seismic Unix Release 34: a free package for seismic research and processing. Center for Wave Phenomena, Colorado School of Mines.

**Contrucci**, I., Matias, L., Moulin, M., Géli, L., Klingelhöfer, F., Nouzé, H., Aslanian, D., Olivet, J.-L., Réhault, J.-P. & Sibuet, J.-C. (2004). Deep structure of the West African continental margin (Congo-Zaïre-Angola) between 5°S and 8°S from reflection/refraction seismics and gravity data. *Geophys. J. Int.*, 158, 529–553.

**Curry**, W.B., Shackleton, N.J. & Richter, C. (1995). *Proc. ODP, Init. Reports Volume 154*, College Station, TX, 719.

**Czuba**, W., Ritzmann, O., Nishimura, Y., Grad, M., Mjelde, R., Guterch, A. & Jokat, W. (2005). Crustal structure of northern Spitsbergen along the deep seismic transect between the Molloy Deep and Nordaustlandet. *Geophys. J. Int.*, 161, 347–364.

**Damuth**, J.E. & Kumar, N. (1975). Amazon Cone: Morphology, sediments, age and growth pattern. *Geol. Soc. Am. Bull.*, 86, 863–878.

**Davies**, R.J., MacLeod, C.J., Morgan, R. & Briggs, S.E. (2005). Termination of a fossil continent-ocean fracture zone imaged with three-dimensional seismic data: The Chain Fracture Zone, eastern equatorial Atlantic. *Geology*, 33(8), 641–644.

**Davis**, M. & Kusznir, N. (2002). Are buoyancy forces important during the formation of rifted margins? *Geophys. J. Int.*, 149, 524–533.

**Dean**, S.M., Minshull, T.A., Henstock, T.J., Murton, B.J., White, R.S. & Fliedner, M. (2001). Numerical modelling of rift-related magmatism and melt chemistry. *EOS Trans. AGU*, Fall Meet. Suppl., Abstract T51B-0861.

**Dean**, S.M., Minshull, T.A., Whitmarsh, R.B. & Louden, K.E. (2000). Deep structure of the ocean-continent transition in the southern Iberia Abyssal Plain from seismic refraction profiles: the IAM-9 transect at 40° 20'N. *J. Geophys. Res.*, 105(B3), 5859–5885.

**Deregowski**, S.M. (1986). What is DMO (dip moveout)? *First Break*, 4(7), 7–24.

**Dick**, J.J.B., Lin, J. & Schouten, H. (2003). An ultraslow-spreading class of ocean ridge. *Nature*, 426, 405–411.

**Dilek**, Y., Moores, E.D. & Furnes, H. (1998). Structure of modern oceanic crust and ophiolites and implications for faulting and magmatism at oceanic spreading centres. In: *Buck, W.R., Delaney, P.T., Karson, J.A. & Lagabrielle, Y.* (eds.), *Faulting and magmatism at mid-ocean ridges*, 359, 219–265. Geophysical Monograph 106, American Geophysical Union, Washington DC.

**Dix**, C.H. (1955). Seismic velocities from surface measurements. *Geophysics*, 20, 68–86.

**Driscoll**, N. & Karner, G. (1998). Lower crustal extension across the Northern Carnarvon basin, Australia: evidence for an eastward dipping detachment. *J. Geophys. Res.*, 103, 4975–4991.

**Duckworth**, G.L. & Baggeroer, A.B. (1985). Inversion of refraction data from the Fram and Nansen basins of the Arctic Ocean. *Tectonophysics*, 114, 55–102.

**Duckworth**, G.L., Baggeroer, A.B. & Jackson, H.R. (1982). Crustal structure measurements from near FRAM II in the Pole Abyssal Plain. *Tectonophysics*, 89, 173–215.

**Dunlop**, D.J. & Prevot, M. (1982). Magnetic properties and opaque mineralogy of drilled submarine intrusive rocks. *Geophys. J. R. Astr. Soc.*, 89, 9800–9990.

**Edgar**, T. & Ewing, J. (1968). Seismic refraction measurements on the continental margin of northeastern South America. *Am. Geophys. Union Trans.*, 49, 197–198.

**Edwards**, R.A., Whitmarsh, R.B. & Scrutton, R.A. (1997). The crustal structure across the transform continental margin off Ghana, eastern equatorial Atlantic. *J. Geophys. Res.*, 102(B1), 747–772.

**Eldholm**, O., Skegseid, J., Planke, S. & Gladczenko, T.P. (1995). Volcanic margins concepts. In: *Banda, E. et al.* (eds.), *Rifted Ocean-Continent Boundaries, NATO ASI Ser. 963*, 1–16.

**Erbacher**, J., Mosher, D.C. & Malone, M.J. *et al.*. (2004). *Proc. ODP, Init. Reports Volume 207*, College Station, TX (Ocean Drilling Program), doi:10.2973/odp.proc.ir.207.2004.

**Escartín**, J., Hirth, G. & Evans, B. (1997). Effects of serpentinisation on the lithospheric strength and the style of normal faulting at slow-spreading ridges. *Earth Planet. Sci. Lett.*, 151, 181–189.

**Faleide**, J.I., Gudlaugsson, S.T., Eldholm, O., Myhre, A.M. & Jackson, H.R. (1991). Deep seismic transects across the sheared western Barents Sea-Svalbard continental margin. *Tectonophysics*, 189, 73–89.

**Flüh**, E. & Bialas, J. (1996). A digital, high data capacity ocean bottom recorder for seismic investigations. *Int. Underwater Systems Design*, 18, 18–20.

**Fowler**, S. & McKenzie, D. (1989). Gravity studies of the Rockall and Exmouth Plateaux using SEASAT. *Basin Res.*, 2, 27–34.

**Fox**, P.J. & Gallo, D.G. (1984). A tectonic model for ridge-transform-ridge plate boundaries: Implications for the structure of oceanic lithosphere. *Tectonophysics*, 104, 205–242.

**Fox**, P.J. & Gallo, D.G. (1986). The geology of North Atlantic transform plate boundaries and their aseismic extensions. In: *Vogt, P.R. & Tucholke, B.E.* (eds.), *The Geology of NorthAmerica, vol. M, The Western North Atlantic Region*, 157–172. Geol. Soc. America.

**Funck**, T., Hopper, J.R., Larsen, H.C., Louden, K.E., Tucholke, B.E. & Holbrook, W.S. (2003). Crustal structure of the ocean-continent transition at Flemish Cap: Seismic refraction results. *J. Geophys. Res.*, 108(B11), 2531, doi: 10.1029/2003JB002434.

**Funck**, T., Jackson, H.R., Louden, K.E., Dehler, S.A. & Wu, Y. (2004). Crustal structure of the northern Nova Scotia rifted continental margin (eastern Canada). *J. Geophys. Res.*, 109, B09102, doi: 10.1029/2004JB003008.

**Gadd**, S.A. & Scrutton, R.A. (1997). An integrated thermomechanical model for transform continental margin evolution. *Geo. Mar. Letts.*, 17, 21–30.

**Gardiner**, A.B. (2003). Segmentation and cycles of crustal accretion at mid-ocean ridges: A study of the Reykjanes Ridge. *Ph.D. thesis*, University of Durham, UK.

**Gardner**, G.H.F., Gardner, L.W. & Gregory, A.R. (1974). Formation velocity and density – the diagnostic basics for stratigraphic traps. *Geophysics*, 39, 770–780.

**Gee**, J. & Kent, D. (1994). Variation in Layer 2A thickness and the origin of the central anomaly magnetic high. *Geophys. Res. Lett.*, 21, 297–300.

**Geoffroy**, L. (2005). Volcanic passive margins. *C.R. Geosci*, 337, 1395–1408.

**Goff**, J.A. (1991). A global and regional stochastic analysis of near-ridge abyssal hill morphology. *J. Geophys. Res.*, 96, 21713–21737.

**Goff**, J.A. (1992). Quantitative characterisation of abyssal hill morphology along flow lines in the Atlantic Ocean. *J. Geophys. Res.*, 97, 9183–9202.

**Gordon**, R.G. & Van der Voo, R. (1995). Mean Paleomagnetic Poles for the Major Continents and the Pacific Plate. *Handbook Phys. Constants, Am. Geophys. Union*, 225–239.

**Gouyet**, S., Unternehr, P. & Mascle, A. (1994). *The French Guyana Margin and the Demerara Plateau: Geological History and Petroleum Plays*, 411–422. Federal Republic of Germany.

**Greenroyd**, C.J., Peirce, C., Rodger, M., Watts, A.B. & Hobbs, R.W. (2007a). Crustal Structure and Evolution of the Demerara Plateau, French Guiana. *Geophys. J. Int.*, in review.

**Greenroyd**, C.J., Peirce, C., Rodger, M., Watts, A.B. & Hobbs, R.W. (2007b). Crustal Structure of the French Guiana margin, West Equatorial Atlantic. *Geophys. J. Int.*, in press.

**Greenroyd**, C.J., Peirce, C., Rodger, M., Watts, A.B. & Hobbs, R.W. (2007c). Rifting and segmentation at the French Guiana continental margin. *Geol. Soc. Spec. Pub.*, in review.

**Grindlay**, N.R., Fox, P.J. & Macdonald, K.C. (1991). Second-order ridge axis discontinuities in the South Atlantic: Morphology, structure, and evolution. *Mar. Geophys. Res.*, 13, 21–49.

**Guedez**, M.C., Zelt, C.A., Magnani, M.B., Levander, A., Christeson, G.L. & Sawyer, D.S. (2005). BOLIVAR: Crustal Structure Across the Caribbean-South American Plate Boundary at 70W: Results from Refraction and Reflection Data. *EOS Trans. AGU*, 86(52), Fall Meet. Suppl., Abstract T11B-0386.

**Harland**, W.B., Armstrong, R.L., Cox, A.V., Craig, L.E., Smith, A.G. & Smith, D.G. (1990). *A Geologic Time Scale.* Cambridge University Press.

**Hinz**, K. (1981). A hypothesis on terrestrial catastrophes: wedges of very thick oceanward dipping layers beneath passive margins – Their origin and paleaoenvironment significance. *Geol. Jahrb.*, 22, 345–363.

**Hinz**, K., Dostmann, H. & Fitsch, J. (1982). The continental margin of Morocco: seismic sequences, structural elements and geological development. In: *Von Rad, U., Hinz, K., Santhein, M. and Seibold, E.* (eds.) *Geology of the Northwest Africa Continental Margin*, 34–60. Springer-Verlag, New York.

**Hobbs**, R.W. (2006). Quantifying uncertainty in margin structure derived from long-offset seismic data. *Ocean Margins LINK Programme Science Meeting: From Margins... to Mainstream.*

**Hobbs**, R.W., Al-Salem, A., Naghi, H., Greenroyd, C.J. & Peirce, C. (2006). Water structure and flow along the north brazil and french guyana margins. *Ocean Margins LINK Programme Science Meeting: From Margins... to Mainstream.*

**Hoffman**, H.-J. & Reston, T.J. (1992). Nature of the S reflector beneath the Galicia Banks rifted margin: Preliminary results from prestack depth migration. *Geology*, 20, 1091–1094.

**Holbrook**, W.S. & Keleman, P.B. (1993). Large igneous province on the US Atlantic margin and implications for magmatism during continental breakup. *Nature*, 364, 433–436.

**Holbrook**, W.S., Purdy, G.M., Sheridan, R.E., Gover III, L., Talwani, M., Ewing, J. & Hutchinson, D. (1994a). Seismic structure of the U.S. Mid-Atlantic continental margin. *J. Geophys. Res.*, 99, 17871–17891.

**Holbrook**, W.S., Reiter, E.C., Purdy, G.M., Sawyer, D., Stoffa, P.L., Austin Jr., J.A., Oh, J. & Makris, J. (1994b). Deep structure of the U.S. Atlantic continental margin offshore South Carolina from coincident ocean bottom and multichannel seismic data. *J. Geophys. Res.*, 99, 9155–9178.

**Holmes**, R., Tolstoy, M., Cochran, J.R. & Floyd, J.S. (2005). Crustal Structure Along the Southeast Indian Ridge From Seismic Refraction Data. *EOS Trans. AGU*, Abstract T33A-0513.

**Hopper**, J.R., Funck, T., Tucholke, B.E., Larsen, H.C., Holbrook, W.S., Louden, K.E., Shillington, D. & Lau, H. (2004). Continental breakup and the onset of ultraslow seafloor spreading off Flemish Cap on the Newfoundland rifted margin. *Geology*, 32, 93–96.

**Hopper**, J.R., Funck, T., Tucholke, B.E., Louden, K.E., Holbrook, W.S. & Larsen, H.C. (2006). A deep seismic investigation of the Flemish Cap margin: implications for the origin of deep reflectivity and evidence for asymmetric break-up between Newfoundland and Iberia. *Geophys. J. Int.*, 164, 501–515.

**Horsefield**, S.J. (1991). Crustal structure across the ocean-continent boundary. *Ph.D. thesis*, University of Cambridge, UK.

**Horsefield**, S.J., Whitmarsh, R.B., White, R.S. & Sibuet, J.-C. (1994). Crustal structure of the Goban Spur rifted continental margin, NE Atlantic. *Geophys. J. Int.*, 119, 1–19.

**Houtz**, R.E. (1977). Sound-velocity characteristics of sediment from the eastern South American margin. *Geol. Soc. Am. Bull.*, 88, 720–722.

**Houtz**, R.E. & Ewing, J. (1976). Upper crustal structure as a function of plate age. *J. Geophys. Res.*, 81, 2490–2498.

**Houtz**, R.E., Ludwig, W.J., Milliman, J.D. & Grow, J.A. (1977). Structure of the northern Brazil continental margin. *Geol. Soc. Am. Bull.*, 88, 711–719.

**Hunt**, E. (2006). Crustal Structure of the Ceara Rise, NE Brazil. *Master's thesis*, University of Durham, UK.

**Hutchinson**, D.A., Grow, J.A., Klitgord, K.D. & Swift, B.A. (1983). Deep structure and evolution of the Carolina trough. In: *Watkins, J.S. and Drake, C.L.* (eds.), *Studies in Continental Margin Geology,* American Association of Petroleum Geologists Memoirs, 129–152.

**IAG** Special Publication No. 3 (1971). *Geodetic Reference System 1967.* Central Bureau IAG; Paris, France.

**Jackson**, H.R., Faleide, J.I. & Eldholm, O. (1990). Crustal structure of the sheared Southwestern Barents Sea continental margin. *Mar. Geol.*, 93, 119–146.

**Jackson**, H.R., Reid, I. & Falconer, R.K.H. (1982). Crustal structure near the Arctic Mid-Ocean Ridge. *J. Geophys. Res.*, 87, 1773–1783.

**Johns**, W.E., Lee, T.N., Beardsley, R.C., Candela, J., Limeburner, R. & Castro, B. (1998). Annual cycle and variability of the North Brazil Current. *J. Phys. Oceanography*, 28(1), 103–128.

**Keen**, C.E., Kay, W.A. & Roest, W.R. (1990). Crustal anatomy of a transform continental margin. *Tectonophysics*, 173, 527–544.

**Keen**, C.E., Peddy, C., de Voogd, B. & Matthews, D. (1989). Conjugate margin of Canada and Europe: results from deep reflection profiling. *Geology*, 17, 173–176.

**Kent**, D.V., Honnerez, B.M., Opdyke, N.D. & Fox, P.J. (1978). Magnetic properties of dredged oceanic gabbros and the source of marine magnetic anomalies. *Geophys. J. R. Astr. Soc.*, 55, 513–537.

**Klingelhöfer**, F., Edwards, R.A., Hobbs, R.W. & England, R.W. (2005). Crustal structure of the NE Rockall Trough from wide-angle seismic data modelling. *J. Geophys. Res.*, 110, B11105, doi: 10.1029/2005JB003763.

**Korenaga**, J., Holbrook, W.S., Kent, G.M., Kelemen, P.B., Detrick, R.S., Larsen, H.-C., Hopper, J.R. & Dahl-Jensen, T. (2000). Crustal structure of the southeast Greenland margin from joint refraction and reflection seismic tomography. *J. Geophys. Res.*, 105(B9), 21591–21614.

**Krawczyk**, C.M. & Reston, T.J. (1995). Detachment faulting and continental breakup: The S reflector offshore Galicia. In: *Banda, E., Torné, M. and Talwani, M.* (eds.), *Rifted Ocean-Continent Boundaries, NATO-Workshop 1994*, 231–246. Kluwer, Dordrecht, Netherlands.

**Krawczyk**, C.M., Reston, T.J., Beslier, M.-O. & Boillot, G. (1996). Evidence for detachment tectonics on the Iberia Abyssal Plain rifted margin. *Proc. ODP, Sci. Results*, 149, 603–615.

**Kristoffersen**, Y., Husebye, E.S., Bungum, H. & Gregersen, S. (1982). Seismic investigation of the Nansen Ridge during the FRAM I experiment. *Tectonophysics*, 82, 57–68.

**Kumar**, N. & Embley, R.W. (1977). Evolution and origin of Ceara Rise: an aseismic rise in the western equatorial Atlantic. *Geol. Soc. Am. Bull.*, 88, 683–694.

**Kuo**, B.Y. & Forsyth, D.W. (1988). Gravity anomalies of the ridge-transform system in the South Atlantic between 31° and 34.5°S upwelling centres and variations in crustal thickness. *Mar. Geophys. Res.*, 10, 205–232.

**LASE Study Group**(1986). Deep structure of the US East Coast passive margin from large aperture seismic experiments (LASE). *Mar. Petr. Geol.*, 3, 234–242.

**Lau**, K.W.H., Louden, K.E., Funck, T., Tucholke, B.E., Holbrook, W.S., Hopper, J.R. & Larsen, H.C. (2006). Crustal structure across the Grand Banks-Newfoundland Basin Continental Margin – I. Results from a seismic refraction profile. *Geophys. J. Int.*, 167(1), 127–156.

**Le Pichon**, X. & Hayes, D. (1971). Marginal offsets, fracture zones and the early opening of the south Atlantic. *J. Geophys. Res.*, 76, 6283–6293.

**Lin**, J., Sibuet, J.-C., Srivastava, S. & Manatschal, G. (2005). Origin of deep-sea magnetic lineations: magnetized oceanic crust or serpentinized exhumed mantle. *EOS Trans. AGU*, Fall Meet. Suppl., Abstract GP33B–06.

**Lines**, L.R. & Ulrych, T.J. (1977). The old and the new in seismic deconvolution and wavelet estimation. *Geophys. Prosp.*, 25, 512–540.

**Lister**, G.S., Ethridge, M.A. & Symonds, P.A. (1986). Detachment faulting and the evolution of passive continental margins. *Geology*, 14, 246–250.

**Loncke**, L., Droz, L., Gaullier, V., Basile, C., Roest, W. & Patriat, M. (2006). Effect of structural inheritance on the distribution and importance of slope instabilities along a passive transform margin. the example of the French Guyana margin. *Geophys. Res. Abst.*, 8, EGU06–A–03803.

**Lorenzo**, J.M., Mutter, J.C., Larson, R.L. & the Northwest Australia Study Group(1991). Development of the continent-ocean transform boundary of the southern Exmouth Plateau. *Geology*, 19, 843–846.

**Lorenzo**, J.M. & Vera, E.E. (1992). Thermal Uplift and Erosion across the Continent-Ocean Transform Boundary of the Southern Exmouth Plateau. *Earth Planet. Sci. Lett.*, 108, 79–82.

**Lorenzo**, J.M. & Wessel, P. (1997). Flexure across a continent-ocean fracture zone: the northern Falkland/Malvinas Plateau, South Atlantic. *Geo. Mar. Letts.*, 17, 110–118.

**Louden**, K.E. & Chian, D. (1999). The deep structure of non-volcanic rifted continental margins. *Phil. Trans. R. Soc. London A*, 357, 767–805.

**Ludwig**, J.W., Nafe, J.E. & Drake, C.L. (1970). Seismic refraction. In: *Maxwell A.E.* (ed.), *The Sea*, 53–84. Wiley-Interscience.

**MacDonald**, K.C., Scheirer, D.S. & Carbotte, S.M. (1991). Mid-ocean ridges: Discontinuities, segments and giant cracks. *Science*, 253, 986–994.

**Malinverno**, A. (1991). Inverse square-root dependence of mid-ocean-ridge flank roughness on spreading rate. *Nature*, 352, 58–60.

**Mandea**, M. & Macmillan, S. (2000). International Geomagnetic Reference Field – the eighth generation. *Earth Plan. Space*, 52, 1119–1124.

**Mascle**, J. & Blarez, E. (1987). Evidence for transform margin evolution from the Ivory Coast-Ghana continental margin. *Nature*, 326, 378–381.

**Mascle**, J., Lohmann, P. & Clift, P. (1997). Development of a passive transform margin: Côte d'Ivoire-Ghana transform margin – ODP Leg 159 preliminary results. *Geo. Mar. Letts.*, 17(1), 4–11.

**Matveenkov**, V.V., Gorshkov, A.G., Popov, K.V. & Safroskin, V.Y. (1996). Magnetic properties of Gorringe ridge serpentinites. *Oceanology*, 35(5), 689–697.

**McElhinny**, M.W. (1973). *Paleomagnetism and plate tectonics*. Cambridge University Press.

**McKenzie**, D.P. (1978). Some remarks on the development of sedimentary basins. *Earth Planet. Sci. Lett.*, 40, 25–32.

**McKenzie**, D.P. & Bickle, M.J. (1988). The volume and composition of melt generated by extension of the lithosphere. *J. Petr.*, 29, 625–679.

**Mello**, M.R., Mosmann, R., Silva, S.R.P., Maciel, R.R. & Miranda, F.P. (2001). Foz do Amazonas area: The last frontier for elephant hydrocarbon accumulations in the South Atlantic realm. In: *Downey, M.W., Threet, J.C. and Morgan, W.A.* (eds.), *Petroleum provinces of the twenty-first century: AAPG Memoir 74*, 403–414.

**Minshull**, T.A. (1999). On the roughness of Mesozoic oceanic crust in the western North Atlantic. *Geophys. J. Int.*, 136, 286–290.

**Minshull**, T.A., Dean, S.M., White, R.S. & Whitmarsh, R.B. (2001). Anomalous melt production after continental breakup in the southern Iberia Abyssal Plain. In: *Wilson, R.C., Whitmarsh, R.B., Taylor, B. and Froitzheim, N.* (eds.), *Non-volcanic rifting of continental margins: a comparison of evidence from land and sea*, 537–550. London, UK, Geological Society of London, Geological Society London Special Publication 187.

**Minshull**, T.A., White, R.S., Mutter, J.C., Buhl, P., Detrick, R.S., Williams, C.A. & Morris, E. (1991). Crustal Structure at the Blake Spur Fracture Zone From Expanding Spread Profiles. *J. Geophys. Res.*, 96(B6), 9955–9984.

**Mjelde**, R., Raum, T., Myhren, B., Shimamura, H., Murai, Y., Takanami, T., Karpuz, R. & Næss, U. (2005). Continent-ocean transition on the Vøring Plateau, NE Atlantic, derived from densely sampled ocean bottom seismometer data. *J. Geophys. Res.*, 110, B05101, doi:10.1029/2004JB003026.

**Mohriak**, W.U., Hobbs, R. & Dewey, J.F. (1990). Basin-forming processes and the deep structure of the Campos basin, offshore Brazil. *Mar. Petr. Geol.*, 7, 94–122.

**Montadert**, L., Roberts, D.G., DeCharpal, D., Guennic, P. & Sibuet, J.-C. (1979). Rifting and subsidence of the northern continental margin of the Bay of Biscay. In: *Montadert, L. and Roberts, D.G.* (eds.), *Init. Repts. DSDP 48*, 1025–1060. Govt. Printing Office, Washington DC.

**Morgan**, J.V. (1988). Seismic studies over Continental Margins. *Ph.D. thesis*, University of Cambridge, UK.

**Morgan**, J.V. & Barton, P.J. (1990). A geophysical study of the Hatton Bank volcanic margin: a summary of the results from a combined seismic, gravity and magnetic experiment. *Tectonophysics*, 173, 517–526.

**Morgan**, J.V., Barton, P.J. & White, R.S. (1989). The Hatton Bank continental margin III, Structure from wide-angle OBS and multichannel seismic refraction profiles. *Geophys. J. Int.*, 98, 367–384.

**Moulin**, M. (2003). Etude géologique et Géophysique des marges continentals passives: example du Zaïre et de l'Angola. *Ph.D. thesis*, Université de Bretagne Occidentale, France.

**Muller**, M.R., Minshull, T.A. & White, R.S. (1995). Crustal structure at the very slow-spreading Southwest Indian Ridge. *Interridge News*, 4, 3–6.

**Müller**, R.D., Roest, W.R., Royer, J.-Y., Gahagan, L.M. & Sclater, J.G. (1997). Digital isochrons of the world's ocean floor. *J. Geophys. Res.*, 102(B2), 3211–3214.

**Mutter**, J.C. (1993). Margins declassified. *Nature*, 364, 393–394.

**Mutter**, J.C., Talwani, M. & Stoffa, P.L. (1982). Origin of Seaward-Dipping Reflectors in Oceanic Crust off the Norwegian Margin by "Sub-Aerial Seafloor Spreading". *Geology*, 10, 353–357.

**Mutter**, J.C., Talwani, M. & Stoffa, P.L. (1984). Evidence for a thick oceanic crust adjacent to the Norwegian margin. *J. Geophys. Res.*, 89, 483–502.

**Mutter**, J.C. & Zehnder, C.M. (1988). Deep Crustal Structure and Magmatic Processes: The inception of Seafloor Spreading in the Norwegian-Greenland Sea. In: *Morton, A.C. and Parson, L.M.* (eds.), *Early Tertiary Volcanism and the Opening of the NE Atlantic, Geological Society Special Publication 39*, 35–48.

**Nafe**, J.E. & Drake, C.L. (1957). Variation with depth in shallow and deep water marine sediments of porosity, density and the velocities of compressional and shear waves. *Geophysics*, 22(3), 523–552.

**Nicolas**, A. & Boudier, F. (1995). Mapping oceanic ridge segments in Oman ophiolite. *J. Geophys. Res.*, 100, 6179–6197.

**Nürnberg**, D. & Müller, R.D. (1991). The tectonic evolution of the South Atlantic from late Jurassic to present. *Tectonophysics*, 191, 27–53.

**Patriat**, P. & Achache, J. (1984). India-Eurasia collision chronology has implications for crustal shortening and driving mechanism of plates. *Nature*, 311, 615–621.

**Pearse**, S. (2002). Inversion and Modelling of Seismic Data to Assess the Evolution of the Rockall Trough. *Ph.D. thesis*, University of Cambridge, UK.

**Peddy**, C., Pinet, B., Masson, D.G., Scrutton, R., Sibuet, J.-C., Warner, M.R., Lefort, J.P. & Schroeder, I.J. (1989). Crustal structure of the Goban Spur continental margin, northeast Atlantic, from deep seismic reflection profiling. *J. Geol. Soc.*, 146, 427–437.

**Peirce**, C., Turner, I.M. & Sinha, M.C. (2001). Crustal structure, accretionary processes and rift propagation: a gravity study of the intermediate-spreading Valu Fa Ridge, Lau Basin. *Geophys. J. Int.*, 146, 53–73.

**Peirce**, C. & Watts, A.B. (2004). RRS *discovery* D275: Cruise Report, unpublished.

**Peirce**, C., Whitmarsh, R.B., Scrutton, R.A., Pontoise, B., Sage, F. & Mascle, J. (1996). Côte d'Ivoire-Ghana margin: seismic imaging of passive rifted crust adjacent to a transform continental margin. *Geophys. J. Int.*, 125, 781–795.

**Pereira da Siva**, S.R. (1989). Bacias da Foz do Amazonas e Para (Aguas Profundas): Une anlise sismoestratigrafica, tectonsedimentar e termica. *Proc. Conf. Braz. Geol. Soc.*, 2, 843–852.

**Pérez-Gussinyé**, M. & Reston, T.J. (2001). Rheological evolution during extension at passive non-volcanic margins: onset of serpentinization and development of detachments to continental break-up. *J. Geophys. Res.*, 106, 3691–3975.

**Pickup**, S.L., Wilson, R.C.L., Pena dos Reis, R., Whitmarsh, R.B. & Ribeiro, A. (1996). The western Iberia margin: A geophysical and geological overview. *Proc. ODP, Sci. Results 149*, 3–23.

**Pinheiro**, L.M., Whitmarsh, R.B. & Miles, P.R. (1992). The ocean-continent boundary off the western continental margin of Iberia II, Crustal structure in the Tagus Abyssal Plain. *Geophys. J. Int.*, 109, 106–124.

**Planke**, S. & Eldholm, O. (1994). Seismic response and construction of seaward dipping wedges of flood basalts. *J. Geophys. Res.*, 99, 9263–9278.

**Planke**, S., Symonds, P.A., Alvestad, E. & Skogseid, J. (2000). Seismic volcanostratigraphy of large-volume basaltic extrusive complexes on rifted margins. *J. Geophys. Res.*, 105(B8), 19335–19351.

**Pollack**, H.N., Hurter, S.J. & Johnson, J.R. (1993). Heat flow from the Earth's interior: Analysis of the global data set. *Rev. Geophys.*, 31, 267–280.

**Rabinowitz**, P.D. & LaBrecque, J.L. (1979). The Mesozoic South Atlantic Ocean and evolution of its continental margins. *J. Geophys. Res.*, 84, 5973–6002.

**Raitt**, R.W. (1963). The crustal rocks. In: *Hill, M.N.* (ed.), *The Sea vol. 3*, 85–102. Wiley (Interscience), New York.

**Reid**, I. & Jackson, H.R. (1981). Oceanic spreading rate and crustal thickness. *Mar. Geophys. Res.*, 5, 165–172.

**Reid**, I.D. (1994). Crustal structure of a nonvolcanic rifted margin east of Newfoundland. *J. Geophys. Res.*, 99(B8), 15161–15180.

**Reston**, T.J. (1996). The S reflector west of Galicia: the seismic structure of a detachment fault. *Geophys. J. Int.*, 127, 230–244.

**Rodger**, M. (2007). A marine geophysical study of the continental margin offshore north eastern Brazil. *Ph.D. thesis*, University of Oxford, UK, in prep.

**Rodger**, M., Watts, A.B., Greenroyd, C.J., Peirce, C. & Hobbs, R.W. (2006). Evidence for unusually thin oceanic crust and strong mantle beneath the Amazon Fan. *Geology*, 34(12), 1081–1084, doi:10.1130/G22966A.1.

**Russell**, S.M. (1999). A magnetic study of the West Iberia and conjugate rifted continental margins: constraints on rift-to-drift processes. *Ph.D. thesis*, University of Durham, UK.

**Russell**, S.M. & Whitmarsh, R.B. (2003). Magmatism at the west Iberia non-volcanic rifted continental margin: evidence from analyses of magnetic anomalies. *Geophys. J. Int.*, 154, 706–730.

**Sandwell**, D.T. & Smith, W.H.F. (1997). Marine gravity anomaly from Geosat and ERS-1 satellite altimetry. *J. Geophys. Res.*, 102(B5), 10039–10054.

**Sandwell**, D.T., Yale, M. & Smith, W.H.F. (1994). ERS-1 Geodetic mission reveals detailed tectonic structures. *EOS Trans. AGU*, 75, 155.

**Scrutton**, R.A. (1979). On sheared passive continental margins. *Tectonophysics*, 59, 293–305.

**Sempéré**, J.-C., Lin, J., Brown, H.S., Schouten, H. & Purdy, G.M. (1993). Segmentation and morphotectonic variations along a slow-spreading center: The Mid-Atlantic Ridge (24°00′N - 30°40′N). *Mar. Geophys. Res.*, 15, 153–200.

**Sheridan**, R.E., Musser, D.L., Glover III, L., Talwani, M., Ewing, J., Holbrook, W.S., Purdy, G.M., Hawman, R. & Smithson, S. (1993). Deep seismic reflection data of EDGE U.S. Mid-Atlantic continental margin experiment: Implications for Appalachian sutures and Mesozoic rifting and magmatic underplating. *Geology*, 21, 563–567.

**Shiobara**, H., Nakanishi, A., Shimamura, H., Mjelde, R., Kanazawa, T. & Berg, E.W. (1997). Precise positioning of ocean bottom seismometer by using acoustic transponder and CTD. *Mar. Geophys. Res.*, 19, 199–209.

**Shuey**, R.T. & Pasquale, A.S. (1973). End corrections in magnetic profile interpretation. *Geophysics*, 38, 507–512.

**Sibuet**, J.-C., Louvel, V., Whitmarsh, R.B., White, R.S., Horsefield, S.J., Sichler, B., Leon, P. & Recq, M. (1995). Constraints on rifting processes from refraction and deep-tow magnetic data: the example of the Galicia continental margin (West Iberia). In: *Banda, E., Torné, M. & Talwani, M.* (eds.), *Rifted ocean-continent boundaries*, 197–218. Amsterdam: Kluwer.

**Silva**, S.R.P., Maciel, R.R. & Severino, M.C.G. (1999). Cenozoic tectonics of Amazon Mouth Basin. *Geo. Mar. Letts.*, 18, 256–262.

**Sleep**, N.H. (1971). Thermal effects of the formation of Atlantic continental margins by continental break-up. *Geophys. J. R. Astr. Soc.*, 24, 325–350.

**Small**, C. (1994). A quantitative analysis of mid-ocean ridge axial topography. *Geophys. J. Int.*, 116, 64–84.

**Smith**, G.M. & Banerjee, S.K. (1986). Magnetic structure of the upper kilometer of the marine crust at Deep Sea Drilling Project hole 504B, Eastern Pacific Ocean. *J. Geophys. Res.*, 91, 10337–10354.

**Spudich**, P. & Orcutt, J. (1980). A new look at the seismic velocity structure of the oceanic crust. *Rev. Geophys.*, 18, 627–645.

**Srivastava**, S.P. & Roest, W.R. (1999). Extent of oceanic crust in the Labrador Sea. *Mar. Petr. Geol.*, 16, 65–84.

**Srivastava**, S.P., Sibuet, J.-C., Cande, S., Roest, W.R. & Reid, I.R. (2000). Magnetic evidence for slow seafloor spreading during the formation of the Newfoundland and Iberian margins. *Earth Planet. Sci. Lett.*, 182, 61–76.

**Stroup**, J.B. & Fox, P.J. (1981). Geologic investigations in the Cayman Trough: Evidence for thin oceanic crust along the mid-Cayman rise. *J. Geol*, 89, 395–420.

**Su**, W., Mutter, C.Z., Mutter, J.C. & Buck, R. (1994). Some theoretical predictions on the relationship among spreading rate, mantle temperature and crustal thickness. *J. Geophys. Res.*, 99, 3215–3227.

**Supko**, P.R. & Perch-Nielson, K. (1977). *Init. Repts. DSDP 39*. Washington (U.S. Govt. Printing Office).

**Talwani**, M. & Abreu, V. (2000). Inferences regarding initiation of oceanic crust formation from the US east coast margin and conjugate south Atlantic margins. In: *Mohriak, W. and Talwani, M.* (eds.), *Atlantic rifts and continental margins*, 211–233. American geophysical Union, Geophysical Monograph 155, Washington DC.

**Talwani**, M., Worzel, J.L. & Landisman, M. (1959). Rapid gravity computations for two-dimensional bodies with application to the Mendocino submarine fracture zone. *J. Geophys. Res.*, 64, 49–59.

**Tarantola**, A. (2005). *Inverse Problem Theory and Methods for Model Parameter Estimation*. SIAM.

**Thinon**, I., Fidalgo-González, L., Réhault, J.-P. & Olivet, J.-L. (2001). Déformations pyrénéennes dans le Golfe de Gasgoigne [Pyrenean deformations in the Bay of Biscay]. *C. R. Acad. Sci., Paris*, 332, 561–568.

**Todd**, B.J. & Keen, C.E. (1989). Temperature effects and their geological consequences at transform margins. *Can. J. Earth Sci.*, 26, 2591–2603.

**Todd**, B.J., Reid, I. & Keen, C. (1988). Crustal structure across the southwest Newfoundland transform margin. *Can. J. Earth Sci.*, 25, 744–759.

**Tréhu**, A.M., Ballard, A., Dorman, L.M., Gettrust, J.F., Klitgord, K.D. & Schreiner, A. (1989). Structure of the lower crust beneath the Carolina Trough, U.S. Atlantic continental margin. *J. Geophys. Res.*, 94, 10585–10600.

**Trinks**, I. (2003). Traveltime tomography of densely sampled seismic data. *Ph.D. thesis*, University of Cambridge, UK.

**Tucholke**, B.E. & Lin, J. (1994). A geological model for the structure of ridge segments in slow spreading ocean crust. *J. Geophys. Res.*, 99(B6), 11937–11958.

**Turner**, I.M., Peirce, C. & Sinha, M.C. (1999). Seismic imaging of the axial region of the Valu Fa Ridge, Lau Basin – the accretionary processes of an intermediate back-arc spreading ridge. *Geophys. J. Int.*, 138, 495–519.

**Turner**, J.P., Rosendahl, B.R. & Wilson, P.G. (2003). Structure and evolution of an obliquely sheared continental margin: Rio Muni, West Africa. *Tectonophysics*, 374, 41–55.

**Unternehr**, P., Curie, D., Olivet, J.L., Goslin, J. & Beuzart, P. (1988). South Atlantic fits and intraplate boundaries in Africa and South America. *Tectonophysics*, 155, 169–179.

**Voicu**, G., Bardoux, M. & Stevenson, R. (2001). Lithostratigraphy, geochronology and gold metallogeny in the northern Guiana Shield, South America: a review. *Ore Geology Rev.*, 18, 211–236.

**Watts**, A.B. (1988). Gravity anomalies, crustal structure and flexure of the lithosphere at the Baltimore Canyon Trough. *Earth Planet. Sci. Lett.*, 89, 221–238.

**Watts**, A.B. & Fairhead, J.D. (1997). Gravity anomalies and magmatism along the western continental margin of the British Isles. *J. Geol. Soc. London*, 154, 523–529.

**Watts**, A.B. & Marr, C. (1995). Gravity anomalies and the thermal and mechanical structure of rifted continental margins. In: *Banda, E. et al.* (eds.) *Rifted ocean-continent boundaries*, 65–94. Kluwer, Dordrecht.

**Watts**, A.B. & Stewart, J. (1998). Gravity anomalies and segmentation of the continental margin offshore West Africa. *Earth Planet. Sci. Lett.*, 156, 239–252.

**Watts**, A.B. & Torné, M. (1992). Subsidence History, Crustal Structure and Thermal Evolution of the Valencia Trough: a young extensional basin in the western Mediterranean. *J. Geophys. Res.*, 97, 13919–13950.

**Weigelt**, E. & Jokat, W. (2001). Peculiarities of roughness and thickness of oceanic crust in the Eurasian Basin, Arctic Ocean. *Geophys. J. Int.*, 145, 505–516.

**Wernicke**, B. (1985). Uniform-sense normal simple shear of the continental lithosphere. *Can. J. Earth Sci.*, 22, 108–125.

**Wessel**, P. & Smith, W.H.F. (1991). Free software helps map and display data. *EOS Trans. AGU*, 72(41), 441, 445–446.

**Wessel**, P. & Smith, W.H.F. (1998). New, improved version of the Generic Mapping Tools released. *EOS Trans. AGU*, 79(47), 579.

**White**, R.S. (1979). Oceanic upper crustal structure from variable angle seismic reflection-refraction profiles. *Geophys. J. R. Astr. Soc.*, 57, 683–726.

**White**, R.S. (1984). Atlantic Ocean crust: seismic structure of a slow spreading ridge. In: *Gass, I.G. and Lippard, S.J. and Shelton, A.N.* (eds.), *Ophiolites and Oceanic Lithosphere*, 13, 34–44. Spec. Publ. Geol. Soc. Lond.

**White**, R.S. (1992). Crustal structure of North Atlantic continental margins. *J. Geol. Soc. London*, 149, 841–854.

**White**, R.S., Christie, P.A.F., Kusznir, N.J., Roberts, A., Davies, A., Hurst, N., Lunnon, Z., Parkin, C.J., Roberts, A.W., Smith, L.K., Spitzer, R., Surendra, A. & Tymms, V. (2002). iSIMM pushes frontiers of marine seismic acquisition. *First Break*, 20, 782–786.

**White**, R.S., Detrick, R.S., Sinha, M.C. & Cormier, M.H. (1984). Anomalous seismic crustal structure of oceanic fracture zones. *Geophys. J. R. Astr. Soc.*, 79, 779–798.

**White**, R.S. & McKenzie, D.P. (1989). Magmatism at rift zones: the generation of volcanic continental margins and flood basalts. *J. Geophys. Res.*, 94, 7685–7729.

**White**, R.S., McKenzie, D.P. & O'Nions, R.K. (1992). Oceanic crustal thickness from seismic measurements and rare earth element inversions. *J. Geophys. Res.*, 97, 439–467.

**White**, R.S., Spence, G.D., Fowler, S.R., McKenzie, D.P., Westbrook, G.K. & Bowen, A.N. (1987). Magmatism at rifted continental margins. *Nature*, 330, 439–444.

**Whitmarsh**, R.B. & Miles, P.R. (1995). Models of the development of the West Iberia rifted continental margin at 40°30′N deduced from surface and deep-tow magnetic anomalies. *J. Geophys. Res.*, 100, 3789–3806.

**Whitmarsh**, R.B., Miles, P.R. & Mauffret, A. (1990). The ocean-continent boundary off the western continental margin of Iberia, I, Crustal structure at 40°30′N. *Geophys. J. Int.*, 103, 509–531.

**Whitmarsh**, R.B., Pinheiro, L.M., Miles, P.R., Recq, M. & Sibuet, J.-C. (1993). Thin crust at the western Iberia ocean-continent transition and ophiolites. *Tectonophysics*, 12, 1230–1239.

**Whitmarsh**, R.B. & Wallace, P.J. (2001). The rift-to-drift development of the west Iberia nonvolcanic continental margin: a summary and review of the contribution of Ocean Drilling Program Leg 173. In: *Beslier, M.O., Whitmarsh, R.B., Wallace, P.J., & Girardeau, J.* (eds.), *Proc. ODP, Sci. Results*, 173, 1–36. Ocean Drilling Program, College Station, Texas.

**Whitmarsh**, R.B., White, R.S., Horsefield, S.J., Sibuet, J.-C., Recq, M. & Louvel, V. (1996). The ocean-continent boundary off the western continental margin of Iberia: crustal structure of Galicia Bank. *J. Geophys. Res.*, 101(B12), 28291–28314.

**Wilson**, D. (2006). The deep crustal structure of the northeast Brazilian passive continental margin determined using seismic refraction modelling over the Amazon Cone. *Master's thesis*, Durham University, UK.

**Wilson**, P.G., Turner, J.P. & Westbrook, G.K. (2003). Structural architecture of the ocean-continent boundary at an oblique transform margin through deep-imaging seismic interpretation and gravity modeling: Equatorial Guinea, West Africa. *Tectonophysics*, 374, 19–40.

**Woollard**, G.P. (1979). The new gravity system – changes in international gravity base values and anomaly values. *Geophysics*, 44, 1352–1366.

**Wu**, Y., Louden, K.E., Funck, T., Jackson, H.R. & Dehler, S.A. (2006). Crustal structure of the central Nova Scotia margin off Eastern Canada. *Geophys. J. Int.*, 166, 878–906.

**Wyer**, P. & Watts, A.B. (2006). Gravity anomalies and segmentation at the East Coast USA continental margin. *Geophys. J. Int.*, 166, 1015–1038.

**Young**, C.J. (1992). Tectonic evolution of the southern African passive margin. *Ph.D. thesis*, University of Leeds, UK.

**Zelt**, C.A. (1999). Modelling strategies and model assessment for wide-angle seismic traveltime data. *Geophys. J. Int.*, 139, 183–204.

**Zelt**, C.A. & Barton, P.J. (1998). Three-dimensional seismic refraction tomography: A comparison of two methods applied to data from the Faeroe Basin. *J. Geophys. Res.*, 108, 7187–7210.

**Zelt**, C.A. & Smith, R.B. (1992). Seismic Traveltime Inversion for 2-D Crustal Velocity Structure. *Geophys. J. Int.*, 108, 16–34.

# Appendices

## A Seismic acquisition parameters

Tables A.1 to A.5 contain a summary of the profiles acquired as part of the ACE, in addition to MCS and WA acquisition details.

| Seismic profile | Start of shooting | | | End of shooting | | | Total shots | Shooting direction | Profile length | OBS/ OBHs | Land stations |
|---|---|---|---|---|---|---|---|---|---|---|---|
| | Location | Time | Shot | Location | Time | Shot | | | | | |
| A | 7.6407°N 49.6846°W | 307:21:07:32 | 1001 | 5.7205°N 51.6208°W | 309:08:21:06 | 4171 | 3171 | NE-SW | 302.09 | 20 | 5 |
| A$^+$ | 7.6054°N 50.1543°W | 308:04:47:09 | 1690 | 5.7205°N 51.6208°W | 309:08:21:06 | 4171 | 2482 | NE-SW | 264.58 | 19 | 5 |
| B | 4.3030°N 47.8154°W | 323:03:44:25 | 996 | 6.5734°N 45.2760°W | 325:02:29:39 | 5204 | 4209 | SW-NE | 377.56 | 18 | - |
| D | 9.9896°N 52.3556°W | 313:14:05:42 | 1015 | 6.6006°N 53.5795°W | 315:14:59:44 | 5416 | 4402 | NE-SW | 400.01 | 20 | 4 |
| D$^+$ | 9.7817°N 52.1110°W | 313:18:16:30 | 1391 | 6.6006°N 53.5795°W | 315:14:59:44 | 5416 | 4026 | NE-SW | 388.89 | 20 | 2 |
| E | 1.8884°N 45.0996°W | 303:15:58:25 | 1 | 3.8316°N 47.5928°W | 304:10:10:27 | 1638 | 1638 | S-N | 350.98 | - | - |
| F | 4.5384°N 45.4317°W | 327:16:09:09 | 971 | 4.3023°N 47.7670°W | 329:00:13:45 | 3857 | 2887 | E-W | 260.06 | 8 | - |
| G | 3.6520°N 44.1510°W | 331:12:52:06 | 971 | 4.7400°N 42.7255°W | 332:05:00:00 | 2423 | 1453 | SW-NE | 198.93 | 6 | - |
| G | 4.6420°N 42.6788°W | 332:08:50:00 | 2766 | 4.5219°N 44.5333°W | 333:18:05:20 | 5760 | 2995 | E-W | 205.85 | 6 | - |

**Table A.1**: Summary of MCS and WA seismic data profiles acquired during ACE cruise D275. Profiles marked $^+$ are the 'on-line' limits of the data used for MCS and WA processing and modelling. Only the OBS/OBH and land station instruments that successfully acquired WA data are shown for these profiles. Times are given in Julian day:hour:minute:second.

| Parameter | Value |
|---|---|
| Energy source | Airguns |
| Number of guns | 14 |
| Total volume | 6520 $in^3$ |
| Shot point time interval | 40 s |
| Shot point distance interval | ~85-110 m |
| Source depth | ~17 m |
| Receiver depth | ~10 m |
| Number of receiver groups | 96 |
| Group interval | 25 m |
| Near trace offset | 242.5 m |
| Far trace offset | 2617.5 m |
| Active streamer length | 2400 m |
| CMP interval | 25 m |
| Shot to CMP ratio | ~4 |
| Fold of coverage | ~24 |
| Sample interval | 4 ms |
| Record length | 20 s |

**Table A.2**: Key MCS acquisition parameters for ACE cruise D275.

| OBS/H number | Deployment location | | Relocated position | | Depth (km) | Offset along profile (km) | Instrument Type | Sampling rate (Hz) |
|---|---|---|---|---|---|---|---|---|
| | Latitude (°N) | Longitude (°W) | Latitude (°N) | Longitude (°W) | | | | |
| A1 | 5.9510 | 51.4440 | 5.9501 | 51.4429 | 1.464 | 193.627 | OBS Klapp | 250 |
| A2 | 6.0220 | 51.3860 | 6.0226 | 51.3867 | 2.009 | 203.795 | OBS Neu | 250 |
| A3 | 6.0930 | 51.3310 | 6.0935 | 51.3317 | 2.413 | 213.761 | OBS Klapp | 250 |
| A4 | 6.1650 | 51.2770 | 6.1646 | 51.2765 | 2.677 | 223.747 | OBH | 200 |
| A5 | 6.2370 | 51.2200 | 6.2372 | 51.2202 | 2.840 | 233.934 | OBS Neu | 250 |
| A6 | 6.3080 | 51.1640 | 6.3086 | 51.1648 | 3.027 | 243.966 | OBS Klapp | 250 |
| A7 | 6.3780 | 51.1090 | 6.3789 | 51.1102 | 3.189 | 253.842 | OBH | 200 |
| A8 | 6.4480 | 51.0550 | 6.4487 | 51.0559 | 3.383 | 263.649 | OBS Klapp | 250 |
| A9 | 6.5270 | 50.9960 | 6.5266 | 50.9954 | 3.480 | 274.586 | OBS Neu | 250 |
| A10 | 6.5910 | 50.9440 | 6.5916 | 50.9448 | 3.581 | 283.729 | OBS Klapp | 250 |
| A11 | 6.6620 | 50.8880 | 6.6630 | 50.8893 | 3.684 | 293.759 | OBH | 200 |
| A12 | 6.7330 | 50.8320 | 6.7344 | 50.8338 | 3.780 | 303.787 | OBS Klapp | 250 |
| A13 | 6.8040 | 50.7760 | 6.8057 | 50.7783 | 3.889 | 313.815 | OBH | 200 |
| A14 | 6.8760 | 50.7220 | 6.8767 | 50.7230 | 3.946 | 323.795 | OBS Neu | 250 |
| A15 | 6.9460 | 50.6670 | 6.9470 | 50.6683 | 4.022 | 333.667 | OBS Klapp | 250 |
| A16 | 7.0180 | 50.6110 | 7.0189 | 50.6122 | 4.097 | 343.781 | OBS Neu | 250 |
| A17 | 7.0890 | 50.5560 | 7.0898 | 50.5570 | 4.152 | 353.739 | OBH | 200 |
| A18 | 7.1600 | 50.5000 | 7.1611 | 50.5014 | 4.159 | 363.764 | OBS Klapp | 250 |
| A19 | 7.2310 | 50.4440 | 7.2324 | 50.4458 | 4.186 | 373.789 | OBH | 200 |
| A20 | 7.3020 | 50.3880 | 7.3036 | 50.3901 | 4.205 | 383.813 | OBS Klapp | 250 |

**Table A.3**: OBS locations for ACE Profile A.

| OBS/H number | Deployment location | | Relocated position | | Depth (km) | Offset along profile (km) | Instrument Type | Sampling rate (Hz) |
|---|---|---|---|---|---|---|---|---|
| | Latitude (°N) | Longitude (°W) | Latitude (°N) | Longitude (°W) | | | | |
| D1 | 7.7108 | 53.0707 | 7.7106 | 53.0700 | 1.104 | 278.880 | OBS Klapp | 250 |
| D2 | 7.7920 | 53.0340 | 7.7910 | 53.0330 | 1.215 | 288.703 | OBH | 200 |
| D3 | 7.8740 | 52.9960 | 7.8731 | 52.9951 | 1.230 | 298.746 | OBS Klapp | 250 |
| D4 | 7.9550 | 52.9577 | 7.9552 | 52.9573 | 1.256 | 308.776 | OBH | 200 |
| D5 | 8.0372 | 52.9205 | 8.0363 | 52.9199 | 1.373 | 318.697 | OBS Klapp | 250 |
| D6 | 8.1195 | 52.8825 | 8.1183 | 52.8821 | 1.658 | 328.720 | OBH | 200 |
| D7 | 8.2010 | 52.8448 | 8.2006 | 52.8441 | 2.101 | 338.776 | OBS Klapp | 250 |
| D8 | 8.2830 | 52.8060 | 8.2813 | 52.8069 | 2.497 | 348.645 | OBH | 200 |
| D9 | 8.3646 | 52.7695 | 8.3626 | 52.7693 | 2.909 | 358.582 | OBS Klapp | 250 |
| D10 | 8.4462 | 52.7321 | 8.4443 | 52.7316 | 3.383 | 368.565 | OBH | 200 |
| D11 | 8.5282 | 52.6937 | 8.5256 | 52.6940 | 3.533 | 378.508 | OBS Klapp | 250 |
| D12 | 8.6098 | 52.6557 | 8.6077 | 52.6560 | 4.679 | 388.543 | OBH | 200 |
| D13 | 8.6917 | 52.6170 | 8.6887 | 52.6186 | 4.655 | 398.450 | OBS Klapp | 250 |
| D14 | 8.7733 | 52.5805 | 8.7715 | 52.5802 | 4.609 | 408.574 | OBH | 200 |
| D15 | 8.8547 | 52.5429 | 8.8525 | 52.5427 | 4.607 | 418.478 | OBS Klapp | 250 |
| D16 | 8.9367 | 52.5046 | 8.9343 | 52.5048 | 4.630 | 428.481 | OBH | 200 |
| D17 | 9.0185 | 52.4668 | 9.0164 | 52.4667 | 4.664 | 438.529 | OBS Klapp | 250 |
| D18 | 9.1000 | 52.4294 | 9.0974 | 52.4292 | 4.697 | 448.429 | OBH | 200 |
| D19 | 9.1815 | 52.3913 | 9.1788 | 52.3914 | 4.725 | 458.385 | OBS Klapp | 250 |
| D20 | 9.2634 | 52.3527 | 9.2609 | 52.3533 | 4.754 | 468.429 | OBH | 200 |

**Table A.4**: OBS locations for ACE Profile D.

| OBS/H number | Deployment location | | Relocated position | | GPS elevation (m) | Offset along profile (km) | Instrument Type | Sampling rate (Hz) |
|---|---|---|---|---|---|---|---|---|
| | Latitude (°N) | Longitude (°W) | Latitude (°N) | Longitude (°W) | | | | |
| A21 | 4.9019 | 52.2657 | 4.8960 | 52.2580 | 14 | 45.703 | SEIS-UK 6TD | 100 |
| A22 | 4.8147 | 52.3377 | 4.8066 | 52.3270 | 14 | 33.161 | SEIS-UK 6TD | 100 |
| A23 | 4.7127 | 52.3871 | 4.7187 | 52.3948 | 20 | 20.830 | SEIS-UK 6TD | 100 |
| A24 | 4.6686 | 52.4400 | 4.6655 | 52.4359 | 25 | 13.370 | SEIS-UK 6TD | 100 |
| A25 | 4.5517 | 52.4853 | 4.5701 | 52.5094 | 9 | 0.000 | SEIS-UK 6TD | 100 |
| D21 | 5.7452 | 53.9359 | 5.5786 | 53.9645 | 14 | 40.363 | SEIS-UK 6TD | 100 |
| D22 | 5.5338 | 53.9471 | 5.5786 | 54.0464 | 12 | 18.446 | SEIS-UK 6TD | 100 |
| D23 | 5.4867 | 54.0410 | 5.5044 | 54.0802 | 37 | 9.382 | SEIS-UK 6TD | 100 |
| D24 | 5.4118 | 54.0803 | 5.4276 | 54.1152 | 5 | 0.000 | SEIS-UK 6TD | 100 |

**Table A.5**: Land station locations for ACE Profiles A and D.

# B Final MCS sections

The final processed MCS data for Profiles A and D, described in Chapter 2 and shown in Figures 2.16 and 2.17, are enclosed as large fold-out sections. These sections are plotted at the same scale to enable direct comparison between the two.

# C Wide-angle seismic dataset and modelling

WA seismic data are reproduced in Figures C.1 to C.39, with phases annotated and the associated ray-trace modelling of arrivals shown. Figures C.1 to C.19 show Profile A OBSs A1 to A20. OBS A8 is not shown as no shot data were recorded. Figures C.20 to C.24 show Profile A land station data. Similarly, Profile D OBSs and land stations are shown in Figures C.25 to C.44 and C.45 to C.46 respectively.

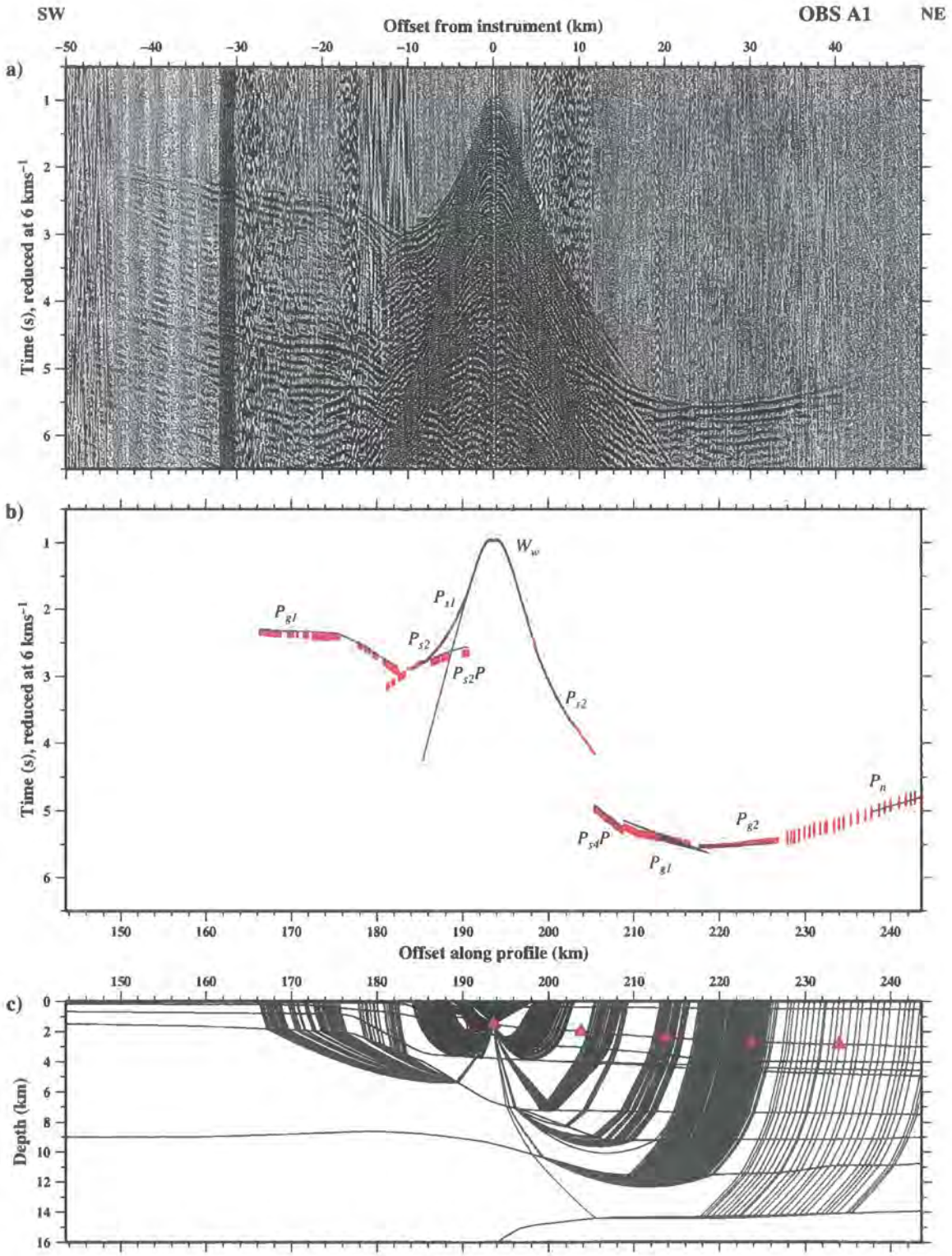


**Figure C.1**: Ray-trace modelling of vertical component geophone data recorded at OBS A1. See Figure 2.2 for instrument location. (Top) Filtered record section plotted at true amplitude. The horizontal axis shows offset from the instrument position. (Middle) Record section showing observed (red vertical bars whose length represents the assigned picking error) and calculated (blue lines) traveltime picks for comparison. For this, and the ray diagram (bottom), the horizontal axis shows model offset along Profile A. Phases are labelled as described in Section 3.4.1. (Bottom) Ray diagram showing modelled arrivals. Red triangles show OBS locations. Both record sections are plotted at a reduction velocity of 6 kms$^{-1}$ and are plotted at the same horizontal scale with each part aligned to the instrument position.

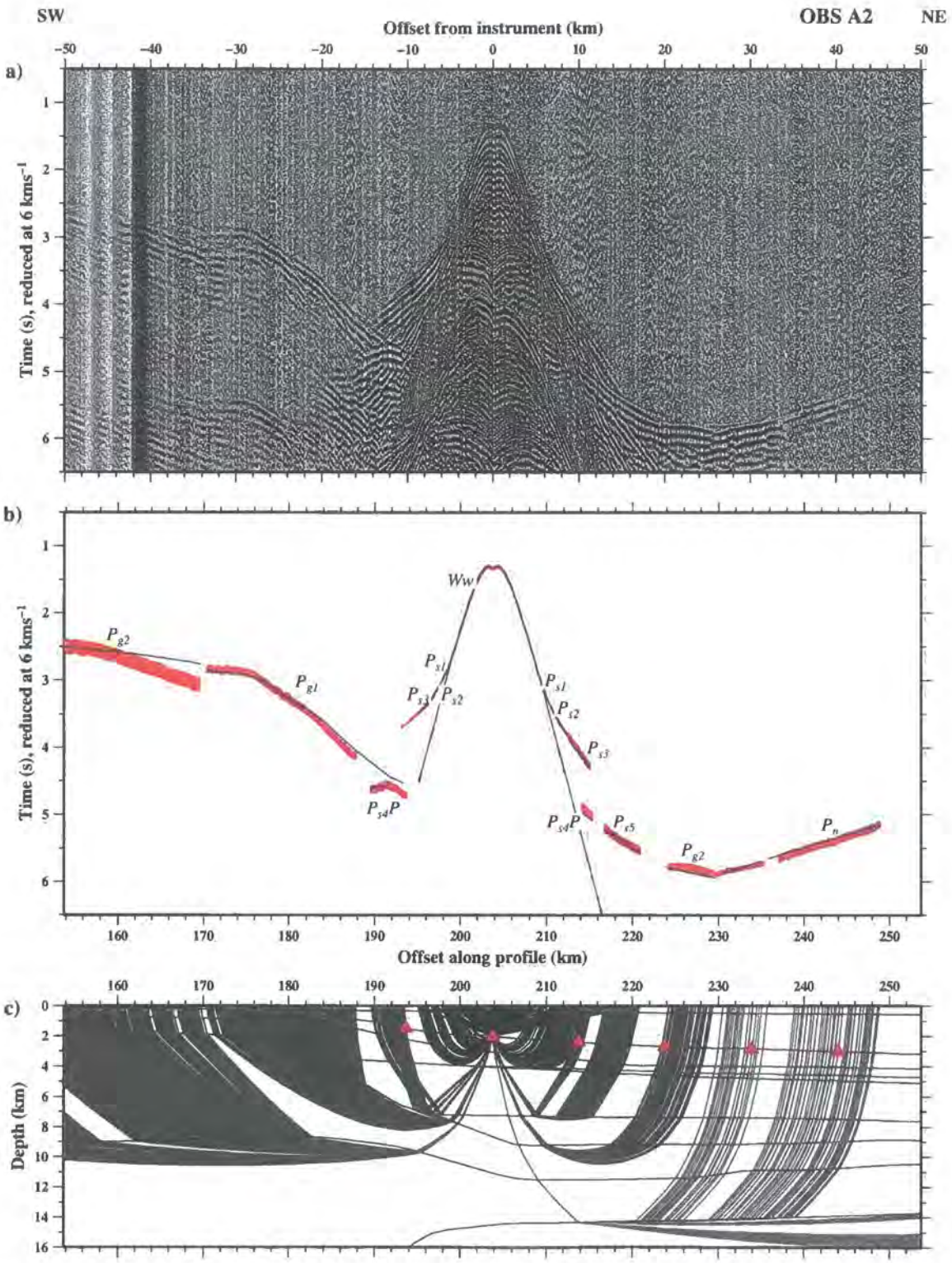


**Figure C.2**: Ray-trace modelling of hydrophone data recorded at OBS A2. See Figure 2.2 for instrument location. See Figure C.1 for details.

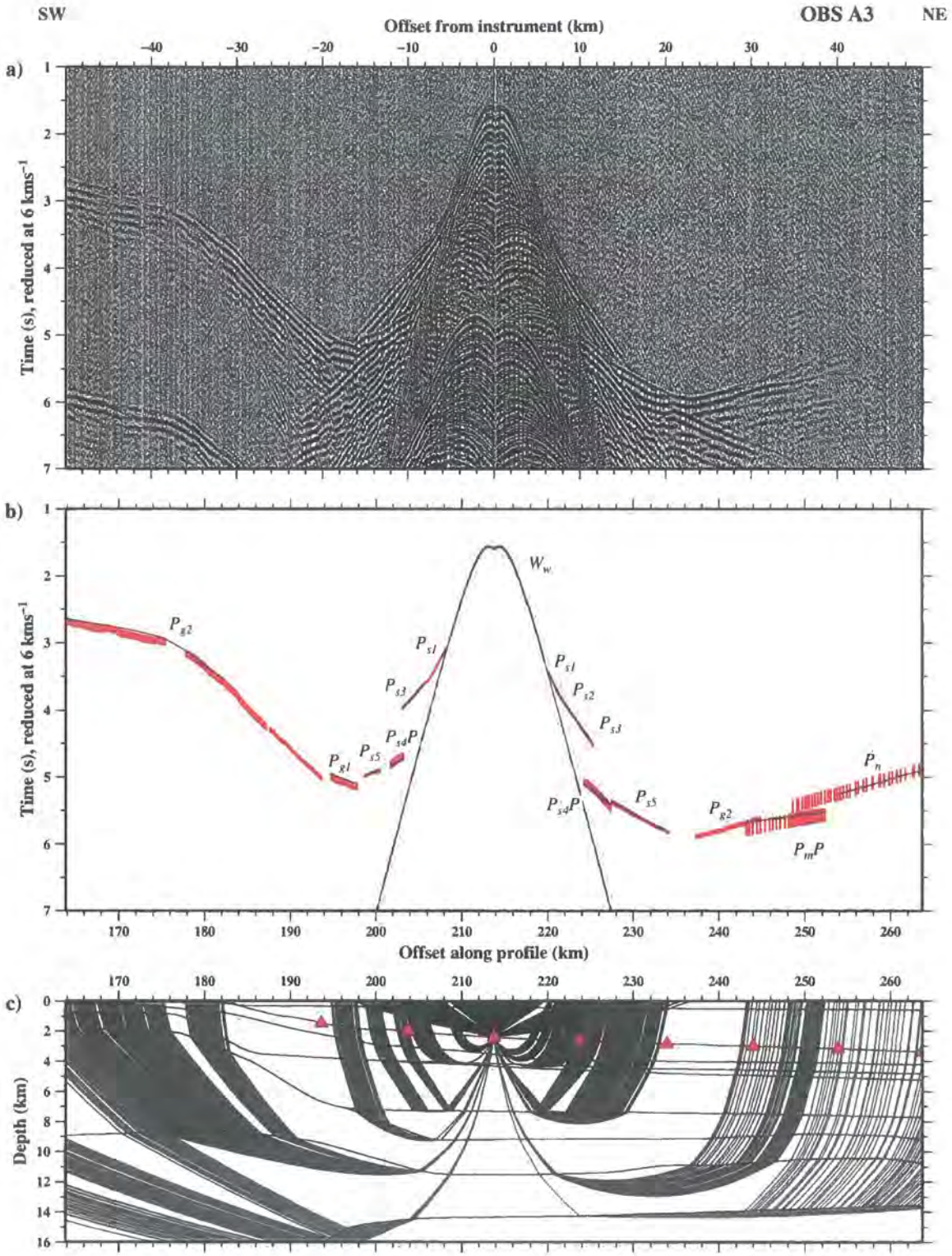


**Figure C.3**: Ray-trace modelling of hydrophone data recorded at OBS A3. See Figure 2.2 for instrument location. See Figure C.1 for details.

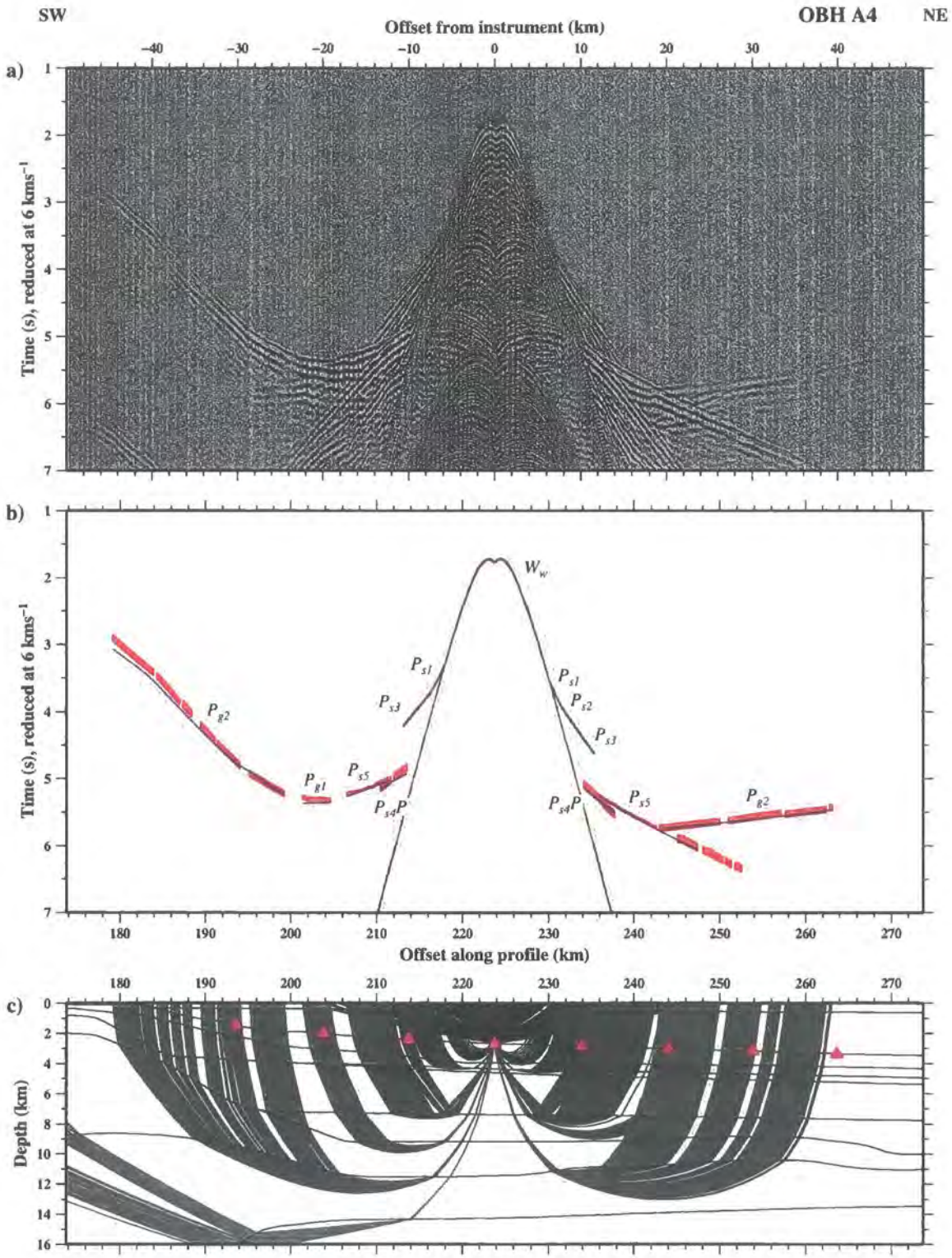


**Figure C.4**: Ray-trace modelling of hydrophone data recorded at OBS A4. See Figure 2.2 for instrument location. See Figure C.1 for details.

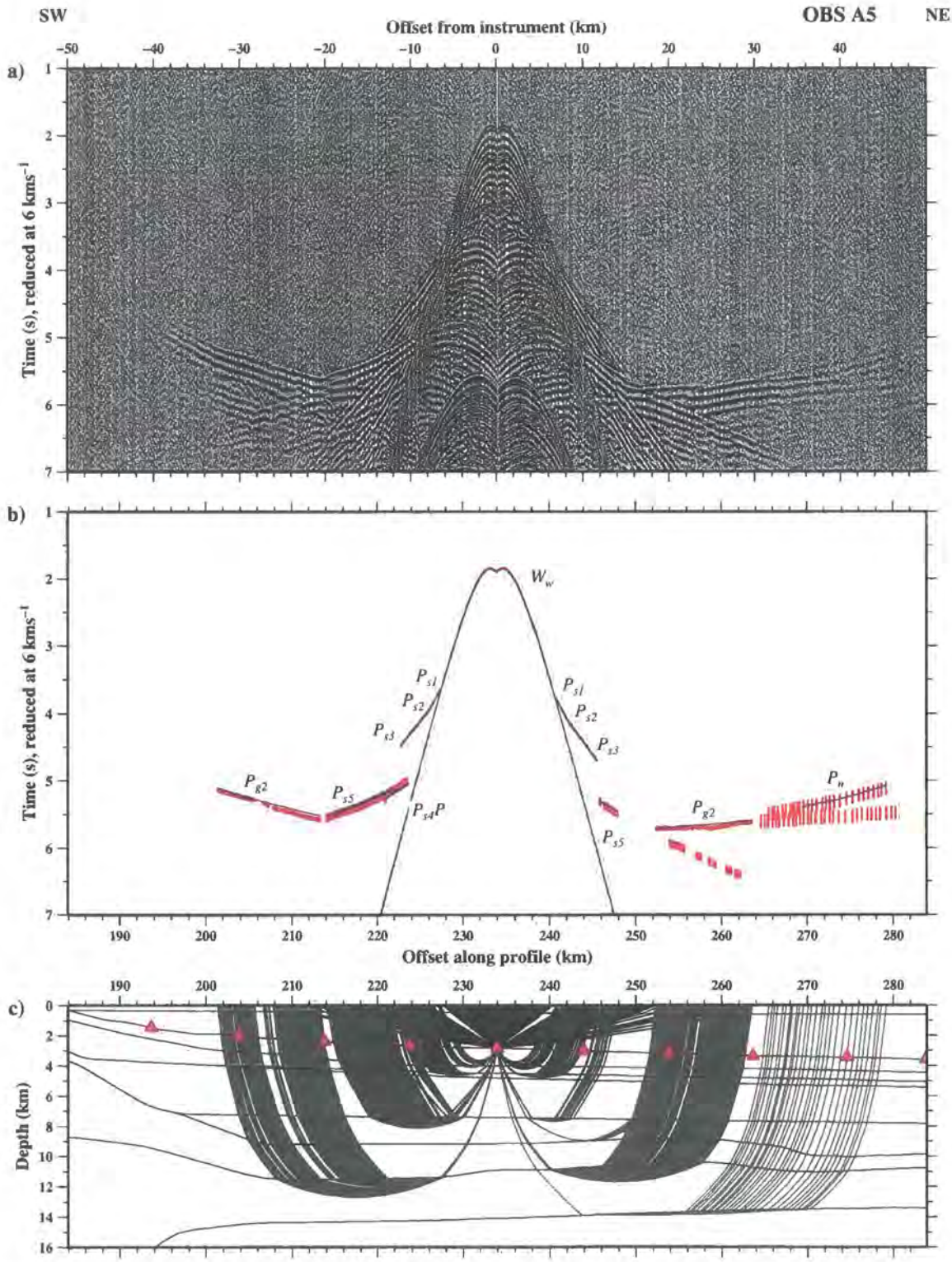


**Figure C.5**: Ray-trace modelling of hydrophone data recorded at OBS A5. See Figure 2.2 for instrument location. See Figure C.1 for details.

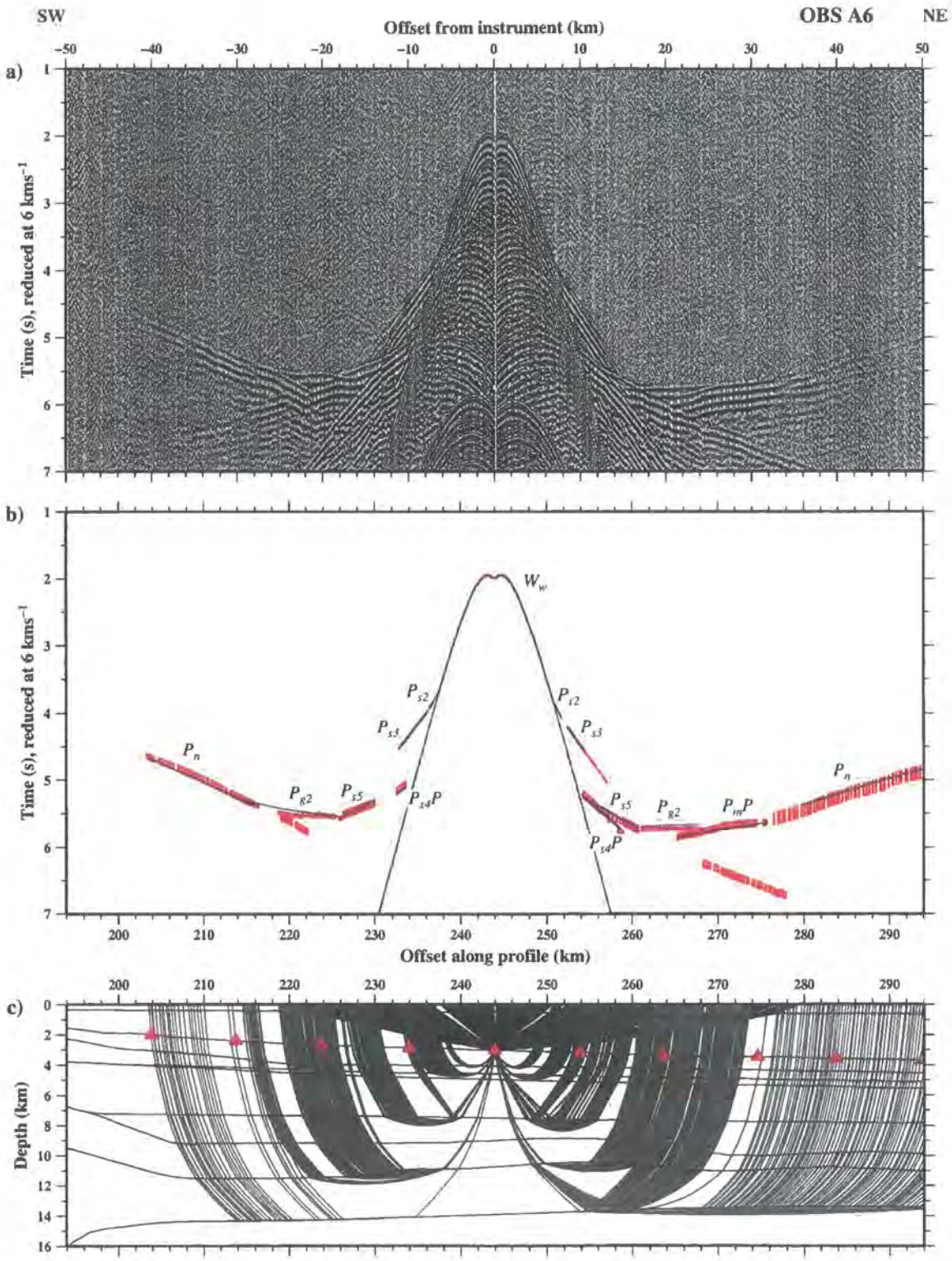


**Figure C.6**: Ray-trace modelling of hydrophone data recorded at OBS A6. See Figure 2.2 for instrument location. See Figure C.1 for details.

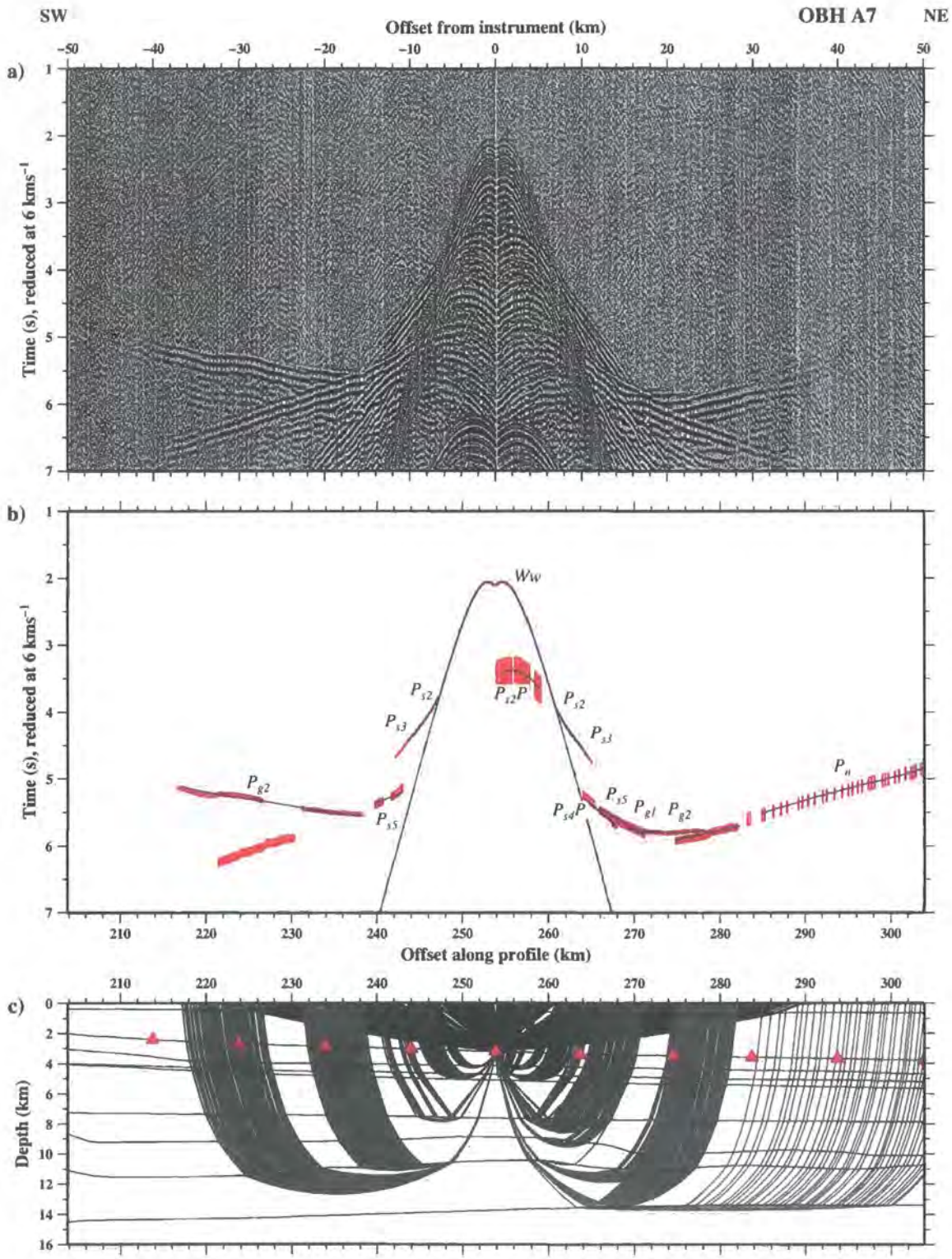


**Figure C.7**: Ray-trace modelling of hydrophone data recorded at OBS A7. See Figure 2.2 for instrument location. See Figure C.1 for details.

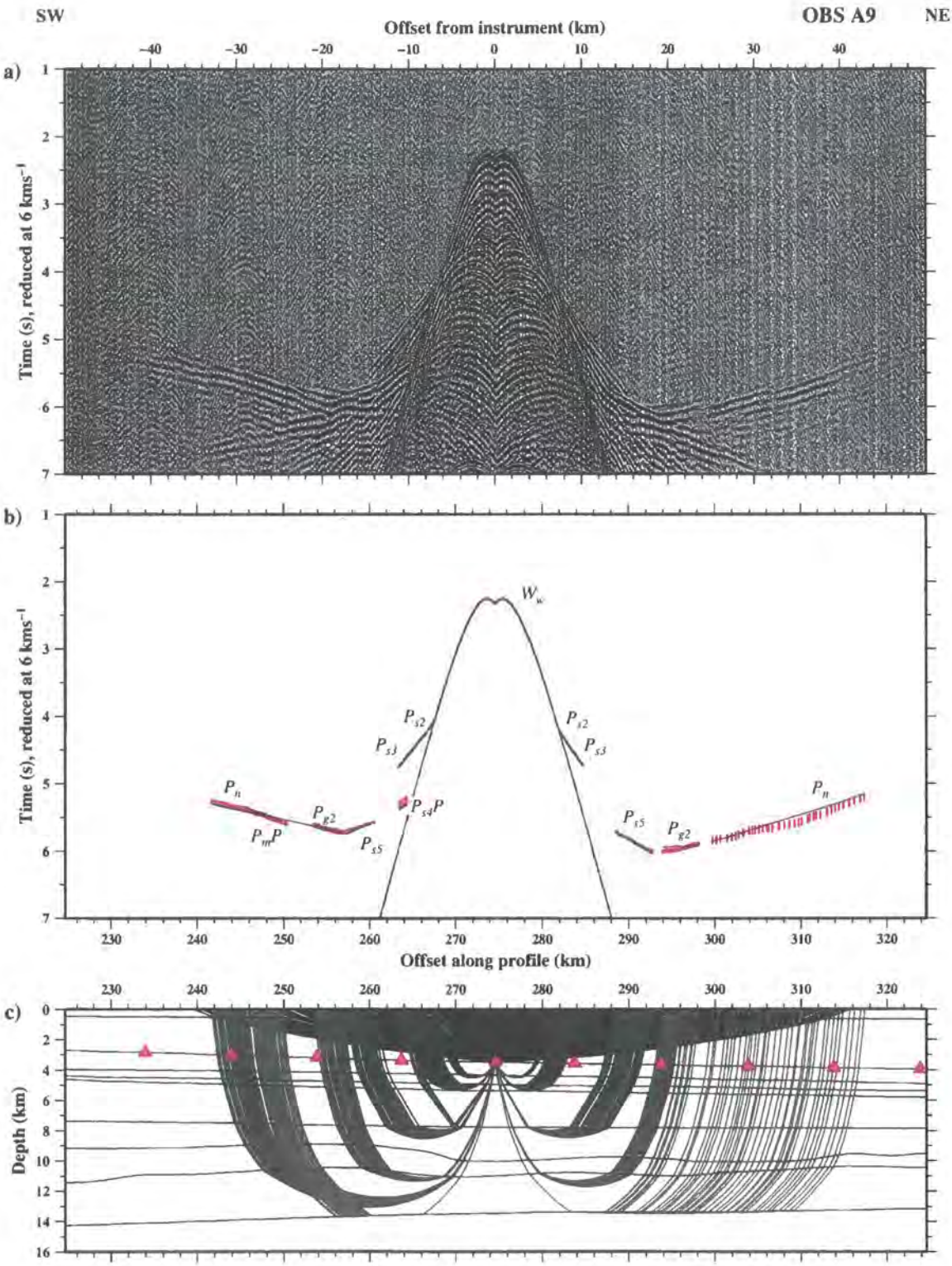


**Figure C.8**: Ray-trace modelling of hydrophone data recorded at OBS A9. See Figure 2.2 for instrument location. See Figure C.1 for details.

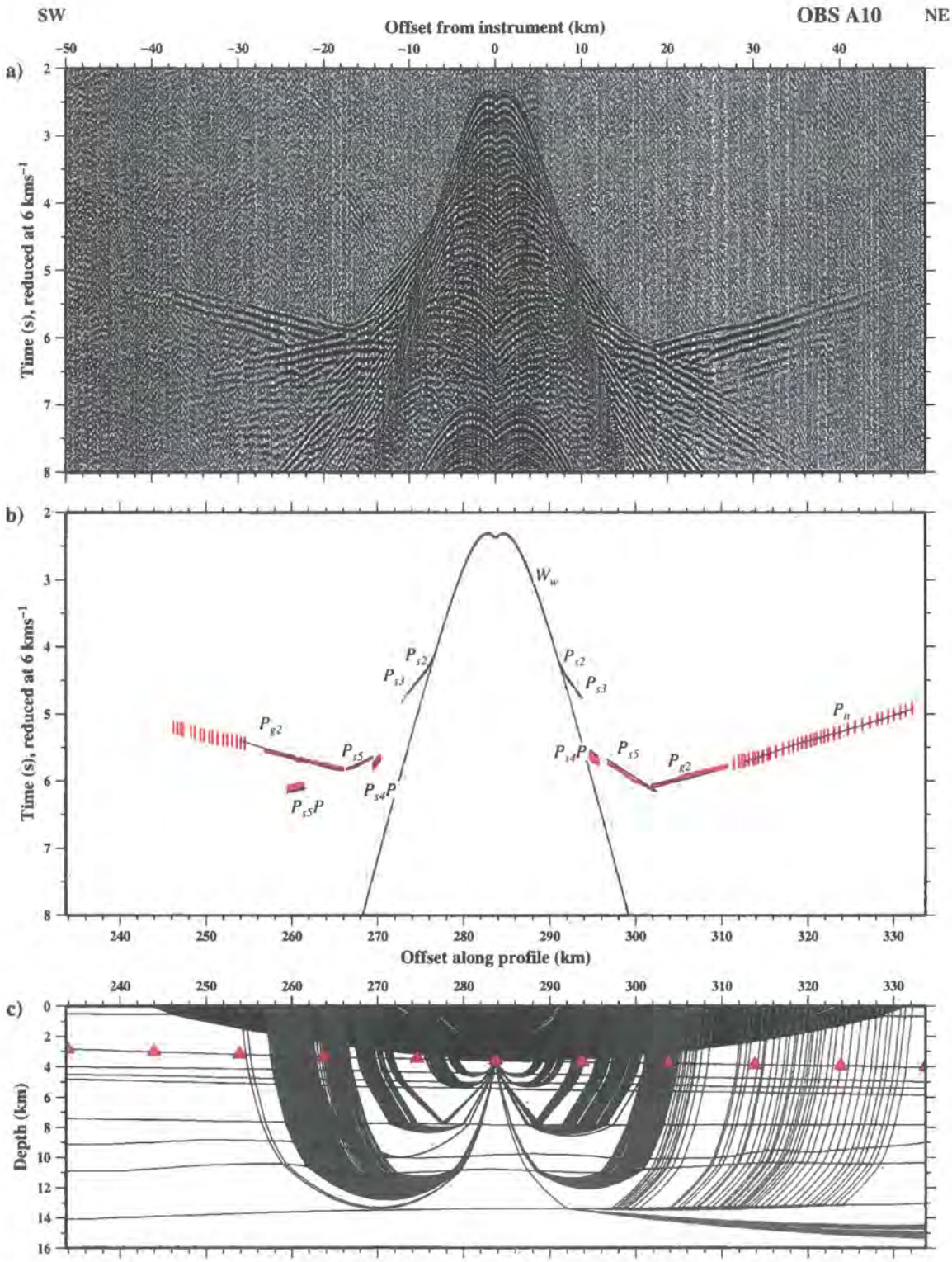


**Figure C.9**: Ray-trace modelling of hydrophone data recorded at OBS A10. See Figure 2.2 for instrument location. See Figure C.1 for details.

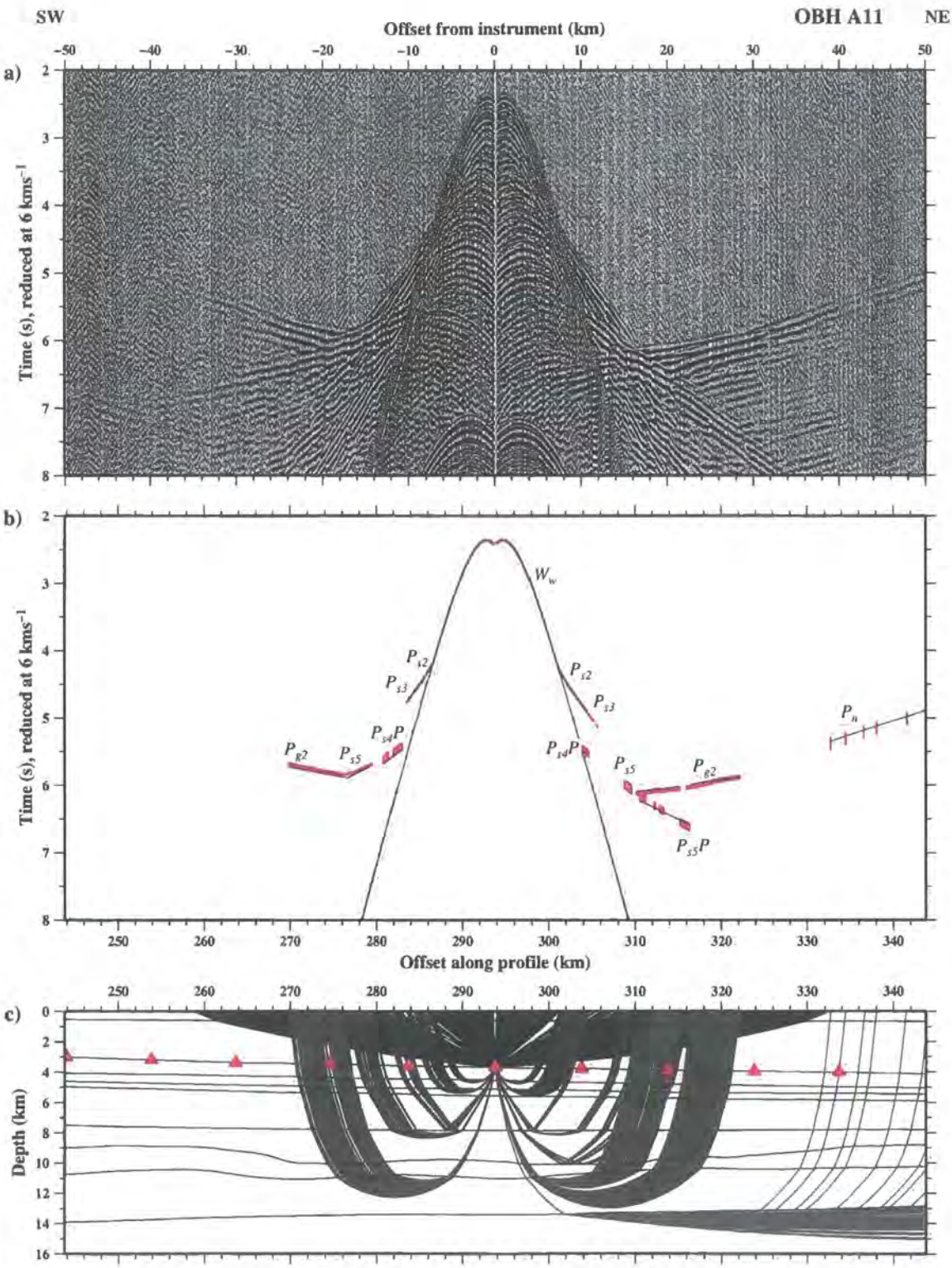


**Figure C.10**: Ray-trace modelling of hydrophone data recorded at OBS A11. See Figure 2.2 for instrument location. See Figure C.1 for details.

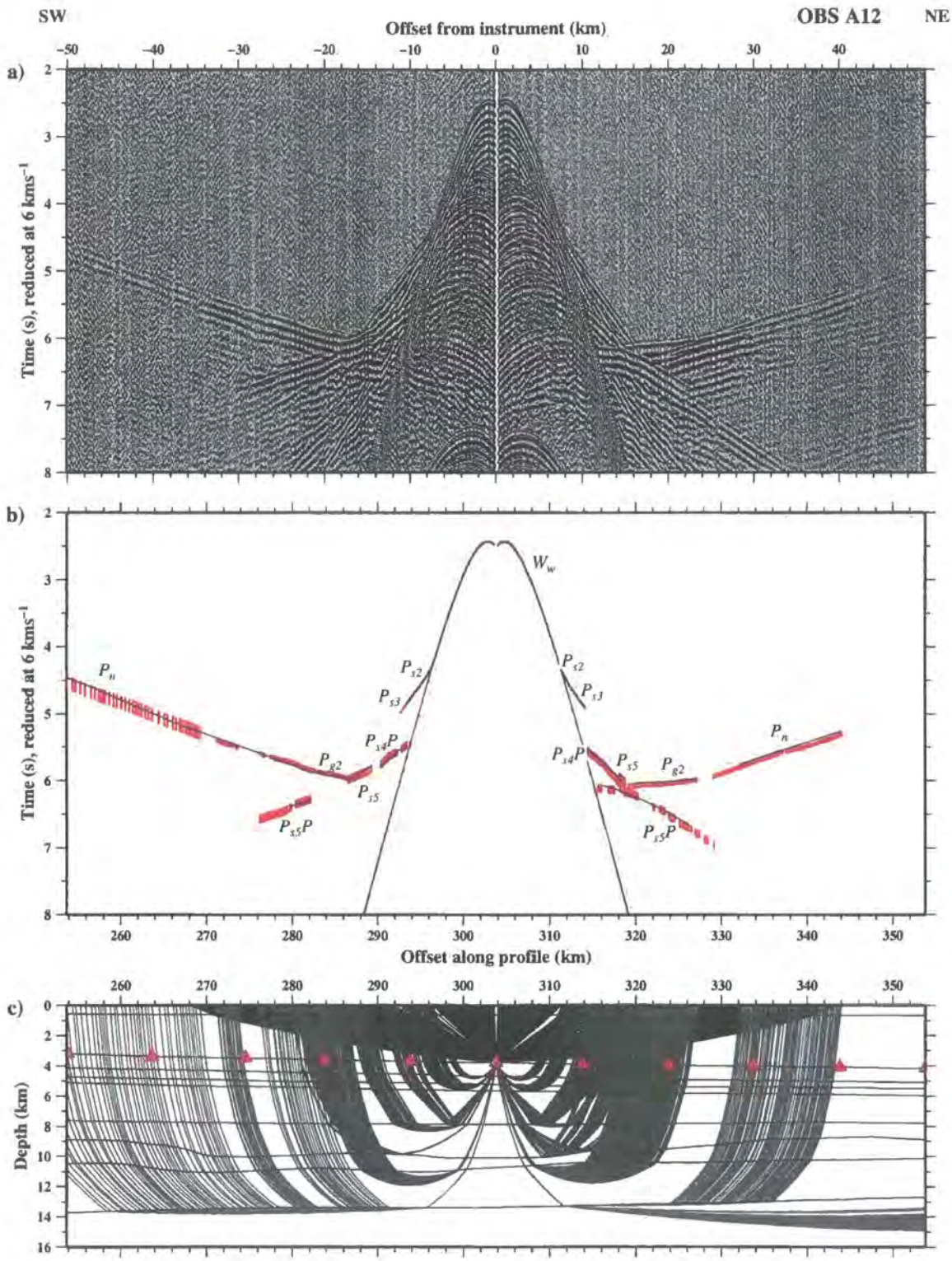


**Figure C.11**: Ray-trace modelling of hydrophone data recorded at OBS A12. See Figure 2.2 for instrument location. See Figure C.1 for details.

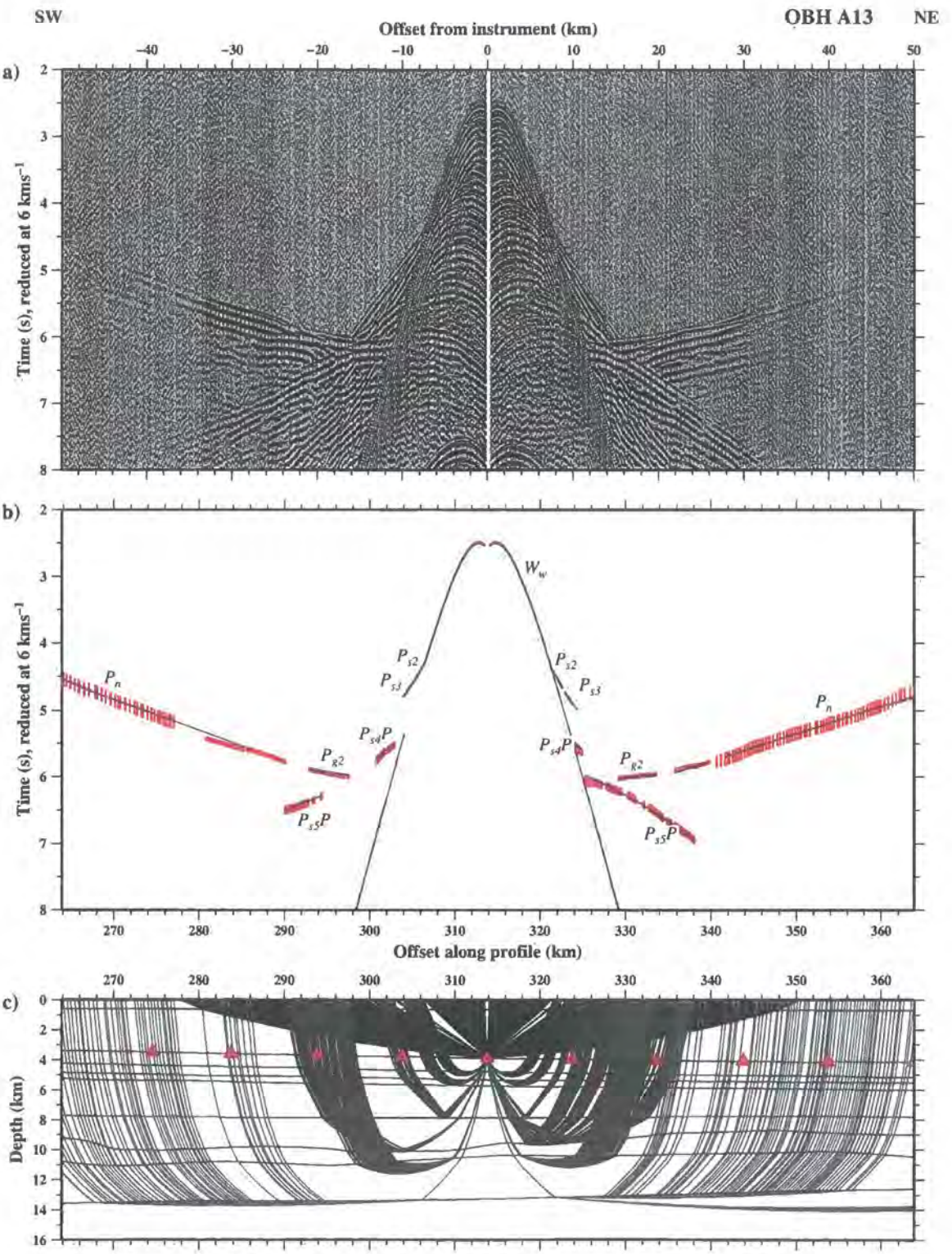


**Figure C.12**: Ray-trace modelling of hydrophone data recorded at OBS A13. See Figure 2.2 for instrument location. See Figure C.1 for details.

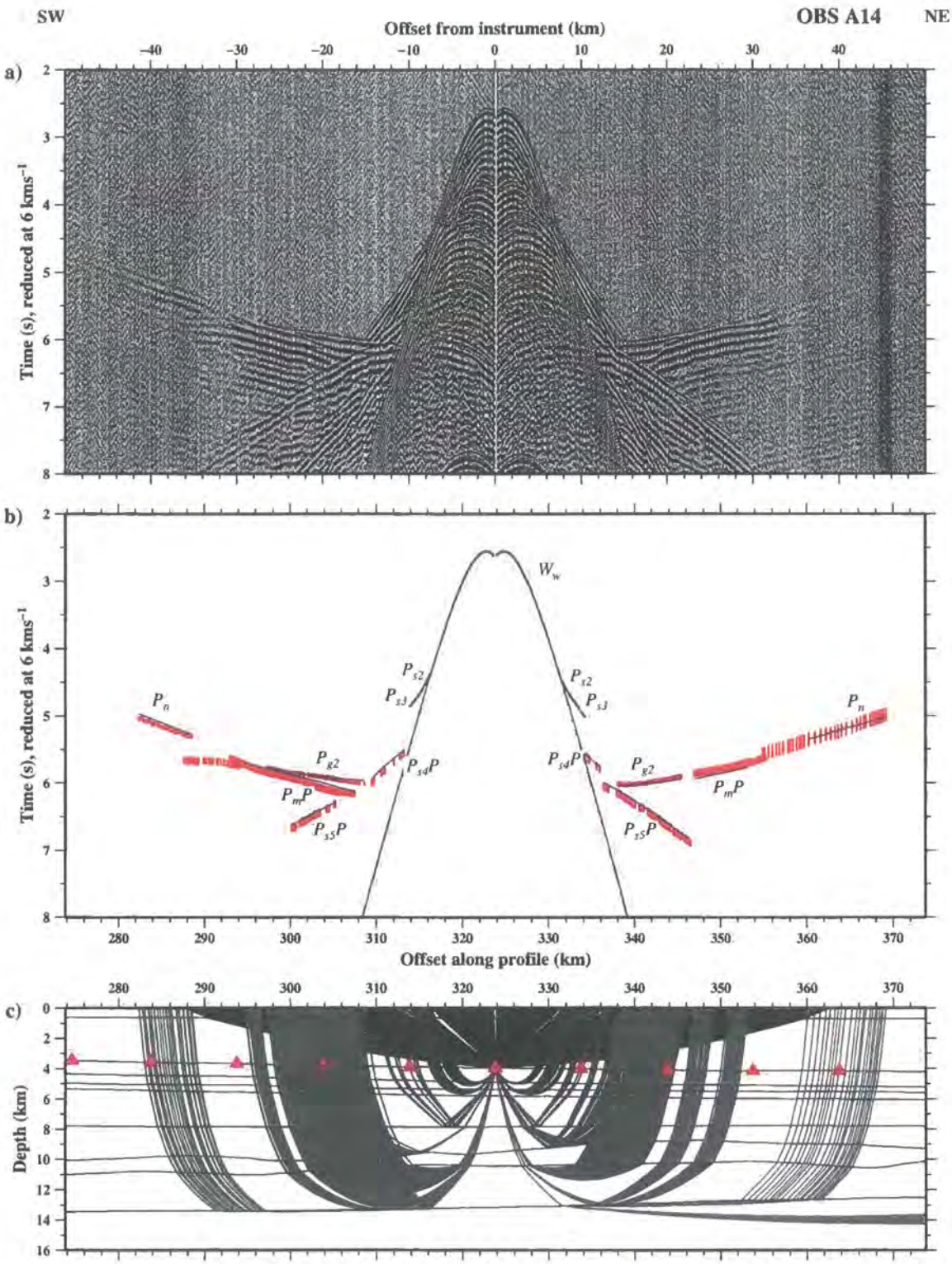


**Figure C.13**: Ray-trace modelling of hydrophone data recorded at OBS A14. See Figure 2.2 for instrument location. See Figure C.1 for details.

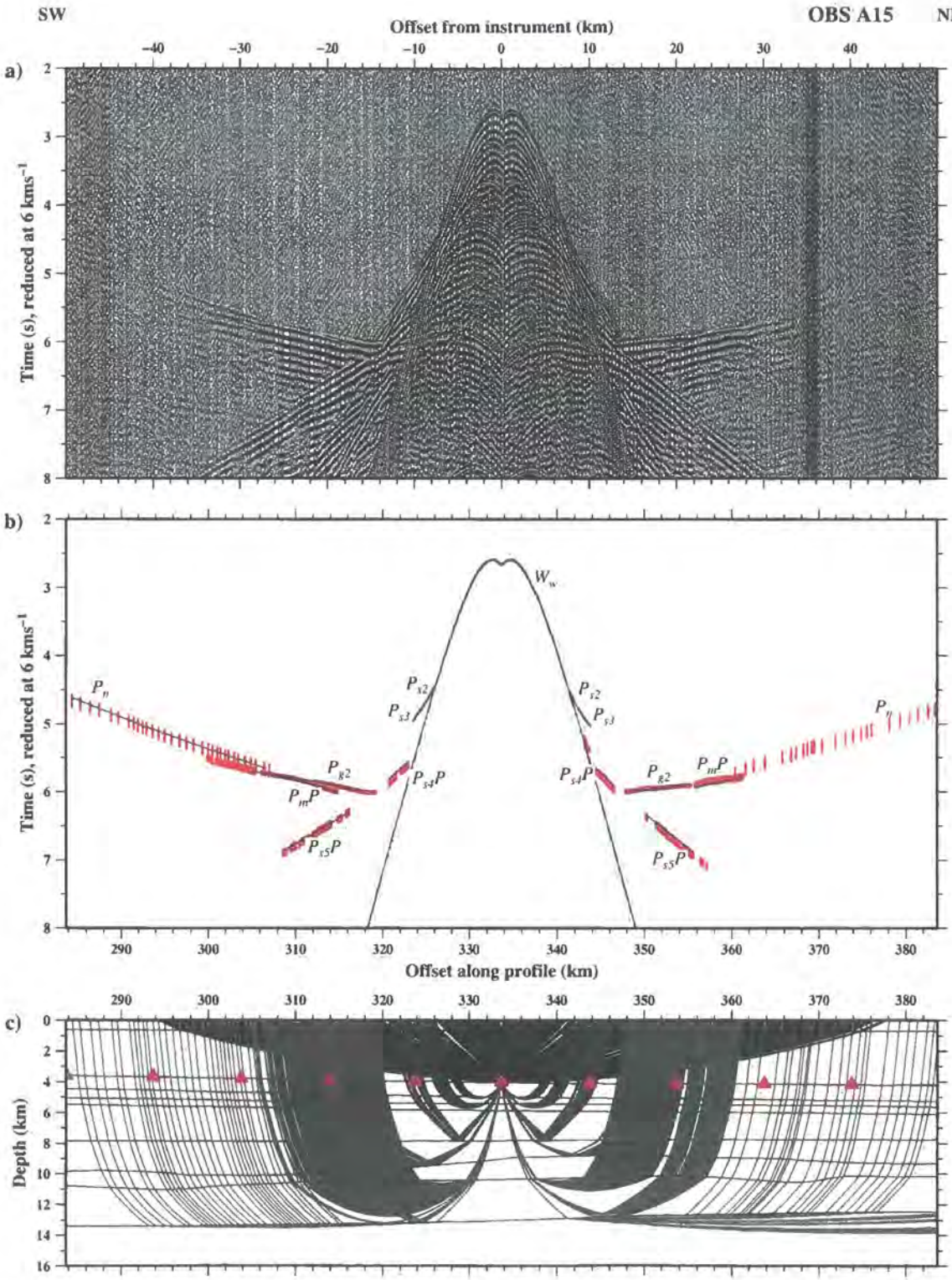


**Figure C.14**: Ray-trace modelling of hydrophone data recorded at OBS A15. See Figure 2.2 for instrument location. See Figure C.1 for details.

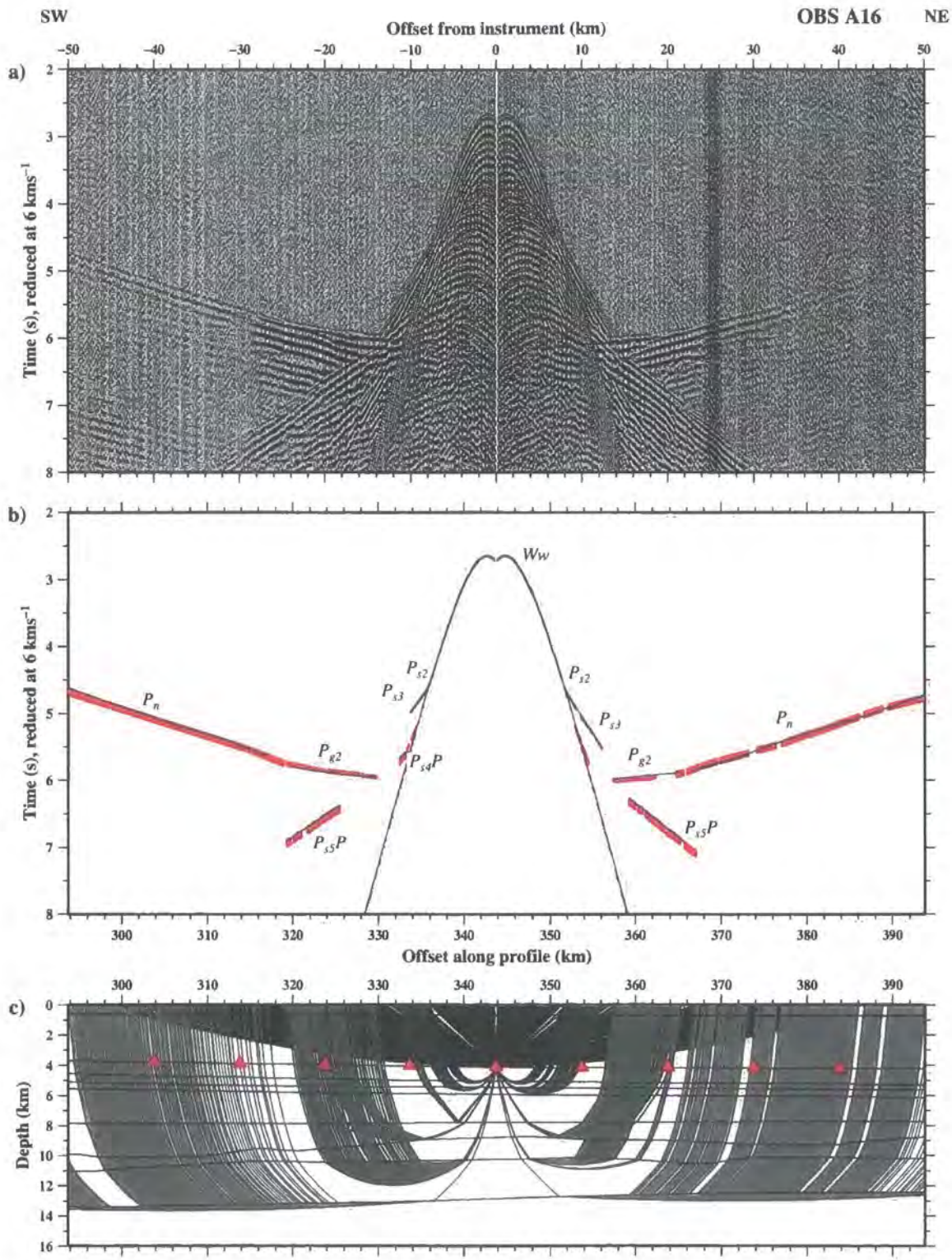


**Figure C.15**: Ray-trace modelling of hydrophone data recorded at OBS A16. See Figure 2.2 for instrument location. See Figure C.1 for details.

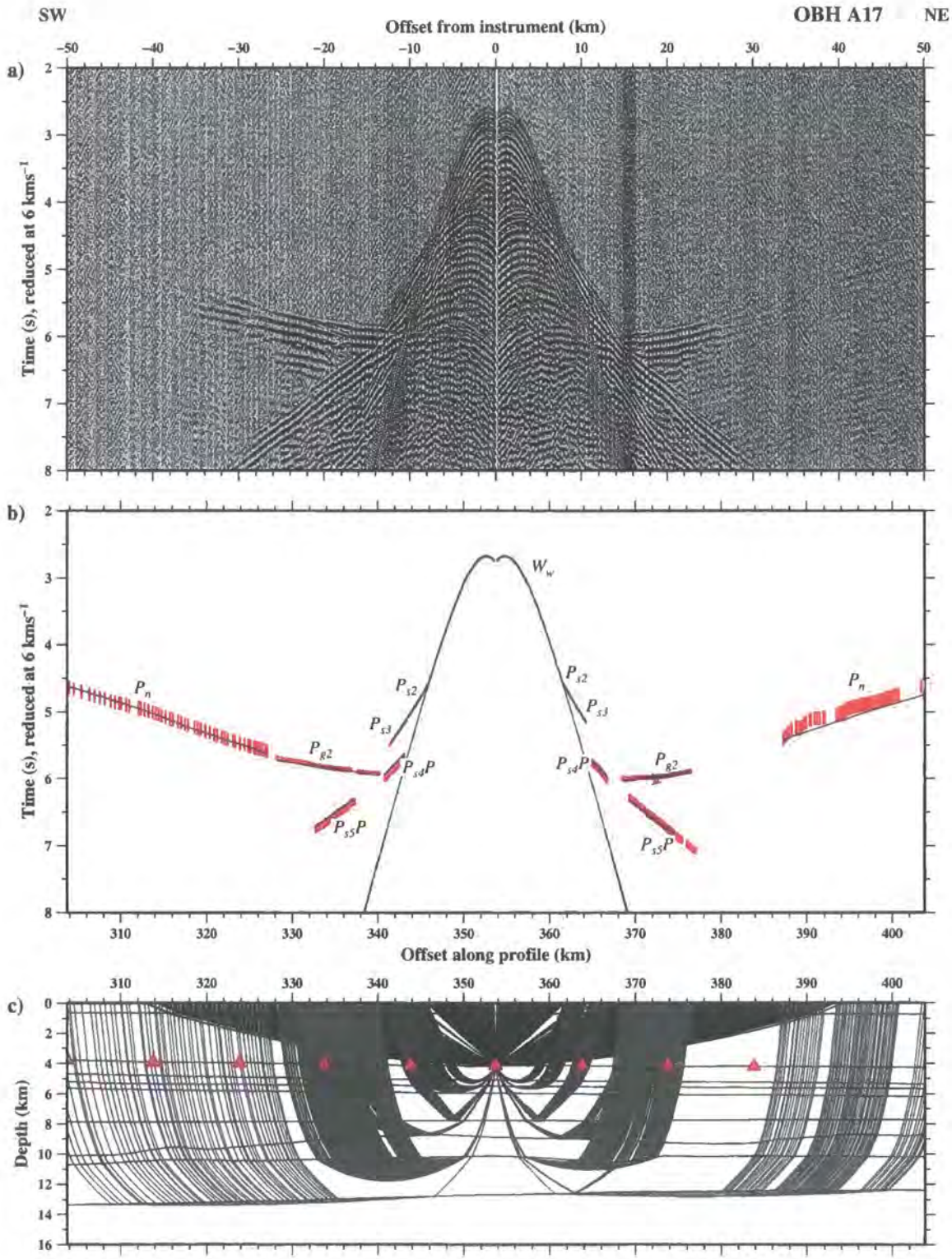


**Figure C.16**: Ray-trace modelling of hydrophone data recorded at OBS A17. See Figure 2.2 for instrument location. See Figure C.1 for details.

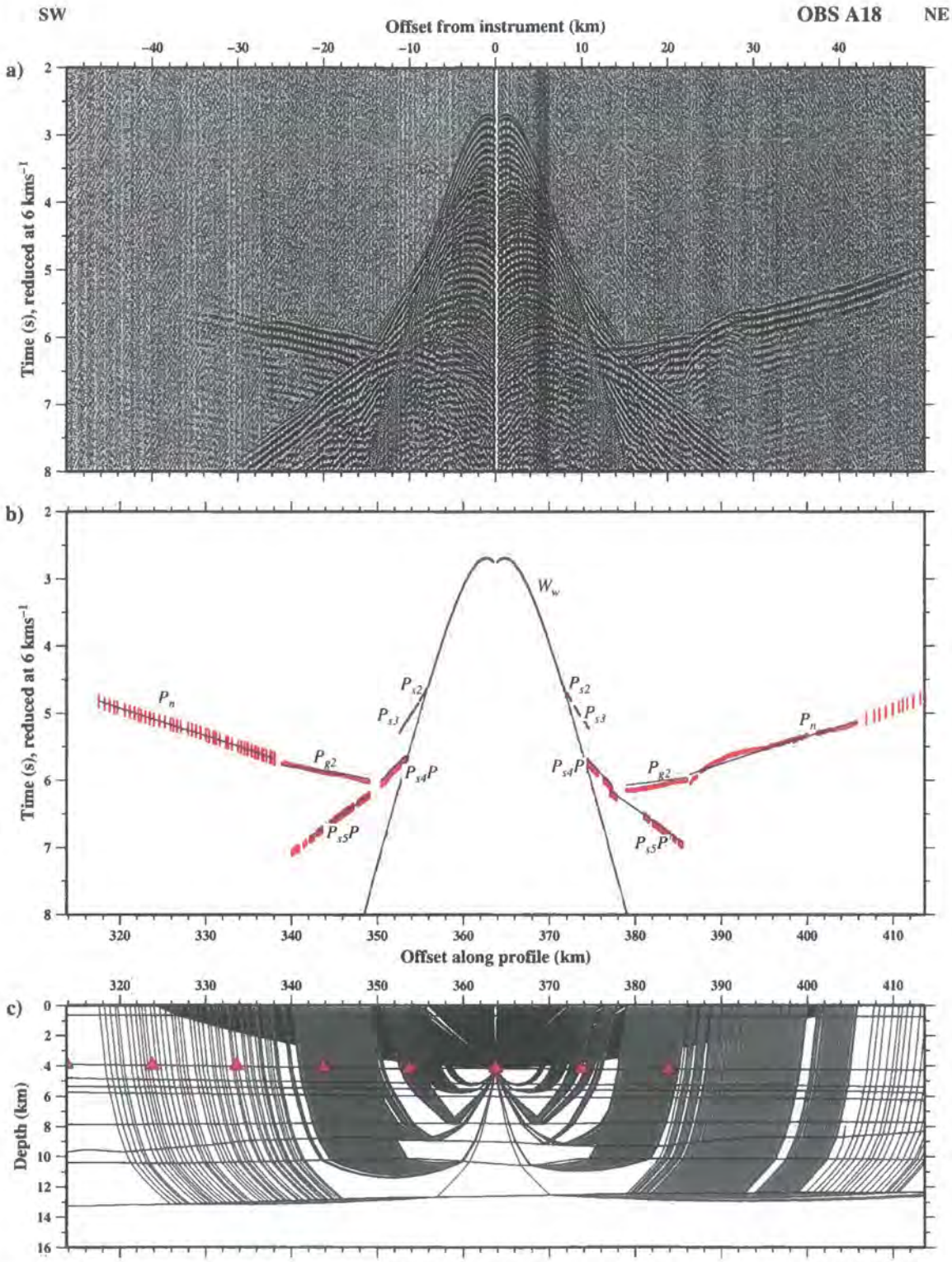


**Figure C.17**: Ray-trace modelling of hydrophone data recorded at OBS A18. See Figure 2.2 for instrument location. See Figure C.1 for details.

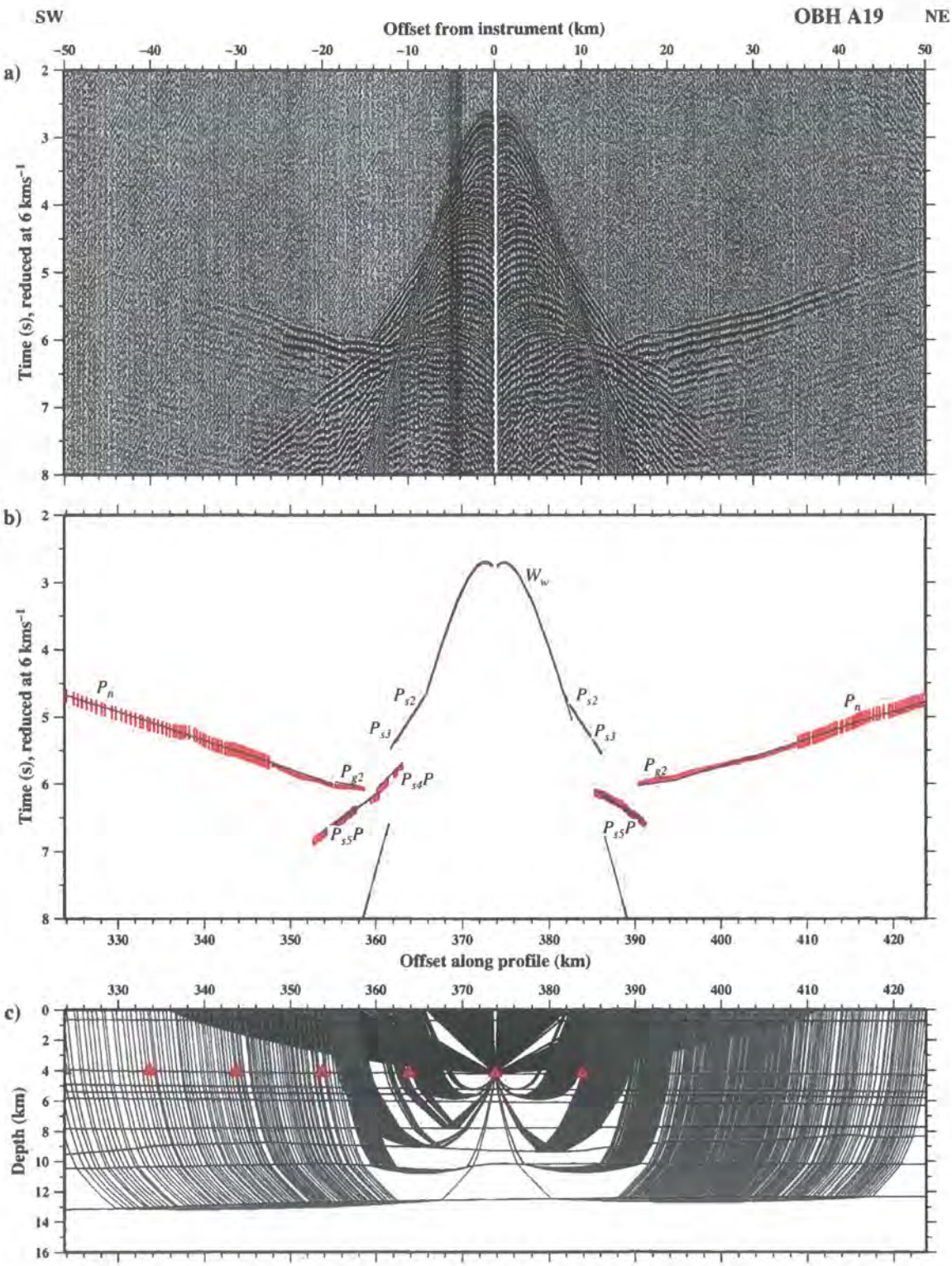


**Figure C.18**: Ray-trace modelling of hydrophone data recorded at OBS A19. See Figure 2.2 for instrument location. See Figure C.1 for details.

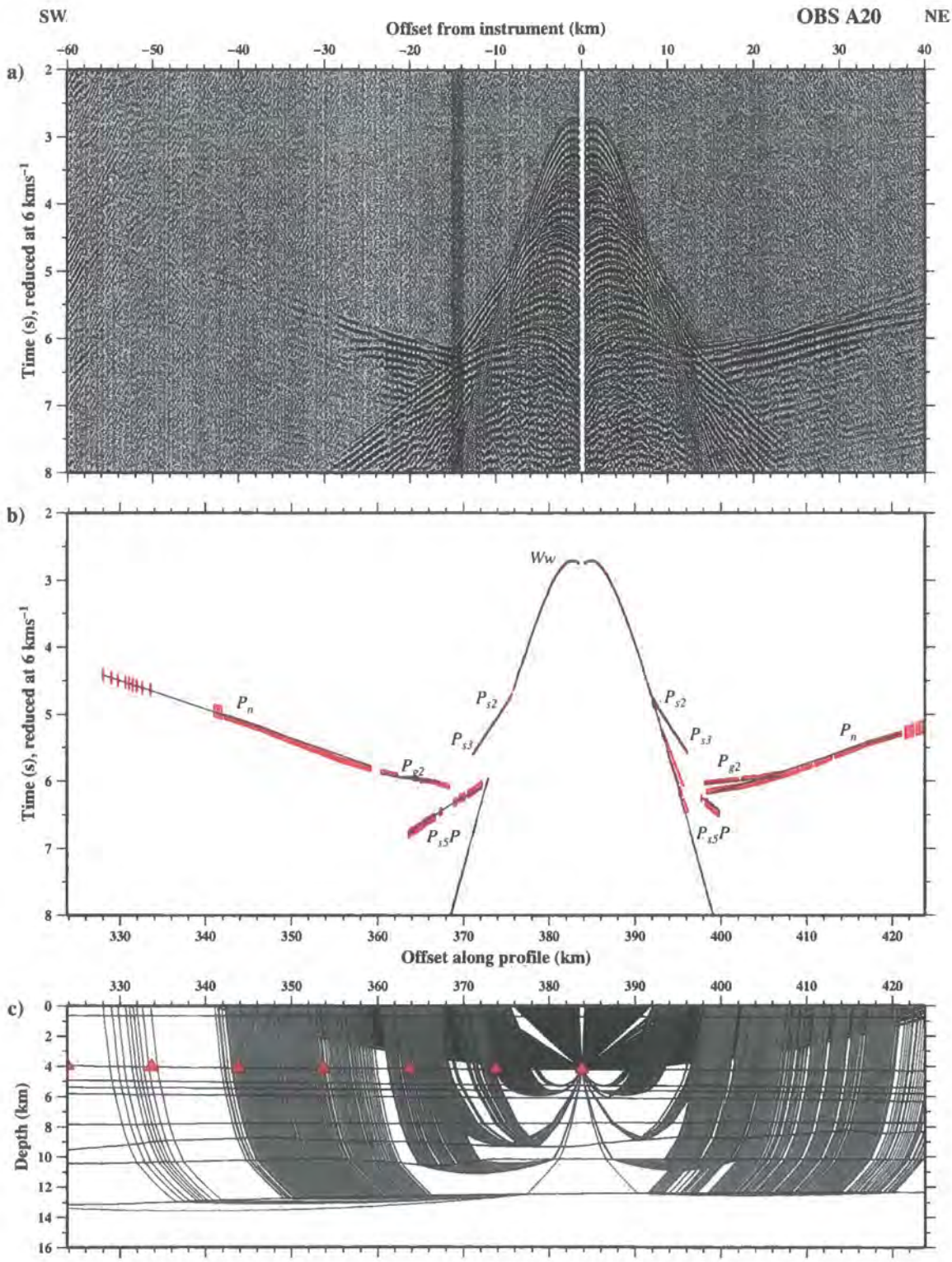


**Figure C.19**: Ray-trace modelling of hydrophone data recorded at OBS A20. See Figure 2.2 for instrument location. See Figure C.1 for details.

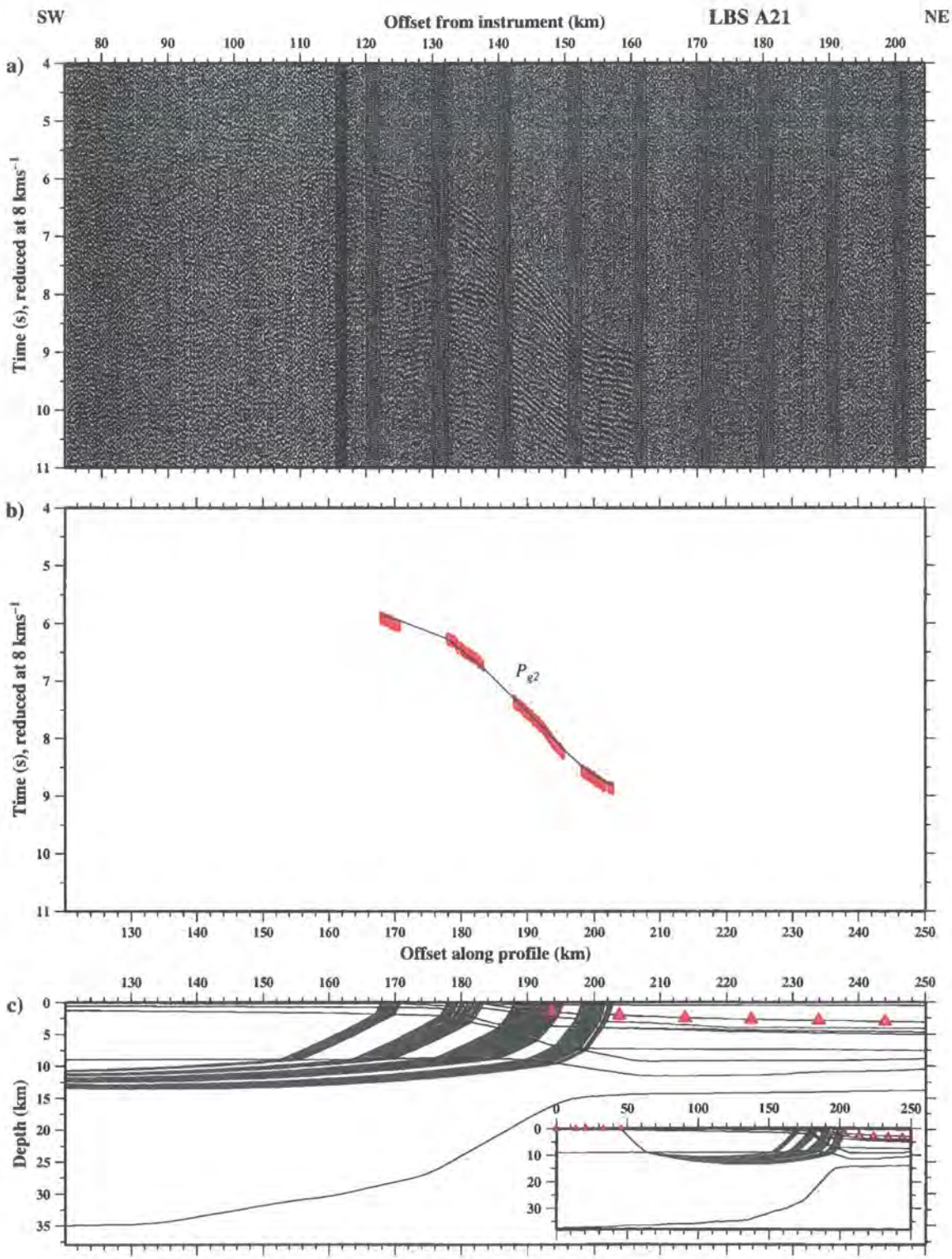


**Figure C.20**: Ray-trace modelling of vertical component geophone data recorded at land station A21. See Figure 2.2 for instrument location. See Figure C.1 for details.

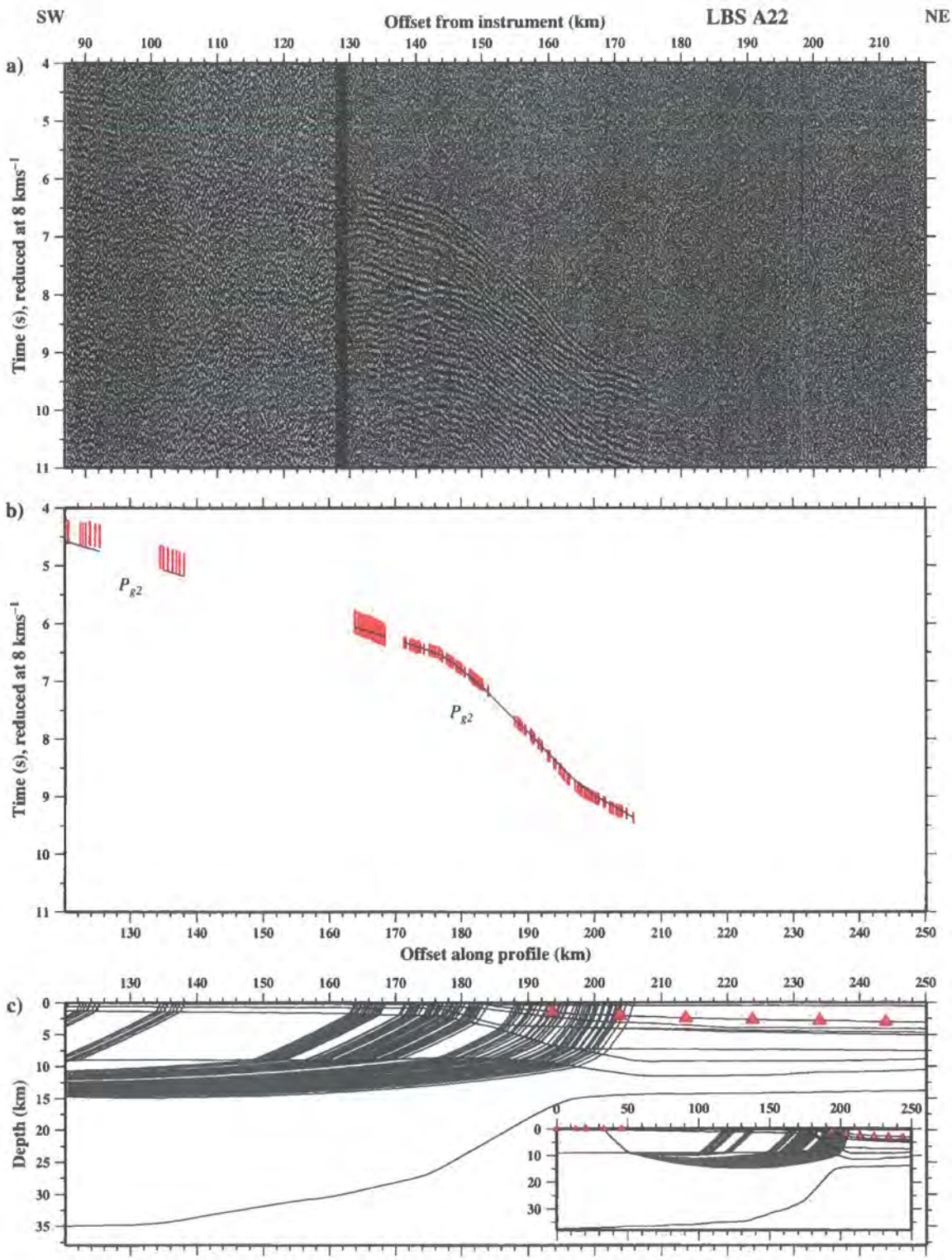


**Figure C.21**: Ray-trace modelling of vertical component geophone data recorded at land station A22. See Figure 2.2 for instrument location. See Figure C.1 for details.

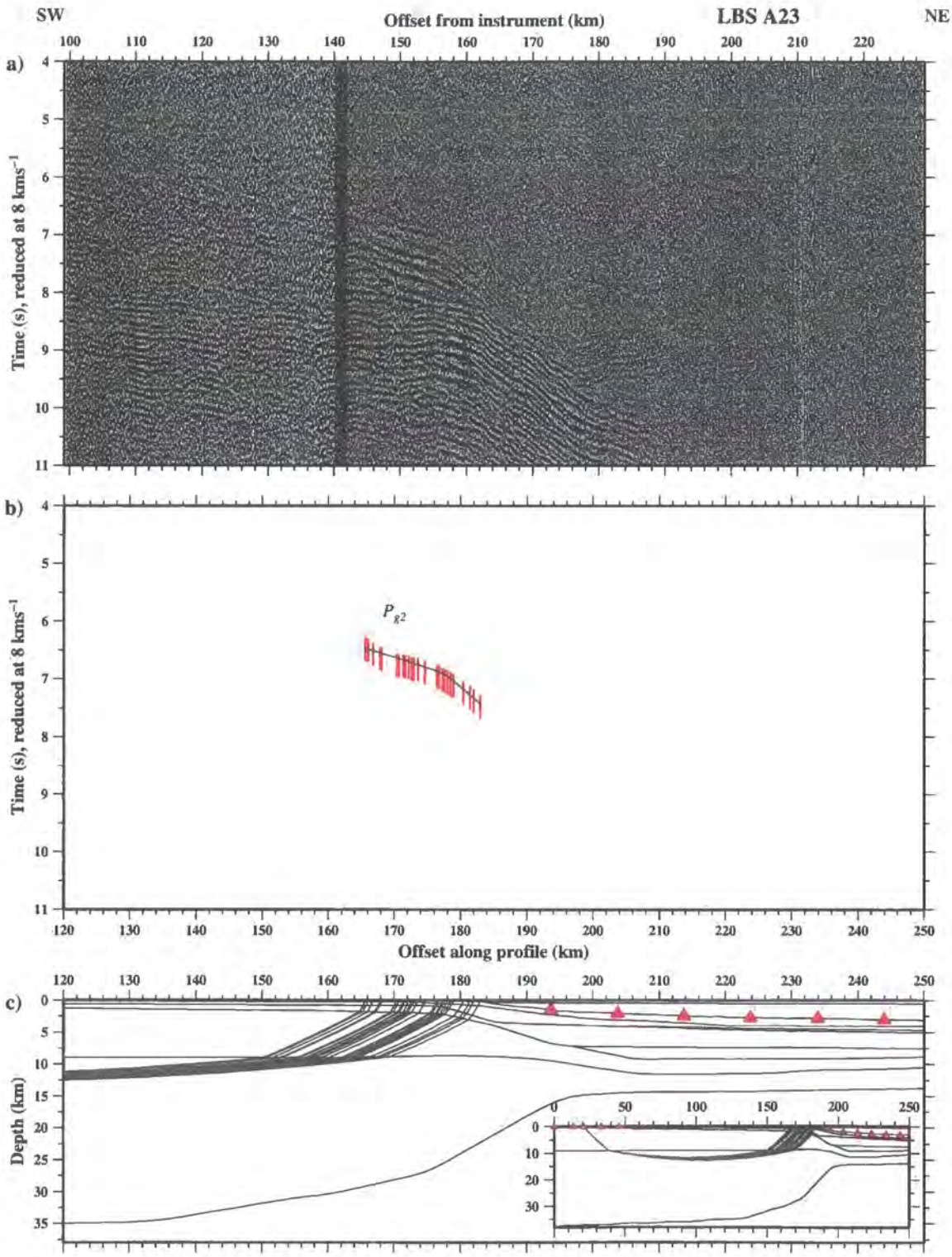


**Figure C.22**: Ray-trace modelling of vertical component geophone data recorded at land station A23. See Figure 2.2 for instrument location. See Figure C.1 for details.

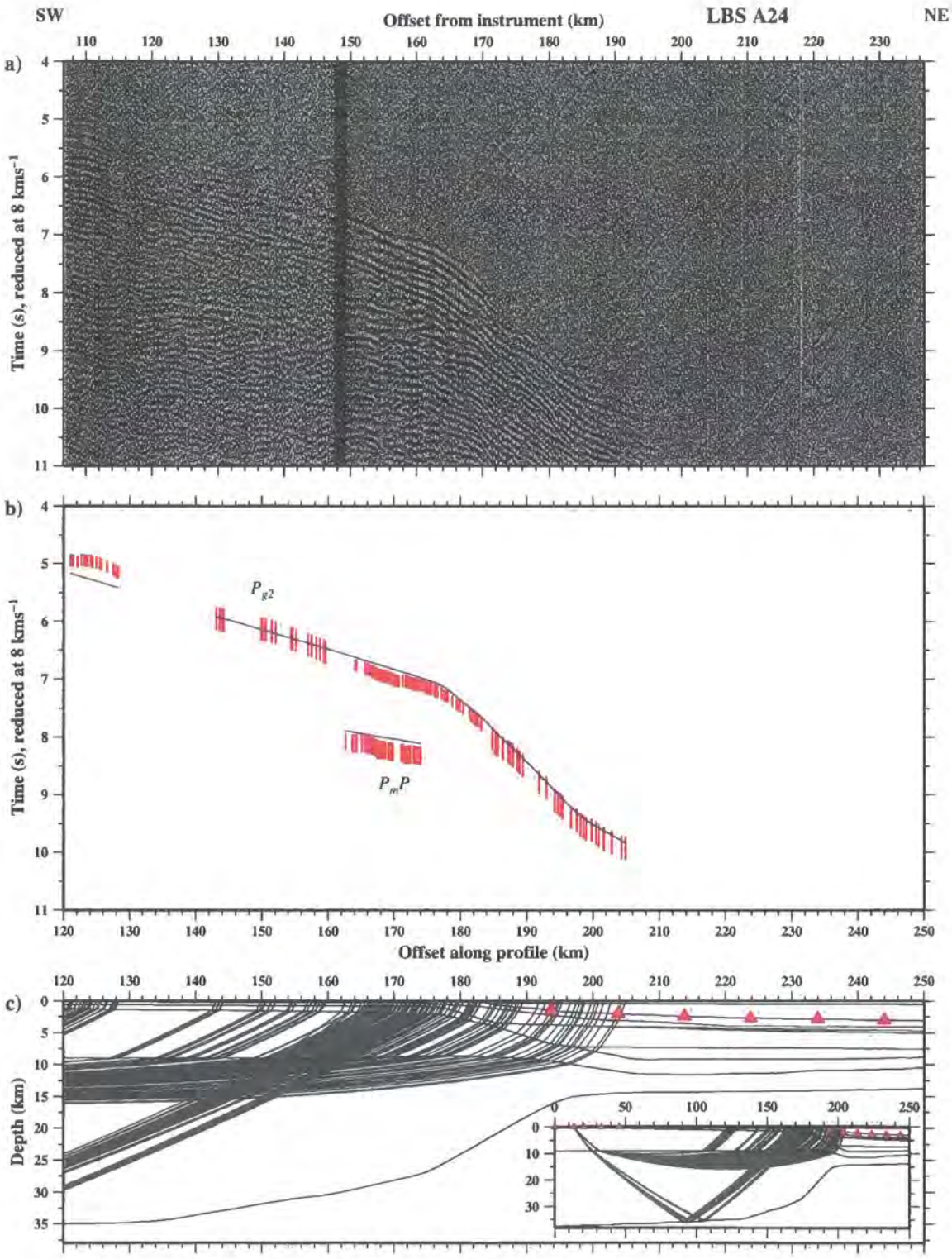


**Figure C.23**: Ray-trace modelling of vertical component geophone data recorded at land station A24. See Figure 2.2 for instrument location. See Figure C.1 for details.

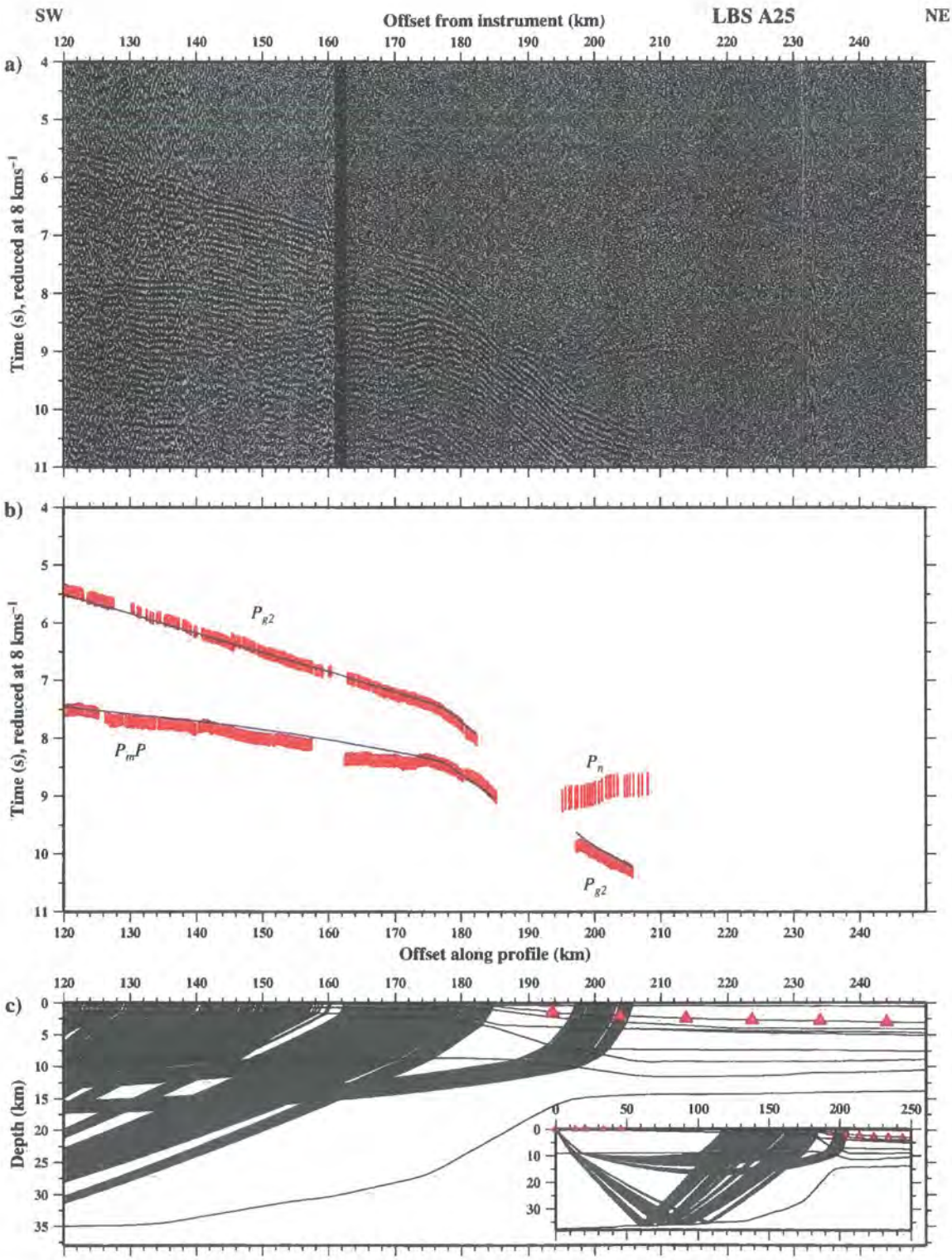


**Figure C.24**: Ray-trace modelling of vertical component geophone data recorded at land station A25. See Figure 2.2 for instrument location. See Figure C.1 for details.

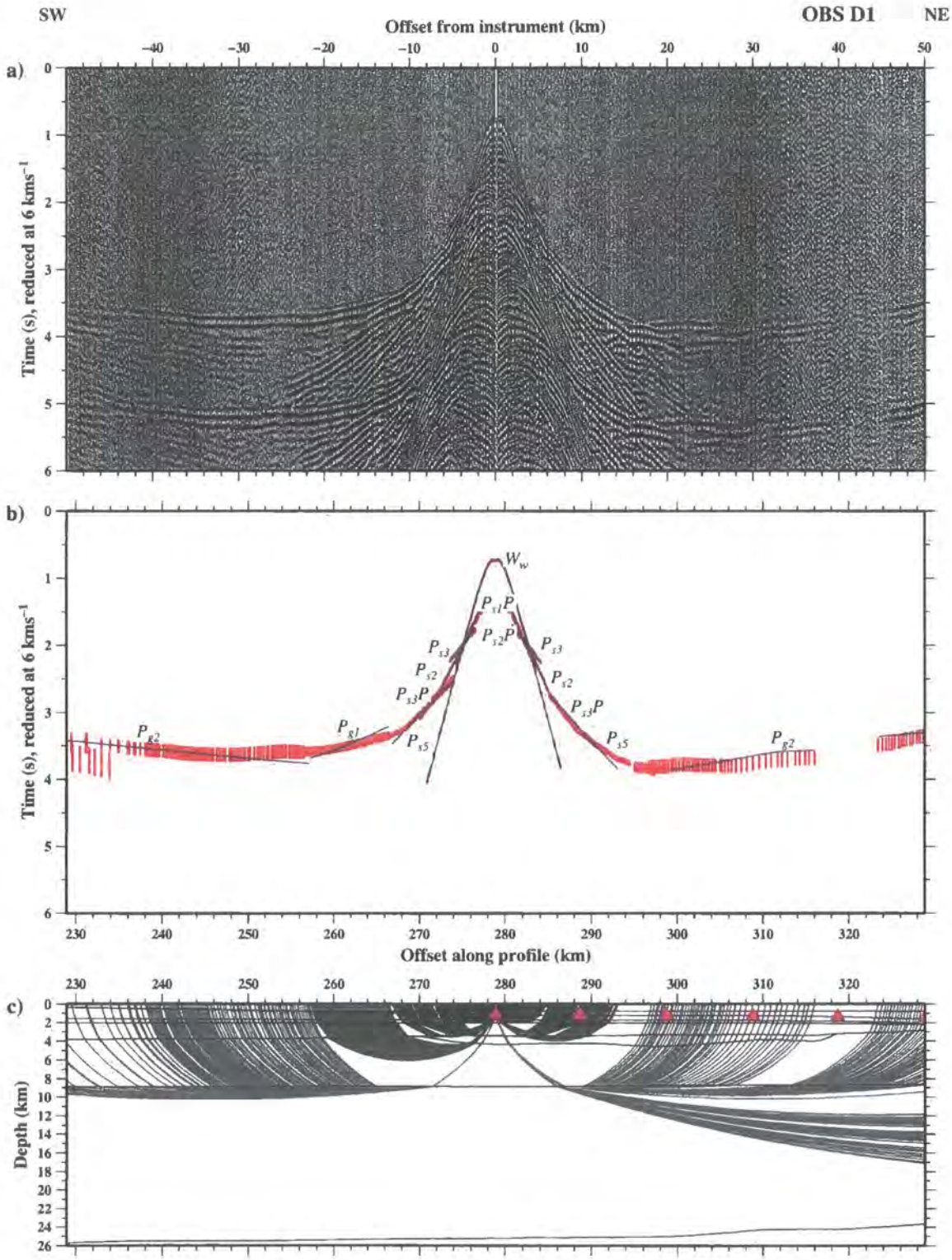


**Figure C.25**: Ray-trace modelling of hydrophone data recorded at OBS D1. See Figure 2.3 for instrument location. See Figure C.1 for details.

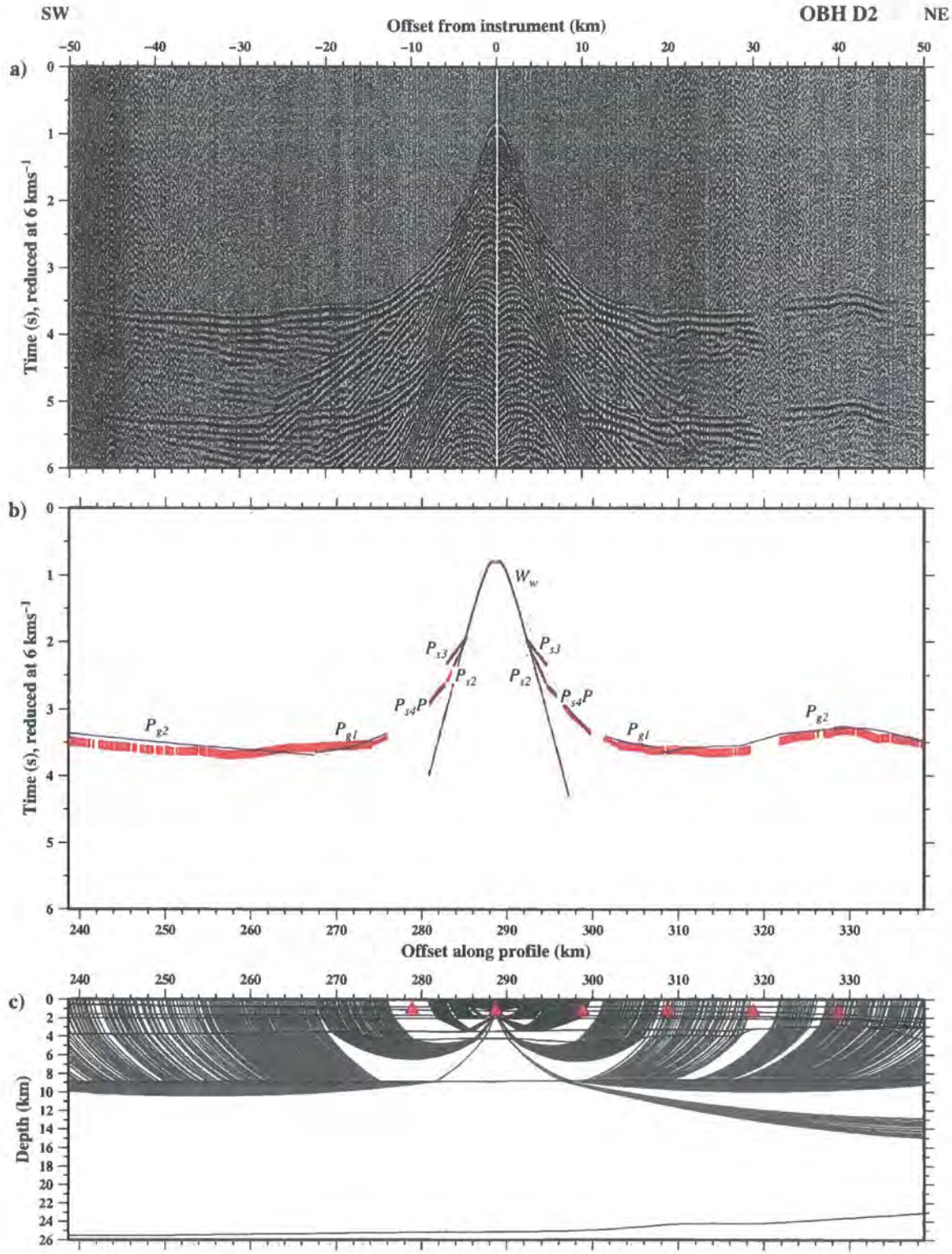


**Figure C.26**: Ray-trace modelling of hydrophone data recorded at OBS D2. See Figure 2.3 for instrument location. See Figure C.1 for details.

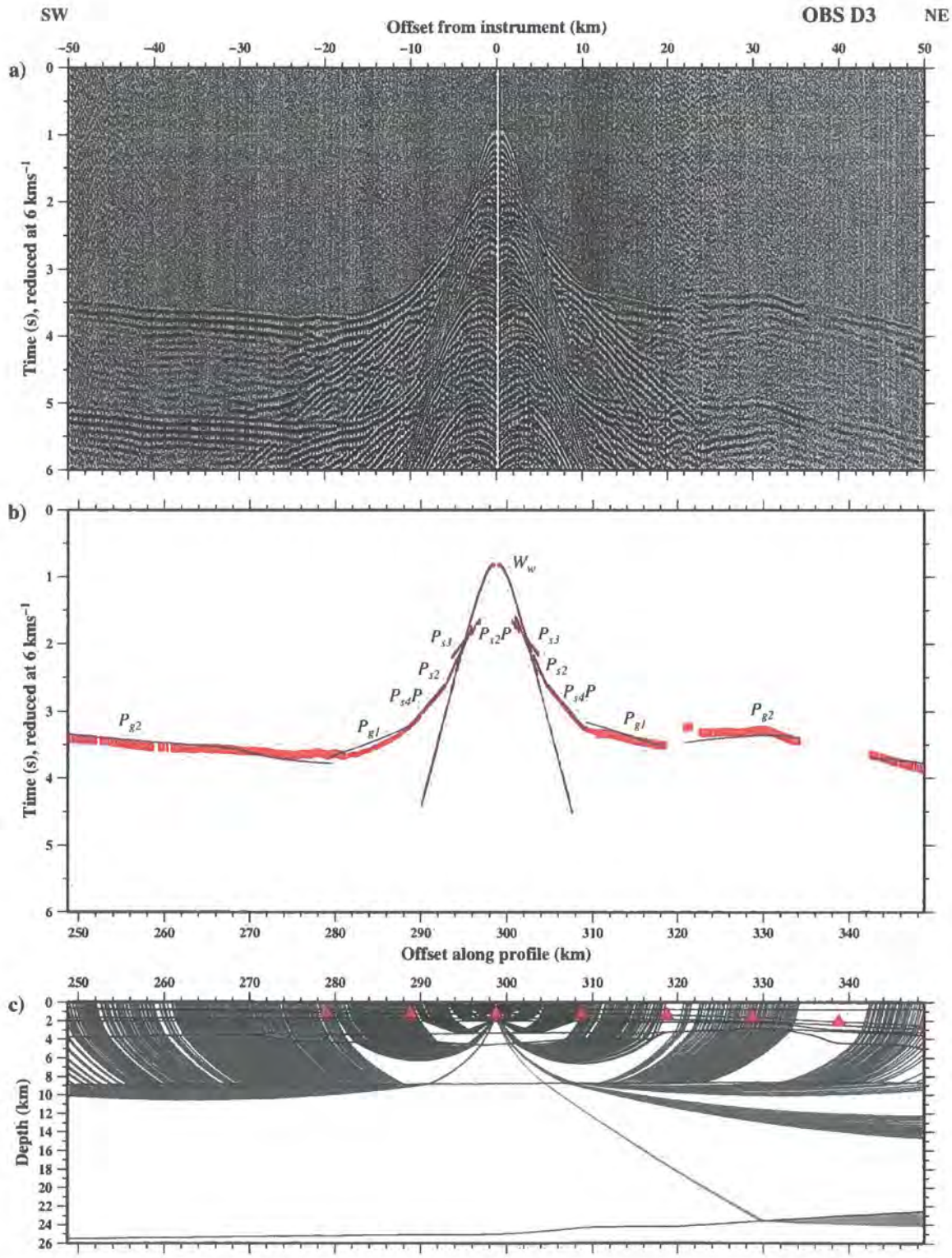


**Figure C.27**: Ray-trace modelling of hydrophone data recorded at OBS D3. See Figure 2.3 for instrument location. See Figure C.1 for details.

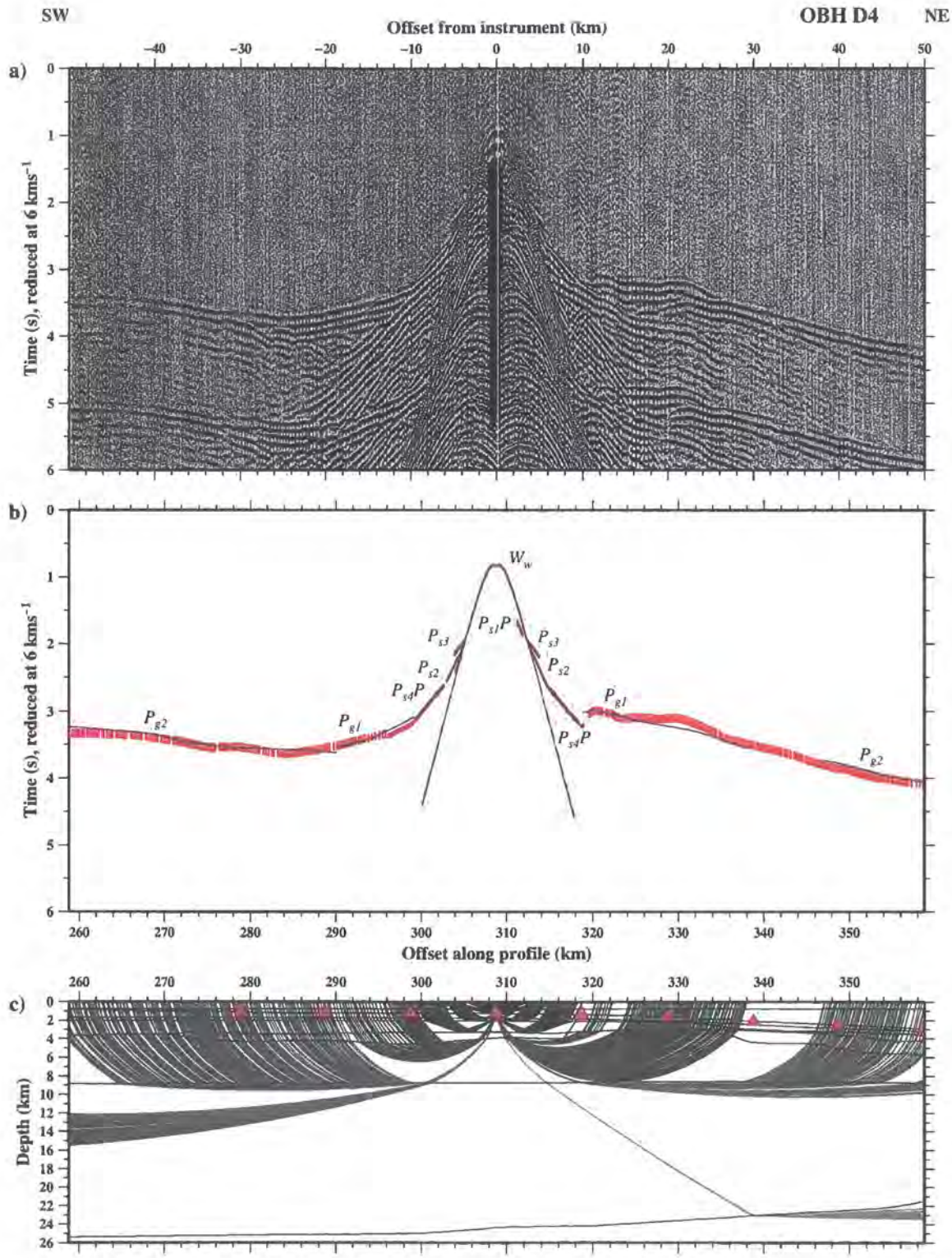


**Figure C.28**: Ray-trace modelling of hydrophone data recorded at OBS D4. See Figure 2.3 for instrument location. See Figure C.1 for details.

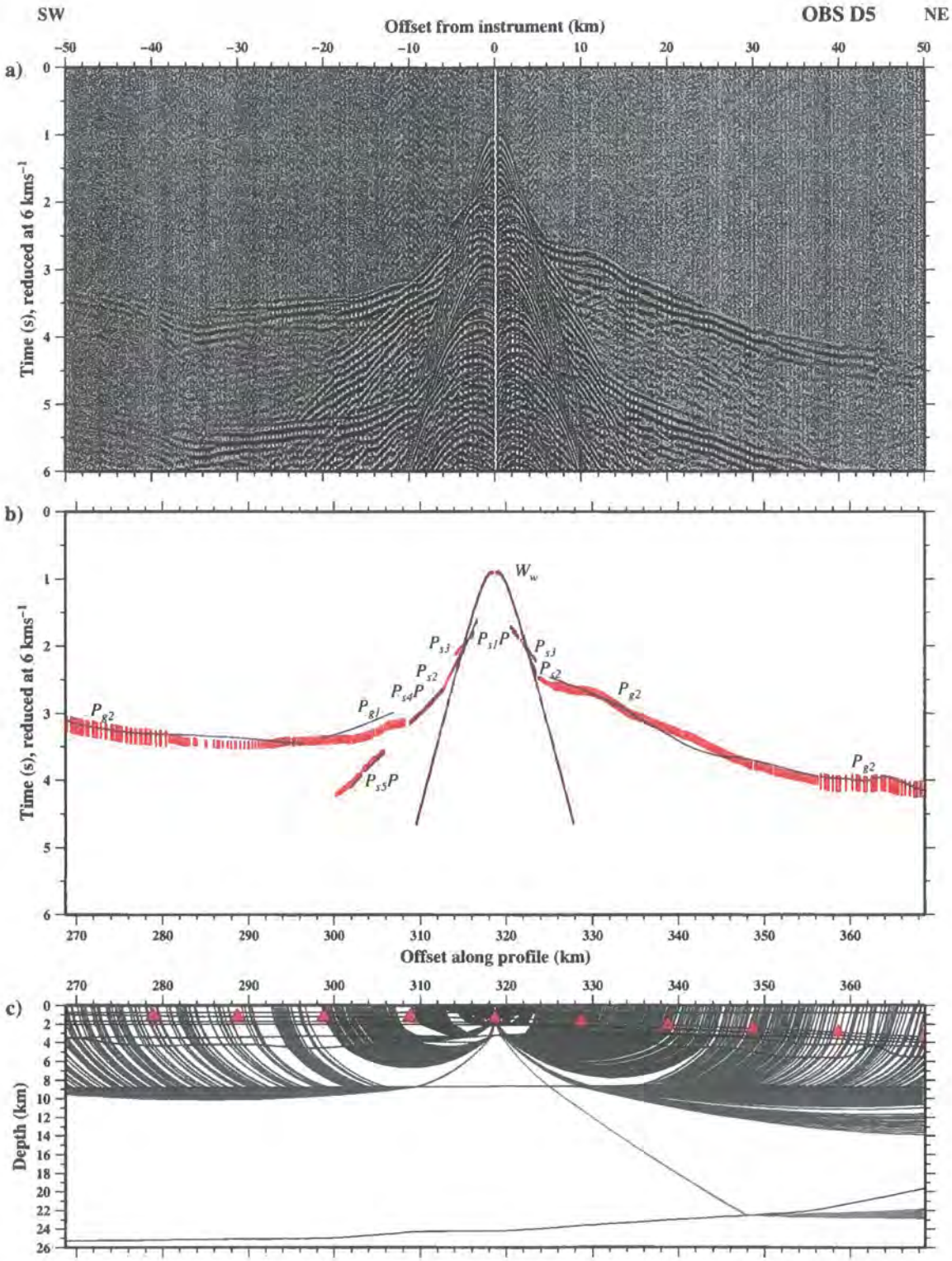


**Figure C.29**: Ray-trace modelling of hydrophone data recorded at OBS D5. See Figure 2.3 for instrument location. See Figure C.1 for details.

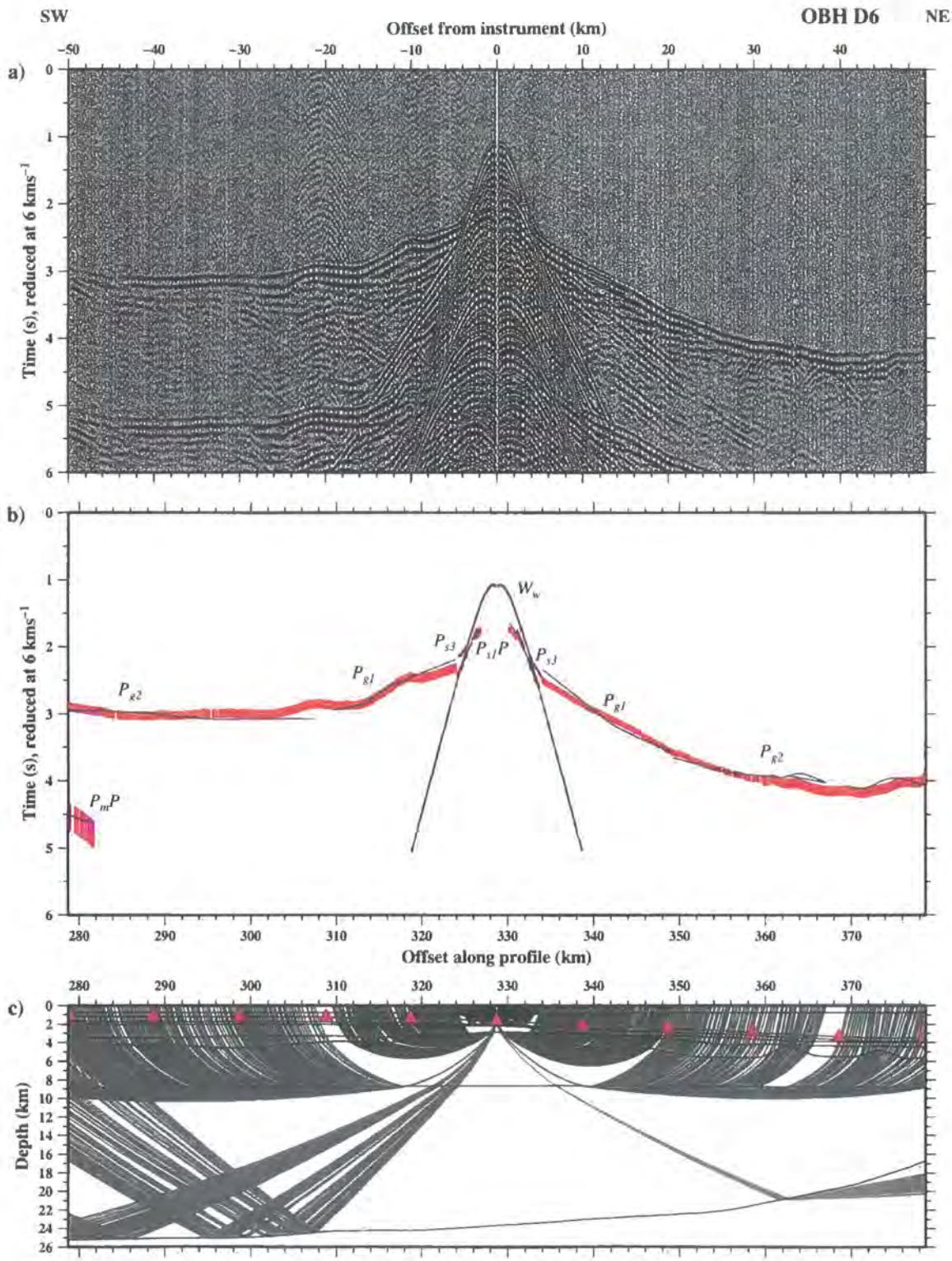


**Figure C.30**: Ray-trace modelling of hydrophone data recorded at OBS D6. See Figure 2.3 for instrument location. See Figure C.1 for details.

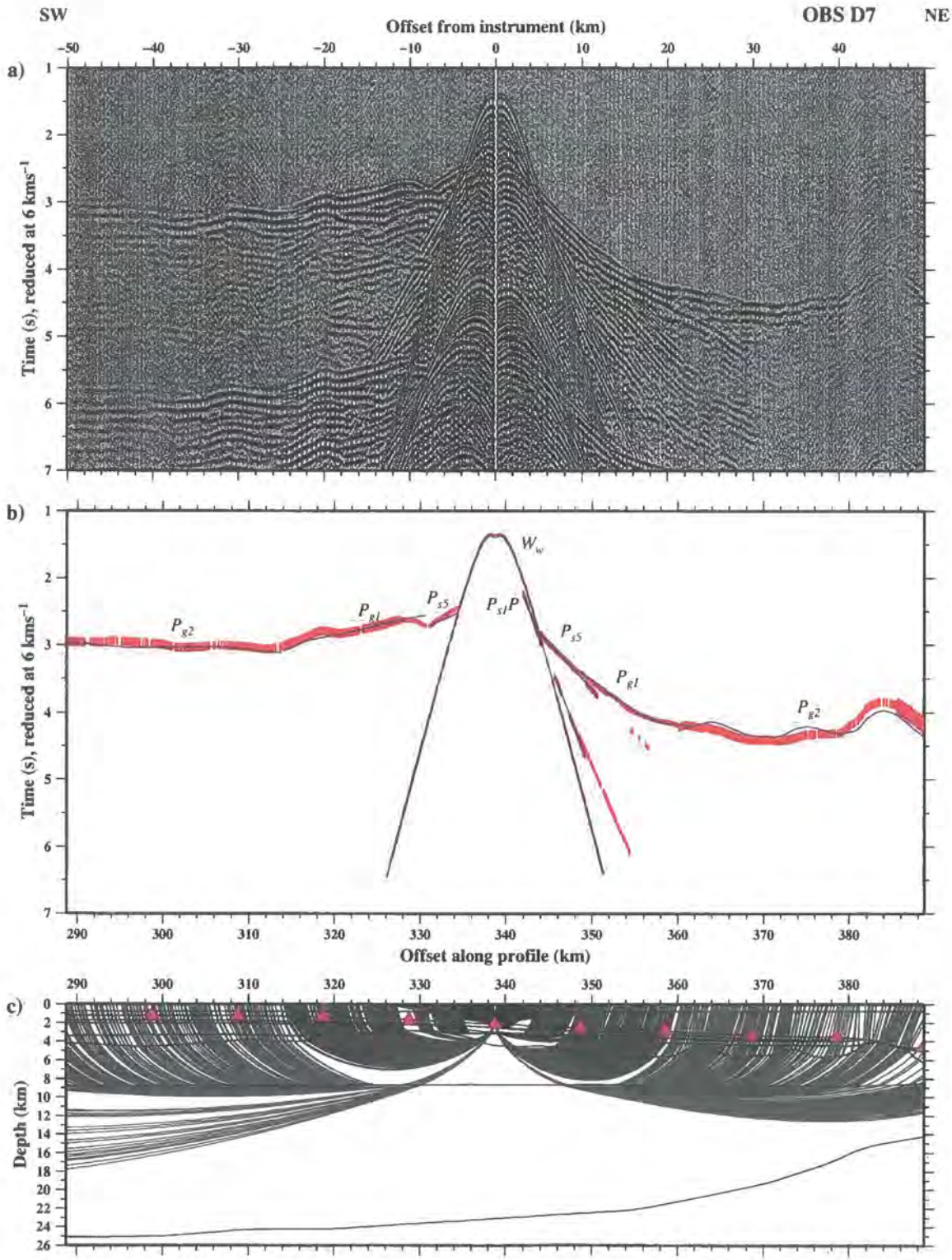


**Figure C.31**: Ray-trace modelling of hydrophone data recorded at OBS D7. See Figure 2.3 for instrument location. See Figure C.1 for details.

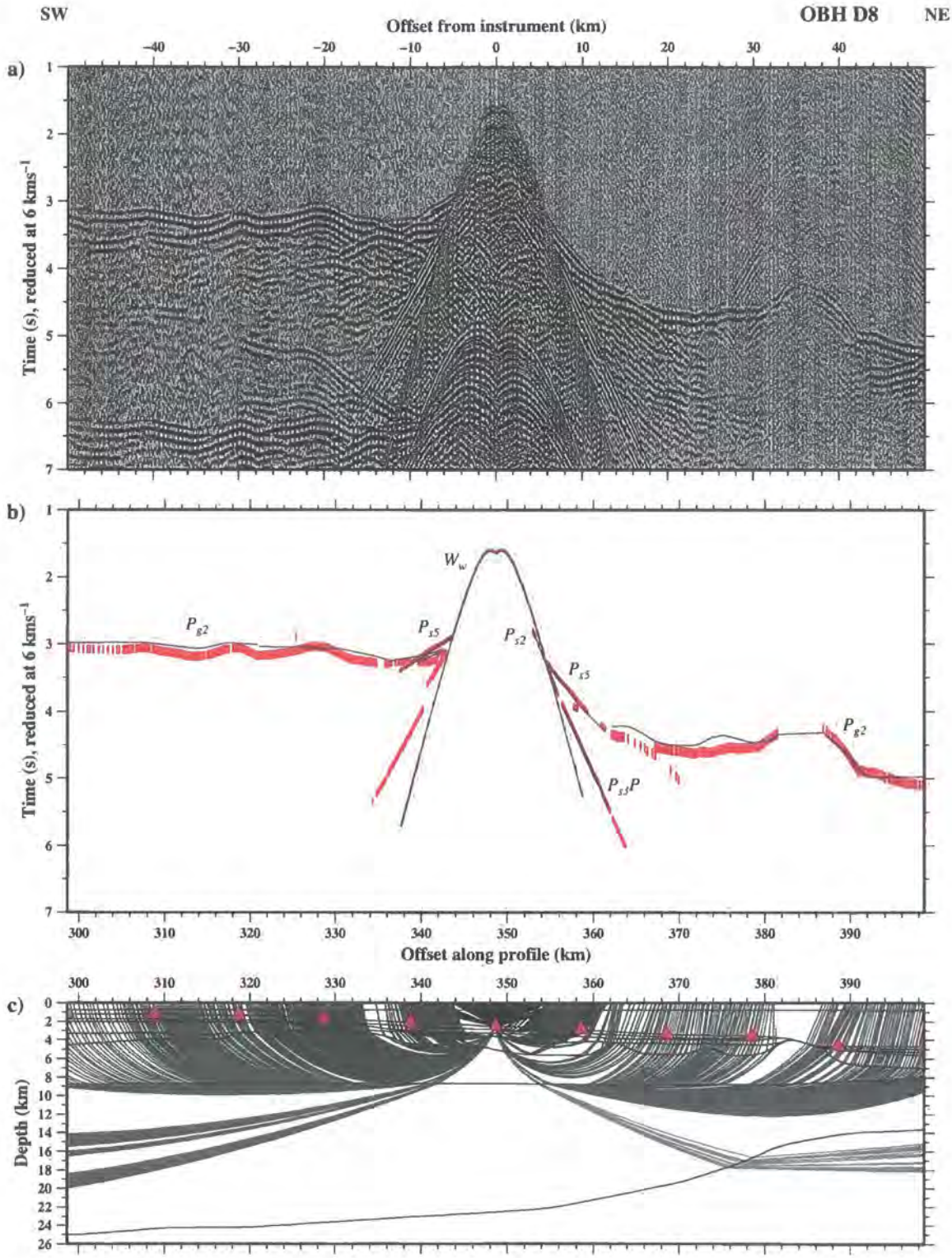


**Figure C.32**: Ray-trace modelling of hydrophone data recorded at OBS D8. See Figure 2.3 for instrument location. See Figure C.1 for details.

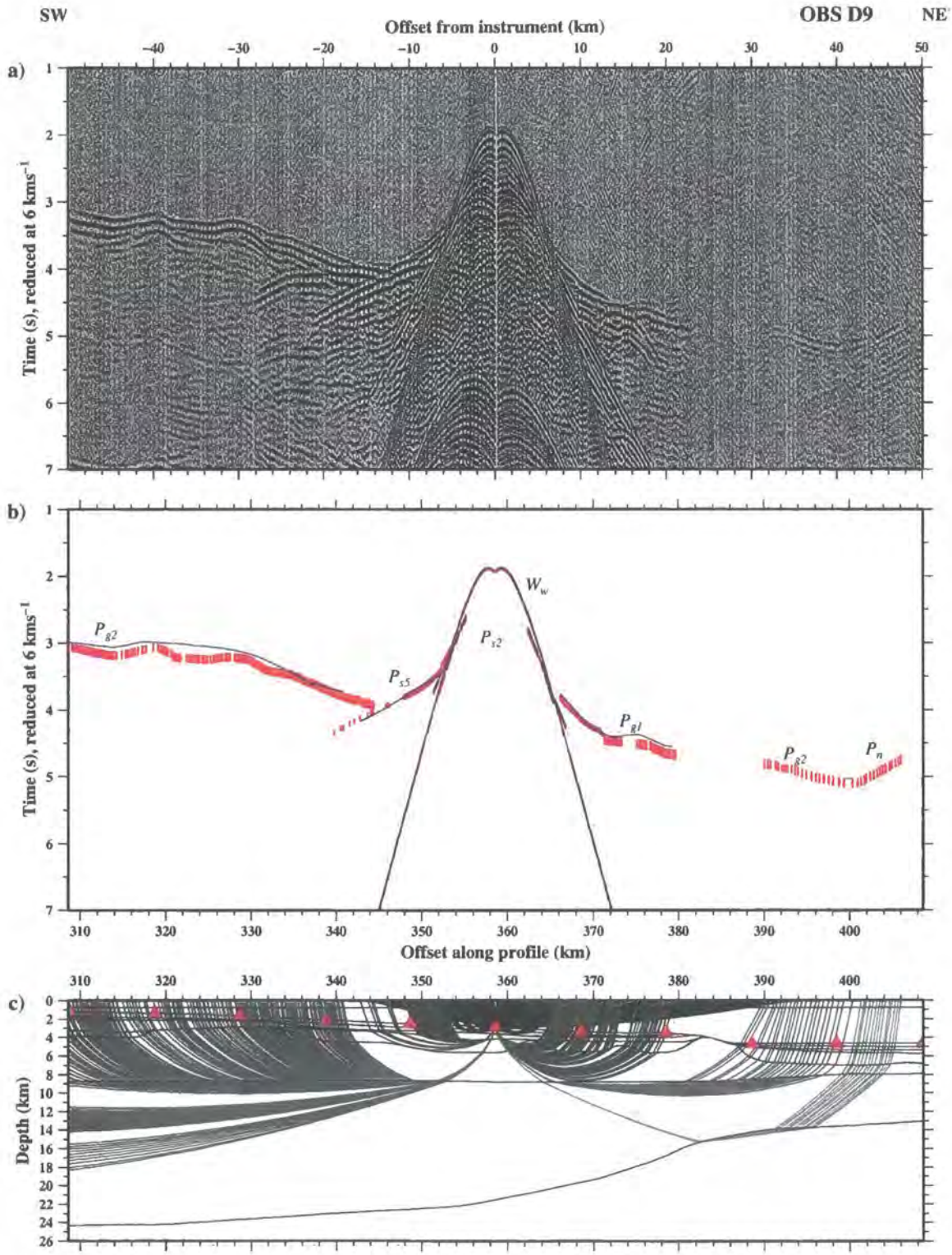


**Figure C.33**: Ray-trace modelling of hydrophone data recorded at OBS D9. See Figure 2.3 for instrument location. See Figure C.1 for details.

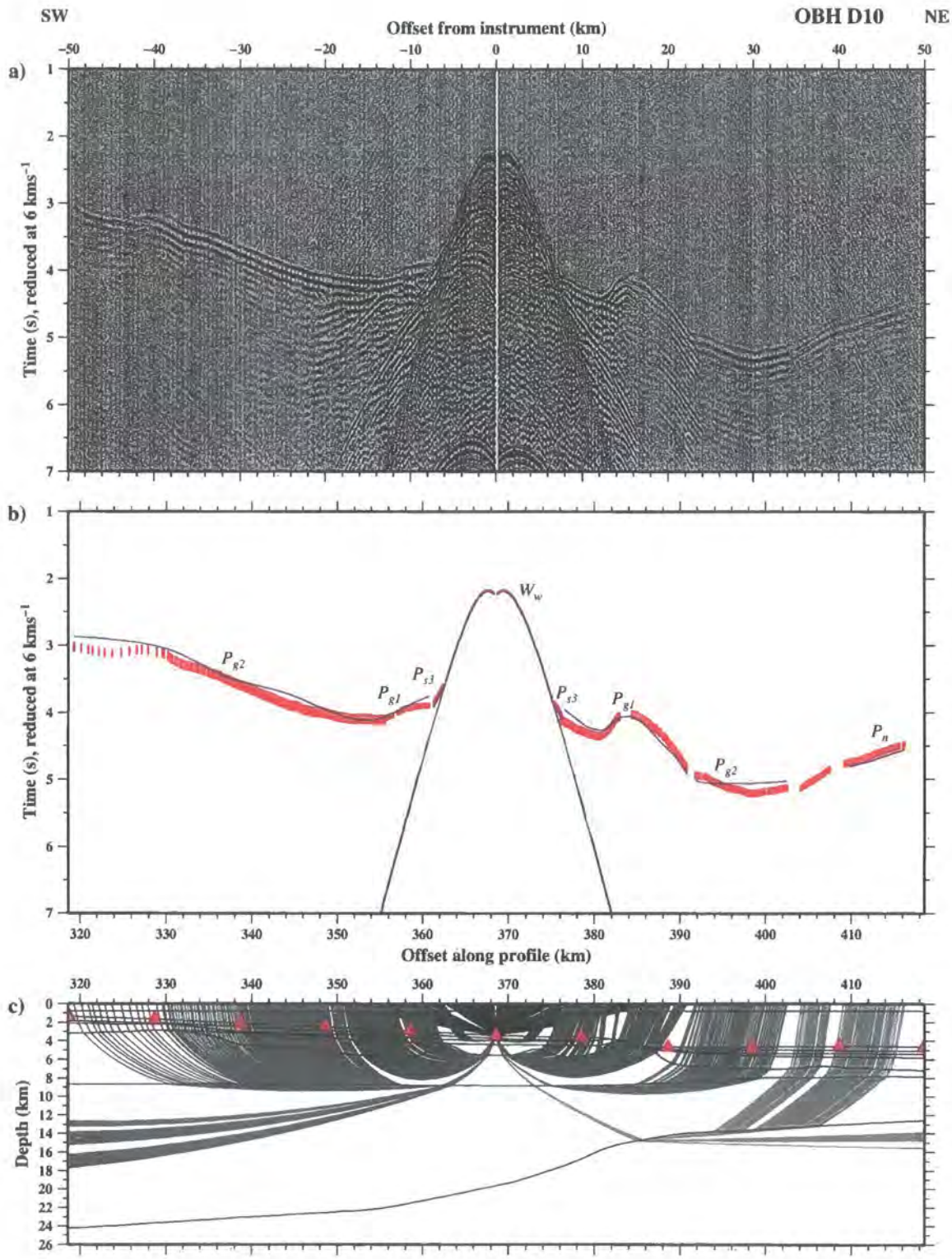


**Figure C.34**: Ray-trace modelling of hydrophone data recorded at OBS D10. See Figure 2.3 for instrument location. See Figure C.1 for details.

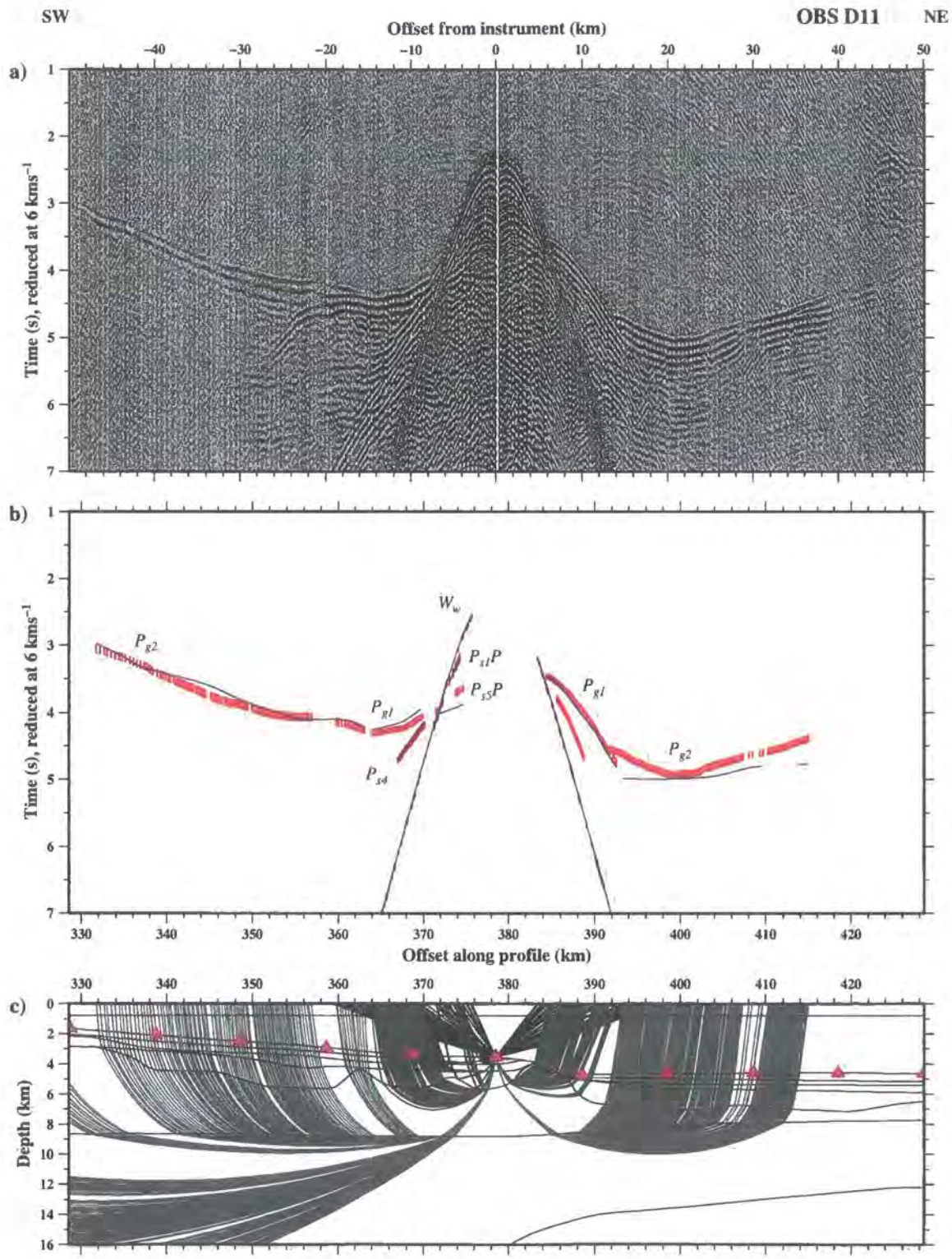


**Figure C.35**: Ray-trace modelling of hydrophone data recorded at OBS D11. See Figure 2.3 for instrument location. See Figure C.1 for details.

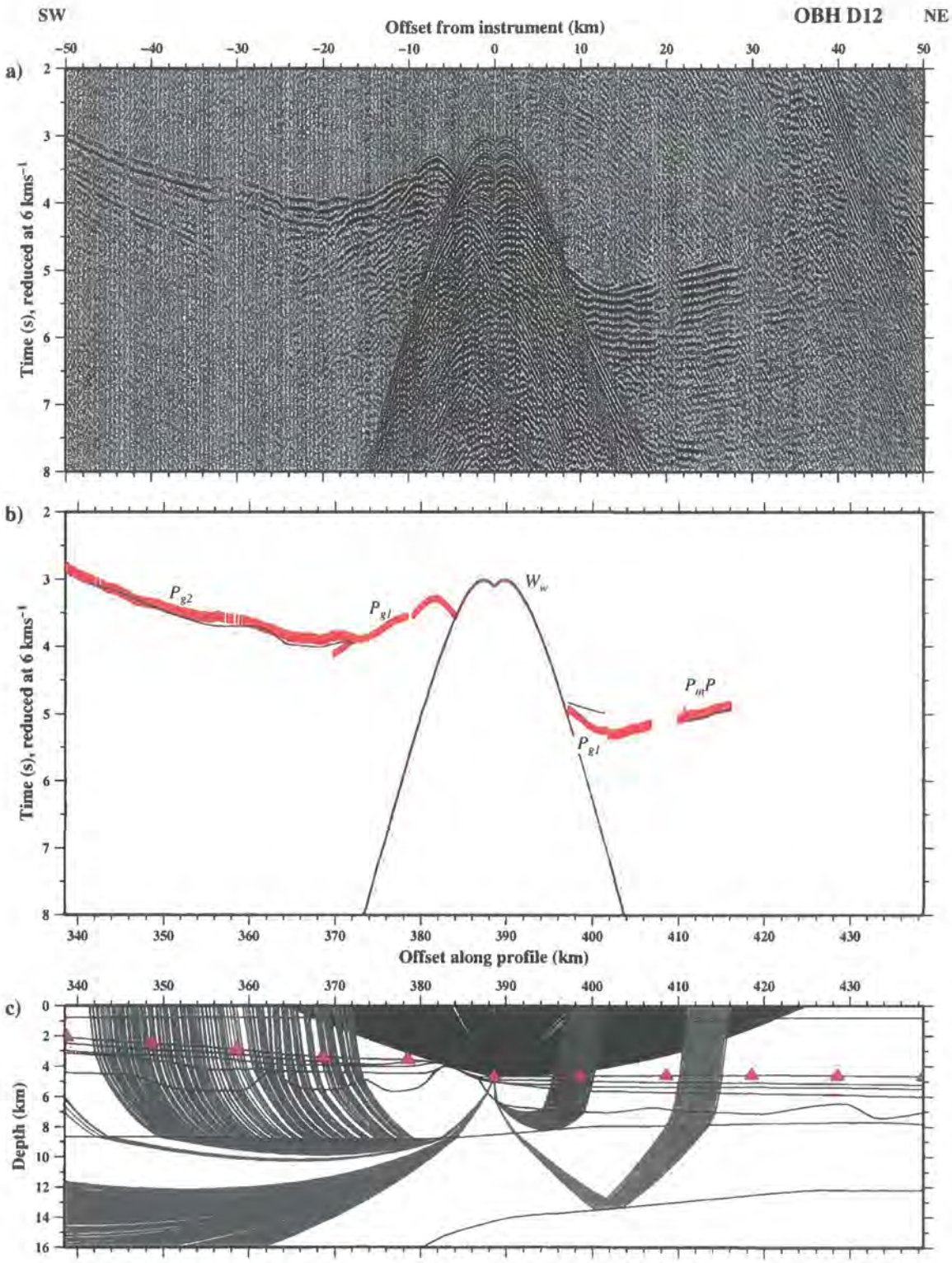


**Figure C.36**: Ray-trace modelling of hydrophone data recorded at OBS D12. See Figure 2.3 for instrument location. See Figure C.1 for details.

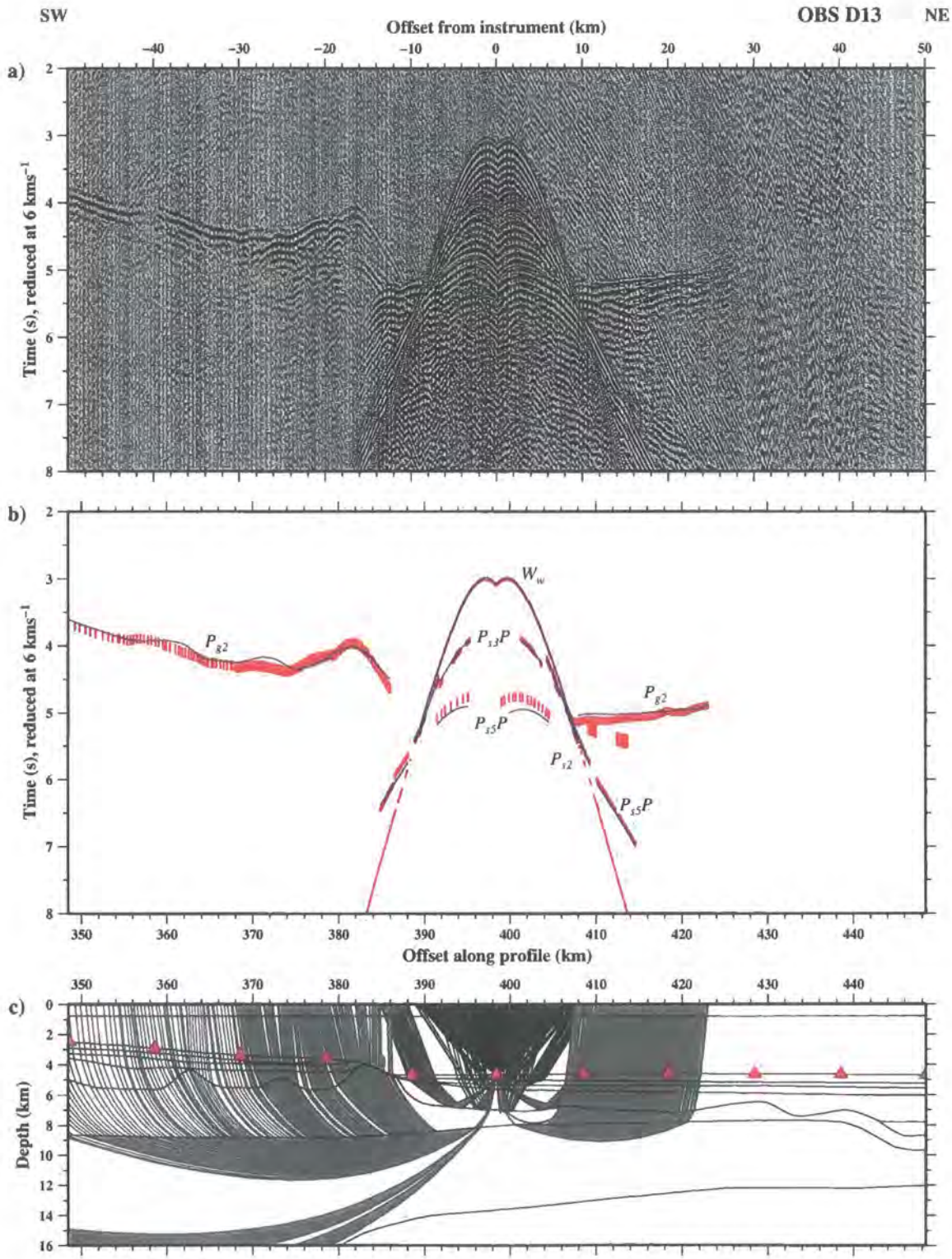


**Figure C.37**: Ray-trace modelling of hydrophone data recorded at OBS D13. See Figure 2.3 for instrument location. See Figure C.1 for details.

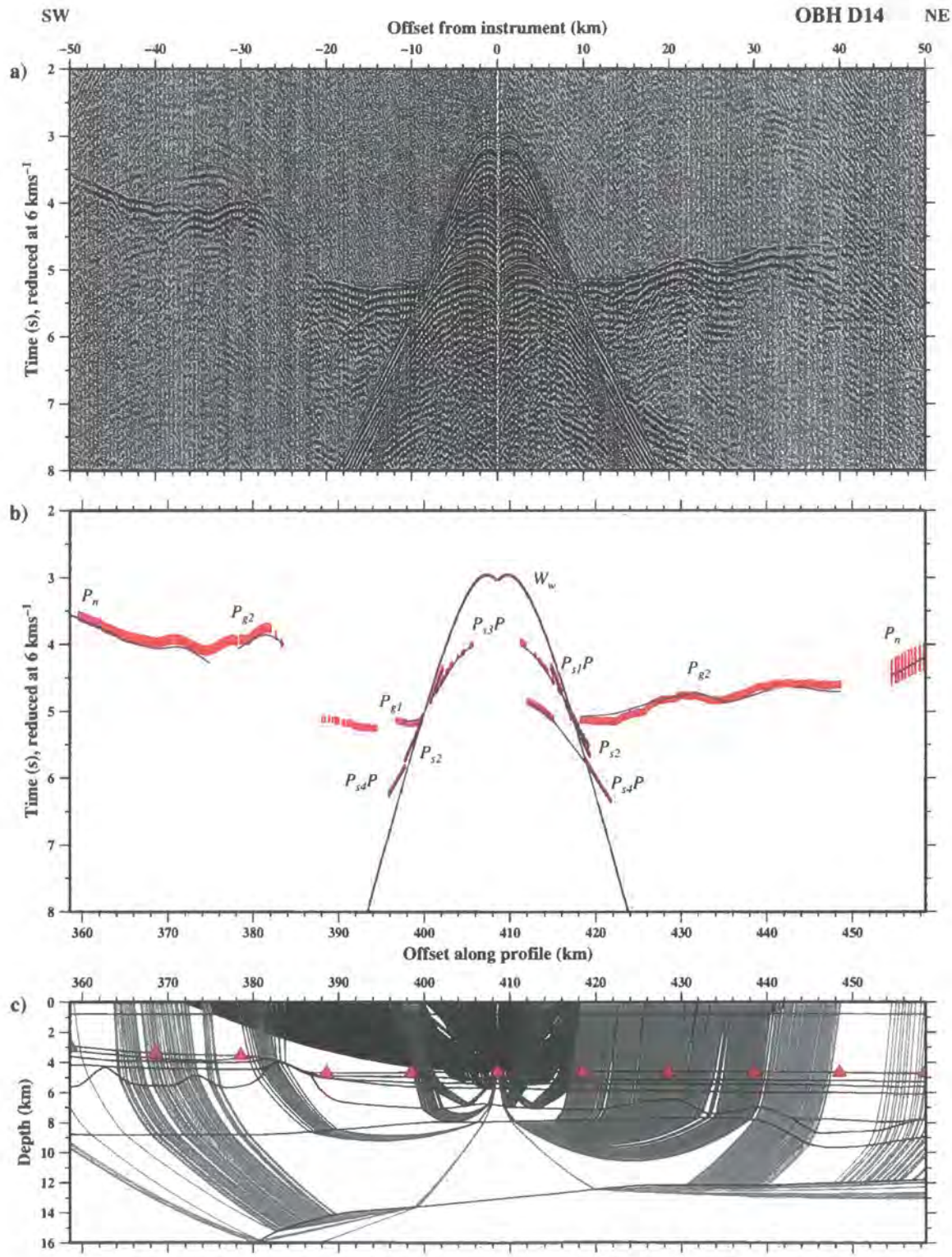


**Figure C.38**: Ray-trace modelling of hydrophone data recorded at OBS D14. See Figure 2.3 for instrument location. See Figure C.1 for details.

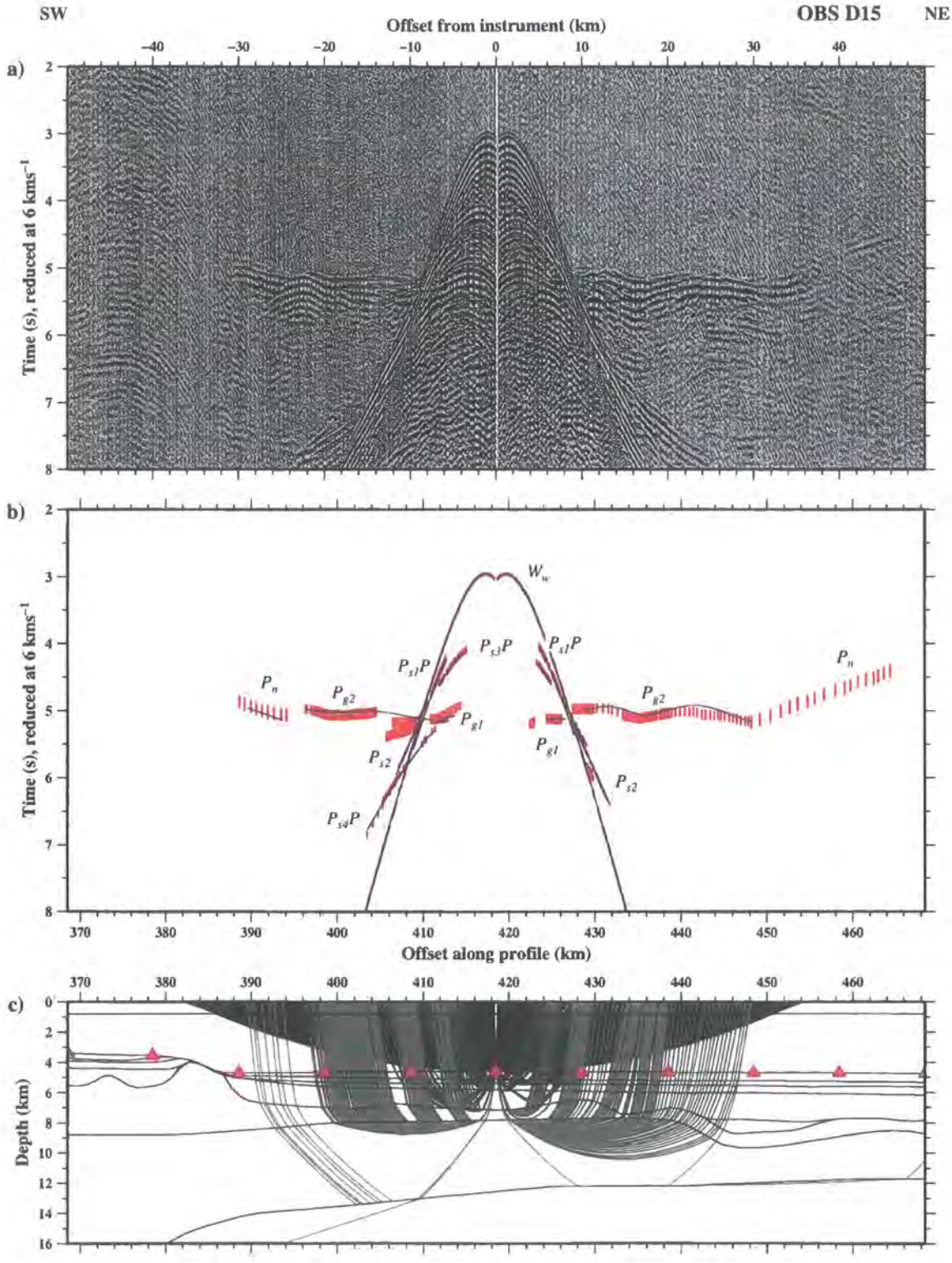


**Figure C.39**: Ray-trace modelling of hydrophone data recorded at OBS D15. See Figure 2.3 for instrument location. See Figure C.1 for details.

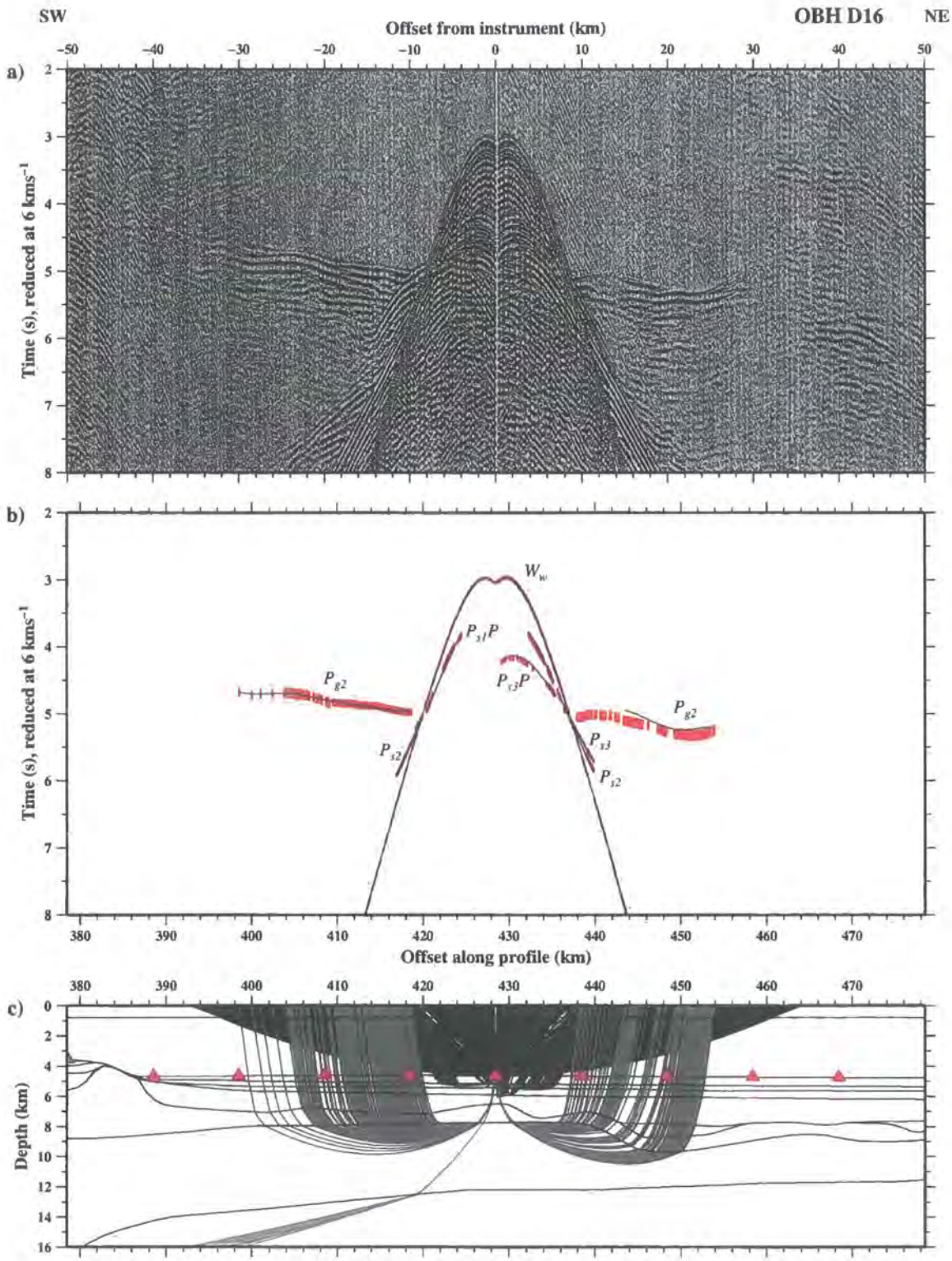


**Figure C.40**: Ray-trace modelling of hydrophone data recorded at OBS D16. See Figure 2.3 for instrument location. See Figure C.1 for details.

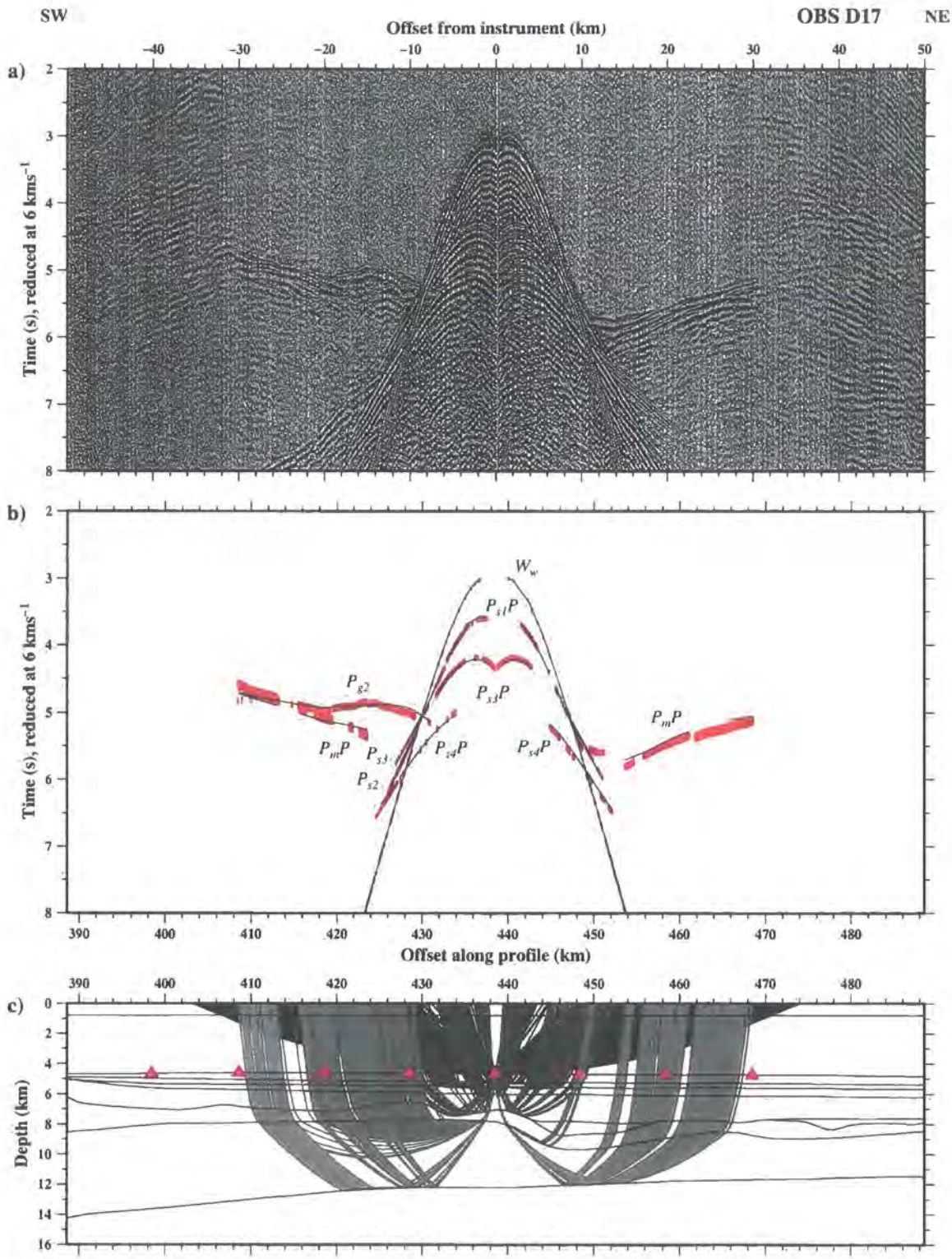


**Figure C.41**: Ray-trace modelling of hydrophone data recorded at OBS D17. See Figure 2.3 for instrument location. See Figure C.1 for details.

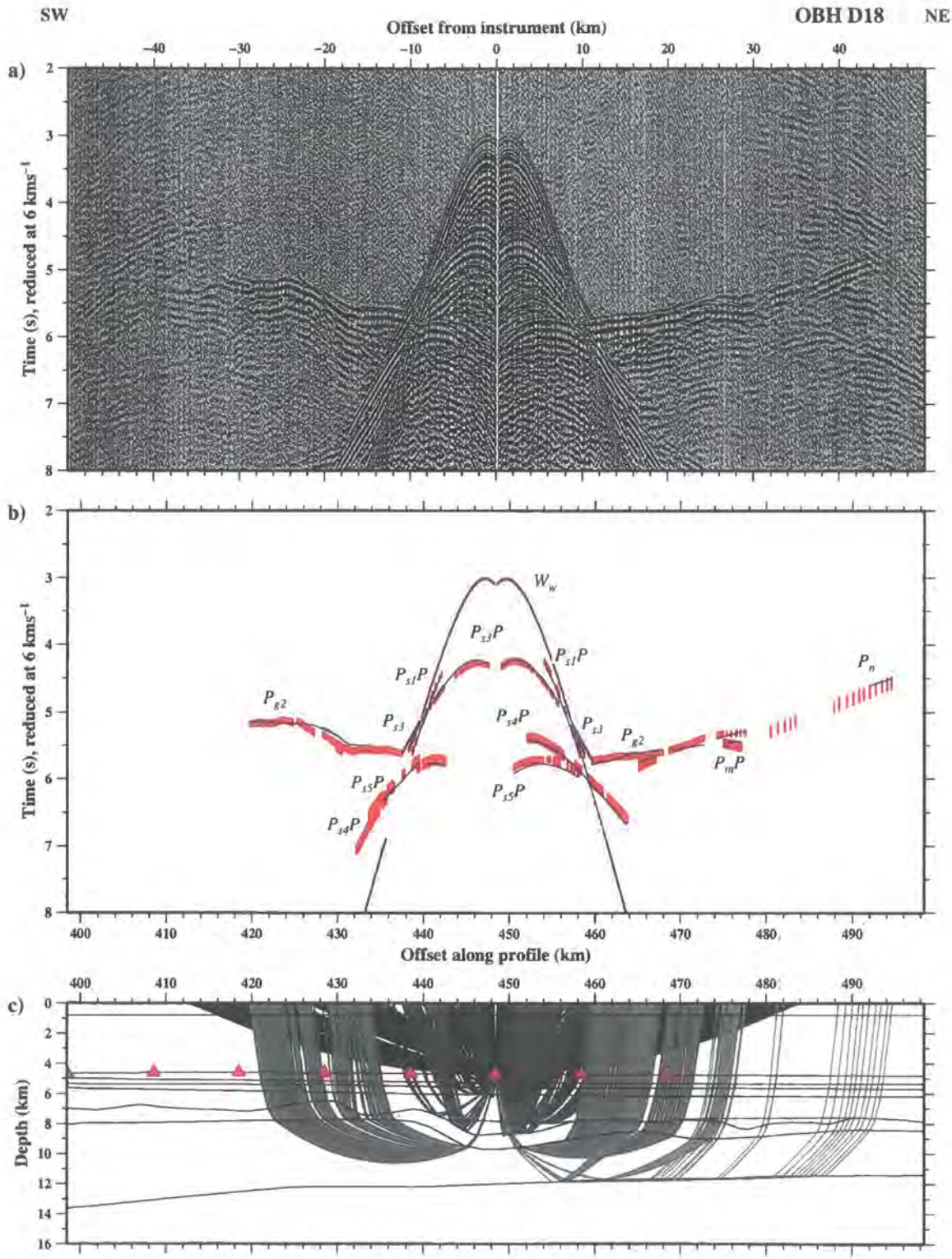


**Figure C.42**: Ray-trace modelling of hydrophone data recorded at OBS D18. See Figure 2.3 for instrument location. See Figure C.1 for details.

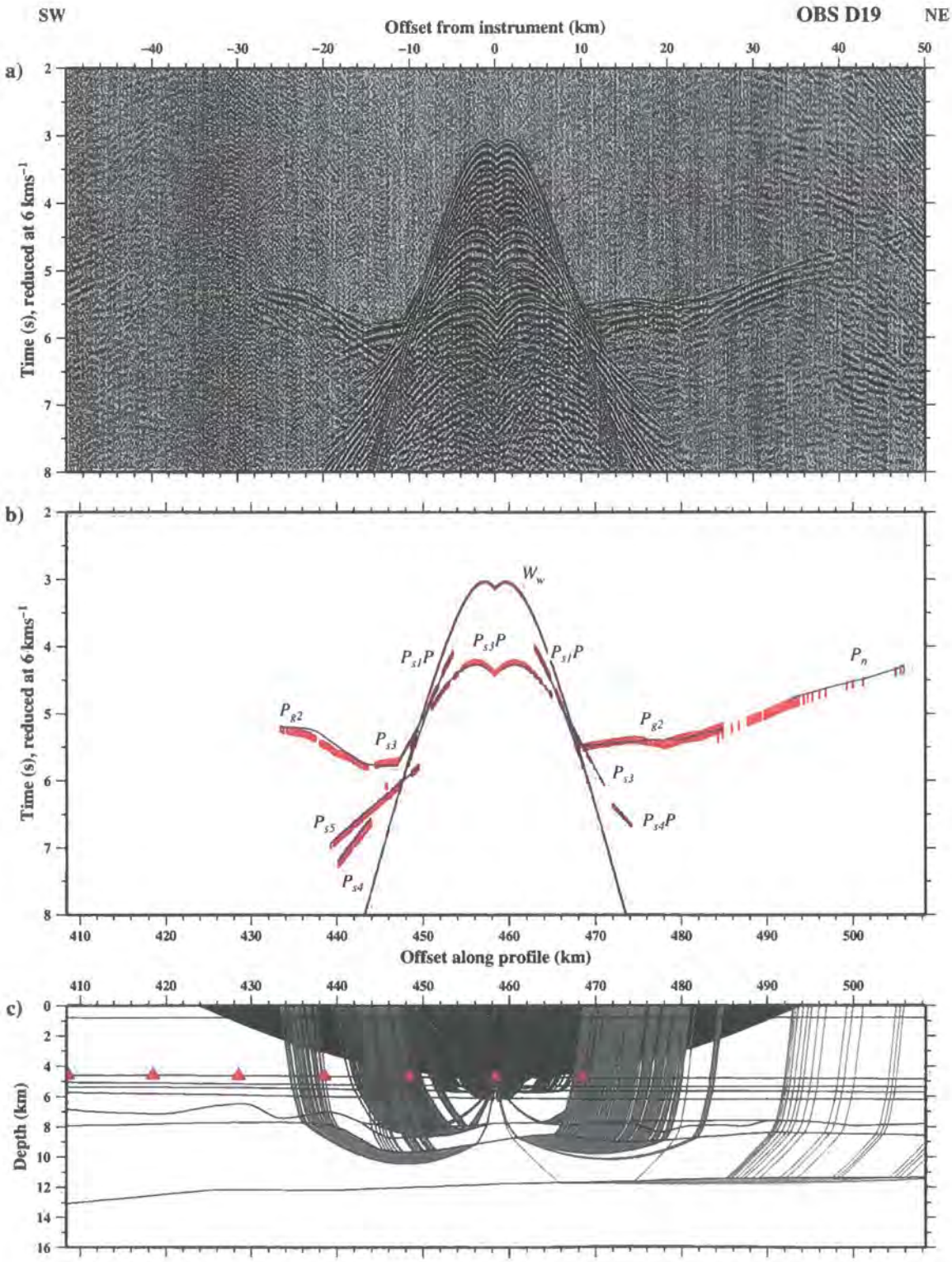


**Figure C.43**: Ray-trace modelling of hydrophone data recorded at OBS D19. See Figure 2.3 for instrument location. See Figure C.1 for details.

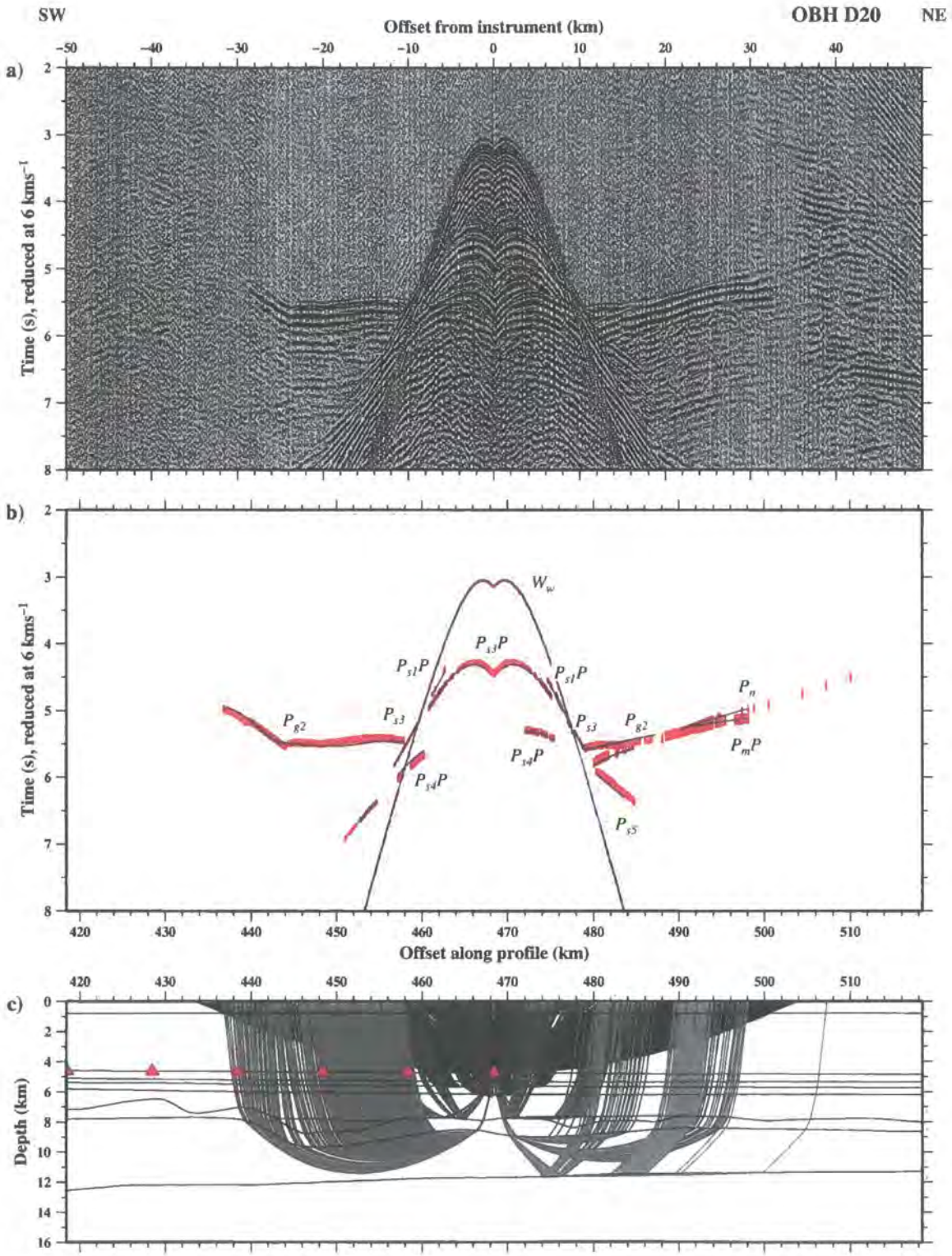


**Figure C.44**: Ray-trace modelling of hydrophone data recorded at OBS D20. See Figure 2.3 for instrument location. See Figure C.1 for details.

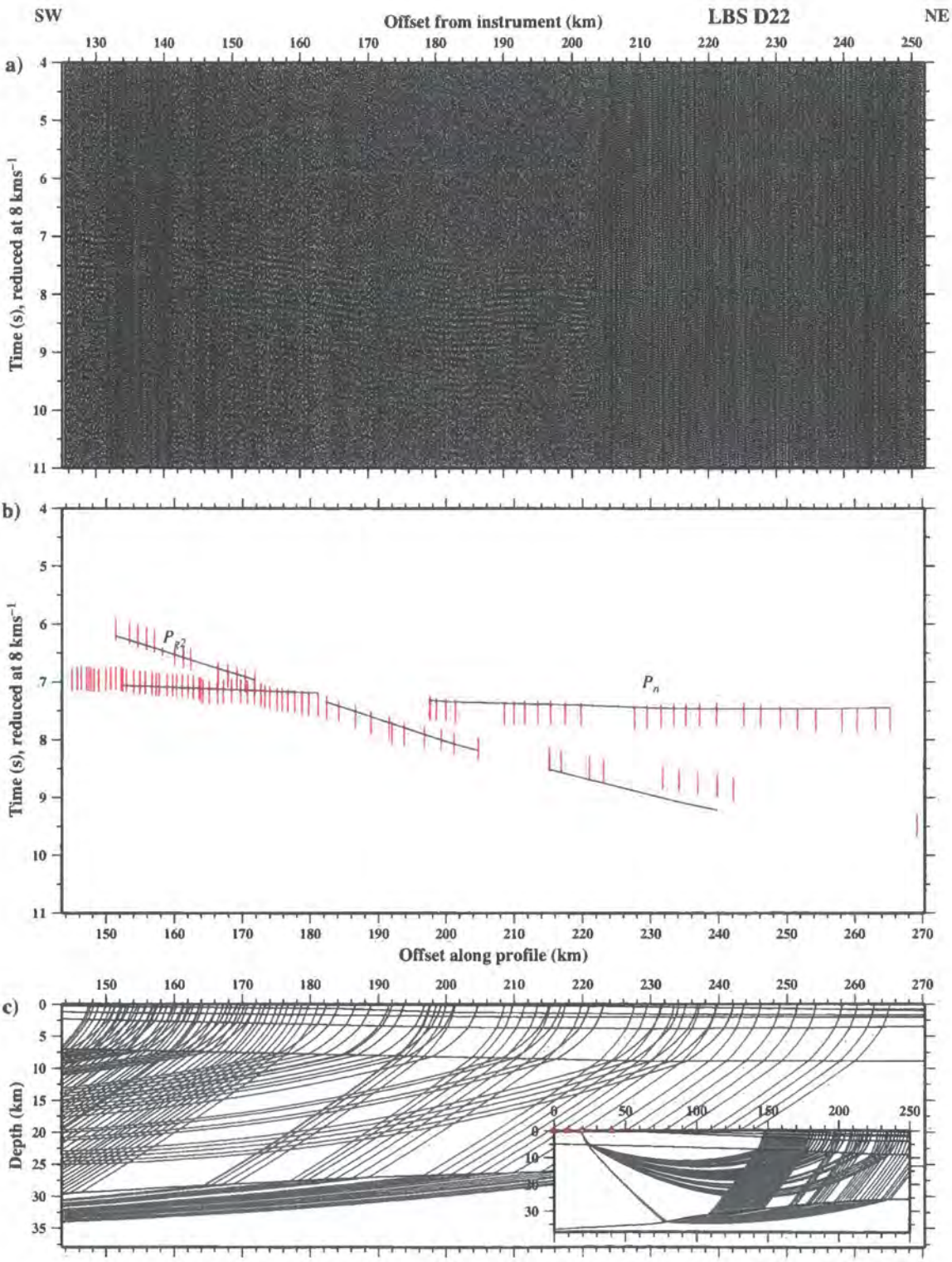


**Figure C.45**: Ray-trace modelling of vertical component geophone data recorded at land station D22. See Figure 2.2 for instrument location. See Figure C.1 for details.

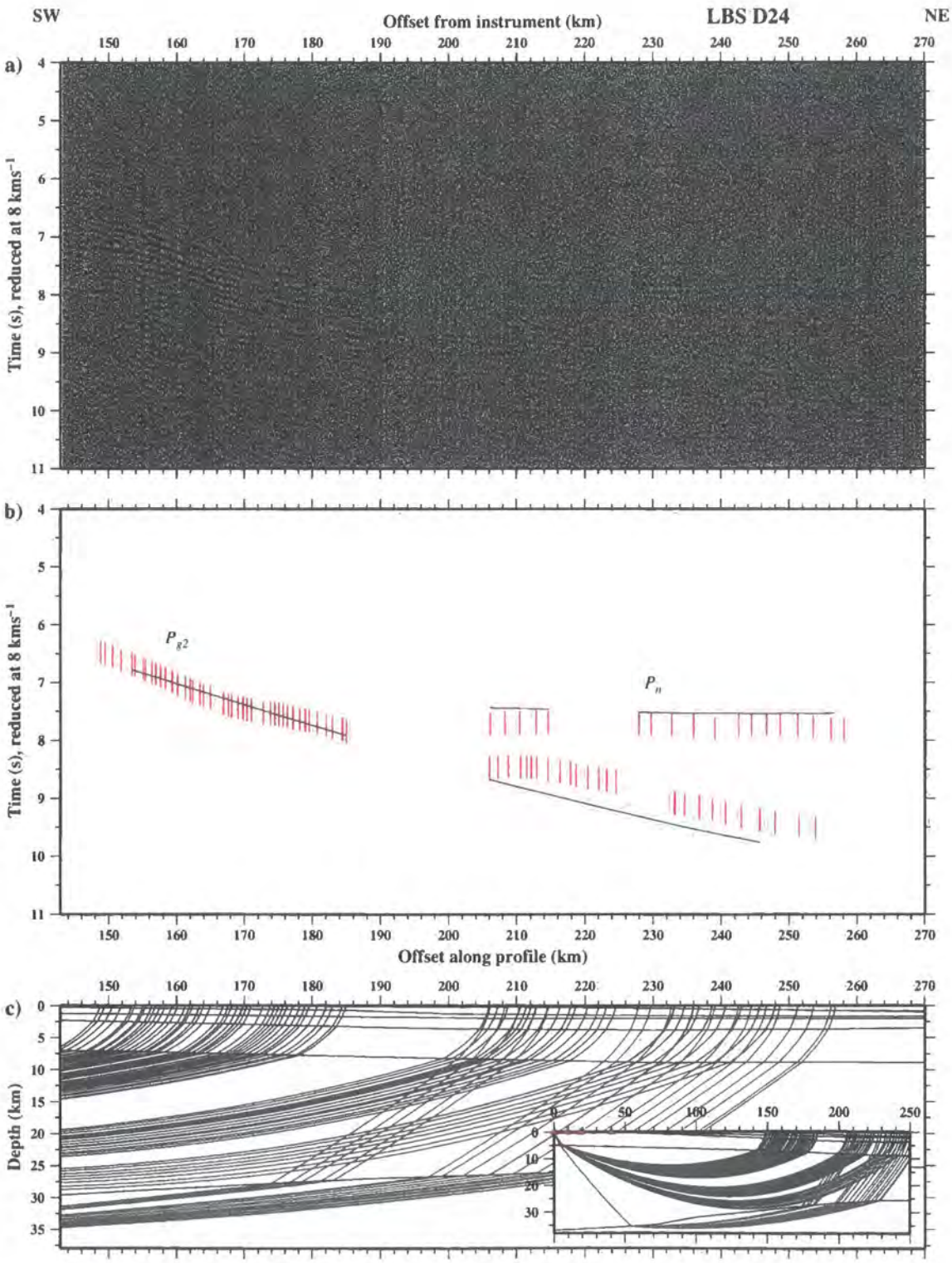


**Figure C.46**: Ray-trace modelling of vertical component geophone data recorded at land station D24. See Figure 2.2 for instrument location. See Figure C.1 for details.

# D Final *P*-wave velocity-depth models

The final *P*-wave velocity-depth models are shown below in *rayinvr* (Zelt & Smith, 1992) format. Lines beginning with a # are comment lines and should be removed before input of a model into *rayinvr*.

## D.1 Profile A

```
#  Layer 1 - Sea surface (Ww)
# ============================
 1    0.00  15.00  45.00  50.00 427.51
 0   -0.02  -0.03  -0.02   0.00   0.00
        1      0      0      0      0
# Top velocity
 1    0.00 427.51
 0    1.48   1.48
        0      0
# Bottom velocity
 1    0.00 427.51
 0    1.47   1.47
        0      0
#
#  Layer 2 - Thermocline (Ww)
# ============================
 2    0.00  15.00  45.00  50.00 161.39 174.39 180.39 183.19 183.99 260.00
 1   -0.02  -0.03  -0.02   0.00   0.07   0.07   0.10   0.14   0.30   0.60
        0      0      0      0      0      0      0      0      0      0
 2  427.51
 0    0.75
        0
# Top velocity
 2    0.00 186.11 260.00 427.51
 0    1.49   1.49   1.50   1.50
        0      0      0      0
# Bottom velocity
 2    0.00 161.39 260.00 275.00 340.00 427.51
 0    1.49   1.49   1.51   1.51   1.52   1.52
        0      0      0      0      0      0
#
#  Layer 3 - Seafloor (Ps1, Ps1P)
# ================================
 3    0.00  15.00  45.00  50.00 161.39 174.39 180.39 183.19 185.14 185.29
 1   -0.02  -0.03  -0.02   0.00   0.08   0.08   0.11   0.14   0.53   0.49
        0      0      0      0      0      0      0      0      0      0
 3  186.39 186.89 187.69 188.49 189.49 190.79 190.99 191.09 191.39 191.89
 1    0.68   0.70   0.87   0.99   1.00   1.10   1.18   1.14   1.14   1.24
        0      0      0      0      0      0      0      0      0      0
 3  192.89 193.79 194.79 195.39 196.39 197.59 198.89 199.71 200.79 201.91
 1    1.36   1.50   1.64   1.67   1.67   1.83   1.94   1.84   1.94   1.86
        0      0      0      0      0      0      0      0      0      0
 3  205.19 208.31 212.39 216.99 221.39 229.39 236.89 240.39 242.39 246.39
 1    2.09   2.20   2.36   2.51   2.62   2.78   2.88   2.96   3.00   3.06
        0      0      0      0      0      0      0      0      0      0
 3  262.39 264.39 266.39 270.39 276.39 287.39 291.89 299.39 305.39 305.69
 1    3.34   3.39   3.39   3.43   3.50   3.63   3.66   3.75   3.79   3.81
        0      0      0      0      0      0      0      0      0      0
 3  308.39 308.89 311.39 316.39 317.59 318.39 325.39 327.39 330.39 332.39
 1    3.83   3.85   3.87   3.91   3.92   3.93   3.96   4.00   4.00   4.05
        0      0      0      0      0      0      0      0      0      0
 3  333.39 336.39 338.11 341.39 341.71 344.51 351.51 354.39 365.39 371.39
 1    4.03   4.04   4.09   4.10   4.12   4.10   4.18   4.15   4.17   4.19
 0       0      0      0      0      0      0      0      0      0
 3  377.39 381.51 386.91 391.51 398.39 399.39 405.39 410.39 415.39 427.51
 0    4.22   4.21   4.22   4.23   4.24   4.26   4.27   4.27   4.30   4.31
        0      0      0      0      0      0      0      0      0      0
# Top velocity
 3    0.00 180.00 190.00 200.00 210.00 220.00 230.00 250.00 260.00 270.00
 1    1.62   1.62   1.61   1.61   1.62   1.65   1.63   1.63   1.62   1.62
        0      0      0      0      0      0      0      0      0      0
```

```
 3  280.00 285.00 290.00 295.00 300.00 310.00 320.00 330.00 340.00 350.00
 1    1.61   1.62   1.62   1.63   1.62   1.64   1.66   1.67   1.66   1.69
        0      0      0      0      0      0      0      0      0      0
 3  427.51
 0    1.69
        0
# Bottom velocity
 3    0.00 180.00 190.00 200.00 210.00 220.00 230.00 240.00 250.00 260.00
 1    2.00   2.00   2.20   2.40   2.46   2.64   2.52   2.47   2.44   2.36
        0      0      0      0      0      0      0      0      0      0
 3  270.00 280.00 285.00 290.00 295.00 300.00 310.00 320.00 330.00 340.00
 1    2.34   2.32   2.33   2.32   2.32   2.38   2.42   2.42   2.44   2.40
        0      0      0      0      0      0      0      0      0      0
 3  350.00 360.00 370.00 380.00 427.51
 0    2.40   2.43   2.45   2.46   2.46
        0      0      0      0      0
#
#  Layer 4 - First subsurface sediment layer (Ps2,Ps2P)
# ====================================================
 4    0.00 160.00 171.51 182.91 190.00 200.00 210.00 220.00 230.00 240.00
 1    0.03   0.19   0.21   0.80   1.80   2.90   3.30   3.95   3.98   4.03
        0      0      0      0      0      0      0      0      0      0
 4  250.00 260.00 270.00 280.00 290.00 295.00 300.00 310.00 320.00 330.00
 1    4.12   4.19   4.30   4.42   4.50   4.54   4.66   4.74   4.87   4.96
        0      0      0      0      0      0      0      0      0      0
 4  340.00 350.00 360.00 370.00 380.00 400.00 407.00 427.51
 0    5.03   5.09   5.15   5.21   5.26   5.34   5.38   5.44
        0      0      0      0      0      0      0      0
# Top velocity
 4    0.00 160.00 177.00 185.50 190.00 200.00 210.00 220.00 230.00 240.00
 1    2.00   2.00   2.05   2.05   2.25   2.40   2.46   2.64   2.52   2.47
        0      0      0      0      0      0      0      0      0      0
 4  250.00 260.00 270.00 280.00 285.00 290.00 295.00 300.00 310.00 320.00
 1    2.47   2.46   2.42   2.38   2.39   2.40   2.40   2.42   2.42   2.44
        0      0      0      0      0      0      0      0      0      0
 4  330.00 340.00 350.00 360.00 370.00 380.00 427.51
 0    2.46   2.42   2.40   2.43   2.45   2.46   2.46
        0      0      0      0      0      0      0
# Bottom velocity
 4    0.00 177.00 185.50 190.00 200.00 210.00 220.00 230.00 260.00 270.00
 1    2.44   2.44   3.54   3.30   3.02   2.98   2.85   2.75   2.75   2.72
        0      0      0      0      0      0      0      0      0      0
 4  280.00 300.00 310.00 320.00 330.00 340.00 427.51
 0    2.66   2.66   2.74   2.70   2.65   2.62   2.62
        0      0      0      0      0      0      0
#
#  Layer 5 - Second subsurface sediment layer (Ps3, Ps3P)
# ======================================================
 5    0.00 160.00 176.00 177.00 185.50 200.00 210.00 220.00 230.00 240.00
 1    0.05   0.75   0.84   0.87   3.50   3.95   4.10   4.28   4.48   4.55
        0      0      0      0      0      0      0      0      0      0
 5  250.00 260.00 270.00 280.00 295.00 300.00 310.00 320.00 330.00 340.00
 1    4.68   4.80   4.90   5.04   5.12   5.16   5.32   5.38   5.42   5.44
        0      0      0      0      0      0      0      0      0      0
 5  350.00 360.00 370.00 380.00 400.00 410.00 427.51
 0    5.50   5.53   5.57   5.62   5.66   5.75   5.83
        0      0      0      0      0      0      0
# Top velocity
 5    0.00 190.00 200.00 210.00 220.00 230.00 240.00 250.00 260.00 270.00
 1    3.00   3.00   3.02   2.98   2.96   2.94   2.92   2.90   2.90   2.92
        0      0      0      0      0      0      0      0      0      0
 5  280.00 290.00 300.00 310.00 320.00 330.00 340.00 350.00 360.00 370.00
 1    2.87   2.85   2.83   2.80   2.78   2.76   2.74   2.70   2.75   2.75
        0      0      0      0      0      0      0      0      0      0
 5  380.00 427.51
 0    2.74   2.73
        0      0
# Bottom velocity
 5    0.00 190.00 200.00 210.00 220.00 230.00 240.00 250.00 260.00 270.00
 1    3.00   3.00   3.02   3.00   2.99   2.98   2.98   3.04   3.04   3.06
        0      0      0      0      0      0      0      0      0      0
 5  280.00 290.00 310.00 320.00 330.00 340.00 350.00 360.00 370.00 380.00
 1    3.02   3.00   3.00   2.98   2.94   2.90   2.82   2.86   2.85   2.84
```

```
        0      0      0      0      0      0      0      0      0      0
 5  427.51
 0    2.83
        0
#
#  Layer 6 - Third subsurface sediment layer (Ps4, Ps4P)
# ======================================================
 6    0.00 160.00 176.00 177.00 185.50 200.00 210.00 220.00 230.00 240.00
 1    0.05   0.75   0.84   0.87   3.50   3.95   4.20   4.52   4.75   4.90
        0      0      0      0      0      0      0      0      0      0
 6  250.00 260.00 270.00 280.00 290.00 300.00 310.00 320.00 330.00 340.00
 1    5.05   5.20   5.34   5.40   5.54   5.62   5.70   5.80   5.85   5.90
        0      0      0      0      0      0      0      0      0      0
 6  350.00 360.00 370.00 380.00 400.00 427.51
 0    5.96   6.01   6.05   6.10   6.18   6.35
        0      0      0      0      0      0
# Top velocity
 6    0.00 170.00 180.00 185.50 190.00 200.00 210.00 220.00 230.00 240.00
 1    3.00   3.00   3.10   3.15   3.20   3.23   3.10   3.03   3.01   3.04
        0      0      0      0      0      0      0      0      0      0
 6  260.00 270.00 280.00 310.00 320.00 330.00 340.00 350.00 360.00 370.00
 1    3.04   3.02   3.00   3.00   2.98   2.94   2.90   2.87   2.86   2.85
        0      0      0      0      0      0      0      0      0      0
 6  427.51
 0    2.85
        0
# Bottom velocity
 6    0.00 160.00 170.00 180.00 185.50 190.00 200.00 210.00 220.00 230.00
 1    3.00   3.10   3.10   3.20   3.25   3.30   3.25   3.18   3.12   3.12
        0      0      0      0      0      0      0      0      0      0
 6  240.00 260.00 270.00 280.00 290.00 320.00 330.00 340.00 350.00 360.00
 1    3.09   3.09   3.07   3.07   3.03   3.03   2.99   2.95   2.91   2.91
        0      0      0      0      0      0      0      0      0      0
 6  370.00 427.51
 0    2.90   2.90
        0      0
#
#  Layer 7 - Fourth subsurface sediment layer (Ps5, Ps5P)
# ======================================================
 7    0.00 160.00 176.00 177.00 185.50 193.00 194.75 197.00 208.00 220.00
 1    0.05   1.65   2.04   2.07   4.00   6.60   6.90   7.20   7.28   7.37
        0      0      0      0      0      0      0      0      0      0
 7  230.00 245.00 250.00 260.00 270.00 280.00 291.00 292.00 300.00 310.00
 1    7.40   7.52   7.60   7.68   7.76   7.82   7.84   7.84   7.88   7.86
        0      0      0      0      0      0      0      0      0      0
 7  320.00 330.00 340.00 360.00 370.00 380.00 390.00 400.00 427.51
 0    7.86   7.84   7.80   7.80   7.82   7.78   7.76   7.74   7.72
        0      0      0      0      0      0      0      0      0
# Top velocity
 7    0.00 197.00 200.00 210.00 220.00 230.00 240.00 250.00 260.00 270.00
 1    4.21   4.21   4.22   4.24   4.24   4.26   4.23   4.18   4.14   4.10
        0      0      0      0      0      0      0      0      0      0
 7  280.00 290.00 300.00 310.00 320.00 330.00 340.00 350.00 360.00 370.00
 1    4.12   4.08   3.93   3.83   3.80   3.77   3.63   3.56   3.53   3.50
        0      0      0      0      0      0      0      0      0      0
 7  380.00 390.00 400.00 427.51
 0    3.50   3.40   3.30   3.20
        0      0      0      0
# Bottom velocity
 7    0.00 197.00 212.00 215.00 227.00 240.00 267.00 272.00 275.00 283.00
 1    4.21   4.21   4.53   4.58   4.63   4.65   4.67   4.70   4.70   4.60
        0      0      0      0      0      0      0      0      0      0
 7  292.00 296.00 300.00 310.00 320.00 330.00 340.00 345.00 360.00 370.00
 1    4.55   4.45   4.45   4.32   4.00   3.91   3.82   3.73   3.76   3.86
        0      0      0      0      0      0      0      0      0      0
 7  380.00 384.00 385.00 395.00 402.00 410.00 415.00 418.00 427.51
 0    3.80   3.80   3.70   3.56   3.58   3.45   3.43   3.46   3.39
        0      0      0      0      0      0      0      0      0
#
#  Layer 8 - Basement (Pg1, Pg1P)
# ================================
 8    0.00 160.00 176.00 177.00 185.50 193.00 194.75 197.00 206.50 212.00
 1    0.05   1.65   2.04   2.07   4.00   6.60   6.90   7.20   9.22   9.21
```

```
         0       0       0       0       0       0       0       0       0       0
 8  215.00 238.00 250.00 260.00 267.00 270.00 275.00 288.00 296.00 297.00
 1    9.18   9.15   8.85   8.95   9.40  10.00  10.05   9.75   9.95  10.10
         0       0       0       0       0       0       0       0       0       0
 8  304.00 310.00 316.00 320.00 330.00 335.00 348.00 354.00 365.00 373.00
 1   10.10  10.05   9.50   9.70   9.25   8.93   8.72   8.92   9.02   9.28
         0       0       0       0       0       0       0       0       0       0
 8  380.00 382.00 384.00 385.00 395.00 402.00 410.00 415.00 418.00 427.51
 0    9.34   9.34   9.34   9.16   8.70   8.80   8.50   8.23   8.48   8.23
         0       0       0       0       0       0       0       0       0       0
# Top velocity
 8    0.00 177.00 208.50 215.00 225.00 240.00 250.00 260.00 270.00 285.00
 1    5.60   5.60   5.20   5.15   5.10   5.10   4.90   4.90   5.10   5.10
         0       0       0       0       0       0       0       0       0       0
 8  290.00 316.00 328.00 427.51
 0    4.90   5.00   4.60   4.60
         0       0       0       0
# Bottom velocity
 8    0.00 160.00 170.00 200.00 210.00 240.00 250.00 290.00 316.00 328.00
 1    5.90   5.90   6.00   6.00   5.80   5.80   5.70   5.70   5.40   5.00
         0       0       0       0       0       0       0       0       0       0
 8  427.51
 0    5.00
         0
#
#  Layer  9 - Inter-crustal boundary (Pg2, PmP)
# ============================================
 9    0.00 160.00 170.00 175.00 180.00 186.00 193.00 206.50 220.00 228.00
 1    9.00   9.00   8.80   8.70   8.60   8.80   9.30  11.50  11.50  11.40
         0       0       0       0       0       0       0       0       0       0
 9  233.00 240.00 250.00 260.00 265.00 270.00 283.00 295.00 296.00 300.00
 1   10.90  10.90  10.50  10.40  10.90  11.10  10.75  11.05  11.10  10.85
         0       0       0       0       0       0       0       0       0       0
 9  316.00 325.00 330.00 355.00 365.00 367.00 368.00 373.00 376.00 384.00
 1   10.35  10.45  10.40  10.12  10.50  10.60  10.70  10.10  10.20  10.16
         0       0       0       0       0       0       0       0       0       0
 9  392.00 427.51
 0   10.20  10.20
         0       0
# Top velocity
 9    0.00 170.00 180.00 190.00 200.00 240.00 250.00 260.00 270.00 283.00
 1    6.40   6.40   6.45   6.55   6.60   6.60   6.55   6.50   6.50   6.45
         0       0       0       0       0       0       0       0       0       0
 9  300.00 316.00 328.00 330.00 340.00 350.00 360.00 369.00 373.00 390.00
 1    6.45   6.35   6.40   6.40   6.50   6.60   6.60   6.70   6.65   6.55
         0       0       0       0       0       0       0       0       0       0
 9  400.00 427.51
 0    6.50   6.50
         0       0
# Bottom velocity
 9    0.00 180.00 192.00 200.00 210.00 220.00 230.00 240.00 250.00 260.00
 1    6.70   6.70   6.90   7.10   7.15   7.10   7.00   7.10   7.10   7.30
         0       0       0       0       0       0       0       0       0       0
 9  270.00 280.00 290.00 300.00 310.00 318.00 330.00 374.00 386.00 390.00
 1    7.40   7.50   7.50   7.40   7.20   7.30   7.30   7.00   6.95   6.90
         0       0       0       0       0       0       0       0       0       0
 9  427.51
 0    6.90
         0
#
#  Layer 10 - Moho (Pn)
# ======================
10    0.00  40.00  50.00  70.00  80.00  90.00 100.00 110.00 120.00 130.00
 1   37.50  37.00  36.50  36.50  36.00  35.90  35.80  35.20  35.00  34.80
         0       0       0       0       0       0       0       0       0       0
10  135.00 155.00 160.00 175.00 192.00 196.00 205.00 225.00 250.00 260.00
 1   34.50  31.00  30.50  27.00  17.00  15.00  14.40  14.25  13.80  13.60
         0       0       0       0       0       0       0       0       0       0
10  270.00 280.00 300.00 310.00 320.00 330.00 340.00 350.00 360.00 370.00
 1   13.50  13.40  13.40  13.30  13.20  13.10  12.92  12.74  12.64  12.54
         0       0       0       0       0       0       0       0       0       0
10  380.00 386.00 427.51
 0   12.48  12.45  12.31
```

```
         0      0      0
# Top velocity
10     0.00 375.00 380.00 427.51
 0     8.00   8.00   7.90   7.90
         0      0      0      0
# Bottom velocity
10     0.00 427.51
 0     8.80   8.80
         0      0
#
#  Layer 11 - Base of model
# ==========================
11     0.00 427.51
 0    80.00  80.00
```

## D.2 Profile D

```
#  Layer 1 - Sea surface (Ww)
# ============================
 1     0.00   9.38  18.45  40.36  45.00 535.00
 0    -0.02  -0.03  -0.04  -0.02  -0.01   0.00
         0      0      0      0      0      0
#
 1     0.00 535.00
 0     1.50   1.50
         0      0
#
 1     0.00 535.00
 0     1.49   1.49
         0      0
#
#  Layer 2 - Thermocline (Ww)
# ============================
 2     0.00   9.38  18.45  40.36  45.00 180.00 214.54 224.12 229.77 235.27
 1    -0.02  -0.03  -0.04  -0.01  -0.01   0.09   0.22   0.31   0.37   0.45
         0      0      0      0      0      0      0      0      0      0
 2   240.27 245.45 251.82 256.82 535.00
 0     0.53   0.61   0.71   0.79   0.79
         0      0      0      0      0
#
 2     0.00 535.00
 0     1.49   1.49
         0      0
#
 2     0.00 256.82 380.00 385.00 535.00
 0     1.49   1.49   1.51   1.53   1.54
         0      0      0      0      0
#
#  Layer 3 - Seafloor (Ps1, Ps1P)
# ================================
 3     0.00   9.38  18.45  45.00 180.00 214.54 224.12 229.77 235.27 240.27
 1    -0.02  -0.02  -0.04   0.00   0.10   0.23   0.32   0.38   0.45   0.53
         0      0      0      0      0      0      0      0      0      0
 3   245.45 251.82 256.82 261.82 266.97 272.05 277.10 282.20 287.42 292.52
 1     0.62   0.72   0.79   0.86   0.93   1.01   1.08   1.15   1.21   1.23
         0      0      0      0      0      0      0      0      0      0
 3   297.85 302.85 308.00 313.05 318.14 323.15 328.27 333.55 338.75 344.07
 1     1.23   1.23   1.25   1.29   1.36   1.48   1.64   1.86   2.10   2.33
         0      0      0      0      0      0      0      0      0      0
 3   349.52 354.87 360.87 361.77 362.72 363.47 364.22 365.12 365.87 366.62
 1     2.53   2.73   3.02   3.09   3.13   3.17   3.21   3.25   3.28   3.31
         0      0      0      0      0      0      0      0      0      0
 3   367.47 368.22 368.97 369.77 370.52 371.27 372.12 372.87 373.67 374.42
 1     3.35   3.37   3.40   3.43   3.45   3.47   3.48   3.49   3.51   3.51
         0      0      0      0      0      0      0      0      0      0
 3   375.17 378.17 378.92 379.67 380.42 381.17 381.50 381.92 382.72 384.05
 1     3.52   3.52   3.55   3.60   3.65   3.69   3.72   3.76   3.81   4.12
         0      0      0      0      0      0      0      0      0      0
 3   385.45 385.80 388.60 389.35 390.85 391.90 394.99 395.84 396.60 397.35
 1     4.40   4.68   4.68   4.69   4.69   4.68   4.68   4.67   4.67   4.66
         0      0      0      0      0      0      0      0      0      0
 3   398.10 398.84 399.64 410.55 420.95 432.07 442.52 452.82 463.35 473.87
 1     4.66   4.65   4.65   4.60   4.61   4.64   4.68   4.71   4.74   4.77
```

```
        0      0      0      0      0      0      0      0      0      0
 3  484.15 494.55 505.05 515.60 526.15 535.00
 0    4.80   4.82   4.84   4.85   4.86   4.86
        0      0      0      0      0      0
#
 3    0.00 387.00 393.00 400.00 408.00 535.00
 0    1.65   1.65   1.70   1.68   1.70   1.70
        0      0      0      0      0      0
#
 3    0.00 260.00 285.00 320.00 330.00 370.00 387.00 393.00 400.00 408.00
 1    2.00   2.00   1.90   1.90   1.85   1.80   1.65   1.72   1.80   1.85
        0      0      0      0      0      0      0      0      0      0
 3  535.00
 0    1.85
        0
#
#  Layer 4 - First subsurface sediment layer (Ps2,Ps2P)
# ====================================================
 4    0.00   9.38  18.45  45.00 140.00 185.00 200.00 230.00 260.00 280.00
 1   -0.02  -0.02  -0.04   0.00   0.20   0.70   1.25   1.55   1.70   1.71
        0      0      0      0      0      0      0      0      0      0
 4  286.00 305.00 320.00 330.55 338.75 350.00 351.00 352.00 355.00 360.00
 1    1.74   1.72   1.88   2.10   2.50   2.95   2.97   2.99   3.05   3.30
        0      0      0      0      0      0      0      0      0      0
 4  370.00 375.00 379.67 380.42 381.17 381.50 381.92 382.72 384.05 385.45
 1    3.80   3.90   3.64   3.65   3.69   3.72   3.76   3.81   4.12   4.40
        0      0      0      0      0      0      0      0      0      0
 4  385.80 386.65 387.00 393.00 400.00 408.00 428.00 448.00 480.00 535.00
 0    4.68   4.68   4.92   4.92   4.98   5.06   5.17   5.25   5.36   5.38
        0      0      0      0      0      0      0      0      0      0
#
 4    0.00 278.00 283.00 315.00 330.00 340.00 350.00 370.00 382.00 393.00
 1    2.30   2.30   2.18   2.22   2.18   2.10   2.05   2.05   2.00   1.95
        0      0      0      0      0      0      0      0      0      0
 4  402.00 408.00 415.00 420.00 450.00 535.00
 0    2.07   2.10   2.16   2.19   2.19   2.18
        0      0      0      0      0      0
#
 4    0.00 270.00 280.00 320.00 335.00 340.00 350.00 380.00 382.00 393.00
 1    2.40   2.45   2.32   2.30   2.20   2.10   2.15   2.15   2.00   2.01
        0      0      0      0      0      0      0      0      0      0
 4  402.00 408.00 415.00 420.00 450.00 535.00
 0    2.11   2.14   2.20   2.21   2.23   2.46
        0      0      0      0      0      0
#
#  Layer 5 - Second subsurface sediment layer (Ps3, Ps3P)
# ======================================================
 5    0.00   9.38  18.45  45.00 210.00 260.00 310.00 325.00 331.00 337.00
 1   -0.02  -0.02  -0.04   0.00   2.00   2.00   2.03   2.14   2.18   2.90
        0      0      0      0      0      0      0      0      0      0
 5  342.00 350.00 353.00 356.00 359.00 362.00 365.00 368.00 371.00 374.00
 1    3.15   3.30   3.38   3.44   3.62   3.82   3.90   3.90   3.95   4.00
        0      0      0      0      0      0      0      0      0      0
 5  379.50 381.50 381.92 382.72 384.05 385.45 385.80 386.65 387.00 390.00
 1    4.00   3.72   3.76   3.81   4.12   4.40   4.68   4.68   4.92   5.11
        0      0      0      0      0      0      0      0      0      0
 5  400.00 410.00 430.00 438.00 445.00 455.00 460.00 470.00 500.00 535.00
 0    5.37   5.38   5.43   5.50   5.54   5.63   5.61   5.63   5.72   5.80
        0      0      0      0      0      0      0      0      0      0
#
 5    0.00 270.00 325.00 337.00 338.00 348.00 359.00 371.00 381.50 382.00
 1    2.90   2.90   2.93   2.38   2.35   2.25   2.28   2.35   2.40   2.30
        0      0      0      0      0      0      0      0      0      0
 5  400.00 420.00 450.00 535.00
 0    2.33   2.37   2.47   2.46
        0      0      0      0
#
 5    0.00 325.00 337.00 338.00 348.00 350.00 359.00 368.00 377.00 381.50
 1    2.96   2.96   2.41   2.36   2.30   2.35   2.38   2.45   2.45   2.40
        0      0      0      0      0      0      0      0      0      0
 5  382.00 400.00 420.00 450.00 535.00
 0    2.30   2.36   2.40   2.50   2.49
        0      0      0      0      0
```

```
#
#  Layer 6 - Third subsurface sediment layer (Ps4, Ps4P)
# ======================================================
 6    0.00   9.38  18.45  45.00 200.00 230.00 255.00 270.00 275.00 282.00
 1   -0.02  -0.02  -0.04   0.00   3.60   3.80   3.70   3.46   3.35   3.45
        1      1      1      1      1      1      1      1      1      1
 6  292.00 298.00 304.00 308.00 316.00 318.50 325.00 328.00 332.00 337.00
 1    3.40   3.29   3.29   3.23   3.40   3.20   3.00   2.85   2.88   3.08
        1      1      1      1      1      1      1      1      1      1
 6  338.00 346.00 350.00 356.00 359.00 362.00 363.00 370.50 372.00 373.00
 1    3.10   3.40   3.68   4.30   4.15   4.20   4.30   4.40   4.39   4.39
        1      1      1      1      1      1      1      1      1      1
 6  375.00 380.50 381.50 382.00 382.42 382.72 384.05 385.45 385.80 387.00
 1    4.45   4.48   4.40   4.32   4.16   3.81   4.12   4.40   4.68   4.92
        1      1      1      1      1      1      1      1      1      1
 6  390.00 396.00 400.00 410.00 420.00 430.00 440.00 450.00 460.00 470.00
 1    5.14   5.52   5.65   5.74   5.83   5.92   6.03   6.05   6.11   6.18
        1      1      1      1      1      1      1      1      1      1
 6  480.00 535.00
 0    6.20   6.22
        1      1
#
 6    0.00 260.00 320.00 363.00 381.50 387.00 400.00 420.00 460.00 535.00
 0    2.98   2.98   2.97   2.81   2.81   2.32   2.37   2.41   2.53   2.79
        1      1      1      1      1      1      1      1      1      1
#
 6    0.00 260.00 310.00 320.00 363.00 366.00 370.50 372.00 373.00 375.00
 1    3.11   2.97   2.98   2.97   2.81   2.85   2.85   2.83   2.83   2.85
        1      1      1      1      1      1      1      1      1      1
 6  381.50 387.00 390.00 402.50 410.00 422.00 425.00 428.00 435.00 437.50
 1    2.81   2.33   2.48   2.49   2.50   2.58   2.57   2.59   2.76   2.74
        1      1      1      1      1      1      1      1      1      1
 6  440.00 442.50 446.00 447.50 450.00 452.50 455.00 457.50 462.50 465.00
 1    2.76   2.84   2.87   2.90   2.93   2.96   2.99   3.02   3.05   3.05
        1      1      1      1      1      1      1      1      1      1
 6  467.50 470.00 485.00 487.50 490.00 535.00
 0    3.08   3.02   3.02   3.01   3.00   3.00
        1      1      1      1      1      1
#
#  Layer 7 - Fourth subsurface sediment layer (Ps5, Ps5P)
# ======================================================
 7    0.00   9.38  18.45  45.00 200.00 230.00 255.00 270.00 275.00 282.00
 1   -0.02  -0.02  -0.04   0.00   3.60   3.80   3.70   3.46   3.35   3.48
        1      1      1      1      1      1      1      1      1      1
 7  292.00 298.00 300.00 304.00 308.00 316.00 318.50 325.00 328.00 332.00
 1    3.40   3.29   3.29   3.29   3.23   3.40   3.20   3.00   2.85   2.88
        1      1      1      1      1      1      1      1      1      1
 7  337.00 338.00 346.00 350.00 356.00 359.00 362.00 363.00 365.50 371.00
 1    3.08   3.10   3.40   3.68   4.30   4.15   4.20   4.30   5.48   5.58
        1      1      1      1      1      1      1      1      1      1
 7  373.00 373.50 376.00 380.50 381.00 381.50 382.00 382.42 382.72 384.05
 1    4.69   4.69   5.75   5.45   4.58   4.40   4.32   4.16   3.81   4.12
        1      1      1      1      1      1      1      1      1      1
 7  385.45 385.80 387.00 387.70 389.76 395.50 402.00 407.00 410.00 420.00
 1    4.40   4.68   4.92   5.89   6.63   6.90   7.10   6.70   6.95   7.20
        1      1      1      1      1      1      1      1      1      1
 7  426.00 430.00 433.00 437.50 439.00 441.50 443.00 446.00 447.50 450.00
 1    6.60   6.45   7.55   7.15   6.95   7.35   7.85   7.80   7.80   7.86
        1      1      1      1      1      1      1      1      1      1
 7  452.50 455.00 457.50 462.50 465.00 467.50 469.00 469.50 470.00 472.50
 1    7.96   7.98   7.80   7.70   7.82   7.95   7.75   7.72   7.72   7.68
        1      1      1      1      1      1      1      1      1      1
 7  475.00 477.50 482.50 485.00 487.50 490.00 492.50 495.00 497.50 500.00
 1    7.68   7.65   7.65   7.62   7.62   7.60   7.65   7.70   7.80   8.00
        1      1      1      1      1      1      1      1      1      1
 7  505.00 513.00 517.00 525.00 535.00
 0    7.85   7.77   8.00   8.00   7.60
        1      1      1      1      1
#
 7    0.00 270.00 318.50 332.00 350.00 362.00 363.00 371.00 441.50 457.50
 1    3.04   3.25   3.20   3.80   3.40   3.40   3.00   3.00   3.50   3.50
        1      1      1      1      1      1      1      1      1      1
 7  469.50 490.00 535.00
```

```
 0    3.63   3.60   3.70
         1      1      1
#
 7    0.00 270.00 275.00 295.00 300.00 310.00 318.50 332.00 359.00 362.00
 1    3.01   3.24   3.40   3.45   3.40   3.30   3.20   3.80   3.75   3.40
         1      1      1      1      1      1      1      1      1      1
 7  363.00 366.00 370.50 371.00 441.50 446.00 447.50 450.00 452.50 455.00
 1    3.00   3.06   3.06   3.00   3.50   3.65   3.65   3.62   3.60   3.55
         1      1      1      1      1      1      1      1      1      1
 7  457.50 462.50 467.50 468.00 469.50 475.00 477.50 480.00 482.50 485.00
 1    3.50   3.78   3.78   3.80   3.63   3.64   3.65   3.68   3.70   3.75
         1      1      1      1      1      1      1      1      1      1
 7  487.50 490.00 535.00
 0    3.70   3.60   3.80
         1      1      1
#
#  Layer 8 - Basement (Pg1, Pg1P)
# ================================
 8    0.00   9.38  18.45  45.00 200.00 230.00 255.00 270.00 275.00 280.00
 1   -0.02  -0.02  -0.04   0.00   3.60   3.80   3.70   3.46   4.18   4.35
         1      1      1      1      1      1      1      1      1      1
 8  285.00 290.00 298.00 305.00 310.00 317.00 317.50 318.25 318.50 325.00
 1    4.20   4.20   4.60   4.15   3.80   4.05   3.60   3.60   3.20   3.00
         1      1      1      1      1      1      1      1      1      1
 8  328.00 332.00 334.00 336.50 338.00 346.00 350.00 352.00 360.00 362.00
 1    2.85   2.88   3.23   3.64   4.45   4.50   5.28   5.55   5.65   4.20
         1      1      1      1      1      1      1      1      1      1
 8  363.00 365.50 371.00 373.00 373.50 376.00 380.50 381.00 381.50 381.70
 1    4.30   5.48   5.58   4.69   4.69   5.75   5.45   4.58   4.40   4.32
         1      1      1      1      1      1      1      1      1      1
 8  382.02 382.72 384.05 385.05 385.80 387.00 387.70 389.76 395.50 402.00
 1    4.16   3.82   4.12   4.40   4.68   4.92   5.89   6.63   6.90   7.10
         1      1      1      1      1      1      1      1      1      1
 8  407.00 410.00 420.00 426.00 430.00 433.00 437.50 439.00 441.50 443.00
 1    6.70   6.95   7.20   6.60   6.45   7.55   7.15   6.95   7.35   7.85
         1      1      1      1      1      1      1      1      1      1
 8  446.00 447.50 450.00 453.50 455.00 457.50 462.50 465.00 467.50 469.00
 1    8.86   8.70   8.64   8.55   8.25   7.80   7.70   7.82   7.95   7.75
         1      1      1      1      1      1      1      1      1      1
 8  469.50 475.00 477.50 480.00 482.50 485.00 487.50 490.00 492.50 495.00
 1    7.72   7.85   8.55   8.00   7.95   7.90   8.07   7.60   7.65   7.70
         1      1      1      1      1      1      1      1      1      1
 8  497.50 500.00 505.00 513.00 517.00 525.00 535.00
 0    7.80   8.00   7.85   7.77   8.00   8.00   7.60
         1      1      1      1      1      1      1
#
 8    0.00 150.00 285.00 305.00 318.50 330.00 356.00 359.00 363.00 368.00
 1    4.40   4.20   4.20   4.40   4.50   4.60   4.50   4.30   3.70   4.40
         1      1      1      1      1      1      1      1      1      1
 8  372.75 378.00 378.50 382.72 388.76 408.00 420.00 428.00 438.00 450.00
 1    4.50   4.70   4.70   4.50   4.90   4.70   4.50   4.30   4.50   4.40
         1      1      1      1      1      1      1      1      1      1
 8  473.50 535.00
 0    4.50   4.50
         1      1
#
 8    0.00 175.00 250.00 280.00 295.00 310.00 330.00 340.00 378.50 395.00
 1    5.70   5.70   5.60   5.60   6.10   6.20   6.25   6.15   5.80   5.80
         1      1      1      1      1      1      1      1      1      1
 8  400.00 420.00 535.00
 0    5.40   5.50   5.50
         1      1      1
#
#  Layer  9 - Inter-crustal boundary (Pg2, PmP)
# ============================================
 9    0.00 150.00 230.00 285.00 295.00 302.00 310.00 320.00 328.00 335.00
 1    4.90   7.10   8.90   8.85   8.80   8.75   8.70   8.68   8.66   8.64
         0      0      0      0      0      0      0      0      0      0
 9  340.00 350.00 360.00 382.00 392.00 400.00 405.00 420.00 433.00 440.00
 1    8.65   8.65   8.80   8.80   8.40   7.95   7.98   7.80   7.70   7.80
         0      0      0      0      0      0      0      0      0      0
 9  445.00 450.00 462.50 466.50 470.00 476.00 490.00 535.00
 0    9.70   9.70   8.57   8.47   9.00   9.00   8.40   8.80
```

```
         0       0       0       0       0       0       0       0
#
 9     0.00 330.00 380.00 405.00 420.00 442.00 444.00 450.00 460.00 535.00
 0     6.40   6.40   6.20   6.40   6.50   6.40   6.50   6.50   6.60   6.60
         0       0       0       0       0       0       0       0       0       0
#
 9     0.00 175.00 220.00 300.00 340.00 357.00 380.00 390.00 400.00 420.00
 1     6.90   6.90   6.80   6.90   6.80   6.75   6.90   6.90   7.00   7.40
         0       0       0       0       0       0       0       0       0       0
 9   425.00 440.00 450.00 535.00
 0     7.40   7.20   7.10   7.10
         0       0       0       0
#
#  Layer 10 - Moho (Pn)
# ======================
10     0.00  70.00 100.00 180.00 190.00 235.00 250.00 270.00 300.00 310.00
 1    37.00  35.00  32.00  27.50  27.00  25.50  25.50  25.25  25.00  24.25
         0       0       0       0       0       0       0       0       0       0
10   320.00 340.00 355.00 370.50 380.00 381.00 390.00 400.00 410.00 425.00
 1    24.20  23.00  22.20  19.30  16.40  15.45  14.00  13.55  13.00  12.20
         0       0       0       0       0       0       0       0       0       0
10   440.00 460.00 475.00 480.00 535.00
 0    12.20  11.75  11.65  11.50  11.20
         0       0       0       0       0
#
10     0.00 535.00
 0     7.90   7.90
         0       0
#
10     0.00 400.00 535.00
 0     8.30   8.41   8.40
         0       0       0
#
#  Layer 11 - Base of model
# ==========================
11     0.00 535.00
 0    80.00  80.00
```